SEISMIC SHEAR STRENGTH OF CIRCULAR BRIDGE PIERS

A thesis

submitted in partial fulfilment

of the requirements for the Degree

of

Doctor of Philosophy in Civil Engineering

at the

University of Canterbury

by

ANG Beng Ghee

University of Canterbury,

Christchurch, New Zealand

1985

ABSTRACT

The project was carried out with the intention to study the shear strength of circular reinforced concrete bridge piers under seismic loading. Two series of tests were conducted. Initially, twenty-five column units were tested by subjecting them to static incremental reversed cyclic loading, to investigate the influence of some main parameters. The columns were loaded into the inelastic range to controlled displacement ductility levels. The second stage of experimental work involved dynamic testing of bridge piers, which were half scale models of the static test units on a shake-table. Altogether eight single pier models and two twin-pier models were tested. The single pier models were subjected to sinusoidal excitation while the twin-pier models were tested using scaled earthquake accelerograms.

The performance of the test units was gauged mainly in terms of shear strength and displacement ductility capacity. Four failure modes were identified according to the displacement ductility level at which significant degradation occurred. The static test results indicated that existing code provisions for shear strength were conservative and suggested that the level of shear strength and the displacement ductility might be related.

The behaviour of single pier models in the dynamic tests was compatible with that of the static test units. The behaviour of the twin-pier models was less predictable, especially when axial tension was acting. The dynamic magnification effect on material strength due to higher strain rate was not significant in the tests.

A design method was proposed as an outcome of the static tests. The proposal allows the shear strength and the displacement ductility capacity to be determined, and has been incorporated into an integral flexure/shear design approach in which the provision of transverse reinforcement is considered for confinement as well as shear resistance.

Some theoretical study was also conducted using 'Diagonal Compression Field Theory'. The theory was adapted using a stress-strain relationship developed for confined concrete. The agreement between the predicted and the experimental behaviour in terms of load-displacement response was reasonable.

ACKNOWLEDGEMENTS

The research reported herein was carried out in the Department of Civil Engineering, University of Canterbury, under the overall guidance of its head, Professor R. Park.

The project was supervised by Dr. M.J.N. Priestley and Professor T. Paulay, whose advice and guidance is gratefully acknowledged.

Special thanks are also due to Professor M.P. Collins, University of Toronto, for his helpful suggestions and comments during his visit to the Department in 1983.

I wish to take this opportunity to express my appreciation for the assistance given by the technical staff of the Department, headed by the Senior Technical Officer, Mr. N.W. Prebble. In particular, my special acknowledgements are given to Mr. G.E. Hill, Mr. G.H. Clarke, Mr. P. Coursey, Mr. J. Ritchie (resigned), Mr. R. Allen and Mr. P.G. Mitchell for their invaluable contribution in terms of technical advice and expertise in the experimental work.

I am also very grateful for the generous financial contribution provided by the Road Research Unit of the N.Z. National Roads Board.

I also wish to register my gratitude to Mrs. D.E. Ball for typing the manuscript, Mrs. V.J. Grey for her draughting work and Mr. L.H. Gardner for his photographic work.

Last but not least, my special thanks to my wife, Jenny, and my family, for their endless support, understanding and encouragement throughout the years.

TABLE OF CONTENTS

PAGE

LIST OF FIGURES

LIST OF TABLES

NOTATION

Unless stated otherwise in the text, definitions of the notations used in the thesis are as follows:

A_{cc} = core concrete area

A_e = $0.8A_g$, effective shear stress area

A_g = gross concrete area

A_ℓ = concrete element area normal to the longitudinal direction

A_t = concrete element area normal to the transverse direction

$A_{s\ell}$ = total area of reinforcement in the longitudinal direction

A_{sp} = area of spiral bar

A_{st} = total area of reinforcement in the transverse direction

ΔA_c = area of a concrete element

ΔA_s = area of a steel element

a = shear span

= response acceleration

b_r = width of a concrete element

b_w = web width

C = compression in the bottom chord member of an analogous truss

C_d = diagonal compressive force in web concrete

$C_{H\mu}$ = horizontal base shear coefficient for design ductility factor μ

C_1, C_2 = resultant concrete force at sections 1 and 2 respectively

D = overall diameter of a circular column

= dynamic magnification factor

D' = pitch circle diameter of longitudinal reinforcement in a circular column

d = effective depth of a section

d_b = spiral bar diameter

$d_{b\ell}$ = longitudinal bar diameter

d_s = diameter of spiral

E = energy dissipated during a load cycle measured from load-deflection hysteresis loops

E_c = modulus of elasticity of concrete

E_i = energy dissipation computed for an idealized system

$E_{s\ell}$ = Young's modulus of longitudinal reinforcement

E_{st} = Young's modulus of transverse reinforcement

F_{c2} = peak strength of biaxially stressed concrete at fixed ε_1 value

F_y = stirrup force at yielding

F_{r-1}, F_r = resultant force in (r-1)th and rth concrete layers respectively

ΔF = additional tensile force in longitudinal reinforcement due to diagonal compression

f_c = concrete stress computed from stress-strain relationship

f'_c = compressive (cylinder) strength of concrete

f'_{cc} = peak strength of confined concrete

f'_{co} = peak strength of unconfined concrete

f_{cr} = diagonal cracking strength of biaxially stressed concrete

f'_{cu} = compressive (cube) strength of concrete

f_{c1} = principal tensile stress in a concrete element

f_{c2} = principal compressive stress in a concrete element

f = total longitudinal stress

f'_ℓ = lateral confining stress

$f_{\ell c}$ = longitudinal stress in a concrete element

$f_{\ell s}$ = stress in a longitudinal steel element

$f_{\ell s,cr}$ = stress in a longitudinal steel element at crack

f'_p = peak strength of biaxially stressed concrete

f_t = total transverse stress

f_{tc} = transverse stress in a concrete element

f_{ts} = stress in a transverse steel element

$f_{ts,cr}$ = stress in a transverse steel element at crack

f_{st} = stirrup stress

f_{yh} = yield strength of hoop steel

$f_{y\ell}$ = yield strength of longitudinal reinforcement

f_{yt} = yield strength of transverse reinforcement

f_1, f_2 = principal stresses

G = gradient of a diagonal crack

g = 9.81 m/s^2, acceleration due to gravity

h = overall thickness of a member

I_{cr} = moment of inertia of a cracked section

jd = moment arm of a section

k = effectiveness coefficient for 45-deg analagous truss

k_e = confinement effectiveness coefficient

k_p = coefficient for different tensile reinforcement ratio (AIJ Standard)

k_u = coefficient for size effect (AIJ standard)

= ratio of neutral axis depth to overall depth at ultimate

k_y = ratio of neutral axis depth to overall depth at first yielding

L = length of a cantilever column from the centre of mass to the critical section

L_c = clear height of a cantilever column

L_p = equivalent plastic hinge length

ℓ = loading height of a cantilever column

M = bending moment

M_b = maximum bending moment at the base of a cantilever column

M_i = ideal moment capacity calculated using an ultimate concrete strain of 0.003 and measured material properties

M_{ib} = ideal moment capacity at the base of a cantilever column

M_{it} = ideal moment capacity at the top of a cantilever column

M_m = modified moment (ACI 318-83)

M_o = decompression moment (CEB-FIP Model Code)

M_p = plastic moment

$M_{p,o}$ = plastic moment for pure flexure

M_t = maximum bending moment at the top of a cantilever column

M_u = ultimate bending moment

$M_{u,ACI}$ = ultimate moment capacity calculated using ACI method

$M_{u,d}$ = dependable moment capacity

M_y = moment at first yield

M_1, M_2 = bending moment at sections 1 and 2 respectively

m = flexural strength enhancement factor

N = axial force due to diagonal compression

P = axial force

P_e = compression load on column due to gravity and seismic loading

P_i = ideal axial load computed using measured material strengths

P_u = axial load acting simultaneously with V_u

P_r = axial tensile resistance of member ignoring any contribution of concrete

R = ratio of strain increase to stress increase at peak strength of confined concrete

r = algebraic ratio (negative) between the maximum and minimum value of shear force at a critical section (NZS 3101:1982)

= $\frac{E_c}{(E_c - E_{sec})}$ in Popovic's equation

r_s = radius of spiral

s = spacing of transverse reinforcement

s' = effective width of a diagonal strut

= clear spacing spiral

T = tension in the top chord member of an analogous truss

T_y = tensile force at yielding of flexural reinforcement

T_1, T_2 = resultant steel force at sections 1 and 2 respectively

UTS = ultimate tensile strength of reinforcing steel

V = shear force or lateral load on a cantilever column

V^L = shear strength computed using the lower bound approach of plastic theory

V^U = shear strength computed using the upper bound approach of plastic theory

V_{Accel} = lateral load computed from response acceleration

V_{ACI} = shear strength specified by ACI 318-83 Building Code

V_{AIJ} = shear strength specified by AIJ Standard

V_{Base} = horizontal base reaction measured by load cell

V_c = shear force carried by concrete shear resisting mechanisms

V_{CAN} = shear strength specified by the Canadian Code

V_{CAN}^r = shear strength specified by the refined method of the Canadian Code

V_{CEB} = shear strength specified by the CEB-FIP Model Code

V_{CEB}^r = shear strength specified by the refined method of the CEB-FIP Model Code

V_{cf} = residual shear strength due to the concrete shear resisting mechanisms

V_{ci} = initial shear strength due to the concrete shear resisting mechanisms

V_{cr} = shear force at diagonal cracking

V_{cr}^o = shear force at diagonal cracking from experimental observations

V_{cr}^ε = shear force at diagonal cracking from measured spiral strains

V_d = shear force corresponding to diagonal crushing

V_E = corrected shear force at east column of a twin-pier unit during the dynamic tests

V_e = shear force corresponding to the maximum elastic displacement during the dynamic tests

V_{east} = horizontal base reaction measured by load cell at east column of a twin-pier unit during the dynamic tests

V_f = residual shear strength applicable at high displacement ductility levels

V_{fr} = measured shear force at first fracture of spiral

V_i = initial shear strength applicable at low displacement ductility levels

V_{if} = shear force corresponding to the development of ideal flexural strength

V^{o}_{if} = shear force corresponding to the development of enhanced flexural strength

V_{iv} = ideal shear strength computed from non-seismic provisions of NZS 3101:1982

V^{s}_{iv} = ideal shear strength computed from seismic provisions of NZS 3101:1982

V_{L} = lateral load on a cantilever column in longitudinal response

V^{o}_{L} = shear force due to enhanced flexural strength in longitudinal response

V_{NZS} = shear strength specified by the NZS 3101:1982 concrete design code

V_{p} = plastic shear force

$V_{p,o}$ = plastic shear force for pure shear

V_{s} = shear force carried by transverse reinforcement

V_{se} = shear force due to service load

V_{sf} = residual shear strength due to transverse reinforcement

V_{si} = initial shear strength due to transverse reinforcement

V_{T} = lateral load on a cantilever column in transverse response

V^{o}_{T} = shear force due to enhanced flexural strength in transverse response

V_{u} = shear force at ultimate

V_{w} = corrected shear force at west column of a twin-pier unit during the dynamic tests

V_{west} = horizontal base reaction measured by load cell at west column of a twin-pier unit during the dynamic tests

$V_{(\mu=4)}$ = shear force measured at $\mu=4$

$V_{(\mu=6)}$ = shear force measured at $\mu=6$

v = shear stress

v_{b} = basic shear stress

v_{c} = shear stress carried by concrete shear resisting mechanisms

v'_{c} = shear stress carried by the concrete element

v_{cf} = residual shear stress carried by concrete shear resisting mechanisms

v_{cr} = shear stress at diagonal cracking

v_i = initial shear stress applicable at low displacement ductility levels

v_{iv} = ideal shear stress

v_r = shear stress acting on rth element

v_s = equivalent shear stress carried by transverse reinforcement

v'_s = shear stress carried by steel element

v_u = ultimate shear stress

W = weight of inertia mass

x = $\frac{\varepsilon}{\varepsilon_{cc}}$ in Popovic's equation

Δx = distance between sections 1 and 2

y_c = centroid of concrete element from extreme compression fibre

y_s = centroid of steel element from extreme compression fibre

Z_H = coefficient related to the return period of an earthquake

α = $\frac{\rho_{s(provided)}}{\rho_{s\ (code)}}$, confinement ratio

α_l = factor to allow for the effect of low aspect ratio

β = angle of inclination of stirrups with respect to the column axis

= ratio of excitation frequency to natural frequency

β_l = factor to allow for the effect of axial compression (CEB-FIP Model Code)

Δ = lateral displacement of a column

Δ_B = displacement component due to bending of foundation beam

Δ_J = displacement component due to joint distortion

Δ_p = column displacement due to plastic hinge rotation

Δ_T = $(\Delta_\phi + \Delta_\gamma + \Delta_B + \Delta_J)$, total computed displacement considering all the displacement components

Δ_{table} = measured shake-table displacement

Δ_u = $(\Delta_y + \Delta_p)$, column displacement at ultimate

Δ_ϕ = displacement component due to curvature

Δ_γ = displacement component due to shear strain

ε_c = concrete strain

ε_{cc} = strain at maximum confined concrete stress f'_{cc}

ε_{co} = strain at maximum stress f'_{co} of unconfined concrete

ε_{cr} = concrete strain at diagonal cracking

ε_ℓ = longitudinal strain

ε_o = strain at concrete cylinder strength f'_c

ε_p = strain at peak strength f'_p of biaxially stressed concrete

ε_R = ratio of mean crack width divided by mean crack spacing

ε_t = transverse strain

$\varepsilon_{y\ell}$ = yield strain of longitudinal reinforcement

ε_{yt} = yield strain of transverse reinforcement

ε_1 = principal tensile strain

ε_2 = principal compressive strain

$\gamma_{\ell t}, \gamma$ = shear strain

γ_m = maximum shear strain

ρ_{cc} = volumetric ratio of the longitudinal reinforcement in the confined core

ρ_ℓ = total longitudinal reinforcement ratio

$\rho_{s\ell}$ = longitudinal reinforcement ratio

ρ_{st} = transverse reinforcement ratio

ρ_t = transverse reinforcement ratio

ρ_w = tensile reinforcement ratio

θ = angle of inclination of diagonal strut in an analogous truss

θ_p = rotation of plastic hinge

λ = $\frac{L_p}{D}$, equivalent plastic hinge length as a fraction of the overall depth of a member

λ_L = geometrical scaling factor

λ_f = stress scaling factor

λ_ρ = density scaling factor

ξ = damping ratio

ν, ν_1 = web effectiveness factor

μ = displacement ductility factor

μ_c = displacement ductility capacity

μ_f = displacement ductility for a ductile member

μ_s = actual structure ductility factor after allowing for flexibility of foundation and bearing

τ_{Rd} = concrete shear stress specified in the CEB-FIP Model Code

τ_g = shear stress due to aggregate interlock action

σ_g = normal stress associated with aggregate interlock action

ψ = $\frac{\rho_t f_{yt}}{f'_c}$, mechanical degree of shear reinforcement

η = $\frac{V_s}{V_u}$, shear coverage ratio

ϕ = strength reduction factor

ϕ_o = overstrength factor

ϕ_u = curvature at ultimate

ϕ_y = curvature at first yield

Chapter One

INTRODUCTION

1.1 GENERAL

Reinforced concrete bridge piers under seismic attack will commonly be subjected to the combined effects of axial load, flexure and shear, and possibly torsion. Since shear failures are non-ductile, the modern earthquake-resistant design methods based on ultimate loading conditions emphasize the need to suppress such failures. However, given the nature of non-linear properties of the composite material together with geometric discontinuities due to cracking, it is obvious that a rigorous analytical approach to optimum design to avoid shear failures is a task of extreme complexity. At present, a measure of conservatism is adopted by over-designing for shear using capacity design principles[1.1-1.2], in order to ensure that a ductile flexural hinging mechanism can always occur. Such an approach may result in uneconomic use of materials in some parts of a structure. On the other hand, the uncertainty in the nature of earthquake attacks makes it difficult to avoid the problem completely. The random nature of the loadings gives rise to a problem which is different from that of monotonic shear. Furthermore, flexural strength may be enhanced above the design strength to the extent that it becomes difficult, if not impossible, to avoid shear failure.

Column shear failures in some recent earthquakes, especially in the Tokachi-Oki Earthquake[1.3], has prompted the investigation of the problem of shear under seismic conditions. The traditional practice of using short columns in buildings in Japan resulted in violent explosive failure in these columns during the earthquake on May 16, 1968. The period of this earthquake was found to be very similar to that of the damaged buildings and the duration of strong ground shaking was long. Consequently, the buildings were subjected to long duration of lateral load equivalent to several times the design force. The inadequate provisions of transverse reinforcement for shear and confinement together with the stiffening effect of secondary elements inevitably forced a shear failure in the columns as shown, for example, in Fig. 1.1.

Over the years of earthquake history there have been many instances of shear failure of columns, including circular columns. The column failure in the Macuto-Sheraton Building during the July 29, 1967 Caracas Earthquake in Venezuela[1.4] is an example involving circular columns (Fig.

1.2). As far as bridge structures are concerned, the February 9, 1971 San Fernando Earthquake in California[1.5] resulted in shear failure in several bridge piers and columns. It appeared that there were two types of failure; one which was similar to a column failure under axial load involving an inclined failure plane, and another with complete destruction of column core. Fig. 1.3 shows some typical examples of column failure during the San Fernando Earthquake.

At present many existing bridges may have inadequate shear strength and detailing to avoid shear failure under strong earthquake attack especially if they were designed before the introduction of modern earthquake-resistant design approaches. These bridges need retrofitting if they are to survive design level earthquakes. The cost of such undertakings depends much on how realistic the assessment of the relative strengths of the bridge is. Unfortunately, the shear provisions of most of the contemporary design codes were derived from monotonic test results and as such, these codes tend to be very cautious and unduly conservative in approaching similar problems under seismic conditions. Hence, any retrofitting program applying these code requirements may face difficulties in satisfying these criteria without incurring substantial expenditure. Nevertheless, the vulnerability of these columns when subjected to earthquake actions is a serious issue and therefore it deserves some attention.

1.2 DESIGN OF BRIDGE STRUCTURES FOR EARTHQUAKE RESISTANCE

1.2.1 Current Design Philosophy And Design Methods

Bridges are important lifeline structures which should remain functional after exposure to the design earthquake. As it is uneconomical to design bridges to withstand the strongest possible earthquake, the common approach is to design so that they can resist small to moderate earthquakes without damage and resist strong earthquakes without collapse but with some structural and non-structural damage. The damage should preferably be visible and accessible for inspection and repair so that at least some temporary measure can be taken to ensure a bridge is usable for light traffic soon after the design earthquake has occurred[1.1-1.2].

There are basically two approaches in modern earthquake-resistant design of bridges. The first method is to design the structure so that it can deform in a ductile manner via some plastic mechanism in parts of the structure. In general, the design of the bridge superstructure is governed by dead load and other imposed load like live load, vehicle

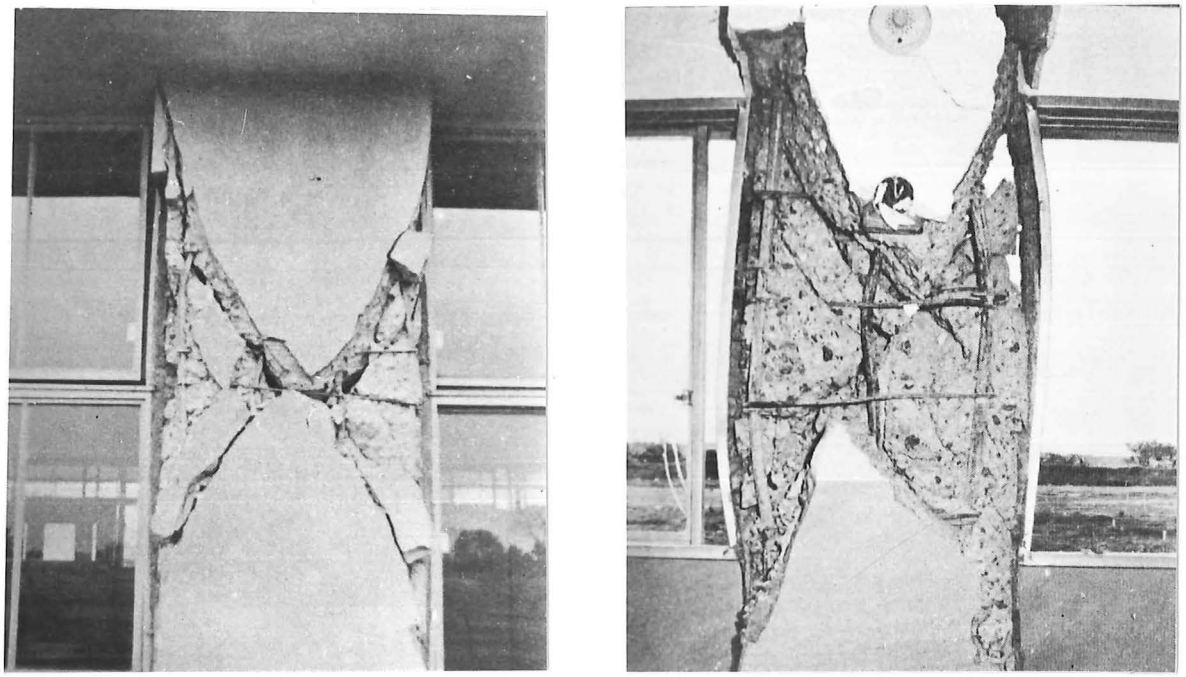

(a) (b)

Fig. 1.1 : Heavily damaged short columns - 1968 Tokachi Oki Earthquake[1.3]

Fig. 1.2 : Column shear failure in 1967 Caracas Earthquake[1.4]

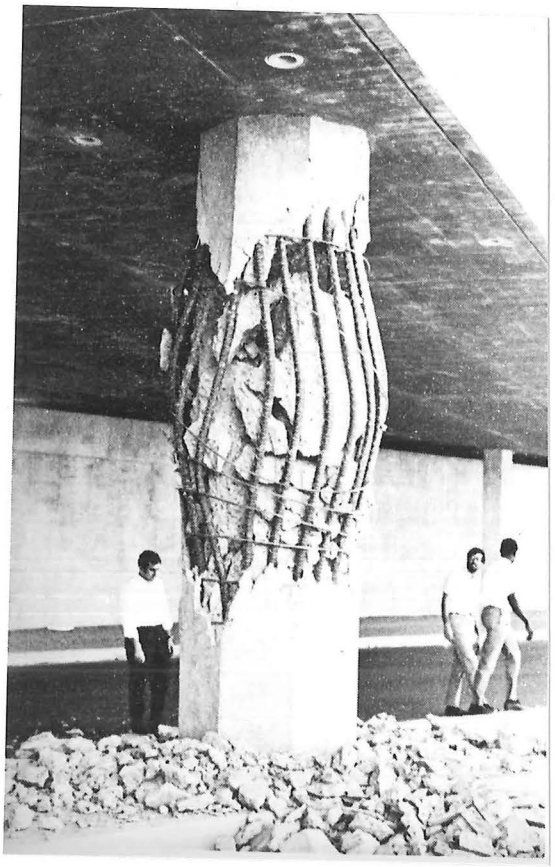

(a)

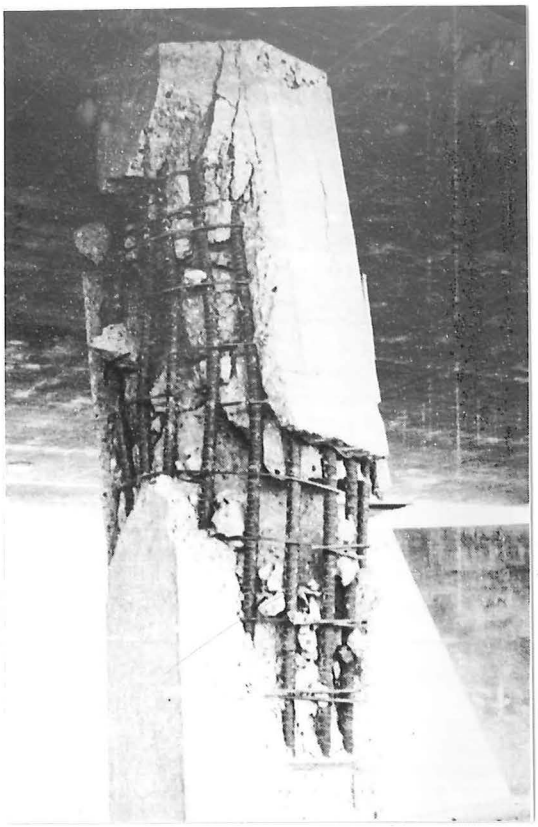

(b)

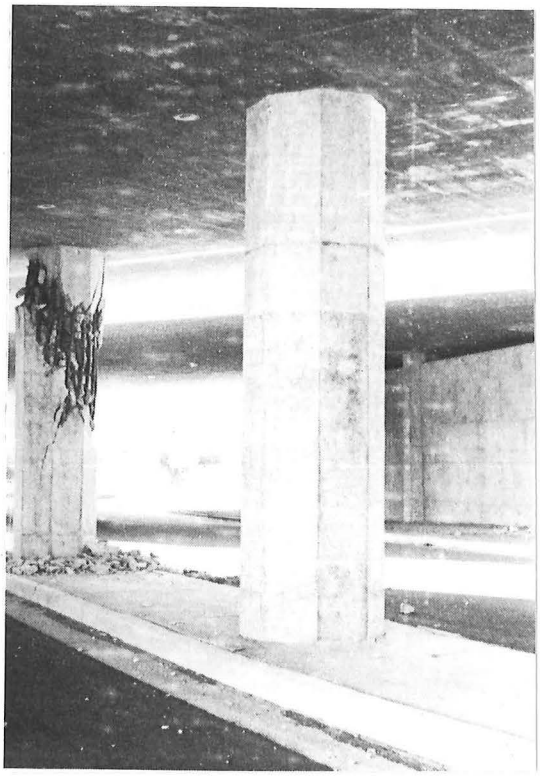

(c)

(d)

Fig. 1.3 : Bridge pier damage during 1971 San Fernando Earthquake[1.5]

impact, temperature, creep and shrinkage. Therefore, it is both impractical and undesirable to design for plastic hinges to form in the superstructure members during an earthquake attack. Also, plastic hinging in foundation structures should be avoided as far as possible in order to reduce the likelihood of damage in less accessible parts of the structure. Hence, it is usually the bridge piers that are designed to yield under strong earthquake attack. Deformation of bridge piers into the inelastic range limits the seismic load input to the structure and therefore allows the piers to be designed for loadings less severe than that due to an elastic response. The piers are able to achieve the necessary energy dissipation through the plastic hinges but a good performance can only be guaranteed if these hinges are properly designed not only for strength but also ductility. The current New Zealand design philosophy is based on a capacity design approach[1.1-1.2] which is outlined in the next section.

An alternative to the first method is to introduce devices which isolate the superstructure from the critical effects of the earthquake and if necessary can also aid energy dissipation[1.6-1.7]. The incorporation of such devices increases the damping in the structure as well as its natural period of vibration because it increases structural flexibility. These two effects generally reduce the elastic acceleration response of the structure to earthquake excitation. Consequently, the strength and ductility demand on the piers will be smaller. However, it should be noted that the method is not very useful if the period is too small because the resulting increase in flexibility brings the structure into a more critical frequency domain.

1.2.2 Capacity Design Approach

The capacity design of bridges follows the hierarchial procedure as outlined by Chapman[1.1-1.2]. Basically, the structural form is decided and the locations of plastic hinges are chosen before analyses are carried out to determine the design loads. The plastic hinges are then designed to have minimum dependable flexural strengths to match these loading requirements. Once this is done, the plastic hinges may be designed for shear and all sections other than the plastic hinges are designed for flexure and shear. The structure is analysed assuming all the plastic hinges to have developed their flexural overstrength. The corresponding shear forces and moments may then be obtained. The shear design of the plastic hinges and the design of all other sections for flexure and shear are based on this resulting distribution of forces. Consequently, the

design shear forces for the bridge piers are not the horizontal base shears as specified by the code but rather they are derived from the maximum flexural strength that is likely to be developed in the plastic hinges. For convenience, the overstrength is computed with the introduction of an overstrength factor. This factor accounts for the increase in strength mainly due to concrete and steel strengths higher than the specified values and the strain-hardening effect of the steel at large deformation. It will be assumed that critical sections are provided with the exact reinforcement content to satisfy the code moments. In this case the flexural overstrength factor, ϕ_o, is taken as 1.25 and 1.40 for grade 275 and grade 380 longitudinal reinforcement respectively.

Under normal conditions, by far the largest part of the weight of a bridge is concentrated in the bridge superstructure and the inertia forces arising from earthquake ground shaking are due predominantly to this superstructure mass. Fig. 1.4 shows a typical bridge structure with piers and the associated bending moment patterns in both transverse and longitudinal directions. As explained by Priestley and Park[1.9], the moment at the base of the pier is governed by the transverse response and that at the top by the longitudinal response. From the figure,

$$M_b = V_T L \tag{1.1a}$$

$$M_t = V_L \frac{L_c}{2} \tag{1.1b}$$

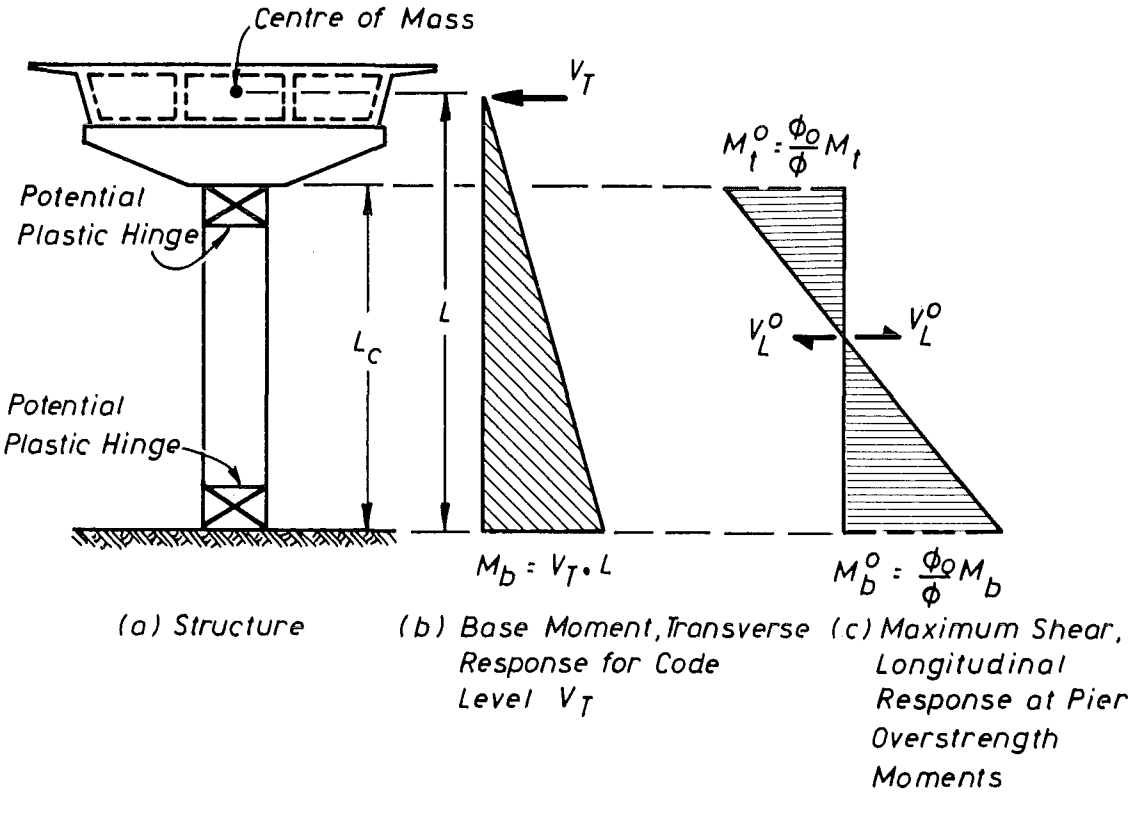

Fig. 1.4 : Capacity design procedure for maximum shear force in a single stem bridge pier

The flexural design ensures that the dependable strength is no less than these moments, i.e.

$$\phi M_{ib} \geq M_b \tag{1.2a}$$

$$\phi M_{it} \geq M_t \tag{1.2b}$$

where M_{ib} and M_{it} are the ideal flexural strengths at the bottom and the top of the pier respectively, and ϕ is the capacity reduction factor.

Then, following the capacity design procedure, the design shear force is computed by considering overstrength developing in these potential plastic hinges. In the transverse direction, plastic hinging can only occur at the pier base and therefore,

$$V_T^o = \frac{\phi_o}{\phi} \frac{M_b}{L}$$

$$= \frac{\phi_o}{\phi} V_T \tag{1.3}$$

Typically $\frac{\phi_o}{\phi}$ is not less than 1.39 for sections with grade 275 reinforcement and 1.55 for grade 380 reinforcement if ϕ is taken as 0.9. In the longitudinal direction, the design shear force results from hinges forming at both the top and bottom of the pier and is given by

$$V_L^o = \frac{\phi_o M_{ib} + \phi_o M_{it}}{L_c}$$

$$= \frac{\phi_o}{\phi} \frac{(M_b + M_t)}{L_c}$$

$$= \frac{\phi_o}{\phi} \left(\frac{L}{L_c} V_T + \frac{1}{2} V_L \right) \tag{1.4}$$

Where more reinforcement is provided than necessary to satisfy M_L and M_t, higher overstrength will results. Typically V_L^o is more than twice V_L[1.9]. If this increase is unaccounted for, a brittle shear failure may occur.

The present practice of using the ACI method to calculate flexural strengths has been found to be conservative and the introduction of ϕ_o to account for overstrength may not be adequate in some instances. Consequently, the design shear forces based on these values may be underestimated. Nevertheless, it should also be noted that the design shear force need not be taken to exceed that of the elastic response spectra.

The above discussion illustrates the severity of the problem because of the high design shear force that may arise. The design for shear, therefore, has to be realistic in order to achieve a satisfactory overall design.

1.3 AIMS AND SCOPE OF THE PROJECT

Extensive study of the flexural behaviour of reinforced concrete members has rendered a comprehensive understanding of requirements for ductile flexural actions. Modern earthquake-resistant design methods are able to enforce a ductile flexural response through proper detailing of the structural members. Provisions for ductility are now incorporated in design codes such as NZS 3101:1982[1.8]. No similar conclusions can be drawn, however, in the case of shear acting in conjunction with other forces.

The behaviour of reinforced concrete members under shear has been extensively studied. However, relatively little research has been done to investigate the performance of spirally reinforced circular columns under the influence of shear combined with other forces. At the commencement of this project, data regarding the effects of repeated reversed cyclic loadings on such columns was not available. The primary aim of this research is therefore to study specifically this aspect in order to achieve a better understanding of the shear performance of spirally reinforced circular bridge piers under seismic loading.

Shear failure mechanisms of columns in seismic conditions usually include the yielding of transverse reinforcement, spalling of concrete cover, loss of bond, and core collapse as a result of repeated abrasion of concrete along wide inclined cracks which are the characteristic features of shear failures.

In the event of an earthquake attack, load reversals will occur and structure members may be subjected to several cycles of inelastic loadings. Consequently, two sets of inclined cracks crossing each other will form a lattice crack pattern. This significantly affects analyses. Research into this area is, therefore, desirable to establish the contribution of various shear resisting mechanisms particularly after several cycles of yield excursion. To this end, both repeated static incremental cyclic loading and rapid dynamic loading were used in this study. The first stage of the project involved the testing of 25 column units by subjecting them to several cycles of inelastic loading with increasing displacement ductility level. The inelastic loading

was achieved by controlled displacement to the top of the column units. The second stage of the project involved the testing of ten bridge pier models (8 single piers and 2 twin-piers) on a shake-table. The pier models were subjected to dynamic loadings with frequency typical of earthquake excitation. The single piers were tested using sinusoidal excitation while the twin-piers were tested using actual earthquake records.

The significance of a number of factors affecting the shear behaviour was investigated. The main parameters studied include:

(a) column aspect ratio;
(b) axial load level; and
(c) amount of transverse reinforcement.

(a) The column aspect ratio:

Columns with low aspect ratio (i.e. ratio of shear span to diameter) are more prone to shear failure than slender columns because of the low moment/shear ratio. Consequently, it was this class of piers that was investigated in the study. Though columns and piers with low aspect ratios are generally avoided in bridge or building constructions in New Zealand, sometimes, because of certain physical constraints or for architectural reasons, they are being used.

Squat columns are used more extensively overseas, especially in Japan where the use of short columns is common, particularly in school and hospital buildings. Flexural action of these columns is typically modified by the stiffening action of other secondary structural or non-structural elements such as filler walls or deep cast-in-situ spandrels. In the case of bridge piers, low aspect ratios usually result from the use of very high seismic design coefficients requiring large diameter piers.

In these circumstances, columns and piers will tend to invite higher earthquake induced shear forces than other more slender elements also participating in the lateral load resisting system and thus, there is the threat of shear failure.

Furthermore, response of any structure to earthquake excitation is sensitive to variation in its natural frequencies which in turn depend on the stiffness. The principal effect of stiffness degradation is an increase in the period of vibration. Unlike a long period of structure, this increase in the period of vibration, in general, will subject an initially stiff structure with small aspect ratio to more vigorous ground shaking. This

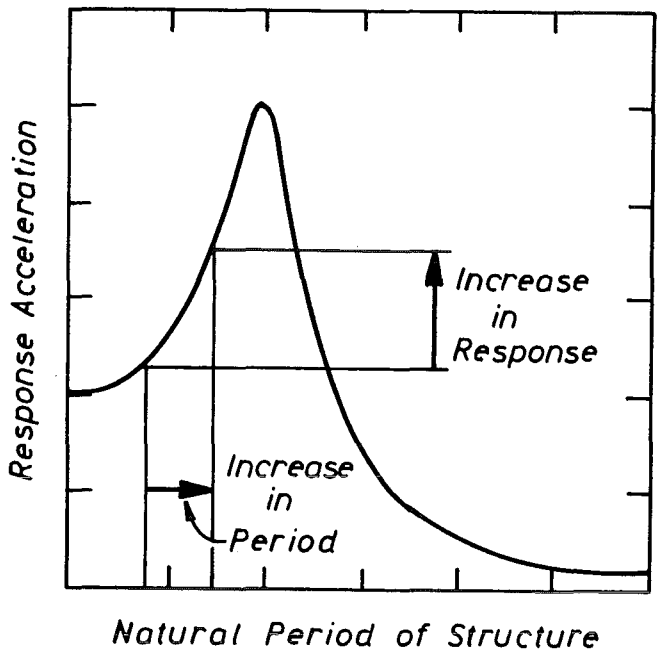

Fig. 1.5 : Increase in response due to change in period of vibration in an initially stiff column

phenomenon is illustrated in Fig. 1.5, using a typical earthquake acceleration response spectrum.

(b) The axial load level:

As columns and piers will always carry a certain amount of axial load, it is important to investigate the influence of this action on shear strength. In general, axial compression places extra demands for confinement of the concrete core while axial tension tends to hasten strength decay under load reversals. The presence of axial force affects the flexural capacity of the critical sections and accordingly the shear demand will be altered as well. The magnitude of the axial loads also affects the strength of the concrete shear resisting mechanisms, as is commonly recognised in many design codes (see Chapter Two). The consequences can be significant especially in the case of unanticipated change in axial load level during an earthquake attack. The vertical component of earthquakes and vertical reactions due to overturning moments can cause a great variation in the level of axial loads. In the case of tall twin or multiple pier systems or in outer columns, especially the corner columns of buildings, the change in axial loads can be much larger. Such change can give rise to detrimental effects in columns and piers.

(c) The amount of transverse reinforcement

Transverse reinforcement in the form of spirals has been found to be more effective in confining the concrete core than rectangular ties[1.9]. Provided fracture of the spirals is prevented, its continuity prevents it from unwinding as freely as in the case of poorly anchored circular hoops.

Recent research[1.9] at the University of Canterbury on ductility of bridge piers indicated the excellent performance of these piers designed according to the present New Zealand Code provisions[1.8]. These piers were large scale models of prototype structures designed specifically to have flexurally predominant behaviour. As such, the confining requirements of the code governed the design and shear strength was normally not a problem. The piers tested included solid circular (or octangonal) sections, solid square sections loaded along a principal axis or a diagonal, and hollow square and circular sections. Among them there were a number of piers with transverse spiral reinforcement. All the piers were able to sustain a load carrying capacity in excess of that predicted by the ACI method using actual material properties. They had a displacement ductility capacity of at least six, but usually more. This observation was attributed to the beneficial effect of confinement afforded by the transverse reinforcement in enhancing both the strength and ductility capacity of the concrete. In view of this, it may be possible to take advantage of the effect of confinement and relax the code requirements somewhat. A suggestion to this effect is given in Ref. 1.9. However, before any step can be taken, it is imperative that the adequacy of the shear strength is assured when the amount of confining reinforcement is to be reduced. Hence, information in this area is essential. A design approach for circular columns confined by spiral reinforcement is proposed as an outcome of this project.

1.4 FORMAT OF THE THESIS

In Chapter Two, the historical perspective of related experimental work on the shear behaviour of reinforced concrete members under seismic situations is outlined. It is not intended to give a thorough literature review. Only a comprehensive summary of the state-of-the-art is given. The discussion is followed by the development of some current theoretical approaches for predicting shear behaviour. To date the variable truss model, used in the so-called 'Diagonal Compression Field Theory' and plastic analyses appears to give the most satisfactory results. Therefore,

these approaches are studied in some detail in the chapter before various contemporary code provisions for shear strength are compared, with emphasis on problems related specifically to circular sections reinforced with transverse spiral reinforcement.

A detailed account of an experimental programme involving testing of 25 circular bridge pier models is reported in Chapter Three. The piers were deliberately designed so that shear limited the strength or ductility capacity. Quasi-static horizontal loading was applied to the vertical piers at a fixed height above the base. The loads were incremented in steps and cycled between various pre-determined peak displacement ductility levels. The results and observations of these tests are presented in Chapter Four. The performance of the piers was monitored mainly in terms of load-deflection hysteresis response. Strength and ductility capacities and energy dissipating characteristics are good indicators of pier performance under the simulated loading conditions, and therefore, are also recorded in Chapter Four. Finally, the experimental results are also compared with the shear strength specified by the contemporary codes examined previously in Chapter Two.

With the knowledge gained in the static tests, a design proposal for shear strength of circular reinforced concrete columns under seismic loadings is given in Chapter Five. This chapter discusses the derivation of design equations for the computation of various strength and ductility values. The proposed design approach allows the shear and flexural strengths of circular reinforced concrete columns and their displacement ductility capacity to be assessed. Based on the calculated value of displacement ductility capacity, the failure mode of the column can then be predicted. In the same chapter, available results from other research are compared with values predicted by the proposal. A brief comparison with the provisions of the New Zealand Concrete Design Code is also included. After the comparisons, an integral flexure/shear ductile design procedure is explained in a step-by-step manner.

In Chapter Six the 'Diagonal Compression Field Theory' is examined further and is adapted for theoretical analyses to predict the behaviour of the column units of the static tests. The biaxial stress-strain relationship of concrete and the computational procedures used in the analytical process are discussed. The predicted results are presented mainly in the form of load-displacement relationship.

Chapter Seven gives a record of experimental aspects of the dynamic tests. This series of tests was conducted to investigate the shear behaviour under the more realistic dynamic loading condition

and in particular the validity of the static test results was to be checked. The tests were carried out on a newly installed shake-table which was designed as part of this project. Altogether 8 single pier and 2 twin-pier models, which were approximately half scale models of the static test units, were tested. The piers were subjected to a sequence of tests, with increasing intensity between tests, using either sinusoidal or simulated earthquake excitations. The results and observations from these tests form the contents of Chapter Eight. Emphasis is placed on comparing the dynamic test results with those from the static tests. The discussion is presented mainly in terms of strength and ductility capacities and is preceded by a brief description of general behaviour and load-deflection hysteresis performance of individual models.

Conclusions regarding the experimental results and observations, and the theoretical analyses are given in Chapter Nine. Some recommendations for future work are suggested after the conclusions are drawn.

The list of references is given in Appendix I while the computer program used in the analysis, with some brief notes and comments, is presented in Appendix II. Details of the earthquake simulating facility and the data acquisition system for the dynamic tests are given in Appendix III. Drawings together with the design considerations for the shake-table are included.

Chapter Two

LITERATURE REVIEW, THEORETICAL APPROACHES AND CODE COMPARISONS

2.1 INTRODUCTION

The early period in the research history on behaviour of reinforced concrete members subjected to shear in conjunction with other actions was an exploratory stage during which research workers studied the shear strength of reinforced concrete members and attempted to identify factors that affected behaviour. It was after the mid-forties that the direction of research was centered on determining the ultimate shear strength of members. A systematic study of shear strength began only in the fifties. Most of the equations derived at that time were either empirical or semi-empirical without much consideration being given to basic shear transfer mechanisms. Based largely on the work of Hognestad[2.1], ACI-ASCE Committee 326[2.2] examined the historical developments at this stage and then proceeded to formulate design equations which later formed the background of the ACI code provisions[2.79]. These equations have been used since 1963. An annotated bibliography[2.4] prepared by ACI-ASCE Committee 326 provides a comprehensive list of literature relevant to research from 1897 to 1961.

In the sixties attempts were made to identify the basic behaviour of various shear resisting mechanisms. These studies enabled a better qualitative description as well as quantitative evaluation of the shear behaviour of the reinforced concrete members to be made. This period of development was summarised, with reference to some 200 publications, in another report of Joint ASCE-ACI TASK Committee 426[2.3] in 1973.

During the last decade the shear behaviour of members subjected to cyclic load reversals was also studied. The present situation is such that within reasonable limits the flexural behaviour of members in seismic situations can be predicted satisfactorily. This is not the case for shear behaviour. Research workers, therefore, attempted to study the influence of shear on strength and stiffness degradation as well as on energy dissipation in these members. The aim was to provide more accurate prediction of behaviour preferably in a rational manner. The following sections give some details of the present state-of-the-art in this specific area.

2.2 PREVIOUS EXPERIMENTAL STUDIES ON SEISMIC SHEAR BEHAVIOUR OF REINFORCED CONCRETE MEMBERS

Most of the studies dealt with subassemblages of buildings.

Jirsa[2.5] selected a number of such projects and commented on their relevance to bridge behaviour. He pointed out the limitations in using small scale specimens and a lack of research into the effect of axial tension on the behaviour of members in which plastic hinges develop. He discussed several possible modes of failure and highlighted the significance of loading history in evaluating seismic performance. An elaborate test programme was subsequently initiated in the University of Texas at Austin[2.6-2.16] to investigate shear behaviour under two- or three-dimensional reversed cyclic loading. As the loading history was the primary variable, the geometry of the specimens was kept identical in all tests. Tests were also carried out with alternating axial tension and compression in addition to lateral loadings in the two orthogonal directions. Results indicated that axial tension or compression influenced member performance only while the tension or compression was applied. Prior tension or compression applied during the loading history did not appear to influence subsequent behaviour. However, lateral loads applied in one direction influenced subsequent performance when load was applied in other directions. Comparisons between one- and two-dimensional load-deformation relationships in the Texas tests showed severe reduction of strength due to prior or simultaneous loading in orthogonal directions where this loading resulted in deflections exceeeding the deflection at which the maximum shear strength of a member under unidirectional loading was reached.

An extensive program to study the performance of bridge piers has been conducted at the University of Canterbury in New Zealand since 1974[2.17-2.20]. The installation of a 10MN Dartec Testing Machine has facilitated the testing of full or near full size columns under combined axial load and inelastic lateral loading (Fig. 2.1). The series of tests included a large number of piers with transverse spiral reinforcement. Tests so far concentrated on the ductility performance of piers. As far as the shear strength was concerned, it was concluded that shear resisting mechanisms in the potential plastic hinge zones other than the transverse reinforcement were able to carry an average shear stress of $0.1\sqrt{f'_c}$ MPa over the gross area even when the axial load was small[2.17]. Lately, it was observed that the shear carried by concrete generally exceeded code predicted values by large margins[2.21]. It was also concluded that ACI 318-77 formulae for shear strength of such columns were inconsistent. An outline of the relevant test program up to 1983 was reported by Priestley and Park[2.20].

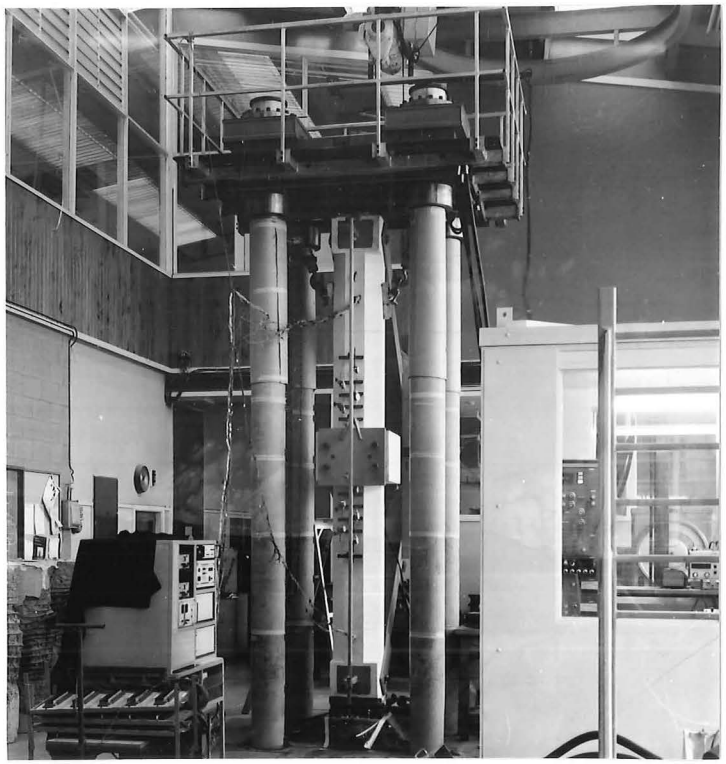

(a) End View

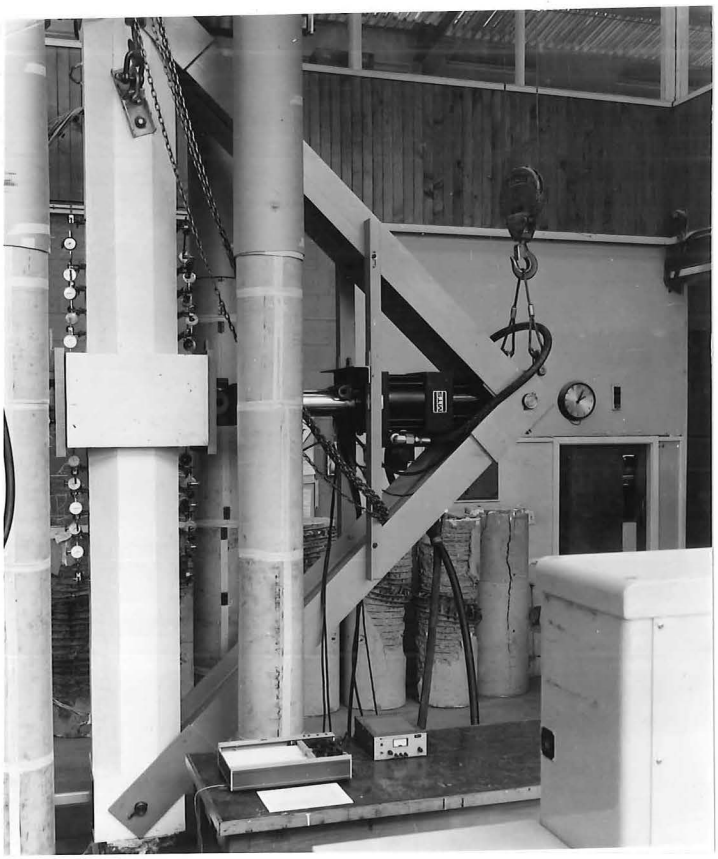

(b) Side View

Fig. 2.1 : Testing of a large bridge column under combined axial load and bending in 10 MN Dartec Testing Machine [2.20]

In Japan, the Building Research Institute of the Ministry of Construction and other institutions initiated a coordinated research programme to study the seismic shear behaviour of short reinforced concrete columns. The need for this work became apparent after numerous column failures in the 1968 Tokachi-Oki Earthquake. Hundreds of specimens covering wide ranging variables were tested. Table 2.1 taken from a comparative study by Kubota and Sozen[2.22] of the American and the Japanese shear design approaches gives some indication of the scope of the programme. A brief account of these tests was also given by Hirosawa, et al[2.23]. They described the loading systems and test specimens used in this research and evaluated qualitatively some initial results.

Brown and Jirsa[2.24] conducted tests to study the effects of inelastic cyclic load reversals on the strength, ductility and mode of failure of reinforced concrete cantilever beams. Their results showed that the ability of members to maintain high resistance and energy dissipating capacity was greatly improved by reducing the stirrup spacing. Shear stress level was found to have a strong influence on the beam performance. A reduction in shear force through changes of the shear-span or of the loading history also improved the performance. Gosain, et al[2.25] found that the shear-span to depth ratio had marked influence on the energy dissipation characteristic of members with the same transverse reinforcement content, i.e. the smaller this ratio the more 'pinched' are the load-deflection hysteresis loops if flexural strength remains unchanged. Wight and others[2.26-2.28] conducted similar studies to examine the effect of axial compression. The presence of axial compression was found to slow down the decay in strength and stiffness with cycling if the hinging zone was properly confined. On the basis of their tests, Wight and Sozen recommended that the transverse reinforcement should be designed to carry the entire shear across a 45-deg failure plane. They also stressed the importance of having the concrete effectively confined in potential plastic hinge regions. Scribner and Wight[2.29,2.30] found in another similar study that intermediate longitudinal reinforcement was effective in improving hysteretic response of doubly reinforced rectangular beams if the maximum shear stress developed was between $0.25\sqrt{f'_c}$ and $0.50\sqrt{f'_c}$ MPa.

Bertero, Popov and others[2.31-2.43] at the University of California, Berkeley, conducted a long-term testing program to study the effect of stiffness degradation due to high shear. Among their findings, they reported that if the maximum deformation of reinforced concrete members

Table 2.1 : A Summary Of Japanese Research[2.22]

Investigator	Section Dimension	$\frac{M}{VD}$	Concrete Strength f'_c (MPa)	Number of Specimens	Major Variables
M. Wakabayashi K. Minami	100 x 150	3.0	28.7 - 40.2	40	ρ_t, P_i/A_g
A. Ikeda	200 x 200	2.5	20.0	18	ρ_ℓ, ρ_t, P_i/A_g
A. Ikeda	200 x 200	2.5	20.0	8	ρ_ℓ, ρ_t, P_i/A_g
A. Ikeda	200 x 200	2.5	21.0	8	ρ_ℓ, P_i/A_g
A. Ikeda	200 x 200	2.5	23.0	4	P_i/A_g
S. Kokusho	200 x 200	2.5	21.9	4	ρ_ℓ
M. Hirosawa	200 x 200	2.5	21.3	7	ρ_ℓ, ρ_t, P_i/A_g
M. Hirosawa	200 x 200	2.5	22.8	7	ρ_ℓ, ρ_t, P_i/A_g
A. Ikeda	200 x 200	2.5	26.7	7	ρ_ℓ, ρ_t, P_i/A_g
A. Ikeda	200 x 200	2.5	29.7	7	ρ_ℓ, ρ_t, P_i/A_g
T. Takeda K. Yoshioka	300 x 300	2.3	20.1 - 22.3	15	ρ_t, P_i/A_g
T. Takeda K. Yoshioka	300 x 300	1.5	18.7 - 22.6	15	ρ_t, P_i/A_g
Y. Suenaga	120 x 120	2.0,3.0, 4.0	12.4 - 24.1	31	$\frac{M}{VD}$, ρ_t
Y. Suenaga	120 x 120	3.0	23.8	6	
M. Ozaki M. Hirosawa	400 x 600	1.0	14.4 - 25.3	18	ρ_t
T. Hisada S. Bessho	350 x 350	2.1	35.8 - 37.7	9	ρ_t
H. Umemura T. Endo	200 x 200	2.0,3.0	18.0	12	ρ_t, P_i/A_g
H. Umemura T. Endo	200 x 200	2.0,3.0	33.6	12	ρ_t
H. Umemura Y. Fukada	200 x 200	2.0	13.4 - 15.1	6	
H. Umemura S. Nakata	250 x 500	1.0,2.0	13.4 - 14.6	4	
A. Ikeda	150 x 150	2.3	21.5 - 24.8	24	$\frac{M}{VD}$, ρ_t, $\frac{P_i}{A_g}$
A. Ikeda	150 x 150	2.3	20.0 - 20.6	16	$\frac{M}{VD}$
M. Yamada	160 x 160	1.0	20.2	4	ρ_t
M. Yamada	160 x 160	1.0-4.0	29.1 - 36.0	6	$\frac{M}{VD}$, $\frac{P_i}{A_g}$
M. Yamada	160 x 160	0.53-2.1	19.7 - 29.1	16	$\frac{M}{VD}$, $\frac{P_i}{A_g}$
K. Ohshima Y. Sonobe	200 x 300	4.0	21.0 - 31.1	10	ρ_ℓ
Y. Sonobe K. Ishibashi	200 x 300	4.0	42.8	6	ρ_ℓ
H. Umemura H. Noguchi	250 x 500	1.0	12.7 - 14.6	8	ρ_t
S. Kokusho E. Yoshizumi	200 x 200	1.5	21.0	27	ρ_t
S. Kokusho	200 x 200	2.5	20.3 - 24.3	6	ρ_ℓ, ρ_t
H. Umemura S. Kokusho	200 x 200	2.5	22.8 - 34.0	10	P_i/A_g
T. Naka	150 x 200	1.25,2.50, 3.95	16.3 - 38.1	59	$\frac{M}{VD}$, ρ_ℓ , ρ_t, $\frac{P_i}{A_g}$
S. Kokusho M. Fukuhara	200 x 200	1.25,2.50, 3.95	22.4	8	ρ_ℓ

Table 2.1 (Contd) : A Summary Of Japanese Research[2.22]

Investigator	Section Dimension	$\frac{M}{VD}$	Concrete Strength, f'_c (MPa)	Number of Specimens	Major Objective
B.R.I.	250 x 250	1.5,3.0	24.0,27.0	36	welded hoop
T.R.I. of Takenaka Komuten	250 x 250	1.0,2.0	16.5	15	loading method
T.I.T.	250 x 250	1.0,2.0	24.5	15	loading method
Meiji Univ. B.R.I.	500 x 500	1.0,2.0	26.5	15	scale effect
T.R.I. of Taisei Const. Co. Ltd.	250 x 250	1.0,2.0	45.3	14	strength of concrete
T.R.I. of Obayashi-Gumi Co. Ltd.	250 x 250	1.0,2.0	27.4	15	welded hoop
T.R.I. of Fujita Kogyo	250 x 250	1.0,2.0	19.0	15	axial stress
T.M.U.	250 x 250	1.0,2.0	15.1	10	wing wall
T.R.I. of Kashima Const. Co. Ltd.	250 x 250	1.0,2.0	27.0,32.2	15	spiral
T.D.C. of Toda Const. Co. Ltd.	250 x 250	1.5,3.0	19.3	17	shear span ratio
T.M.U.	250 x 250	2.0	24.0	10	loading program
M.I.T.	250 x 250	2.0,2.5, 3.0	19.8 - 24.4	12	spacing of web reinforcement
R.I. of Shimizu Const. Co. Ltd	250 x 250	1.5,2.0	12.4,15.3	13	arrangement of reinforcement
M.I.T.	250 x 250	2.0,2.5, 3.0	18.5 - 21.7	6	spacing of web reinforcement
R.I. of Shimizu Const. Co. Ltd.	250 x 250	2.0	26.1	16	arrangement of reinforcement
T.M.U.	250 x 250	1.0	14.6	6	loading program
T.M.U.	250 x 250	1.0,2.0	18.7	6	wing wall
B.R.I.	250 x 250	1.0,2.0	14.0,18.0	6	plain bar
B.R.I.	250 x 250	1.5,2.0	26.3	6	plain bar
T.M.U.	250 x 250	2.0	24.1	7	axial stress
T.R.I. of Obayashi-Gumi Co. Ltd.	400 x 400	1.5,2.0	24.0,27.7	5	closed hoop
B.R.I.*	250 x 250	2.0	21.0	3	shape of hoop
M.I.T.*	250 x 250	1.0,1.5 2.0	20.3 - 26.4	27	ties
M.I.T.*	250 x 250	2.0,2.5, 3.0	20.9 - 24.6	18	shape of hoops

* parallel investigations

B.R.I. = Building Research Institute, Ministry of Construction
T.I.T. = Tokyo Institute of Technology
T.M.U. = Tokyo Metropolitan University
M.I.T. = Muroran Institute of Technology
T.R.I. = Technical Research Institute
R.I. = Research Institute
T.D.C. = Technical Development Center

in either direction was increased, initial stiffness and energy dissipation per cycle degraded during the following cycle. Their results showed that the hysteresis behaviour of a structure appeared to be very sensitive to the history of excitations. In particular in members subjected to high shear, they found that the effect of shear deformation was significant and most of the deformation was caused by large transverse displacement across one or two pairs of intersecting flexural and diagonal tension cracks. Their results indicated that moderate ductile behaviour and high shear were not incompatible but, to develop large deformations while maintaining full shear strength, the contribution of concrete shear resisting mechanisms as defined in ACI Code should be ignored unless the core concrete of the members could be kept effectively confined with sufficient and properly detailed transverse reinforcement. Furthermore, they recommended that the shear stress in the critical regions should be limited to a value lower than that allowed by the ACI 318-71 Building Code if excessive damage leading to stiffness and strength degradation was to be avoided.

In 1977 a research program was initiated at the University of Auckland in New Zealand by Fenwick and his co-workers[2.44-2.51] to study the influence of shear stress level on the performance of plastic hinge zones of reinforced concrete beams under reversed cyclic loading. The emphasis of the research has been to study the shear deformation mechanisms in the beams after several cycles of yield excursion and the effects of this shear deformation on the performance of the beams. Three modes of shear deformation mechanisms were identified from their test observations. It was noted that the main effect of shear deformation was a reduction of the stiffness. For beams with closely spaced stirrups which were proportioned to carry the entire applied shear across a 45-deg plane and where the shear stress was not high, strength degradation was found to be not significant.

Many of the tests mentioned, e.g. those at the University of Texas at Austin and in Japan, involved specimens which would not meet the detailing requirements of NZS 3101 to provide adequate confining and anti-buckling reinforcement in the potential plastic hinge regions. Typically intermediate ties for column bars were omitted as shown for example in Fig. 2.2. Failure of these specimens could involve buckling of flexural bars and loss of confinement and therefore the test results did not necessarily reflect the influence of shear only. Better performance of these columns could have been obtained if more care had been taken in the detailing of critical regions in the column specimens.

It was also found that research which addresses specifically the problem of shear strength of reinforced concrete members with circular cross-section or members with circular hoops or spirals as transverse reinforcement was very limited. The only example cited by Committee 426[2.3] was the work by Farodji and Diaz de Cassio who tested twenty-one 250 mm diameter circular specimens. However, only four of the specimens contained web reinforcement.

Though the tests at the University of Canterbury in New Zealand involved some fifteen bridge pier models with spiral reinforcement, the main objective of the tests was to study the ductility performance of these piers. Consequently, the design of transverse reinforcement was governed by confinement rather than shear strength requirement.

Similarly, the study by Karlsson et al[2.52], who tested six spirally reinforced concrete columns with constant axial load and subjected to reversed cyclic lateral loading, was intended to develop a hysteresis model to be used in the dynamic analysis of structures supported by such columns.

A more systematic study of the shear strength of circular columns was conducted at the University of Toronto[2.77]. Khalifa and Collins tested five circular columns with circular hoops. Four of their columns were tested with monotonic loading while one column was tested with load reversals. They found that shear strengths were typically 20 percent higher than predicted by ACI[2.79] equations, and that the Compression Field Theory (reviewed subsequently) gave a more accurate prediction.

Presently information on the shear strength of circular members with or without axial load and subjected to reversed cyclic lateral loading is unavailable. Most studies were carried out using conventionally reinforced beams. It was found that the beams were prone to sliding shear failure along a plane perpendicular to the axis of the beams when high shear stress was involved. In the case of circular members, the longitudinal reinforcement is usually distributed uniformly around spirals of the section. With this arrangement, the flexural reinforcement does not yield all at the same time when the ideal flexural strength is developed. The bars closer to neutral axis will not be as heavily strained as those near the extreme fibres. There will always be a concrete flexural compression zone even if no axial compression is present. Hence, it is possible to mobilize the concrete in this zone to resist part of the applied shear. Moreover, the flexural bars at mid-depth of the member are able to participate in resisting the applied

shear through dowel action because of better support provided by the core concrete. Consequently, the tendency to sliding shear failure is reduced. Because of this, the behaviour of the potential plastic hinge region in such members is likely to be different from that observed with rectangular members which were reviewed above.

2.3 THEORETICAL APPROACHES USED TO PREDICT SHEAR BEHAVIOUR OF REINFORCED CONCRETE MEMBERS

2.3.1 General

A large part of early research was conducted on members without web reinforcement because they afforded an opportunity to study basic components of shear resistance and also shear failure mechanisms in relatively simple circumstances. Several early theories therefore focused mainly on members without web reinforcement.

However, as it is common to use web reinforcement in main structural elements, the truss analogy received more attention than other approaches. The classical truss analogy was introduced by Ritter and Mörsch[2.1] at the turn of this century. They postulated that the entire shear in cracked reinforced concrete beams is resisted by a truss, the web members of which consist of vertical or inclined shear reinforcement and of 45-deg inclined concrete compression struts. The conservative nature of their proposal has been consistently observed in later research. Hence, the aim in later research was to improve this model in order to achieve a better correlation between theoretical prediction and actual behaviour.

Today, there are basically two lines of approach. The first is the familiar additive principle in which the strength in excess of that predicted by the classical truss model is attributed to concrete shear resisting mechanisms, such as aggregate interlock, dowel action and shear transfer in the concrete flexural compression zone. The second approach is to modify the 45-deg truss by adopting a model in which both forces and deformations within the failure region are considered. Variable inclination of cracks and diagonal compression struts are used and failure conditions include yielding of web and/or flexural reinforcement, crushing of concrete in the flexural compression zone, crushing of the diagonal concrete struts and some combination of these.

Seismic loading introduces additional complexity because repeated cyclic loading in the inelastic range can be expected to modify the shear strength and associated mechanisms in members. Most research so far has

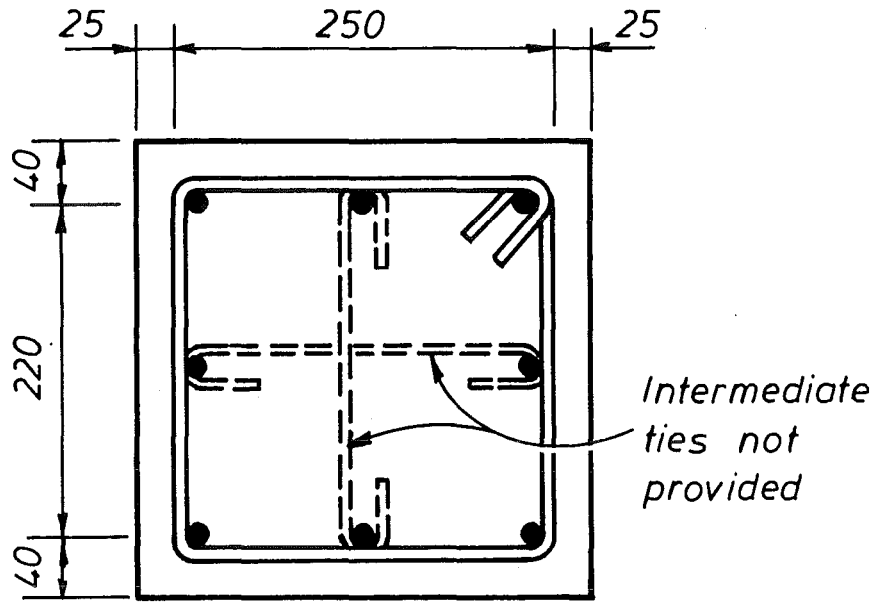

Fig. 2.2 : A typical column cross-section of Texas test[2.6-2.9]

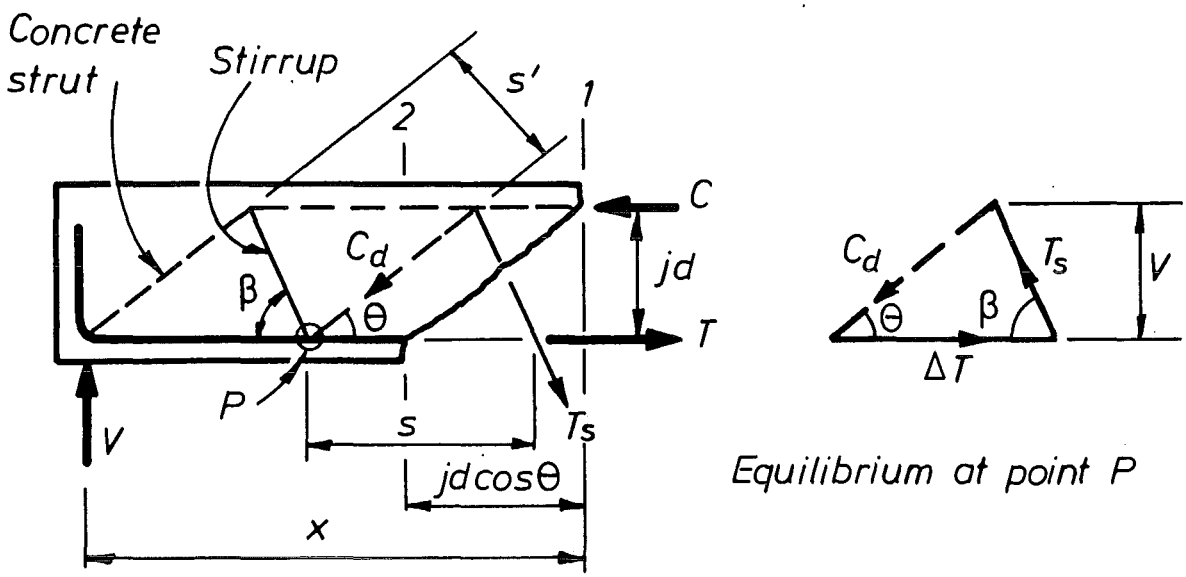

Fig. 2.3 : Internal forces in an analogous truss [2.53]

been concerned with the modelling of the loss in stiffness due to shear deformation of the members. The important characteristics of available strength and ductility have received relatively little attention.

The following sections review the main schools of theoretical approaches. Seismic loading requires the provision of a certain amount of web reinforcement. Therefore this discussion will consider members with transverse reinforcement. These methods are described in some detail as subsequently they are used in further theoretical developments and in the assessment of experimental results obtained in this study. The theoretical methods reviewed apply to monotonic loading. It is uncertain whether they will be applicable to cases involving inelastic cyclic loading.

2.3.2 The Truss Analogy

The 'Truss Analogy' was postulated by Ritter (in 1899) and Mörsch (in 1902) who assumed the shear resistance of reinforced concrete beams to arise from 'truss-action'. Their analogous truss is composed of the flexural concrete compression region and the longitudinal tensile reinforcement as the two parallel top and bottom chords, while the vertical or inclined stirrups and concrete struts at 45-deg form the web members of the equivalent 'pin-jointed' truss. The transverse and longitudinal reinforcement were to carry tension because the concrete was assumed to have no tensile strength. This assumption together with the assumption of 45-deg inclination of the diagonal struts formed the two primary assumptions of the classical truss analogy.

Fig. 2.3 depicts a segment of the analogous truss with general stirrup (β) and crack inclinations (θ) . The chord members are at distance jd apart. From consideration of equilibrium only, the stirrup force per unit length of the beam is

$$\frac{A_{st}\, f_{st}}{s} = \frac{V}{jd \sin\beta\,(\cot\theta + \cot\beta)} \qquad (2.1)$$

where V is the external shear force, A_{st} is the area of stirrup spaced at distance s and f_{st} is the stirrup stress. In the specific case of β = 90-deg and θ = 45-deg Eq.2.1 reduces to

$$\frac{A_{st}\, f_{st}}{s} = \frac{V}{jd} \qquad (2.1a)$$

which, when rearranged, gives

$$V = \frac{A_{st} f_{st} jd}{s} \qquad (2.1b)$$

i.e. the original form of equation proposed by Ritter.

Referring again to Fig. 2.3, the diagonal compressive stresses acting in the web can be approximated by

$$f_{c2} = \frac{C_d}{b_w s'} = \frac{V}{b_w jd \sin^2\theta (\cot\theta + \cot\beta)} = \frac{v_s}{\sin^2\theta (\cot\theta + \cot\beta)} \qquad (2.2)$$

where $v_s = \frac{A_{st} f_{st}}{b_w jd}$ is defined as the shear stress carried by the stirrups and $s' = s \sin\theta$ is the effective width of the diagonal struts. It can be seen that the magnitude of the shear force and the inclination of concrete struts affect the magnitude of diagonal compressive stress. Failure by crushing of web concrete is possible if this stress is large and especially when the compressive strength of web concrete is weakened due to the effects of other secondary actions as outlined in Ref. 2.53.

In deriving the above equations, the strain incompatibility due to differences in stiffness of shear resisting mechanisms was ignored. The diagonal compression members composed of concrete are much stiffer than the steel tension members. Beam geometry and state of cracking affect the stiffness ratio between the concrete and the reinforcement. Leonhardt postulated[2.54-2.57], that the stresses are governed by the principle of minimum energy. He showed that the stirrup stresses of beams with the same effective depth increased with decreasing web width as shown in Fig. 2.4a. The increase of the measured stresses in the stirrups due to increased shear load consistently exhibited the characteristic pattern whereby the values always followed a line almost parallel to the one computed using the classical 45-deg truss analogy. This line was displaced horizontally by a distance that corresponded to a fixed amount of shear force, V_c. The value of V_c was found to be approximately equal to the diagonal cracking load. This in turn was found to be independent of the amount of shear reinforcement used as is shown in Fig. 2.4b in which stirrup stress in beams with different transverse reinforcement content is plotted against the applied shear load. Leonhardt suggested that the shear force V_c is carried by the top flexural concrete compression chord which must therefore be inclined towards the support.

Leonhardt and others also observed that the inclination of shear cracks was not always 45-deg. It varied in the range between 30-deg to

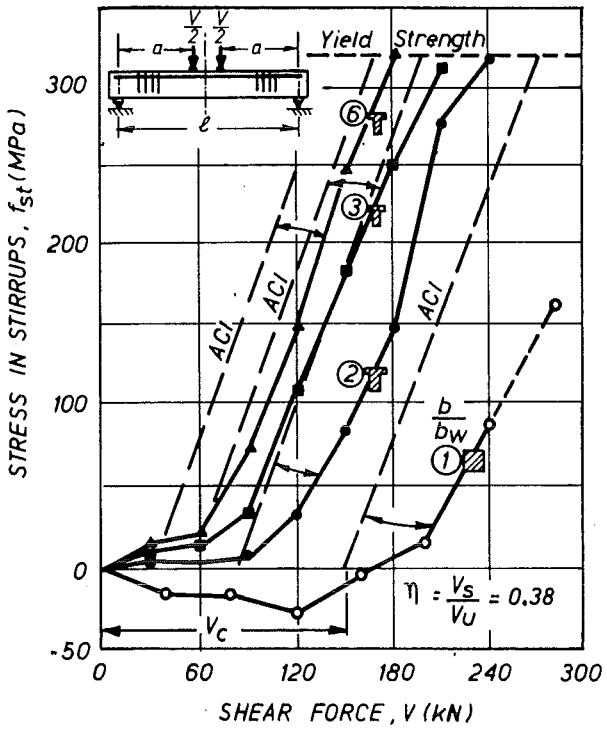

(a) Fixed shear coverage ratio, η

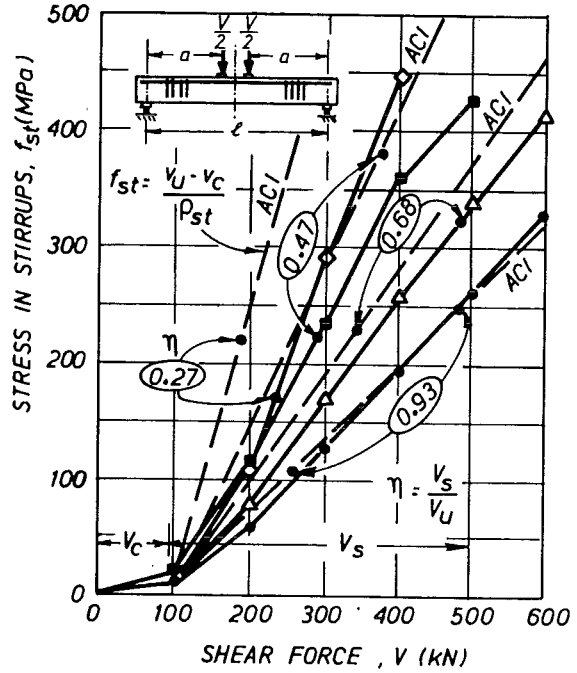

(b) Variable shear coverage ratio, η

Fig. 2.4 : Stirrup stress - shear force relationship [2.56]

40-deg and was found to be influenced by the percentage of shear coverage, η , i.e. the ratio of the amount of shear reinforcement provided to the full amount needed for the ultimate shear force ($\eta = V_s/V_u$).

Other research workers, including Bresler and Scordelis[2.58], Attiogbe, et al[2.59] and Haddadin, et al[2.60] had also studied the effectiveness of web reinforcement with particular attention to lightly reinforced members. They drew similar conclusions that the web reinforcement was more effective than was suggested by the classical approach based on a 45-deg truss model. The effectiveness they reported was 50 to 80 percent in excess of the classical value.

To overcome the conservatism inherent in the classical approach, the results of the 45-deg truss model was modified either by introducing a correction term v_c to Eq. 2.1b, or by multiplying Eq. 2.1b with an effectiveness factor, k , or employing both, i.e.

$$v_i = k \rho_t f_{yt} + v_c \qquad (2.1c)$$

where $\rho_t = \frac{A_{st}}{b_w s}$ is the transverse reinforcement ratio. Originally, Ritter and Mörsch assumed $k = 1.0$ and $v_c = 0$ but over the years, a number of research workers have suggested different values for k and v_c . These were based on results obtained from tests with monotonic loading. As pointed out earlier, the reliability of the so-called 'concrete contribution' as implied in the second term of Eq. 2.1c was considered questionable. Consequently some research workers who studied the seismic shear behaviour of reinforced members recommended that this term be ignored in the design of members for shear. Their concern is reflected in some current design code provisions outlined in Section 2.4.

In the case of members subjected to seismic loading, the transverse reinforcement has additional roles. Besides carrying part or all of the applied shear, the transverse reinforcement also helps to confine the concrete and provides lateral restraint to the flexural compression bars.

2.3.3 Plastic Analyses

The classical truss analogy has its limitations as an analytical tool. Much effort has since been directed to devising improved truss models, especially in terms of the angle of inclination of the concrete diagonals. It was found that a more realistic strut inclination at the development of ideal shear strength giving more reliable prediction can be obtained from plastic analyses. The progress of work in this area is

promising. The approach has gained acceptance in CEB-FIP Model Code[2.81] 1978 as the basis of an alternative design method. Notable examples of contribution are those of Thürlimann and his co-workers in Zürich[2.61-2.63] and of Nielsen and his co-workers in Copenhagen[2.64-2.68]. A similar approach is also being used by some Japanese research workers in this field[2.89].

The model consists of the same components as used in the classical 45-deg truss analogy. However, the diagonal concrete struts may be inclined at angles other than 45-deg. Either of the lower-bound or upper-bound approaches can be used to determine the angle of inclination if the mechanical degree of shear reinforcement (ψ) given by Eq. 2.7a is known. The strut inclination does not remain constant as the shear load on the member is increased. The stresses adjust themselves to carry the changing load through some form of redistribution; the higher the shear force the flatter the diagonal struts will be. This implies that diagonal stresses have to be transferred across cracks which formed initially at approximately 45-deg. Hence, satisfactory performance can be ensured only if shear transfer across cracks can be maintained.

The analyses involve the following assumptions:

(1) The stress field in the beam is planar. The web concrete is in a state of uniaxial compression and the action of stirrups is described by an equivalent stress parallel to the stirrup direction.

(2) The response of steel is rigid-perfectly plastic. Bars can only resist forces in their axial direction only.

(3) The response of concrete is rigid-perfectly plastic with the square yield condition for plane stress. The tensile strength of concrete is zero and its compressive strength is the cylinder strength f'_c.

Fig. 2.5 shows the postulated yield criteria for steel and concrete in a normalised form.

(a) Lower Bound Solution

To obtain the lower-bound solution, the equilibrium conditions of a statically admissible and safe stress field have to be considered with all boundary conditions being satisfied. The static theorem states that the highest value for the bending moment and shear force will lead to collapse provided that equilibrium is maintained and that nowhere in the member are the yield conditions violated. Fig. 2.6 shows a sketch of a typical element in the idealized stress field with concrete struts

inclined at angle θ . Taking tensile values as positive, the diagonal concrete compression stress can be shown to give rise to the following components of normal stress and shear stress,

$$f_{\ell c} = - f'_c \cos^2 \theta \tag{2.3a}$$

$$f_{tc} = - f'_c \sin^2 \theta \tag{2.3b}$$

$$v = \frac{V}{b_w jd}$$

$$= f'_c \sin\theta \cos\theta \tag{2.3c}$$

where subscripts ℓ and t denote stresses in longitudinal and transverse directions respectively and f refers to normal stress while v refers to shear stress. This convention is used throughout this chapter unless defined otherwise. A limit state is considered.

To these components one must add the other components due to an equivalent stirrup stress which, by virtue of assumption (2), contributes only to the transverse component, i.e.

$$f_{ts} = \frac{A_{st} f_{yt}}{b_w s}$$

$$= \rho_t f_{yt} \tag{2.4}$$

where f_{yt} is the yield strength of transverse reinforcement and $\rho_t = \frac{A_{st}}{b_w s}$. Combining the two effects, the resulting stresses are

$$f_\ell = - f'_c \cos^2\theta \tag{2.5a}$$

$$f_t = - f'_c \sin^2\theta + \rho_t f_{yt} \tag{2.5b}$$

$$v = f'_c \sin\theta \cos\theta \tag{2.5c}$$

The boundary condition is $f_t = 0$ and this implies that at failure

$$\rho_t f_{yt} = f'_c \sin^2\theta$$

$$= v \tan\theta \tag{2.6}$$

The mechanical degree of shear reinforcement is defined as

$$\psi = \frac{\rho_t f_{yt}}{f'_c} \tag{2.7a}$$

and from Eq. 2.6

$$\psi = \sin^2\theta \tag{2.7b}$$

or

$$\frac{1}{\psi} = \operatorname{cosec}^2\theta = 1 + \cot^2\theta \tag{2.7c}$$

Therefore,

$$\tan\theta = \sqrt{\frac{\psi}{1-\psi}} \tag{2.8}$$

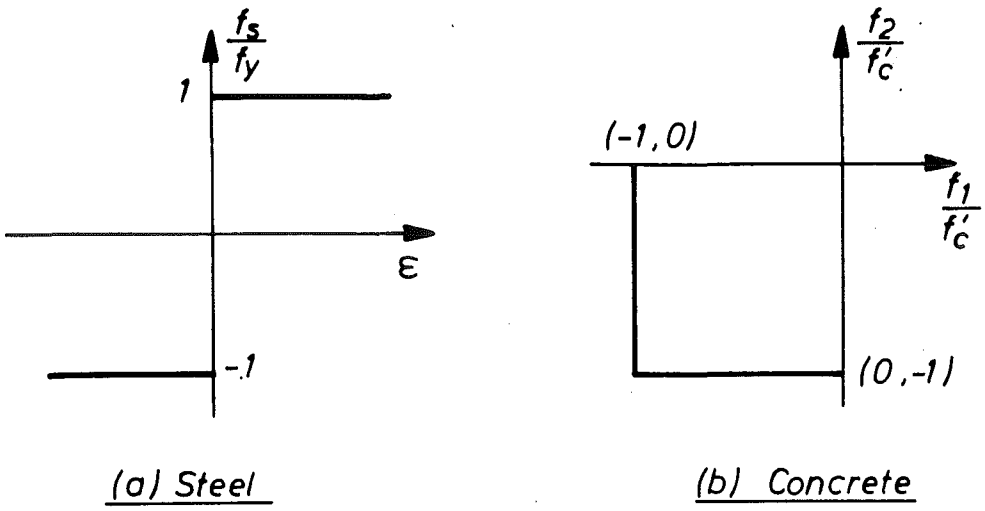

Fig. 2.5 : Yield criteria for steel and concrete

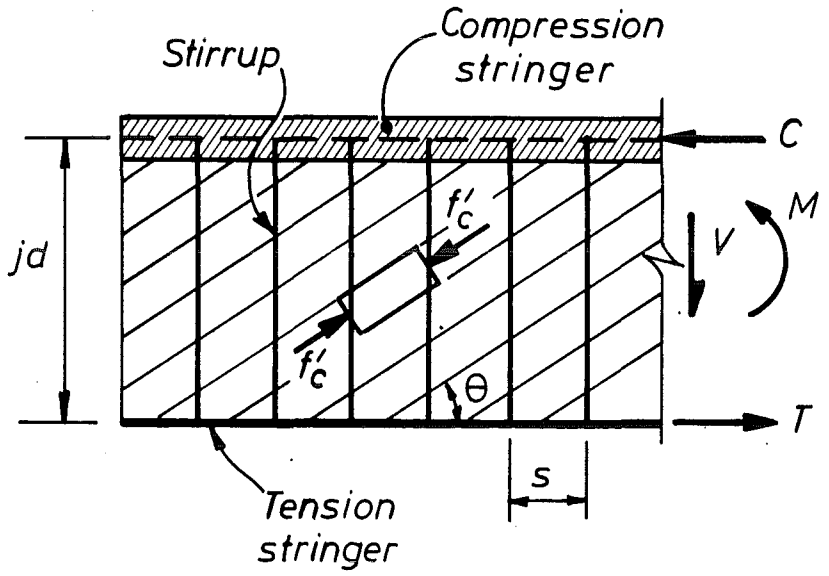

Fig. 2.6 : A typical element of an idealized stress field

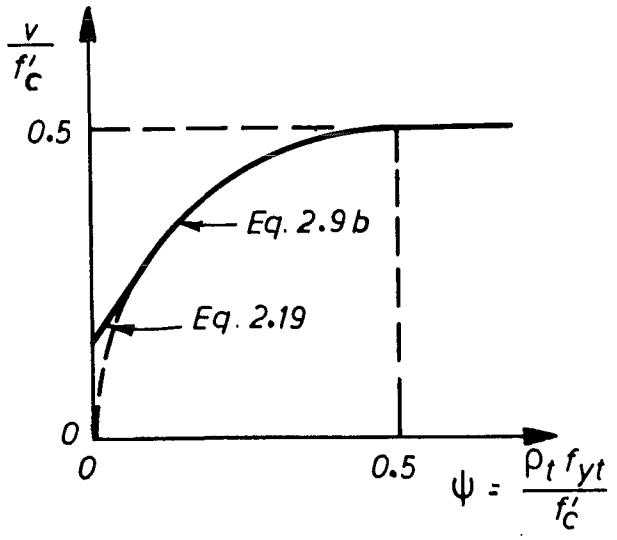

Fig. 2.7 : The upper and lower bound solutions

Also, from Eq. 2.6 and Eq. 2.8,

$$\psi = \frac{\rho_t f_{yt}}{f'_c} = \frac{v}{f'_c} \tan\theta$$

$$= \frac{v}{f'_c}\sqrt{\frac{\psi}{1-\psi}} \qquad (2.9a)$$

Therefore,

$$\frac{v}{f'_c} = \sqrt{\psi(1-\psi)} \qquad (2.9b)$$

Eq. 2.9b represents a circle in the coordinate system as shown in Fig. 2.7. The maximum value of v/f'_c is 0.5, corresponding to $\psi = 0.5$. For $\psi > 0.5$, the best lower bound was found to be $v/f'_c = 0.5$ [2.69] and the complete lower-bound solution becomes

$$\frac{v}{f'_c} = \sqrt{\psi(1-\psi)} \quad \text{for} \quad \psi \leq 0.5 \qquad (2.10a)$$

$$= 0.5 \quad \text{for} \quad \psi > 0.5 \qquad (2.10b)$$

The beam is able to achieve this maximum shear resistance given by the web crushing criterion only if the stringers are sufficiently strong. The normal stress component introduced by the stress field has to be added to the stringer forces due to other actions. From static relations, they should have the values:

$$T = \frac{M}{jd} + \frac{V}{2}\cot\theta \qquad (2.11a)$$

$$C = \frac{M}{jd} - \frac{V}{2}\cot\theta \qquad (2.11b)$$

where T and C are the tension and compression in the chord members and M is the bending moment at the section considered. (Fig. 2.6)

If the longitudinal and transverse reinforcement are chosen such that the resistance is governed by the yielding of these reinforcement but not crushing of the concrete diagonals, then

$$T_y = \frac{M}{jd} + \frac{V}{2}\cot\theta \qquad (2.12)$$

where T_y is the tensile force at yielding of flexural reinforcement. From Eq. 2.6

$$\cot\theta = \frac{v\, b_w\, jd}{\rho_t f_{yt} b_w jd} = \frac{V}{A_{st} f_{yt} \frac{jd}{s}}$$

$$= \frac{V}{F_y \frac{jd}{s}} \qquad (2.13)$$

where $F_y = A_{st} f_{yt}$ is the stirrup force at yielding.

Using subscript 'p' to denote plastic moment and shear and substituting cot θ from Eq. 2.13, Eq. 2.12 becomes

$$T_y = \frac{M_p}{jd} + \frac{V_p^2}{2 F_y \frac{jd}{s}} \tag{2.14}$$

Eq. 2.14 can further be transformed into an interaction equation such that

$$\frac{M_p}{M_{p,o}} + \left(\frac{V_p}{V_{p,o}} \right)^2 = 1 \tag{2.15}$$

where $M_{p,o} = T_y jd$ for $V_p = 0$ is the plastic moment for pure flexure; and $V_{p,o} = \sqrt{2 T_y F_y \frac{jd}{s}}$ for $M_p = 0$ is the plastic shear force for pure shear.

The theoretical development of the model in the preceding paragraphs assumed the development of full concrete compression strength as a yield criterion. However, having studied experimental results, Nielsen, et al[2.66,2.67] saw the need to introduce a web effectiveness factor, ν, so as to obtain better correlation between experimental results and theoretical predictions. The primary reason given for this is that, although the ductility of the concrete can be rather high in compression, its strength reduces drastically when the peak of the stress-strain curve has been reached. Values of ν suggested vary between 0.7 and 0.9. The effective compressive strength, $\nu f'_c$, represents an average stress in the actual strain region. As will be explained in Section 2.3.4, the reduction in strength is primarily due to tensile strains transverse to the diagonal compressive stress field.

(b) Upper Bound Solution

To complete the plastic analyses, an upper bound solution is briefly outlined in this section. A possible failure mechanism is sketched in Fig. 2.8 for the upper-bound or kinematic solution. A single displacement field is shown where the portion between the two yield lines inclining at angle γ is given a downward displacement, u. According to the upper-bound theorem, the structure will collapse if there is a compatible pattern of plastic deformation for which the rate at which the external forces do work exceeds the rate of internal energy dissipation. With the same assumptions that were stated earlier, the rate of internal work dissipated in the failure mechanism can be

computed. The work equation[2.69] corresponding to the failure mechanism shown can then be expressed as

$$Vu = (\rho_t f_{yt} b_w d \cot\gamma)\, u + \frac{1}{2} f'_c b_w (1 - \cos\gamma) \frac{d}{\sin\gamma} u \qquad (2.16)$$

or $$\frac{v}{f'_c} = \frac{V}{b_w d f'_c} = \psi \cot\gamma + \frac{1}{2} (1 - \cos\gamma) \frac{1}{\sin\gamma} \qquad (2.17)$$

with $\psi = \dfrac{\rho_t f_{yt}}{f'_c}$ as before.

The expression $v = V/(b_w d)$ is a slight variation of the definition given by Eq. 2.3c because the effective depth, d , instead of jd , is used.

The lowest upper bound is then determined by minimising the work with respect to the yield line inclination, γ , i.e.

$$\frac{\partial v}{\partial \gamma} = 0 \Longrightarrow \tan\gamma = \frac{2\sqrt{\psi(1-\psi)}}{1 - 2\psi} \qquad (2.18)$$

which when substituted back into Eq. 2.17 leads to

$$\frac{v}{f'_c} = \sqrt{\psi(1-\psi)}$$

This is identical to Eq. 2.10a obtained using lower-bound approach if the angle γ is twice the angle θ of the lower-bound solution. The geometrical boundary conditions require the angle to lie within the range

$$\frac{d}{a} \leq \tan\gamma \leq \infty$$

Substituting the lower limit of $\tan\gamma = d/a$ into Eq. 2.17 gives the following result:

$$\frac{v}{f'_c} = \frac{1}{2} \left\{ \left[1 + \left(\frac{a}{d}\right)^2\right]^{\frac{1}{2}} - \frac{a}{d} \right\} + \psi \frac{a}{d} \qquad (2.19)$$

This is a straight line tangent to the circle at the point where the angle is equal to $\tan^{-1} d/a$ (Fig. 2.7). The upper-limit corresponds to $\gamma = \pi/2$ and $\psi = 0.5$ i.e. the case of vertical yield line. Obviously, increasing the shear reinforcement under the circumstances will not increase the load carrying capacity. Therefore, for $\psi > 0.5$, $v/f'_c = 0.5$ is still valid.

The kinematic considerations were also used to establish the limitations on the inclination of the concrete compression field of the

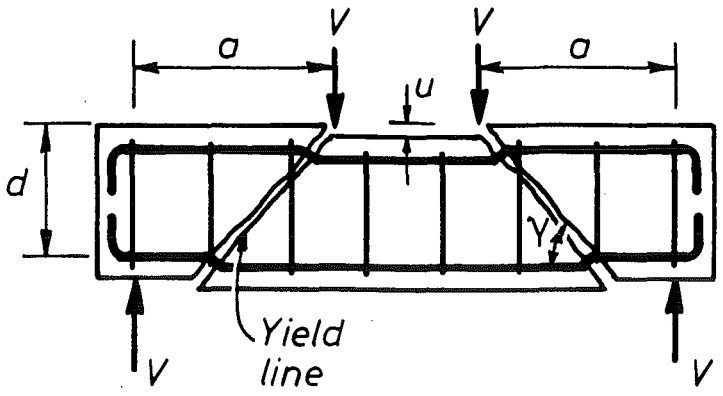

Fig. 2.8 : A failure mechanism for upper bound solution

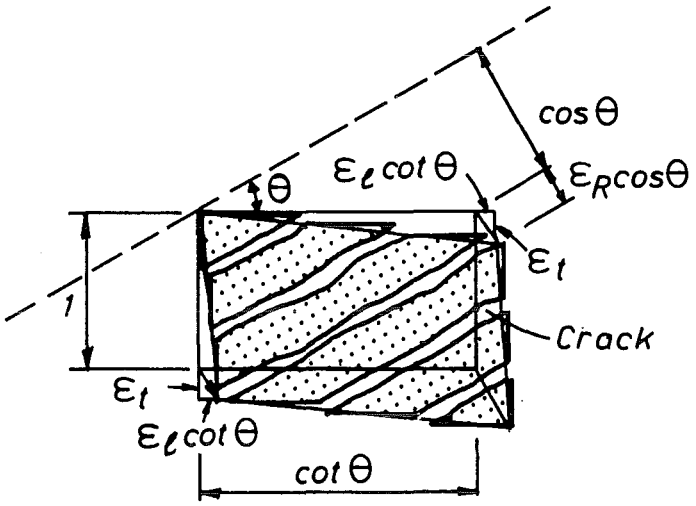

Fig. 2.9 : Plastic strain diagram [2.61]

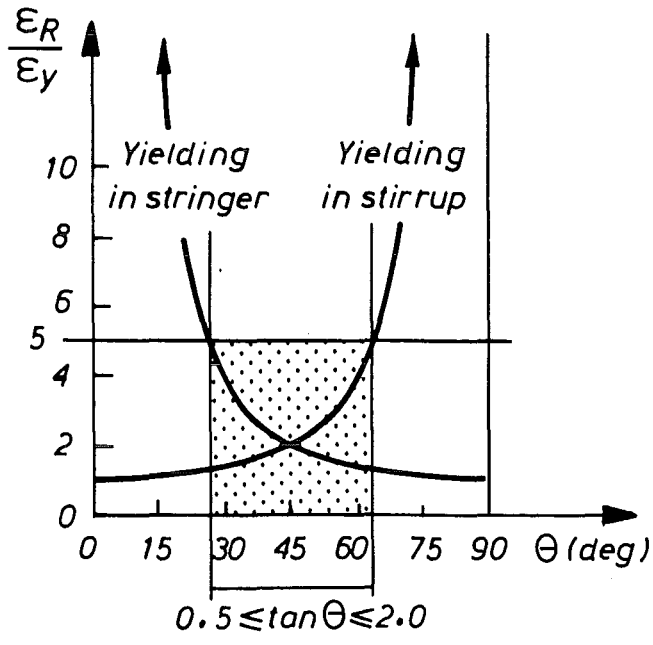

Fig. 2.10 : Stirrup and stringer strains versus diagonal strut inclination [2.61]

lower bound approach. Thürlimann, et al[2.61] arrived at the limits on angle θ by considering the deformation diagram as shown in Fig. 2.9. The concrete was assumed to be rigid and the crack opening was assumed to be normal to the crack direction. The displacement parameter, ε_R, was taken to be the mean crack width divided by the mean crack spacing. It was related to strains in the longitudinal reinforcement (ε_ℓ) and transverse reinforcement (ε_t) in the following manner,

$$\varepsilon_R \sin^2\theta = \varepsilon_\ell \tag{2.20a}$$

$$\varepsilon_R \cos^2\theta = \varepsilon_t \tag{2.20b}$$

$$\varepsilon_R = \varepsilon_\ell + \varepsilon_t \tag{2.20c}$$

The deformations illustrated in Fig. 2.9, if obtained for the ultimate stage, set the limits for the inclination of the compressive stress field as well as the crack widths. Thus, from Eq. 2.20a, at yielding of longitudinal reinforcement, i.e. $\varepsilon_\ell = \varepsilon_{y\ell}$

$$\frac{\varepsilon_R}{\varepsilon_{y\ell}} = 1 + \cot^2\theta \tag{2.21a}$$

Similarly, at yielding of transverse reinforcement, i.e. $\varepsilon_t = \varepsilon_{yt}$

$$\frac{\varepsilon_R}{\varepsilon_{yt}} = 1 + \tan^2\theta \tag{2.21b}$$

Both the last two equations are plotted in Fig. 2.10. The parameter $\varepsilon_R/\varepsilon_y$ reaches a minimum at θ = 45-deg and increase to infinity on approaching θ = 0 or 90-deg. It is understood that once the cracks start to open at an accelerated rate, the shear transfer across the cracks due to changing θ will deteriorate rapidly and further redistribution of stresses will be hindered. The limit was then chosen such that

$$0.5 \leq \tan\theta \leq 2.0$$

Fig. 2.11 illustrates how the change in angle θ influences the strain values ε_R, ε_ℓ and ε_t, and Fig. 2.12 shows a plot of the interaction diagram for the lower bound approach with zones of different mechanisms as distinguished by the limits of the angle of inclination, θ. With the lower limit of $\tan\theta = 0.5$, Eq. 2.13 gives the highest shear capacity, i.e.

$$V_p = 2 F_y \frac{jd}{s} \tag{2.22}$$

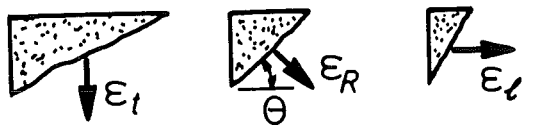

Tan θ	0.5	1	2
Long Strain $\varepsilon_\ell / \varepsilon_{y\ell}$	1	1	4
Stirrup Strain $\varepsilon_t / \varepsilon_{yt}$	4	1	1
Crack Strain $\varepsilon_R / \varepsilon_y$	5	2	5
Failure Mechanism	Shear	Combined	Bending

Fig. 2.11 : Failure mechanisms due to different diagonal strut inclinations[2.61]

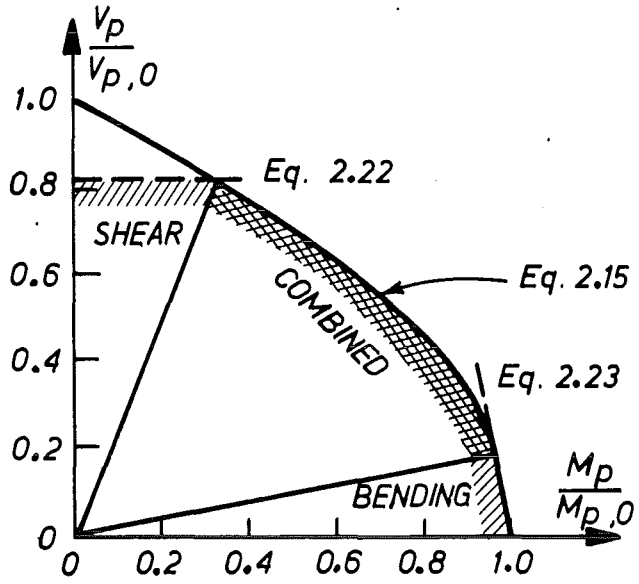

Fig. 2.12 : Interaction diagram for bending and shear

and with the upper limit of $\tan \theta = 2.0$ Eq.2.15 becomes

$$\frac{M_p}{M_{p,o}} + \frac{1}{4} \frac{V_p}{T_y} = 1 \qquad (2.23)$$

Within the two limits of θ the diagonal compressive stress does not vary significantly. It is influenced more by the shear intensity than the angle of inclination.

2.3.4 The Diagonal Compression Field Theory

Similar to the plastic models developed in Europe, Collins and his co-workers[2.70-2.78] in Toronto have put forward another variable truss model, using the so-called Diagonal Compression Field Theory. The merit of this new approach lies in its ability not only to predict the shear strength of both reinforced and prestressed concrete members with higher accuracy but also to follow the complete load-deformation response, in similar fashion to that which has been achieved in the case of bending and axial load.

This theory was derived from Wagner's concept[2.74] of 'diagonal tension field' for thin webbed metal girders with the post-buckling tension field of metal replaced by a diagonal compression field of concrete in the post-cracking state as a load carrying mechanism. The tensile strength of concrete was ignored when the theory was first proposed. The approach was, thus, named 'Diagonal Compression Field Theory'. However, it is now understood that though there are no concrete tensile stresses at cracks, the concrete between cracks will be subjected to tensile stresses as stresses from reinforcement are transferred to adjacent concrete through bond. Experimental evidence[2.76] supported this view and the theory was subsequently modified by Collins, et al to take into account of this tension stiffening effect.

The analysis is carried out using a section which is subdivided into a series of strips or laminae as shown in Fig. 2.13. Under normal loading circumstances, each layer can be treated as a plane stress-plane strain element. The loading in each element is assumed to consist of uniform normal and shear stresses and the deformation is assumed such that the edges remain straight and parallel as shown in Fig. 2.14b. Mohr's circles can then be used to depict the accompanying states of stresses and strains. Knowing any three independent variables in these circles is sufficient to define the circles and hence, allowing other values to be found. The central concept of the theory is the establishment of the relationship between the stress circle and the co-existing

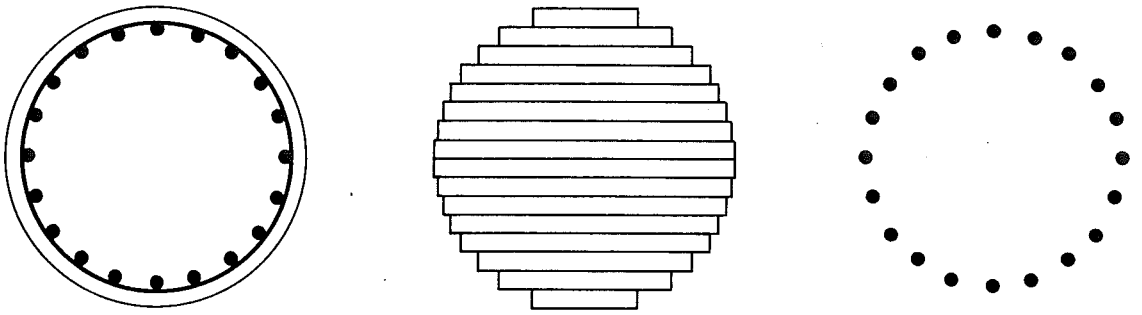

Fig. 2.13 : Discretization of member cross-section into concrete laminae and longitudinal steel elements

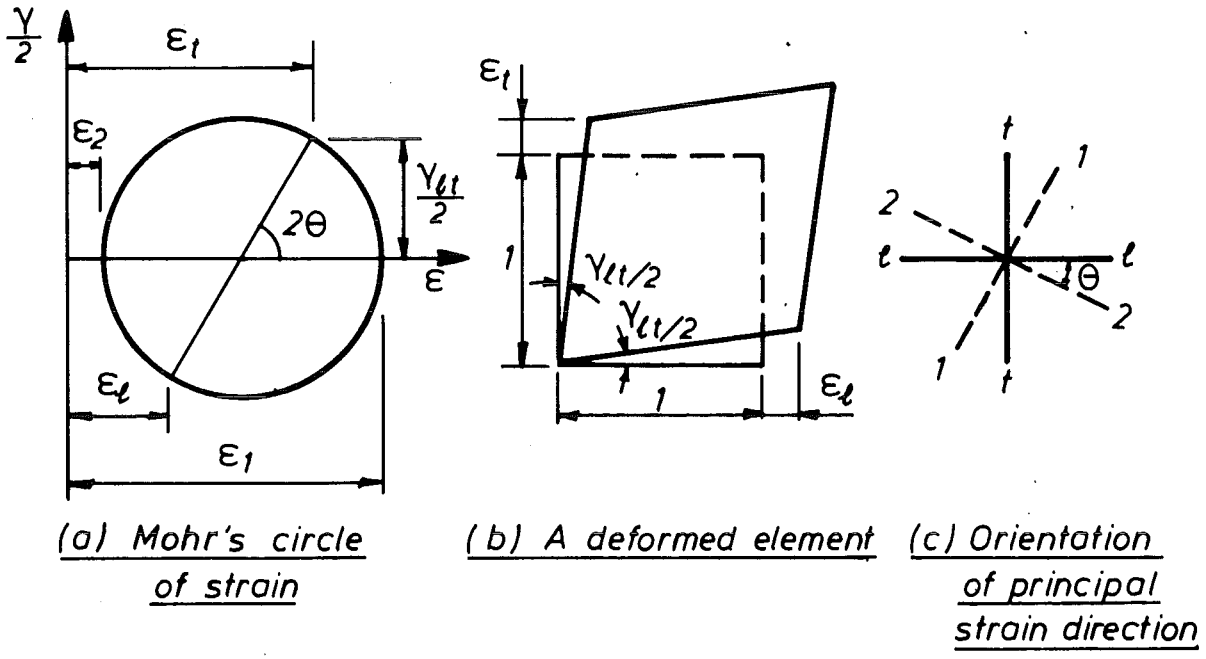

Fig. 2.14 : Strain state representation

strain circle. The fundamental assumption is that the direction of largest average compressive (or tensile) stress coincides with that of the largest compressive (or tensile) strain in the cracked concrete. In other words, the angle between any plane and either of the principal planes of the cracked concrete is the same whether the state of stresses or strains is considered. Generally, the inclination of overall principal stresses applied to the element does not coincide with the inclination of the corresponding principal strains. The term 'overall' refers to the cracked concrete together with the reinforcement.

The approach adopts a smearing procedure whereby the effect of cracks is distributed evenly within the element which, therefore, needs to be large enough to include several cracks and still representative of the particular section to be considered. Consequently, only average values of stresses and strains are of interest.

In the approach the reinforcement and the cracked concrete are treated separately. However, they are required to satisfy the compatibility requirements such that they both experience the same average strains as the overall average strains in the element. Perfect bond between concrete and reinforcement is not necessary. Local slipping at cracks can occur without violating the above compatibility conditions since only average values of strains are considered.

At element level, if any three independent strain components are known, the Mohr's circle of strains for that particular strain state is fixed and deformation in any other direction can be found from geometry. From Fig. 2.14a, the geometry of circle implies that

$$\varepsilon_\ell + \varepsilon_t = \varepsilon_1 + \varepsilon_2 \tag{2.24}$$

$$\gamma_{\ell t} = \frac{2(\varepsilon_\ell - \varepsilon_2)}{\tan\theta} \tag{2.25}$$

$$\gamma_{\ell t} = 2(\varepsilon_t - \varepsilon_2)\tan\theta \tag{2.26}$$

where θ is the inclination of the principal compressive strain, ε_2, with respect to the longitudinal direction, ε_1 is the principal tensile strain and $\gamma_{\ell t}$ is the shear strain.

By eliminating $\gamma_{\ell t}$ from Eq. 2.25 and Eq. 2.26, the following relation is obtained

$$\tan^2\theta = \frac{\varepsilon_\ell - \varepsilon_2}{\varepsilon_t - \varepsilon_2} \tag{2.27}$$

From Eq. 2.24 and Eq. 2.27, similar relations can be obtained for different combinations of strain variables, e.g.

$$\tan^2\theta = \frac{\varepsilon_1 - \varepsilon_t}{\varepsilon_1 - \varepsilon_\ell} = \frac{\varepsilon_1 - \varepsilon_t}{\varepsilon_t - \varepsilon_2} = \frac{\varepsilon_\ell - \varepsilon_2}{\varepsilon_1 - \varepsilon_\ell} \tag{2.28}$$

These expressions for $\tan^2\theta$ are the basic compatibility relationship linking the strains in the concrete, the longitudinal and the transverse reinforcement. Note that Eq. 2.21a and b used by Thürlimann to establish the limits on angle θ as discussed in Section 2.3.3(b) can be obtained if the following substitutions are made in Eq. 2.28,

$\varepsilon_1 = \varepsilon_R$ i.e. the crack inclination is in the principal strain direction.

$\varepsilon_2 = 0$ because concrete was assumed to be rigid.

$\varepsilon_\ell = \varepsilon_{y\ell}$ implies Eq. 2.21a, and

$\varepsilon_t = \varepsilon_{yt}$ implies Eq. 2.21b.

The equilibrium conditions of the corresponding stress state, as given in Fig. 2.15a are

$$f_\ell = f_{\ell c} + \rho_{s\ell}\, f_{\ell s} \tag{2.29}$$

$$f_t = f_{tc} + \rho_{st}\, f_{ts} \tag{2.30}$$

where $\rho_{s\ell} = \frac{A_{s\ell}}{A_\ell}$ and $\rho_{st} = \frac{A_{st}}{A_t}$ are the longitudinal and transverse reinforcement content respectively.

Usually the reinforcement normal to the plane is assumed to have no contribution in resisting shear stress in that plane. In the case of orthogonal reinforcement as shown in Fig. 2.15a, the concrete therefore carries the entire shear stress and the angle, θ_s', and the average shear stress in reinforcement, v_s', will be zero in Fig. 2.16 which, otherwise, represents a general situation in which θ_s' is the angle between the longitudinal reinforcement and the principal compressive stress direction.

The stress-strain relationship for reinforcing steel is well established but the actual strain distribution along the reinforcement in the concrete is unknown. For simplicity, it is assumed that the average stress is related to the average strain by the following equations:

$$f_{\ell s} = E_{s\ell}\, \varepsilon_\ell \leq f_{y\ell} \tag{2.31a}$$

$$f_{ts} = E_{st}\, \varepsilon_t \leq f_{yt} \tag{2.31b}$$

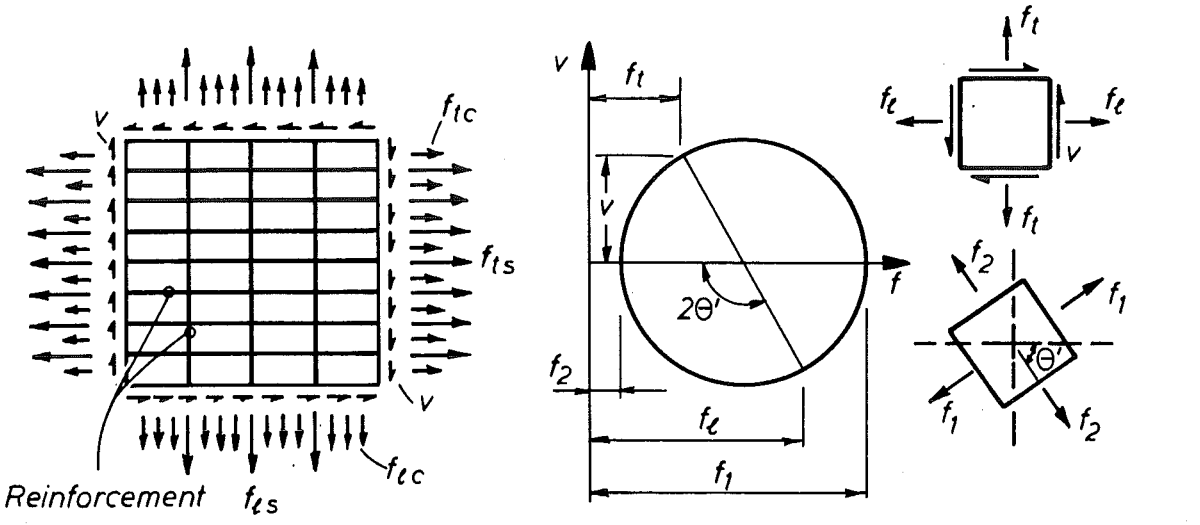

(a) Element of reinforced concrete (b) Mohr's circle of stress (c) Orientation of principal stress direction

Fig. 2.15 : Stress state representation

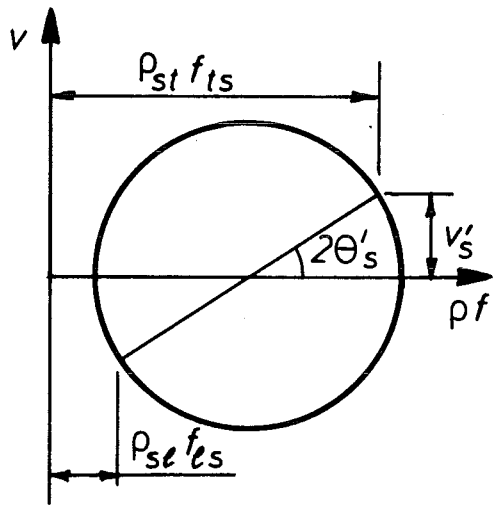

Fig. 2.16 : Stress circle for reinforcement

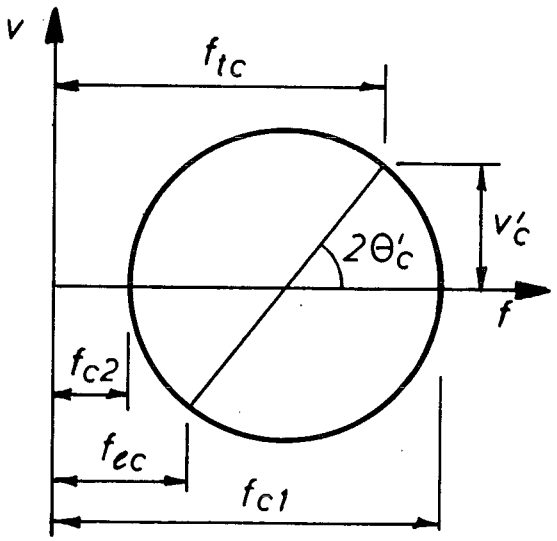

Fig. 2.17 : Stress circle for cracked concrete

With the appropriate sign convention taken into consideration, the equations are valid for both tension and compression.

Subtracting the steel stress circle (Fig. 2.16) from the overall stress circle (Fig. 2.15b) the resulting circle represents the stress state in the cracked concrete (Fig. 2.17). Typically, the angle between the longitudinal and principal stress directions in cracked concrete, θ'_c, is not equal to corresponding angle, θ', of the overall stress state. Again, from the geometry of the stress circle, some useful relationships can be extracted, such as

$$f_{\ell c} = f_{cl} - \frac{v'_c}{\tan \theta'_c} \tag{2.32}$$

$$f_{tc} = f_{cl} - v'_c \tan \theta'_c \tag{2.33}$$

$$f_{c2} = f_{cl} - v'_c \left(\tan \theta'_c + \frac{1}{\tan \theta'_c}\right) \tag{2.34}$$

in which f_{cl} and f_{c2} are the normal stresses in the two principal directions and v'_c is the shear stress in the cracked concrete. By rearranging the above equations one can obtain $\tan \theta$ as a function of stresses, for example

$$\tan \theta = \sqrt{\frac{f_{cl} - f_{tc}}{f_{tc} - f_{c2}}}$$

for $f_{cl} = 0$, $f_{c2} = -f'_c$ and $f_{tc} = -\rho_t f_{yt}$

$$\tan \theta = \sqrt{\frac{\rho_t f_{yt}}{-\rho_t f_{yt} - (-f'_c)}} = \sqrt{\frac{\rho_t f_{yt}}{f'_c - \rho_t f_{yt}}}$$

$$= \sqrt{\frac{\psi}{1 - \psi}}$$

where $$\psi = \frac{\rho_t f_{yt}}{f'_c}$$

which is the equation (Eq. 2.8) derived using the lower bound approach of the plastic analyses.

The biaxial average stress-average strain relationship of cracked concrete is not easy to model. Traditionally, the tensile strength is neglected and the stress circle is assumed to correspond to the strain circle by relating the principal compressive stress to the strength in uniaxial loading. However, experimental results have shown that the large principal tensile strain present normal to the compression field has a significant influence on the stress-strain

response of the concrete. The presence of tensile strain in particular tends to reduce the principal compressive strength. According to Collins[2.71], the strength is probably not governed by the ability of the uncracked portion of the concrete to transmit compression but rather the ability of the interface shear transfer mechanism to transmit the shear stress across existing cracks. This mode of shear transfer depends on the crack width which in turn is related to the average principal tensile strain in the concrete. From their studies, Collins and his co-workers[2.72,2.75,2.76,2.78] proposed relationships for the stress-strain behaviour of concrete which are discussed further in Chapter Six.

On the basis of the above development of the theory, all the stress parameters have been found, and they can be combined with Eq. 2.29 and Eq. 2.30 to give

$$f_{\ell} = f_{cl} - \frac{v'_c}{\tan\theta'_c} + \rho_{s\ell}\, f_{\ell s} \tag{2.35a}$$

$$f_t = f_{cl} - v'_c \tan\theta'_c + \rho_{st} f_{ts} \tag{2.36a}$$

$$v = v'_s + v'_c \tag{2.37a}$$

From the fundamental assumption, $\theta'_c = \theta$, and in the case of beams with vertical stirrups and longitudinal reinforcement, $v'_s = 0$. Therefore,

$$f_{\ell} = f_{cl} - \frac{v'_c}{\tan\theta} + \rho_{s\ell} f_{\ell s} \tag{2.35b}$$

$$f_t = f_{cl} - v'_c \tan\theta + \rho_{st} f_{ts} \tag{2.36b}$$

$$v = v'_c \tag{2.37b}$$

The equilibrium condition in the transverse direction implies $f_t = 0$ if no transverse prestress is present and the section is far away from local effect of support and load application point. Hence, from Eq. 2.36b,

$$v \tan\theta = f_{cl} + \rho_{st} f_{ts} \tag{2.36c}$$

which resembles the familiar truss equation if θ is assumed to be 45-deg and f_{cl} is taken to be zero. In fact the modified truss equation given by Eq. 2.1c is a variation of the above equation if k is taken to be $\cot\theta$ and v_c is taken to be f_{cl}. Note that the shear stress distribution across the section is assumed to be uniform in this approach.

The analytical process involves an iterative procedure whereby the solution is reached for which the strain values in each layer must satisfy the compatibility condition of Eq. 2.27 or Eq. 2.28 and the corresponding stresses, as obtained from their respective stress-strain relations, have to satisfy equilibrium requirements of Eq. 2.35a, Eq. 2.36a and Eq. 2.37a. The process is simpler in the case of axial load and shear force only. In fact, the angle θ can be obtained directly if f_{cl} is taken to be zero[2.71]. At locations where flexural stresses are significant, the procedure is not as straightforward because the variation of shear stresses over the section complicates the analysis. The iterative procedure involves a further assumption on the distribution of shear stresses which has to be checked using the method described by Collins and Vecchio[2.75,2.76,2.78]. This is also discussed further in Chapter Six.

The shear behaviour of reinforced concrete members under monotonic loading has been predicted reasonably well using this theory and design rules based on this approach have been incorporated in the new Canadian Code[2.82] as an alternative design procedure.

2.4 CONTEMPORARY DESIGN CODE APPROACHES

2.4.1 General

A number of current design codes still follow the additive principle of the modified truss analogy in the design for shear, whereby the total shear strength is taken to be the sum of 'concrete contribution' and that of transverse reinforcement assuming a 45-deg truss. The calculation of the latter component is straightforward but the former component has to be determined from semi-empirical equations. The rules stipulating the 'concrete contribution' vary among the codes and they are compared in Section 2.4.2.

Presently there is a trend towards a more rational approach with the development of plastic analyses and the Diagonal Compression Field Theory as outlined in the last two sections. Both the CEB-FIP Model Code[2.81] and the Canadian Code[2.82] adopted the variable truss model as an alternative to conventional approach. These codes allow a more liberal selection within a range of angles instead of the commonly used 45-deg. It is claimed that the new method will result in more economic design. However, since the demand on both types of reinforcement varies in opposite directions as the angle changes, an optimum angle should be chosen to achieve the desired economy[2.61,2.87].

2.4.2 The Traditional Approach

Tables 2.2a and b compare the shear provisions of various contemporary codes for non-seismic and seismic situations respectively. For simplicity, only the case of web reinforcement perpendicular to the axis of the member is considered.

The ACI design formulae[2.79] for calculating the concrete shear strength were developed semi-empirically from test results of some 194 beams in 1962[2.2]. The original form of the equations has been retained since then and the code allows the use of an approximate or a more 'exact' equation.

The ACI approach is largely followed in NZS 3101[2.80]. However, there are two major differences between the two code provisions. The use of a basic shear stress, v_b, in NZS 3101 represents a first departure from the ACI provisions. The introduction of basic shear stress is to unify the design for slender and deep reinforced concrete members and prestressed concrete members. This approach was actually a recommendation by the ACI-ASCE Committee 426 in 1979[2.80] but was not adopted by ACI 318 Committee. The equation for v_b takes into account the reduction in 'concrete contribution' due to low flexural reinforcement content that has been noted in some past research[2.86,2.88]. Secondly, NZS 3101 differentiates between the provisions within and outside the potential plastic hinge regions; the 'concrete contribution' in the plastic hinge regions is ignored unless the axial compression is greater than $0.1f'_c A_g$. Also, since the design shear force is established on the basis of capacity design principles (Chapter One), the capacity reduction factor is not used. Note that the latest ACI Building Code also specifies v_c to be zero if the factored axial compression including the earthquake effects is less than $0.05f'_c A_g$ and the earthquake induced shear force is greater than half the total design shear.

The Canadian Code[2.82] uses expressions similar to the ACI approximate equations to compute concrete shear stress while the CEB-FIP Model Code specifies the concrete shear stress in terms of concrete cube strength (f'_{cu}) as shown in Fig. 2.18. The curves are fitted by the author to the values listed in Table 2.3. In addition, the seismic design section of the CEB-FIP Model Code considers the 'concrete contribution' to be 80 percent of the non-seismic value if the axial compression is greater than $0.1f'_{cu} A_g$, otherwise the 'concrete contribution' is ignored.

Table 2.2a : Comparison Of Non-Seismic Shear Design Provisions of Different Codes

	ACI [2.79]		NZS [2.80]	CAN [2.82]	CEB-FIP [2.81]
	Approximate	More 'exact'			
v_c (flexure only)	$0.17\sqrt{f'_c}$	$0.16\sqrt{f'_c} + 17.2\rho_w \frac{V_u d}{M_u}$ $\leq 0.29\sqrt{f'_c}$ $\frac{V_u d}{M_u} \leq 1.0$	$v_b = 0.07 + 10\rho_w\sqrt{f'_c}$ $0.08\sqrt{f'_c} \leq v_b \leq 0.2\sqrt{f'_c}$	$0.2\sqrt{f'_c}$	$2.5\ \tau_{Rd}$ τ_{Rd} as given in Table 2.3
v_c (with axial tension)	zero	$0.17(1 + 0.29\frac{P_u}{A_g})\sqrt{f'_c}$ P_u is negative for tension	$(1 + 12\frac{P_u}{f'_c A_g})\ v_b$ P_u is negative for tension	$0.2\sqrt{f'_c}(1 - \frac{P_u}{P_r})$ P_u is positive for tension P_r axial tensile resistance of member ignoring any contribution of concrete (P_r may be taken as $0.6\sqrt{f'_c}\ A_g$ for simplicity)	$2.5\ \tau_{Rd}$ unless the position of N-A is outside the cross-section
v_c (with axial compression)	$0.17(1 + 0.073\frac{P_u}{A_g})\sqrt{f'_c}$	$0.16\sqrt{f'_c} + 17.2\rho_w \frac{V_u d}{M_m}$ $M_m = M_u - P_u \frac{(4h-d)}{8} > 0$ upper bound is $0.29\sqrt{f'_c}\sqrt{1 + 0.2\frac{P_u}{A_g}}$	$(1 + \frac{3P_u}{f'_c A_g})\ v_b$	$0.2\sqrt{f'_c}\ (1 + \frac{3P_u}{f'_c A_g})$	$2.5\ \tau_{Rd}\ \beta_1$ $\beta_1 = 1 + \frac{M_o}{M_u} \geq 2$ M_o = decompression moment
Maximum allowable shear stress	$v_s \leq 0.67\sqrt{f'_c}$	$v_s \leq 0.67\sqrt{f'_c}$	$v_u \leq 0.2\ f'_c$ ≤ 6 MPa	$v_u \leq 0.8\sqrt{f'_c}$	$v_u \leq 0.3\ f'_{cu}$
Minimum transverse reinforcement required	$0.35\frac{b_w s}{f_{yt}}$	$0.35\frac{b_w s}{f_{yt}}$	$0.35\frac{b_w s}{f_{yt}}$	$0.35\frac{b_w s}{f_{yt}}$	$(0.01\ f'_{cu} + 0.2)\frac{b_w s}{f_{yt}}$
Spacing limits	$s \leq d/2$ ≤ 600 mm s reduced by ½ if $v_s > 0.33\sqrt{f'_c}$	$s \leq d/2$ ≤ 600 mm s reduced by ½ if $v_s > 0.33\sqrt{f'_c}$	$s \leq d/2$ ≤ 600 mm s reduced by ½ if $v_s > 0.07\ f'_c$ $s < 0.75D$ When $P_u/A_g > 0.12\ f'_c$	$s \leq d/2$ ≤ 600 mm s reduced by ½ if $v_c > 0.4\sqrt{f'_c}$	-

Note: In all equations f'_c to be in MPa units

Table 2.2b : Comparison of Seismic Shear Design Provisions Of Different Codes

	ACI	NZS	CEB-FIP
v_c (flexure only)	-	Zero	Zero
v_c (with axial tension)	-	Zero	Zero
v_c (with axial compression)	When the earthquake induced shear force is more than half the total design shear force, $v_c = 0$ if $\frac{P_e}{f'_c A_g} < 0.05$ otherwise as for non-seismic situations	$4 v_b \sqrt{\frac{P_e}{f'_c A_g} - 0.1}$ for $\frac{P_e}{f'_c A_g} > 0.1$ otherwise zero v_b as given in Table 2.2a	For $P_e > 0.1 f'_{cu} A_g$ $2.0\ \tau_{Rd}\ \beta_1$ $\beta_1 = 1 + \frac{M_o}{M_u} \not> 2$ M_o = decompression moment τ_{Rd} as given in Table 2.3
Maximum allowable shear stress	-	For $\frac{P_e \text{ (comp)}}{f'_c A_g} \leq 0.1$ (i) if $v_u > 0.9\sqrt{f'_c}$ the entire shear is resisted by diagonal reinforcement. (ii) if $0.9\sqrt{f'_c} < v_u < 0.3(2+r)\sqrt{f'_c}$ diagonal reinforcement carries part of the shear. Otherwise the non-seismic requirements govern.	For $\frac{P_e \text{ (comp)}}{f'_{cu} A_g} \leq 0.1$ (i) if $v_u > 6(2+r)\ \tau_{Rd}$ entire shear is resisted by diagonal reinforcement. (ii) if $6(2+r)\tau_{Rd} < v_u < 3(2+r)\tau_{Rd}$ half the applied shear is carried by diagonal reinforcement. Otherwise the non-seismic requirements govern.

Note: In all equations f'_c to be in MPa units

From a large number of tests that have been conducted, the Architectural Institute of Japan (AIJ) adopted an empirical approach in determining the shear strength of reinforced concrete members. The formulae used in the AIJ Standard are modified versions of equations proposed by Ohno and Arakawa in 1960 based on test results of some 156 beam specimens[2.83,2.84]. The two commonly used equations in MKS units are,

$$v_u = (0.9 + 0.004 \frac{P_u}{A_g}) \left[\frac{0.23 k_u k_p (f'_c + 180)}{\frac{2M}{Vd} + 0.23} + 2.7\sqrt{\rho_t f_{yt}} \right] \quad (2.38)$$

and

$$v_u = \frac{0.23 k_u k_p (f'_c + 180)}{\frac{2M}{Vd} + 0.23} + 0.1 \frac{P_u}{A_g} + 2.7 \sqrt{\rho_t f_{yt}} \quad (2.39)$$

where k_u and k_p are coefficients depending on the size of member and tensile reinforcement ratio respectively. Their values are given as shown in Fig. 2.19a and b. Note that the contribution from transverse reinforcement does not appear in the usual form as in the truss analogy.

Fig. 2.20 to Fig. 2.22 compare various code equations for shear strength provided by concrete, in graphical form. The shear strength provided by concrete of the AIJ standard is taken to be that given by Eq. 2.38 and Eq. 2.39 without the term involving the contribution from transverse reinforcement, and the concrete cube strength, f'_{cu}, is assumed to be $f'_c/0.85$. The comparison is based on typical details of the specimens tested in this project and the shear strengths are normalised with respect to the square root of f'_c. The strength reduction factor is not used in these calculations. Some brief notes on the comparison are given below. The equation numbers of the codes are retained in the discussions.

(a) Only the ACI and AIJ equations consider the effect of shear-span to depth ratio but as shown in Fig. 2.20, the AIJ equation gives a more drastic variation of v_c with a/d than the ACI equation.

(b) The tensile reinforcement ratio, ρ_w, appears in three code equations compared in Fig. 2.21. In the case of NZS 3101, it was suggested[2.85] that the upper limit of $0.2\sqrt{f'_c}$ be used in seismic design of continuous beams because the flexural reinforcement content at a section would seldom be less than 1.3 percent in such situations.

(c) Most codes recognise the contribution of axial compression in increasing the concrete shear strength, and the opposite effect of axial tension. Usually the effect is allowed for by multiplying the concrete shear strength with a factor involving the axial load. The seismic shear

Table 2.3 : Design Concrete Shear Stress - CEB-FIP Model Code (MPa)

f'_{cu}	12	16	20	25	30	35	40	45	50
τ_{Rd}	0.18	0.22	0.26	0.30	0.34	0.38	0.42	0.46	0.50

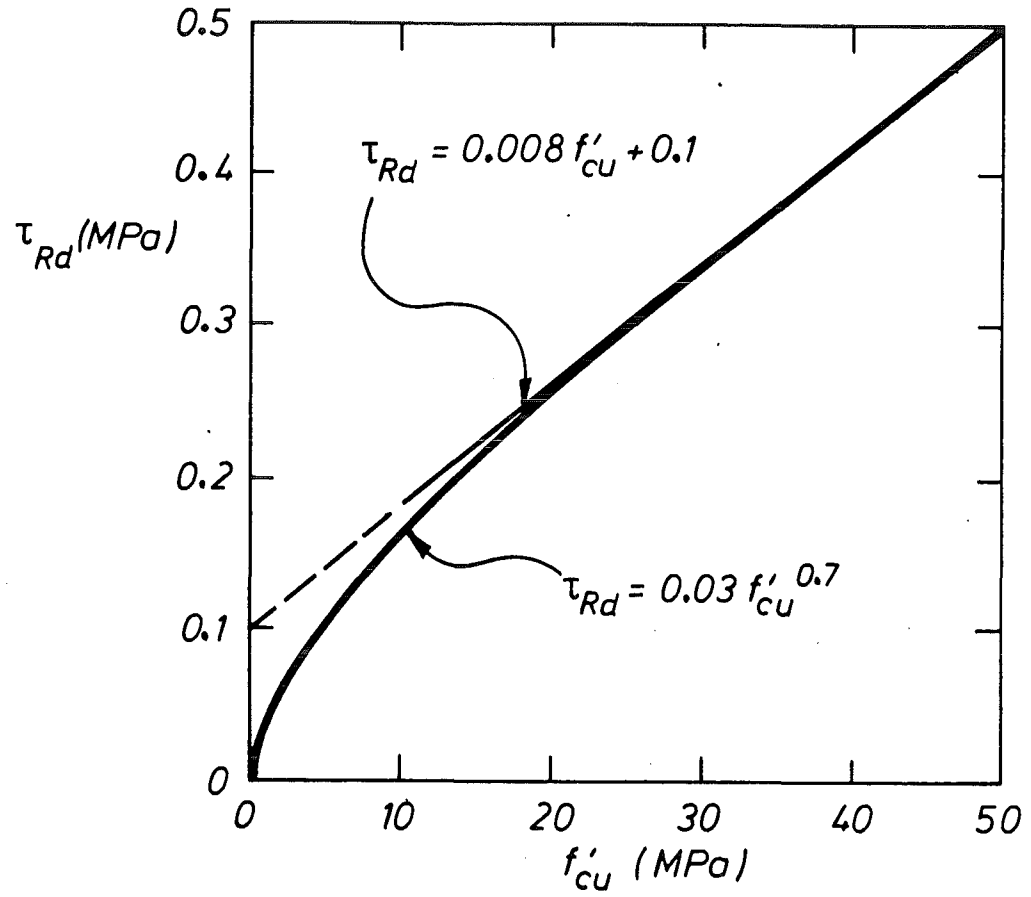

Fig. 2.18 : Design concrete shear stress - CEB-FIP Model Code [2.81]

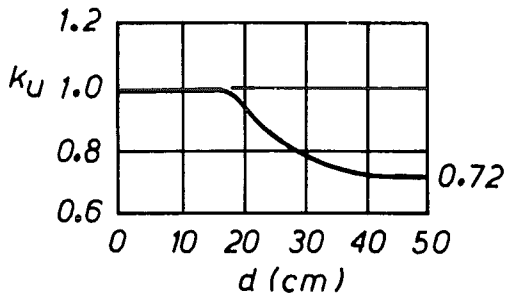

(a) k_u for size effect

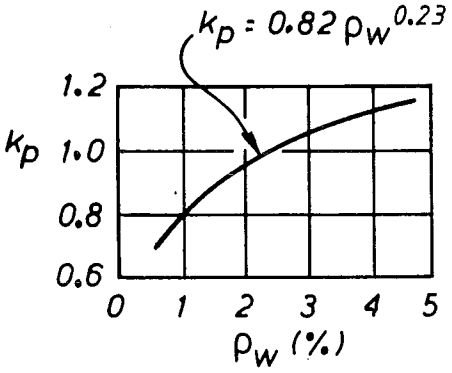

(b) k_p for different tensile reinforcement ratios

Fig. 2.19 : Multiplication factors, k_u and k_p - AIJ Standard [2.83,2.84]

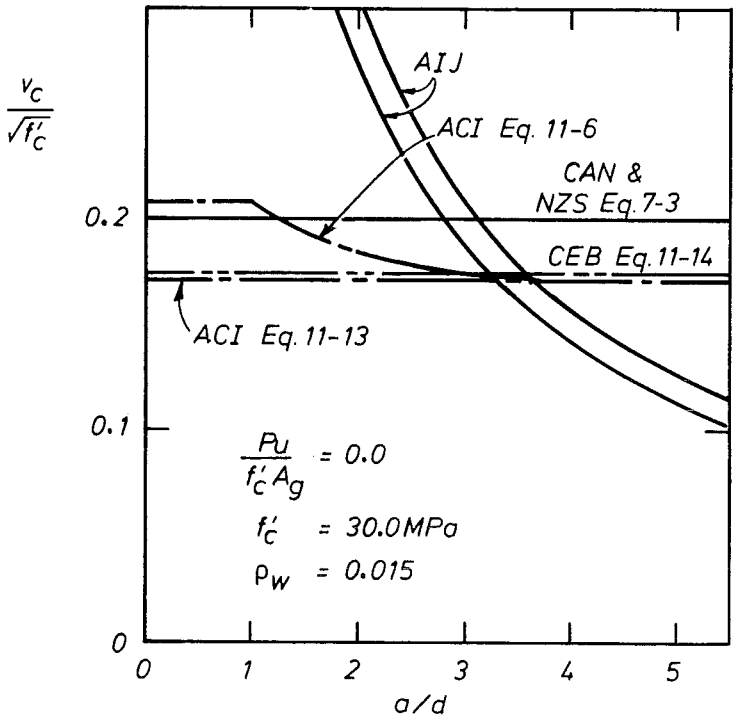

Fig. 2.20 : Variation of shear strength provided by concrete with aspect ratio in different design codes

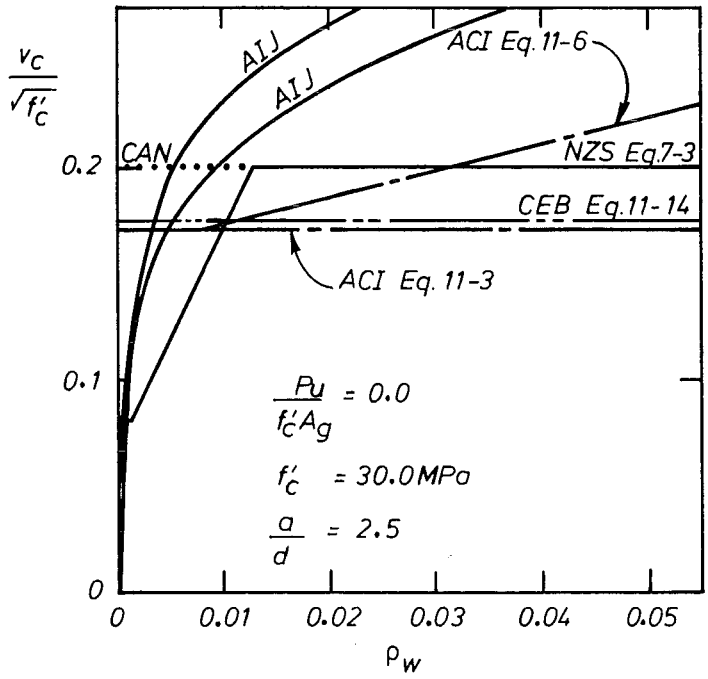

Fig. 2.21 : Variation of shear strength provided by concrete with tensile reinforcement ratios in different design codes

provision of NZS 3101 is a parabolic transition from $v_c = 0$ for an axial compression of $0.1f'_c A_g$ to the full non-seismic value at $0.4f'_c A_g$ (see Fig. 2.22). According to the ACI code, three equations are applicable in the design of members for shear with axial compression. The ACI Eq. 11-6 and Eq. 11-7 specify values for v_c that are relatively insensitive to axial load level until M_m approaches zero, whereupon v_c increases rapidly towards the limiting value set by ACI Eq. 11-8 for comparatively small change in axial compression. The differences between the two provisions is large if the axial compression is small and there is little justification for such a hyperbolic relationship between shear strength provided and axial load level.

(d) Concrete strength is another quantity found to have influence on the shear strength. In general, the code equations specify an increase in shear strength with increasing concrete strength. However, owing to its form, the NZS 3101 equation indicates a drop in seismic v_c value with increasing concrete strength at fixed axial compression as shown in Fig. 2.23. Within practical limits, the non-seismic provision specified an increase in shear strength provided by concrete with concrete strength.

(e) A minimum amount of web reinforcement is required in most codes if the design shear force exceeds half the shear strength provided by the concrete, V_c. The purpose of this provision is to restrain growth of inclined cracking and thereby increase ductility.

(f) To guard against web crushing due to diagonal compression of the truss action, an upper limit is imposed on the total shear stress or the shear carried by the web reinforcement. This upper limit on V_s is also intended to prevent unsightly inclined cracks at working loads[2.86].

(g) In NZS 3101 and CEB-FIP Model Code, the seismic design section specifies the use of diagonal reinforcement if high shear stress cannot be avoided. The primary purpose of the diagonal reinforcement is to effectively cross every potential full depth crack after the bottom and top flexural reinforcement have yielded so as to safeguard against sliding shear failure and to enhance energy dissipating capacity. The level of shear stress above which diagonal reinforcement is required in NZS 3101 is given in Table 2.2b. In members with symmetrical arrangement of flexural reinforcement the value of r may be close to -1 when the upper limit for shear stress is $0.3\sqrt{f'_c}$ when axial compression is not greater than $0.1f'_c A_g$. If the axial compression is greater than $0.1f'_c A_g$ this limit is governed by the non-seismic requirement, i.e.

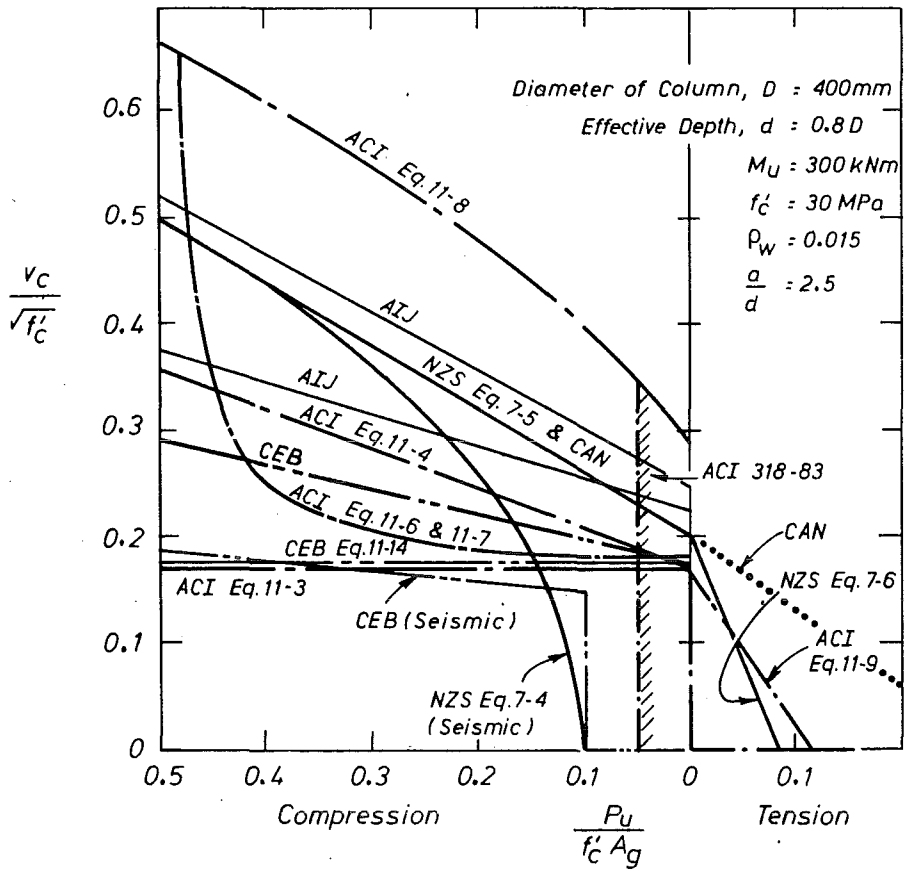

Fig. 2.22 : Variation of shear strength provided by concrete with axial load level in different design codes

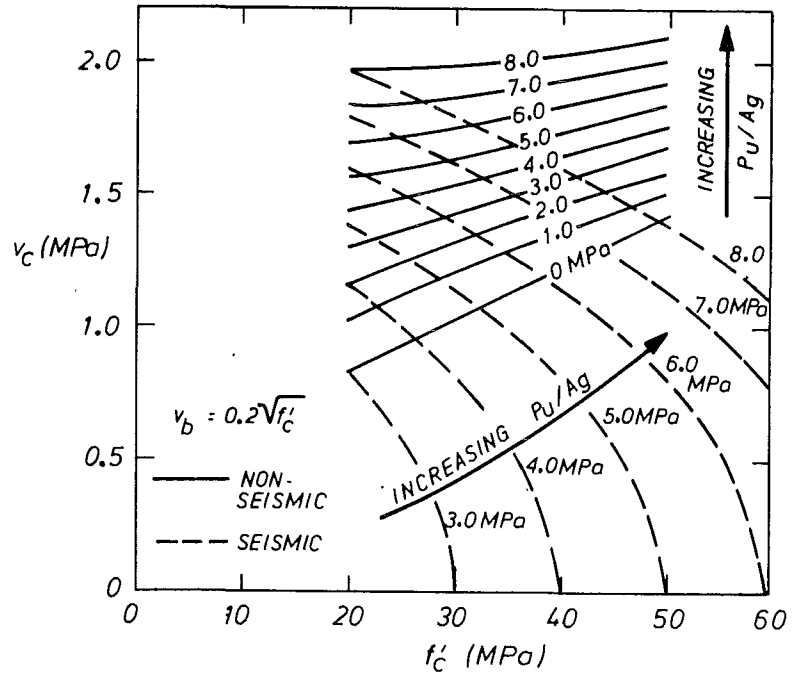

Fig. 2.23 : Variation of shear strength provided by concrete with specified concrete strength (NZS 3101)

v_u must not be greater than $0.2f'_c$ nor 6 MPa . There is a drastic increase in the limiting shear stress due to a change in axial load from $0.1f'_c A_g$ (or lower) to a higher value. There is little justification for such a big difference between the two limits especially in members with distributed flexural reinforcement. In both cases if v_u is greater than $0.9\sqrt{f'_c}$ the entire shear has to be resisted by diagonal reinforcement.

(h) The diagonal compression of the analogous truss introduces an additional force to the flexural reinforcement on top of that due to bending and axial load. Most design codes, rather than specifying the amount of additional tensile reinforcement needed to resist this increase in tension, choose to spell this out in terms of curtailment and development requirements of the longitudinal reinforcement. Usually the flexural bars are required to extend beyond the point at which they are no longer needed to resist flexure over a distance equal to the effective depth of the member.

2.4.3 The Refined Method

The Canadian Code[2.82] and CEB-FIP Model Code[2.81] include the method using a variable truss model as an alternative to the traditional design approach. The former code is mainly influenced by the Diagonal Compression Field Theory while the latter by the plastic analyses. The provisions in both codes are compared in Table 2.4. Only members with web reinforcement perpendicular to the axis of the members are considered.

A wider range of diagonal strut inclination, θ , is allowed in the Canadian Code. The range of angle in the CEB-FIP Model Code has been chosen conservatively for a few reasons. Firstly, they are chosen to ensure reasonable control of crack width under service load. Another consideration is the limited shear transfer capacity across cracks which form initially at approximately 45-deg. The restriction imposed on the choice of angle is intended to avoid the need for excessive adaptation of the internal mechanism. Finally, the strain in either of the reinforcement which yields first can be very large if the angle deviates too greatly from 45-deg. This excessive yielding of steel gives rise to large crack openings which, in turn, can lead to disintegration of interface shear transfer capacity.

Because of the conservative range of angle permitted, the CEB-FIP Model Code introduces an empirical correction term, V_c , in the calculat-

Table 2.4 : Comparison Of The Refined Method For Shear Design In The Canadian Code And CEB-FIB Model Code

	CANADIAN CODE	CEB-FIP MODEL CODE
Limits on θ	$15^{o} \leq \theta \leq 75^{o}$	$3/5 \leq \cot\theta \leq 5/3$ i.e. $30^{o} \leq \theta \leq 60^{o}$
Check for diagonal compressive stress	$f_{c2} \leq F_{c2}$ where $f_{c2} = (\tan\theta + \frac{1}{\tan\theta})\left(\frac{V_u}{b_w jd}\right)$ $F_{c2} = \frac{f'_c}{(0.8 + 170\varepsilon_1)} \leq f'_c$ $\varepsilon_1 = \varepsilon_\ell + \frac{\varepsilon_\ell + 0.002}{\tan^2\theta}$ (ε_1 may be taken as 0.002 for simplicity)	$V_u \leq V_d$ $V_d = 0.30\, f'_{cu}\, b_w d \sin 2\theta$
Design of transverse reinforcement	$V_u = \frac{A_{st} f_{yt}}{s} jd \cot\theta$ $A_{st} = \frac{V_u S}{f_{yt} jd} \tan\theta$	$V_u = \frac{A_{st} f_{yt}}{s} 0.9d \cot\theta + V_c$ $A_{st} = \frac{(V_u - V_c)\, s}{0.9 f_{yt} d} \tan\theta$ where $V_c = \frac{1}{2}(7.5\, \tau_{Rd}\, b_w d - V_u)$ $0 \leq V_c \leq 2.5\, \tau_{Rd}\, b_w d$ τ_{Rd} as given in Table 2.3 N.B. For members subjected to significant axial tension or if repeated loads of high intensity can occur, v_c is taken to be zero.
Minimum transverse reinforcement required	$0.35 \frac{b_w s}{f_{yt}}$	$(0.01 f'_{cu} + 0.2) \frac{b_w s}{f_{yt}}$
Check yielding of transverse reinforcement	$\varepsilon_t > \frac{f_{yt}}{E_{st}}$ $\varepsilon_t = \varepsilon_1 - \varepsilon_\ell - 0.002$	-
Spacing limits	$S < \frac{jd}{3} \cot\theta$ $< jd$ < 600 mm	-
Design for longitudinal reinforcement	Design for additional axial tension acting at mid-depth given by $N = V_u \cot\theta$ It may be more convenient to design only for a larger moment of $(M_u + Njd/2)$	Design for additional tensile force given by $\Delta F = \frac{V_u^2 S}{2 A_{st} f_{yt} d}$

ion of total shear strength, V_i . The value of V_c decreases linearly with the design shear force and is valid only within a narrow range of the shear force.

Both approaches assume a uniformly distributed shear stress over the effective depth and a constant angle of inclination, θ , of the principal compressive stress. The Canadian Code requires the check for the magnitude of this compressive strength explicitly. Ignoring the tensile strength of the concrete, the principal compressive stress, f_{c2} , can be derived from the Mohr's circle shown in Fig. 2.17 with $f_{c1} = 0$ and $\theta'_c = \theta$. This principal compressive stress must not exceed the diagonal crushing strength of the concrete, F_{c2} . Apart from the problems of actual distribution of the principal compressive stress, the transmission of this shear stress across cracked concrete is substantially hindered by the severely deformed concrete. An equation, relating the diagonal crushing strength of concrete to the principal tensile strain, ε_1 , was derived from test results in Ref. 2.78, and this is discussed in Chapter Six. The compatability equation involving the three strain components is obtained from Fig. 2.14a in which ε_2 is assumed to be -0.002 in the code. As θ is increased, the diagonal compressive stress, f_{c2} , due to the applied shear becomes larger and the limiting value, F_{c2} , becomes smaller.

The CEB-FIP Model Code chooses to express the check on diagonal compressive stress in terms of shear stress. From Fig. 2.3, with β = 90-deg , the diagonal compressive stress is given as follows,

$$f_{c2} = \frac{V}{b_w\, jd \sin\theta\, \cos\theta} = \frac{2V}{b_w\, jd \sin 2\theta} \qquad (2.40)$$

If $V = V_d$ of the design equation given in Table 2.4, then

$$f_{c2} = \frac{2 \times 0.3\, f'_{cu}}{j} \qquad (2.41)$$

$$= \frac{2}{3} f'_{cu} \quad \text{if} \quad j \quad \text{is taken to be 0.9.}$$

This equation implies a design ultimate compressive strength for the diagonal strut of 2/3 the concrete strength, f'_{cu} .

The design of transverse reinforcement is similar to the traditional 45-deg truss approach except that a factor of $\cot\theta$ is introduced to allow for different angles used. In the Canadian Code, a further check on the adequacy of the cross-section and reinforcement properties is required to ensure that the transverse reinforcement yields before the diagonal crushing of the concrete. This requirement limits

the maximum shear that a given cross-section can resist.

Unlike the usual approach as outlined in Section 2.4.2(h), the two codes require the flexural reinforcement to be designed for an additional force required to balance a horizontal component of the diagonal compression force. The CEB-FIP Model Code specifies an additional tensile force given by

$$\Delta F = \frac{V_u^2 \, s}{2 \, A_{st} \, f_{yt} \, d} \tag{2.42}$$

which is one half of the tensile force balancing the diagonal compression. The other half may be subtracted from the flexural compression force.

The Canadian Code requires the flexural reinforcement to be designed with the additional tensile force due to an axial force, N, acting at mid-depth and N is computed by Eq. 2.43,

$$N = V_u \cot \theta \tag{2.43}$$

Alternatively, it suggests a more convenient way to design only for a larger moment given by $(M + 0.5Njd)$ to achieve the same result. The increase in tensile force due to the additional moment of $0.5Njd$ is the same as that given explicitly in CEB-FIP Model Code.

The Canadian Code specifies different design rules for regions near discontinuities where it is inappropriate to assume that the shear stresses are uniformly distributed over the depth of the member. The same code also requires the diagonal cracking at service loads to be controlled by limiting the spacing of the reinforcement and the strain in the transverse reinforcement at service loads.

Finally, the refined method is compared with the traditional method in Fig. 2.24. The comparison is made with respect to the transverse stress at yielding of web reinforcement, $\rho_t f_{yt}$. The values for both the upper and lower bounds of the refined methods are included. The effective stress area was taken to be 80 percent of the gross area. Also included in the figure is the design proposal by Collins and Mitchell[2.74]. Among other things in their proposal, the angle θ chosen must satisfy the two conditions:

(a) To ensure that the reinforcement yields prior to crushing of concrete

$$10 + \frac{35 \left(\frac{v_i}{f'_c} \right)}{(0.42 - 50 \varepsilon_\ell)} < \theta < 80 - \frac{35 \left(\frac{v_i}{f'_c} \right)}{(0.42 - 65 \varepsilon_{yt})} \tag{2.44}$$

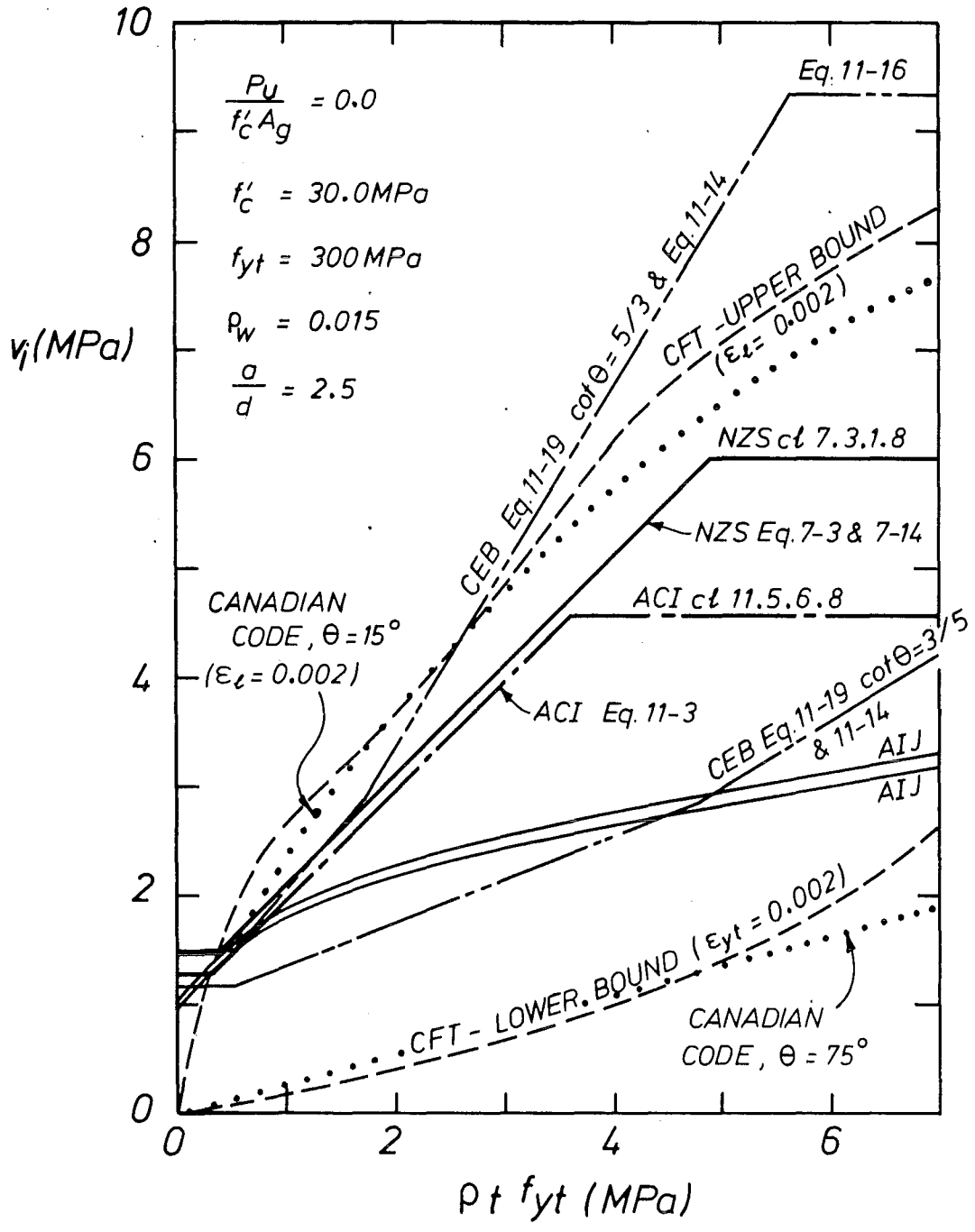

CFT : Compression Field Theory

Fig.2.24 : Comparison between the refined method and the traditional method in the prediction of shear strength

(b) To ensure that at service loads the control of diagonal cracking is adequate,

$$\tan\theta \geq \left[\frac{f_{yt}}{200}\,\frac{V_{se}}{V_i}\right]^2\left[1-\left(\frac{V_{cr}}{V_{se}}\right)^3\right]^2 \qquad (2.45)$$

where V_{cr} = cracking shear under combined loading; and

V_{se} = shear force due to service load.

The allowable range of angle θ is very wide but is reduced as the nominal shear stress, v_i, is increased.

It can be seen that the upper bound predictions of the refined method and the traditional approach give quite similar results at low shear stress levels but for members subjected to very high shear stresses there is a considerable difference between predictions. On the whole the variable truss model gives a more rational approach without introducing undue difficulty in computation.

2.4.4 Spirals As Shear Reinforcement In Circular Sections

2.4.4.1 Definition of effective area

In the previous section, reference was made to the effective area for shear, taken as $0.8A_g$. Unlike rectangular or flanged sections, the effective area of circular sections over which the concrete shear stress acts is not well-defined in the literature. According to ASCE-ACI Task Committee 426[2.3], the usual equations for rectangular sections are applicable also to circular sections if the external diameter is used for the effective depth, d, and the gross area of circular sections for the stress area, $b_w d$. In other words, the effective depth is taken as $d = D$, and the effective width is taken as $b_w = \frac{\pi}{4}D$ giving an effective area equal to $\frac{\pi}{4}D^2$. Following the CEB-FIP Model Code[2.81], Collins and Mitchell[2.74] assumed the effective area for circular section to be as shown in Fig. 2.25. However, in this case, the assumed value of b_v shown in the figure was not defined.

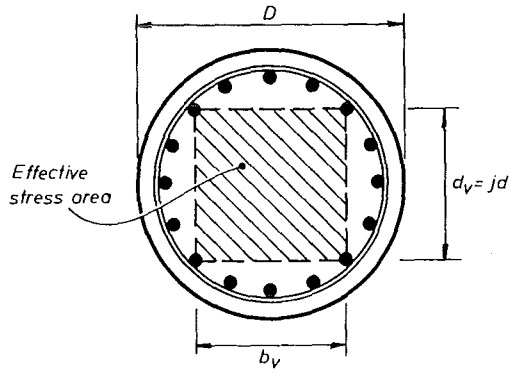

Fig. 2.25 : Effective stress area assumed by Collins and Mitchell[2.74]

In ACI 318-83[2.79] and NZS 3101[2.80], b_w is defined to be the diameter of the circular sections, D , and the effective depth, d , need not be taken as less than the distance drom the extreme compression fibre to the centroid of the longitudinal reinforcement in the opposite half of the members.

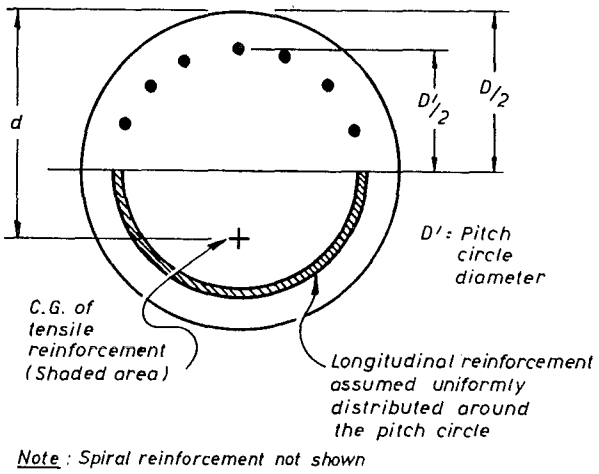

Fig. 2.26 : Definition of effective depth in ACI 318-83[2.79] and NZS 3101[2.80]

Referring to Fig. 2.26, the effective depth defined in this way is equivalent to

$$d \geq 0.5D + \frac{\int_0^{\pi} \left(\frac{D'}{2}\right) \sin\alpha \, d\alpha}{\frac{\pi D'}{2}}$$

$$= 0.5D + \frac{D'}{\pi}$$

$$\approx 0.5D + 0.318D'$$

where D' is the pitch circle diameter of longitudinal reinforcement. For large circular sections $\frac{D'}{D} \geq 0.9$ and hence the effective depth will typically be at least 78.6 percent of the overall diameter, D , so the product $b_w d$ will be no less than $0.786\,D^2$ which is about equal to the gross area $\frac{\pi D^2}{4}$. Note that $0.786\,D$ is the minimum value for d so in other situations the effective stress area, $b_w d$, will actually be greater than the gross area. However, at large shear stresses, the cover concrete may spall off and the effective stress area will be less than the gross area. In this project the effective shear area is taken to be 80 percent of the gross area, as is common practice in New Zealand bridge design, and is about equal to the core area measured to the centre-line

of spirals of the columns tested.

2.4.4.2 Shear force carried by spiral reinforcement

As discussed in Section 2.3.2 the shear carried by transverse reinforcement can be expressed in the general form

$$V_s = A_{st} f_{yt} \frac{d}{s} \cot \theta \qquad (2.46)$$

where θ is the inclination of the potential failure plane and A_{st} is the total steel area in the direction of applied shear. This equation was derived from truss model of rectangular beams with parallel legged stirrups and it is not immediately obvious that it is applicable to circular sections. Most codes, however, allow the same equation to be used in the shear design of rectangular and circular sections. In the case of circular sections, the tension is tangential to the spiral or circular hoop at the location where the inclined crack intercepts the transverse reinforcement. However, only the component of steel force parallel to the loading direction is effective in resisting the applied shear. From Fig. 2.27a, assuming all spiral reinforcement is at yield stress (f_{yt}), the component for one hoop or spiral is

$$\Delta V_s = 2A_{sp} f_{yt} \cos \alpha \qquad (2.47)$$

The angle α varies depending on where the crack crosses the spiral or circular hoop. The component force is zero when α is 90 or 270-deg and reaches a maximum at the centre-line of the members (i.e. α = 0 or 180-deg). The current practice in New Zealand is to average the value of $\cos \alpha$ over a large number of spirals using the following procedure:

$$\begin{aligned} V_s &= \sum^{n} \Delta V_s = \sum^{n} 2 A_{sp} f_{yt} \cos \alpha \\ &= 2 A_{sp} f_{yt} \sum^{n} \cos \alpha \\ &= 2 A_{sp} f_{yt} \, n \, \overline{\cos \alpha} \end{aligned} \qquad (2.48)$$

where n is the number of spirals or circular hoops crossed by the crack and is given by

$$n = \frac{d_s \cot \theta}{s} \qquad (2.49)$$

where d_s is the diameter of the spirals. $\overline{\cos \alpha}$ is the average value of $\cos \alpha$ and is taken to be

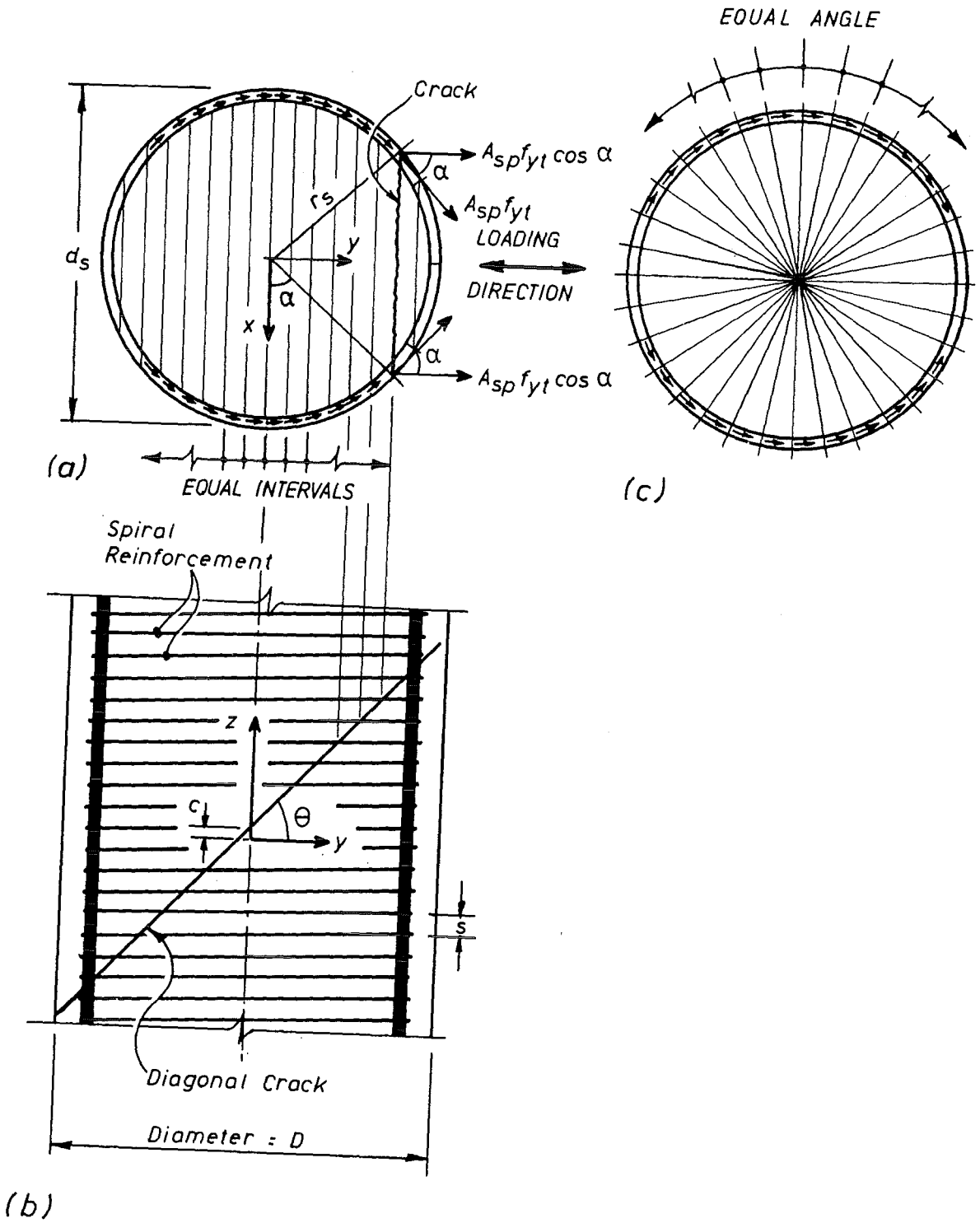

Fig. 2.27 : Spiral force components in the loading direction

$$\frac{\int_0^{\frac{\pi}{2}} \cos\alpha \, d\alpha}{\frac{\pi}{2}} = \frac{2}{\pi} \tag{2.50}$$

Combining Eqs. 2.48, 2.49 and 2.50 gives the following equation

$$V_s = \frac{4}{\pi} A_{sp} f_{yt} \frac{d_s \cot\theta}{s} \tag{2.51}$$

The averaging process using Eq. 2.50 assumes the inclined cracks intercept the spirals or circular hoops at points which subtend equal angle at the centre of the circular section as shown in Fig. 2.27c. This is however incorrect because the inclined crack actually cuts the spirals or circular hoops at equal intervals of distance along a line parallel to the loading direction, with the value depending on the crack inclination and the spiral pitch as shown in Fig. 2.27b. In this case the integration process will be as follows,

$$\overline{\cos\alpha} = \frac{1}{r} \int_0^r \cos\alpha \, dy \tag{2.52}$$

but $y = r \sin\alpha$ so $dy = r \cos\alpha \, d\alpha$

Therefore, Eq. 2.52 becomes

$$\overline{\cos\alpha} = \frac{1}{r} \int_0^{\frac{\pi}{2}} r \cos^2\alpha \, d\alpha$$

$$= \int_0^{\frac{\pi}{2}} \cos^2\alpha \, d\alpha$$

$$= \frac{\pi}{4}$$

Thus, the total shear force carried by the spirals or circular hoops is

$$V_s = \frac{\pi}{4} (2 A_{sp} f_{yt}) \frac{d_s \cot\theta}{s} \tag{2.53}$$

$$= \frac{\pi}{2} A_{sp} f_{yt} \frac{d_s \cot\theta}{s} \tag{2.53}$$

The ratio between the two V_s values given by Eqs. 2.51 and 2.53 is $\frac{8}{\pi^2} = 0.81$. The difference in the values of V_s between Eq. 2.46 (i.e. the code equation) and Eq. 2.53 is typically about 10 percent if appropriate values of d_s and d are used; for example, $d_s = 0.9D$ and $d = 0.786D$ (see Section 2.4.4.1) imply a ratio of $(4 \times 0.786/0.9\pi) = 1.11$. However, it is recommended that the more rigorous Eq. 2.53 be used because no additional computational effort is required in using the equation.

To be more accurate in calculating V_s, the spiral force components should be summed discretely instead of using the averaging process above, particularly when a large spiral pitch is used. From Fig. 2.27b the equation of spirals can be expressed vectorically as

$$\underset{\sim}{r}(\alpha) = r_s \cos\alpha \, \underset{\sim}{i} + r_s \sin\alpha \, \underset{\sim}{j} + (c + \frac{s}{2\pi}\alpha)\underset{\sim}{k} \qquad (2.54)$$

where $r_s = \frac{d_s}{2}$ is the radius of the spirals

α is the angle measured in the horizontal plane from the x-axis

c is a constant depending on the position of the inclined crack, $0 \leq c \leq s$

Also, for a given crack inclination, the equation of the crack plane shown in the same figure is

$$\frac{z}{y} = G = \cot\theta \qquad (2.55)$$

The expression for y and z from Eq. 2.54 can be substituted into Eq. 2.55 to get

$$\frac{c + \frac{s}{2\pi}\alpha}{r_s \sin\alpha} = G$$

Therefore,
$$\sin\alpha = \frac{s}{Gr_s}\frac{\alpha}{2\pi} + \frac{c}{Gr_s}$$

$$= \frac{s}{Gd_s}\frac{\alpha}{\pi} + \frac{2s}{Gd_s} \qquad (2.56)$$

Eq. 2.56 can be solved numerically by an iterative process. The values of α obtained at various points of intersection give the angles to which the spiral force, $A_{sf} f_{yt}$, has to be resolved. Hence, all the $\cos\alpha$ values can be discretely summed (i.e. $\sum \cos\alpha$) to obtain the total spiral contribution in the loading direction. A simple computer program was written to solve Eq. 2.56 a hundred times for different values of the constant c in order to get a mean value for $\sum \cos\alpha$. The calculations were carried out for different spiral spacings which were expressed as a fraction of the spiral diameter, d_s. The results are tabulated in Table 2.5 and plotted in Fig. 2.28 for two crack inclinations ($G = 1.0$ and 1.5). Depending on the crack position and inclination, the number of spirals crossed by the crack varies and hence so does the sum of the components. Within the practical range of spiral pitch, the results show that the discrete summation process outlined above gives

Table 2.5 : Discrete Summation Versus Average Value For Prediction Of Spiral Shear Force For Circular Columns

s/d_s	$\bar{x}^*$	$\frac{\pi}{2}\frac{G d_s}{s}$	(2)/(3)	$\frac{(4)}{\sqrt{1+(\frac{s}{2\pi r_s})^2}}$
(1)	(2)	(3)	(4)	(5)
0.001	1570.780	1570.796	1.00	1.00
0.01	156.989	157.080	1.00	1.00
0.1	15.443	15.708	0.98	0.98
0.2	7.498	7.854	0.95	0.95
0.3	4.839	5.236	0.92	0.92
0.4	3.462	3.927	0.88	0.87
0.5	2.636	3.142	0.84	0.83

(a) G = 1.0

s/d_s	$\bar{x}^*$	$\frac{\pi}{2}\frac{G d_s}{s}$	(2)/(3)	$\frac{(4)}{\sqrt{1+(\frac{s}{2\pi r_s})^2}}$
(1)	(2)	(3)	(4)	(5)
0.001	2356.176	2356.194	1.00	1.00
0.01	235.578	235.619	1.00	1.00
0.1	23.340	23.562	0.99	0.99
0.2	11.481	11.781	0.97	0.97
0.3	7.481	7.854	0.95	0.95
0.4	5.484	5.890	0.93	0.92
0.5	4.277	4.712	0.91	0.90

(b) G = 1.5

* $\bar{x}$ = average value of $\sum \cos \alpha$

G = cot θ, θ = crack inclination

lower values of V_s than that given by the averaging process of Eq. 2.53. The ratio of the former to the latter decreases as the spiral pitch increases and the discrepenacy between the two values is greater if the value of G (i.e. cot θ) is smaller.

Referring to Eq. 2.54 again, differentiating with respect to α yields

$$\dot{\underset{\sim}{r}}(\alpha) = - r_s \sin\alpha \, \underset{\sim}{i} + r_s \cos\alpha \, \underset{\sim}{j} + \frac{s}{2\pi} \underset{\sim}{k} \qquad (2.57a)$$

Therefore, the unit tangent vector is

$$\frac{\dot{\underset{\sim}{r}}(\alpha)}{|\dot{\underset{\sim}{r}}|} = \frac{-r_s \sin\alpha \, \underset{\sim}{i} + r_s \cos\alpha \, \underset{\sim}{j} + \frac{s}{2\pi} \underset{\sim}{k}}{\sqrt{r_s^2 + (\frac{s}{2\pi})^2}} \qquad (2.57b)$$

Hence, a mathematically more accurate expression for the component of spiral force in the loading direction (i.e. along the y-axis) including the influence of spiral force inclination to the horizontal plane resulting from the pitch of spirals is

$$\Delta V_s = \frac{r_s \cos\alpha}{\sqrt{r_s^2 + (\frac{s}{2\pi})^2}} A_{sp} f_{yt}$$

$$= \frac{\cos\alpha}{\sqrt{1 + (\frac{s}{2\pi r_s})^2}} A_{sp} f_{yt}$$

$$= \frac{\cos\alpha}{\sqrt{1 + (\frac{s}{\pi d_s})^2}} A_{sp} f_{yt} \qquad (2.58)$$

Since d_s and s are fixed for a particular spiral arrangement, the coefficient is constant and can be included later after the summation process. Unlike circular hoops, the spirals do not remain in the x-y plane so this factor is actually to allow for the angle in the vertical direction. For a spiral pitch of one half the spiral diameter (or $\frac{1}{2}$ x 0.9D = 0.45D) this factor is 0.988 so the influence of this factor on the spiral shear force is negligible. In this project Eq. 2.53 is used to calculate the spiral shear force because in actual design situations the use of the discrete summation is not practical. The error is typically less than 10% for common ratios of $\frac{s}{d_s}$. Moreover, as will be shown in Chapter Four, analysis of experimental results based on the overestimation of V_s in Eq. 2.53 results in a conservative estimate of other shear resisting mechanisms - the so-called 'concrete contribution'.

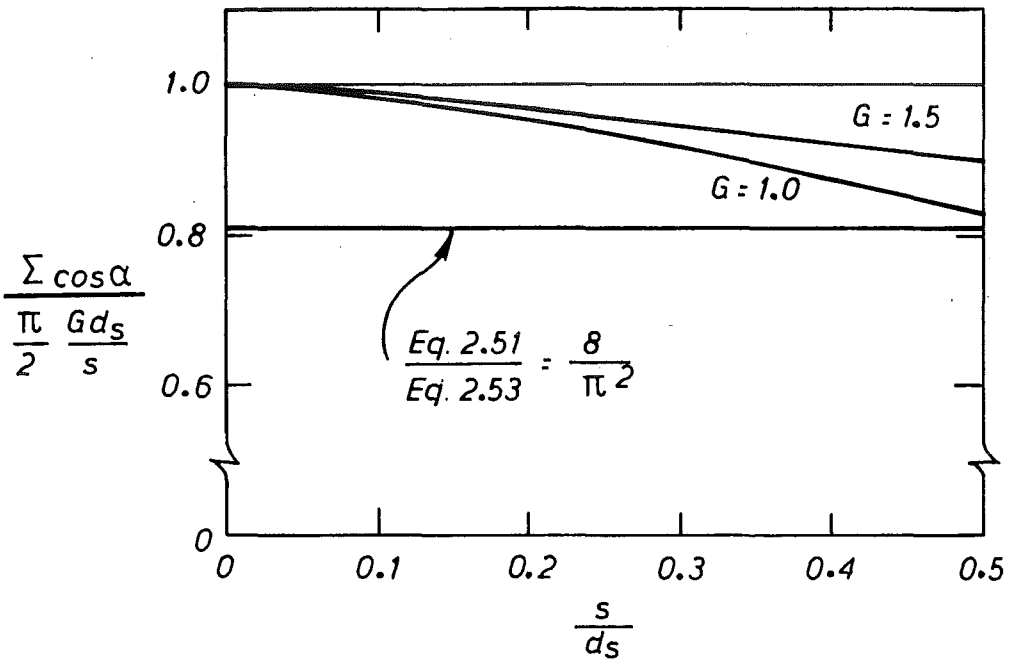

Fig. 2.28 : Comparison between the results of the averaging and discrete summation processes

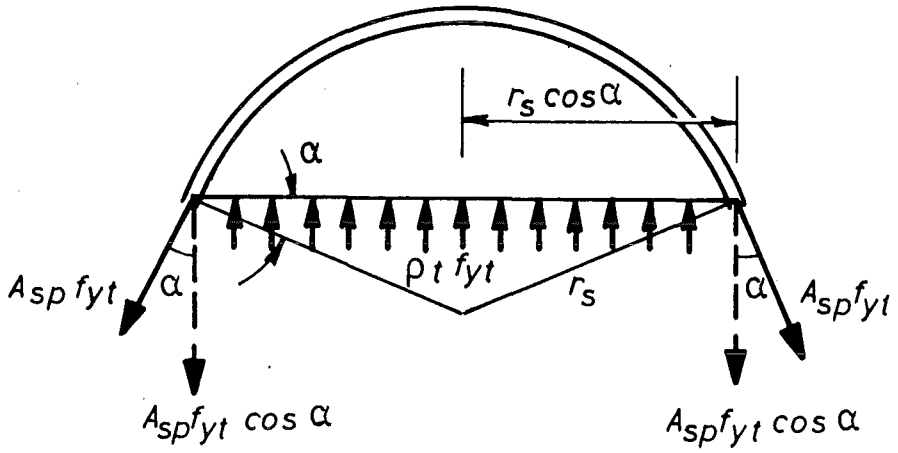

Fig. 2.29 : Equivalent spiral stress for circular section

Finally, in some codes[2.79], the shear strengths are sometimes specified in terms of shear stresses and the equivalent shear stress of transverse reinforcement is usually given as

$$v_s = \rho_t f_{yt} \tag{2.59}$$

where $\rho_t = \frac{A_{st}}{b_w s}$ for parallel legged stirrups perpendicular to the axis of the member. In the case of members with transverse spiral reinforcement, the term ρ_t is not well-defined. Referring to Fig. 2.29, assuming that the spiral shear force gives rise to a uniform equivalent stress, then

$$\begin{aligned} v_s &= \frac{2 A_{sp} f_{yt} \cos\alpha}{2 r_s \cos\alpha \; s} \\ &= \frac{2 A_{sp} f_{yt}}{d_s s} \\ &= \frac{1}{2}\left[\frac{4 A_{sp}}{d_s s}\right] f_{yt} \\ &= \frac{1}{2} \rho_s f_{yt} \\ &= \rho_t f_{yt} , \end{aligned} \tag{2.60}$$

if ρ_t is taken to be one-half the volumetric spiral reinforcement content, ρ_s. The values of ρ_t used in analyses in later chapters are based on this approach.

2.5 CONCLUSIONS

From a brief review of related experimental work on the shear behaviour of reinforced concrete members, it was found that the research on shear strength of circular reinforced concrete columns with transverse spiral reinforcement is very limited. The work in this area under seismic situations is practically non-existent. The shear provisions in most of the contemporary design codes were derived from test results of rectangular sections with parallel legged stirrups, and concentrated top and bottom layers of flexural reinforcement. Hence, the applicability of these code provisions to the case of circular sections with spiral reinforcement and distributed flexural rebars is

not immediately obvious. Moreover, most of the work considered only monotonic loading and as such, extrapolation of the results to seismic situations was approached in the codes with caution and tended to be unduly conservative. From the theoretical consideration, and also past experimental evidence, it appears that the variable truss model adopted in the 'Diagonal Compression Field Theory' and plastic analyses may be a better and more rational approach than the traditional 45-deg truss analogy. The approach has been accepted as an alternative to the conventional design approach, and has been included in some of the codes examined in this chapter.

Chapter Three

— STATIC TESTS OF CIRCULAR COLUMNS — DESIGN, CONSTRUCTION AND TESTING PROCESSES

3.1 INTRODUCTION

The experimental programme of the project was divided into two stages. In the initial stage, cantilever column models were subjected to slow cyclic loading with gradually increasing displacement limits to simulate earthquake loadings. This stage involved twenty-five column units, which were tested in three batches over a period of eighteen months. The aim of these preliminary tests was to gain some insight into the behaviour of columns dominated by shear and to establish the influence of various parameters. The conclusion drawn from these static tests were then examined in dynamic tests on a shake-table in the second stage of the project. This chapter describes the design, construction and experimental processes of the static tests, while the following chapter deals with the evaluation of the results from these tests.

3.2 DESIGN CONSIDERATIONS

3.2.1 Parameters To Be Studied

The main parameters studied in static tests included the aspect ratio ($\frac{M}{VD}$) , the relative axial load level ($\frac{P_i}{f'_c A_g}$) and the volumetric spiral reinforcement content ($\rho_s = \frac{4 A_{sp}}{d_s s}$) .

The main aspect ratios used were 1.5, 2.0, 2.5, with Unit 20 being the only exception with $\frac{M}{VD} = 1.75$. The variation was achieved by using different loading heights (i.e. ℓ = 600, 800, 1000 mm respectively) while keeping the overall diameter of column, D , constant at 400 mm. The section diameter was considered to represent a model scale of about 1/5 to 2/5, while the low aspect ratios allowed realistic proportioning of shear and longitudinal reinforcement to be adopted to obtain a shear failure mode.

Three levels of axial compression ($\frac{P_i}{f'_c A_g}$ = 0, 0.1, 0.2) were used in the investigation. Because of limitations of the lateral loading capacity, the axial load level on Unit 20 had to be reduced to 0.175 during testing. The axial load level was chosen not be be greater than 0.2 because above this value the confinement requirements of

NZS 3101 [3.1] rather than the shear requirements are likely to govern the amount of transverse reinforcement required unless shear stresses are very high. This is illustrated in Fig. 3.1 which compares confinement and shear requirements for potential plastic hinge regions of columns designed to NZS 3101. In Fig. 3.1, the straight line represents the confinement requirements of NZS 3101 as given by Eq. 3.5. This equation prevails over Eq. 3.4 in the design of confinement reinforcement if the cover concrete is less than 5.6 percent of the column diameter. In practice Eq. 3.5 is applicable to large diameter columns or bridge piers typically with a diameter of 700 mm or more. For $\frac{P_i}{f'_c A_g} < 0.1$ the shear strength provided by concrete is taken to be zero (see Table 2.2b) so the spiral reinforcement has to carry the entire shear. This, in turn, sets the upper limit for spiral reinforcement content, ρ_s, which is determined by assuming a 45-deg failure plane. The demand on the spiral reinforcement to participate in resisting the applied shear decreases as the axial compression increases beyond $0.1f'_c A_g$. This is because the code allows increase in shear strength provided by concrete for high axial compression levels. Consequently, the higher the axial compression the less likely is the design of spiral reinforcement governed by shear unless the shear stress is unusually high.

The influence of spiral reinforcement was studied by either varying the spiral pitch (s) and bar diameter (d_b) while maintaining a constant ρ_s or the spiral pitch was changed to obtain different values of ρ_s. For simplicity, the spiral pitch was kept constant over the entire height of the columns, rather than increasing the pitch outside the potential plastic hinge region.

It was assumed that the influence of the above three parameters would be the most significant. The details of the column units are listed in Table 3.1. Note that the longitudinal reinforcement detail is different in Units 2, 14, 15 and 25. Grade 275 steel was used instead of Grade 380 steel for Units 2 and 25. In Unit 14, nine 24 mm diameter bars, giving the same flexural reinforcement content as the other column units, were used. In Unit 15 the twelve 16 mm diameter bars give only 60 percent of the flexural reinforcement content of the other column units.

3.2.2 The Design Of Column Units

Fig. 3.2 gives the overall dimensions of the column units of this test series. These dimensions were chosen to suit the loading system, the

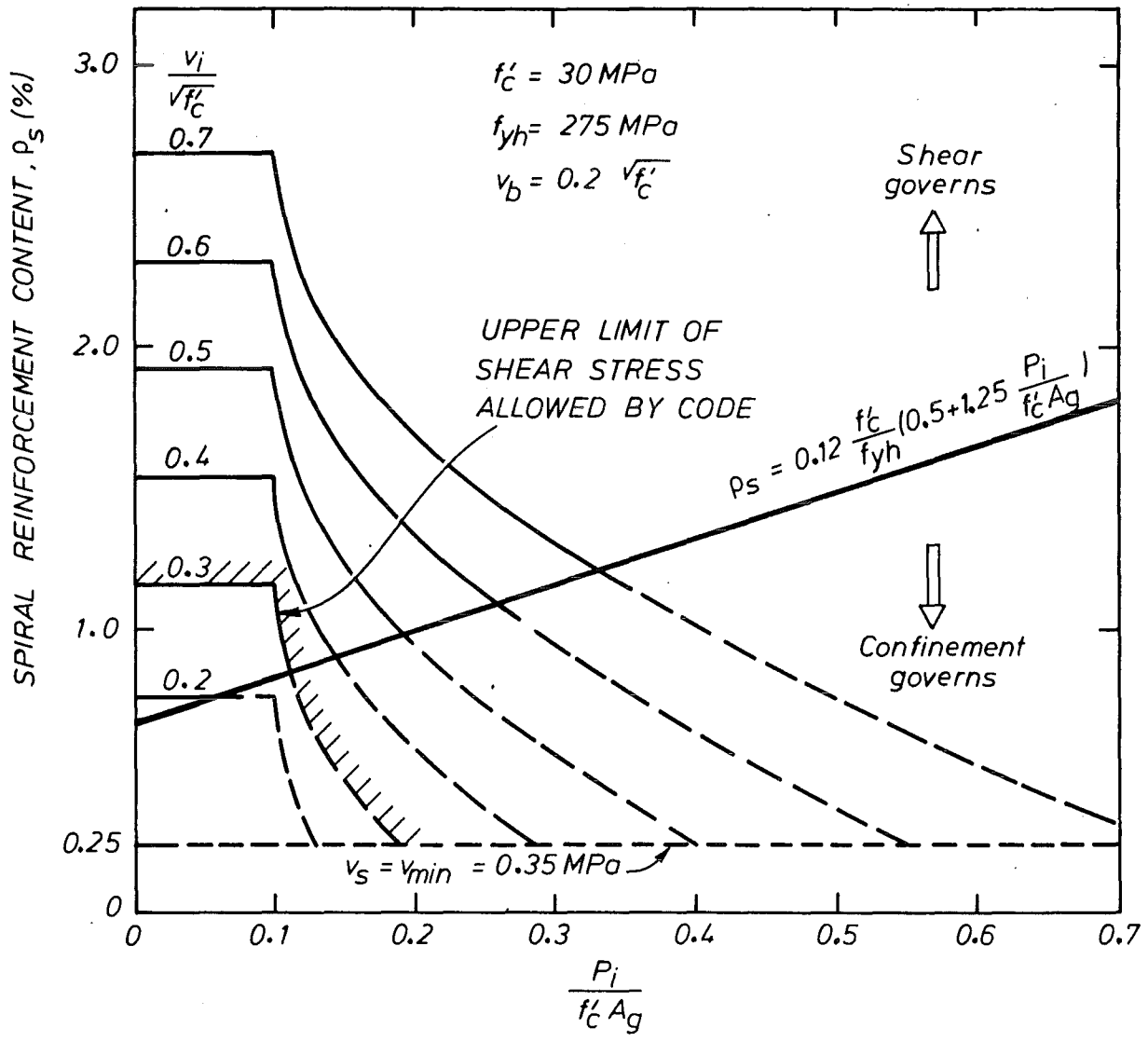

Fig. 3.1 : Comparison between shear and confinement requirements for large circular columns designed to NZS 3101 [3.1]

Table 3.1 : Reinforcing Details Of Column Units

Unit	Aspect ratio $\frac{M}{VD}$	$\frac{P_i}{f'_c A_g}$	Transverse * Reinforcement			Longitudinal Reinforcement	
			d_b (mm)	s (mm)	$\rho_s (\times 10^{-3})$	Quantity	ρ_ℓ
1	2.0	0	6	60	5.094	20-HD16	0.0320
2	2.0	0	6	60	5.094	20-D16	0.0320
3	2.5	0	6	60	5.094	20-HD16	0.0320
4	2.0	0	10	165	5.146	20-HD16	0.0320
5	2.0	0	6	40	7.642	20-HD16	0.0320
6	1.5	0	6	60	5.094	20-HD16	0.0320
7	2.0	0	6	80	3.821	20-HD16	0.0320
8	2.0	0.2	6	30	10.189	20-HD16	0.0320
9	2.5	0.2	6	30	10.189	20-HD16	0.0320
10	2.0	0.2	12	120	10.189	20-HD16	0.0320
11	2.0	0.2	6	60	5.094	20-HD16	0.0320
12	1.5	0.1	6	30	10.189	20-HD16	0.0320
13	2.0	0.1	6	30	10.189	20-HD16	0.0320
14	2.0	0	6	60	5.094	9-HD24	0.0324
15	2.0	0	6	60	5.094	12-HD16	0.0192
16	2.0	0.1	6	60	5.094	20-HD16	0.0320
17	2.5	0.1	6	60	5.094	20-HD16	0.0320
18	1.5	0.1	6	60	5.094	20-HD16	0.0320
19	1.5	0.1	6	80	3.821	20-HD16	0.0320
20	1.75	0.175	6	80	3.821	20-HD16	0.0320
21	2.0	0	6	80	3.821	20-HD16	0.0320
22	2.0	0	10	220	3.859	20-HD16	0.0320
23	2.0	0	12	160	7.642	20-HD16	0.0320
24	2.0	0	10	110	7.719	20-HD16	0.0320
25	1.5	0	-	-	-	20-D16	0.0320

D16 = 16 mm Grade 275 Deformed bar

HD16 = 16 mm Grade 380 Deformed bar

HD24 = 24 mm Grade 280 Deformed bar

* Plain round bars, such as R6, were used

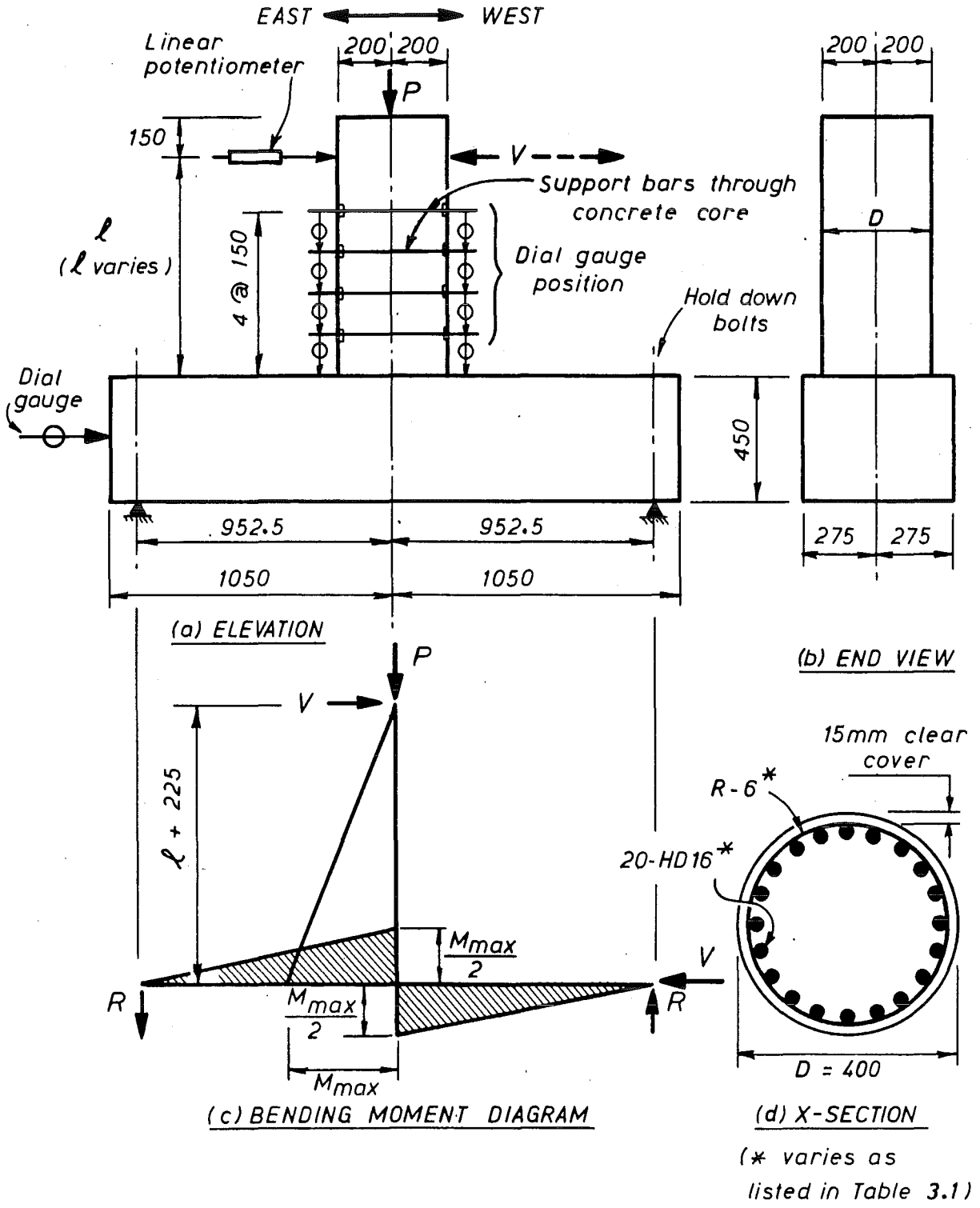

Fig. 3.2 : Details of column units

jack capacity and the layout of the laboratory strong floor. The support beams were designed by conservative capacity design principles to ensure that they would suffer negligible damage during the test. Hence, more than sufficient reinforcement was provided, especially in the joint area. Also, higher concrete strength (f'_c = 35 MPa) was specified for the concrete used in the support beams.

The support beams were held down at both ends giving rise to the bending moments shown in Fig. 3.2(c). Fig. 3.3b shows a typical beam reinforcement arrangement. Reinforcement details in general were similar in all twenty-five column units; only minor adjustment in the joint reinforcement details was needed to satisfy the different levels of axial load used.

Shear reinforcement for the columns was deliberately chosen to force the columns to show a shear dominated behaviour. The basic criterion was to provide less spiral reinforcement than that required by code to resist the shear force developed at ideal flexural strength, V_{if}. Table 3.2 lists the ideal shear strength calculated using the design approach of NZS 3101, based on

$$v_{iv} = v_s + v_c \tag{3.1}$$

The above equation gives the strengths in terms of stresses but, for purpose of comparison, shear forces in kilonewtons (kN) were used. Hence,

$$V_{iv} = V_s + V_c \tag{3.2}$$

where $V_c = 0.8A_g v_c$

A_g = gross concrete cross-sectional area

and the NZS 3101 equations used in computing the value of v_c are as given in Table 2.2.

V_s in Table 3.2 was calculated assuming a 45-deg potential failure plane. The equation used is

$$V_s = \frac{\pi}{2} A_{sp} f_{yt} \frac{d_s}{s} \tag{3.3}$$

The derivation of the above equation was discussed in Chapter Two.

Also listed in Table 3.2 is the shear stress corresponding to the development of ideal flexural strength v_{if} normalised with respect to the square root of the actual concrete strength in MPa. As discussed in Section 2.4.2(g), the upper limit of shear stress allowed in NZS 3101 is $0.3\sqrt{f'_c}$ if the axial compression is not greater than $0.1 f'_c A_g$,

Table 3.2 : Flexural And Shear Strengths Of Column Units Based On Actual Material Properties

Unit	V_s (kN)	V_c (kN)		V_{iv} (kN)		M_i (kNm)	V_{if} (kN)	$\frac{v_{if}}{\sqrt{f'_c}}$	V^o_{if}
		Non-seismic	Seismic	Non-Seismic	Seismic				
1	88	123	0	211	88	245	306	0.50	373
2	88	123	0	211	88	176	220	0.36	239
3	88	121	0	209	88	242	242	0.40	295
4	85	111	0	196	85	239	299	0.54	364
5	131	112	0	243	131	241	301	0.54	366
6	88	110	0	198	88	241	402	0.73	489
7	74	109	0	183	74	234	293	0.54	357
8	198	172	136	370	334	285	356	0.66	433
9	198	176	139	374	337	281	281	0.51	342
10	176	180	142	356	318	288	360	0.64	438
11	100	176	139	276	239	281	351	0.64	427
12	175	140	0	315	175	262	437	0.81	532
13	174	157	0	331	174	290	363	0.60	442
14	86	117	0	203	86	243	304	0.52	370
15	86	98	0	184	86	163	204	0.34	248
16	86	151	0	237	86	276	345	0.59	420
17	86	153	0	239	86	281	281	0.48	342
18	86	155	0	241	86	277	462	0.78	562
19	65	153	0	218	65	281	468	0.79	569
20	65	186	133	251	198	334	477	0.78	581
21	65	116	0	181	65	250	313	0.54	381
22	62	112	0	174	62	235	294	0.53	358
23	124	114	0	238	124	236	295	0.52	359
24	125	116	0	241	125	244	305	0.53	371
25	-	112	0	112	0	178	297	0.52	323

f'_c as given in Table 3.4

$V^o_{if} = 1.4\ V_{if}/1.15$

$= 1.22\ V_{if}$

unless diagonal reinforcement is provided to carry part of the applied shear. However, as can be seen in Table 3.2, for all column units with an axial compression of $0.1f'_c A_g$ or without axial compression this upper limit specified in NZS 3101 is exceeded even if only ideal flexural strength is considered.

The flexural strengths given in Table 3.2 were based on actual material properties measured and calculated using the design charts of New Zealand Concrete Design Handbook [3.2] with the strength reduction factor, ϕ, set equal to unity. Intermediate values were determined by linear interpolation. In NZS 3101, the probable strength of member is suggested to be 1.15 times the ideal strength while the overstrength is 1.40 times the ideal strength for members reinforced with Grade 380 steel. As the actual material properties were used in the calculations, the flexural strengths listed in Table 3.2 are the probable strengths of the column units and hence the corresponding ideal strengths are $\frac{V_{if}}{1.15}$ and the overstrengths, V^o_{if}, are $\frac{1.4\ V_{if}}{1.15} = 1.22\ V_{if}$. Note that though the values were computed using actual material properties, the terms V_{iv} and V_{if} are referred to as ideal shear and flexural strengths respectively in the thesis. The overstrengths calculated in this manner are also listed in Table 3.2 and as can be seen from the tabulated values, except for Unit 9, the design of all the other column units violated the capacity design principle. The ideal shear strength provided is less than the shear corresponding with the anticipated flexural overstrength of the column units. Unit 9 was the only column with the ideal seismic shear strength matching the flexural overstrength.

To complete the column design, the seismic provisions for confinement of the potential plastic hinge region had to be checked. Accordingly the confinement requirements of NZS 3101 are

$$\rho_s = 0.45 \left(\frac{A_g}{A_c} - 1 \right) \frac{f'_c}{f_{yh}} \left(0.5 + 1.25 \frac{P_i}{f'_c A_g}\right) \qquad (3.4)$$

or

$$\rho_s = 0.12 \frac{f'_c}{f_{yh}} \left(0.5 + 1.25 \frac{P_i}{f'_c A_g}\right) \qquad (3.5)$$

where

$$\rho_s = \frac{4\ A_{sp}}{d_s\ s} \qquad (3.6)$$

The greater of the two ρ_s values must be provided in the potential plastic regions. However, in order to achieve shear failure in these tests, this requirement was not rigidly adhered to. Similarly, the spacing restrictions of the code on transverse reinforcement were not followed strictly either.

3.3 PREPARATION OF COLUMN UNITS

3.3.1 Mould Construction

As the specified concrete strength for support beams was different from that of columns, the two components had to be cast separately. Except for Unit 25, all the support beams were cast in sets of three as shown in Fig. 3.3a. Sides and base of the moulds shown in the figure were made from plywood with a thickness of 20 mm.

Because the casting of columns was not dependent on the wooden moulds, they could be cast in any number. However, a minimum of three columns was considered to be necessary to ensure an economic pour and enough quantity of concrete to achieve reasonably uniform strength. The circular form for the columns was obtained using a flexible sheet metal mould made from 2 mm thick stainless steel rolled to the required diameter and rivetted together with sufficient overlap to ensure adequate strength. A steel annular plate serving as the bar anchorage also served to position the mould at the top. The diameter of the columns was kept uniform as far as possible by positioning two external wooden rings along their heights; one at the base and the other at about mid-height.

3.3.2 Fabrication Of Reinforcing Cages

The support beam reinforcing cage was fabricated first and the vertical column bars were then tied to the completed cage. All the column bars were provided with a 90-deg hook at the end where they were embedded in the beam. The top ends were welded to an annular steel plate to ensure adequate anchorage. A typical joint detail in the support beam showing how the column bars were anchored is as shown in Fig. 3.3b. Enough spirals were provided to hold the column bars in place; with only one or two turns emerging above the beam surface. This was to facilitate the application of 'Febol' concrete retarding agent and chipping and wire-brushing of the beam-column interface to create a good bonding construction joint.

After the support beams were cast and roughening of beam-column interface was done, the spirals were placed and tied to the vertical column bars. The spirals were joined with single V flare weld over a lap length of 150 mm. Strain gauging (described in Section 3.4.2) was carried out after the cage was completed. The vertical column bars were welded to the top face of the steel annular plate only after the mould was placed in position. The excess length of bars was then cut off with a gas torch.

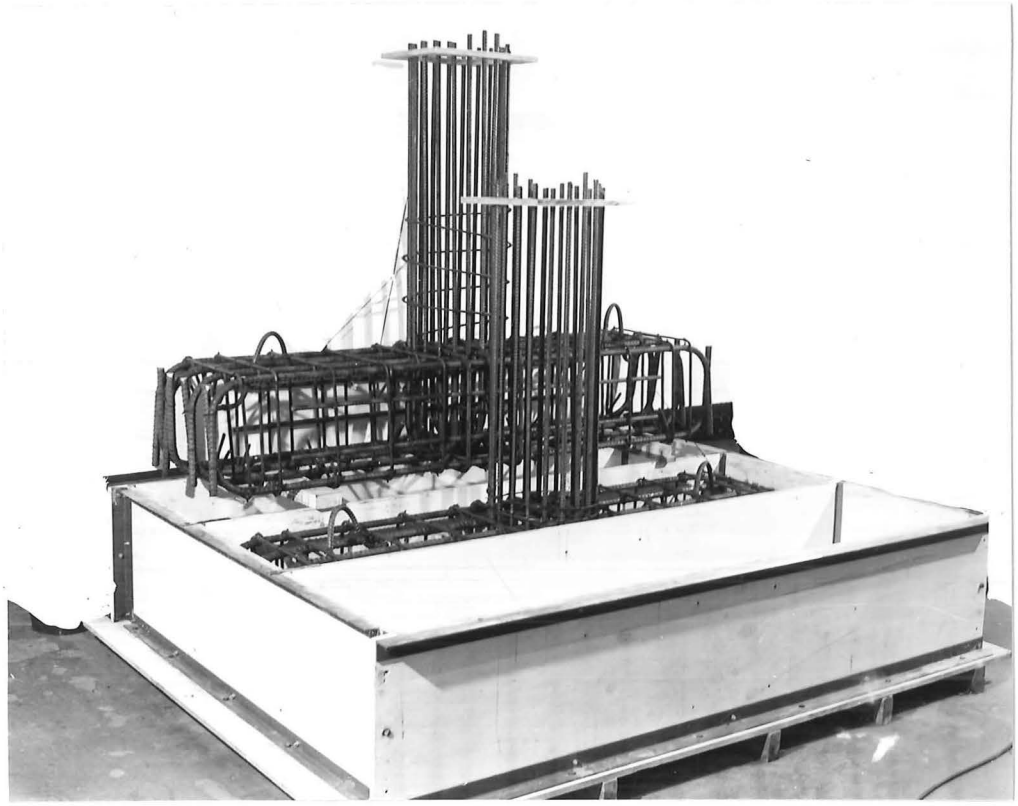

(a) Beam reinforcement and mould

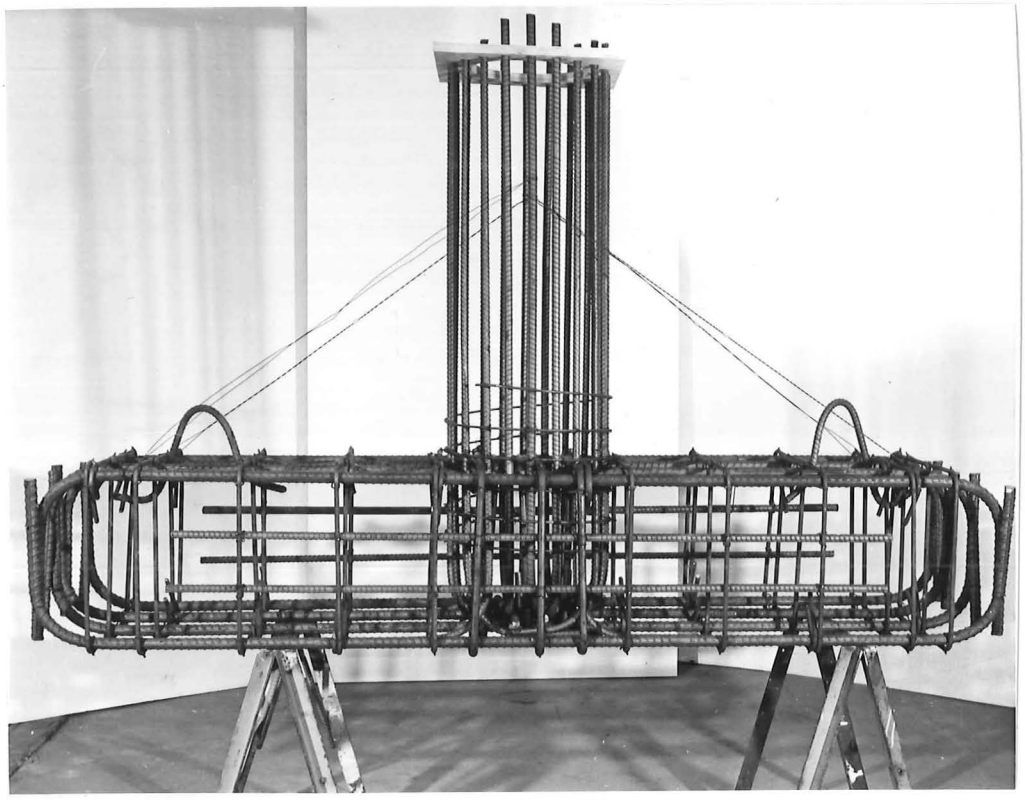

(b) Beam reinforcement

Fig. 3.3 : Beam reinforcement details

3.3.3 Placing Of Concrete

Just prior to placing the concrete, any gap along joining edges of the wooden moulds was sealed with water-proofing tape and the moulds were then given a thin coat of oil to assist stripping of formwork after curing. When casting the column, the gaps due to irregularities of beam-column interface were sealed with expendite sealing compound.

All the columns were cast in a vertical position and support beams were cast horizontally. Placing of concrete in support beams was simultaneously done in the three adjacent moulds. The concrete was compacted using an internal vibrator. After the moulds were full, the top was screeded to remove any excess concrete and then floated. To eliminate blow holes when casting the columns, the top steel plate was lightly tapped to remove any air bubbles which might have been trapped underneath.

After initial set of the concrete, the support beams or the columns were covered with damp sacks and plastic sheeting for at least a week before stripping the formwork. All column units were then given a coat of white paint to facilitate crack identification during testing.

Before every pour, a slump test was carried out to check against the value specified. Three concrete cylinders for each column unit were also taken for later determination of concrete strength.

3.3.4 Material Properties

All the reinforcing bars were bent to the required shape by a commercial steel fabricator. Except for Units 2 and 25, the specified yield strength for the longitudinal reinforcement was 380 MPa. Longitudinal reinforcement for Units 2 and 25 and all the transverse reinforcement had a specified yield strength of 275 MPa. Deformed bars were used for flexural reinforcement and plain bars for transverse reinforcement. Coupons of these bars were tested in an Avery Universal Testing Machine to determine the strength properties of the steel. Figs. 3.4a to d give the stress-strain curves of the steel used for the column units. Note that there is no obvious difference in the ratios of actual yield strength to the specified yield strength (which are listed in Table 3.3) between Grade 275 and Grade 380 steel. An average value of 1.18 was obtained for all the steel used.

The concrete was supplied by a ready mix plant. The target concrete properties specified were as follows:

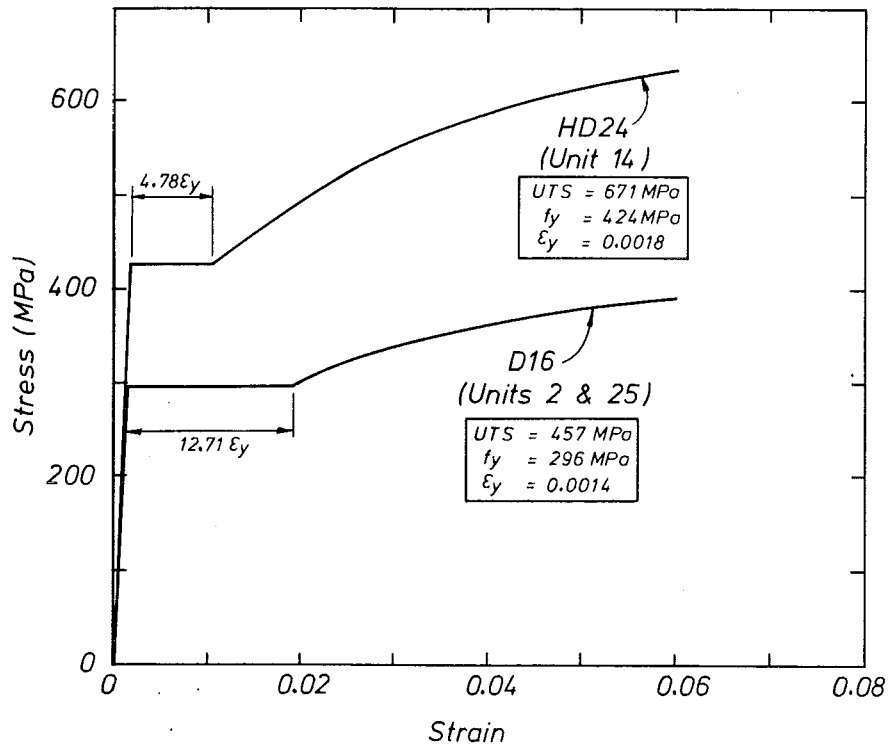

(a) Longitudinal reinforcement

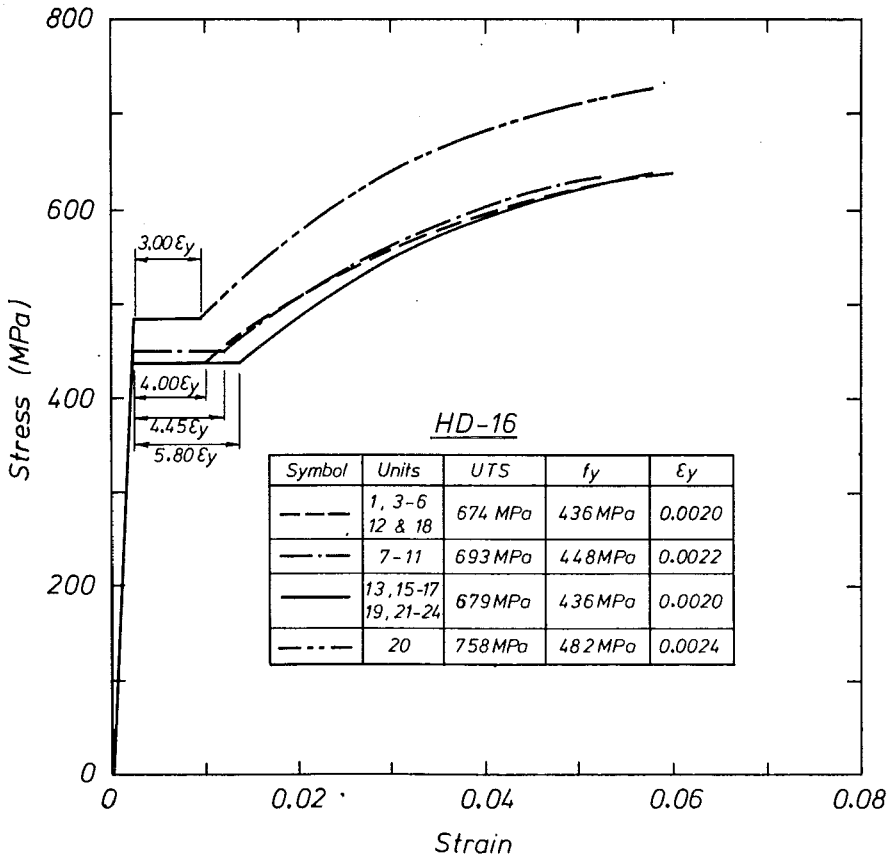

(b) Longitudinal reinforcement

Fig. 3.4 : Stress-strain curves for reinforcing steel

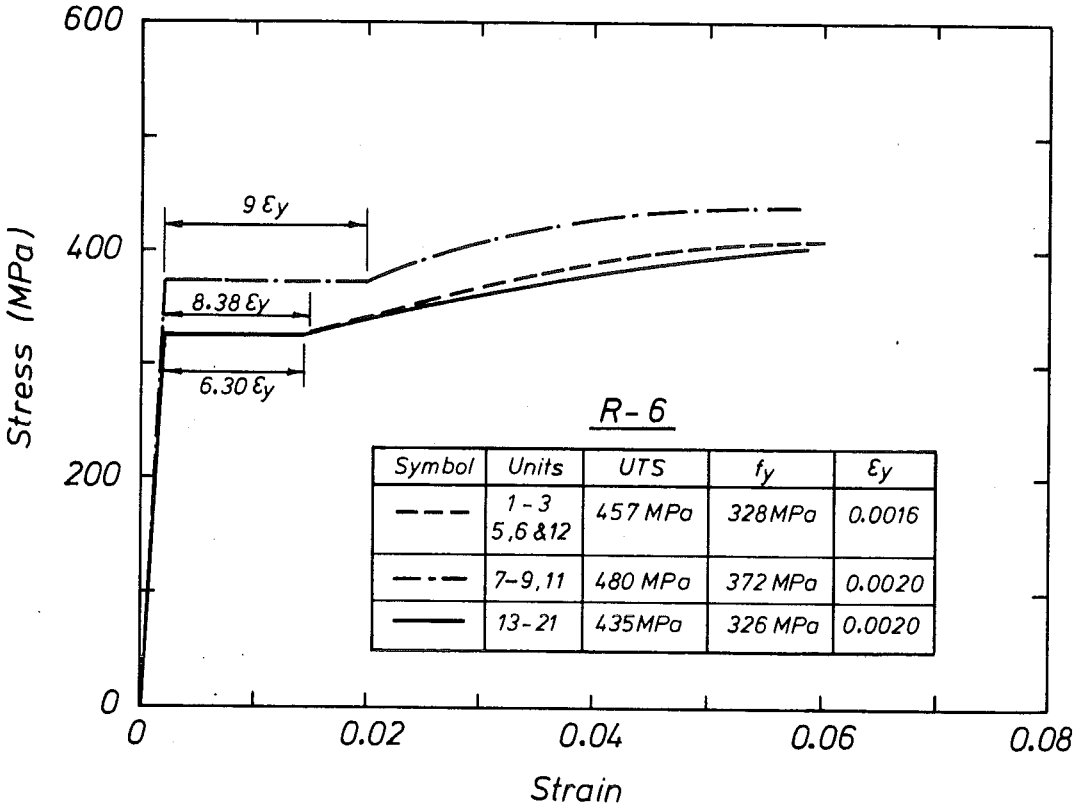

(c) Transverse reinforcement

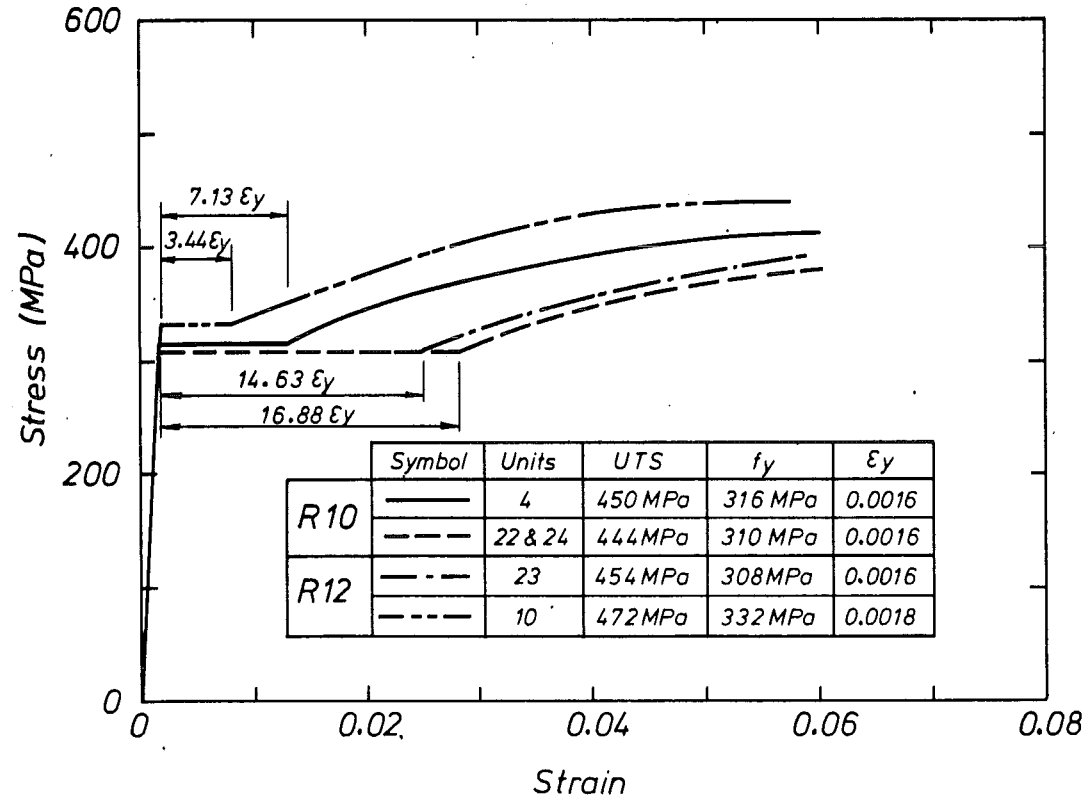

(d) Transverse reinforcement

Fig. 3.4 (Contd.) : Stress-strain curves for reinforcing steel

Table 3.3 : Material Properties - Reinforcing Steel

Bar Designation	Yield Strength (MPa)	Yield Strain ($\times 10^{-6}$)	Strain at Strain Hardening ($\times 10^{-6}$)	UTS (MPa)	Units*	Measured f_y / Specified f_y
R6	328	1600	15000	457	1-3,5,6 & 12	1.19
	372	2000	20000	480	7-9, 11	1.35
	326	2000	14600	435	13-21	1.19
R10	316	1600	13000	450	4	1.15
	310	1600	28600	444	22 & 24	1.13
R12	332	1800	8000	472	10	1.21
	308	1600	25000	454	23	1.12
D16	296	1400	19200	445	2 & 25	1.08
HD16	436	2000	10000	674	1,3-6,12 & 18	1.15
	448	2200	12000	693	7 - 11	1.18
	436	2000	13600	679	13,15-17,19, 21-24	1.15
	482	2400	9600	758	20	1.27
HD24	424	1800	10400	671	14	1.12
					Ave	1.18
					σ	0.07

* Units using the particular steel listed

UTS = Ultimate Tensile Strength of steel

Maximum aggregate size = 20 mm

Slump = 75 mm

Concrete strength at 28 day = 30 MPa for columns

= 35 MPa for support beams.

At the start of every test, the concrete cylinders were crushed to determine the actual concrete compressive strength at the time of testing. The values obtained are listed in Table 3.4.

3.4 INSTRUMENTATION

3.4.1 Load Application and Measurement

The simulated lateral seismic load was applied through an MTS (204.81 model) hydraulic jack connected to a loading 'collar' via a 40 mm pin. The double acting MTS hydraulic jack was operated by a servo-hydraulic closed-loop control system and had a force capacity of approximately 500 kN, and a maximum stroke of 150 mm. Maximum velocity of ram operation (64 mm/s) was controlled by the size of the pumping unit. The load was monitored by a strain-gauged load-cell between the jack and the test column. The load-cell was calibrated in an Avery Universal Testing Machine before the tests.

A Simplex 100 Ton single acting jack was used to provide the required constant axial compression to column units subjected to axial load. A pressure gauge used to measure this compression was calibrated beforehand.

An existing reaction frame (Fig. 3.5a and b) was used to resist lateral load from the MTS jack. To avoid loading through a pin positioned within the columns, a loading 'collar' was designed to fit the columns as shown in Fig. 3.5b. The 'collar' was held by means of a steel wedge which was, in turn, bolted to the 'collar' as a safety precaution. Clamps were used to drive the wedge into position before the bolts in the slotted holes were tightened to secure the wedge.

The hydraulic jack providing the axial compression reacted against a cross-beam and four tensioning rods. The jack was plastered to the top of the columns and held down with four bolts into the 'Terrier' concrete inserts provided. The steel cross-beam was fitted with a matching scalloped plate and supported against the cylindrical roller bearing on top of the jack to allow for any rotation that might occur. The rods were anchored to two steel beams at the base of the support beam. The steel beams had clearance holes and were fitted with spherical washers to accommodate the rotation. The concrete and steel contacting surfaces

Table 3.4 : Material Properties - Concrete

Unit	Concrete Strength, f'_c (MPa)	
	Beam	Column
1	39.1	37.5
2	41.3	37.2
3	38.6	36.0
4	35.9	30.6
5	36.5	31.1
6	36.5	30.1
7	31.3	29.5
8	34.4	28.7
9	38.0	29.9
10	38.1	31.2
11	35.8	29.9
12	32.1	28.6
13	43.7	36.2
14	49.7	33.7
15	39.9	34.8
16	51.4	33.4
17	44.8	34.3
18	42.2	35.0
19	43.0	34.4
20	43.6	36.7
21	41.9	33.2
22	37.7	30.9
23	44.1	32.3
24	44.6	33.1
25	31.2	32.8
	Average:	32.8
	Standard Deviation : σ	2.7

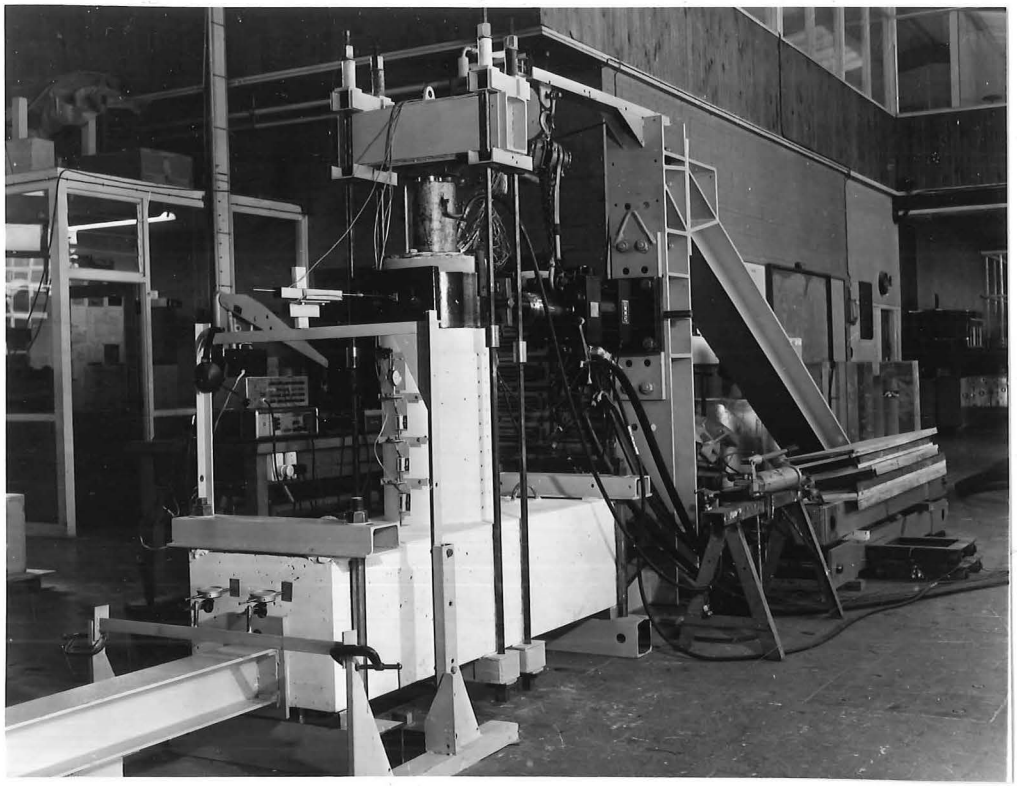

(a) Oblique View

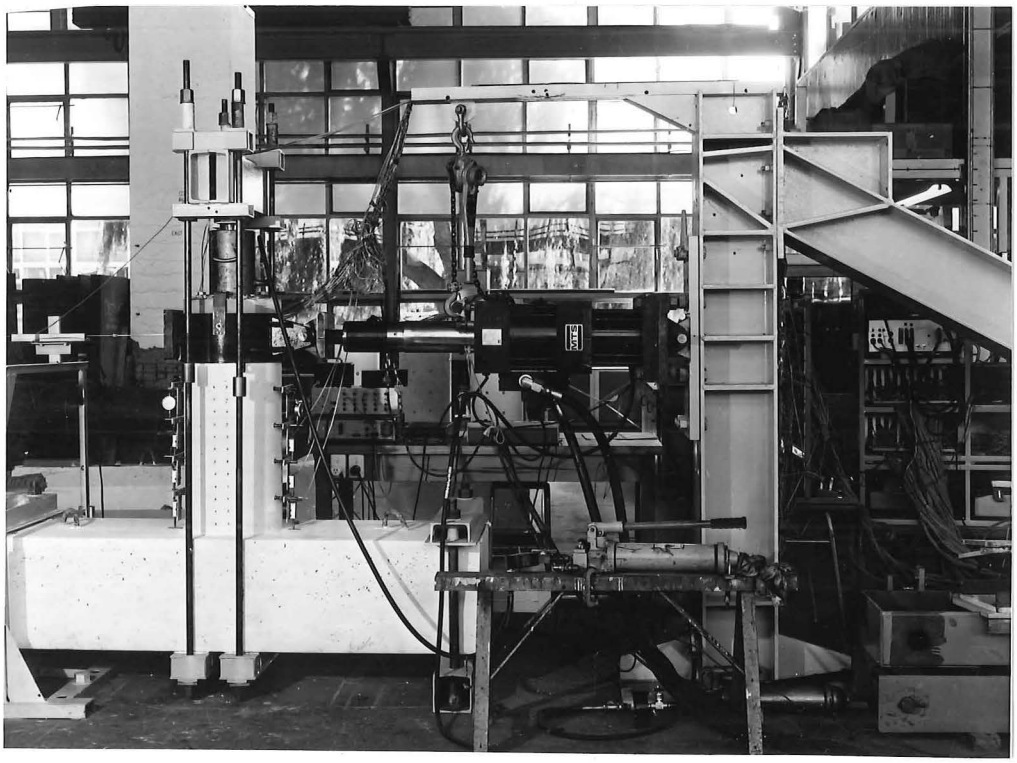

(b) Side view

Fig. 3.5 : Reaction frame and test set-up

were separated by a small steel plate plastered to the concrete to avoid crushing the concrete corners.

3.4.2 Strain Gauges

Strain gauges were mounted on the reinforcing bars using normal procedures. All gauges were 5 mm electric resistance strain gauges of type Kyowa-5-Cl-11 and were used together with Showa SFG-ST self-adhesive terminal strips. Care was taken to ensure adequate water-proofing (with Shinkoh SN/4) for optimum performance of the gauges.

For the first six column units, the strain gauges were positioned following a likely 45-deg crack pattern in both loading directions. However, after this first batch of testing, it was apparent that a steeper crack inclination was possible. The pattern for the remaining column units was then changed to follow an inclination of about 35-deg with respect to the column axis as shown for a typical column unit in Fig. 3.6. Spirals at both the north and south faces of the columns were strain-gauged but those within the beams were not. For a typical column unit with a spiral pitch of 60 mm, the number of gauges used was about 40 and this number varied according to the spiral pitch.

3.4.3 Displacement Transducers

A 30LP200 Sakae linear potentiometer having a resistance of 10 KΩ was used to measure displacement of the columns. The total range of travel was 200 mm with a sensitivity of 0.04 mm. The potentiometer was set close to its mid-travel initially and positioned at the same level as the line of application of the lateral load (see Fig. 3.2). Because of small horizontal movement of the beams on their supports, the readings from this potentiometer gave only the overall displacement of the column. In order to obtain the actual displacement, the movement of the support beam was monitored independently by a pair of horizontal displacement transducers made up of either dial gauges or linear potentiometers at the mid-depth of the beam (see Fig. 3.2). This displacement was subtracted from the potentiometer readings to give the true column displacement.

3.4.4 Rotation and Curvature Measurement

Steel rods cast in the core along the loading axis provided the anchorage for the transducers used for curvature measurement. The spacing of these rods was intended to be 150 mm as shown in Fig. 3.2 but sometimes this desired spacing was slightly altered to avoid the spirals. These rods were internally threaded at both ends for the mounting of

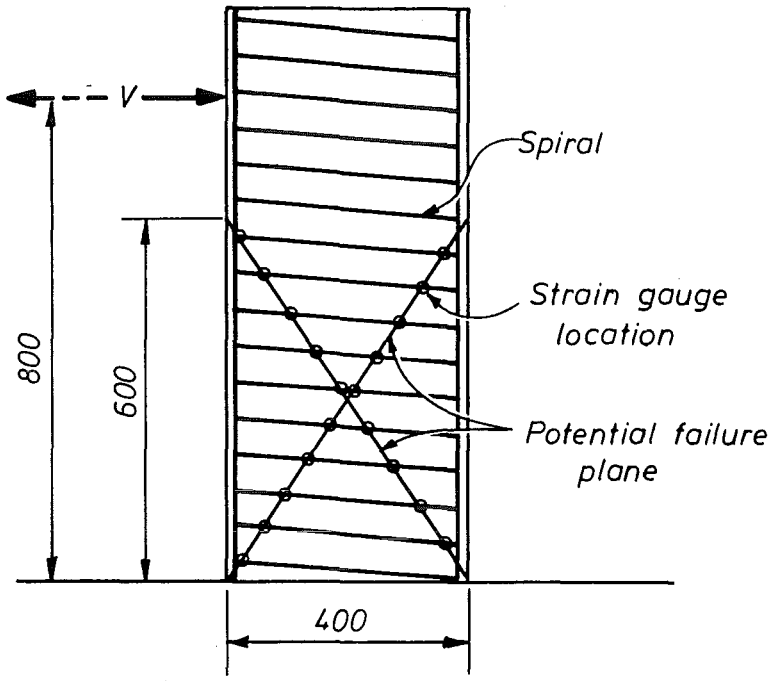

Fig. 3.6 : A typical arrangement of strain gauges (North and South sides)

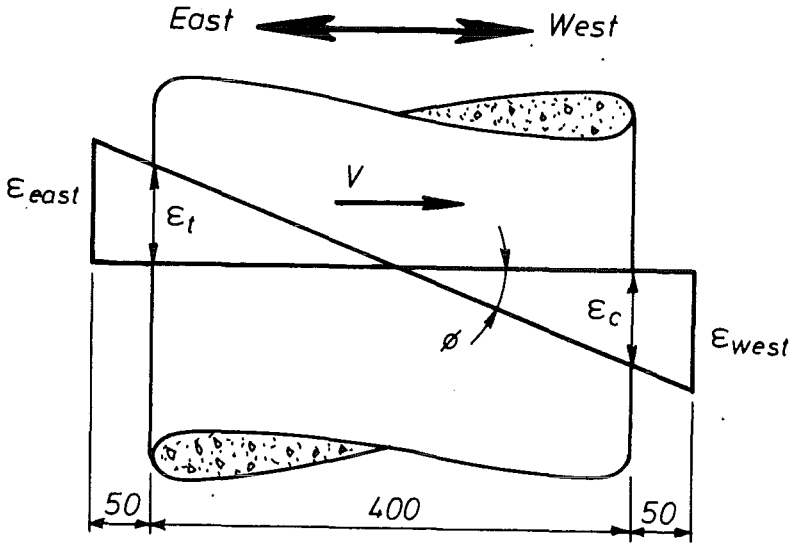

$$\varepsilon_{west} = \Delta_{west}/\text{gauge length} \quad \left.\right\} \text{-ve for compression}$$
$$\varepsilon_{east} = \Delta_{east}/\text{gauge length} \quad \left.\right\} \text{+ve for tension}$$

$$\text{Curvature}, \phi = \frac{\varepsilon_{east} - \varepsilon_{west}}{500} \text{ rad/mm}$$

$$\varepsilon_c = \varepsilon_{west} + \phi \times 50$$

$$\varepsilon_t = \varepsilon_{west} + \phi \times 450$$

Fig. 3.7 : Curvature and concrete strain calculations

transducers. Polystyrene pieces were sleeved at both ends of the rods to create a clear space between the rods and the surrounding cover concrete to avoid interference by spalling cover concrete. In shorter specimens (ℓ = 600 to 700 mm) only three pairs of transducers were used instead of four shown in Fig. 3.2. The transducers measured changes in length over the vertical gauge length concerned. The change in length can then be converted to strain and the rotation and curvature can be calculated as illustrated in Fig. 3.7.

The curvature or rotation readings were not very meaningful when the effect of shear displacement became predominant. An attempt was made to monitor the shear displacement using two rows of demountable mechanical gauges (DEMEC) at the centre-line of the columns as can be seen in Fig. 3.5b. However, the spalling of concrete in the critical regions resulted in loss of these gauges and hence no useful results were obtained.

3.4.5 Data Acquisition System

An integral system consisting of a 200 channel Solartron Analogue Scanner, Data Transfer Unit, Digital Voltmeter and Facit Printer (or Tape Puncher) was used to record the readings from strain gauges and the transducers. At first the readings were printed by the Facit printer but later on, with the development of a computer program for data reduction, punched paper tapes were used to speed up the process. The paper tapes were read through a tape reader and the data were stored in the CANDEPACK facility of the University for data reduction that followed.

A Hewlett Packard X-Y plotter and later, Watanabe X-Y recorder, was used to plot the load-displacement hysteresis loops as the tests progressed. Displacements were taken from the 30LP200 Sakae linear potentiometer rather than the displacement readings of the MTS jack, since the latter included a component of lateral displacement of the loading frame.

To safeguard against any loss of displacement data due to failure or undetected fault in the integral Solartron electronic system, the horizontal displacement readings from the 30LP200 Sakaw linear potentiometer were also read through a Hewlett Packard digital voltmeter display unit. In the case where potentiometers were used to measure the beam movement, their readings were also recorded through the same unit.

3.5 TESTING PROCEDURES

For the first six column units, a more cautious step was taken in applying the static lateral loads. Ten cycles at about half the ideal flexural strength (V_{if}) followed by another ten cycles at ideal shear strength (V_{iv}) or the strength at first yielding of the extreme longitudinal bar, whichever was smaller, were carried out before the standard loading sequence to be outlined below was applied. However, for the subsequent column units, the first twenty cycles of loading mentioned above were discarded and only the standard loading sequence was followed. This started with an initial five cycles of horizontal load (load controlled) to about 75 percent of the ideal flexural strength, V_{if}, to establish the yield displacement, Δy. As shown in Fig. 3.8, Δy was found by extrapolating the first cycle of experimental curve to the theoretical ideal strength level, V_{if}, and the yield displacement was obtained by proportion. The average of the values in both positive and negative direction was taken as the yield displacement, Δy, and the displacement ductility factor, μ, is defined as the ratio of actual displacement to yield displacement.

Once the yield displacement was established, subsequent loadings beyond this yield displacement were controlled by displacement increments to pre-determined value of displacement ductility level (i.e. multiple values of Δy). Five complete cycles to displacement ductility factor, μ, of 1.5, 2, 4, 6 and possibly 8 were carried out in turn (Fig. 3.9). Variation in the sequence or the number of cycles were necessary in some circumstances.

Incremental loading was used in every first cycle to a new peak displacement whereas for all subsequent loadings to the same displacement level the loadings were cycled from positive peak to negative peak without stopping at intermediate values. The initial part of every first cycle to a new peak displacement was load-controlled until $\mu = 1$, after which displacement control was used. The testing was concluded when significant deterioration in both strength and stiffness had taken place.

Complete sets of readings were taken before horizontal load application and also after axial load, if any, was applied. These readings gave the initial zero readings for later data reduction. Subsequently, strain and displacement readings were taken during load increments but only displacement readings were recorded during unloading. Complete sets of readings were taken at every new peak, positive and negative, and every last cycle to the same displacement ductility level. They

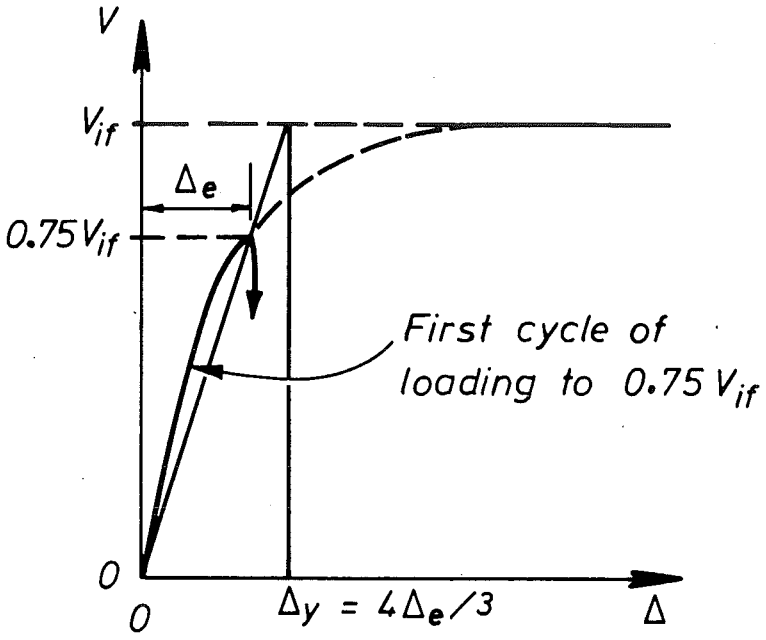

Fig. 3.8 : Definition of yield displacement

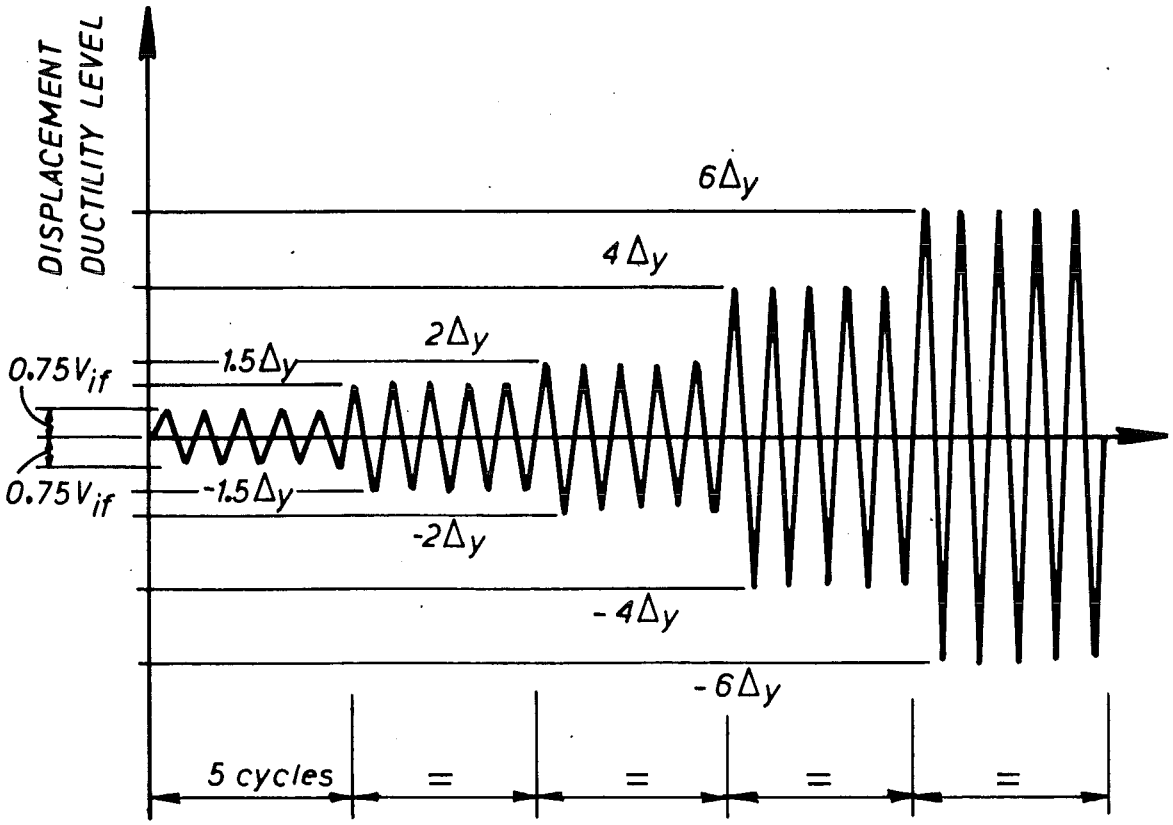

Fig. 3.9 : Loading sequence

were also taken at zero load levels when unloading from every first positive as well as negative peak but not for intermediate cycles unless necessary. Axial load was adjusted every time before any reading was taken.

At every new loading increment and at the peaks of first and last load cycles all the cracks were marked. The crack patterns were only photographed at the peaks of first and last cycles at a given ductility. Photos of crack patterns were taken during intermediate cycles if they were of particular interest. These photos provided a visual record of the cracking patterns at different load stages.

Chapter Four

— STATIC TESTS OF CIRCULAR COLUMNS — RESULTS AND OBSERVATIONS

4.1 INTRODUCTION

The experimental results and observations of twenty-five column units tested statically are given in this chapter. Instead of discussing the results of each column unit individually, the results are studied collectively to facilitate correlation of the influence of various parameters with column performance. The column performance is gauged with respect to the shear strengths and displacement ductility attained as well as the overall hysteresis behaviour and energy dissipation characteristics. Other quantities such as spiral strains and forces, curvature distributions and concrete strains are also discussed. Detailed comparisons of results with code specified shear strengths and prediction by plastic theory are presented.

4.2 GENERAL OBSERVATIONS

4.2.1 Classification of Failure Modes

Table 4.1 lists the ideal shear strengths (V^s_{iv} and V_{iv}) based respectively on the seismic and non-seismic code equations of NZS 3101[4.2] for concrete contribution, and a 45-deg truss analogy for spiral contribution. The code equations used are as listed in Table 2.2 and the spiral shear forces were calculated using Eq. 2.53. In the same table the ideal flexural strengths (V_{if}) were calculated using the column design charts of New Zealand Reinforced Concrete Design Handbook[4.1]. The actual material properties were used in the calculations and the strength reduction factors were taken to be unity.

Except for Unit 9, all column units had insufficient margin of ideal shear strength over the ideal flexural strength to satisfy capacity design requirements. Note that the capacity design principle requires the shear strength to be at least 1.22 (i.e. $\frac{1.4}{1.15}$) times the flexural strength of the member reinforced with Grade 380 steel when both strengths are based on known steel strengths and if this is followed strictly, even the shear strength of Unit 9 would be deemed to be inadequate to ensure a satisfactory performance. The final failure mode was found to be very much dependent upon the ratio between these two quantities (i.e. $\frac{V^s_{iv}}{V_{if}}$ or $\frac{V_{iv}}{V_{if}}$ in Table 4.1). This ratio is referred to as relative strength index in the discussions that follow. As it will be shown that

Table 4.1 : Ultimate Shear Strength And Failure Mode of Column Units

UNIT	$\frac{M}{VD}$	$\frac{P_i}{f'_c A_g}$	Ideal Shear Strength (kN)		Ideal Flexural Strength V_{if} (kN)	Relative Strength Index		Ultimate Exptal. Strength V_u (kN)	$\frac{V_u}{V_{if}}$	μ at V_u	$\frac{v_u}{\sqrt{f'_c}}$	Failure Mode
			V_{iv}	V_{is}		$\frac{V_{iv}}{V_{if}}$	$\frac{V_{is}}{V_{if}}$					
(1)	(2)	(3)	(4)	(5)	(6)	(7)	(8)	(9)	(10)	(11)	(12)	(13)
9	2.5	0.2	374	337	281	1.331	1.199	385	1.370	7.8	0.70	D-F
2	2.0	0	211	88	220	0.959	0.400	228	1.036	4.0	0.37	
15	2.0	0	184	86	204	0.902	0.422	230	1.127	4.0	0.39	
13	2.0	0.1	331	174	363	0.912	0.479	443	1.220	4.0	0.73	MD-S
8	2.0	0.2	370	334	356	1.039	0.938	475	1.334	4.0	0.88	
10	2.0	0.2	356	318	360	0.989	0.883	450	1.250	4.0	0.80	
1	2.0	0	211	88	306	0.690	0.288	320	1.046	2.5	0.52	
5	2.0	0	243	131	301	0.807	0.435	340	1.130	2.4	0.61	
14	2.0	0	203	86	304	0.668	0.283	311	1.023	2.0	0.53	
23	2.0	0	238	124	295	0.807	0.420	339	1.149	2.0	0.59	LD-S
24	2.0	0	241	125	305	0.790	0.410	338	1.108	4.0	0.58	
3	2.5	0	209	88	242	0.865	0.364	298	1.231	4.0	0.49	
12*	1.5	0.1	315	175	437	0.721	0.400	527	1.206	3.0	0.98	
17	2.5	0.1	239	86	281	0.851	0.306	329	1.171	2.0	0.56	
25	1.5	0	112	0	297	0.377	0	233	0.785	1.2	0.40	
6	1.5	0	198	88	402	0.493	0.219	390	0.970	1.3	0.71	
4	2.0	0	196	85	299	0.656	0.284	295	0.987	1.4	0.53	
7	2.0	0	183	74	293	0.625	0.253	280	0.956	1.6	0.51	
21	2.0	0	181	65	313	0.578	0.208	258	0.824	1.1	0.45	B-S
22	2.0	0	174	62	294	0.592	0.211	280	0.952	1.5	0.50	
18	1.5	0.1	241	86	462	0.522	0.186	507	1.097	1.4	0.85	
19	1.5	0.1	218	65	468	0.466	0.139	436	0.932	1.3	0.74	
16	2.0	0.1	237	86	345	0.687	0.249	379	1.099	1.5	0.48	
20	1.75	0.175	251	198	477	0.527	0.415	487	1.021	1.5	0.80	
11	2.0	0.2	276	239	351	0.786	0.681	404	1.151	2.5	0.73	

D-F : Ductile flexural failure; LD-S : Shear failure with limited ductility;
MD-S : Shear failure with moderate ductility; B-S : Brittle Shear failure.

* The ultimate load in Unit 12 was achieved after the axial load was lowered from 0.2 to $0.1 f'_c A_g$.

the code provisions for shear strength are very conservative even if the non-seismic values were used, the relative strength index as represented by $\frac{V_{iv}}{V_{if}}$ is used in the discussion most of the time.

The column units are broadly divided into four groups of different failure modes in Table 4.1. Among them Unit 9 had the largest margin of shear strength over the flexural strength and was the only column unit to have a ductile flexural mode of failure. In general, if $\frac{V_{iv}}{V_{if}}$ (non-seismic) was close to unity, e.g. the next five column units in Table 4.1, shear failure did not occur until a displacement ductility level of about $\mu = 6$ was attained. If the non-seismic shear strength was not less than 65 percent of the ideal flexural strength, the column units possessed limited ductility and failed in shear at a lower displacement ductility level, typically $\mu = 4$ or less. If the shear strength of the column was very inadequate, brittle shear failure was the consequence. These column units usually were not able to attain their flexural strength, with maximum load being reached prior to $\mu = 2$. Frequently, this peak strength could only be held momentarily. The failure modes are classified according to the displacement ductility level at which failure took place and they are as follows:

Ductile flexural failure (D-F) :	$\mu > 6$
Shear failure with moderate ductility (MD-S) :	$4 < \mu \leq 6$
Shear failure with limited ductility (LD-S) :	$2 < \mu \leq 4$
Brittle shear failure (B-S) :	$\mu \leq 2$

The general observations made during testing are presented in the following sections according to the category of failure mode. It should be noted that the maximum experimental displacements (at ultimate) represent drifts of 3 to 6 percent. Though these values are acceptable to bridge design they would be excessive for building design where drift must be limited to protect non-structural components and because of detrimental P-delta effects.

4.2.2 Ductile Flexural Failure (Unit 9 : $\frac{M}{VD} = 2.5$ and $\frac{P_i}{f'_c A_g} = 0.2$)

The behaviour is discussed with reference to load-deflection hysteresis loops of the specimen as shown in Fig. 4.1. The load-deflection hysteresis loops shown in Fig. 4.1 and subsequently in other figures were plotted directly by x-y plotter during testing. For reference, the ideal flexural strength, V_{if}, has been included and shown as a dashed line in the figures. The P-Δ effect due to axial compression was taken

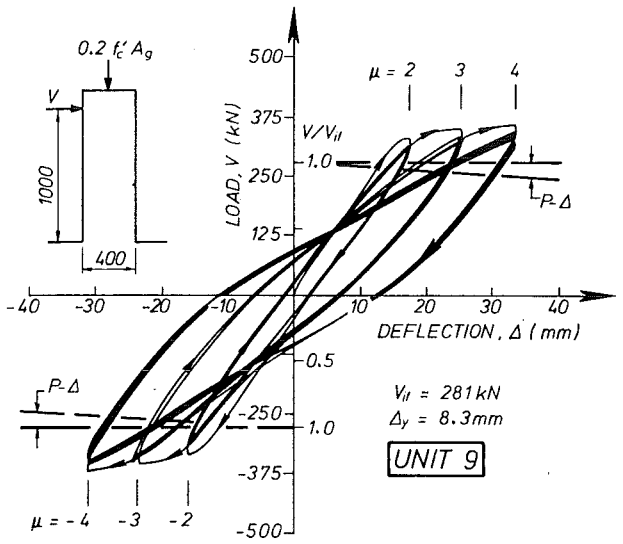

(a) $\mu \leq 4$

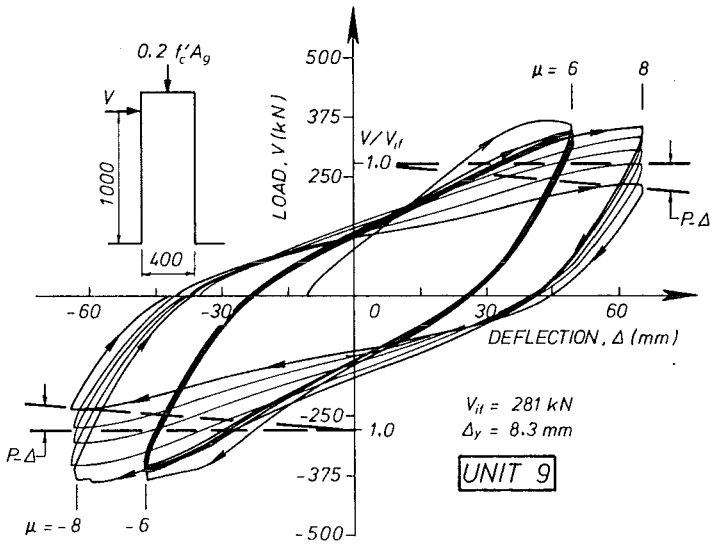

(b) $6 \leq \mu \leq 8$

Fig. 4.1 : Load-deflection hysteresis curves - UNIT 9 (ductile flexural failure)

into account and consequently, the dashed line dips downward at higher displacement ductility levels if axial compression was present.

The ideal non-seismic shear strength of Unit 9 exceeded the ideal flexural strength by about 33 percent. This column failed in a very ductile manner, sustaining five cycles each at μ = 1.5, 2, 3, 4, 6 and 8 .

As discussed in Section 3.5, the initial elastic cycles brought the column to about 75 percent of its ideal flexural strength. Flexural cracks first appeared at about 43 percent of V_{if} and by the end of the first elastic cycle the flexural cracking zone had extended over 60 percent of the column height.

There was no obvious sign of flexural cracks becoming inclined until μ = 1.5 . The crack inclination near the centre-line was about 45-deg at this stage. These diagonal cracks lengthened and widened as the testing progressed. During the later stages of loading, these cracks formed a pattern fanning away from the compression zone at the base of the column.

At μ = 1.5 , the load at peak displacement exceeded the ideal flexural strength for the first time. Initial crushing of concrete took place at μ = 2 but the load at peak displacement continued to increase until a maximum value was reached at μ = 8 . The rate of this increase, however, dropped as the peak load reached the plateau at μ = 8 . Some spalling of the concrete was detected at μ = 3 but it became extensive only at μ = 4 . No sign of strength and stiffness degradation accompanied the spalling of concrete and the stability of load-deflection response was remarkable even at μ = 6 (see Fig. 4.1). Strength degradation became more significant at μ = 8 but the resistance of the column at the conclusion of the test still exceeded the ideal flexural strength with P-Δ effect being taken into account.

Incipient signs of buckling of longitudinal reinforcement were observed at the third cycle to μ = 8 and the test was terminated with two additional cycles at the same ductility level. Most damage was concentrated in the hinging region within 200 mm at the column base as shown in Fig. 4.2a. The foundation beam provided some confining effect and there was a conical zone within which the concrete remained intact. Fig. 4.2b gives a close-up view of the buckled longitudinal reinforcement in the compression zone. Note that even though the shear strength of this column did not quite meet the capacity design requirements, its performance has been very satisfactory.

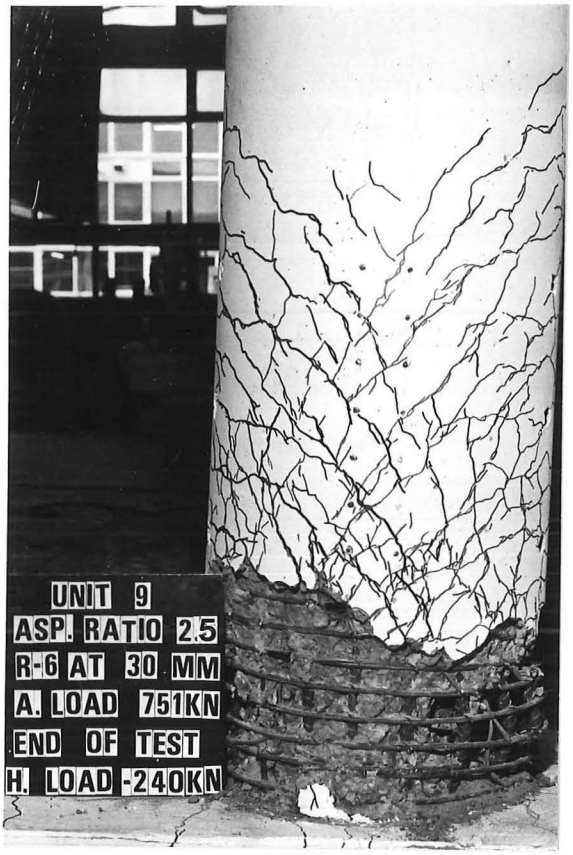

(a) Plastic hinge at column base

(b) Close-up view showing buckling of longitudinal bars

Fig. 4.2 : Damage in UNIT 9 (ductile flexural failure)

4.2.3 Shear Failure With Moderate Ductility (Units 2, 8, 10, 13, 15)

These five column units were provided with about equal ideal flexural and non-seismic shear strengths. They all had an aspect ratio of 2.0 and Units 2 and 15 were without axial load while the axial compression on the other three columns was $0.2f'_c A_g$. The load-deflection hysteresis loops of these columns shown in Figs. 4.3 to 4.7 were typical of predominant flexural behaviour initially. Until $\mu = 4$, the pinching effect on the hysteresis loops was secondary and the columns were able to sustain a large shear force of at least V_{if} without significant degradation. However, once the columns were displaced beyond $\mu = 4$, stability in the load-deflection response could no longer be held and failure was imminent. Nevertheless, given the amount of shear strength provided, the performance of these column units can still be considered satisfactory if the ductility demand on them is not very great.

Loading to about 75 percent of ideal flexural strength was carried out initially and flexural cracks first appeared at about 40 percent of V_{if}. Initiation of diagonal cracking also took place during the elastic cycles. In general, the presence of axial compression tended to delay the onset of diagonal cracking and therefore the diagonal cracking loads of Units 8, 10 and 13 were higher than those of the other two columns. Initially the diagonal cracks were inclined at about 40-deg with respect to column axis. The diagonal cracks fanned out from the compression zone and most of the damage was concentrated in regions adjacent to column base as shown in Fig. 4.8.

In all five column units, the ideal flexural strength was reached or exceeded at $\mu = 1.5$. Peak loads in Unit 2 were, however, unable to exceed V_{if} but this value was maintained until $\mu = 6$ (see Fig. 4.3). All the other columns attained maximum load higher than V_{if} at $\mu = 4$. Crushing of concrete was first detected at $\mu = 1.5$ to 2 while spalling took place at a higher displacement ductility level, typically $\mu = 2$ to 4. Crushing and spalling of concrete did not seem to have any influence on the initiation of shear failure. As is evident in Figs. 4.3 to 4.7, the peak strengths were maintained above or at the ideal flexural strength until $\mu = 4$. On further loading to displace the specimens beyond $\mu = 4$, sudden degradation in strength and stiffness occurred. Excessive widening of diagonal cracks caused loss of aggregate interlock capacity and hence, demanded more contribution from spiral reinforcement to carry the applied shear. Coupling with this, high

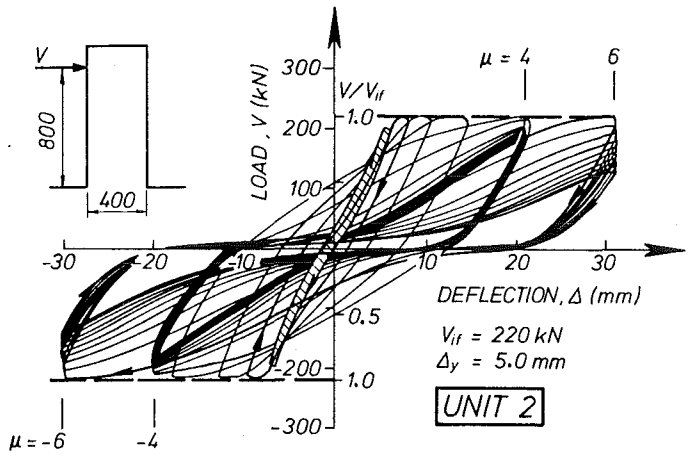

Fig. 4.3 : Load-deflection hysteresis curves - UNIT 2 (moderate ductility)

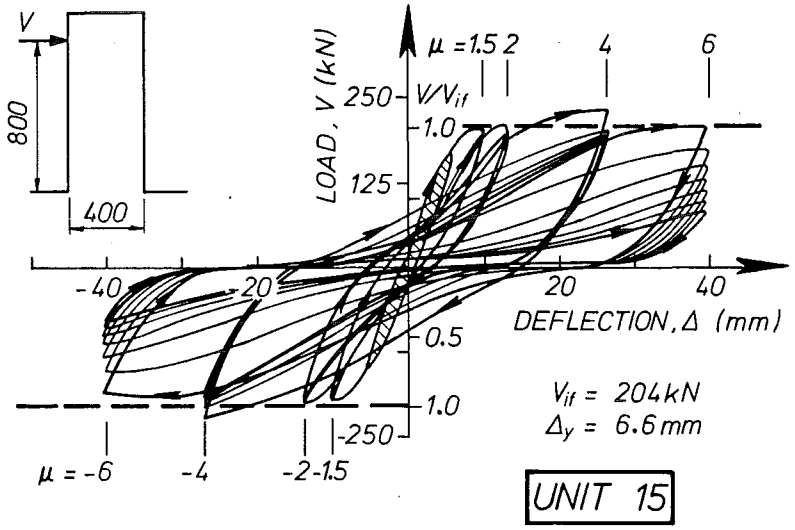

Fig. 4.4 : Load-deflection hysteresis curves - UNIT 15 (moderate ductility)

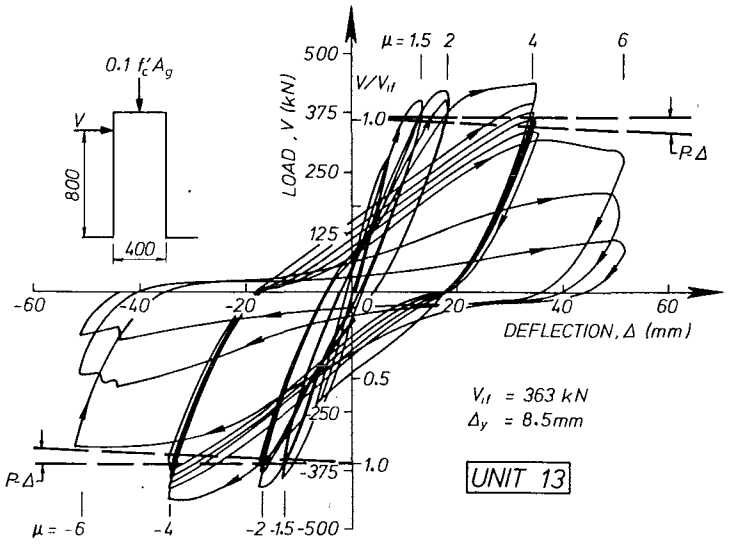

Fig. 4.5 : Load-deflection hysteresis curves - UNIT 13 (moderate ductility)

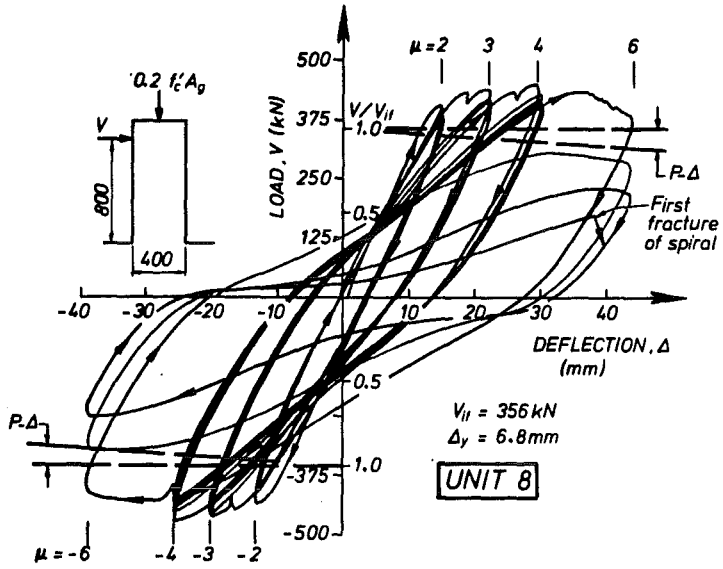

Fig. 4.6 : Load-deflection hysteresis curves - UNIT 8 (moderate ductility)

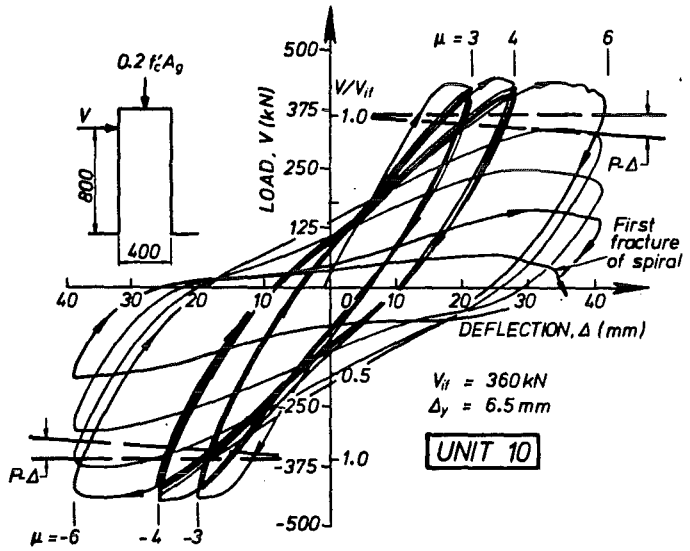

Fig. 4.7 : Load-deflection hysteresis curves - UNIT 10 (moderate ductility)

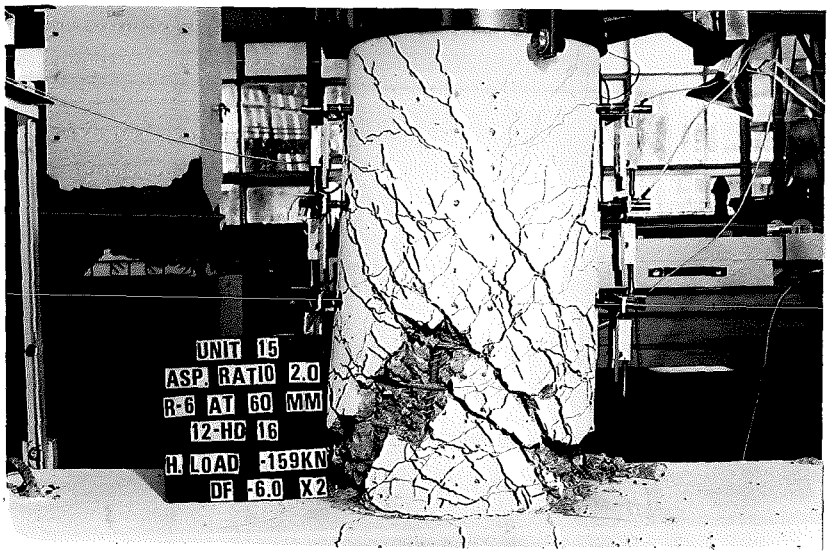

Fig. 4.8 : Damage near column base of UNIT 15 (moderate ductility)

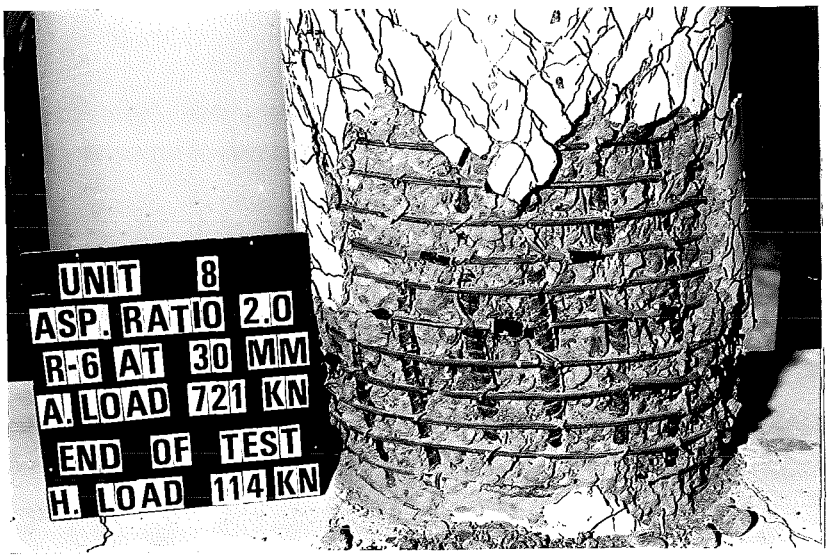

Fig. 4.9 : Final appearance of UNIT 8 after test (moderate ductility)

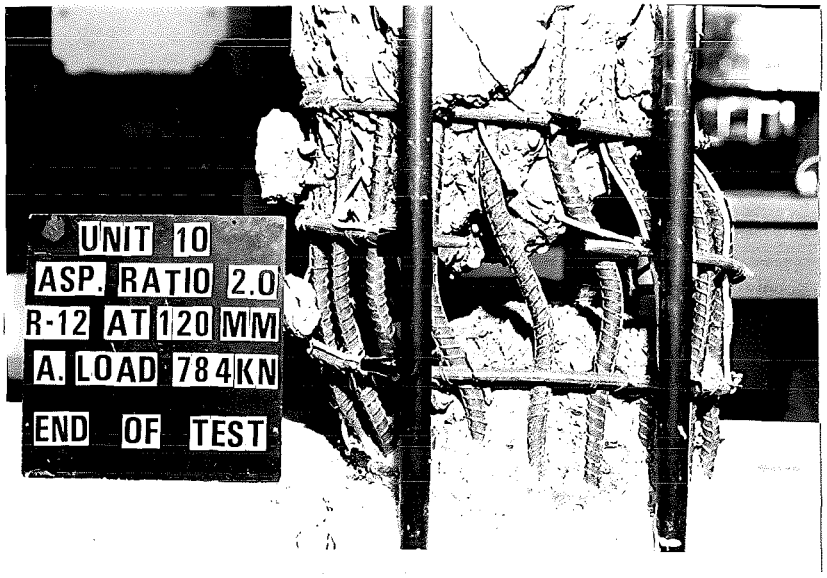

Fig. 4.10 : Final appearance of UNIT 10 after test (moderate ductility)

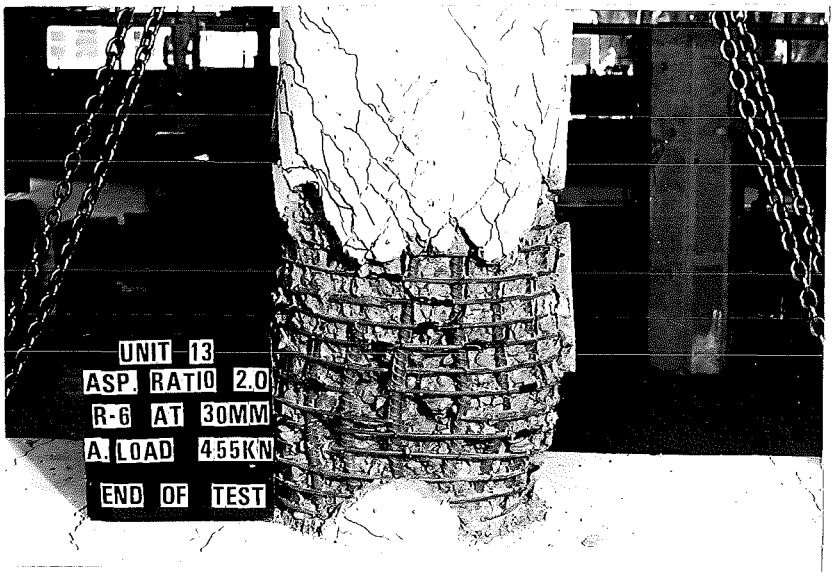

Fig. 4.11 : Final appearance of UNIT 13 after test (moderate ductility)

strain was also imposed on the spirals as they were mobilised to confine the dilating cracked concrete. In some cases, especially with the presence of axial compression as in Units 8, 10 and 13, the strain was so high that spirals fractured during the first few cycles at $\mu = 6$.

Figs. 4.9, 4.10 and 4.11 show Units 8, 10 and 13 respectively at the end of the test. In Unit 10 the large spiral pitch failed to prevent buckling of longitudinal reinforcement at $\mu = 6$. It appears from Fig. 4.10 that the fracture of the spiral created a plane of weakness a short distance away from the beam-column interface and resulted in a form of sliding shear failure at the location of the broken spiral. Fig. 4.11 shows fracture of spirals in Unit 13. The locations of the fracture followed closely the inclined failure plane. Note that due to the confining effect of the foundation beam the concrete at the base remained relatively intact.

4.2.4 Shear Failure With Limited Ductility (Units 1, 3, 5, 12, 14, 17, 23, 24)

The eight column units within this category of failure mode had ideal non-seismic shear strength of no less than 65 percent of the ideal flexural strength. Units 12 and 17 had an axial compression of $0.1f'_c A_g$ while the other columns were without axial load. Except for Units 3, 12 and 17, the aspect ratio of the columns was 2.0 . Units 3, 12 and 17 had an aspect ratio of 2.5, 1.5 and 2.5 respectively. Typically, they all possessed limited ductility with shear failure occurring prior to or at $\mu = 4$. The load-deflection hysteresis loops of these columns are as shown in Figs. 4.12 to 4.19.

The columns were loaded to approximately 75 percent of their ideal flexural strength during the initial elastic load cycles. Flexural cracks first appeared at about 40 percent of the ideal flexural strength on average. Diagonal cracking also took place during the initial elastic cycles. In general, diagonal cracking was delayed by the presence of axial compression. The initial angle of crack inclination with respect to column axis varied between 40 and 50-deg. All diagonal cracks widened and lengthened with further loading. In most cases, a pair of wide intersecting main diagonal cracks eventually formed. They were usually at a smaller angle than the initial crack inclination and in some shorter columns they ran from corner to corner forming two inclined planes of diagonal tension failure in the loading directions, along which deformation and degradation concentrated.

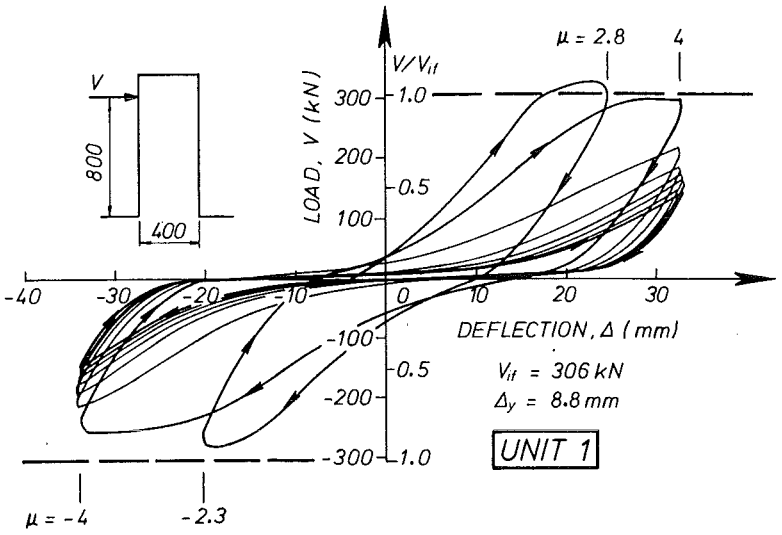

Fig. 4.12 : Load-deflection hysteresis curves - UNIT 1 (limited ductility)

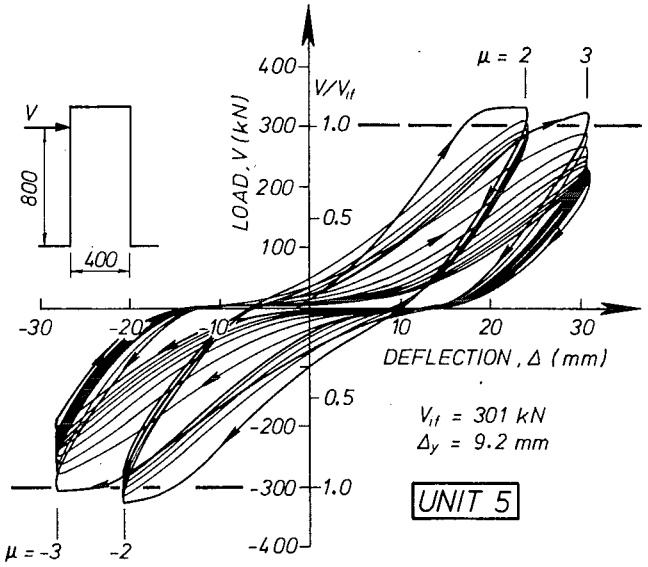

Fig. 4.13 : Load-deflection hysteresis curves - UNIT 5 (limited ductility)

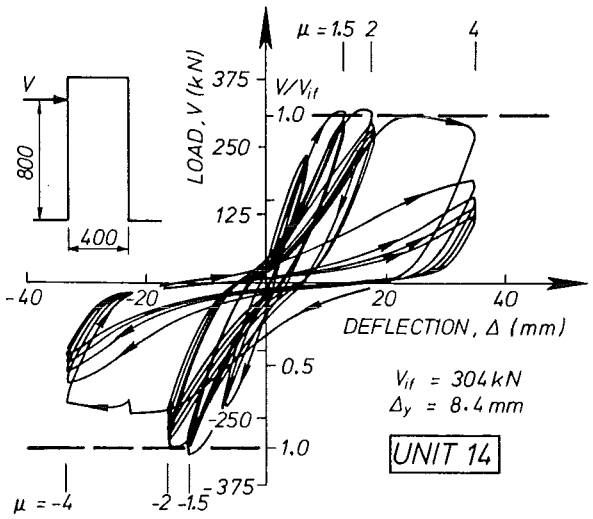

Fig. 4.14 : Load-deflection hysteresis curves - UNIT 14 (limited ductility)

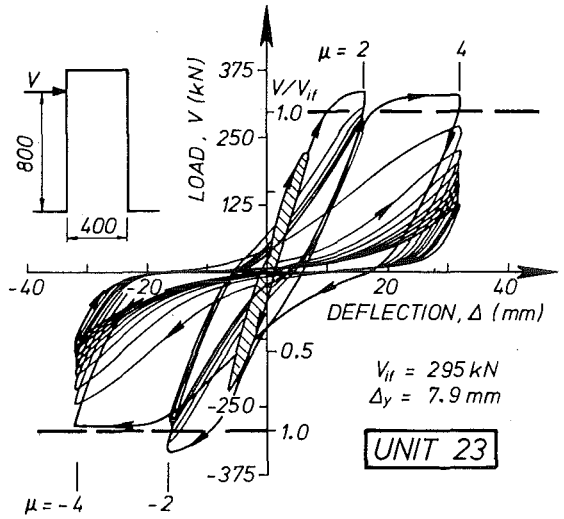

Fig. 4.15 : Load-deflection hysteresis curves - UNIT 23 (limited ductility)

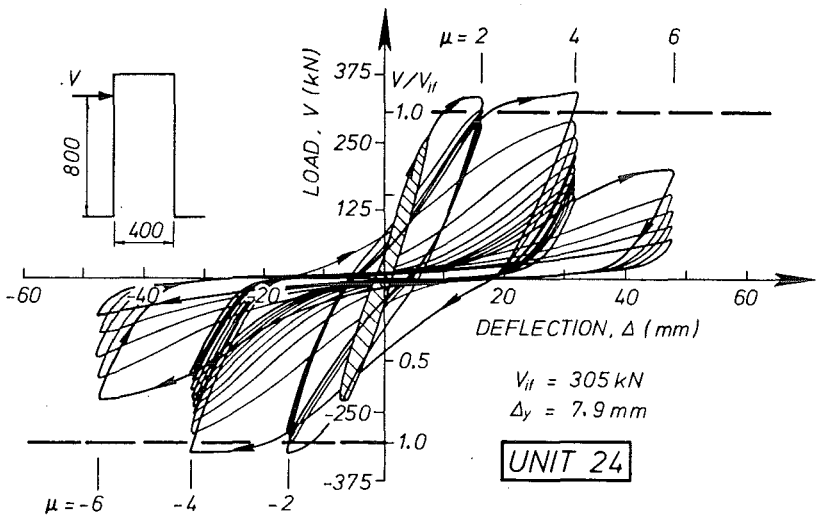

Fig. 4.16 : Load-deflection hysteresis curves - UNIT 24 (limited ductility)

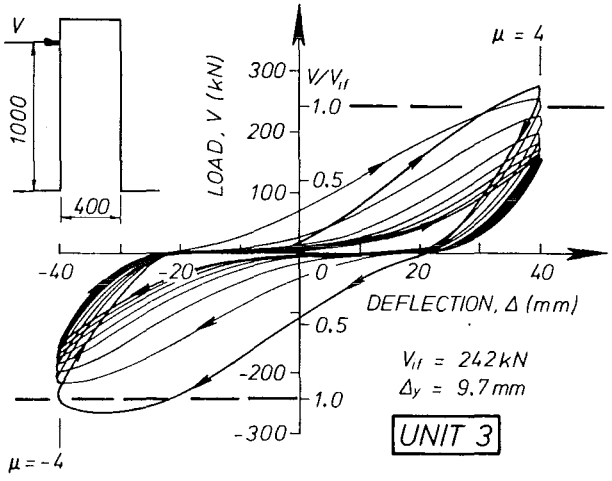

Fig. 4.17 : Load-deflection hysteresis curves - UNIT 3 (limited ductility)

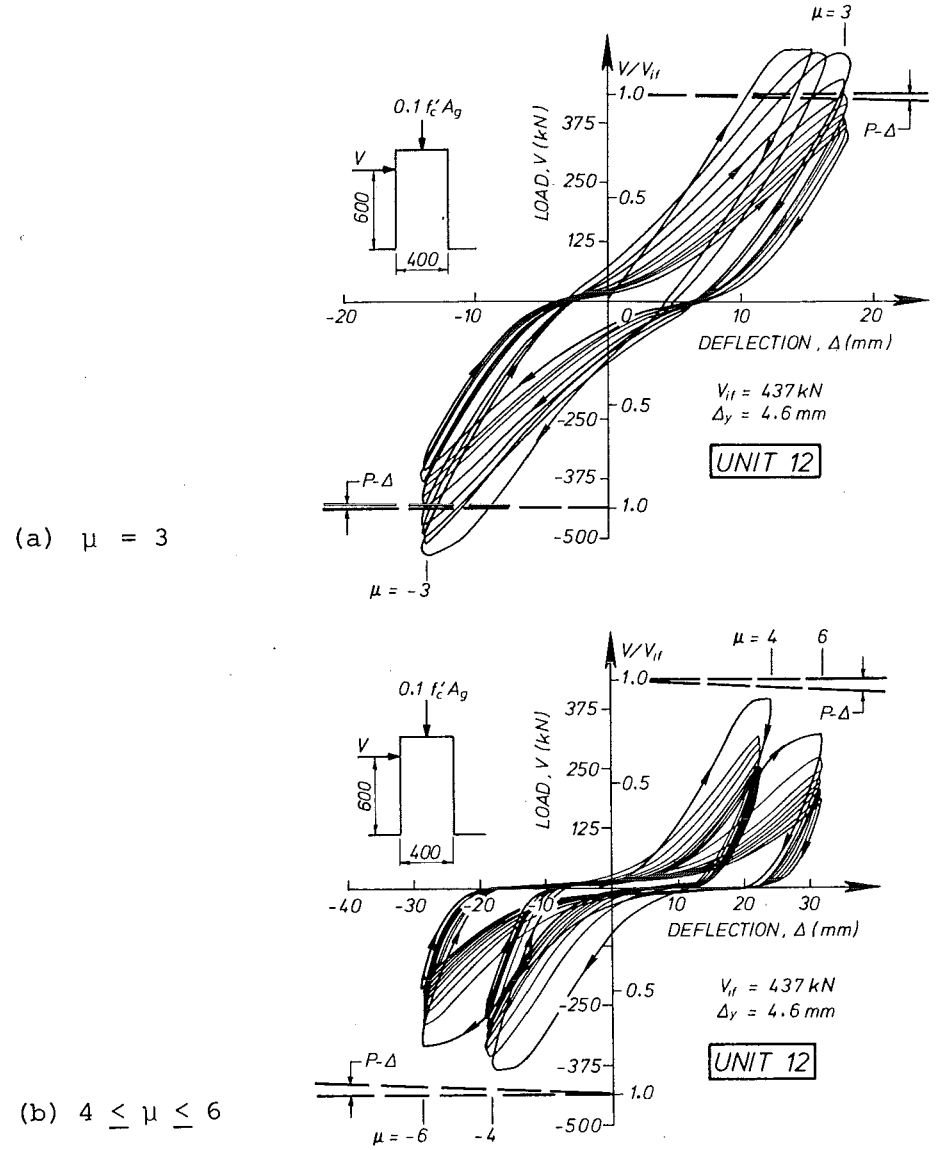

(a) μ = 3

(b) 4 ≤ μ ≤ 6

Fig. 4.18 : Load-deflection hysteresis curves - UNIT 12 (limited ductility)

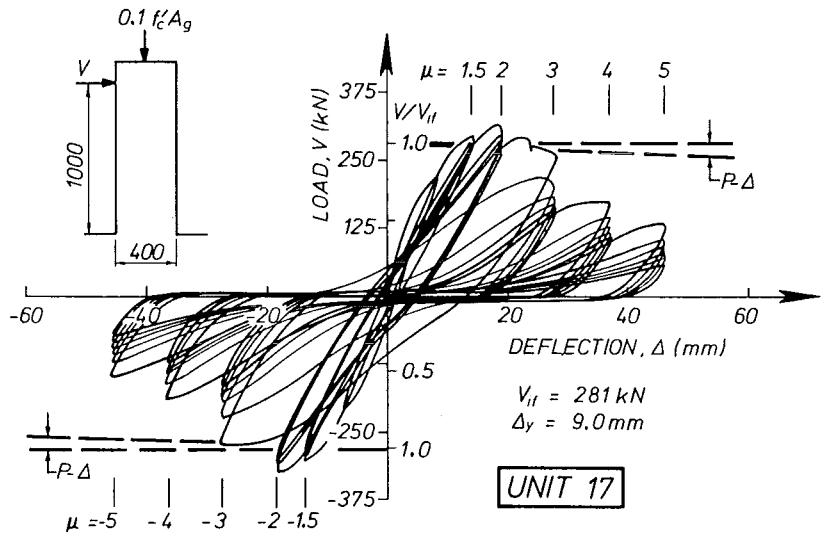

Fig. 4.19 : Load-deflection hysteresis curves - UNIT 17 (limited ductility)

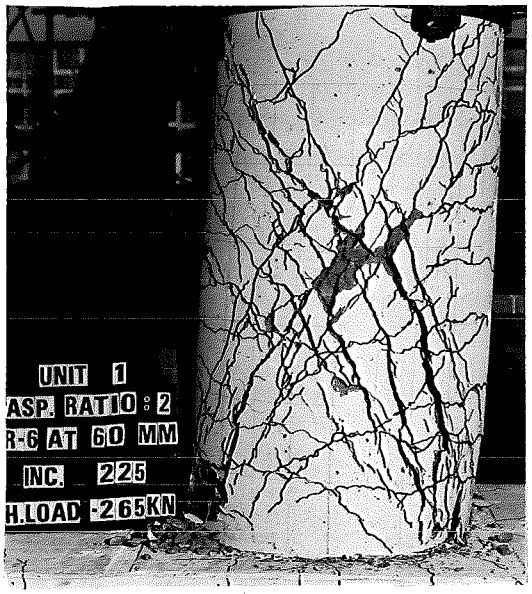

Fig. 4.20 : Damage along main diagonal cracks - UNIT 1 (limited ductility)

Fig. 4.21 : Damage along main diagonal cracks - UNIT 12 (limited ductility)

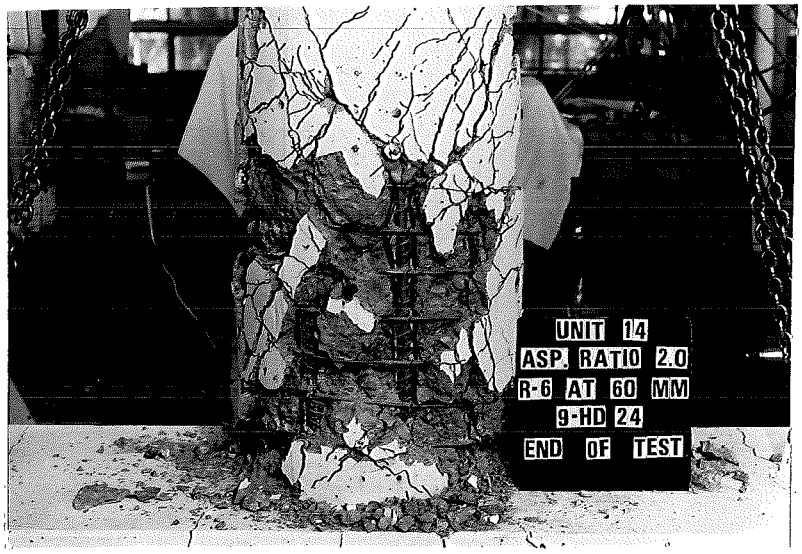

Fig. 4.22 : Final appearance of UNIT 14 after test (limited ductility)

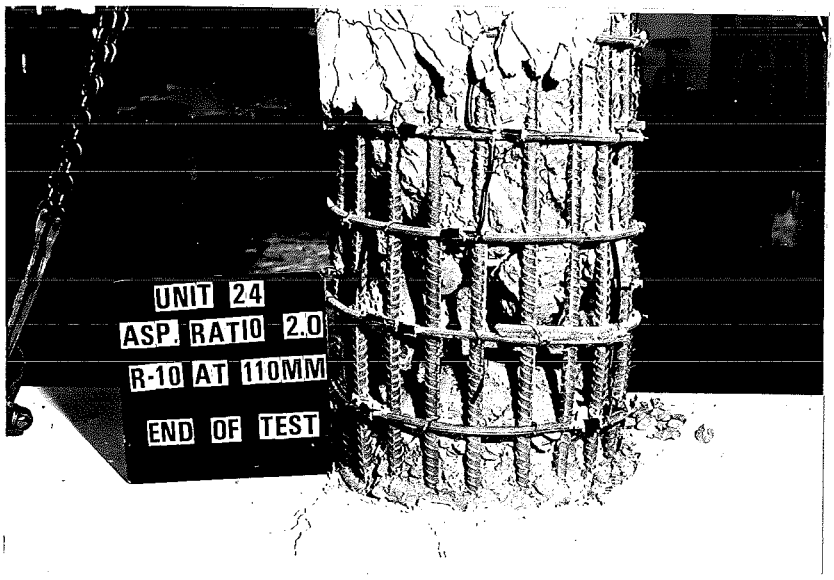

Fig. 4.23 : Final appearance of UNIT 24 after test (limited ductility)

All columns attained their ideal flexural strength at some stage. Usually the peak strength was reached at a displacement ductility of $\mu = 2$ or slightly higher. The axial load on Unit 12 was lowered from the planned $0.2f'_c A_g$ to $0.1f'_c A_g$ after $\mu = 1.5$ because the load capacity of the MTS jack had been reached. In most columns, crushing of concrete was observed at $\mu = 1.5$ or 2 and spalling of cover concrete followed not long after. The only exceptions were Units 3 and 12 in which the spalling took place at $\mu = 4$ and 3 respectively.

Prior to the formation of diagonal failure cracks, the load-deflection response, as shown for typical cases in Figs. 4.14 to 4.16, remained relatively stable, though the effect of shear, as manifested in the pinching of the hysteresis loops, could be easily detected in many cases. The later stage of loadings concentrated the displacements along the two main intersecting diagonal cracks, with reduced flexural activity. Because of the inability to restrain diagonal crack opening, the integrity of the concrete could not be maintained. Due to repeated abrasion, the concrete disintegrated along the two main diagonal cracks and more severely so at their intersection. Figs. 4.20 and 4.21 show the extent of spalling of concrete in the vicinity of these shear cracks. The concrete lost its aggregate interlock capacity and at the same time the broken blocks of concrete wedged against the spirals laterally. These two effects imposed large strain on the spirals and in some cases, e.g. Units 14 and 17, led to fracture of the spirals.

The tests ended after substantial strength and stiffened degradation had taken place. Figs. 4.22 and 4.23 show the appearance of typical columns after the tests were completed. In both cases the failure plane did not run from corner to corner. It is interesting to note that the restraining effect of the foundation beam prevented a conical block of concrete at the column base from disintegration.

4.2.5 Brittle Shear Failure (Units 4, 6, 7, 11, 16, 18, 19, 20, 21, 22, 25)

The performance of these column units was rather poor. With few exceptions they were not able to sustain the ideal flexural strength and failure occurred at very low displacement ductility level of about 1.5. The details of the column units are as given in Table 4.1. Typically, the ideal non-seismic shear strength was less than 65 percent of the ideal flexural strength. The load-deflection hysteresis loops are as shown in Figs. 4.24 to 4.34. Unit 11 is included in this group despite

a displacement ductility of $\mu > 2$ at V_u because fracture of spirals (see Fig. 4.35) at an early stage ($\mu = 2.7$) resulted in little strength and stiffness at low displacement ductility level as is apparent in Fig. 4.34. Note that with an axial compression of $0.2f'_c A_g$, the spiral reinforcement content of 0.0051 provided in Unit 11 was insufficient according to NZS 3101 requirements for confinement (required $\rho_s = 0.0072$), which might have contributed to early failure of this column.

During the initial elastic cycle to $0.75V_{if}$, flexural cracking took place on average at about 30 percent of V_{if}. These cracks soon became inclined to the column axis and the range of angle was between 40 to 50-deg.

The peak strength of the columns was reached at about $\mu = 1.5$. Though Units 11, 18 and 20 achieved their ideal flexural strength, these columns together with five other columns (Units 6, 18, 19, 21, 22) were only able to sustain their maximum load momentarily. The sudden drop in load carrying capacity from the maximum load corresponded to excessive widening of diagonal cracks which opened up suddenly and extended almost from corner to corner. Subsequent loadings concentrated the damage along the inclined failure plane so formed and this is illustrated in Figs. 4.36 and 4.37 for Units 7 and 16 respectively. Large crack width and repeated abrasion of concrete resulted in loss of aggregate interlock. The combined effect of shear and dilatancy of the concrete led to fracture of spirals and consequently the load carrying capacity degraded. Sometimes, more fracture of spirals might follow once the first fracture had taken place. This led to progressive decay in load carrying capacity and is reflected in step-wise reduction in the load-deflection hysteresis loops as depicted in Figs. 4.31 and 4.33 for Units 19 and 20 respectively. The final appearance of these two columns was as shown in Figs. 4.38 and 4.39. The corner-to-corner failure planes can be seen in these figures. Note that though much damage has taken place along the failure planes, the concrete at the base remained relatively intact, indicating reduced flexural activity.

Also included in this group of column units are Units 21 and 25. Unit 21 was the only column loaded monotonically to $\mu = 6$ before load reversal. The non-seismic relative strength index of this column was 0.578. The first flexural crack appeared at about 20 percent of V_{if}. Diagonal cracks also formed and ran from corner to corner before loading into the inelastic range was carried out. A maximum load of less

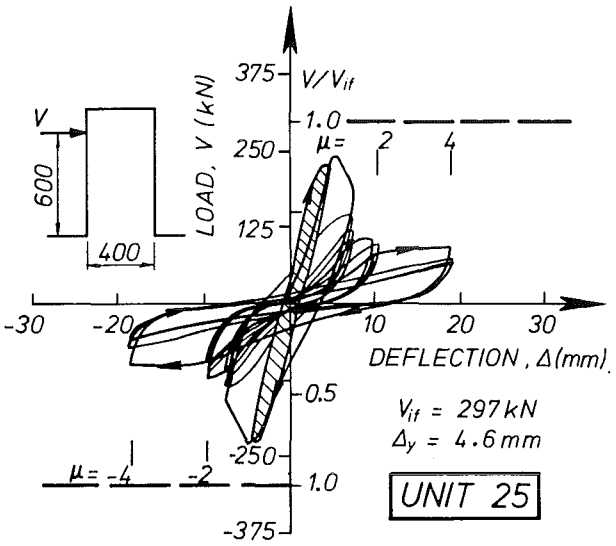

Fig. 4.24 : Load-deflection hysteresis curves - UNIT 25 (brittle shear failure)

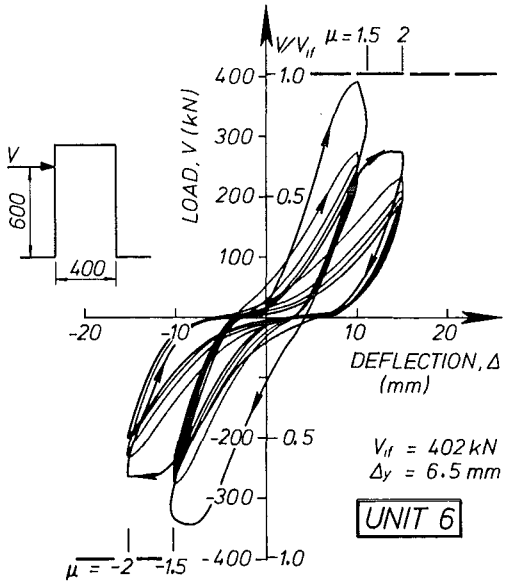

Fig. 4.25 : Load-deflection hysteresis curves - UNIT 6 (brittle shear failure)

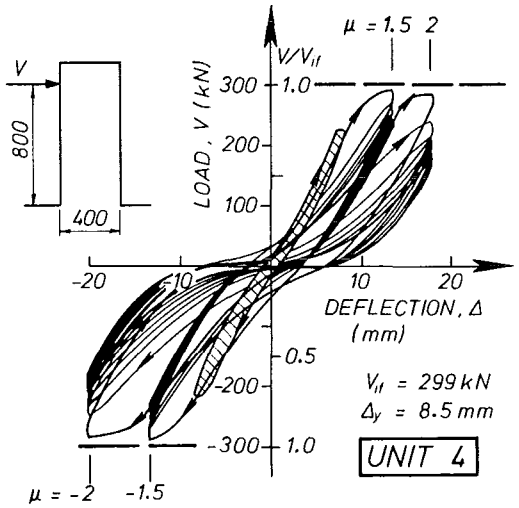

Fig. 4.26 : Load-deflection hysteresis curves - UNIT 4 (brittle shear failure)

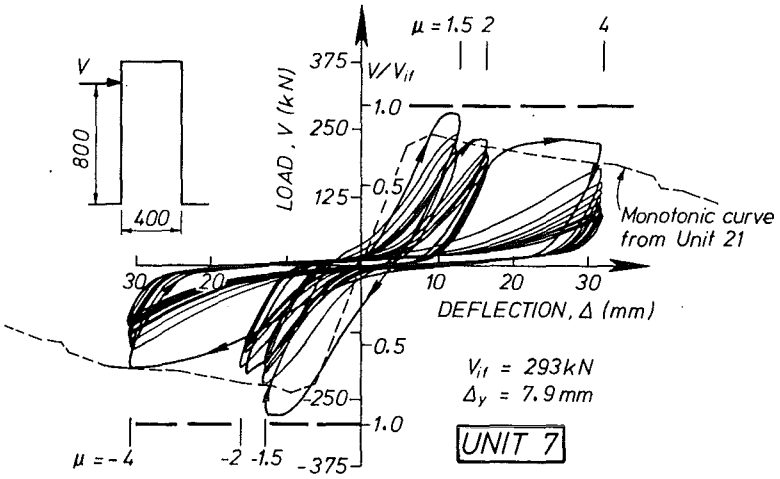

Fig. 4.27 : Load-deflection hysteresis curves - UNIT 7 (brittle shear failure)

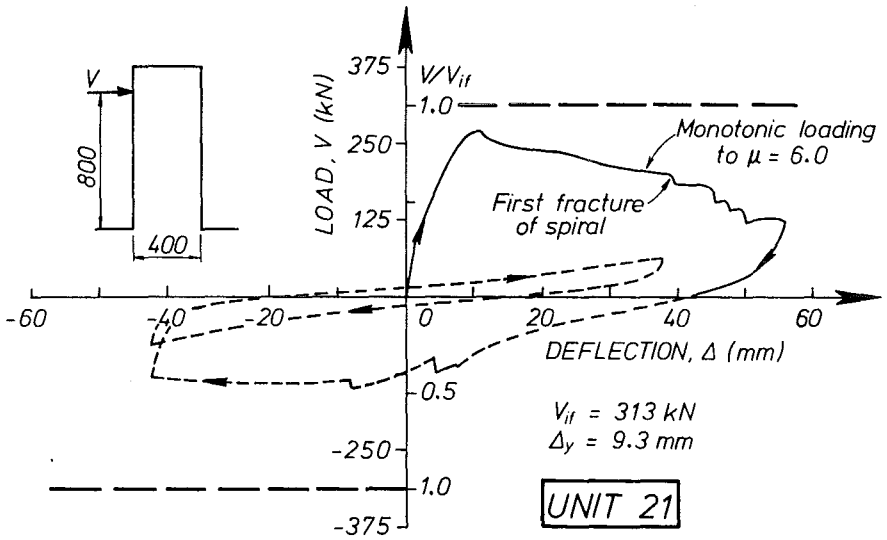

Fig. 4.28 : Load-deflection hysteresis curves - UNIT 21 (brittle shear failure)

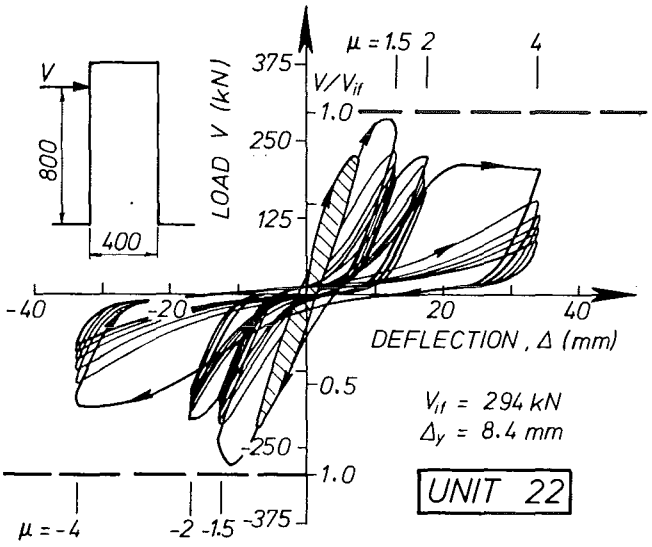

Fig. 4.29 : Load-deflection hysteresis curves - UNIT 22 (brittle shear failure)

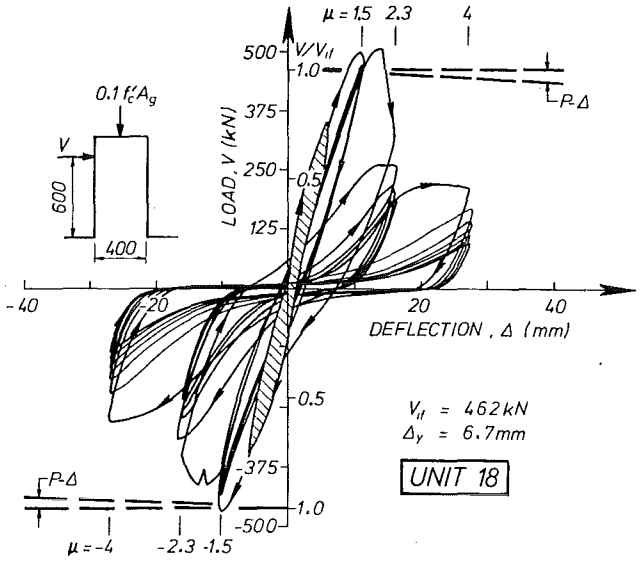

Fig. 4.30 : Load-deflection hysteresis curves - UNIT 18 (brittle shear failure)

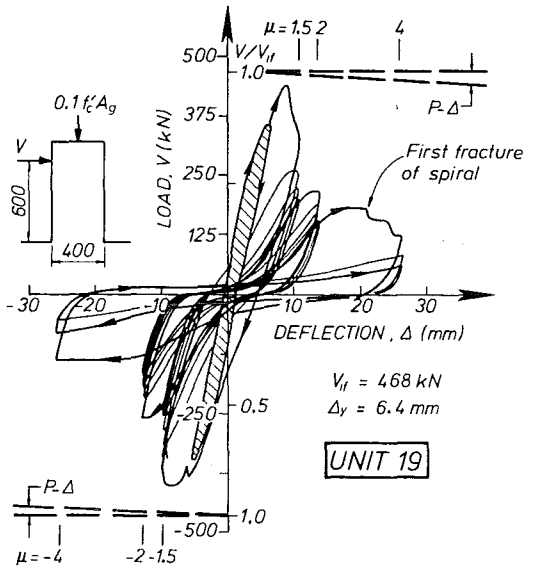

Fig. 4.31 : Load-deflection hysteresis curves - UNIT 19 (brittle shear failure)

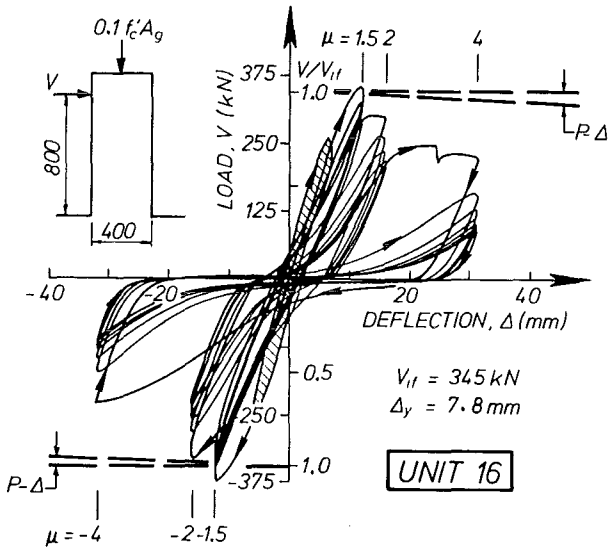

Fig. 4.32 : Load-deflection hysteresis curves - UNIT 16 (brittle shear failure)

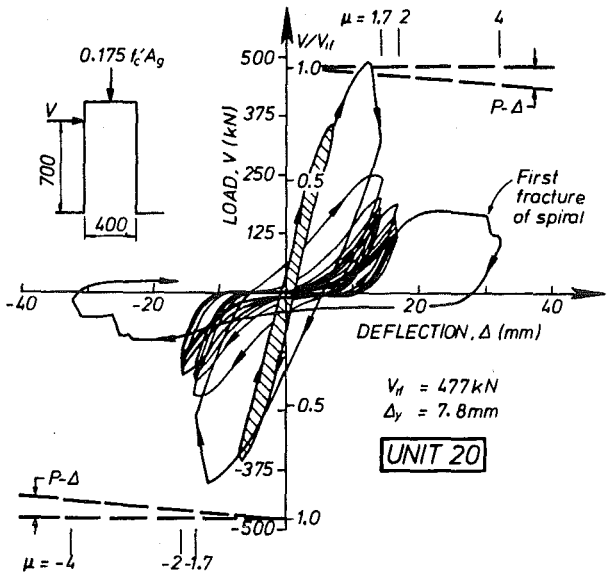

Fig. 4.33 : Load-deflection hysteresis curves - UNIT 20 (brittle shear failure)

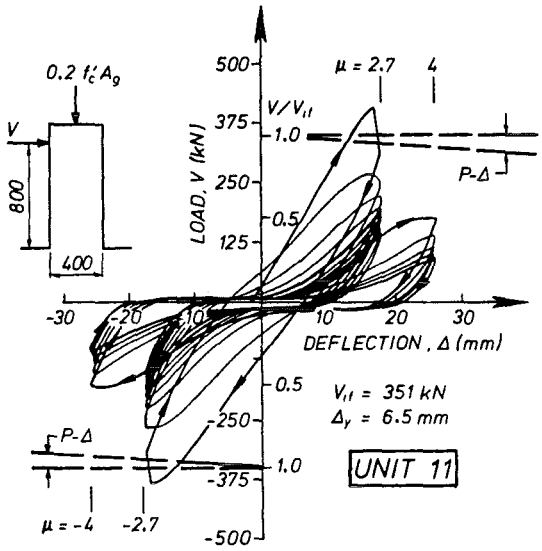

Fig. 4.34 : Load-deflection hysteresis curves - UNIT 11 (brittle shear failure)

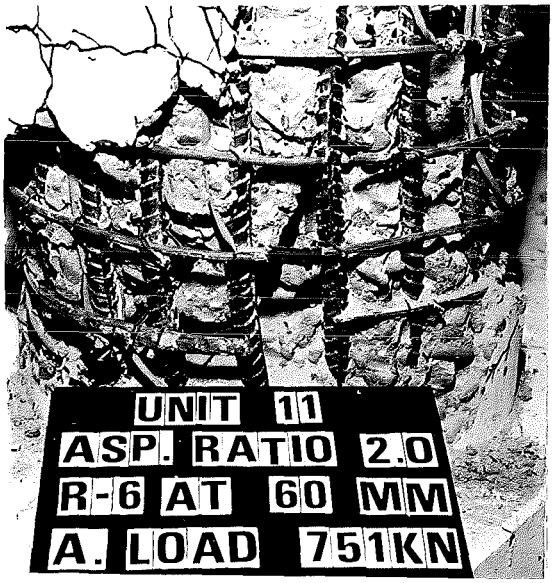

Fig. 4.35 : Fractures of spiral in UNIT 11

Fig. 4.36 : Damage along the main diagonal cracks in UNIT 7 (brittle shear failure)

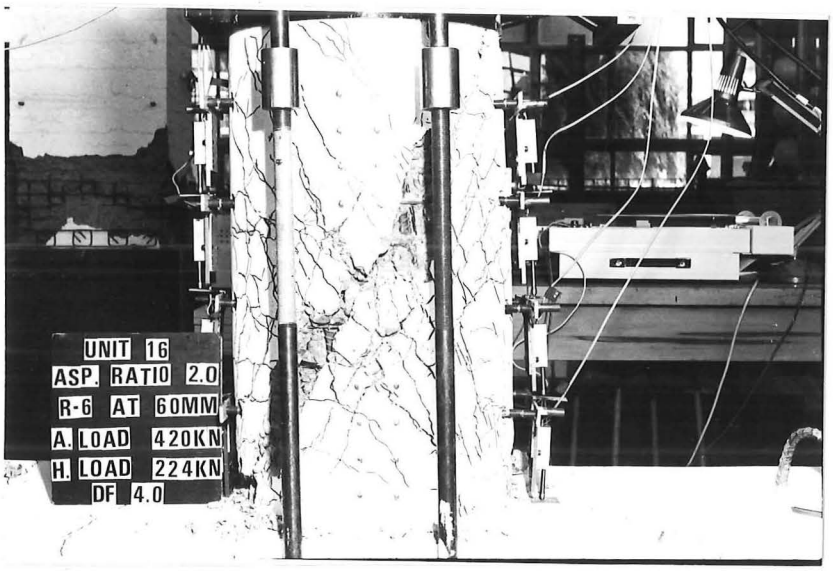

Fig. 4.37 : Damage along the main diagonal cracks in UNIT 16 (brittle shear failure)

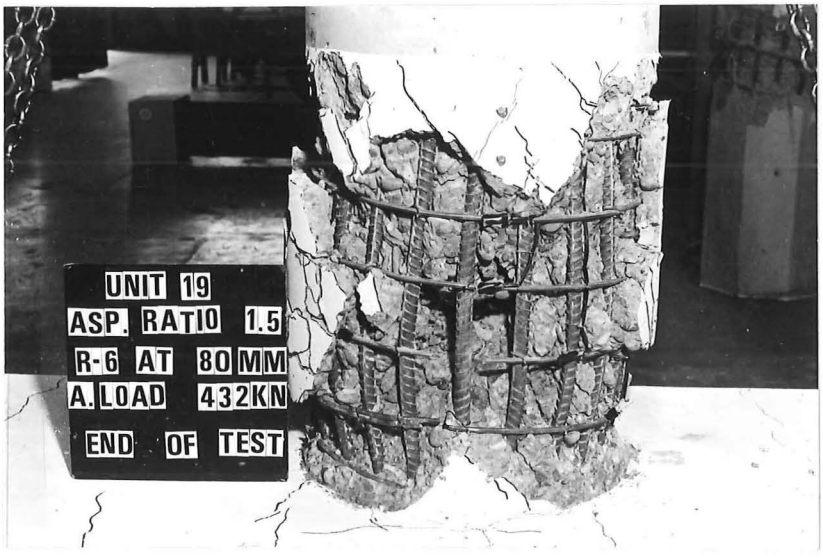

Fig. 4.38 : Final appearance of UNIT 19 after test (brittle shear failure)

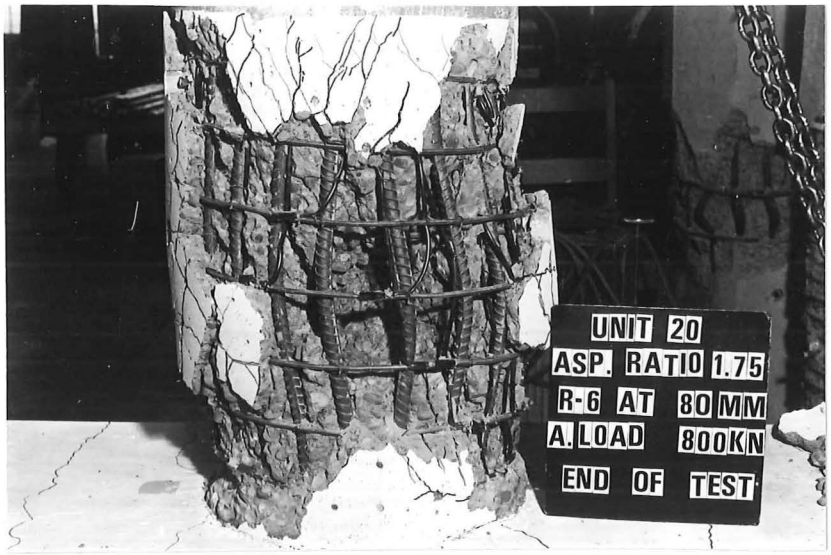

Fig. 4.39 : Final appearance of UNIT 20 after test (brittle shear failure)

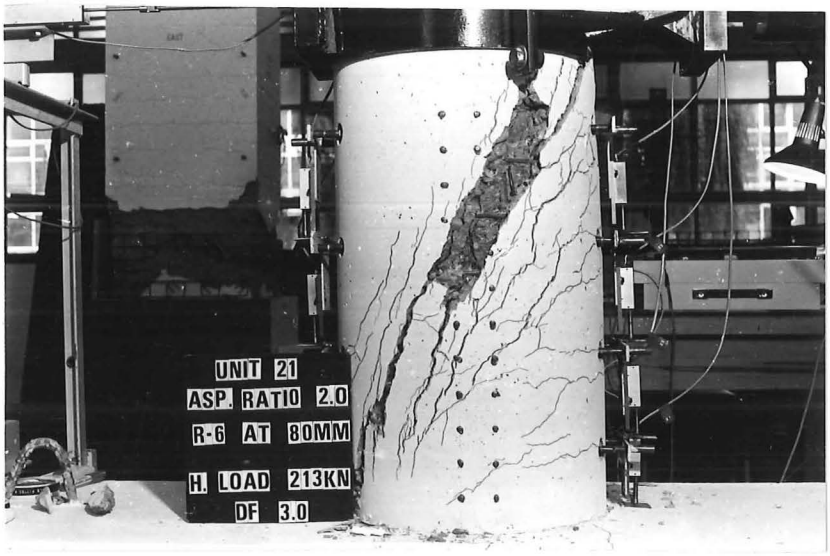

Fig. 4.40 : Damage along main diagonal cracks of UNIT 21 (brittle shear failure - monotonic loading)

Fig. 4.41 : Final appearance of UNIT 25 (brittle shear failure - no transverse reinforcement)

than V_{if} was attained at about $\mu = 1.5$ ($\frac{V_u}{V_{if}} = 0.824$) but thereafter the load carrying capacity dropped continuously. As can be seen in Fig. 4.40, the main diagonal cracks opened widely and severe spalling of concrete took place in the vicinity of these cracks. The spiral reinforcement began to carry a larger proportion of the applied shear as the concrete disintegrated. The high strain imposed resulted in progressive fracture of spirals from $\mu = 4$ onwards. The step-wise drop in the load-deflection curve shown in Fig. 4.28 is a consequence of this. This 'unbuttoning' effect severely affected the structural integrity of this unit. On reversing the loading direction at $\mu = 6$, both strength and stiffness remained very small. The first peak load to $\mu = 4$ in the reversed direction was only 43 percent of V_{if} and this dropped to about 25 percent in the next cycle. Unit 21 was a companion unit of Unit 7 ($\frac{M}{VD} = 2.0$ and $\frac{P_i}{f'_c A_g} = 0$) with a spiral reinforcement content of 0.0038. The monotonic load-deflection curve of Unit 21 normalized with respect to the ideal flexural strength and the yield displacement is transposed onto Fig. 4.27 of Unit 7. The results showed that the monotonic curve is similar to the envelope of the response of Unit 7, though rather surprisingly, Unit 7 attained higher peak loads at $\mu = 1.5$ and $\mu = 4$.

Unit 25 was the only column without any transverse reinforcement. Flexural cracking in this column commenced at about 20 percent of V_{if}. The main diagonal cracks, formed in the elastic cycles, soon extended from corner to corner during subsequent loading and the column had essentially failed once these cracks were formed. The load carrying capacity during the inelastic cycles could never reach the ideal flexural strength and the first excursion into the inelastic range brought about a drastic drop in strength at a point not far beyond the peak load of the elastic cycles as is evident in Fig. 4.24. The hysteresis loops thereafter remained flat, indicating very low stiffness and load carrying capacity. Nevertheless, the load sustained by the shear resisting mechanism that existed was quite substantial during the early stage of loading. The final appearance of Unit 25 is as shown in Fig. 4.41.

4.3 SHEAR CARRYING CAPACITY

Shear strengths at various stages of loading history are studied in this section. Shear strength is expressed in the non-dimensional form $\frac{v}{\sqrt{f'_c}} = \frac{V}{A_e\sqrt{f'_c}}$ where the effective stress area, A_e, is taken to be 80 percent of the gross area of cross-section. This area is approx-

mately equal to the concrete core area taken to the centre-line of spirals for the column units in this project.

4.3.1 Shear Carrying Capacity At Onset Of Diagonal Cracking

As the so-called 'concrete contribution' in a number of code equations is taken to be the load at onset of diagonal cracking, the diagonal cracking load of the specimens is studied in this section. During the elastic load cycles, diagonal cracks formed only after flexural cracking had taken place. Because the loading was carried out in increments, the loads at which diagonal cracks first appeared might not coincide with the end of an increment. As these increments were not very large, the average load at two successive increments was usually taken as the experimentally observed diagonal cracking load. Also, before diagonal cracking, shear strain in the spirals remained practically zero. Therefore, the load at which the spiral strain became significant gave a good indication of the onset of diagonal cracking. Extrapolating backwards from spiral strain readings measured during increments subsequent to diagonal cracking gave a good estimate of diagonal cracking load. Values of loads at diagonal cracking obtained from strain readings are listed together with the observed values in Table 4.2. These two values compared favourably and their average was used to calculate the non-dimensional shear stress at diagonal cracking $(\frac{v_{cr}}{\sqrt{f'_c}})$. Also listed in Table 4.2 is the initial crack inclination with respect to the column axis, θ, as measured from photos taken during testing. These angles appear to fall in the range 40 to 50-deg with an average value of about 43-deg.

(a) The influence of aspect ratio

The non-dimensional shear stress, $\frac{v_{cr}}{\sqrt{f'_c}}$, is plotted against the reciprocal of aspect ratio in Fig. 4.42a for three axial load levels. The plots show that shear stress at diagonal cracking varies almost linearly with the reciprocal of aspect ratio for the three levels of axial load considered. However, it appears from the plots that the variation in v_{cr} is not very large for aspect ratio greater than 2.0 and it might thus be reasonable to take $\frac{M}{VD} = 2.0$ as the limit beyond which the influence of aspect ratio on diagonal cracking load can be considered insignificant.

(b) The influence of axial load

In general the presence of axial compression delayed the onset of diagonal cracking, i.e. the diagonal cracking load increases with axial

Table 4.2 : Shear Force At Diagonal Cracking

UNIT	$\frac{M}{VD}$	$\frac{P_i}{f'_c A_g}$	Diagonal Cracking Load (kN)			$\frac{v_{cr}}{\sqrt{f'_c}}$ (expt)	$\frac{v_{cr}}{\sqrt{f'_c}}$ (Eq.4.1)	(7)/(8)	Crack Inclination θ (deg)
			V^o_{cr}	V^ε_{cr}	V_{cr}				
(1)	(2)	(3)	(4)	(5)	(6)	(7)	(8)	(9)	(10)
1	2.0	0	153	153	153.0	0.249	0.280	0.89	50
2	2.0	0	180	175	177.5	0.290	0.280	1.04	38
3	2.5	0	142	160	151.0	0.250	0.280	0.89	45
4	2.0	0	150	150	150.0	0.270	0.280	0.96	48
5	2.0	0	150	150	150.0	0.268	0.280	0.96	40
6	1.5	0	183	172	177.5	0.322	0.373	0.86	45
7	2.0	0	150	175	162.5	0.298	0.280	1.06	45
8	2.0	0.2	254	250	252.0	0.468	0.454	1.03	40
9	2.5	0.2	289	200	244.5	0.445	0.454	0.98	45
10	2.0	0.2	270	253	261.5	0.466	0.454	1.03	43
11	2.0	0.2	222	257	239.5	0.436	0.454	0.96	47
12*	1.5	0.2	324	325	324.5	0.604	0.605	1.00	47
13	2.0	0.1	210	210	210.0	0.348	0.367	0.95	43
14	2.0	0	150	167	158.5	0.272	0.280	0.97	46
15	2.0	0	127	140	133.5	0.225	0.280	0.80	42
16	2.0	0.1	220	218	219.0	0.377	0.367	1.03	42
17	2.5	0.1	211	195	203.0	0.344	0.367	0.94	37
18	1.5	0.1	300	280	290.0	0.487	0.489	1.00	38
19	1.5	0.1	270	275	272.5	0.462	0.489	0.94	42
20	1.75	0.175	328	325	326.5	0.537	0.494	1.09	37
21	2.0	0	150	164	157.0	0.271	0.280	0.97	45
22	2.0	0	150	168	159.0	0.284	0.280	1.01	38
23	2.0	0	201	185	193.0	0.338	0.280	1.21	45
24	2.0	0	205	190	197.5	0.341	0.280	1.22	42
25	1.5	0	180	-	180.0	0.321	0.373	0.86	50
							Ave	0.99	43
							σ	0.09	3.8

* The initial axial load on Unit 12 was $0.2f'_c A_g$

V^o_{cr} = Diagonal cracking load observed during testing

V^ε_{cr} = Diagonal cracking load extrapolated from measured spiral strains

$V_{cr} = (V^o_{cr} + V^\varepsilon_{cr})/2$

θ was measured with respect to column axis

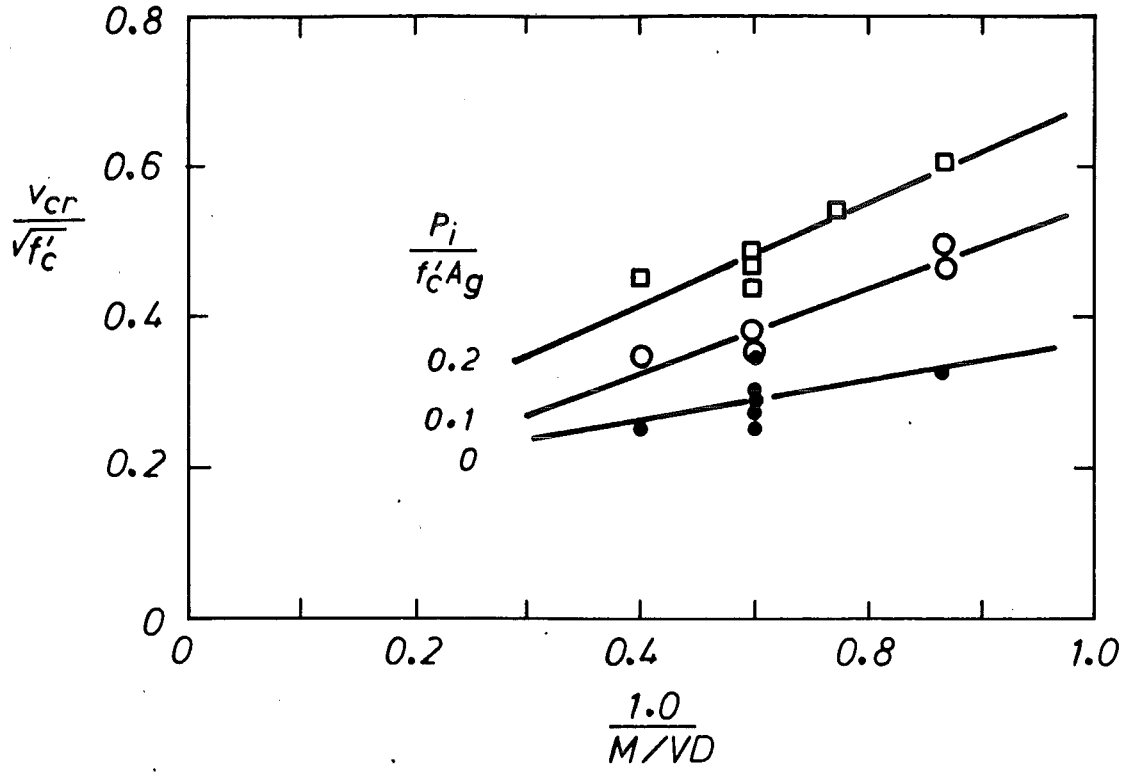

(a) at onset of diagonal cracking

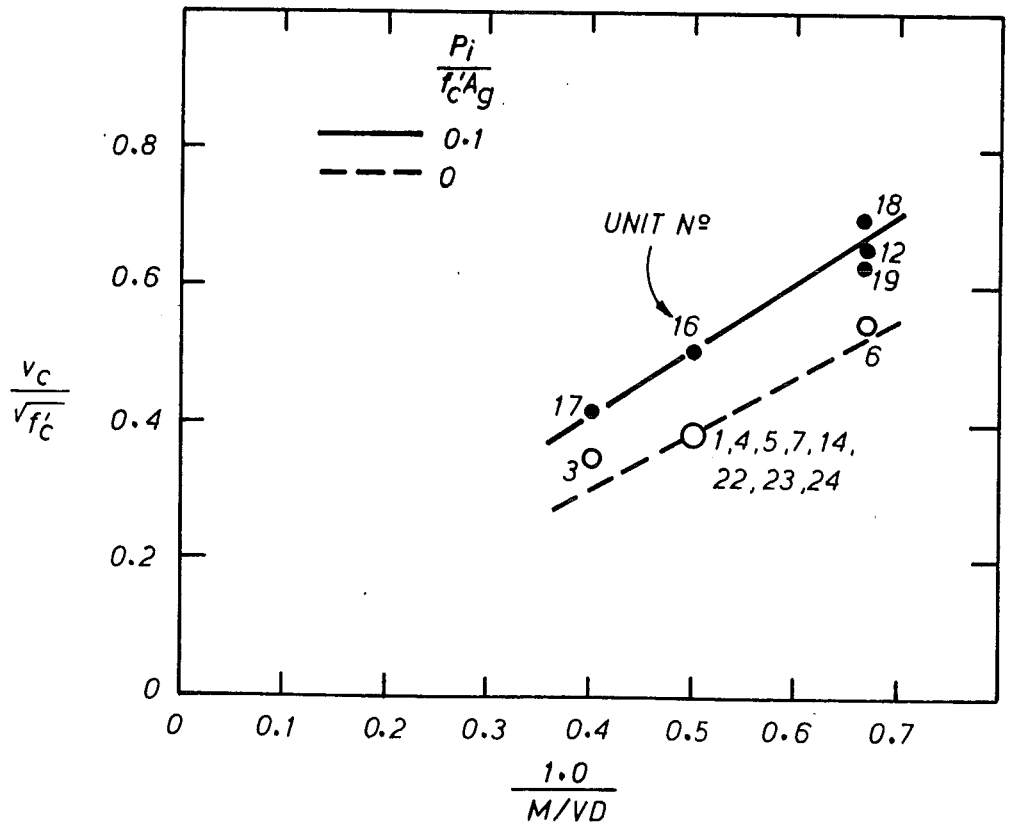

(b) at ultimate

Fig. 4.42 : Effect of aspect ratio on 'concrete contribution' in shear strength

compression. The influence of axial load on shear stress at diagonal cracking is illustrated in Fig. 4.43a in which the non-dimensional shear stress is plotted against the axial load level for three different aspect ratios. A linear relationship between the two quantities was obtained. For aspect ratios of 2.0 and 2.5 the points are quite close to each other and a single straight line was used to fit these points.

(c) The combined effect of aspect ratio and axial load

The combined effect of the two factors was studied by introducing a factor, α_1, such that

$$\alpha_1 = \frac{2.0}{\frac{M}{VD}} \geq 1.0$$

This factor is to allow for the increase in shear stress at onset of diagonal cracking due to decrease in aspect ratio for $\frac{M}{VD}$ less than 2.0 . The non-dimensional shear stress multiplied by the factor $\frac{1}{\alpha_1}$ is plotted against axial load level in Fig. 4.44a. The results indicated a linear increase in v_{cr} as the axial compression was increased. The equation for the best-fit straight line can be expressed as follows

$$\frac{v_{cr}}{\sqrt{f'_c}} = 0.28 \left(1 + 3.1 \frac{P_i}{f'_c A_g}\right) \alpha_1 \qquad (4.1)$$

Also included in Fig. 4.44a is a straight line representing the upper limit of the non-seismic code equation for concrete shear stress from NZS 3101, viz

$$\frac{v_c}{\sqrt{f'_c}} = 0.2 \left(1 + \frac{3 P_i}{f'_c A_g}\right) \qquad (4.2)$$

The two relationships are very similar except that the experimental results are about 1.4 times those specified by the code equation. The results predicted by Eq. 4.1 and the ratios between the experimental and predicted values are also listed in Table 4.2. The average value of the ratios is close to 0.99 with a standard deviation of 0.09.

4.3.2 Shear Carrying Capacity At Ultimate

4.3.2.1 Strength and ductility at ultimate

The ultimate capacity (V_u) is defined here as the load at which the shear carrying capacity reaches its maximum value during testing. The displacement ductility level at which this maximum load was achieved varied considerably. Depending on the non-seismic relative strength

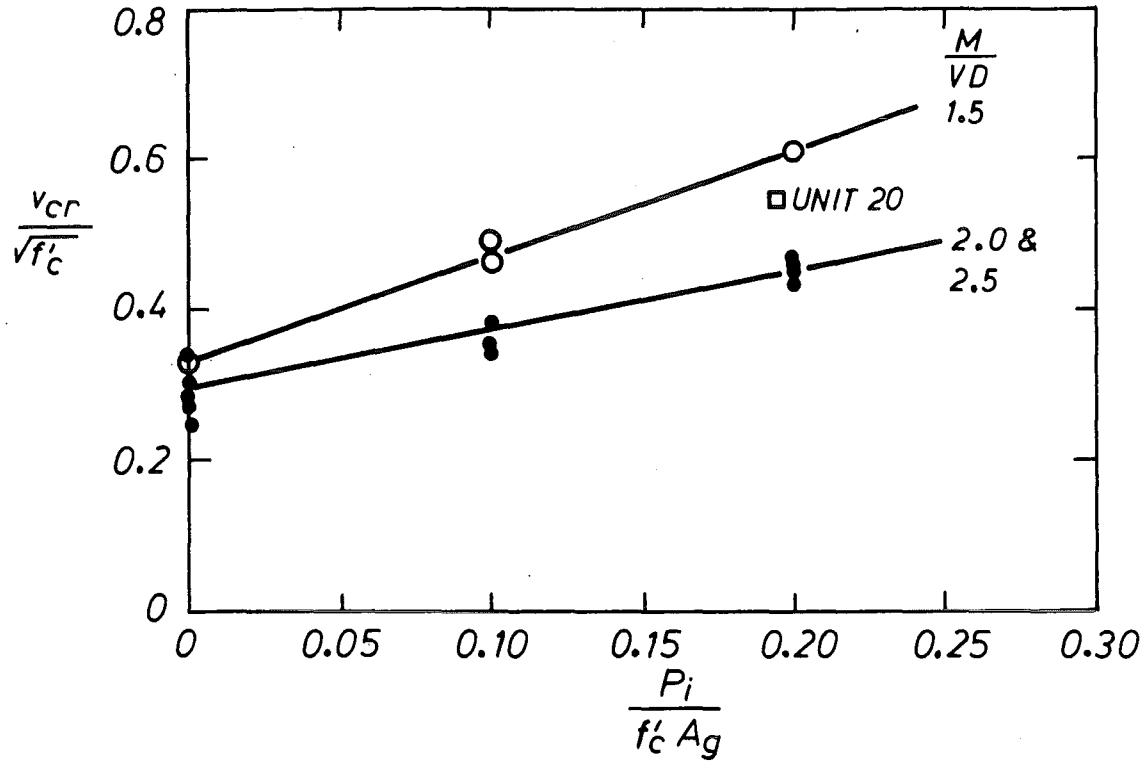

(a) at onset of diagonal cracking

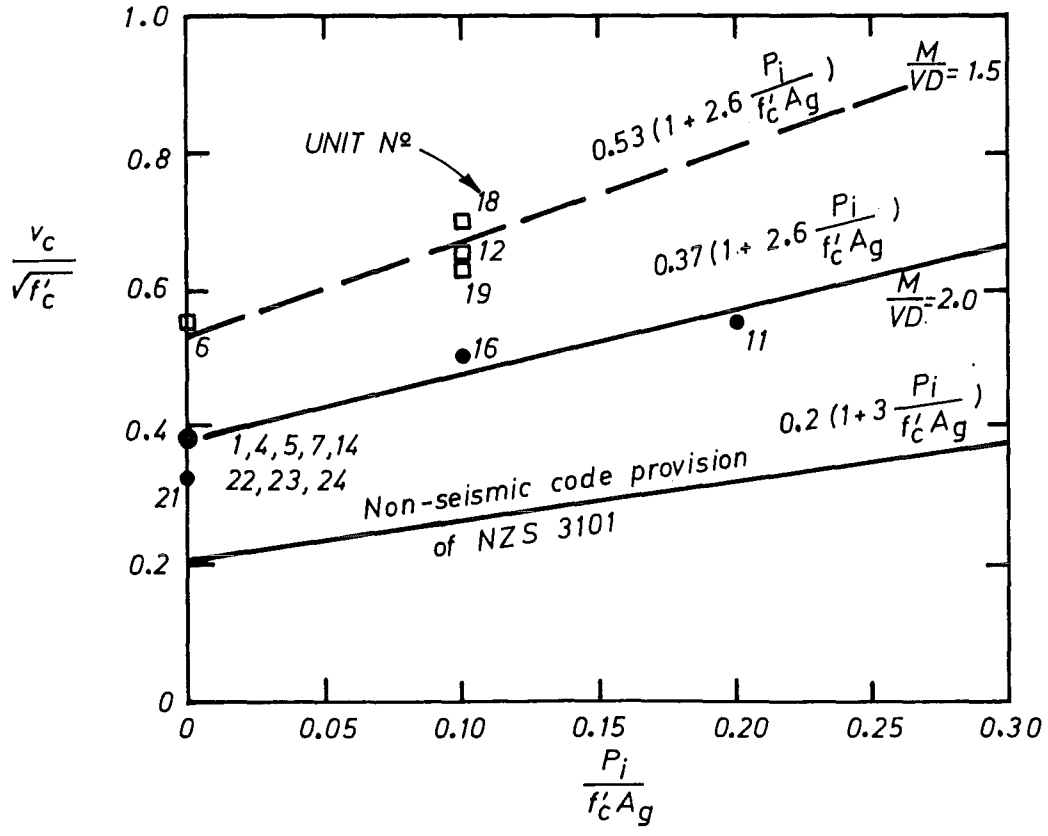

(b) at ultimate

Fig. 4.43 : Effect of axial load on 'concrete contribution' in shear strength

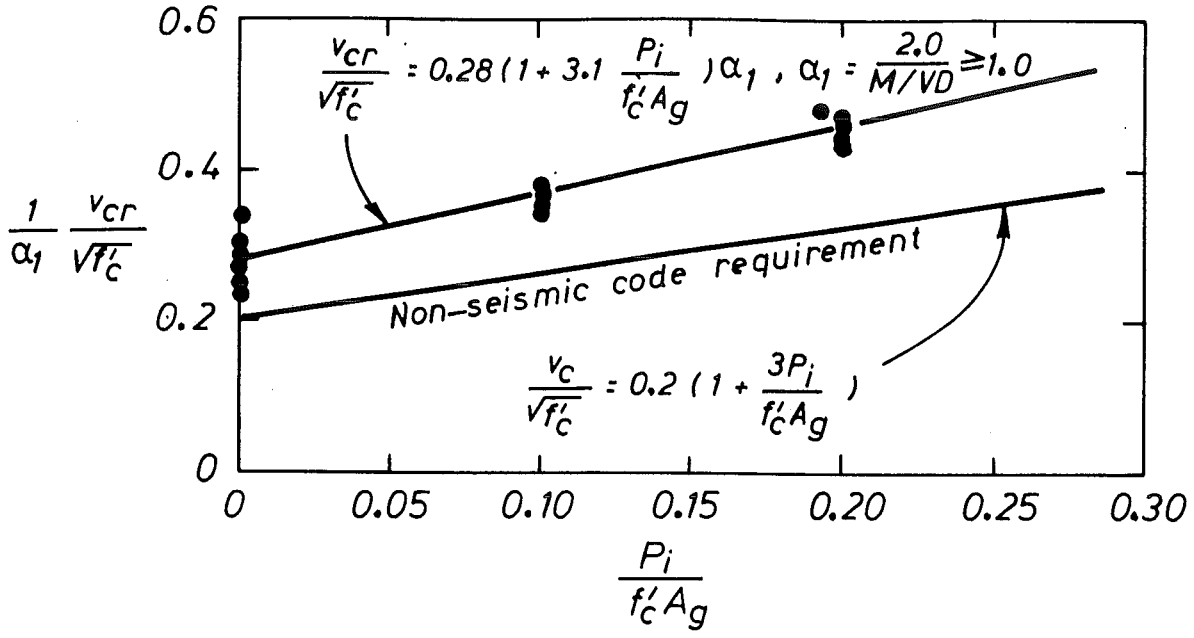

(a) at onset of diagonal cracking

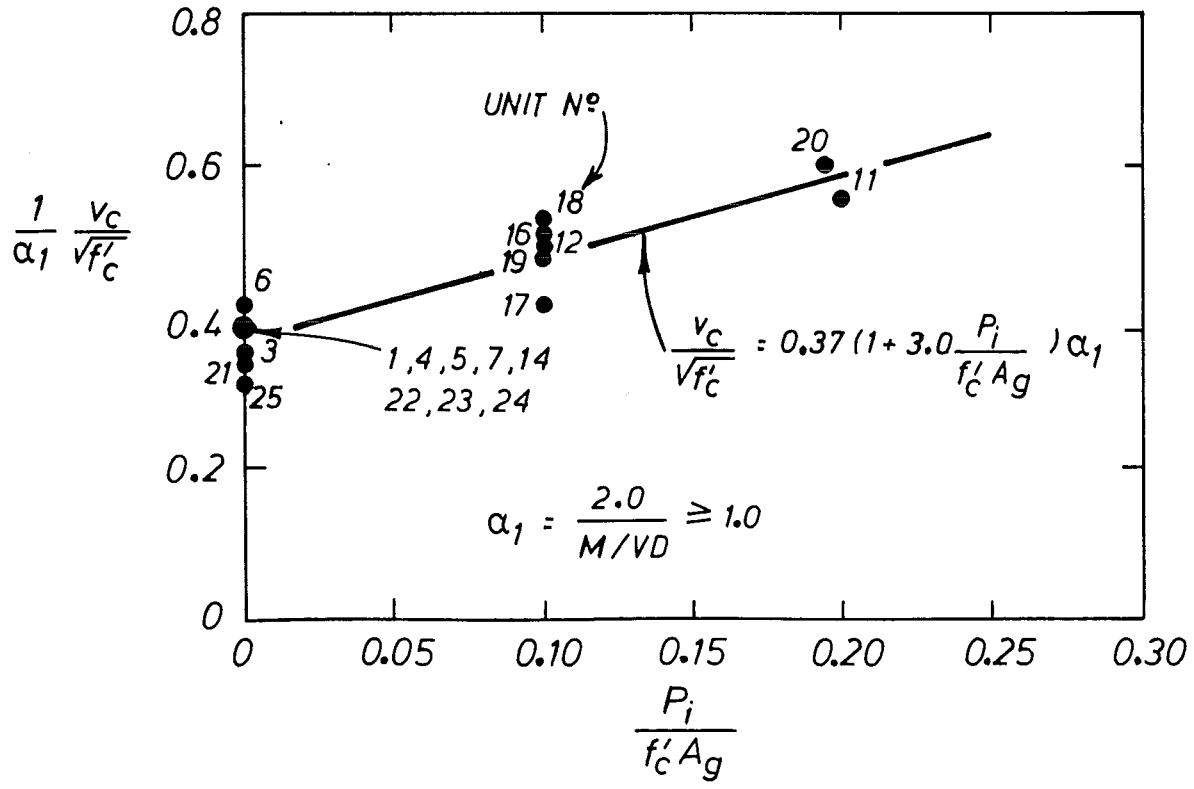

(b) at ultimate

Fig. 4.44 : The combined effect of aspect ratio and axial load on concrete shear strength

index, μ at V_u, as listed in Table 4.1, ranges from about 1 to 8. A plot of these ductility values versus $\frac{V_{iv}}{V_{if}}$ is shown in Fig. 4.45. In general, the value of μ achieved at ultimate increases as the relative strength index increases. From the plot, a design with equal ideal flexural and shear strengths using the current non-seismic code provisions NZS3101 implies a ductility of about 4.3 at ultimate.

Also included in Table 4.1 are the values of V_u expressed as ratios of $\frac{V_u}{V_{if}}$. To assess the effect of the relative strength index $\frac{V_{iv}}{V_{if}}$, the $\frac{V_u}{V_{if}}$ ratio is plotted against $\frac{V_{iv}}{V_{if}}$ in Fig. 4.46a. The general trend shows that the $\frac{V_u}{V_{if}}$ ratio increases almost linearly with the relative strength index. The average value of $\frac{V_u}{V_{if}}$ for columns which attained a displacement ductility factor of at least 4 before failure is about 1.23 which is similar to, but slightly higher than the flexural overstrength ratio expected for members reinforced with Grade 380 steel.

In Table 4.1, the ultimate shear stresses are non-dimensionalised as explained earlier. Results from nine column units having 800 mm shear-span and without axial load are plotted against the spiral reinforcement content, ρ_s, in Fig. 4.47a. All these column units failed in shear with limited or no ductility. They appear to vary linearly with the spiral reinforcement content and the best-fit straight line gives the relationship as

$$\frac{v_u}{\sqrt{f'_c}} = 28\ \rho_s + 0.38 \qquad (4.3)$$

Using the conventional additive principle, the theoretical equation for ultimate shear strength can be written as

$$V_i = V_s + V_c$$

In terms of shear stresses and assuming a 45-deg truss, the above equation can be transformed into

$$\frac{v_i}{\sqrt{f'_c}} = \frac{V_i}{A_e\sqrt{f'_c}} = \frac{(\frac{\pi}{8}\ d_s^2\ f_{yt})\ \rho_s}{0.8A_g\sqrt{f'_c}} + \frac{v_c}{\sqrt{f'_c}}$$

$$\approx \frac{f_{yt}}{2\sqrt{f'_c}}\ \rho_s + \frac{v_c}{\sqrt{f'_c}} \qquad (4.4)$$

Taking average values of material strengths (f_{yt} = 332 MPa and f'_c = 33 MPa) the above equation becomes

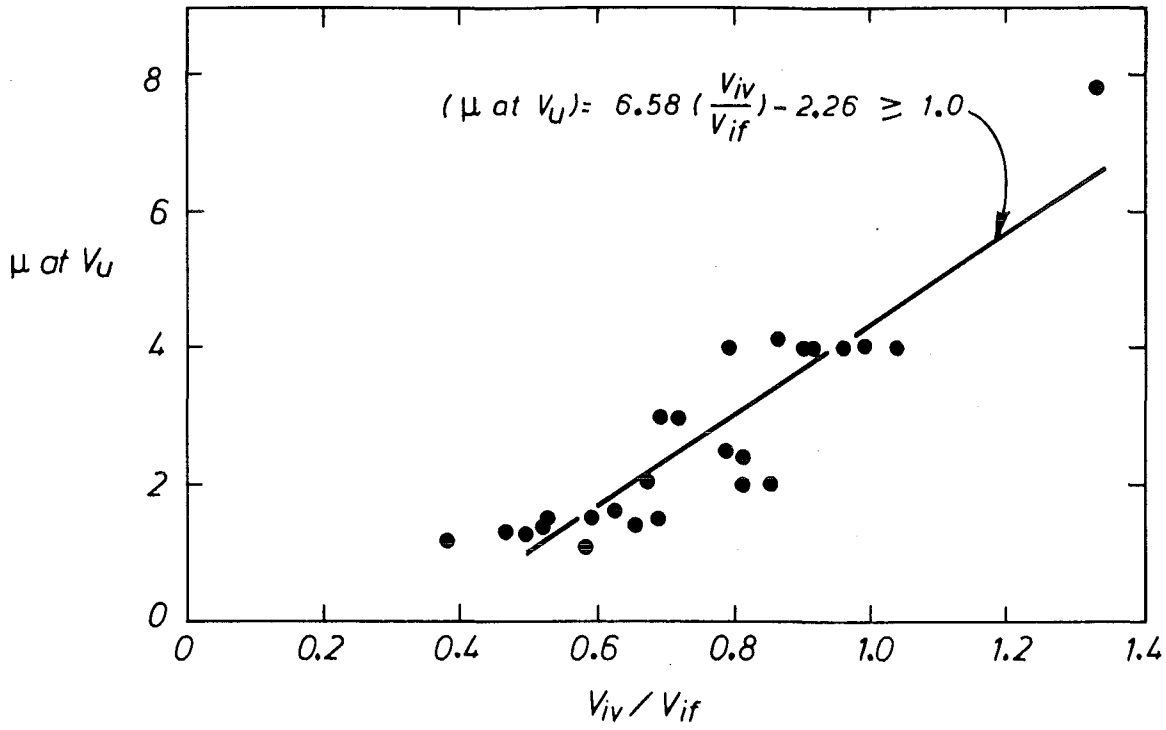

Fig. 4.45 : Displacement ductility level at ultimate as a function of non-seismic relative strength index

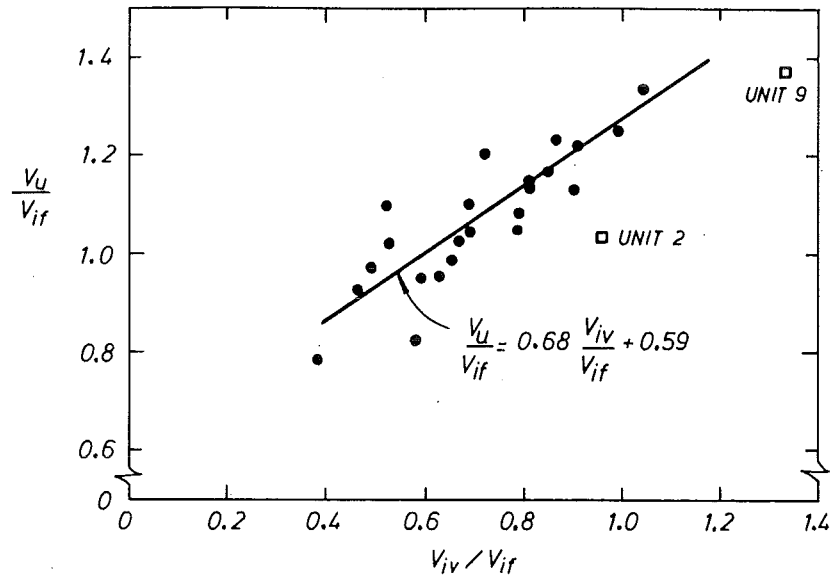

(a) at ultimate

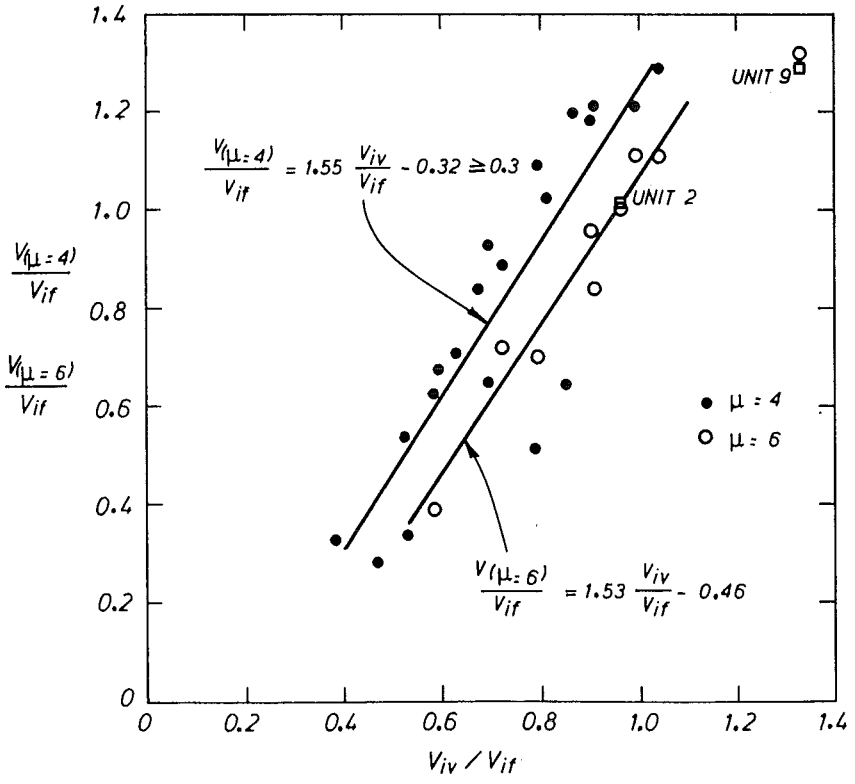

(b) at μ = 4 and μ = 6

Fig. 4.46 : Shear strength versus non-seismic relative strength index

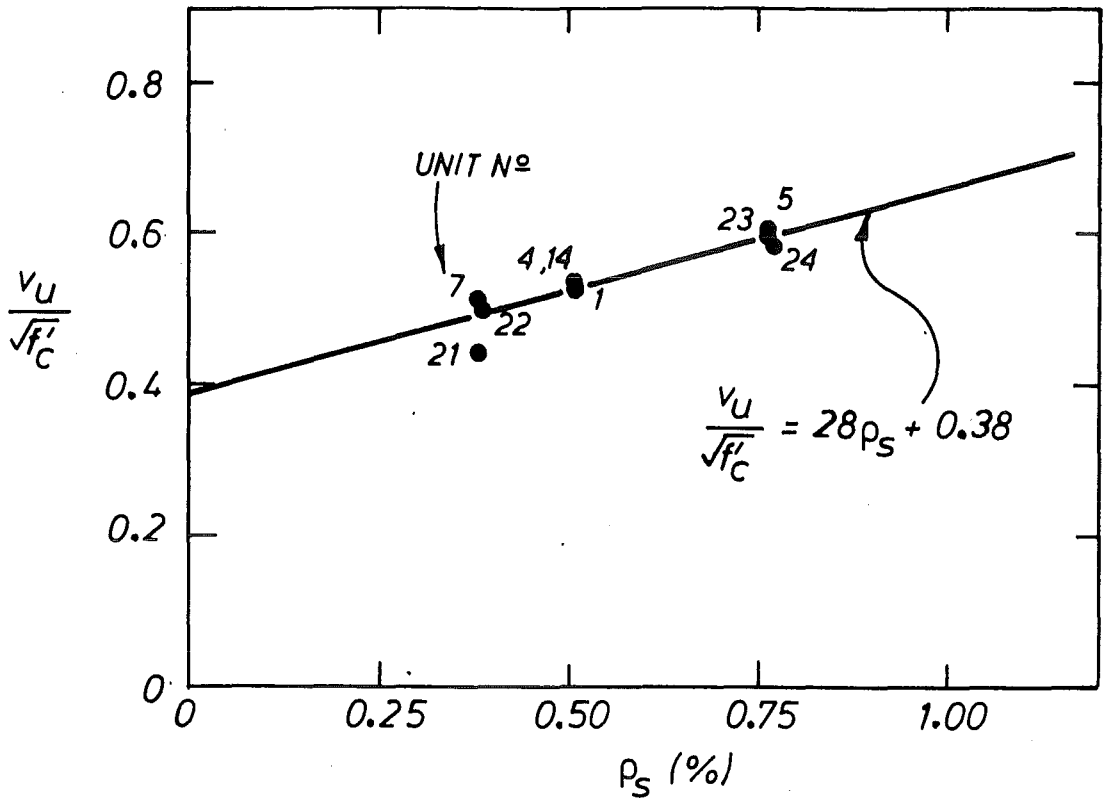

(a) at ultimate

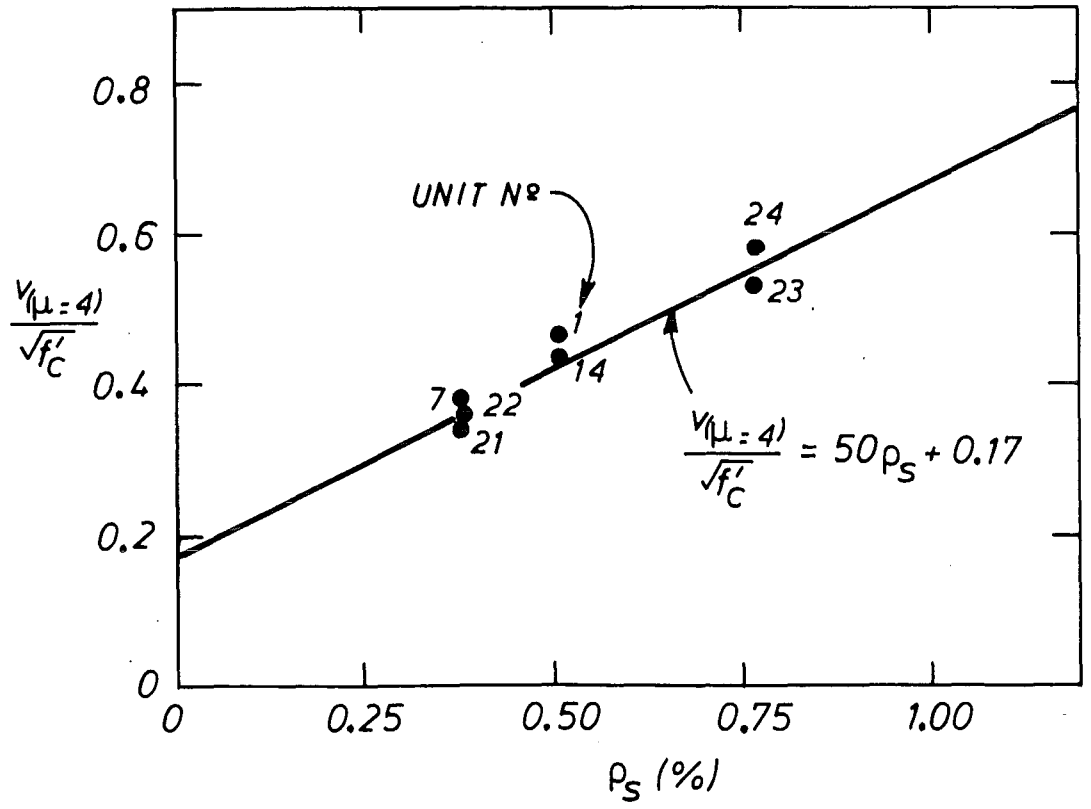

(b) at $\mu = 4$

Fig. 4.47 : Shear stress at ultimate and $\mu = 4$ versus spiral reinforcement content ($\frac{M}{VD} = 2.0$, $\frac{P_i}{f'_c A_g} = 0$)

$$\frac{v_u}{\sqrt{f'_c}} = 29\,\rho_s + \frac{v_c}{\sqrt{f'_c}} \qquad (4.5)$$

which is very similar to that obtained from experimental data (Eq. 4.3). Comparing Eqs. 4.3 and 4.5 the value for $\rho_s = 0$ implies $v_c = 0.38\sqrt{f'_c}$. The fact that the constant associated with ρ_s differs by only 3.5 percent between Eqs. 4.3 and 4.5 indicates that the assumption of a 45-deg truss appears to be reasonable in this case.

The non-dimensional shear stresses at ultimate listed in Table 4.1 vary between 0.37 (Unit 2) and 0.98 (Unit 12). The seismic provisions of NZS 3101 requires diagonal reinforcement to be provided in members with axial compression no greater than $0.1f'_c A_g$ if the ultimate shear stress exceeds $0.3\sqrt{f'_c}$ (Chapter Two). This very low upper limit was exceeded by all column units tested in this project. The average concrete strength for all the column units was 32.8 MPa (Chapter Three) and if the code requirements are followed strictly, diagonal reinforcement should have been provided if the shear force at ultimate exceeded 173 kN (i.e. $0.3\sqrt{32.8}$ x 0.8 A_g) and if the axial compression was less than or equal to $0.1f'_c A_g$. However, as can be seen from the table, the shear stress levels of column units (excluding Units 8, 9, 10, 11, 20) at ultimate exceeded the code specified upper limit despite the absence of diagonal reinforcement. The ultimate shear stresses of the named five column units with axial compression of $0.2f'_c A_g$ fall within the code specied upper limit of $0.9\sqrt{f'_c}$. The results are plotted for different axial load levels in Fig. 4.48 which

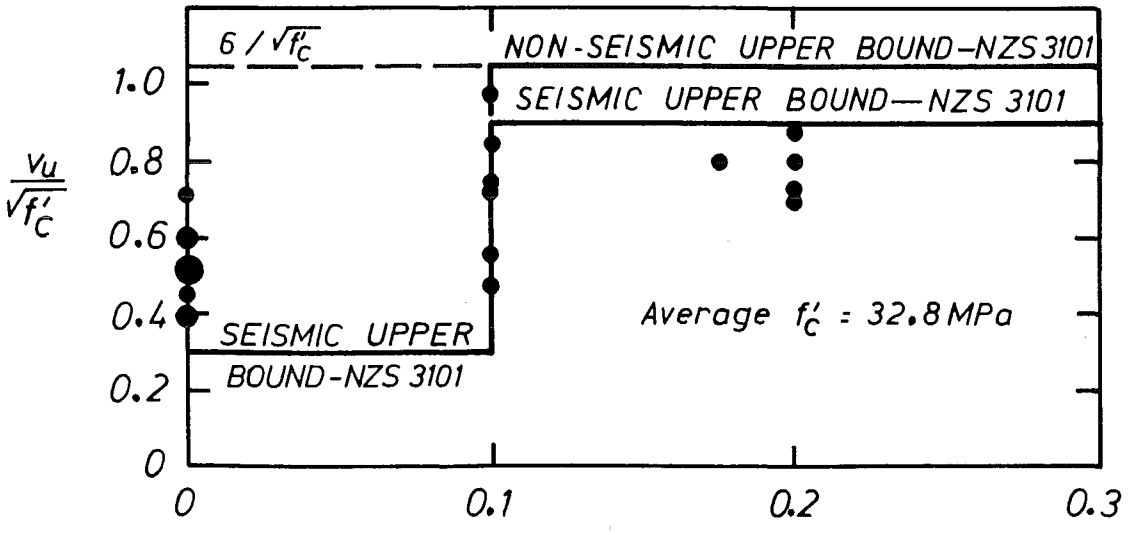

Fig. 4.48 : Shear stress at ultimate for different axial load levels

also illustrates how the code specified upper limit on shear stress changes due to change in axial load level. Also included in the figure is the non-seismic upper limit as dictated by the criterion to avoid diagonal crushing of concrete. The figure shows that the ultimate shear stresses of column units with no axial compression are closer together while a wider spread of data is observed in the case when $\frac{P_i}{f'_c A_g} = 0.1$. However, all the points are well above the code limit of $0.3\sqrt{f'_c}$. It should be noted that the diagonal reinforcement in NZS 3101 was recommended to control sliding shear displacement and hence, to improve energy dissipation, and it was not envisaged to increase shear strength, although the diagonal tension reinforcement may be included in deriving V_s.

4.3.2.2 Concrete shear stress at ultimate

For discussion purposes, the difference between the ultimate shear force and the theoretical spiral force across a 45-deg crack given by Eq. 2.53 divided by the effective stress area ($0.8A_g$) is termed concrete shear stress. The magnitude of concrete shear stress at ultimate as outlined in the last section is greater than that given by Eq. 4.1 for the case of no axial load, implying the 'concrete contribution' increased after onset of diagonal cracking.

(a) The influence of aspect ratio

The non-dimensional values of concrete shear stress from Table 4.3 are plotted against the reciprocal of aspect ratio in Fig. 4.42b. It appears from the figure that the concrete shear stress has an inverse relationship with the aspect ratio within the range considered. However, the variation $\frac{v_c}{\sqrt{f'_c}}$ with aspect ratio was not very significant for aspect ratio greater than 2.0. The big open circle in the figure encompasses the results from the eight specimens labelled.

(b) The influence of axial load

To examine the effect of axial load, the dimensionless concrete shear stress is plotted against $\frac{P_i}{f'_c A_g}$ as shown in Fig. 4.43b and the numerical values are tabulated in Table 4.4. As was the case with diagonal cracking load, the tendency of increasing axial compression is to increase the concrete shear stress. Results from other column units with different ratios indicate similar trend of increase in concrete shear stress with axial load level. The resulting plot for column units with an aspect ratio of 2.0 implies a linear relationship as follows,

Table 4.3 : Influence Of Aspect Ratio On Concrete Shear Stress At Ultimate

UNIT	$\frac{P_i}{f'_c A_g} = 0$		UNIT	$\frac{P_i}{f'_c A_g} = 0.1$	
	$\frac{M}{VD}$	$\frac{v_c}{\sqrt{f'_c}}$		$\frac{M}{VD}$	$\frac{v_c}{\sqrt{f'_c}}$
1	2.0	0.377	12	1.5	0.655
3	2.5	0.349	13	2.0	-
4	2.0	0.377	16	2.0	0.503
5	2.0	0.373	17	2.5	0.413
6	1.5	0.549	18	1.5	0.699
7	2.0	0.376	19	1.5	0.630
14	2.0	0.385			
22	2.0	0.389			
23	2.0	0.377			
24	2.0	0.369			

Table 4.4 : Experimental And Predicted Concrete Shear Stress At Ultimate

UNIT	$\frac{M}{VD}$	$\frac{P_i}{f'_c A_g}$	$\frac{v_c}{\sqrt{f'_c}}$ (Expt)	$\frac{v_c}{\sqrt{f'_c}}$ (Eq.4.7)	$\frac{(4)}{(5)}$
(1)	(2)	(3)	(4)	(5)	(6)
1	2.0	0	0.377	0.370	1.02
2	2.0	0	-	-	-
3	2.5	0	0.349	0.370	0.94
4	2.0	0	0.377	0.370	1.02
5	2.0	0	0.373	0.370	1.01
6	1.5	0	0.549	0.493	1.11
7	2.0	0	0.376	0.370	1.02
8	2.0	0.2	-	-	-
9	2.5	0.2	-	-	-
10	2.0	0.2	-	-	-
11	2.0	0.2	0.553	0.592	0.93
12	1.5	0.1	0.655	0.641	1.02
13	2.0	0.1	-	-	-
14	2.0	0	0.385	0.370	1.04
15	2.0	0	-	-	-
16	2.0	0.1	0.503	0.481	1.05
17	2.5	0.1	0.413	0.481	0.86
18	1.5	0.1	0.699	0.641	1.09
19	1.5	0.1	0.630	0.641	0.98
20	1.75	0.175	0.693	0.645	1.07
21	2.0	0	0.333	0.370	0.90
22	2.0	0	0.389	0.370	1.05
23	2.0	0	0.377	0.370	1.02
24	2.0	0	0.369	0.370	1.00
25	1.5	0	0.414	0.493	0.84
				Ave	1.00
				σ	0.07

$$\frac{v_c}{\sqrt{f'_c}} = 0.37 \left(1 + 2.6 \frac{P_i}{f'_c A_g}\right) \qquad (4.6)$$

Also included in the figure for comparison is the non-seismic provision of NZS 3101 as given by Eq. 4.2. It is evident that the code equation is conservative in predicting the ultimate strength even if the non-seismic provision is used.

However, as noted in Chapter Two, it must be remembered that the NZS 3101 provisions were based on behaviour of rectangular sections, with flexural reinforcement concentrated at opposite faces. Although applied to circular sections in the absence of specific information, their applicability has always been suspect.

(c) The combined effect of aspect ratio and axial load

The same procedure as described in the last section was employed to study the combined effect of aspect ratio and axial load. The results are plotted as shown in Fig. 4.44b and the best-fit straight line is given by

$$\frac{v_c}{\sqrt{f'_c}} = 0.37 \left(1 + 3.0 \frac{P_i}{f'_c A_g}\right) \alpha_1 \qquad (4.7)$$

where $\alpha_1 = \dfrac{2.0}{\dfrac{M}{VD}} \geq 1.0$

The values predicted by the above equation are listed in Table 4.4. The ratios between the experimental and predicted results had an average value of 1.00 with a standard of deviation of 0.07.

(c) The influence of spiral pitch and bar diameter

The use of different bar diamater for a constant spiral reinforcement content requires a change in the spiral pitch. However, as is evident in Fig. 4.49, which shows shear strengths of groups of specimens with the same spiral reinforcement content but different spiral pitch and bar diameter, the spiral pitch did not have much effect on the ultimate shear strengths of the column units within the limits considered. For the cases without axial load, the non-dimensional ultimate shear stress remained practically constant. The effect could be more significant where axial load was present. For $\frac{P_i}{f'_c A_g} = 0.2$, a reduction of about 10 percent in Unit 10, which had a wider spiral pitch, was recorded. Also shown in the figure is the corresponding concrete shear stress deduced experimentally as outlined before. The difference was again negligible.

4.3.3 Shear Carrying Capacity At $\mu = 4$ And $\mu = 6$

To look at the strength developed at high displacement ductility levels, the shear carrying capacity at $\mu = 4$ and $\mu = 6$ from Tables 4.5 and 4.6 respectively are studied. The values listed are the average of both positive and negative peak loads at the first cycle to $\mu = 4$ or $\mu = 6$. Also listed in the tables are the relative strength indices for both seismic and non-seismic values. Comparing these values with the experimental results indicates, in general, that the ratios of $\frac{V_{(\mu=4)}}{V_{if}}$ and $\frac{V_{(\mu=6)}}{V_{if}}$ might not reach the non-seismic values but exceeded the seismic values by a significant margin, even when shear failure had already occurred. Units 11 and 20 were the two exceptions. It is felt that insufficient provision of confining reinforcement for the levels of axial compression applied might have contributed to the poor performance of these latter units.

The effect of providing different ratios of ideal flexural and shear strengths is illustrated in Fig. 4.46b. The strength at $\mu = 4$ again increases with increasing relative strength index ($\frac{V_{iv}}{V_{if}}$) but at a faster rate if compared to similar plot at ultimate (Fig. 4.46a). The limited data for $\frac{V_{(\mu=6)}}{V_{if}}$ were also plotted in Fig. 4.46b as open circles. The pattern of variation is very similar to that of $\frac{V_{(\mu=4)}}{V_{if}}$ with only very slightly reduced rate of increase.

The degradation in strength can be significant if axial compression is present. As it is meaningless to include column units which attained their ultimate strengths at $\mu = 4$ or higher, the data from these column units were excluded in Table 4.7 which lists the ratios of measured strength reduction ($V_u - V_{(\mu-4)}$) to the ideal flexural strength These data indicated that the degradation in strength from ultimate was significantly influenced by the presence of axial compression. Even with a magnitude as low as $0.1f'_c A_g$ it caused a drop of about 55 percent of ideal flexural strength on average. A plot of these data versus axial load level in Fig. 4.50 shows that drop in strength varies almost linearly with axial load level.

In similar fashion to Fig. 4.47a, the dimensionless shear stress at $\mu = 4$ from Table 4.5 for column units with aspect ratio of 2.0 and without axial load is plotted in Fig. 4.47b. Again the results appear to vary in a linear fashion but with a drop in the vertical intercept representing the 'concrete contribution' and a steeper gradient indicating a deviation in crack inclination from 45-deg. The coefficient of ρ_s in the expression shown in Fig. 4.47b is 50 at $\mu = 4$ while the correspond-

Table 4.5 : Shear Force Developed At $\mu = 4$

UNIT	$\frac{M}{VD}$	$\frac{P_i}{f'_c A_g}$	$\frac{V_{iv}}{V_{if}}$	$\frac{V^s_{iv}}{V_{if}}$	$V_{(\mu=4)}$ (kN)	$\frac{V_{(\mu=4)}}{V_{if}}$	$\frac{V_{(\mu=4)}}{\sqrt{f'_c}}$
1	2.0	0	0.690	0.288	283	0.925	0.46
2	2.0	0	0.959	0.400	222	1.009	0.36
3	2.5	0	0.864	0.364	289	1.194	0.48
4	2.0	0	0.656	0.284	-	-	-
5	2.0	0	0.807	0.435	-	-	-
6	1.5	0	0.493	0.219	-	-	-
7	2.0	0	0.625	0.253	206	0.703	0.38
8	2.0	0.2	1.039	0.938	458	1.287	0.85
9	2.5	0.2	1.331	1.199	362	1.288	0.66
10	2.0	0.2	0.989	0.883	436	1.211	0.78
11	2.0	0.2	0.786	0.681	180	0.513	0.33
12*	1.5	0.1	0.721	0.400	387	0.886	0.72
13	2.0	0.1	0.912	0.479	438	1.207	0.72
14	2.0	0	0.668	0.283	254	0.836	0.44
15	2.0	0	0.902	0.422	228	1.118	0.38
16	2.0	0.1	0.687	0.249	228	0.646	0.39
17	2.5	0.1	0.851	0.306	181	0.644	0.31
18	1.5	0.1	0.522	0.186	247	0.535	0.42
19	1.5	0.1	0.466	0.139	132	0.282	0.22
20	1.75	0.175	0.527	0.415	160	0.335	0.26
21	2.0	0	0.578	0.208	196	0.626	0.34
22	2.0	0	0.592	0.211	198	0.673	0.35
23	2.0	0	0.807	0.420	301	1.020	0.53
24	2.0	0	0.790	0.410	332	1.089	0.57
25	1.5	0	0.377	0	95	0.327	0.17

* Axial load of Unit 12 was reduced to $0.1 f'_c A_g$

Table 4.6 : Shear Force Developed At $\mu = 6$

UNIT	$\frac{M}{VD}$	$\frac{P_i}{f'_c A_g}$	$\frac{V_{iv}}{V_{if}}$	$\frac{V^s_{iv}}{V_{if}}$	$V_{(\mu=6)}$ (kN)	$\frac{V_{(\mu=6)}}{V_{if}}$	$\frac{V_{(\mu=6)}}{\sqrt{f'_c}}$
2	2.0	0	0.959	0.400	221	1.002	0.36
8	2.0	0.2	1.039	0.938	396	1.112	0.74
9	2.5	0.2	1.331	1.199	371	1.319	0.67
10	2.0	0.2	0.989	0.883	409	1.111	0.71
12	1.5	0.1	0.721	0.400	323	0.739	0.60
13	2.0	0.1	0.912	0.479	279	0.767	0.46
15	2.0	0	0.902	0.422	197	0.963	0.33
21	2.0	0	0.578	0.208	121	0.387	0.21
24	2.0	0	0.790	0.410	214	0.700	0.37

Table 4.7 : Shear Strength Degradation Between Ultimate And μ=4
For Column Units With Limited Ductility Or No Ductility

UNIT	$\frac{P_i}{f'_c A_g}$	V_{if} (kN)	V_u (kN)	$V_{(\mu=4)}$ (kN)	$\frac{V_u - V_{(\mu=4)}}{V_{if}}$
1	0.0	306	320	283	0.121
7	0.0	293	280	206	0.253
11	0.2	351	404	180	0.638
14	0.0	304	311	254	0.187
16	0.1	345	379	223	0.453
17	0.1	281	329	181	0.527
18	0.1	462	507	247	0.563
19	0.1	468	436	132	0.650
20	0.175	477	487	160	0.686
21	0.0	313	258	196	0.198
22	0.0	294	280	198	0.279
23	0.0	295	339	301	0.129

ing value at ultimate is 29 (see Fig. 4.47a) so the angle of crack inclination can be estimated to be

$$90^o - \tan^{-1} \frac{50}{29} = 30.1^o$$

This agrees reasonably well with the observed value of about 26.6 (i.e. $\tan^{-1} 0.5$) for a corner-to-corner crack for the columns with aspect ratio of 2.0.

4.3.4 Shear Carrying Capacity At First Fracture Of Spirals

In a number of column units the high strain imposed on the spirals resulted in fracture of these spirals. Following each fracture there would usually be a drop in load carrying capacity. However, it is the load which caused the fracture, i.e. before the drop, which is of interest here. These values, V_{fr}, are listed in Table 4.8 for the ten column units involved. As the ideal flexural strength is irrelevant at the verge of failure since significant degradation of load carrying capacity had already occurred, the shear force, V_{fr}, was divided by the design spiral force, V_s, based on a 45-deg truss. For Units 8, 10 and 13, the fracture occurred at about $\mu = 5.5$ or higher but in the other columns, which demonstrated limited or no ductility (Units 11, 14, 16, 17, 19-21), the average value of μ at V_{fr} was about 3.4.

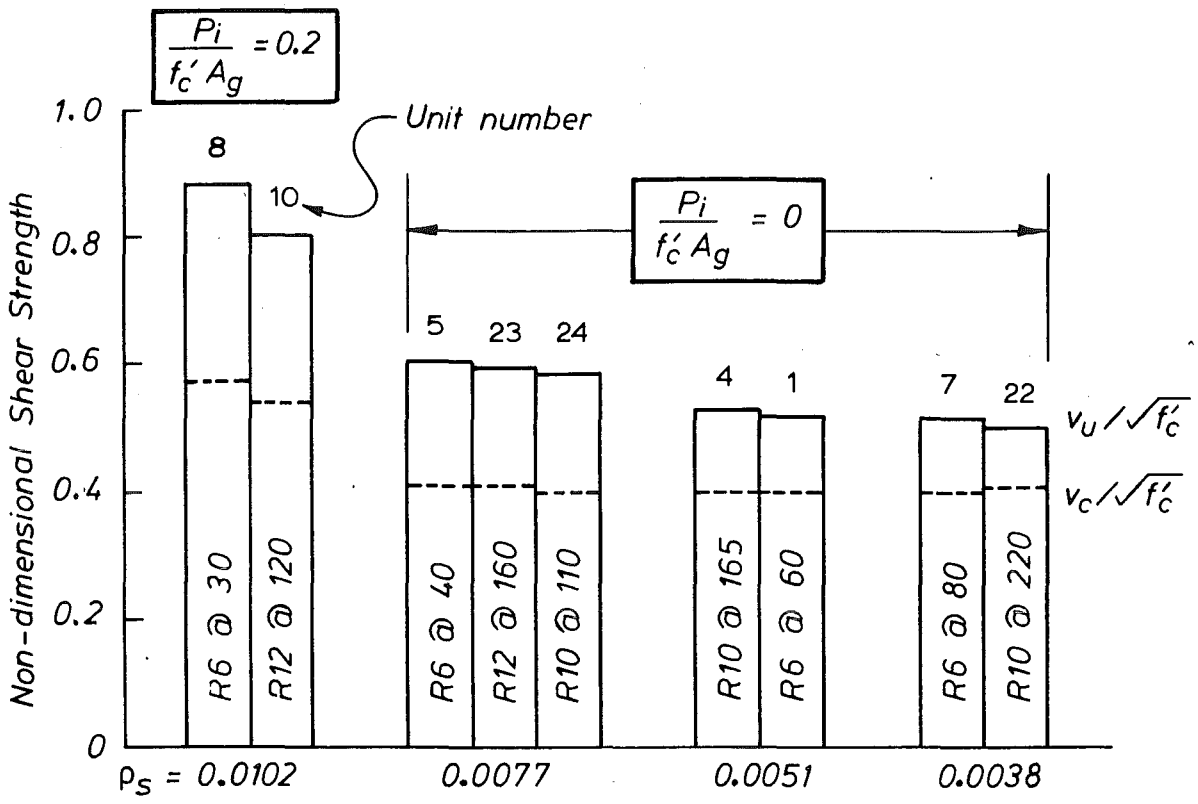

Fig. 4.49 : Comparison of shear strength of column units with different spiral spacings

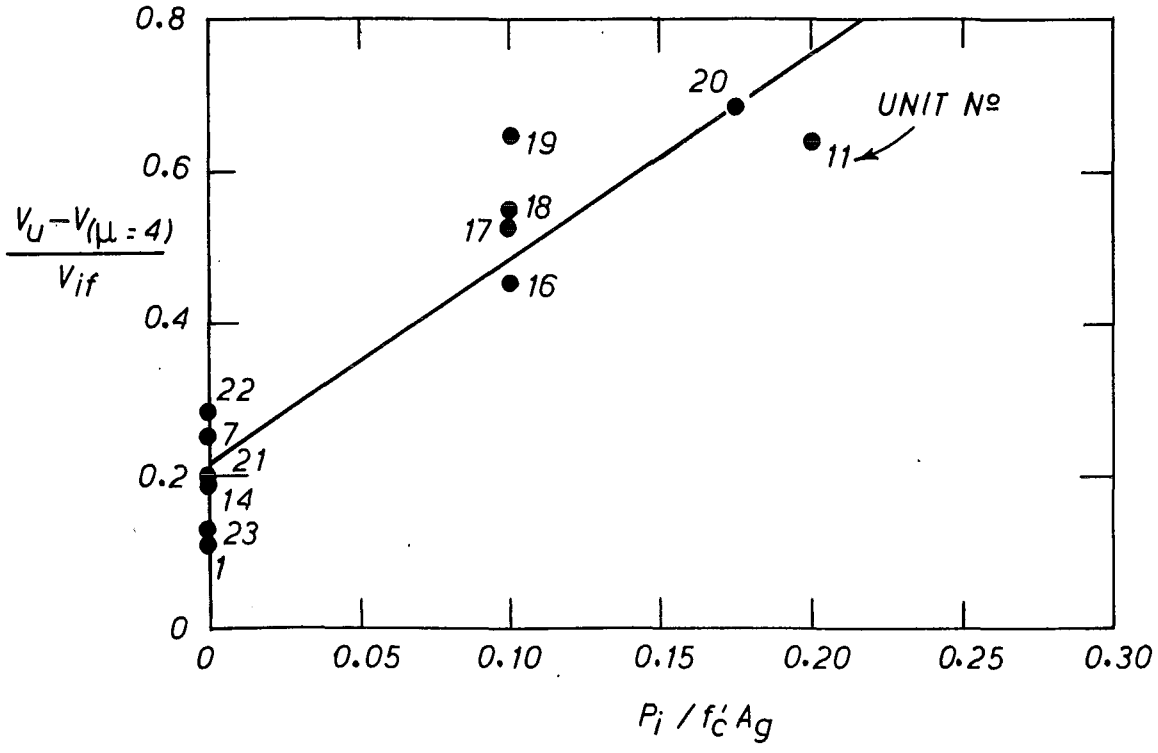

Fig. 4.50 : Effect of axial compression on strength degradation between ultimate and μ = 4

Table 4.8 : Shear Force At First Fracture Of Spirals

UNIT	V_s (kN)	$\frac{UTS}{f_{yt}}$	V_{fr} (kN)	$\frac{V_{fr}}{V_s}$	μ at V_{fr}
8	198	1.29	114	0.576	5.6
10	176	1.42	37	0.210	5.4
11	100	1.29	141	1.410	2.7
13	174	1.33	327	1.879	6.0
14	86	1.33	240	2.791	2.8
16	86	1.33	244	2.837	3.5
17	86	1.33	215	2.500	3.0
19	65	1.33	180	2.769	3.3
20	65	1.33	160	2.462	3.9
21	65	1.33	196	3.015	4.3

For these seven columns the ratio, $\frac{V_{fr}}{V_s}$, appears to remain essentially constant with an average of 2.54. If all the applied shear is assumed to be carried by the spirals and the ultimate tensile strength (UTS) of the spiral steel is taken as the spiral stress at failure (note that the average failure stress should be less than UTS) then, with a corner-to-corner crack as observed, the spiral force, V_s, at failure would have to be multiplied by a factor

$$\left(\frac{50}{29}\right) \times \frac{UTS}{f_{yt}} = 2.28$$

After modification, the average ratio $\frac{V_{fr}}{V_s}$ would be 1.11 (i.e. $\frac{2.54}{2.28}$) and this implies that there were still some 11 percent (or perhaps more) of the applied shear carried by other means than the spirals.

4.4 SHEAR STRENGTH ENVELOPE

Strength envelope curves adjusted to some compatible scales for column units with different properties are compared in this section. The maximum shear force attained at peak displacements is divided by the ideal flexural strength before plotting against the displacement ductility, μ. Since quantitative account has been given in the previous section of shear carrying capacities at different stages, only a qualitative discussion will be offered here. The emphasis is on the effects of the main parameters on the envelope curves, particularly the decaying characteristics.

Figs. 4.51 to 4.53 show the envelope curves grouped according to the parameter to be assessed. Only the average values of the positive and negative peak loads of the first and fifth cycles at different displacement ductility levels are shown in the figures. These points are then joined by straight lines to form the envelope curves. In cases where not enough points were available to complete the fifth cycle envelope, the third cycle envelope was included to illustrate the extent of degradation.

(a) The influence of spiral reinforcement content

Generally, the envelope curves (e.g. Fig. 4.51a and Units 8 and 10 in Fig. 4.51c) were quite similar for the same spiral reinforcement content regardless of the change in spiral pitch and bar diameter. Unless the spiral reinforcement content was insufficient to prevent premature shear failure, the column units were mostly able to reach their ideal flexural strength at some stage. The greater the spiral reinforcement content the greater the maximum load achieved. This is to be expected because the spiral reinforcement content increases the ideal strength and resulted in an increase in relative strength index which was found previously to indicate improved performance. In most cases, the ascending portions on envelopes followed each other very closely but the amount of spiral reinforcement determined the point where the curves began to decline. In other words, the increase in spiral reinforcement content delayed the onset of shear strength decay to higher displacement ductility levels. The initial rate of decrease of shear strength was generally greater if less spiral reinforcement was provided and the rate of decay had a tendency to taper off at later stages (e.g. Fig. 4.51d). Degradation of strength at fixed displacement ductility levels became more severe during the post-ultimate stage. It was especially so in Units 8, 10 and 13 (Figs. 4.51b and c). The contrast between the pre- and post-ultimate stages in these columns can be seen in the difference between the first and third cycle envelopes in the figures. This is probably due to axial compression present in these specimens.

(b) The influence of aspect ratio

The aspect ratio dictated the point at which decay commenced, resulting in later initiation of shear strength degradation if a larger shear-span was used. This is, of course, expected since an increase in the shear-span while the flexural capacity remains unchanged implies a lower value of V_{if} or in other words, a higher relative strength index.

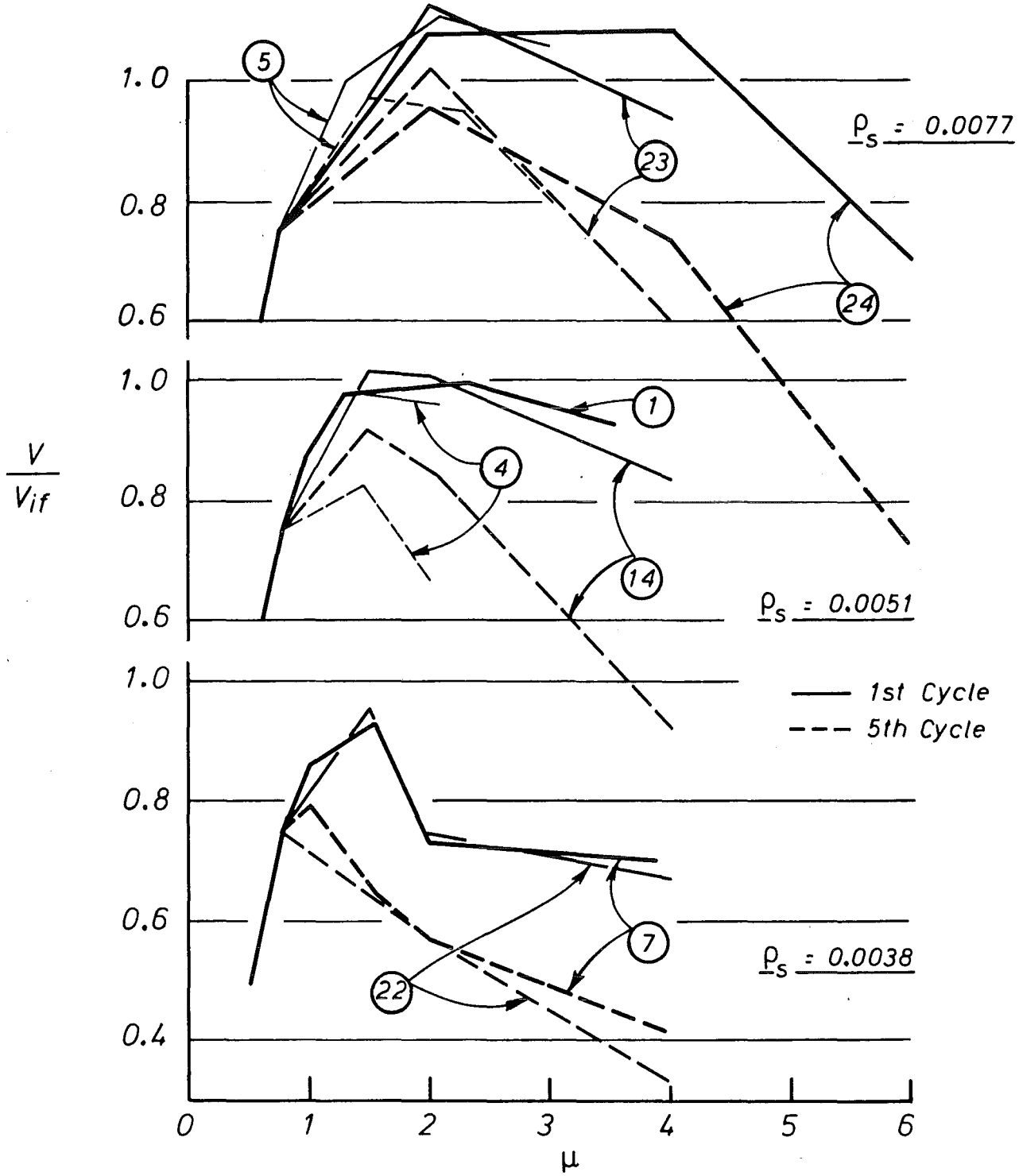

(a) $\frac{M}{VD} = 2.0$, $\frac{P_i}{f'_c A_g} = 0$

Fig. 4.51 : Influence of spiral reinforcement content on envelope curves

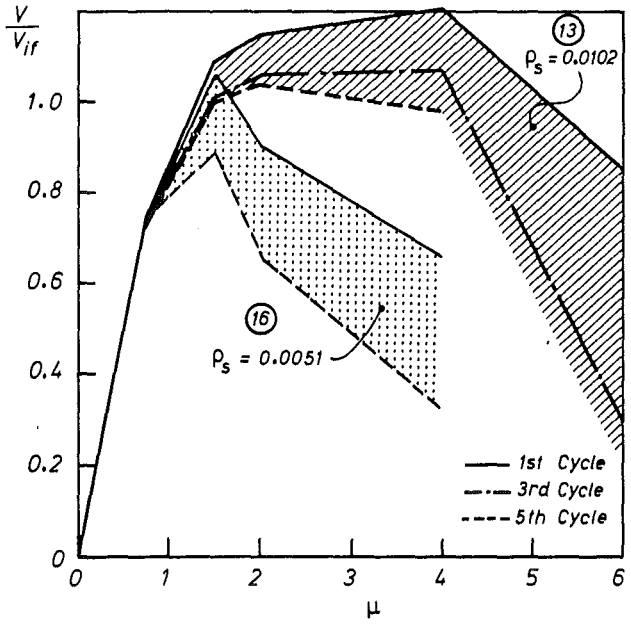

(b) $\frac{M}{VD} = 2.0$, $\frac{P_i}{f'_c A_g} = 0.1$

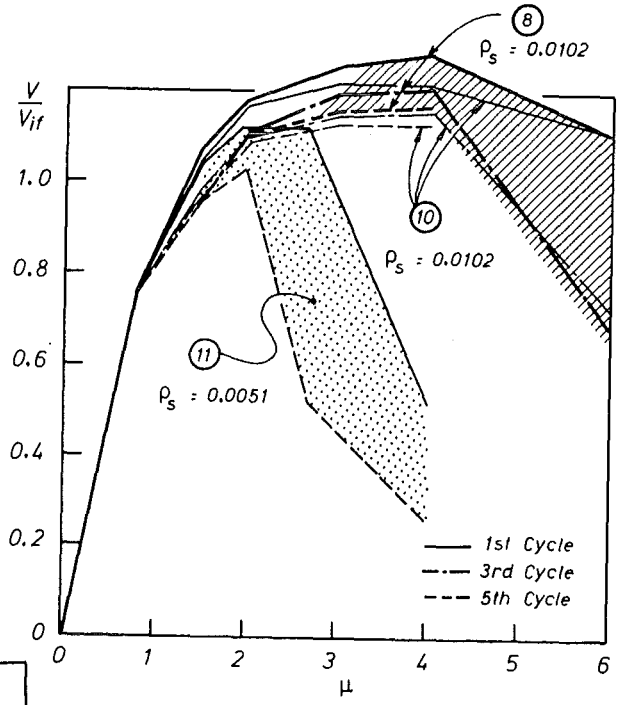

(c) $\frac{M}{VD} = 2.0$, $\frac{P_i}{f'_c A_g} = 0.2$

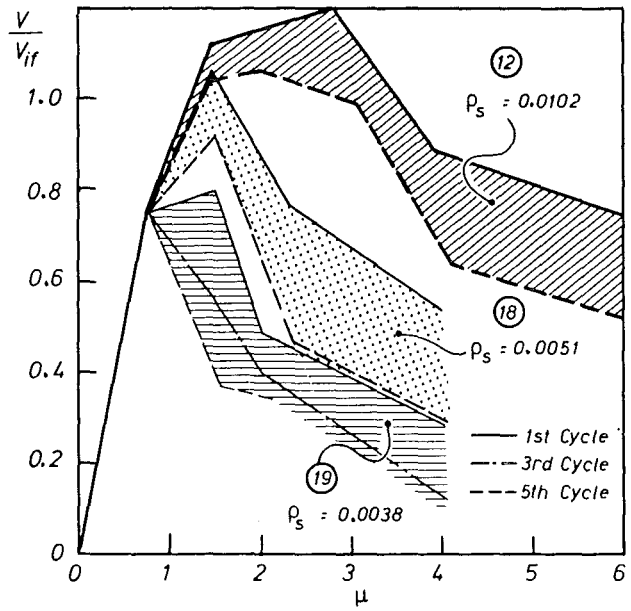

(d) $\frac{M}{VD} = 1.5$, $\frac{P_i}{f'_c A_g} = 0.1$

Fig. 4.51 (contd) : Influence of spiral reinforcement content on envelope curves

Hence, a better performance can be achieved. The envelope curves of column units with lower aspect ratio tended to fall below those of higher aspect ratio if comparison is made within the same group as in Fig. 4.52a. The rate of decay within the group, however, did not seem to be significantly affected by the change in aspect ratio. The drop in strength from first cycle to fifth cycle was more or less constant at different ductility levels in column units with limited or no ductility like those in Fig. 4.52a or Unit 12 in Fig. 4.52b. On the other hand, the drop in load carrying capacity associated with the failure in the other column units such as Units 8, 9 and 13 in Figs. 4.52b and c had been more drastic between the first and fifth cycles with the same ductility level.

(c) The influence of axial load

If the amount of spiral reinforcement was not sufficient to prevent premature shear failure, the presence of axial compression accelerated the rate of decay of strength during the post-ultimate stage. For example, from Figs. 4.53a and b, it is evident that the slope of the falling branch became steeper as the axial compression was increased. On the other hand, if the spiral reinforcement content was adequate for shear resistance, the effect of axial load was not very significant, e.g. Units 8 and 13 in Fig. 4.53c.

(c) Strength decay at fixed displacement ductility level

Until the ultimate strength was reached, the extent of strength decay with respect to the number of cycles was usually small and the load carrying capacity tended to approach some asymptotic value. However, this decaying rate tended to become greater as the displacement ductility was increased. To examine the decaying characteristics, the average loads at positive and negative peaks at $\mu = 4$ and $\mu = 6$ of a few selected column units are plotted in Fig. 4.54a against the number of cycles applied. From the figure, the rates of decay for column units with moderate ductility were very similar at $\mu = 4$, though the loads at first cycle might be different. All these column units sustained more than five cycles at $\mu = 4$ without losing more than 20 percent of V_{if} in their load carrying capacities. The decay at $\mu = 6$ was more drastic. As noted earlier, the presence of axial load accelerated strength decay and this is clearly seen in Fig. 4.54b when comparing column units with and without axial compression.

For comparison, similar results at $\mu = 4$ for five column units in the categories of shear failure with limited or no ductility, are

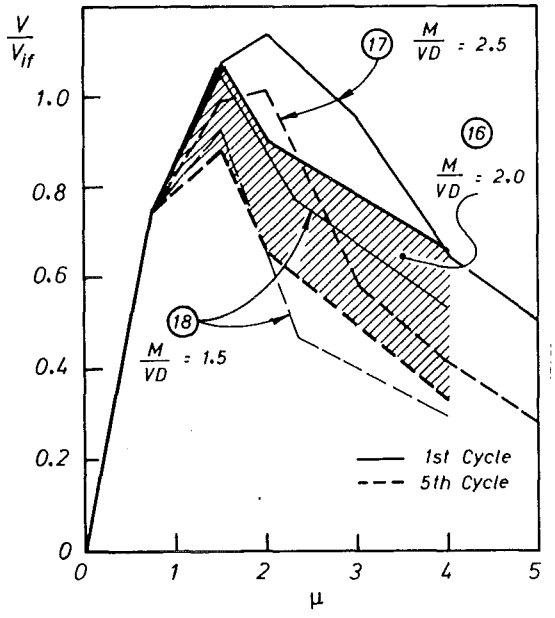

(a) $\rho_s = 0.0051, \frac{P_i}{f'_c A_g} = 0.1$

(b) $\rho_s = 0.0102, \frac{P_i}{f'_c A_g} = 0.1$

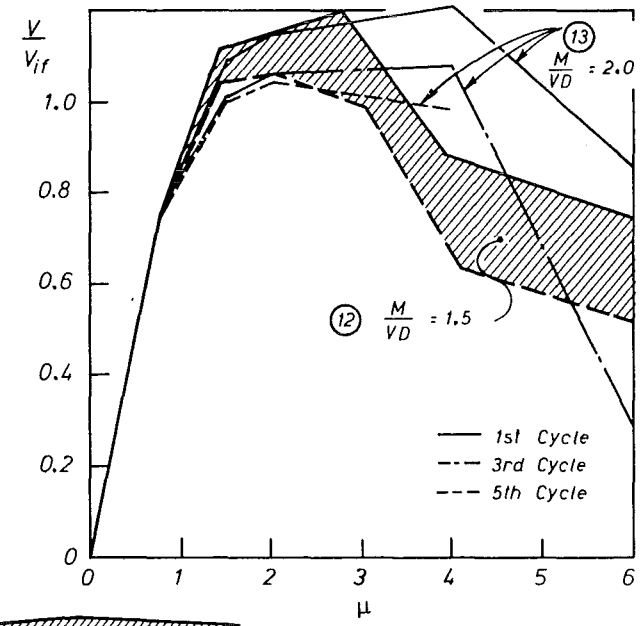

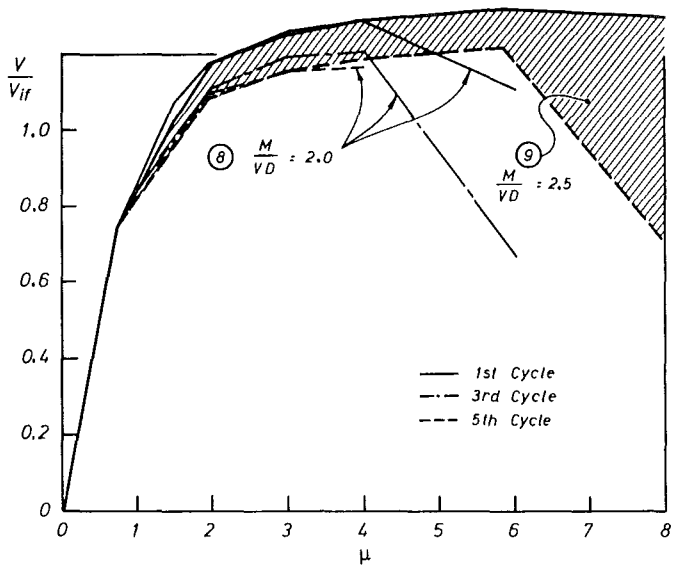

(c) $\rho_s = 0.0102, \frac{P_i}{f'_c A_g} = 0.2$

Fig. 4.5.2 : Influence of aspect ratio on envelope curves

(a) $\rho_s = 0.0051$, $\frac{M}{VD} = 2.5$

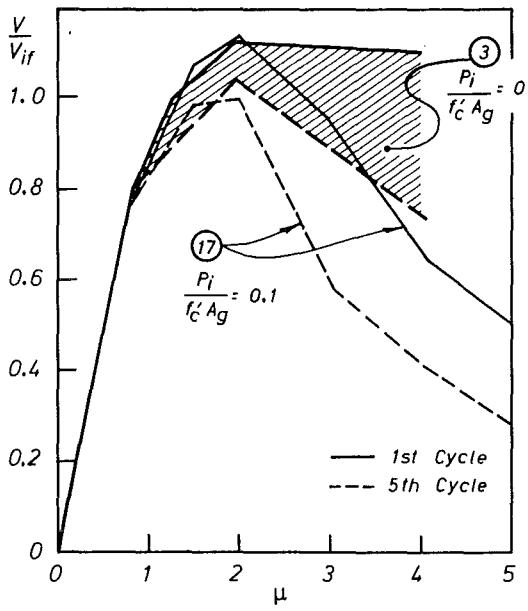

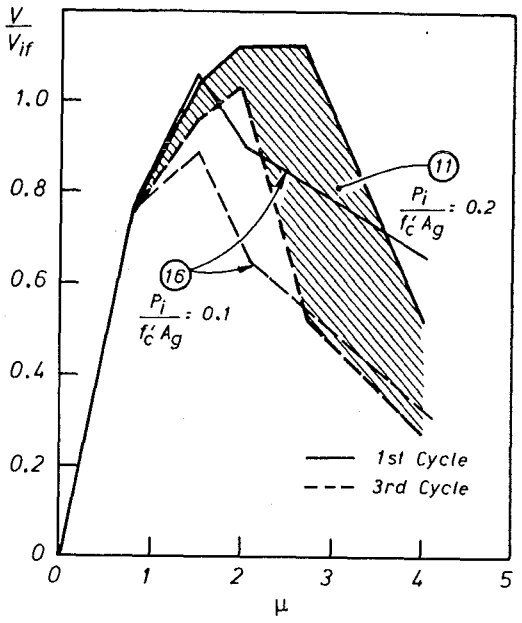

(b) $\rho_s = 0.0051$, $\frac{M}{VD} = 2.0$

(c) $\rho_s = 0.0102$, $\frac{M}{VD} = 2.0$

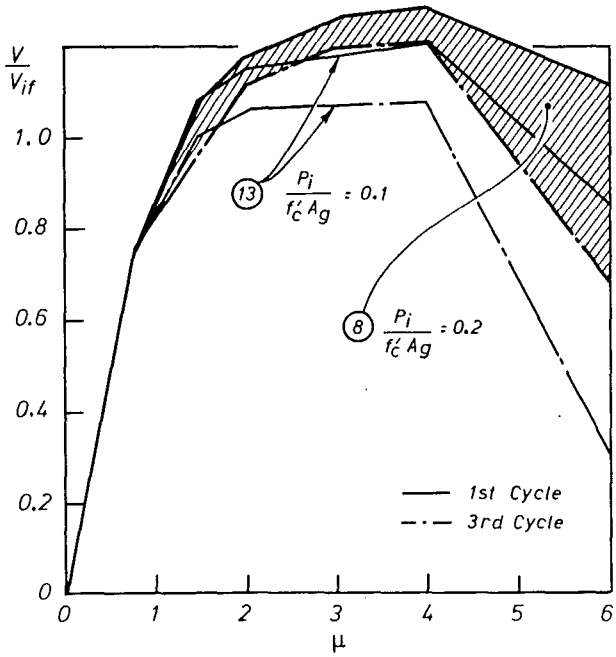

Fig. 4.53 : Influence of axial load on envelope curves

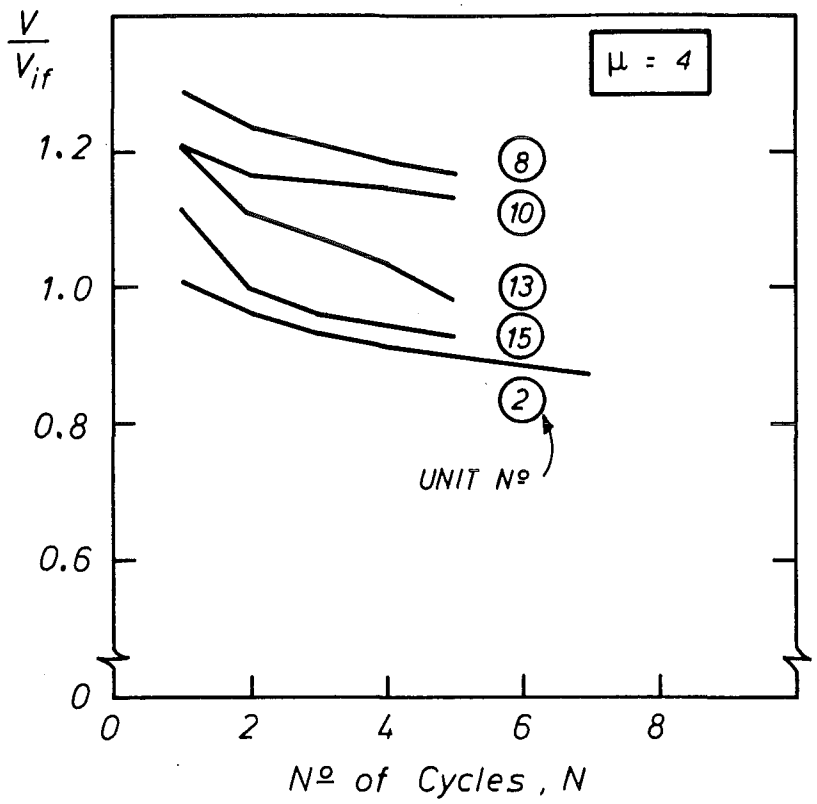

(a) Column units with moderate ductility (μ = 4)

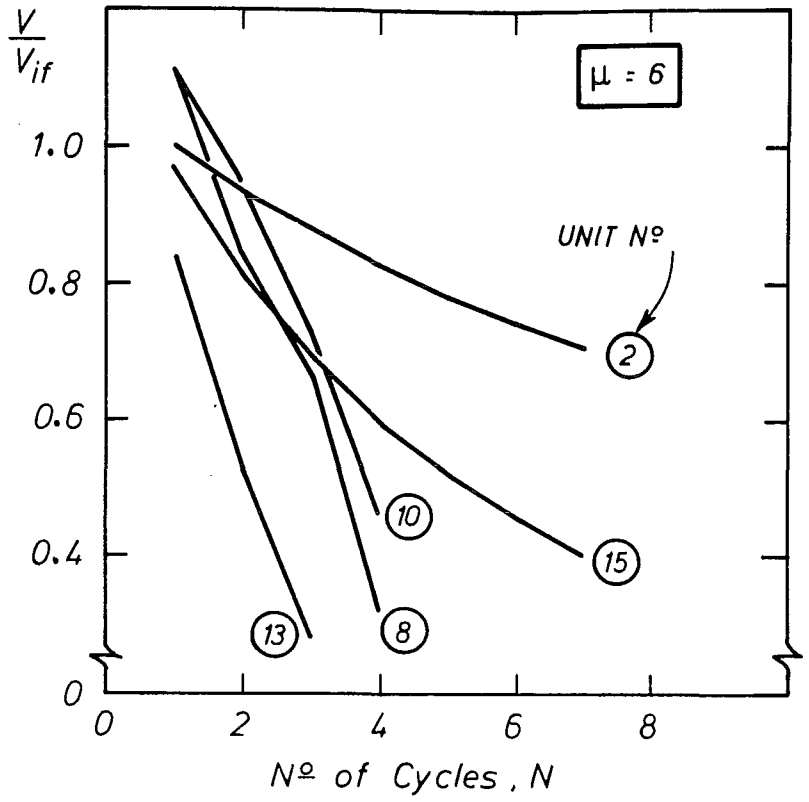

(b) Column units with moderate ductility (μ = 6)

Fig. 4.54 : Shear strength degradation with the number of cycles at fixed displacement ductility levels

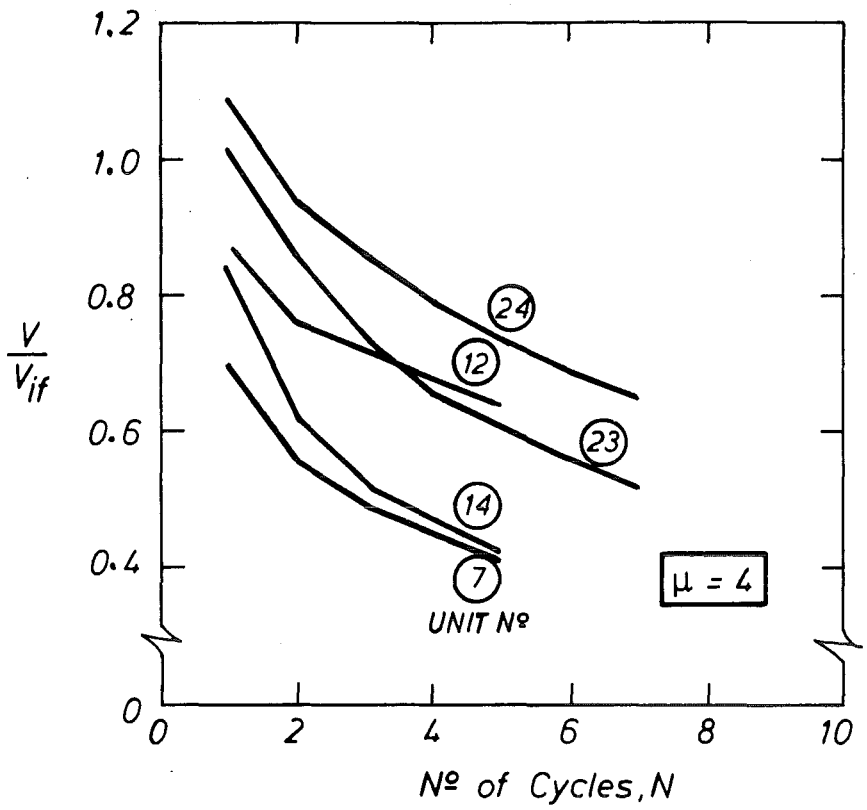

(c) Column units with limited or no ductility (μ = 4)

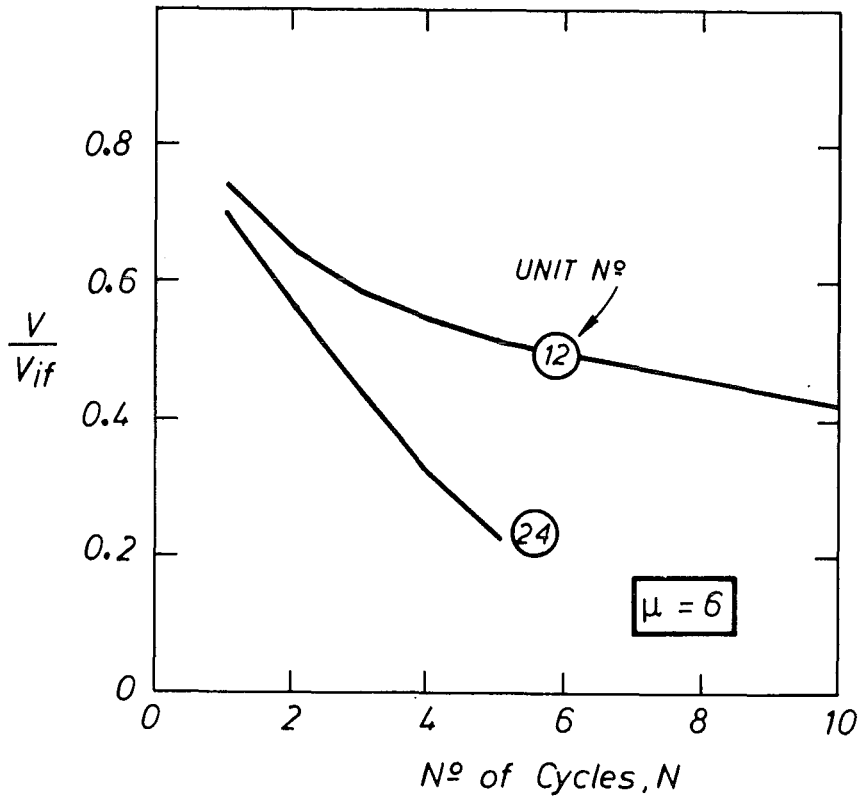

(d) Column units with limited or no ductility (μ = 6)

Fig. 4.54 (contd) : Shear strength degradation with the number of cycles at fixed displacement ductility levels

also included in Fig. 4.54c. They were from the column units which still possessed substantial strength in the initial cycle to $\mu = 4$. The decaying rates within this group are also quite similar but the rates are faster if compared to that of the other five column units. None of these columns maintained a strength of 80 percent of V_{if} after five cycles at $\mu = 4$. Fig. 4.54d shows the decaying rate of two of the column units (Units 2 and 24) at $\mu = 6$. The rate of decay is similar to that of Units 2 and 15 shown in Fig. 4.54b.

4.5 SPIRAL STRAIN AND SPIRAL FORCE

Spiral strains were measured as far as far as possible throughout the loading history. A typical trace of strain history is shown in Fig. 4.55. It represents the spiral response at gauge 1A of Unit 13 situated near the intersection of two diagonal cracks (see Fig. 4.55). In general, negligible spiral strain was recorded until diagonal cracking occurred and thereafter the strain readings increased as the loading continued. Unloading to zero load did not release all the strain in the spirals and this residual strain accumulated as testing proceeded. An increase in spiral strain was recorded with increasing number of cycles at constant as well as increasing displacement ductility levels, indicating a reduction in shear carried by concrete. Initially the residual strain in the spirals was due to incomplete closure of cracks. Subsequent to the formation of main failure cracks, the concrete wedges so formed (see Fig. 4.56) tended to be pushed outward, especially with the presence of axial compression, and this imposed additional strain on the spirals. Due to this wedging action, the strain could only be partly relieved on unloading and hence there was a marked increase in residual strain. Because of this wedging action, the spiral strains measured did not represent the actual values due to the applied shear and, therefore, to use the entire spiral strain measured to calculate the spiral shear force will inevitably overestimate the contribution of spiral reinforcement in shear resistance. Nevertheless, this practice results in a conservative prediction of the other component of shear resistance, i.e. the 'concrete contribution'.

For clarity only the strain history of first cycle loadings is included in Fig. 4.55. The increase in spiral strain indirectly indicated the deterioration in concrete shear carrying capacity. Hence, the increase in spiral strain with the number of cycles at low displacement ductility levels was expectedly small because the damage then was minimal. At high displacement ductility levels, the damage in concrete

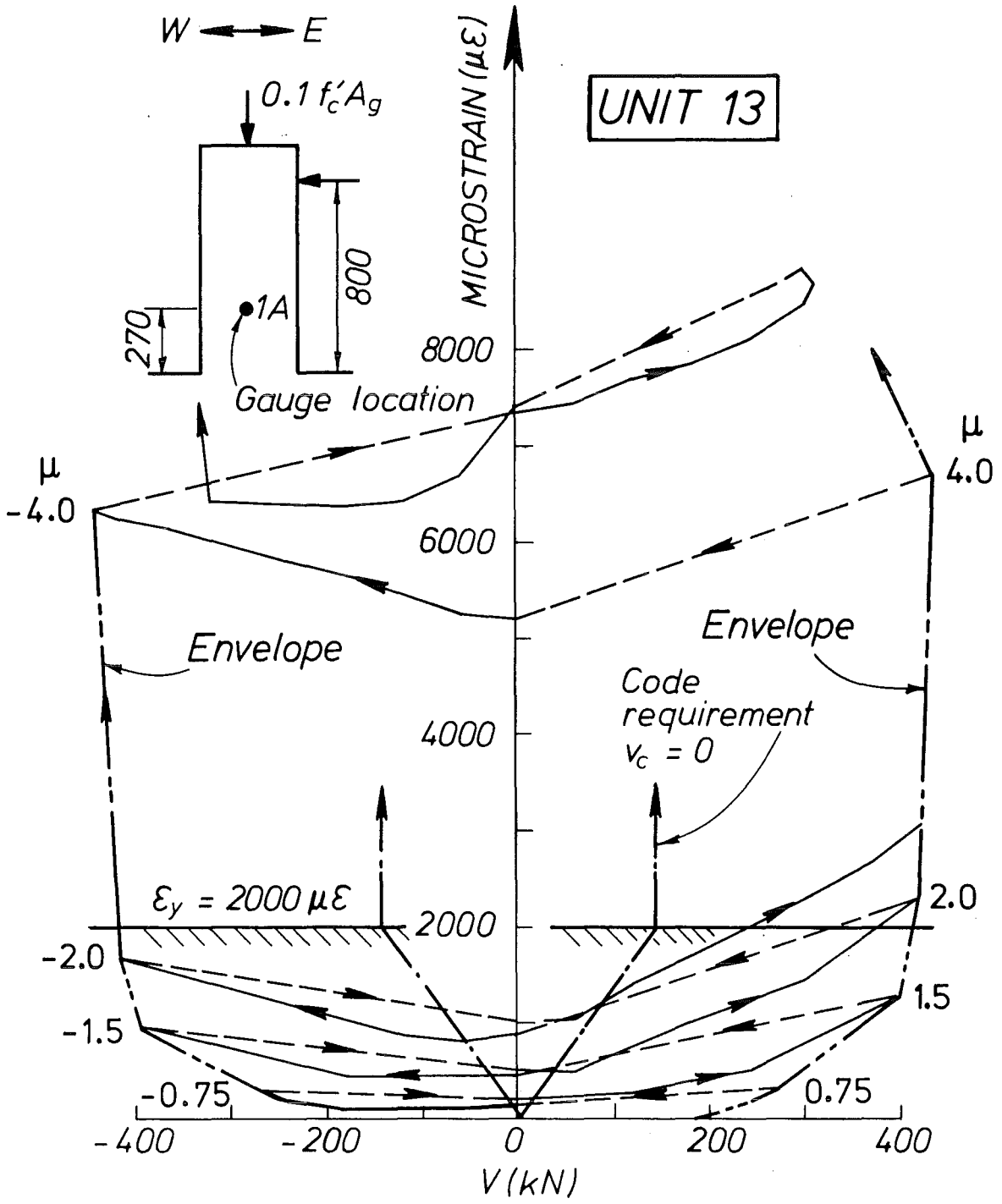

Fig. 4.55 : A typical strain history of spiral reinforcement

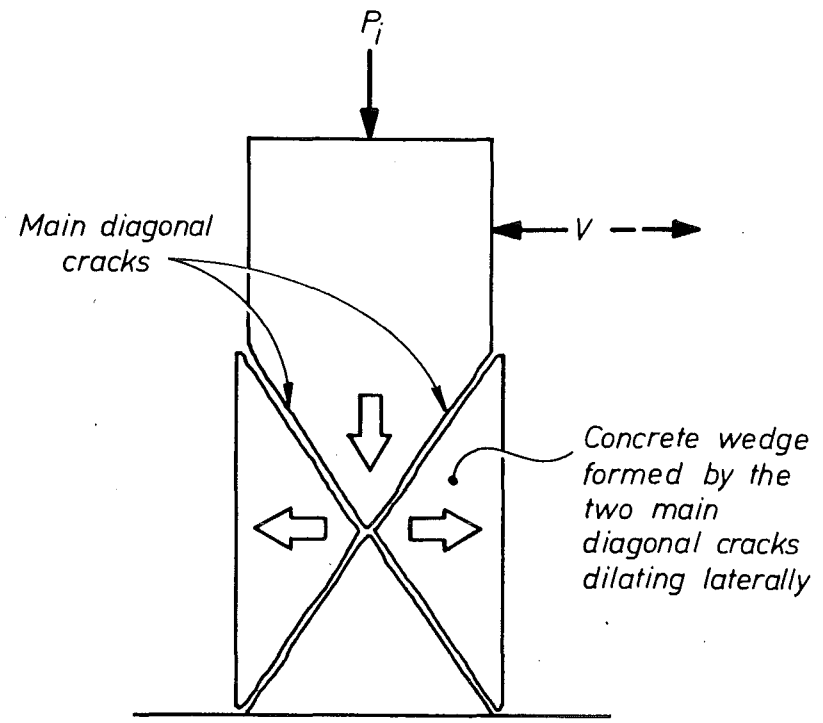

Fig. 4.56 : Wedging action of concrete blocks formed by the main diagonal cracks

as the load cycles were carried out was considerable even if the peak displacement was unchanged. By virtue of this, the increase in spiral strain with the number of cycles tended to be higher. Also, the fact that spirals in some column units were stressed to the point of fracture showed that strain-hardening in the spiral reinforcement had taken place. However, at such a high strain level, the strain gauge performance was rather doubtful and it was common towards the end of the tests to have some strain gauge circuits not operational.

The extremities in the strain history were joined by straight lines to form strain envelopes as illustrated in Fig. 4.55. Strain gauges were positioned following possible main diagonal crack directions. So, selecting the strain gauges according to the loading direction and averaging their results gave an average strain envelope in that particular loading direction. Points for both positive and negative loads are plotted for some typical examples in Figs. 4.57a to c. The positive and negative points follow each other very closely. A single strain envelope curve can therefore be used to represent the behaviour of the two opposite loading directions. As usual, the average strain envelope does not originate from zero load level. The point from which

substantial spiral strain began to be recorded should correspond to the onset of diagonal cracking. Hence, on extrapolation, the intercept on the horizontal axis in the figure can be taken as the diagonal cracking load. As was mentioned earlier, the values obtained in this manner agreed with experimentally obtained values and they are listed in Table 4.2.

From Figs. 4.57a to c, it is evident that once spirals started to carry part of the applied shear, the strain in the spirals increased with the applied shear and reached the yield value near ultimate. The spiral strain kept increasing though the load carrying capacity of a column unit might have dropped during the post-ultimate stage. This indicates the increasing proportion of shear was being carried by the spirals. This trend continued well into the strain-hardening range, though the envelopes shown do not extend that far.

With knowledge of the spiral strain and an estimate of the angle of crack inclination, the total spiral force developed across the potential diagonal failure plane, V_s, can be calculated. The slight influence on the stress-strain property resulting from cold-working to form the spirals was ignored. The results are plotted against the applied shear below their respective strain envelope in Figs. 4.57a to c. Also shown in the figures is a straight line representing the theoretical value (i.e. 45-deg truss analogy) if the spirals were to carry all the applied shear. The region between the straight line and the experimental values gave the portion of applied shear not carried by the spirals. This remaining part of the shear is usually attributed to the concrete and commonly known as the 'concrete contribution', details of which were summarized in Section 2.3.2. As can be seen, this 'concrete contribution' was very significant during early stage of loadings but was reduced subsequently during the post-ultimate stage. During this later stage, crack inclination was assumed to be that of a corner-to-corner crack (e.g. Figs. 4.38 and 4.39) but no smaller than 25-deg with respect to the column axis. The effect of strain-hardening was ignored. The spiral force at this stage is denoted by the broken line in the plots. With this approach, the deterioration in concrete shear carrying capacity shown is not as great as it would otherwise be. However, it should be noted that part of the spiral strain at this stage might be due to confining pressure and not the applied shear so to calculate the spiral shear force using the entire spiral strain may not be appropriate. Nevertheless, it does give an indication of the level of reliable 'concrete contribution'.

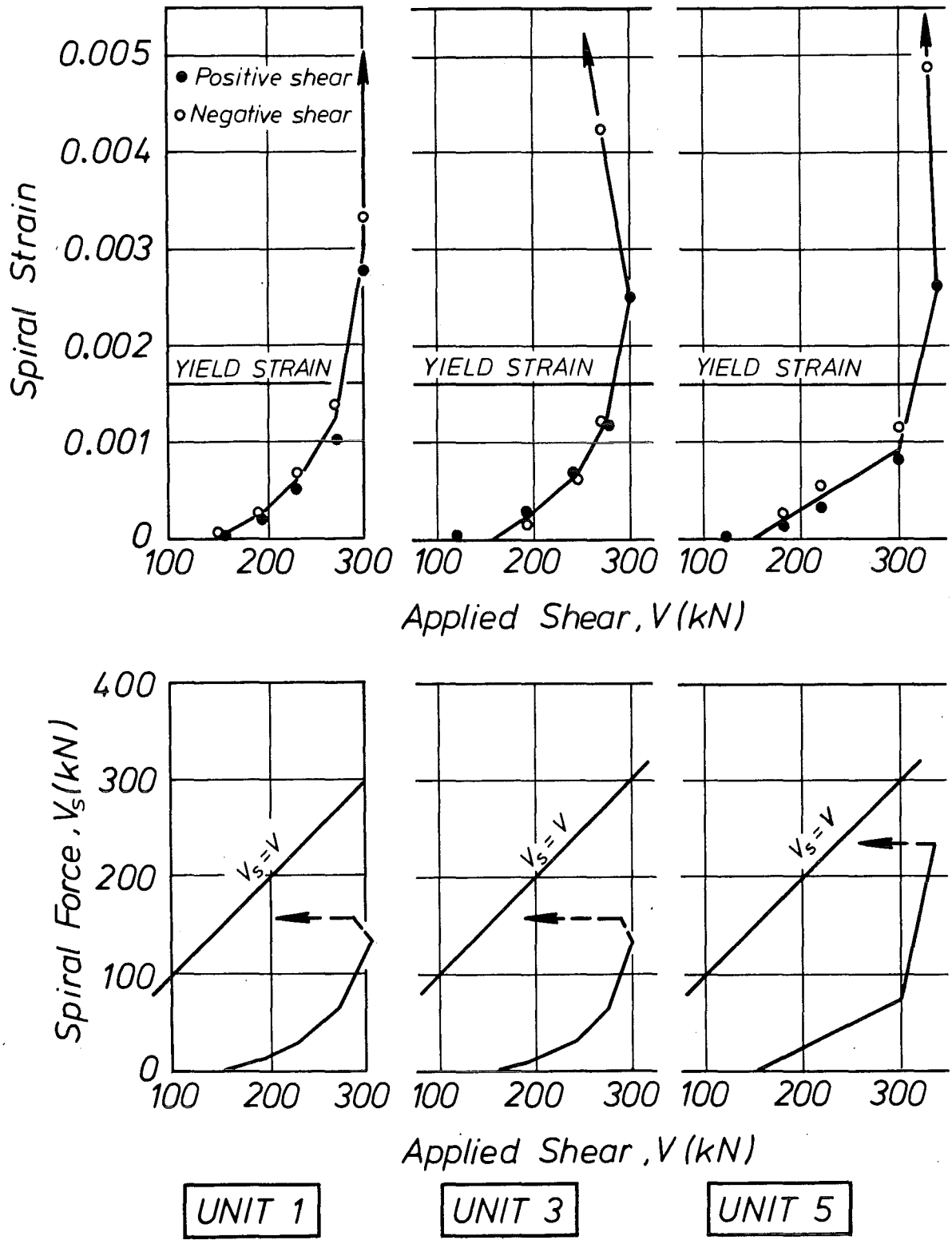

Fig. 4.57(a) : Average spiral strain envelopes and the associated spiral forces

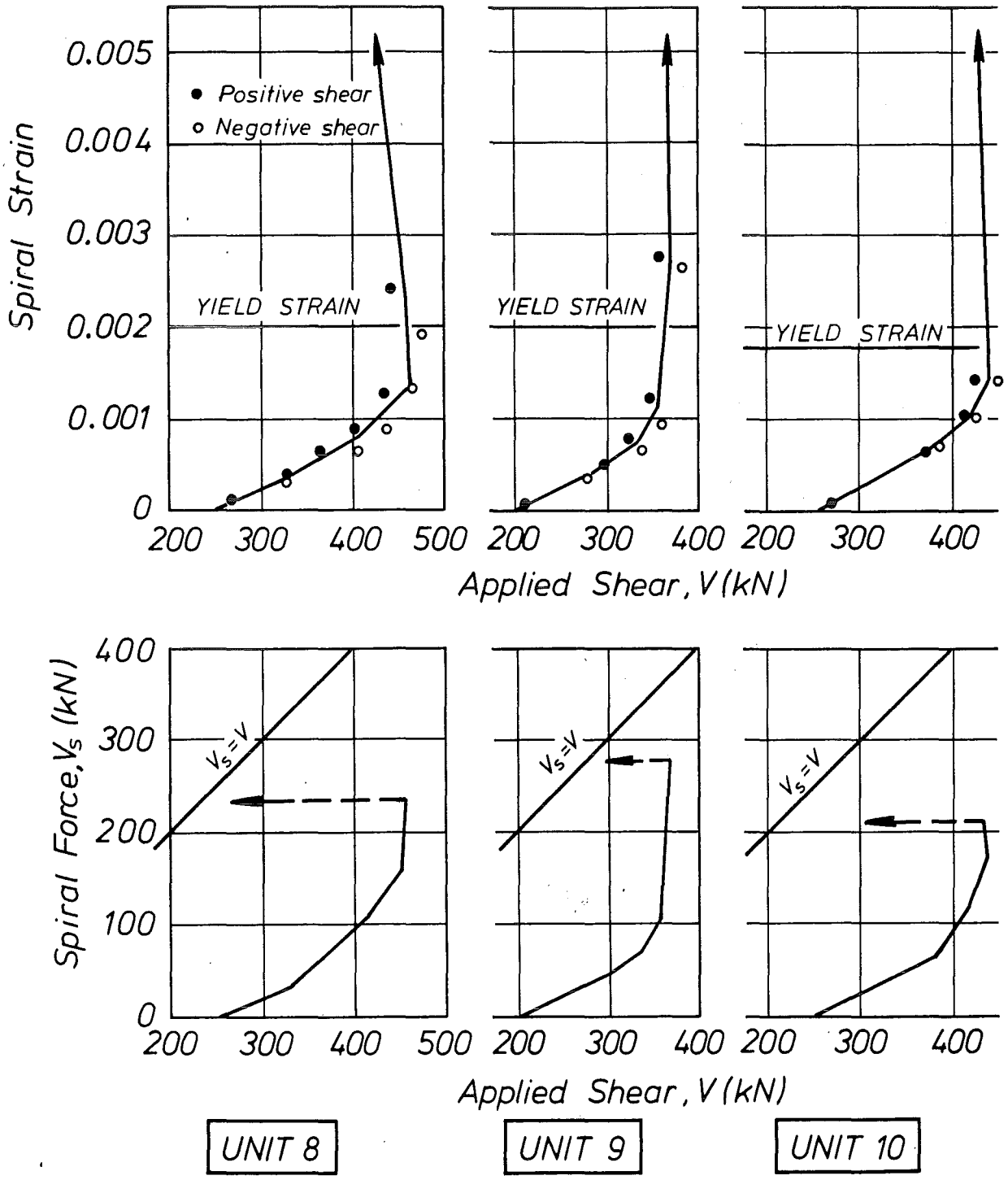

Fig. 4.57(b) (contd) : Average spiral strain envelopes and the associated spiral forces

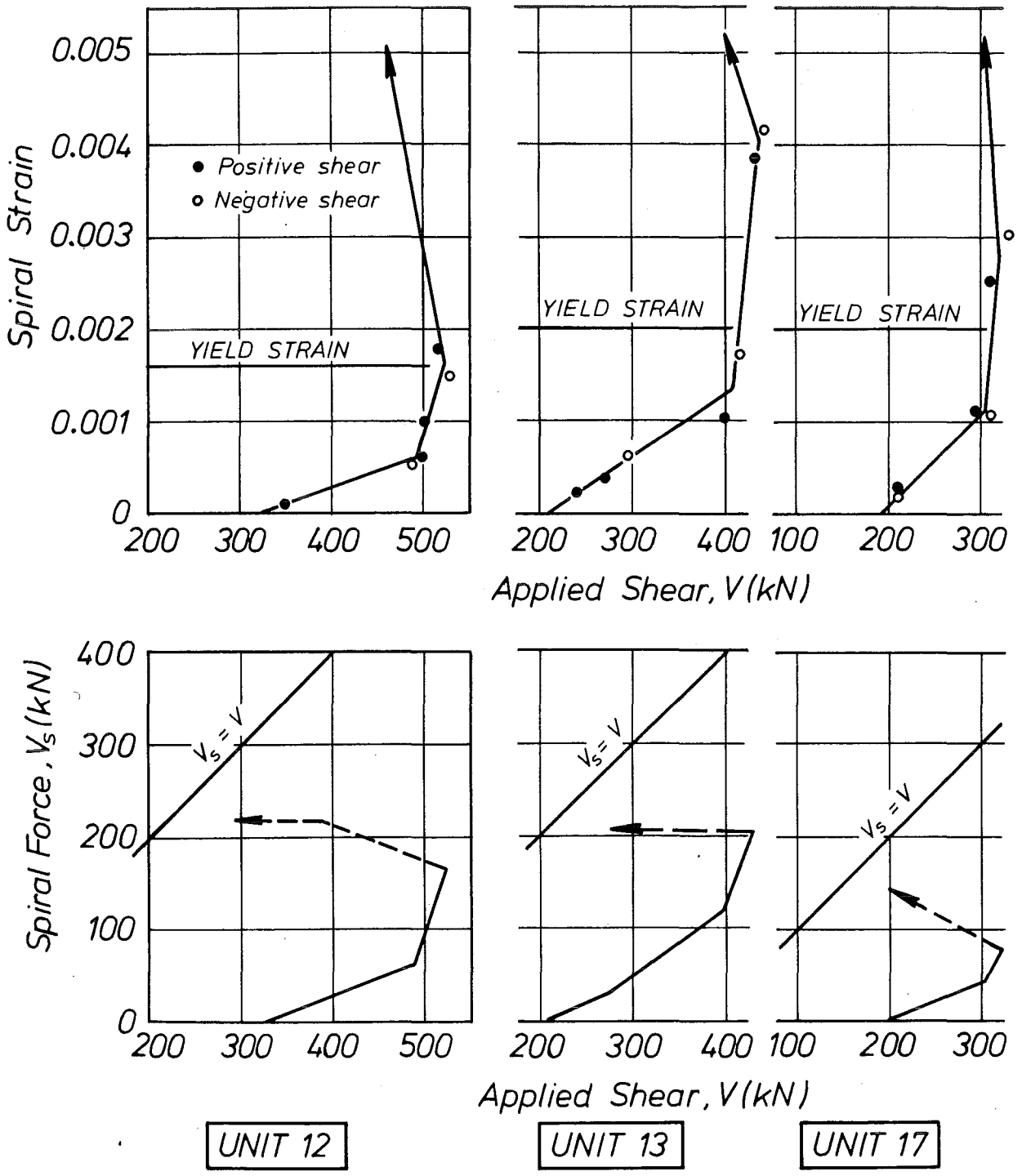

Fig. 4.57(c) (contd) : Average spiral strain envelopes and the associated spiral forces

The normalized applied shear force and shear carried by spiral reinforcement are plotted against cumulative ductility levels for three typical units in Fig. 4.58. In the figure, the applied shear is plotted as a full line while the corresponding spiral force is shown as a broken line. The region between them again represents 'concrete contribution'. Unit 1 possessed limited ductility and the ultimate load was achieved before reaching a cumulative ductility of 50. Earlier deterioration saw the region between the two lines narrowed as the loading continued beyond the ultimate stage. In the other two cases the ultimate load was reached at higher cumulative ductilities. The loss in concrete shear carrying capacity, however, could not be avoided in Unit 8 which finally failed in shear.

Unit 9 represents a typical ductile flexural failure. After yielding of all spirals the two lines plotted for this column unit in Fig. 4.58c remained almost parallel even at high cumulative ductility levels. As stated previously the spirals in this column were not designed to resist shear corresponding to flexural overstrength. Even with shear strength not quite meeting the capacity design requirement, this column still withstood the imposed loading of greater than ideal flexural strength and maintained its integrity at high displacement ductility levels, but of course, at the expense of extensive yielding of the spirals.

Also shown in Figs. 4.58b and c is a dotted line denoting the level of spiral force required if the current non-seismic design concrete shear force of NZS 3101 is deducted from the applied shear. The difference in the so-called 'concrete contribution' between the design and experimental values is self-evident. The code is very conservative in its non-seismic provisions and even more so in the seismic provisions.

To further examine the change in observed 'concrete contribution', determined indirectly by subtracting the spiral contribution across an estimated crack inclination from the applied shear, with displacement ductility level, the value of $\frac{v_c}{\sqrt{f'_c}}$ for all the column units are plotted against μ in Figs. 4.59a to d. The plots are grouped according to the failure mode. In general they show that the value of $\frac{v_c}{\sqrt{f'_c}}$ increases after the onset of diagonal cracking. It reaches maximum at about $\mu = 1.5$ to 2.0 and thereafter the 'concrete contribution' decreases. In the case of Unit 9, the drop in v_c tapered off to a value of about $0.16\sqrt{f'_c}$. Comparing the plots for column units

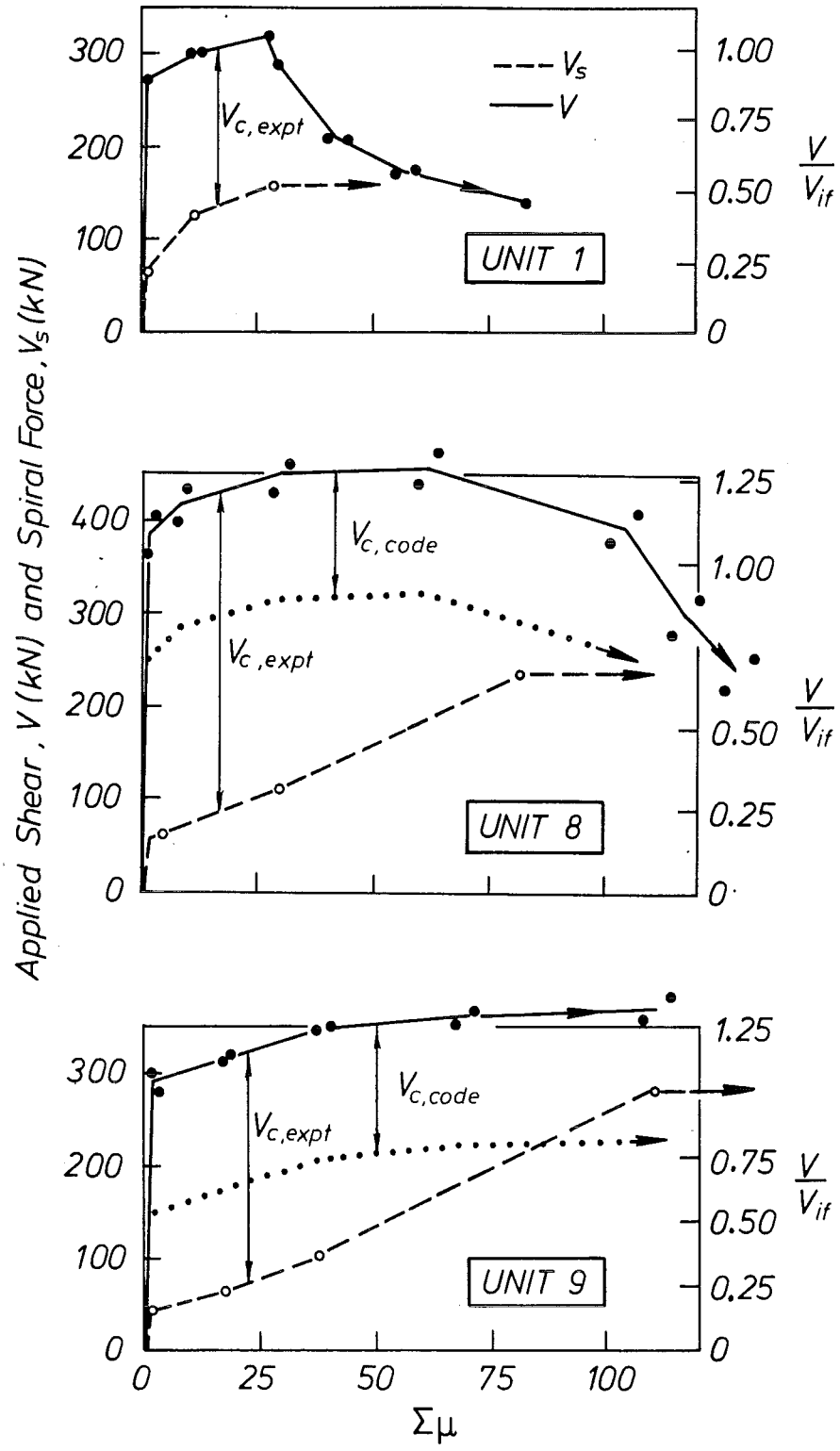

Fig. 4.58 : Spiral forces versus cumulative ductility

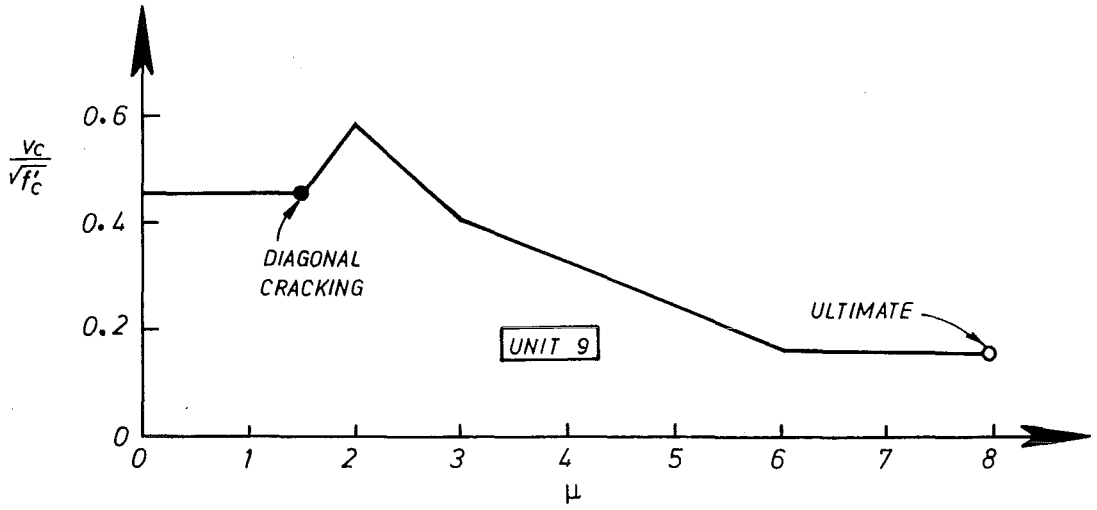

(a) Ductile flexural failure

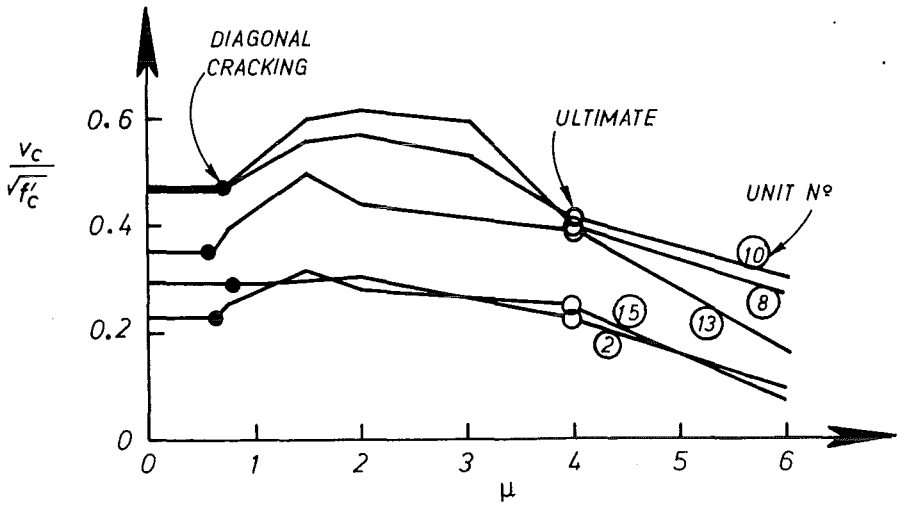

(b) Shear failure with moderate ductility

Fig. 4.59 : Experimental shear strength of concrete at different displacement ductility levels

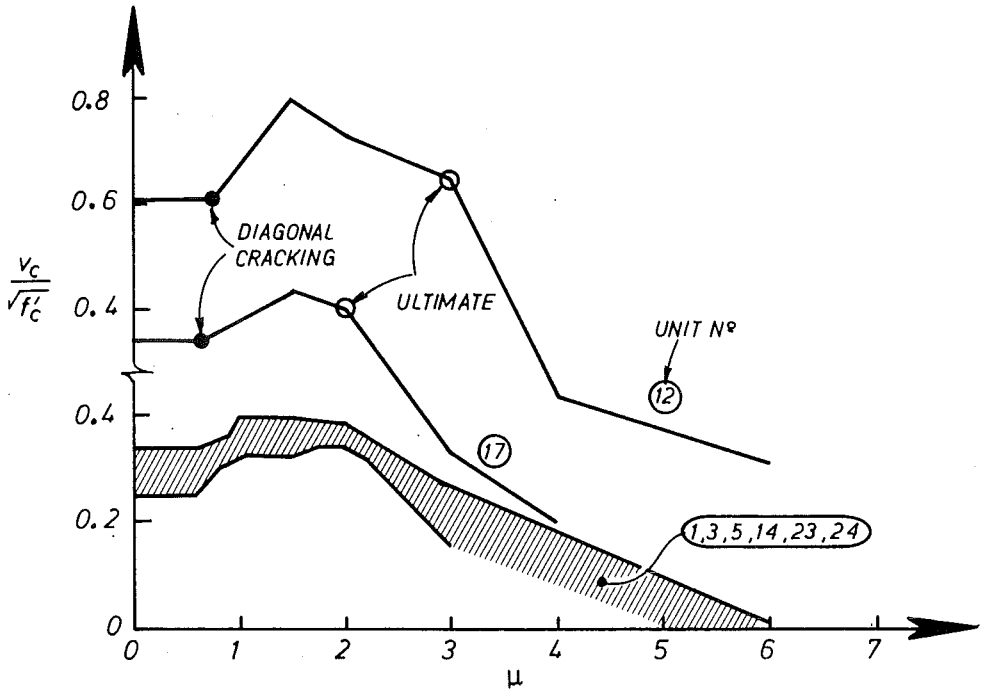

(c) Shear failure with limited ductility

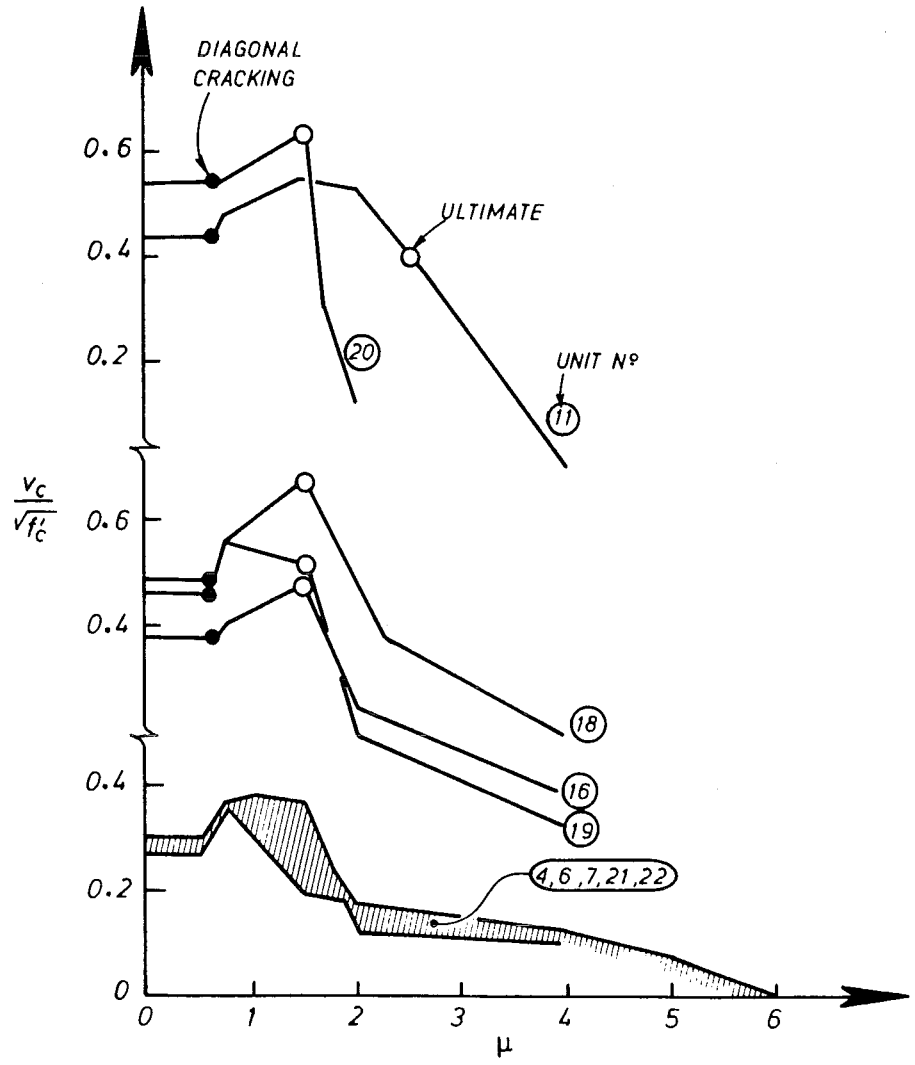

(d) Brittle shear failure

Fig. 4.59 (contd) : Experimental shear strength of concrete at different displacement ductility levels

with axial compression with those without axial compression shows that the drop in v_c is more drastic in the case of column units with axial compression. However, it should be noted that the higher spiral strain due to wedging action discussed earlier might be the cause of such a drastic drop in v_c. The values of v_c in this case did not approach a fixed value as in the case of Unit 9. The same observation is made in the case of column units that failed in shear with limited or no ductility (see Figs. 4.59c and d) except that in these columns the ultimate load was reached at low displacement ductility levels and hence the deterioration of 'concrete contribution' occurred earlier. Note the severe effect of axial compression on v_c in Units 11 and 20 shown in Fig. 4.59d. Insufficient confinement is believed to be a contributing factor and the values of v_c implied are thus probably conservative.

4.6 ENERGY DISSIPATION PERFORMANCE

Other than strength and ductility, energy dissipation is another important property necessary for satisfactory performance under seismic attack. In order for a structure to survive an earthquake attack, it must, without undue damage, be able to temporarily store part of the input energy as strain energy and then subsequently dissipate energy by inelastic deformation in the members. The energy dissipated in this way is represented by the area enclosed by the hysteresis loops. In members where shear effects are predominant, the pinching nature of the hysteresis loops inevitably causes reduction in the enclosed area and thus results in less energy dissipation.

A perfectly elasto-plastic member performance has the load-deflection response as shown in Fig. 4.60. The energy dissipated by the perfectly elasto-plastic system during a complete displacement cycle, is the shaded area of the parallelogram BCDE. At displacement ductility level, μ, the ideal energy, E_i, dissipated can be computed as follows:

$$E_i = 4(\mu - 1)\, V_{if}\, \Delta_y \qquad (4.8)$$

where V_{if} is the ideal flexural strength and Δ_y is the yield displacement. As it is impossible to achieve this idealised system in reality, the actual energy dissipated will be less than E_i.

The area within the experimental load-deflection hysteresis loops was measured with the aid of a planimeter to get the amount of energy, E, dissipated in a particular load cycle. For comparison purpose, the

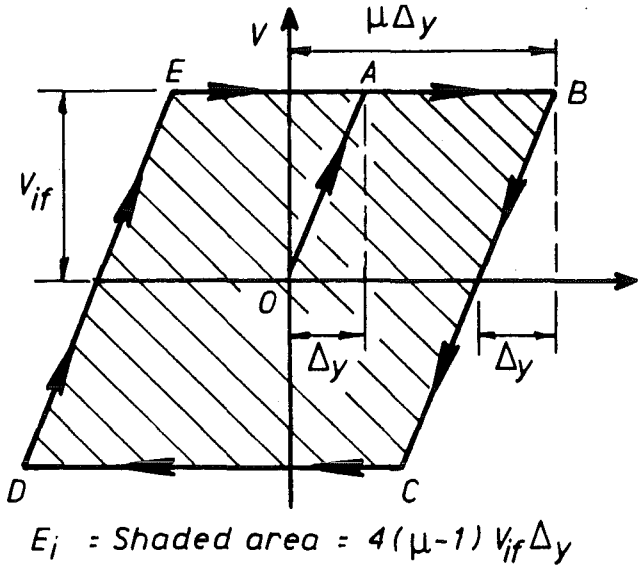

Fig. 4.60 : Energy dissipation in an idealized perfectly elasto-plastic system

measured energy dissipation was divided by the E_i value of the column for the same ductility level and this ratio is referred to as relative energy dissipation index. A number of research workers[4.7] have attempted to represent the energy dissipated in a system by the product of peak load and displacement of a particular cycle. To establish if there is any relationship between these two quantities, the energy associated with a given displacement, Δ , is expressed in a more convenient form as follows:

$$(\mu - 1)\frac{E}{E_i} = \frac{E}{4V_{if}\,\Delta_y} \qquad (4.9)$$

The results from all column units are plotted against

$$\mu\frac{V}{V_{if}} = \frac{V\Delta}{V_{if}\,\Delta_y} \qquad (4.10)$$

in Fig. 4.61. A bilinear curve fitted to the experimental points gives a representation of the energy dissipated. The expression for the two straight lines are

$$(\mu - 1)\frac{E}{E_i} = 0.14\,\mu\frac{V}{V_{if}} \quad \text{for} \quad \mu\frac{V}{V_{if}} \leq 2.5 \qquad (4.11a)$$

$$(\mu - 1)\frac{E}{E_i} = -0.741 + 0.438\,\mu\frac{V}{V_{if}} \quad \text{for} \quad \mu\frac{V}{V_{if}} > 2.5 \qquad (4.11b)$$

A typical plot of $\frac{E}{E_i}$ versus the number of cycles from a predominantly flexural response (Unit 9) is as shown in Fig. 4.62. As full plasticity would not have developed at $\mu = 2$, the relative energy dissipation index remained low. This index, however, increased with increasing displacement ductility level. Before $\mu = 8$, there was evidence that the system tended to become stabilized after a few cycles at fixed ductility levels. This stability was lost at $\mu = 8$ but during the last cycle of the test the column still dissipated about 40 percent of the amount of energy dissipated in the ideal system. Note that the actual hysteresis loops occupied mainly the first and third quadrants of the parallelogram BCDE so a value of 40 percent of E_i is not surprising.

The relative energy dissipation index for three groups of column units are shown in the next three plots in Figs. 4.63a to c. Each of these groups consists of two column units with the same spiral reinforcement content but different spiral pitch and bar diameter. As can be seen, the change in spiral pitch and bar diameter did not significantly alter the energy dissipation characteristics so long as the spiral reinforcement content remained constant.

To study the influence of spiral reinforcement content, a series of four plots is shown in Figs. 4.64a to d. Each of them include column units similar in every aspect but their spiral reinforcement content. They are plots of relative energy dissipation index versus the number of cycles at $\mu = 4$. The greatest difference in performance was not a direct results of the variations in spiral reinforcement content but rather due to the way in which the spiral reinforcement content changed the failure mode. The most significant difference was between Units 13 and 16 (Fig. 4.64c) and Units 8, 10 and 11 (Fig. 4.64b). Units 8, 10 and 13 were columns with moderate ductility and expectedly a stable energy dissipation performance was maintained at $\mu = 4$. On the other hand, Units 11 and 16 failed prematurely in shear and the amount of energy dissipated was considerably lower than that of the above three column units. Among the column units which failed in shear with limited or no ductility (e.g. Figs. 4.64a and d), the differences in energy dissipation in performance are insignificant after a few cycles at $\mu = 4$.

Figs. 4.65 and 4.66 show how the aspect ratio and the axial load level respectively affected the energy dissipation performance. It is

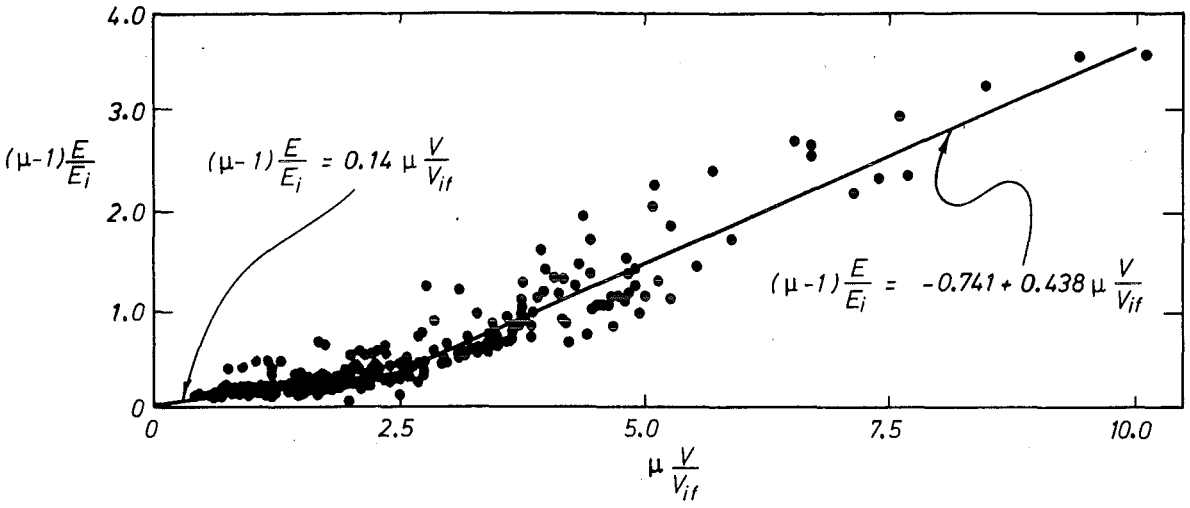

Fig. 4.61 : Relationship between energy dissipation and the product of peak load and peak displacement

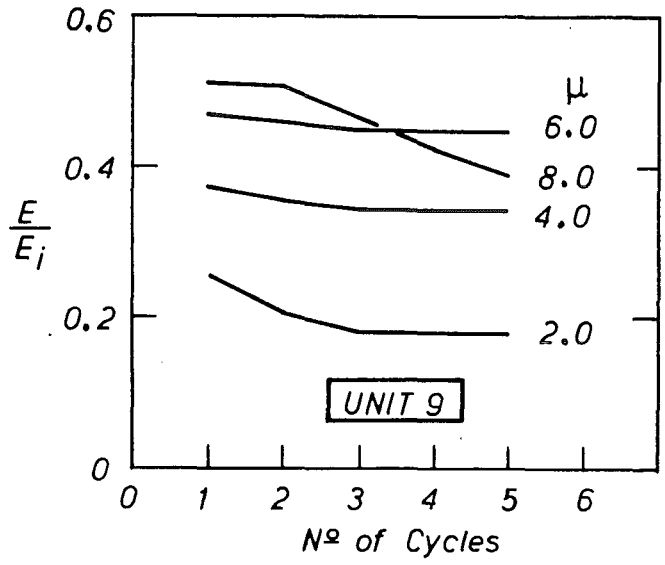

Fig. 4.62 : Relative energy dissipation index of UNIT 9 at different displacement ductility levels (ductile flexural failure)

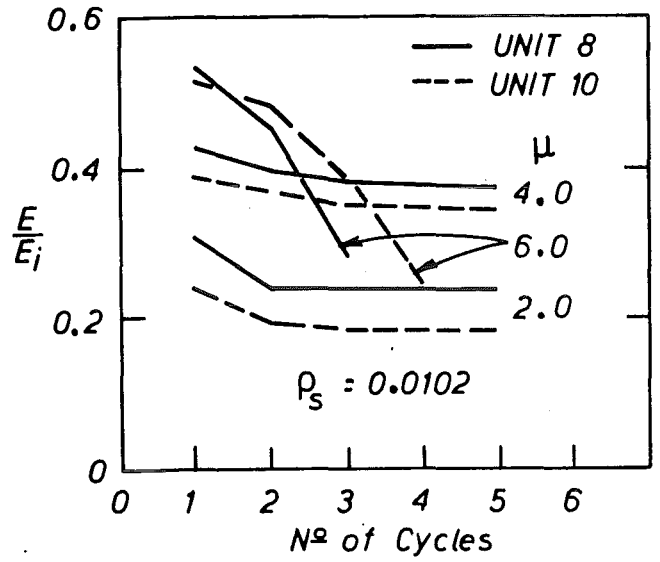

(a) Shear failure with moderate ductility

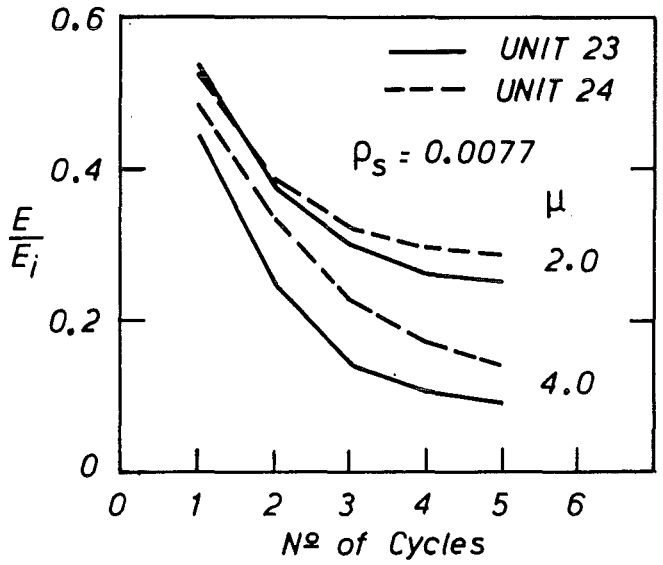

(b) Shear failure with limited ductility

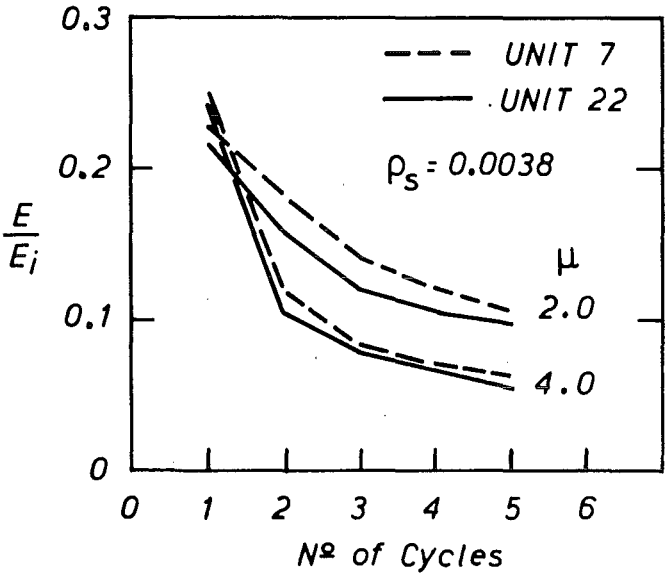

(c) Brittle shear failure

Fig. 4.63 : Relative energy dissipation index at different displacement ductility levels

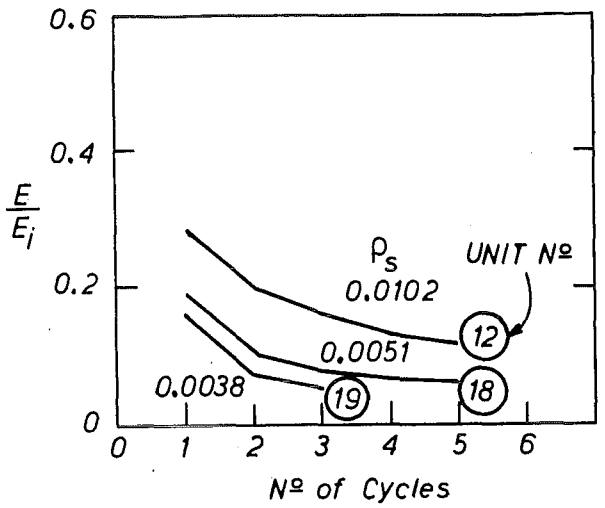

(a) $\frac{M}{VD} = 1.5, \frac{P_i}{f'_c A_g} = 0.1$

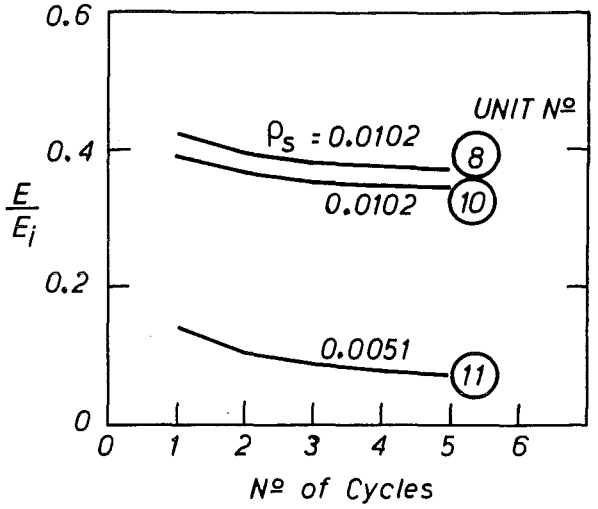

(b) $\frac{M}{VD} = 2,0, \frac{P_i}{f'_c A_g} = 0.2$

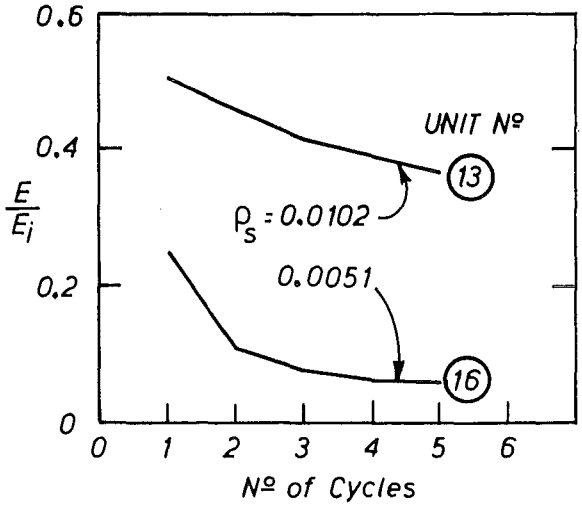

(c) $\frac{M}{VD} = 2.0, \frac{P_i}{f'_c A_g} = 0.1$

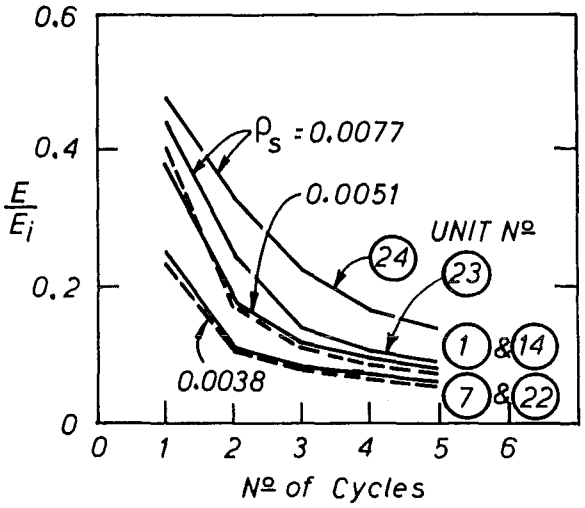

(d) $\frac{M}{VD} = 2.0, \frac{P_i}{f'_c A_g} = 0$

Fig. 4.64 : The influence of spiral reinforcement content on relative energy dissipation index at $\mu = 4$

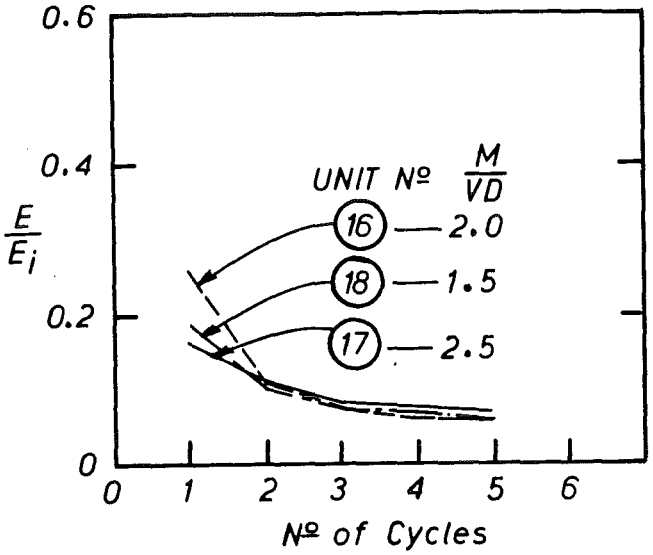

(a) $\rho_s = 0.0051$, $\frac{P_i}{f'_c A_g} = 0.1$

(b) $\rho_s = 0.0102$, $\frac{P_i}{f'_c A_g} = 0.2$

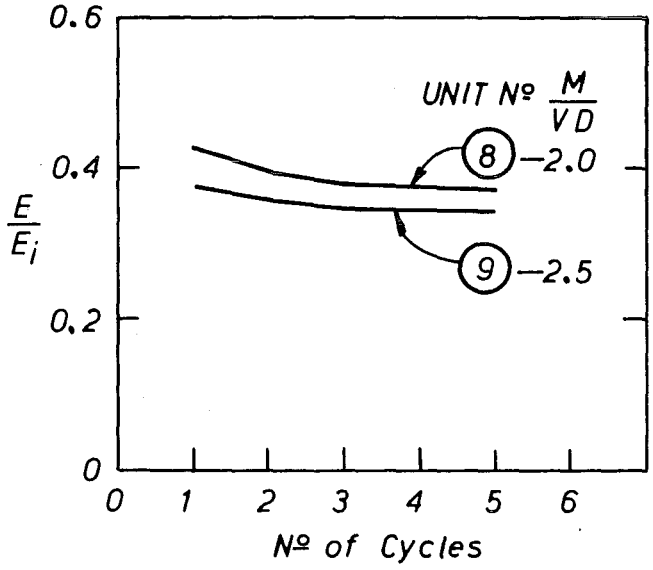

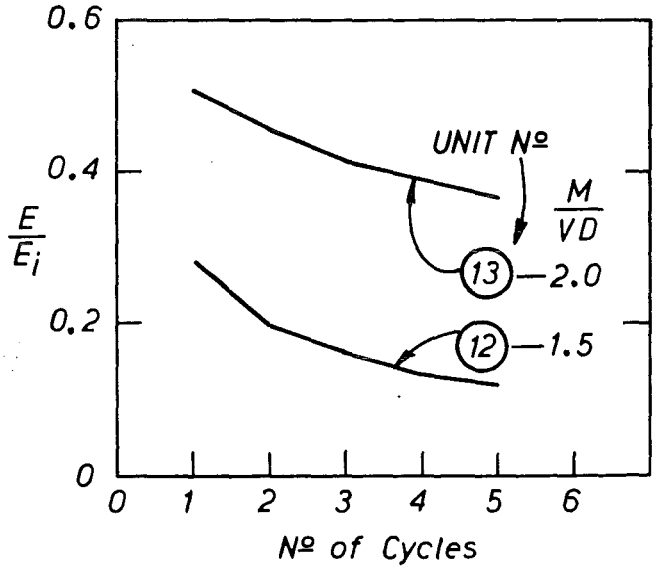

(c) $\rho_s = 0.0102$, $\frac{P_i}{f'_c A_g} = 0.1$

Fig. 4.65 : Influence of aspect ratio on relative energy dissipation index at $\mu = 4$

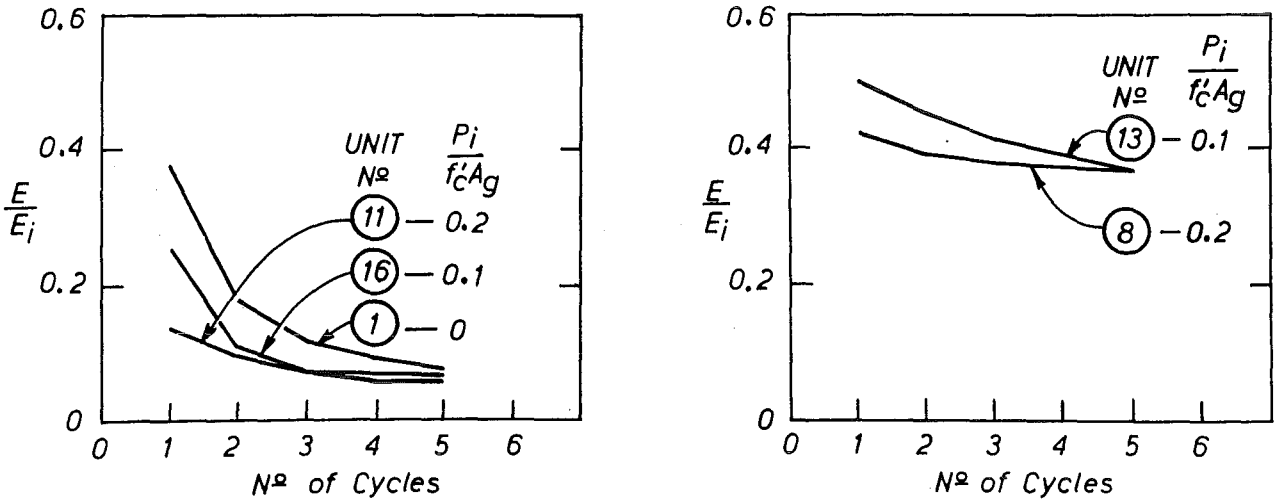

(a) $\rho_s = 0.0051$, $\frac{M}{VD} = 2.0$ (b) $\rho_s = 0.0102$, $\frac{M}{VD} = 2.0$

Fig. 4.66 : Influence of axial load on relative energy dissipation index at $\mu = 4$

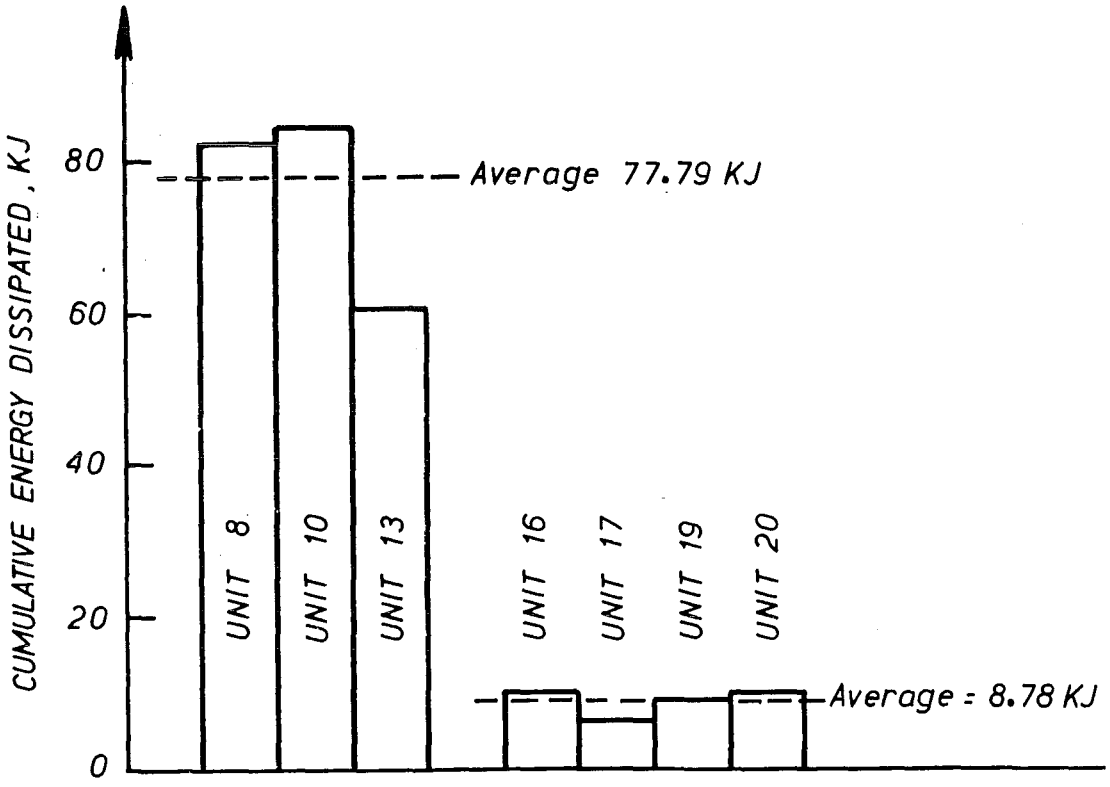

Fig. 4.67 : Cumulative energy dissipation to fracture of first spiral

again evident that the mode of failure is the main determining factor in controlling the energy dissipation property (e.g. Units 12 and 13 in Fig. 4.65c). The influence of aspect ratio in column units that failed prematurely in shear was negligible (Fig. 4.65a). The increase in axial load, however, tended to slightly worsen the situation but the effect eventually disappeared after five cycles at $\mu = 4$ (Fig. 4.66a). The above observations point to the fact that the relative strength index ($\frac{V_{iv}}{V_{if}}$) is a critical factor in the energy dissipation performance.

Among the few column units which experienced fracture of spirals during testing, Units 8, 10 and 13 belong to the category of shear failure with moderate ductility and Units 16, 17, 19 and 20 belong to the categories with limited or no ductility. The total energy dissipated until first fracture of spirals was summed for these column units and plotted in Fig. 4.67. The first three had an average value of 77.79 KJ of cumulated energy dissipation. Note that Units 8 and 10 had higher cumulated values owing to additional five cycles of loadings at $\mu = 3$. The average value of the cumulated energy dissipation until first fracture of spirals of the remaining four column units was 8.78 KJ. This is almost an order of magnitude lower than that of the former group. The difference in performance between the failure categories is therefore self-evident.

4.7 CURVATURE DISTRIBUTION AND CONCRETE CRUSHING AND SPALLING STRAINS

4.7.1 Curvature Profile

Observed curvatures were calculated as described in Section 3.4.4. They were taken as average values over the gauge length over which the readings were taken. The calculated values were plotted at the mid-point of the gauge length and successive points were connected by straight lines to form the curvature profiles as shown in Figs. 4.68a to f. Normally, an increase in curvature was found with increasing bending moment down the length of the columns, with non-linearity of the profiles due to the concentration of plasticity in the hinging region.

Fig. 4.68a shows the curvature distribution for a typical ductile member (Unit 9). As the displacement ductility was increased, the curvature increased but the spread of plasticity was somewhat limited to the critical region at the column base. The region of high plasticity appears to be concentrated within 200 mm of the base and this coincides with the region of severe damage observed during testing of the column unit.

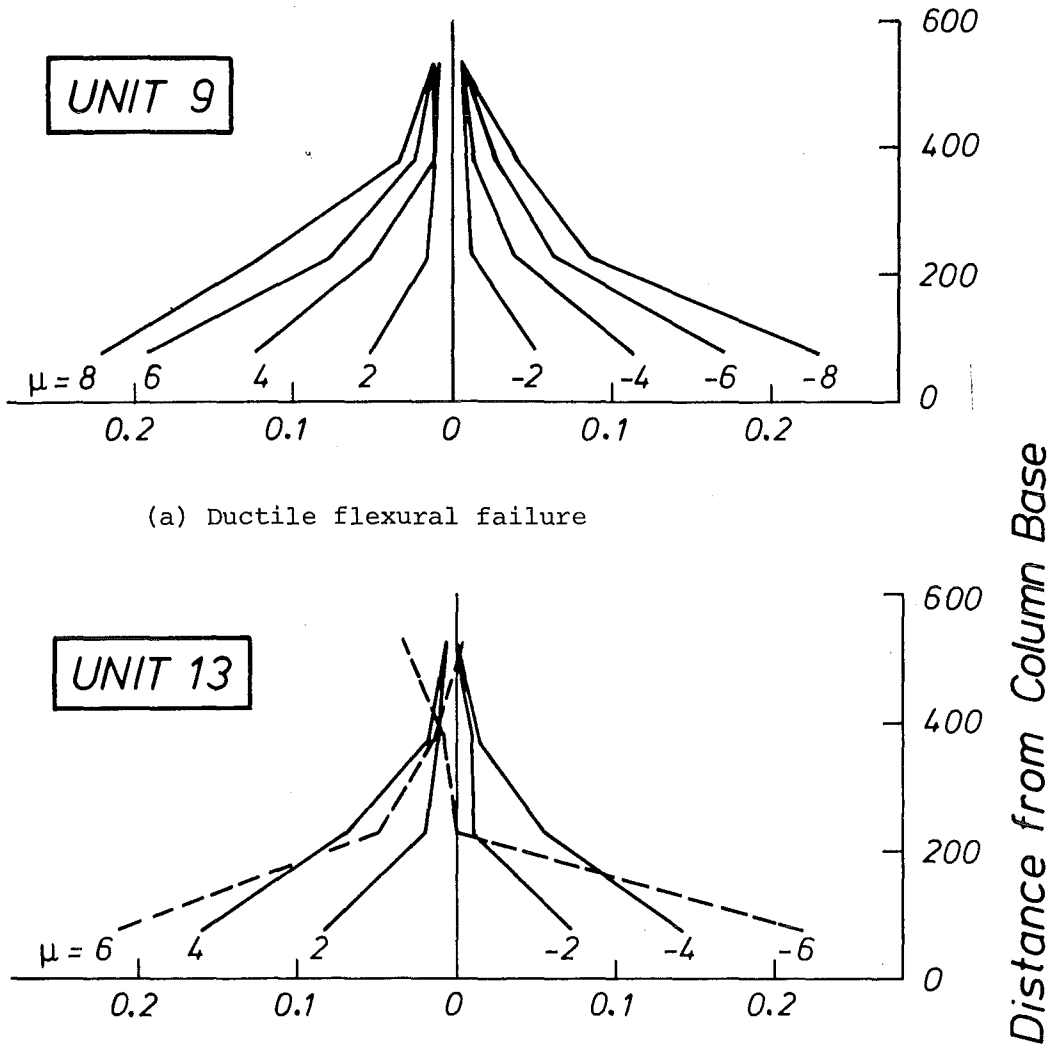

(a) Ductile flexural failure

(b) Shear failure with moderate ductility

(c) Shear failure with moderate ductility

Fig. 4.68 : Curvature profiles (rad/m)

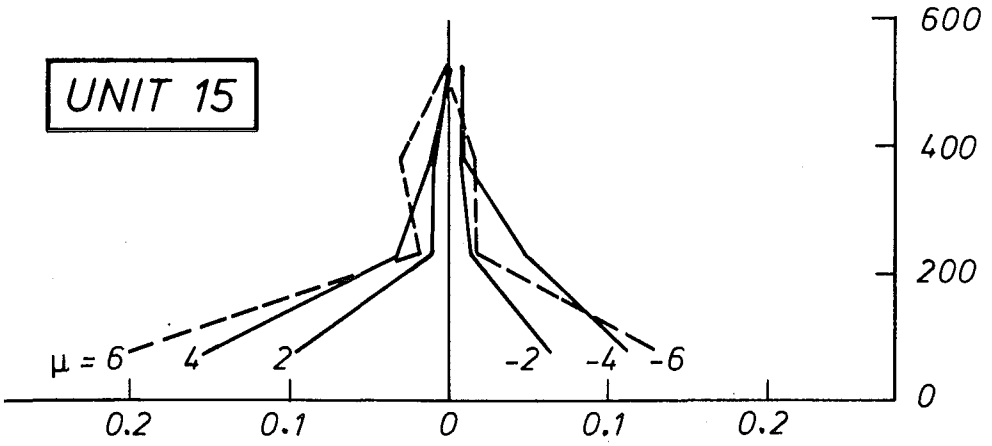

(d) Shear failure with moderate ductility

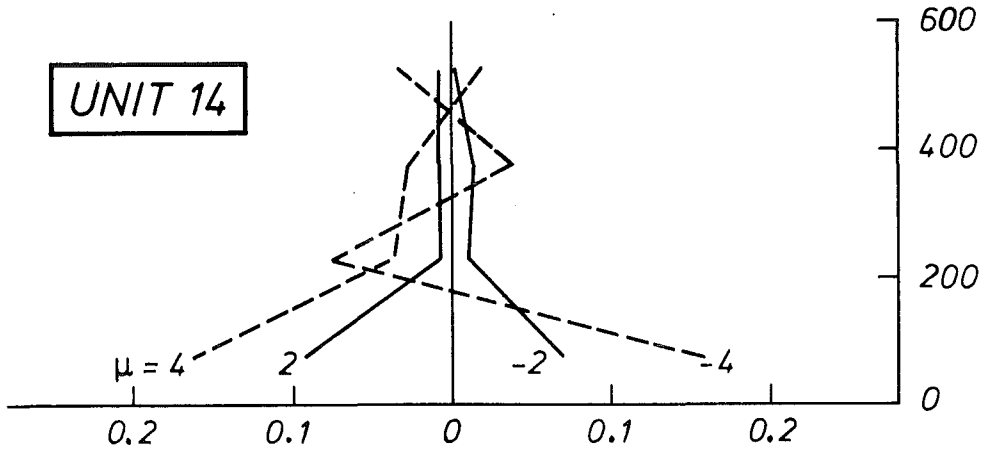

(e) Shear failure with limited ductility

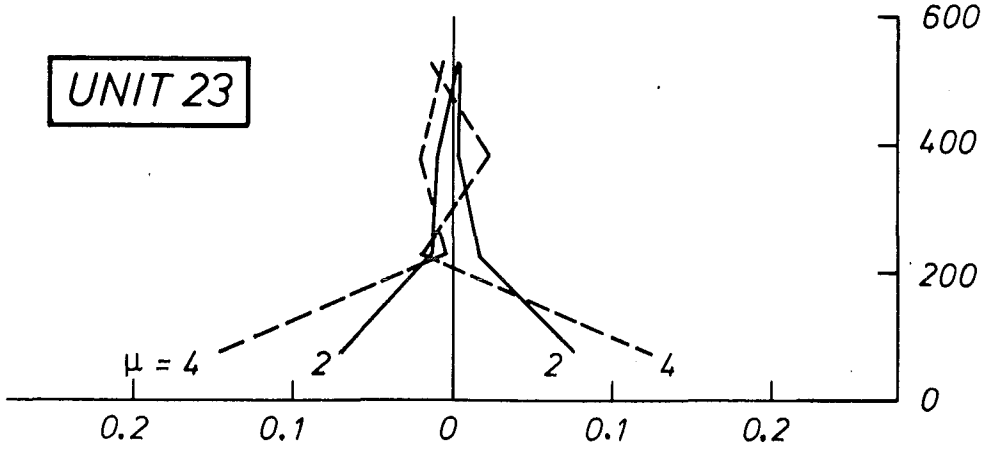

(f) Shear failure with limited ductility

Distance from Column Base

Fig. 4.68 (contd) : Curvature profiles (rad/m)

When the effect of shear deformation began to play a major role, the curvature profiles tended to be more irregular. In the case of column units which failed in shear with moderate ductility, as shown in Figs. 4.68b to d, the irregularity set in during later stages of testing, at $\mu = 6$. Up to and including $\mu = 4$, the appearance of the profiles still maintained the shape typical of flexural performance. At $\mu = 6$, the shape of the profiles changed and there was a tendency to have the curvature reversed near the loading end. This could be due to the dominating effect of shear deformation at that stage.

For comparison, Figs. 4.68e to f show two typical examples in the other categories of shear failure (Units 14 and 23). The early onset of irregularity in curvature distribution gave an indication of the dominating shear effects in these columns. Until $\mu = 2$, the profiles were still typical of that due to flexure but the profiles at $\mu = 4$ became very irregular.

4.7.2 Concrete Strains At Crushing And Spalling

From the strain measurements at the gauge locations (see Fig. 3.2), the concrete strains can be estimated by linear interpolation (see Section 3.4.4). In this manner, the extreme concrete compressive strain at incipient crushing and spalling were calculated and are listed in Table 4.9. The crushing and spalling of concrete were observed during testing but the timing of these events in terms of ductility level might not be precise. Only readings from the lowest pair of transducers were used because crushing and spalling first took place at the location of maximum bending moment. Undoubtedly, the concrete strain would not remain constant throughout the gauge length but the results should give an indication of average strain values to be expected when crushing and spalling occurred. It should be noted that the calculations were based on the readings at the end of a load increment and therefore, the results are likely to overestimate the actual values.

The displacement ductility at crushing and spalling of concrete are also listed in Table 4.9. Crushing of concrete took place at a displacement ductility of about 1.5 to 2.0 while spalling occurred at slightly higher values. At such low displacement ductility levels the effects of shear remained small and the curvature and strain calculation procedures outlined in Section 3.4.4 are considered to be still valid.

In a few column units (Units 19-24), crushing and spalling of concrete occurred almost at the same time. Inevitably the concrete

Table 4.9 : Concrete Strain At Crushing And Spalling

UNIT	Crushing		Spalling	
	μ	ε	μ	ε
1	1.5	0.0063	2.5	0.0141
2	2.0	0.0084	4.0	0.0147
3	2.0	0.0080	4.0	0.0214
4	1.5	0.0090	2.0	0.0135
5	1.5	0.0082	2.0	0.0133
6	1.5	0.0105	2.0	-
7	1.5	0.0103	2.0	0.0154
8	1.5	0.0099	3.0	0.0163
9	2.0	0.0094	3.0	0.0152
10	1.5	0.0067	2.0	0.0092
11	1.5	0.0069	2.0	0.0096
12	2.0	0.0082	3.0	0.0091
13	1.5	0.0074	2.0	0.0106
14	1.5	0.0068	2.0	0.0093
15	2.0	0.0054	4.0	0.0122
16	1.5	0.0088	2.0	0.0150
17	1.5	0.0069	2.0	0.0110
18	1.5	0.0098	2.5	0.0154
19	-	-	1.5	0.0112
20	-	-	2.0	0.0115
21	-	-	1.5	0.0159
22	-	-	1.5	0.0121
23	-	-	2.0	0.0100
24	-	-	2.0	0.0114
25	1.5	0.0044	2.0	0.0093
	Ave. =	0.0080	Ave. =	0.0128
	σ =	0.0016	σ =	0.0029

crushing strain of these column units would be over-estimated. If these six columns were excluded, the average crushing strain was found to be 0.008. On the other hand, the average spalling strain was computed with the inclusion of these columns and the resulting value was 0.0128, i.e. 1.6 times the average crushing strain. These are values well in excess of the value of 0.003 used in strength design. Allowing for any discrepancy between the calculated and actual values, a crushing strain of 0.006 and spalling of 0.0096, i.e. 75 percent of the experimental values, appear to be reasonable for the purpose of analysis and design of circular columns of similar proportions.

4.8 COMPARISONS OF EXPERIMENTAL RESULTS WITH SHEAR STRENGTHS SPECIFIED BY VARIOUS CODES

In the presentation of experimental results earlier in this chapter, the code requirements of NZS 3101 have been used to provide a datum for comparison. In this section, the results are further compared with NZS 3101 and the other code approaches presented in Chapter Two. The experimental and code specified results are tabulated in Tables 4.10 and 4.11, and comparisons are made in terms of the ratio of experimental ultimate shear strength (in kN) to the code specified shear strength (in kN). The spiral shear force was calculated using Eq. 2.53, with the appropriate value of $\cot\theta$, and the code specified shear strength of concrete, if any, was assumed acting uniformly over an effective area equal to 80 percent of the gross area. The code equations used are as given in Tables 2.2 and 2.4. In cases when the ideal flexural strength is lower than the code specified shear strength, no value is shown in the tables for the column units concerned.

4.8.1 The Traditional Method

4.8.1.1 The New Zealand Code (NZS 3101[4.2])

From Table 4.10 it is obvious that the experimental shear strengths achieved at ultimate far exceeded the ductile seismic shear strengths (V^s_{NZS} or V^s_{iv}) specified by NZS 3101. This is especially so for column units with axial compression of $0.1f'_c A_g$ or less because for these columns the shear strength of concrete shear resisting mechanisms is ignored by the code. The experimental values are plotted against the code specified values in Fig. 4.69a. Similar plots are also used for the comparison between experimental and other code specified results in subsequent figures. Also included in the figure is a straight line showing $V_u = V^s_{iv}$ and it can be seen that most of the points plotted

Table 4.10 : Comparisons Of Experimental And Code Specified Shear Strengths At Ultimate

UNIT	$\frac{M}{VD}$	$\frac{P_i}{f'_c A_g}$	V_u (kN)	V^s_{NZS} seismic (kN)	$\frac{V_u}{V^s_{NZS}}$	V_{NZS} non-seismic (kN)	$\frac{V_u}{V_{NZS}}$	V_{CAN} (kN)	$\frac{V_u}{V_{CAN}}$	V_{CEB} (kN)	$\frac{V_u}{V_{CEB}}$
1	2.0	0	320	88	3.64	211	1.52	211	1.52	202	1.58
2	2.0	0	228	88	2.59	211	1.08	211	1.08	201	1.13
3	2.5	0	298	88	3.39	209	1.43	209	1.43	198	1.51
4	2.0	0	295	85	3.47	196	1.51	196	1.51	183	1.61
5	2.0	0	340	131	2.60	243	1.40	243	1.40	210	1.62
6	1.5	0	390	88	4.43	198	1.97	198	1.97	184	2.12
7	2.0	0	280	74	3.78	183	1.53	183	1.53	169	1.66
8	2.0	0.2	475	334	1.42	370	*	370	*	304	1.56
9	2.5	0.2	385	337	*	374	*	374	*	308	*
10	2.0	0.2	450	318	1.42	346	1.26	356	1.26	289	1.56
11	2.0	0.2	404	239	1.69	276	1.46	276	1.46	210	1.92
12	1.5	0.1	527	175	3.01	315	1.67	315	1.67	275	1.92
13	2.0	0.1	443	174	2.55	331	1.34	331	1.34	294	1.51
14	2.0	0	311	86	3.61	203	1.53	203	1.53	191	1.63
15	2.0	0	230	86	2.67	184	1.25	184	1.25	193	1.19
16	2.0	0.1	379	86	4.41	237	1.60	237	1.60	199	1.90
17	2.5	0.1	329	86	3.83	239	1.38	239	1.38	201	1.64
18	1.5	0.1	507	86	5.90	241	2.10	241	2.10	203	2.50
19	1.5	0.1	436	65	6.71	218	2.00	218	2.00	180	2.42
20	1.75	0.175	487	198	2.46	251	1.94	251	1.94	191	2.55
21	2.0	0	258	65	3.97	181	1.43	181	1.43	169	1.53
22	2.0	0	280	62	4.52	174	1.61	174	1.61	160	1.75
23	2.0	0	339	124	2.73	238	1.42	238	1.42	226	1.50
24	2.0	0	338	125	2.70	241	1.40	241	1.40	228	1.48
25	1.5	0	233	0	-	112	2.08	112	2.08	103	2.26
				Ave.	3.37		1.56		1.56		1.75
				σ	1.26		0.27		0.27		0.37

* flexure governs

Table 4.10 (Contd.) Comparisons Of Experimental And Code Specified Shear Strengths At Ultimate

UNIT	$\frac{M}{VD}$	$\frac{P_i}{f'_c A_g}$	V_u (kN)	V_{ACI} Approx. (kN)	$\frac{V_u}{V_{ACI}}$ Approx.	V_{ACI} exact (kN)	$\frac{V_u}{V_{ACI}}$ exact	V_{AIJ} Eq.2.38 (kN)	$\frac{V_u}{V_{AIJ}}$ Eq. 2.38	V_{AIJ} Eq.2.39 (kN)	$\frac{V_u}{V_{AIJ}}$ Eq. 2.39
1	2.0	0	320	193	1.66	197	1.62	246	1.30	273	1.17
2	2.0	0	228	192	1.16	196	1.16	245	*	272	*
3	2.5	0	298	191	1.56	193	1.54	209	1.43	232	1.28
4	2.0	0	295	180	1.64	184	1.60	223	1.32	248	1.19
5	2.0	0	340	226	1.50	231	1.47	241	1.41	268	1.27
6	1.5	0	390	182	2.14	190	2.05	270	1.44	300	1.30
7	2.0	0	280	167	1.68	172	1.63	215	1.30	239	1.17
8	2.0	0.2	475	328	1.45	302	1.57	319	1.49	339	1.40
9	2.5	0.2	385	332	*	300	*	289	*	313	*
10	2.0	0.2	450	315	1.43	284	1.58	328	1.37	347	1.30
11	2.0	0.2	404	234	1.73	206	1.96	287	1.41	311	1.30
12	1.5	0.1	527	285	1.85	279	1.89	330	1.60	354	1.49
13	2.0	0.1	443	304	1.46	285	1.55	315	1.41	337	1.31
14	2.0	0	311	185	1.68	182	1.71	215	1.45	239	1.30
15	2.0	0	230	187	1.23	191	1.20	237	*	263	*
16	2.0	0.1	379	209	1.81	193	1.96	267	1.42	292	1.30
17	2.5	0.1	329	211	1.56	191	1.72	235	1.40	260	1.27
18	1.5	0.1	507	213	2.38	200	2.54	335	1.51	356	1.42
19	1.5	0.1	436	190	2.29	178	2.45	321	1.36	344	1.27
20	1.75	0.175	487	217	2.24	182	268	331	1.47	350	1.39
21	2.0	0	258	163	1.58	168	1.54	222	1.16	247	1.04
22	2.0	0	280	157	1.78	162	1.73	214	1.31	238	1.18
23	2.0	0	339	221	1.53	226	1.50	242	1.40	269	1.26
24	2.0	0	338	223	1.52	228	1.48	246	1.37	273	1.24
25	1.5	0	233	98	2.38	106	2.20	211	1.10	234	1.00
				Ave.	1.72		1.76		1.38		1.27
				σ	0.33		0.38		0.11		0.11

* flexure governs

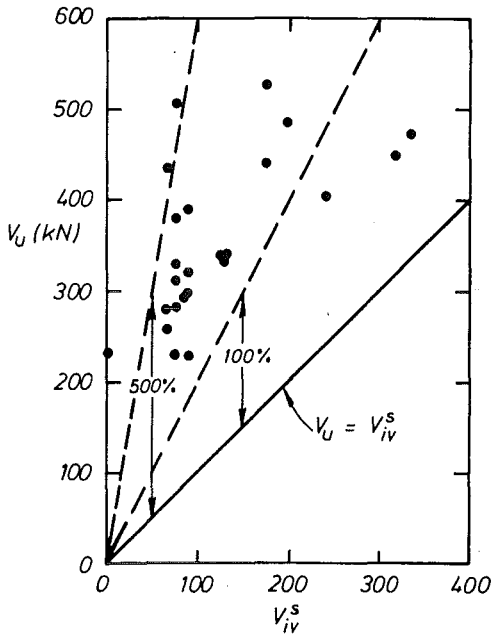

(a) Seismic provisions

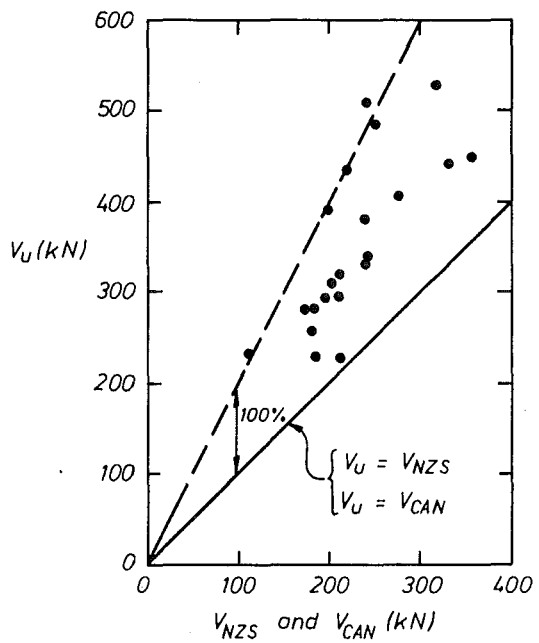

(b) Non-seismic provisions

Fig. 4.69 : Comparisons of experimental and code specified shear strengths at ultimate (NZS 3101 and Candadian Code)

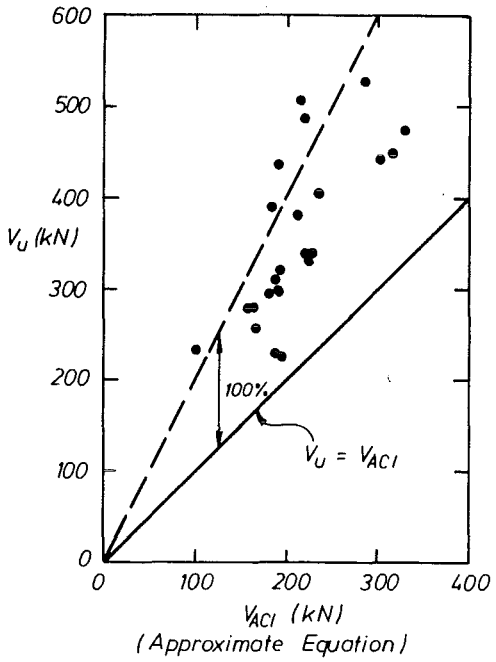

(a) Approximate equation

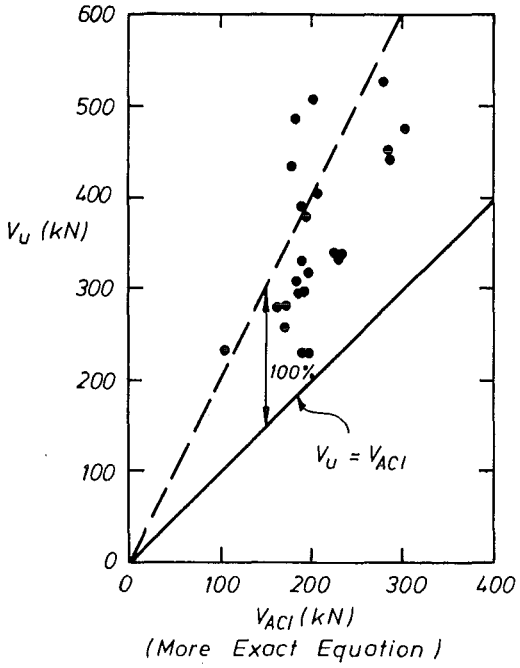

(b) More exact equation

Fig. 4.70 : Comparisons of experimental and code specified shear strengths at ultimate (ACI 318-83)

are more than twice the code specified values. In general, they fall within the range 2 to 6 times V_{iv}^s. The three points closer to the straight line $V_u = V_{iv}^s$ belong to column units with axial compression of $0.2f'_c A_g$ in which the shear strength provided by the concrete was non-zero according to NZS 3101. The average of the ratio $\frac{V_u}{V_{iv}^s}$ from Table 4.10 is 3.37 with a standard deviation of 1.26. On the other hand, the non-seismic provisions of NZS 3101, with basic shear stress, v_b, taken to be $0.2\sqrt{f'_c}$, are still conservative but most of the points fall within the range greater than the ideal shear strength but less than twice this value (see Fig. 4.69b). Note that V_{NZS} and similar terms used for other codes are synonymous with V_{iv} used elsewhere. On average the experimental values are 56 percent higher than the code specified values and the standard deviation is 0.27 for the ratio $\frac{V_u}{V_{NZS}}$.

4.8.1.2 The Canadian Code[4.3]

The shear strengths specified by the Canadian Code are identical to those of the non-seismic provisions of NZS 3101 with $v_b = 0.2\sqrt{f'_c}$ and so the accuracy of the code specified results is the same as that of the latter.

4.8.1.3 The American Code (ACI 318-83[4.4])

The shear strengths specified by both the approximate and the more exact ACI equations are included in the comparison. The values were calculated assuming that the effective depth, d, is equal to 80 percent of the overall diameter of the cross-section. The results from Table 4.10 are compared as shown in Figs. 4.70a and b. From the results it appears that the ACI results are more conservative than the non-seismic provision of NZS 3101 (or the Canadian Code). The average of the ratio $\frac{V_u}{V_{ACI}}$ is 1.72 (standard deviation = 0.33) if the approximate equation is used and 1.76 (standard deviation = 0.38) if the more exact equation is used.

4.8.1.4 The European Code (CEB-FIP Model Code[4.5])

In CEB-FIP Model Code the specified concrete strength is the cube strength of concrete, f'_{cu}, and for simplicity it was taken to be $\frac{f'_c}{0.85}$. The values of τ_{Rd} are as given in Table 2.3 and appropriate value of β_1 was used if axial compression was present. Generally the shear strengths, plotted in Fig. 4.71, are very similar to those by the more exact equation of ACI 318-83. The average of the ratio $\frac{V_u}{V_{CEB}}$ is 1.75 with a standard deviation of 0.37.

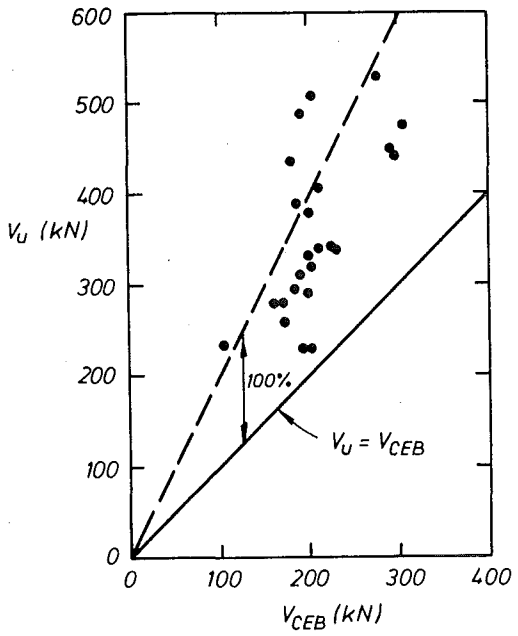

Fig. 4.71 : Comparisons of experimental and code specified shear strengths at ultimate (CEB-FIP Model Code)

4.8.1.5 The Japanese Code (AIJ Standard[4.6])

The empirical expressions (Eqs. 2.38 and 2.39) used in AIJ Standard involve a number of multiplying factors to allow for the influence of various parameters, The AIJ Standard uses the MKS system and the conversion factor used is 1 Kgf/cm^2 = 0.0981 MPa. The results predicted by the AIJ equations give the best agreement with experimental results and the spread of the data is not as great as in the other cases (Figs. 4.72a and b). The experimental results exceeded the predicted results of Eqs. 2.38 and 2.39 by 38 and 27 percent respectively on average. The standard deviation in both cases is 0.11 for $\frac{V_u}{V_{AIJ}}$ (see Table 4.10).

4.8.2 The Refined Method

The CEB-FIP Model Code[4.3] and the Canadian Code[4.5] allow the use of smaller diagonal strut inclination in the shear design of reinforced concrete members such that

$$V^r_{CAN} = V_{s(45^o)} \cot \theta \qquad (4.12a)$$

$$\text{or} \quad V^r_{CEB} = V_{s(45^o)} \cot \theta + V_c \qquad (4.12b)$$

where θ is the angle of diagonal strut inclination with respect to

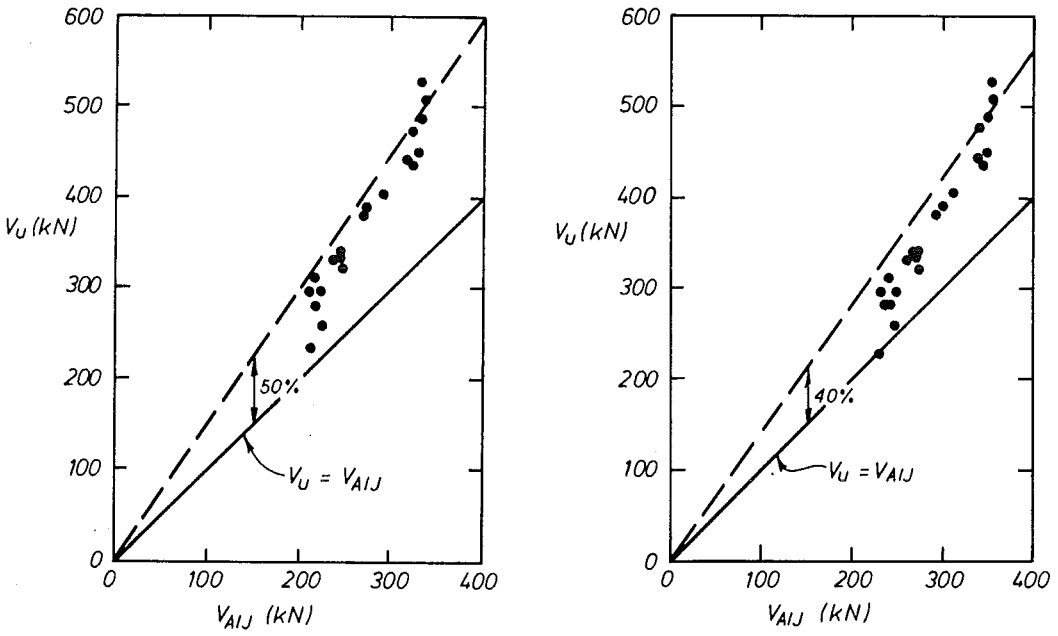

(a) Eq. 2.38 (b) Eq. 2.39

Fig. 4.72 : Comparisons of experimental and code specified shear strength at ultimate (AIJ standard)

member axis and can be selected within the allowable range of values specified by the codes. However, it should be noted that a smaller value of θ than that of a corner-to-corner crack is of no significance because the number of spirals available for the truss-action is fixed by the total number of spirals within the shear-span; no additional spirals are available to help in carrying the applied shear if the angle is lowered below the angle of the diagonal.

4.8.2.1 The Canadian Code[4.3]

The Canadian Code allows a wider range of angle in determining the shear strength of a member but as is discussed above this angle is limited by the aspect ratio of the column. The code also required the flexural reinforcement to be designed for an increase in tensile force due to the diagonal compression. For simplicity the code recommends that the moment resistance of the section must be designed such that they are greater than that due to other actions plus an additional moment of $\frac{Njd}{2}$, where $N = V \cot \theta$. However, at the base of the cantilever columns, within a distance of $jd \cot \theta$, the angle of diagonal strut inclination has to vary between θ and 90-deg. The above consideration is therefore not applicable in this region and the resulting bending moment diagram is as shown in Fig. 4.73, with a

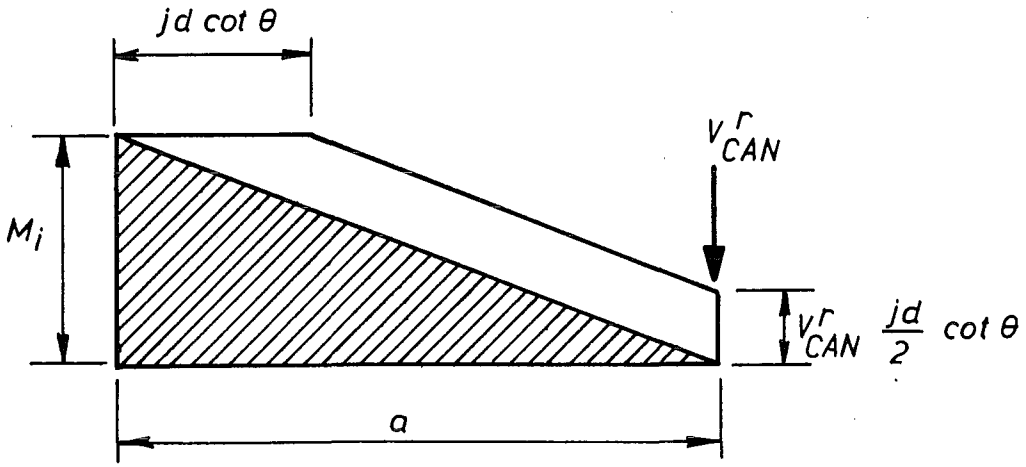

Fig. 4.73 : Increase in required moment of resistance due to diagonal compression - the Canadian Code approach

constant value equal to the moment at the base of the cantilever within a distance of $jd \cot \theta$ from this critical section. Hence, the angle θ should also be checked so that

$$V^r_{CAN}\, a = V_s \cot\theta\, a \leq M_i \qquad (4.13)$$

However, in the case when Eq. 4.13 is not satisfied, the prediction of shear strength is irrelevant because it is the flexural overstrength that is likely to govern.

The specified shear strength was calculated by multiplying $V_{s(45^o)}$ with a factor $\cot\theta$ where θ was appropriately chosen within the constraint of geometry. The results calculated accordingly are much lower than the experimental shear strengths at ultimate. The ratio $\frac{V_u}{V^r_{CAN}}$ has an average of 2.06 and a standard deviation of 0.95 (Table 4.11).

4.8.2.2. The CEB-FIP Model Code[4.5]

The range of angle θ allowed in CEB-FIP Model Code is narrower but the code introduces a correction term, V_c, similar to the so-called 'concrete contribution' used in the traditional approach of the modified truss analogy. The values of V_c is dependent on the design shear force level and is non-zero only within a narrow range of design shear force. From Table 2.4,

$$V_c = 0.5(7.5\,\tau_{Rd}\, b_w d - V_u),\ 0 \leq V_c \leq 2.5\,\tau_{Rd}\, b_w d \qquad (4.14)$$

If $V_u = V_{iv}$ and $V_u \leq 7.5\,\tau_{Rd}\, b_w d$

$$V_{iv} = V_s \cot\theta + V_c$$

$$= V_s \cot\theta + 0.5(7.5\,\tau_{Rd}\, b_w d - V_{iv})$$

$$1.5V_{iv} = V_s \cot\theta + 3.75\,\tau_{Rd}\, b_w d$$

$$V_{iv} = \frac{2}{3} V_s \cot\theta + 2.5\,\tau_{Rd}\, b_w d \qquad (4.15)$$

with the lower limit of $\tan\theta = \frac{3}{5}$ the above equation becomes

$$V^r_{CEB} = V_{iv} = \frac{10}{9} V_s + 2.5\,\tau_{Rd}\, b_w d \qquad (4.16)$$

Note that this lower limit is still greater than the slope of a corner-to-corner crack in column units with aspect ratio of 1.5 and hence, the appropriate value of $\cot\theta = 1.5$ should be used for these column units. Thus for these units Eq. 4.16 is reduced to

$$V^r_{CEB} = V_s + 2.5\,\tau_{Rd}\, b_w d \qquad (4.17)$$

which is equivalent to that of the traditional method allowed by the same code.

Because of the introduction of the correction term, the results

Table 4.11 : Comparisons Of Experimental Shear Strengths At Ultimate With The Values Specified By The Refined Method

UNIT	$\frac{M}{VD}$	V_s 45-deg (kN)	V_u (kN)	V^r_{CAN} (kN)	$\frac{V_u}{V^r_{CAN}}$	V^r_{CEB} (kN)	$\frac{V_u}{V^r_{CEB}}$
1	2.0	88	320	176	1.82	212	1.51
2	2.0	88	228	176	1.30	165	1.38
3	2.5	88	298	220	1.35	186	1.60
4	2.0	85	295	170	1.74	192	1.54
5	2.0	131	340	262	1.30	220	1.48
6	1.5	88	390	132	2.95	184	2.12
7	2.0	74	280	148	1.89	177	1.58
8	2.0	198	475	396	*	283	1.68
9	2.5	198	385	495	*	239	1.61
10	2.0	176	450	352	1.28	280	1.61
11	2.0	100	404	200	2.02	207	1.95
12	1.5	175	527	263	2.00	268	1.97
13	2.0	174	443	348	1.27	281	1.58
14	2.0	86	311	172	1.81	200	1.56
15	2.0	86	230	172	1.34	154	1.49
16	2.0	86	379	172	2.20	200	1.90
17	2.5	86	329	215	1.53	208	1.58
18	1.5	86	507	129	3.93	194	2.61
19	1.5	65	436	98	4.45	172	2.53
20	1.75	65	487	114	4.27	184	2.65
21	2.0	65	258	130	1.98	176	1.47
22	2.0	62	280	124	2.26	167	1.68
23	2.0	124	339	248	1.37	223	1.52
24	2.0	125	338	250	1.35	229	1.48
25	1.5	-	233	-	-	103	2.26
				Ave.	2.06		1.77
				σ	0.95		0.37

* $(V^r_{CAN} \cdot a) \geq M_i$ (flexure governs)

specified by CEB-FIP Model Code agree better with experimental values than those predicted by the Canadian Code. The average of the ratio $\frac{V_u}{V^r_{CEB}}$ is 1.77 with a standard deviation of 0.37 (see Table 4.11).

4.9 PREDICTION OF SHEAR STRENGTH USING PLASTIC THEORY

The lower and upper bound approaches of the plastic analyses outlined in Chapter Two were also used to predict the strength of the test columns. The value of ρ_t used in calculating the mechanical degree of transverse reinforcement ($\psi = \frac{\rho_t f_{yt}}{f'_c}$) was taken to be $0.5\ \rho_s$ as was discussed in Section 2.4.4.2. The results predicted by both approaches are listed in Table 4.12. The angle θ calculated using Eq. 2.8 (see Section 2.3.3.) resulted in values of $\cot\theta$ which are outside the range allowed. Hence, the limit of $\tan\theta = \frac{1}{2}$ was used in the prediction. However, in cases where the aspect ratio was less than 2.0 (e.g. Units 6, 12, 18, 19 and 20) the value of θ was taken to be that due to the corner-to-corner crack for the reason given in Section 4.8.2. For Units 8, 9 and 10 the predicted values were limited by the ideal flexural strength, V_{if}, of the column units and therefore no prediction of shear strength was made.

It is obvious from Table 4.12 that the lower-bound approach gives very conservative results (average value of the ratios $\frac{V_u}{V^L}$ is 2.14 and the standard deviation is 0.94) and this shows that the prediction of ultimate strength cannot be achieved by changing the angle θ alone. On the other hand, except for Units 8, 9 and 10, the upper bound solutions were also limited by the geometry of the columns and Eq. 2.19 was therefore used to calculate the upper bound results, V^U. $\frac{M}{VD}$ was used in place of $\frac{a}{d}$ for simplicity.

An upper bound approach is expected to be non-conservative. In this case the predicted results all exceeded the experimental results by substantial margins (Table 4.12) indicating that the approach is inappropriate. On average the experimental results are only 59 percent of the predicted values. The standard deviation of the ratios $\frac{V_u}{V^U}$ is 0.11. However, it is interesting to see that the solution as given by Eq. 2.19 can be expressed as

$$v = \frac{f'_c}{2}\left\{\left[1 + \left(\frac{a}{d}\right)^2\right]^{\frac{1}{2}} - \frac{a}{d}\right\} + \rho_t f_{yt} \frac{a}{d} \qquad (4.18)$$

The second term on the right hand side of the equation is the contribution from transverse reinforcement across the corner-to-corner crack and the equation resembles the familiar additive principle if the first term

Table 4.12 : Lower And Upper Bound Predictions Of The Plastic Theory

UNIT	$\frac{M}{VD}$	ρ_s ($\times 1^{-3}$)	$\psi = \frac{\rho_s f_{yt}}{2f'_c}$ ($\times 10^{-3}$)	V_u (kN)	V_s 45-deg (kN)	Lower Bound Approach			Upper Bound Approach		
						cot θ	V^L (kN)	$\frac{V_u}{V^L}$	cot γ	V^U (kN)	$\frac{V_u}{V^U}$
1	2.0	5.094	22.28	320	88	6.6	176	1.82	3.2	613	0.52
2	2.0	5.094	22.46	228	88	6.6	176	1.30	3.2	609	0.37
3	2.5	5.094	23.21	298	88	6.5	176	1.69	3.2	558	0.53
4	2.0	5.146	26.57	295	85	6.1	170	1.74	2.9	527	0.56
5	2.0	7.642	40.30	340	131	4.9	262	1.30	2.3	621	0.55
6	1.5	5.094	27.76	390	88	5.9	132	2.95	2.9	584	0.67
7	2.0	3.821	24.09	280	74	6.4	148	1.89	3.1	493	0.57
8	2.0	10.189	66.03	475	198	3.8	-	-	1.7	717	0.66
9	2.5	10.189	63.38	385	198	3.8	-	-	1.8	732	0.53
10	2.0	10.189	54.21	450	176	4.2	-	-	2.0	710	0.63
11	2.0	5.094	31.69	404	100	5.5	200	2.02	2.7	545	0.74
12	1.5	10.189	58.43	527	175	4.0	263	2.00	1.9	687	0.77
13	2.0	10.189	45.88	443	174	4.6	348	1.27	2.2	763	0.58
14	2.0	5.094	24.64	311	86	6.3	172	1.81	3.1	567	0.55
15	2.0	5.094	23.86	230	86	6.4	172	1.34	3.1	580	0.40
16	2.0	5.094	24.86	379	86	6.3	172	2.20	3.1	563	0.67
17	2.5	5.094	24.21	329	86	6.3	172	1.91	3.1	541	0.61
18	1.5	5.094	23.72	507	86	6.4	129	3.93	3.1	658	0.77
19	1.5	3.821	18.11	436	65	7.4	98	4.45	3.6	617	0.71
20	1.75	3.821	16.97	487	65	7.6	114	4.27	3.7	599	0.81
21	2.0	3.821	18.76	258	65	7.2	130	1.98	3.5	519	0.50
22	2.0	3.859	19.36	280	62	7.1	124	2.26	3.5	487	0.57
23	2.0	7.642	36.44	339	124	5.1	248	1.37	2.5	620	0.55
24	2.0	7.719	36.15	338	125	5.2	250	1.35	2.5	633	0.53
25	1.5	-	-	233	-	-	-	-	-	499	0.47
							Ave	2.14			0.59
							σ	0.94			0.11

on the right hand side is regarded as the 'concrete contribution', i.e.

$$v_c = \frac{f'_c}{2} \{ [1 + (\frac{a}{d})^2]^{\frac{1}{2}} - \frac{a}{d} \} \qquad (4.19)$$

The variation of $\frac{v_c}{f'_c}$ according to Eq. 4.19 is plotted against $\frac{a}{d}$

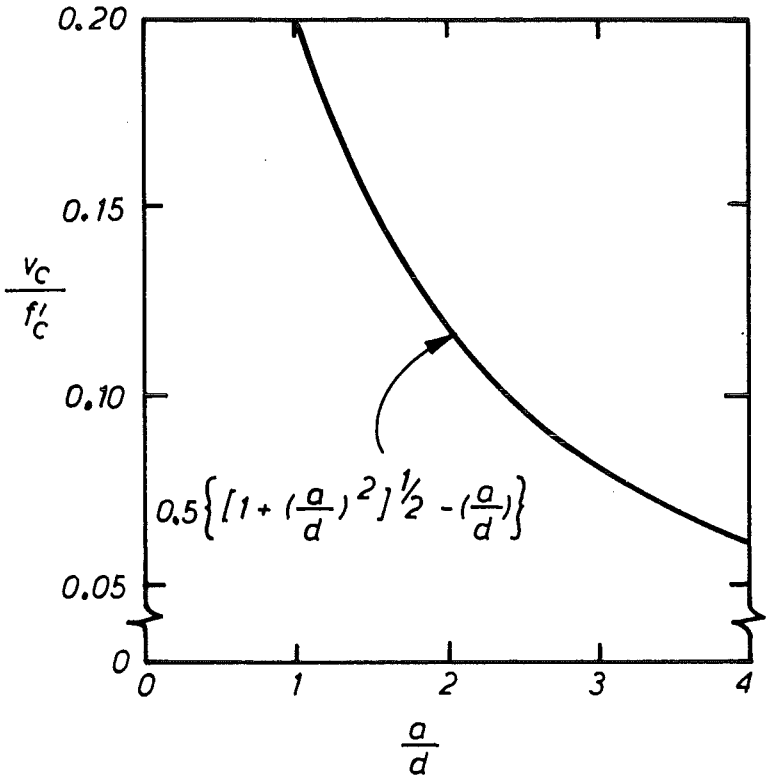

Fig. 4.74 : 'Concrete contribution' in upper bound solution

in Fig. 4.74. Within the possible range of aspect ratio ($\frac{a}{d}$ greater than 4.0 would imply a very small angle for a corner-to-corner failure crack) it appears that there is an inverse relationship between the 'concrete contribution' implied in the approach and the $\frac{a}{d}$ ratio. However, using Eq. 4.19 in its original form would give rise to very high value of v_c if the full concrete strength, f'_c , is used. Perhaps, a better prediction may be achieved if a similar web effectiveness factor, ν , as discussed in Section 2.3.3 is incorporated so that the actual concrete strength is represented by $\nu f'_c$. Nevertheless, it does reveal that even with the use of upper bound approach the resulting equation still involves a term similar to the 'concrete contribution' if the inclination of the failure plane is limited by the geometry of the member.

4.10 CONCLUSIONS

The main conclusions drawn from the experimental results are briefly summarised below.

(a) The NZS 3101 provisions for shear when applied to circular sections with uniformly distributed longitudinal reinforcement around the spiral are very conservative even if the non-seismic equations are used. The shear strength provided by 'concrete' is substantial even under the simulated seismic loading situation. It appears that the shear strength provided by 'concrete' is dependent on the displacement ductility level. Similar conservatism was also noted in other code provisions.

(b) The experimental shear strength could not be satisfactorily predicted by changing the diagonal strut inclination alone. The angle of inclination tended to be limited by the geometry of the column units, and the results predicted by considering solely the spiral contribution across a corner-to-corner failure plane still underestimated the actual shear strength.

(c) The relative strength index as represented by the ratio of ideal shear strength to ideal flexural strength was found to be a strong indicator of the column performance. The ideal shear strengths were based on the non-seismic provisions of NZS 3101.

According to the tests results the column performance is classified in four categories, viz.

Relative Strength Index	Failure Mode	Ductility Capacity
greater than 1.3	Ductile flexural failure	$\mu > 6$
between 0.9 and 1.10	Shear failure with moderate ductility	$4 < \mu \leq 6$
between 0.65 and 0.9	Shear failure with limited ductility	$2 < \mu \leq 4$
less than 0.65	Brittle shear failure	$\mu \leq 2$

(d) The use of a 45-deg truss, though apparently reasonable at low displacement ductility level, may not be valid when the displacement ductility is large. For column units which achieved ultimate shear strength at displacement ductility of no greater than 2.0, the 45-deg truss can be used to calculate the ultimate shear strength if an

appropriate value of shear strength provided by 'concrete' is used.

(e) Increasing the spiral reinforcement content has the following effects,

i) enhancement of shear strength at all stages;

ii) increase in displacement ductility before onset of failure;

iii) improvement in energy dissipation capacity.

If the spiral reinforcement content remained constant, changing the spiral pitch and bar diameter did not result in any significant change in performance.

(f) Decreasing the aspect ratio has the following effects,

i) earlier onset of strength and stiffness degradation;

ii) increase in shear stress carried by 'concrete' if $\frac{M}{VD} < 2.0$.

(g) Increase in axial compression has the following effects,

i) increase in shear stress carried by 'concrete';

ii) increase in rate of decay during the post-ultimate stage.

Chapter Five

A PROPOSAL FOR SHEAR DESIGN OF CIRCULAR COLUMNS UNDER SEISMIC LOADING

5.1 INTRODUCTION

From Chapter Four, the study of test results indicated that neither the traditional method of modified truss analogy, based on a 45-deg truss and a correction term known as the 'concrete condition', nor the refined approach based on a variable angle truss model alone is able to satisfactorily predict the shear strength of circular columns under seismic loading.

The 'concrete contribution', v_c , of the additive principle used in many codes was derived from tests on rectangular beams. It is doubtful whether the same term is applicable to circular members reinforced with well distributed longitudinal reinforcement and transversely with spirals or circular hoops. The experimental results indicated that v_c for circular members could be higher than that currently specified in the codes which therefore tend to under-estimate the shear strength of these members. The code specified shear strengths are even more conservative when the 'concrete contribution' is reduced or ignored under seismic situations, as is frequently specified. This is especially so when no provision is allowed for the change in diagonal strut inclination from 45-deg during the inelastic stage of loading.

On the other hand, the variable-angle truss approach, though being more rational, still gave conservative predictions because the diagonal strut inclination tended to be restricted by member geometry. The introduction of a correction term as in the case of CEB-FIP Model Code might improve the prediction accuracy if a good estimate of this term could be obtained.

The experimental results indicate that under simulated seismic loading situations, the concrete shear carrying mechanisms are still operational before significant plasticity is developed; the magnitude of 'concrete contribution' is substantial and the angle of crack inclination remains close to 45-deg.

At high displacement ductility level, especially with the yielding of both longitudinal and transverse reinforcement, the cracks open excessively and the integrity of concrete cannot be maintained under repeated abrasion. Hence, the 'concrete contribution' is reduced.

On the other hand, the contribution from the yielding transverse reinforcement can only be increased by a change in the angle of diagonal strut inclination of the analogous truss. The extent of degradation in concrete shear carrying mechanisms and an adjustment in the diagonal strut inclination depends on the amount of transverse reinforcement provided.

The shear strength of members therefore changes with the displacement ductility level; the lower the ductility demand the higher is the shear resistance of the member or conversely, the available ductility capacity of the member at full strength is a function of its shear strength. This is the basis of the design approach proposed in the following sections. The approach is subsequently used to predict the strength and ductility capacity of the test columns and columns in other tests.

5.2 THE PROPOSAL

5.2.1 Outline Of The Proposal

The above idea is illustrated graphically in Fig. 5.1. It is a modification of a proposal by ATC-6-2[5.1] and it represents a skeleton curve from which the strength and available ductility capacity, μ_c, of the member can be assessed by comparing the shear and flexural strengths of the member. The skeleton curve is made up of two piecewise linear curves, viz. AB and BC. The two levels of shear strength, V_i and V_f refer respectively to the initial shear strength before significant plasticity is developed and the residual shear strength after degradation in concrete shear carrying mechanisms has taken place.

The shear carrying capacity of a member is assumed to remain constant at V_i until $\mu = 2.0$ (line AB) and the residual shear strength V_f is assumed to be achieved at $\mu = \mu_f$, the flexural displacement ductility capacity, defined in Section 5.2.5. If the shear corresponding to flexural overstrength, V_{if}^o, falls below V_f a ductile flexural failure can be ensured (curve 1 in Fig. 5.1). The drop from V_i to V_f is assumed to be linear (line BC) so if V_{if}^o lies between V_i and V_f inclusively, the value of μ_c can be determined by interpolation between $\mu = 2$ and $\mu = \mu_f$ (curve 2 in Fig. 5.1). Depending on the value of μ_c obtained, a ductile flexural failure ($\mu_c > 6$) or shear failure with moderate ductility ($4 < \mu_c \leq 6$) or with limited ductility ($2 \leq \mu_c \leq 4$) can be achieved. In all these cases the flexural overstrength of the member can still be fully developed.

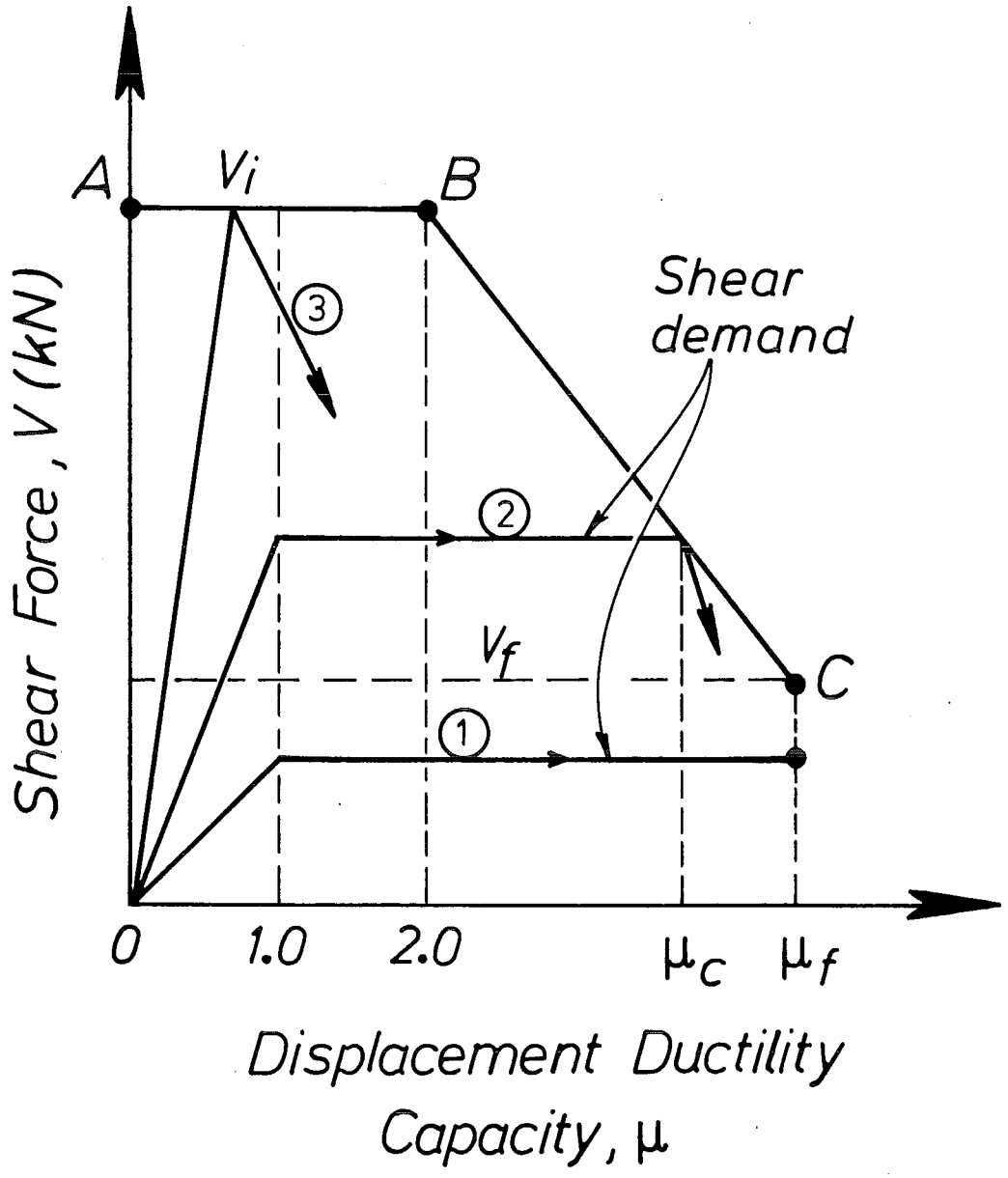

Fig. 5.1 : Relationship between shear strength and displacement ductility capacity

However, if V_{if}^{o} is greater than V_i but the ideal flexural strength, V_{if}, is less than V_i, the ultimate strength is assumed to be V_i and the dependable displacement ductility capacity is 2. On the other hand, if even the ideal flexural strength cannot be achieved (i.e. $V_i < V_{if}$) brittle shear failure ($\mu < 1.0$) will be the consequence (curve 3 in Fig. 5.1).

5.2.2 Shear At Flexural Overstrength, V_{if}^{o}

It is well established that the flexural strength as computed using the ACI method is very conservative for reinforced concrete columns designed for ductile flexural response to earthquakes[5.2]. Enhancement in concrete strength due to confinement, strain-hardening of steel and other effects can lead to a substantially higher flexural strength than that obtained using the ACI method. According to the capacity design principles outlined in Chapter One, the shear strength of a member should be such that it is not lower than the shear demand developed with flexural overstrength. Hence, it is crucial to have a reliable estimate of the flexural overstrength. The relative magnitude of shear strength and flexural overstrength is an important criterion for the member performance.

Table 5.1 lists the results of some 31 column units tested at the University of Canterbury since 1974[5.3-5.10]. The columns were subjected to several inelastic lateral load cycles and under different magnitudes of axial compression. All the column units were reinforced with Grade 275 flexural steel and were of different cross-sections. Note that Unit 2 included in the table is the only column unit with Grade 275 flexural steel from the present series of tests. The ideal flexural strength (in terms of M_i) of these columns are listed together with the corresponding maximum experimental value, M_u, and the ratio $\frac{M_u}{M_i}$. The ideal flexural strength was calculated using the ACI method based on a crushing concrete compressive strain of 0.003, measured material strength properties, and a strength reduction factor of unity.

The strength ratio, $\frac{M_u}{M_i}$, is plotted against axial load level in Fig. 5.2. It is apparent from the figure that axial compression has a very strong influence on the strength ratio which also can be considered as a strength enhancement factor. Fig. 5.2 includes a best-fit curve fitted using regression analysis and defined by the following equations:

$$\text{For } \frac{P_i}{f'_c A_g} > 0.1, \quad m = \frac{M_u}{M_i} = 2.35 \left(\frac{P_i}{f'_c A_g} - 0.1\right)^2 + m_1 \qquad (5.1a)$$

Table 5.1 : Experimental To Predicted Strength Ratios For Column Units Tested At The University of Canterbury since 1974

UNIT	Cross Section	$\frac{P_i}{f'_c A_g}$	Confinement ratio, α	M_i (ACI) kNm	M_u (Expt) kNm	$\frac{M_u}{M_i}$	Predicted Ratio (Eq. 5.1)	$\frac{(7)}{(8)}$	Reference
(1)	(2)	(3)	(4)	(5)	(6)	(7)	(8)	(9)	(10)
D1		0.06	0.599	421	470	1.12	1.13	0.99	
D2		0.06	0.574	419	520	1.24	1.13	1.10	5.3
D3		0.06	0.647	428	460	1.07	1.13	0.95	
M1		0.03	1.905	323	370	1.15	1.13	1.02	5.4
N2		0.01	2.268	44	50	1.14	1.13	1.01	
N3		0.33	1.422	59	71	1.20	1.25	0.96	5.5
P1		0.23	0.836	723	890	1.23	1.17	1.05	
P3		0.54	0.897	672	966	1.44	1.58	0.91	
P4		0.39	0.869	803	1041	1.30	1.33	0.98	5.6
P5-1		0.35	2.000	807	1079	1.34	1.28	1.05	
P5-2		0.70	1.363	564	1276	2.26	1.98	1.14	
G1		0.26	0.983	691	864	1.25	1.19	1.05	
G2		0.21	1.019	905	1010	1.12	1.16	0.97	5.7
G3		0.42	0.870	646	843	1.30	1.37	0.95	
G4		0.60	0.715	598	911	1.52	1.72	0.88	
A1		0.12	0.995	222	262	1.18	1.13	1.04	
A2		0.53	1.042	219	417	1.90	1.56	1.22	5.8
A3		0.38	1.477	270	336	1.24	1.31	0.95	
A4		0.21	1.217	257	322	1.25	1.16	1.08	
Z1		0.27	1.000	273	368	1.35	1.20	1.13	
Z2		0.45	1.150	259	400	1.54	1.42	1.08	
Z3		0.23	1.040	274	357	1.31	1.17	1.12	
Z4		0.48	1.340	234	397	1.70	1.47	1.16	5.9
Z5		0.13	1.110	217	234	1.08	1.13	0.96	
Z6		0.67	1.350	193	325	1.68	1.89	0.89	
Z7		0.23	1.260	284	335	1.18	1.17	1.01	
Z8		0.42	0.930	352	433	1.23	1.37	0.90	
MA		0.10	0.740	255	282	1.11	1.13	0.98	
MB		0.50	0.830	373	496	1.33	1.51	0.88	5.10
MC		0.30	0.830	368	415	1.13	1.22	0.93	
MD		0.30	0.550	368	418	1.14	1.22	0.93	
UNIT 2		0.00	0.749	220	228	1.04	1.13	0.92	Present Project
							Ave	1.00	
							σ	0.09	

$$\text{For} \quad \frac{P_i}{f'_c A_g} \leq 0.1 \ , \quad m = m_1 \tag{5.1b}$$

where $m_1 = 1.13$. It can be seen from Fig. 5.2 that all except one data point are within ±15 percent of this curve. The strength ratios predicted by the above equations are also listed in Table 5.1. The standard deviation of the ratios of observed to predicted values is 0.09 from a mean value of 1.00.

To further check if the amount of confinement provided has any influence on the strength ratio, the same data are plotted against the confinement ratio, α , where $\alpha = \frac{\rho_{s(provided)}}{\rho_{s(code)}}$ in Fig. 5.3. The numerator of the ratio refers to the amount of confining reinforcement provided in the column units and the denominator refers to the amount of confining reinforcement required in accordance with NZS 3101[5.13]. Values of α are included in Table 5.1. The figure shows that there is no clear pattern of variation unless the points are separated according to the axial load level. For column units with axial compression of less than $0.4f'_c A_g$ the strength ratios remained relatively constant. For higher axial load levels the ratio increases linearly as shown in Fig. 5.3. This is expected, because the enhancement in concrete strength due to confinement can cause a significant increase in moment capacity only if the depth of neutral-axis is large, i.e. high axial compression is present. For simplicity Eqs. 5.1a and b are adopted but as the results were derived from column units with Grade 275 flexural steel, the equations have to be modified so that they can be used for the present series of tests which involved column units with Grade 380 flexural steel which would be expected to develop greater strain hardening due to the reduced yield plateau. In the absence of experimental data prior to the tests, m_1 is taken to be 1.22 which is the value implied in NZS 3101 (see Chapter Three) and the form of Eq. 5.1a is retained.

For shear design purposes, it is recommended that the value of m as obtained from Eqs. 5.1a and b be multiplied by a factor of 1.15 (i.e. the curve corresponding to the upper bound shown in Fig. 5.1, in order not to under-estimate the flexural overstrength of a member. In addition, since the measured (i.e. probable) strength was used in the calculations of M_i , and according to NZS 3101, the ratio of measured strength to specified strength is taken to be 1.15, the strength enhancement factor had to be further multiplied by a factor of 1.15 in design situations in which specified material properties are used in calculations.

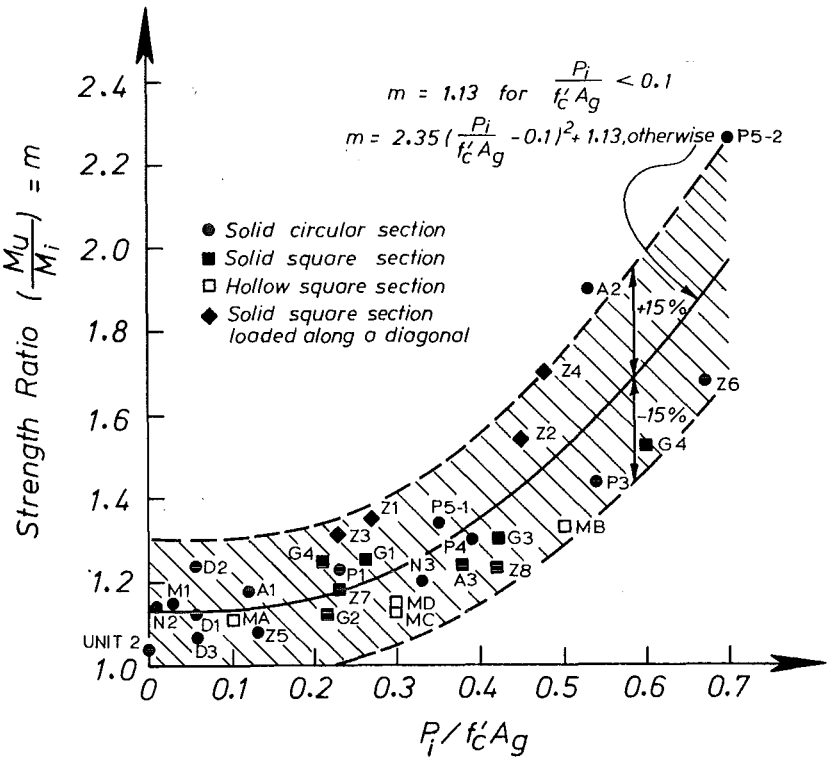

Fig. 5.2 : Variation of strength ratio with axial compression level

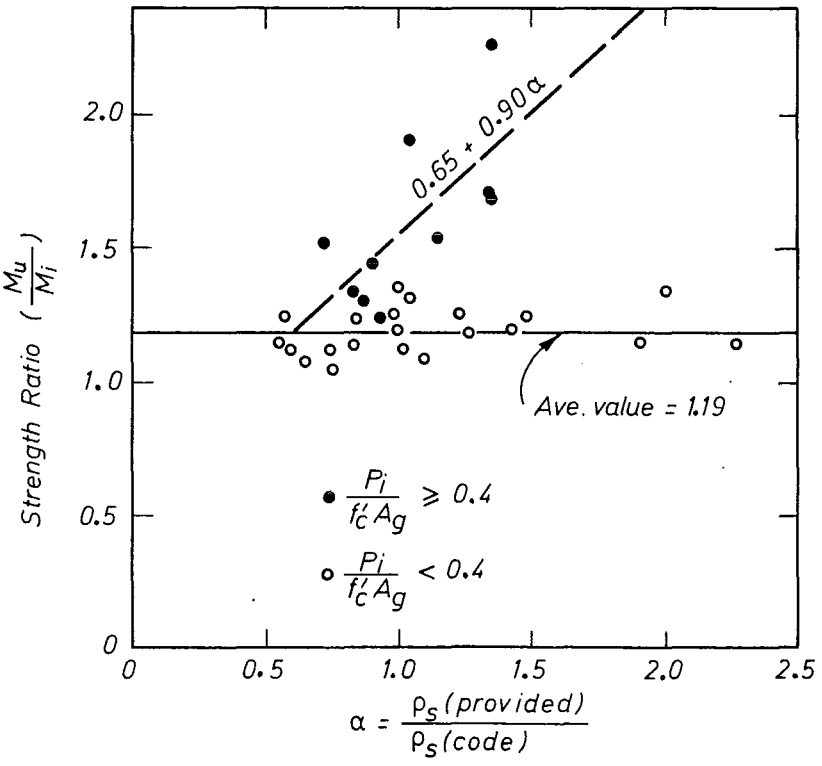

Fig. 5.3 : Variation of strength ratio with confinement ratio

5.2.3 Shear Strength Before Degradation, V_i

Following the additive principle, the shear strength before degradation for circular columns with spiral reinforcement is taken to be

$$V_i = V_{si} + V_{ci} \tag{5.2}$$

where $$V_{si} = V_s = \frac{\pi}{2} A_{sp} f_{yt} \frac{d_s}{s} \tag{5.3a}$$

and $$V_{ci} = \alpha_1 \left(1 + \frac{3P_i}{f'_c A_g}\right) v_b A_e \tag{5.3b}$$

in which $$\alpha_1 = \frac{2.0}{\frac{M}{VD}} \geq 1.0 \tag{5.3c}$$

$$v_b = 0.37\sqrt{f'_c} \tag{5.3d}$$

and the effective stress area, A_e, is 80 percent of the gross area. The above equations were obtained from test results and were presented in Chapter Four. The factor α_1 is to allow for increase in shear strength provided by concrete due to an aspect ratio lower than 2.0, as noted earlier, and the term inside the brackets of Eq. 5.3b is to allow for increase in concrete shear strength due to increase in axial compression. The basic shear stress, v_b, is taken to be $0.37\sqrt{f'_c}$ rather than the $0.2\sqrt{f'_c}$ limit used in NZS 3101. The larger value was also obtained experimentally (Chapter Four) and since the tensile reinforcement content, ρ_w, was not the main variable in the tests, the basic shear stress is made independent of ρ_w. However, it should be noted that circular columns with lower levels of longitudinal reinforcement may have lower values of basic shear stress. Fig. 5.4 shows how the basic shear stress specified by NZS 3101 varies with tensile reinforcement content. Also shown are the average values of $0.37\sqrt{f'_c}$ from nine column units. From the tests, Unit 15 had 12 bars compared to 20 bars of other column units and it failed in shear with moderate ductility. However, if the value of v_c (and hence v_b) of this column at $\mu = 2.0$ is calculated by subtracting the shear force carried by the spirals, which were still in their elastic range, from the applied shear force, the result is as plotted in the figure. The very limited data from the tests indicate that the form of code equation is reasonable but the values given by the dashed line may be a more likely path along which the value of v_b should vary with ρ_w. The following tentative equation involving the term ρ_w is suggested.

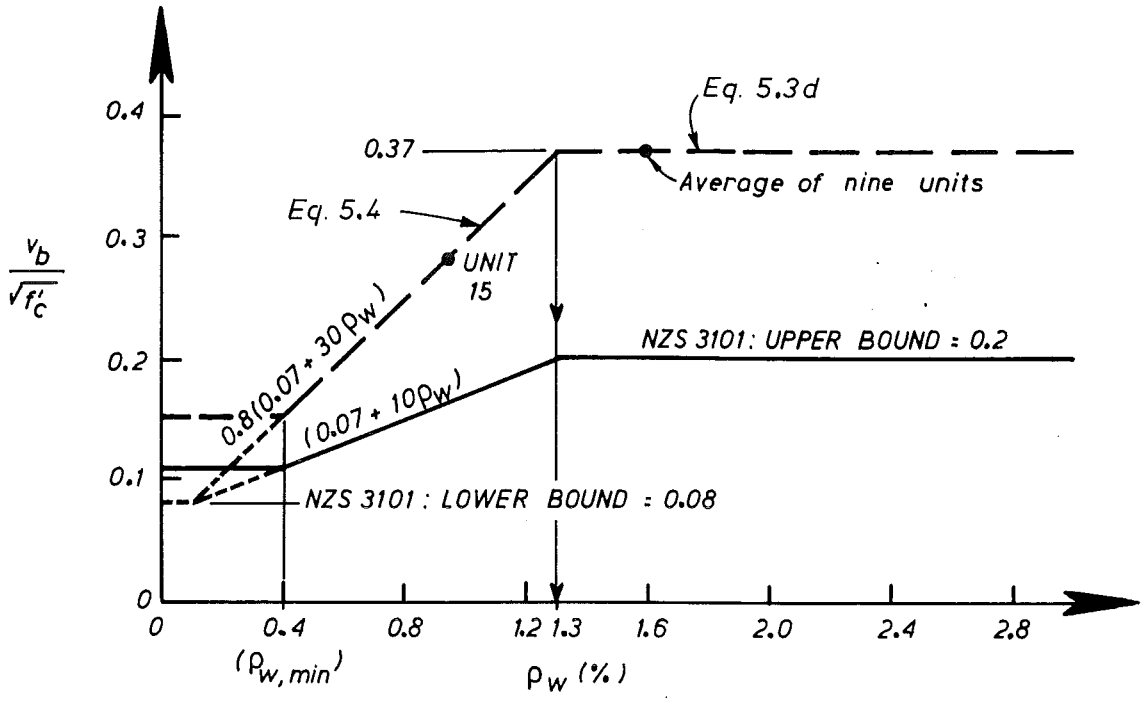

Fig. 5.4 : Variation of basic shear stress with tensile reinforcement content

$$v_b = 0.8\ (0.07 + 30\ \rho_w)\sqrt{f'_c} \leq 0.37\sqrt{f'_c} \qquad (5.4)$$

During the initial stage, before significant plasticity is developed (i.e. $\mu \leq 2.0$) , the full participation of concrete shear resisting mechanisms, expressed by Eq. 5.3, is still possible. The spiral contribution at this stage is therefore calculated using the 45-deg truss model, as was evident from the test results presented in Chapter Four.

5.2.4 Residual Shear Strength, V_f

The degradation in the strength of concrete shear resisting mechanisms demands more participation from transverse reinforcement at high ductilities. However, as the transverse reinforcement yields at high displacement ductility level, its contribution can only be increased by lowering the diagonal strut inclination of the analogous truss. The extent of the degradation in concrete shear resisting mechanisms depends very much upon how well the concrete is confined. The greater is the amount of transverse reinforcement, the better is the confinement of core concrete and at the same time, the later is the onset of yielding of transverse reinforcement. Hence, degradation is smaller and higher displacement ductility can be achieved.

The shear strength, V_f , at this stage is also obtained using the additive principle but with factors introduced to allow for degradation in concrete shear strength and possible the lowering of diagonal strut inclination such that

$$V_f = V_{sf} + V_{cf} \leq V_i \tag{5.5}$$

where $$V_{sf} = k\, V_s = k \frac{\pi}{2} A_{sp} f_{yt} \frac{d_s}{s} \tag{5.6a}$$

and $$V_{cf} = v_{cf} A_e \tag{5.6b}$$

To allow for a diagonal strut inclinations smaller than 45-deg, the spiral force, V_s , is multiplied by a factor k greater than unity. This factor can be considered to be $\cot \theta$, where θ is the inclination of the diagonal strut with respect to the column axis, while the value of V_s is based on the 45-deg truss analogy. According to the lower bound solution of the plastic theory, the angle θ can be calculated as follows,

$$\tan \theta = \sqrt{\frac{\psi}{1-\psi}} \tag{5.7a}$$

where the mechanical degree of shear reinforcement, $\psi = \frac{\rho_t f_{yt}}{f'_c}$ is calculated assuming full concrete strength. This was found (in Chapter Two) to be inaccurate and if a web effectiveness factor, ν , is introduced such that $\psi' = \frac{\rho_t f_{yt}}{\nu f'_c} = \frac{\psi}{\nu}$ then

$$\tan \theta = \sqrt{\frac{\psi'}{1-\psi'}} = \sqrt{\frac{\psi}{\nu-\psi}} \tag{5.7b}$$

The value of ν was found by calibrating with the results of Unit 9, which exhibited ductile flexural behaviour. The angle of crack inclination for this column unit at high displacement ductility level was found to be about 35-deg (see Fig. 4.2). Substituting $\psi = 0.06338$ from Table 5.2 for this column unit, the value of ν was found to be 0.193 and hence

$$k = \cot \theta = \sqrt{\frac{0.193-\psi}{\psi}} \tag{5.7c}$$

where $45^o \geq \theta \geq 25^o$ (or $1 \leq k \leq 2$) and $k \leq \frac{M}{VD}$

The limit on k is such that the value of θ is not greater than that of a corner-to-corner failure plane in the case of a column with aspect ratio lower than 2.0. Otherwise, the lower limit on θ is set at 25-deg which was the value suggested by Thürlimann[5.11] and was discussed in Chapter Two.

The concrete shear stress, v_{cf}, at this stage is taken to be one-half the basic shear stress, $v_b = 0.37\sqrt{f'_c}$, if the concrete is sufficiently well confined. This gives rise to a v_{cf} value of about $0.185\sqrt{f'_c}$ which is close to the corresponding value obtained experimentally for Unit 9 which possessed a volumetric spiral reinforcement content of about 1 percent. Hence it is assumed that

$$v_{cf} = 0.185\sqrt{f'_c} \quad \text{for} \quad \rho_s \geq 0.01 \tag{5.8a}$$

and $$v_{cf} = \frac{0.185\,\rho_s}{0.01}\sqrt{f'_c} \quad \text{for } \rho_s < 0.01$$

$$= 18.5\,\rho_s\sqrt{f'_c} \tag{5.8b}$$

The second expression is based on the premise that the extent of degradation in concrete shear strength is directly proportional to the amount of spiral reinforcement provided if the amount is less than 1 percent. Comparison with experimental results later in this chapter justifies this assumption. Note that the value of v_{cf} given by Eq. 5.8a is close to the limit of $0.2\sqrt{f'_c}$ of the non-seismic provision of NZS 3101.

5.2.5 Flexural Displacement Ductility Capacity For Ductile Members

Let μ_f be the displacement ductility capacity of the member if shear failure can be avoided. It is determined in the following manner:

Referring to Fig. 5.5, which shows a single stem pier with a plastic hinge forming at the pier base, the yield displacement (Δ_y) and yield curvature (ϕ_y) can be calculated as follows, assuming linear elastic behaviour up to first yield:

$$\Delta_y = \frac{1}{3}\,\frac{M_y L^2}{EI_{cr}} \tag{5.9a}$$

and $$\phi_y = \frac{M_y}{EI_{cr}} \tag{5.9b}$$

where I_{cr} is the moment of inertia of the cracked section.

Therefore, $$\Delta_y = \frac{1}{3}\,\phi_y L^2 \tag{5.10}$$

Also $$\Delta_u = \Delta_y + \Delta_p \tag{5.11}$$

where Δ_p is due to plastic hinge rotation about the centre of the hinge. Substituting $\Delta_p = \theta_p\,(L - \frac{L_p}{2})$ into Eq. 5.11 gives

$$\Delta_u = \Delta_y + \theta_p\,(L - \frac{L_p}{2})$$

$$= \Delta_y + (\phi_u - \phi_y)L_p(L - \frac{L_p}{2}) \tag{5.12}$$

The displacement ductility is defined as $\mu = \frac{\Delta_u}{\Delta_y}$, hence

$$\mu = \frac{\Delta_u}{\Delta_y} = 1 + 1.5 \left(\frac{\phi_u}{\phi_y} - 1\right) \frac{L_p}{L} \left(2 - \frac{L_p}{L}\right) \tag{5.13}$$

The curvature ductility $\frac{\phi_u}{\phi_y}$ can be expressed explicitly by rearrangung Eq. 5.13 such that

$$\frac{\phi_u}{\phi_y} = 1 + \frac{2}{3} \frac{(\mu - 1)}{\frac{L_p}{L}\left(2 - \frac{L_p}{L}\right)} \tag{5.14}$$

From test results[5.8], column units with $\frac{M}{VD} = 4.0$ and with confinement to the requirement of NZS 3101 were found to possess a dependable displacement ductility capacity of at least 6.0. Substituting $L = 4D$ and $\mu = 6$ into Eq. 5.14, the following expression is obtained for these column units, i.e.

$$\frac{\phi_u}{\phi_y} = 1 + \frac{2}{3} \frac{(6 - 1)}{\frac{L_p}{4D}\left(2 - \frac{L_p}{4D}\right)}$$

$$= 1 + \frac{20}{3} \frac{1}{\frac{L_p}{D}\left(1 - \frac{L_p}{8D}\right)} \tag{5.15}$$

Let $L_p = \lambda D$, then Eq. 5.15 becomes

$$\frac{\phi_u}{\phi_y} = 1 + \frac{2}{3} \frac{5}{0.25\lambda(2 - 0.25\lambda)}$$

$$= 1 + \frac{160}{3} \frac{1}{\lambda(8 - \lambda)} \tag{5.16}$$

From earlier test results of column units tested at the University of Canterbury, the equivalent plastic hinge length, L_p, for the loading shown in Fig. 5.5 has been found to be dependent on the shear-span length, L, and flexural bar diameter, $d_{b\ell}$, and an approximate equation to calculate the value of L_p was proposed by Priestley and Park[5.2], viz.

$$L_p = 0.08L + 6\, d_{b\ell} \tag{5.17}$$

i.e.
$$\lambda = \frac{L_p}{D} = 0.08 \frac{L}{D} + \frac{6d_{b\ell}}{D}$$

$$= 0.08 \frac{M}{VD} + \frac{6d_{b\ell}}{D} \tag{5.18}$$

In the case of the column units referred to earlier, $\frac{M}{VD} = 4$ and $d_{b\ell} = 16$ give rise to $\lambda = 0.56$ from Eq. 5.18.

The energy balance method proposed by Mander[5.10] indicates that the available curvature ductility is effectively proportional to the volumetric ratio of confining reinforcement provided. Hence, it is assumed that the curvature ductility capacity increases linearly with α from some values at $\alpha = 0$, where $\alpha = \frac{\rho_{s(provided)}}{\rho_{s(code)}}$ as before. In determining the available curvature ductility of unconfined members ($\alpha = 0$), the curvature at first yield (Fig. 5.6a) is calculated assuming a typical yield strain of 0.0015 for flexural rebar, arranged with a pitch circle diameter equal to 0.9D. Since it has been consistently found that the value of 0.003 assumed in the ACI method for concrete crushing strain is a very conservative estimate[5.2], the unconfined concrete crushing strain applicable to seismic situations is assumed to be 0.005 in Fig. 5.6b. This appears to be a lower bound value from the results of column units tested at the University of Canterbury. Hence, referring to Figs. 5.6a and b,

$$\phi_y = \frac{0.0015}{(0.95 - k_y)D} \tag{5.19a}$$

and

$$\phi_u = \frac{0.005}{k_u D} \tag{5.19b}$$

Therefore,

$$\frac{\phi_u}{\phi_y} = \frac{0.005}{0.0015} \frac{k_u}{(0.95 - k_y)}$$

$$= 3.0$$

with $\frac{k_u}{(0.95 - k_y)}$ assumed to be 0.9

Hence, for members with confining reinforcement,

$$\frac{\phi_u}{\phi_y} = 3.0 + A\alpha \tag{5.20}$$

in which the constant of proportionality, A, is to be calibrated using the test data of column units mentioned above.

Comparing Eqs. 5.16 and 5.20 and substituting $\lambda = 0.56$, $\alpha = 1.0$, it is found that

$$1 + \frac{160}{3} \frac{1}{0.56(8 - 0.56)} = 3.0 + A$$

thus $A = 10.8$

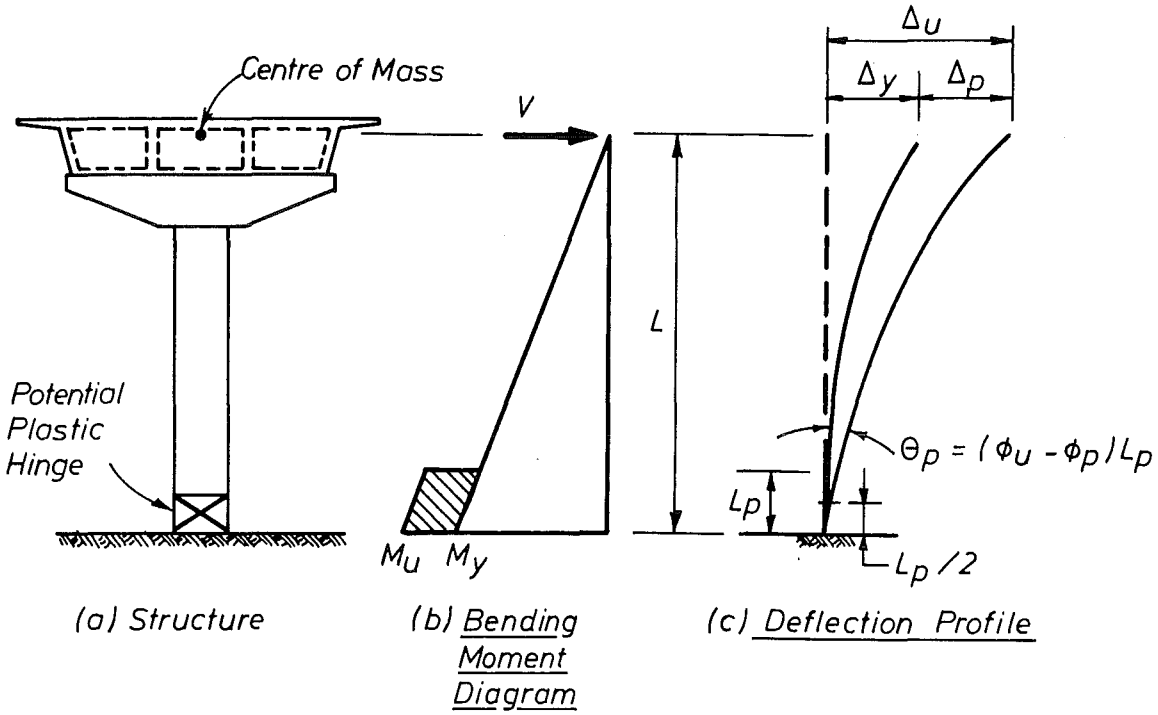

Fig. 5.5 : The bending moment diagram and deflection profile of a single stem cantilever bridge pier loaded to inelastic range

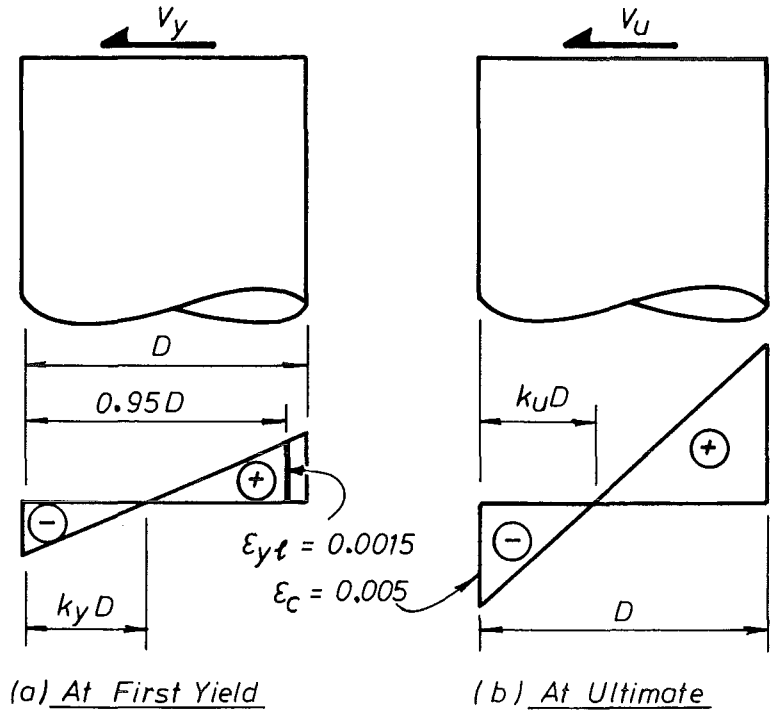

Fig. 5.6 : Strain profile of critical section for an unconfined circular section at first yield and at ultimate

Hence,

$$\frac{\phi_u}{\phi_y} = 3.0 + 10.8\alpha \quad = 1 + \frac{2}{3} \frac{(\mu - 1)}{\frac{L_p}{L}\left(2 - \frac{L_p}{L}\right)} \tag{5.21}$$

Therefore,

$$\mu = 1 + 3(1 + 5.4\alpha) \frac{\lambda}{\frac{M}{VD}} \left(2 - \frac{\lambda}{\frac{M}{VD}} \right) \tag{5.22}$$

The relationship is plotted in Fig. 5.7 for three different values of $\frac{D}{d_{b\ell}}$, enabling the available displacement ductility capacity, $\mu (= \mu_f)$ to be determined.

5.2.6 Ductility Capacity When V_{if}^o Is Between V_i And V_f

If the shear at flexural overstrength, V_{if}^o, of the member is in-between V_i and V_f then the member displacement ductility capacity, μ_c, is between 2.0 and μ_f, where μ_f takes the value of μ as given by Eq. 5.22 in the last section. The value of μ_c can easily be obtained by interpolation as follows:

$$\mu_c = \frac{(V_i - V_{if}^o)}{(V_i - V_f)} (\mu_f - 2) + 2 \tag{5.23}$$

Eq. 5.23 gives the available ductility capacity of the member and as outlined in Section 5.2.1, its value determines the category of failure mode the member belongs to.

The procedure outlined above is developed for analytical purposes. That is, given details of column geometry and reinforcement, and axial load level, the available ductility can be estimated. In typical design situations, the required ductility will be specified. For such situations Eq. 5.23 can be rearranged to enable the shear strength to be checked. Thus

$$\frac{(\mu_f - \mu_c)}{(\mu_f - 2)} (V_i - V_f) + V_f \geq V_{if}^o \tag{5.24}$$

5.3 COMPARISON BETWEEN EXPERIMENTAL AND PREDICTED RESULTS

5.3.1 Tests Reported In Chapter Four

The ultimate strength of the twenty five column units tested are predicted using the approach described in the preceding section. The various strength values are listed in Table 5.2. The predicted ultimate strength is taken to be the smaller of V_i (Eqs. 5.2 and 5.3) and V_{if}^o (Eqs. 5.1a and b) and is listed together with the experimental ultimate

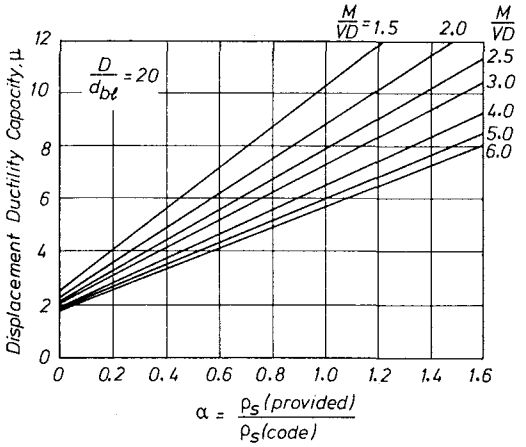

(a) $\frac{D}{d_{b\ell}} = 20$

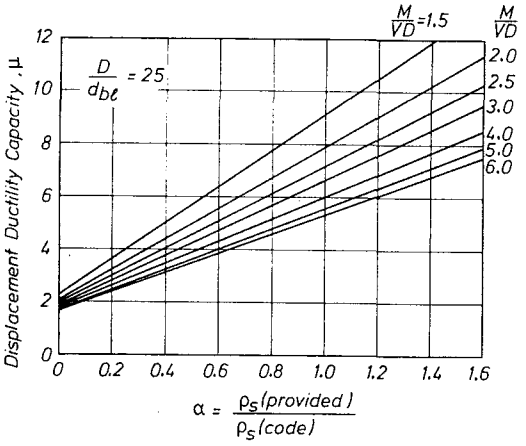

(b) $\frac{D}{d_{b\ell}} = 25$

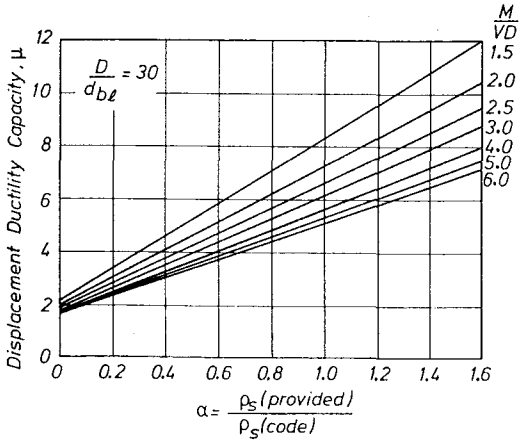

(c) $\frac{D}{d_{b\ell}} = 30$

Fig. 5.7 : Displacement ductility capacity as a function of confinement ratio and aspect ratio

Table 5.2 : Shear And Flexural Strengths Predicted By The Design Proposal

UNIT	$\frac{M}{VD}$	$\frac{P_i}{f'_c A_g}$	ρ_s ($\times 10^{-3}$)	ψ ($\times 10^{-3}$)	μ_f	V_{si} (kN)	V_{ci} (kN)	V_i (kN)	V_{sf} (kN)	V_{cf} (kN)	V_f (kN)	V_{if} (kN)	V_{if}^o (kN)
1	2.0	0	5.094	22.28	6.4	88	228	(316)*	-	-	-	306	373
2	2.0	0	5.094	22.46	6.5	88	227	315	176	58	234	220	(249)
3	2.5	0	5.094	23.21	6.0	88	223	311	189	57	246	242	(295)
4	2.0	0	5.146	26.57	7.3	85	206	(291)	-	-	-	299	365
5	2.0	0	7.642	40.30	9.9	131	207	(338)	-	-	-	301	367
6	1.5	0	5.094	27.76	8.6	88	272	(360)	-	-	-	402	490
7	2.0	0	3.821	24.09	6.8	74	202	(276)	-	-	-	293	357
8	2.0	0.2	10.189	66.03	10.6	198	319	517	275	100	375	356	(443)
9	2.5	0.2	10.189	63.38	9.3	198	325	523	283	102	385	281	(349)
10	2.0	0.2	10.189	54.21	9.1	176	332	508	282	104	386	360	(448)
11	2.0	0.2	5.094	31.69	6.2	100	325	(425)	-	-	-	351	436
12	1.5	0.1	10.189	58.43	12.9	175	345	(520)	-	-	-	437	533
13	2.0	0.1	10.189	45.88	9.2	174	291	465	312	112	424	363	(443)
14	2.0	0	5.094	24.64	8.4	86	216	(302)	-	-	-	304	371
15	2.0	0	5.094	23.86	6.7	86	219	305	172	56	229	204	(249)
16	2.0	0.1	5.094	24.86	6.0	86	279	(365)	-	-	-	345	421
17	2.5	0.1	5.094	24.21	5.3	86	283	369	184	55	241	281	(343)
18	1.5	0.1	5.094	23.72	6.6	86	381	(467)	-	-	-	462	564
19	1.5	0.1	3.821	18.11	5.6	65	378	(443)	-	-	-	468	571
20	1.75	0.175	3.821	16.97	4.6	65	393	(458)	-	-	-	477	588
21	2.0	0	3.821	18.76	5.7	65	214	(279)	-	-	-	313	382
22	2.0	0	3.859	19.36	5.8	62	207	(269)	-	-	-	294	359
23	2.0	0	7.642	36.44	9.2	124	211	(335)	-	-	-	295	360
24	2.0	0	7.719	36.15	9.1	125	214	(339)	-	-	-	305	372
25	1.5	0	-	-	2.1	0	284	(284)	-	-	-	297	336

* Value within brackets gives the predicted ultimate strength

strength in Table 5.3. The ratio of the latter to the former is 1.00 with a standard deviation of 0.06. The proposed method not only allows the ultimate strength to be calculated; the available displacement ductility capacity and hence, the failure mode can also be assessed. Excluding the two extreme categories of $V_{if}^{o} \leq V_f$ (i.e. ductile flexural failure) and $V_i \leq V_{if}$ (i.e. brittle shear failure), the displacement ductility capacity can be determined by interpolation using Eq. 5.23. The corresponding experimental value was estimated from the load-deflection hysteresis loops presented in Chapter Four and was taken to be the value at which the stability of the hysteresis loops could no longer be maintained. The results are also tabulated in Table 5.3 and on the whole, the predicted values agree reasonably well with the observed values.

The last two columns of Table 5.3 compare the experimentally observed and the predicted failure mode of various column units. On the whole the prediction has been reasonably accurate except for the two border-line cases such as Units 16 and 18 and the exceptional case of Unit 11. Unit 8 is predicted to fail in a ductile manner because the value of μ_c calculated is greater than 6.0. However, the value of V_{if}^{o} predicted for this column unit is less than that obtained from the test. If a higher value of V_{if}^{o} $(= V_u)$ is used in the calculation, a lower value of μ_c $(= 4.5)$ will be predicted and then the predicted failure mode will agree with the experimental observation.

Fig. 5.8 shows some numerical examples of the shear-ductility relationship for three groups of column units, with one of the three main parameters $(\rho_s$, $\frac{M}{VD}$ or $\frac{P_i}{f'_c A_g})$ as the only variable within each group. The column units have an overall diameter, D , of 400 m and are reinforced transversely with R-6 spirals $(A_{sp} = 28\ mm^2)$. The concrete strength, f'_c , is taken to be 32.5 MPa and the yield strength of spiral steel, f_{yt} , is 325 MPa. These values are typical of the column units tested. They are assumed to be the same in all the column units in the examples so as to give a more meaningful comparison to illustrate how the three main parameters influence the two levels of shear strengths and the degradation between them. The calculated results are listed in Table 5.4. In general, the drop from V_i to V_f is greater if the spiral reinforcement content is lower (Fig. 5.8a), or the aspect ratio is smaller (Fig. 5.8b) or if higher axial compression is present (Fig. 5.8c).

Table 5.3 : Predicted Ultimate Strength And Ductility Capacity Versus Experimental Values

UNIT	V_u (kN)		(2)/(3)	$V_{(\mu=4)}$ (kN)		(5)/(6)	Ductility Capacity, μ_c		Failure Mode *	
	(Expt)	(Predicted)		(Expt)	(Predicted)		(Expt)	(Predicted)	(Expt)	(Predicted)
(1)	(2)	(3)	(4)	(5)	(6)	(7)	(8)	(9)	(10)	(11)
1	320	316	1.01	-	-	-	2.5	2.0	LD-S	LD-S
2	228	249	0.92	222	249	0.89	6.0	5.7	MD-S	MD-S
3	298	295	1.01	-	-	-	4.0	3.0	LD-S	LD-S
4	295	291	1.01	-	-	-	1.4	$\leq$1.0	B-S	B-S
5	340	338	1.01	-	-	-	3.0	2.0	LD-S	LD-S
6	390	360	1.08	-	-	-	1.3	$\leq$1.0	B-S	B-S
7	280	276	1.01	-	-	-	1.6	$\leq$1.0	B-S	B-S
8	475	443	1.07	458	443	1.03	6.0	6.5	D-F	MD-S
9	385	349	1.10	362	349	1.04	8.0	9.3	D-F	D-F
10	450	448	1.00	436	448	0.97	6.0	5.5	MD-S	MD-S
11	404	425	0.95	-	-	-	2.5	2.0	LD-S	B-S
12	527	520	1.01	-	-	-	3.0	2.0	LD-S	LD-S
13	443	443	1.00	438	443	0.99	6.0	5.9	MD-S	MD-S
14	311	302	1.03	-	-	-	3.0	2.0	LD-S	LD-S
15	230	249	0.92	228	249	0.92	6.0	5.5	MD-S	MD-S
16	379	365	1.04	-	-	-	1.5	2.0	LD-S	B-S
17	329	343	0.96	-	-	-	2.5	2.7	LD-S	LD-S
18	507	467	1.09	-	-	-	1.4	2.0	LD-S	B-S
19	436	443	0.98	-	-	-	1.3	$\leq$1.0	B-S	B-S
20	487	458	1.06	-	-	-	1.5	$\leq$1.0	B-S	B-S
21	258	279	0.92	-	-	-	1.1	$\leq$1.0	B-S	B-S
22	280	269	1.04	-	-	-	1.5	$\leq$1.0	B-S	B-S
23	339	335	1.01	-	-	-	4.0	2.0	LD-S	LD-S
24	338	339	1.00	-	-	-	4.0	2.0	LD-S	LD-S
25	233	284	0.82	-	-	-	1.2	$\leq$1.0	B-S	LD-S
		Ave	1.00		Ave	0.97				
		σ	0.06		σ	0.05				

* B-S : Brittle shear failure
LD-S : Shear failure with limited ductility
MD-S : Shear failure with moderate ductility
D-F : Ductile flexural failure

Table 5.4 : Numerical Examples For Three Groups Of Column Units (f'_c = 32.5 MPa, f_{yt} = 325 MPa, D = 400 mm, A_{sp} = 28 mm^2)

UNIT	$\frac{M}{VD}$	$\frac{P_i}{f'_c A_g}$	ρ_s ($x10^{-3}$)	ψ ($x10^{-3}$)	μ_f	V_{si} (kN)	V_{ci} (kN)	V_i (kN)	V_{sf} (kN)	V_{cf} (kN)	V_f (kN)
A	2.0	0	7.768	38.84	9.6	131	214	345	261	82	343
B	2.0	0	5.178	25.89	7.1	88	214	302	176	55	231
C	2.0	0	3.884	19.42	5.9	66	214	280	132	41	173
P	1.5	0	5.178	25.89	8.9	88	285	373	132	55	187
Q	2.0	0	5.178	25.89	7.1	88	214	302	176	55	231
R	2.5	0	5.178	25.89	6.0	88	214	302	189	55	244
X	2.0	0	5.178	25.89	7.1	88	214	302	176	55	231
Y	2.0	0.1	5.178	25.89	6.1	88	278	366	176	55	231
Z	2.0	0.2	5.178	25.89	5.4	88	342	430	176	55	231

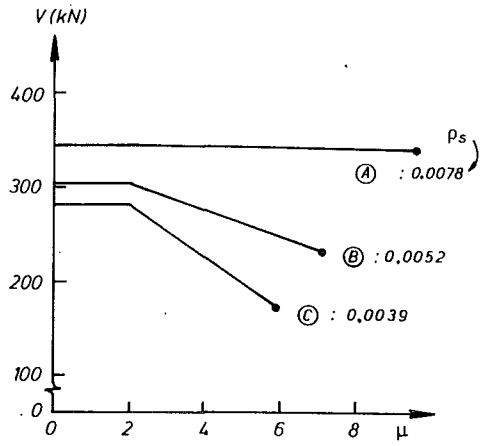

(a) Influence of spiral reinforcement ratio ($\frac{M}{VD} = 2.0$, $\frac{P_i}{f'_c A_g} = 0$)

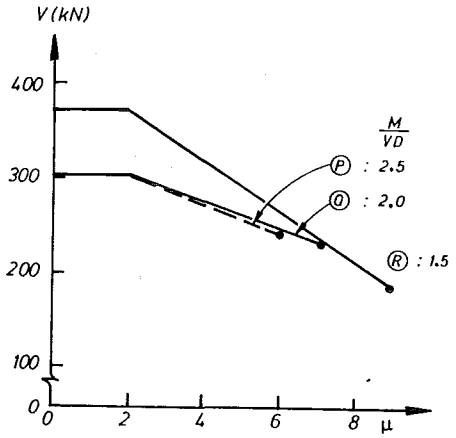

(b) Influence of aspect ratio ($\rho_s = 0.0052$, $\frac{P_i}{f'_c A_g} = 0$)

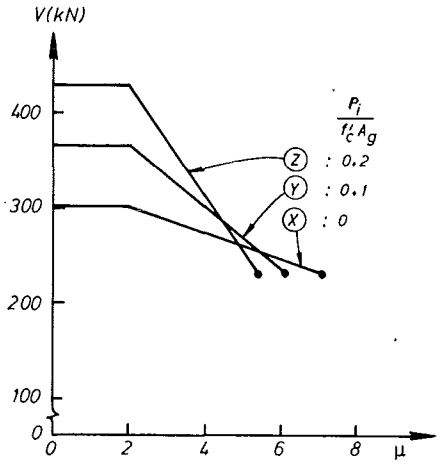

(c) Influence of axial load level ($\rho_s = 0.0052$, $\frac{M}{VD} = 2.0$)

Fig. 5.8 : Examples of shear-ductility relationship

5.3.2 Earlier Tests At The University Of Canterbury

In addition, various strength values for similar column units tested at the University of Canterbury from Refs. 5.4-5.6, 5.8 and 5.9 are tabulated in Table 5.5. The intention is to check whether the method proposed would predict the failure mode of these column units, all of which failed in a ductile manner. Except for Unit P4, which was predicted to have a slightly lower value of V_f than V_{if}^o, the V_f values exceeded those of V_{if}^o in all the other column units, indicating a ductile flexural failure. For Unit P4 the displacement ductility capacity was found to be greater than 6.0 and thus, it also can be classified as a ductile column under the present proposal.

5.3.3 Tests At The University Of Toronto

Khalifa and Collins[5.12] tested five circular columns under double curvature bending at the University of Toronto. Their test units (as shown in Fig. 5.9a) had an overall diameter of 445 mm and the test region was 1270 mm long. The axial compression (1050 kN) was applied by post-tensioning and the only variable was the amount of transverse reinforcement provided. All the test units were reported to have failed in shear. The shear strengths of these column units were also evaluated with the proposal using Eqs. 5.2 and 5.3 and are listed together with the experimentally obtained shear strengths in Table 5.6. The columns are assumed to have effective fixity at the end of the test region. Because of higher moment associated with the applied shear (see Fig. 5.9d), the more critical section is taken to be the one at the south end. This is supported by test observations and is illustrated in Fig. 5.10, showing relatively more damage at the south end, for three of the column units tested. The predicted shear strengths are consistently higher than the experimental results. On average, the experimental values are only about 63 percent of the predicted values and the standard deviation of the ratios of the former to the latter is 0.04.

However, it was reported in Ref. 5.12 that significant cracking and, in two cases (Units SC3 and SC4), crushing of concrete did occur in the south end blocks where higher bending moment was applied, implying that the effective fixity might have been further away from the end of the intended test regions. Crack penetration into the end blocks is clearly visible in the crack pattern of the test units shown in Fig. 5.10. Calculations were therefore re-done by assuming the effective fixity to be at the end of the transition 200 mm away from the end of

Table 5.5 : Predicted Shear And Flexural Strengths Of Some Column Units Tested At the University of Canterbury

UNIT	$\frac{M}{VD}$	$\frac{P_i}{f'_c A_g}$	ρ_s ($\times 10^{-3}$)	ψ ($\times 10^{-3}$)	μ_f	V_{si} (kN)	V_{ci} (kN)	V_i (kN)	V_{sf} (kN)	V_{cf} (kN)	V_f (kN)	V_{if} (kN)	V_{if}^o (kN)
M1[5.4]	5.5	0.03	12.636	61.14	8.0	414	422	837	608	194	802	117	132
N2[5.5]	5.4	0.01	18.661	69.91	11.2	103	93	196	137	45	182	31	35
N3[5.5]	3.7	0.33	24.824	77.86	8.6	109	175	284	133	44	177	64	80
P1[5.6]	2.0	0.23	7.480	39.51	7.0	271	795	1066	534	176	710	602	704
P4[5.6]	2.0	0.39	8.014	51.52	7.2	408	1098	1506	676	203	879	669	888
P5-1[5.6]	2.0	0.35	26.112	112.48	13.7	872	1031	1903	872	251	1123	673	859
P5-2[5.6]	2.0	0.70	26.112	112.48	10.0	872	1559	2431	872	251	1123	470	929
A1[5.8]	4.0	0.20	7.560	44.78	6.0	125	320	445	227	76	303	139	160
A2[5.8]	4.0	0.56	15.273	75.03	6.2	228	561	789	286	105	391	137	223
Z5[5.9]	4.0	0.13	6.1	44.28	6.5	159	308	457	291	68	359	136	154
Z6[5.9]	4.0	0.67	10.9	108.07	7.5	286	572	858	286	95	381	121	229

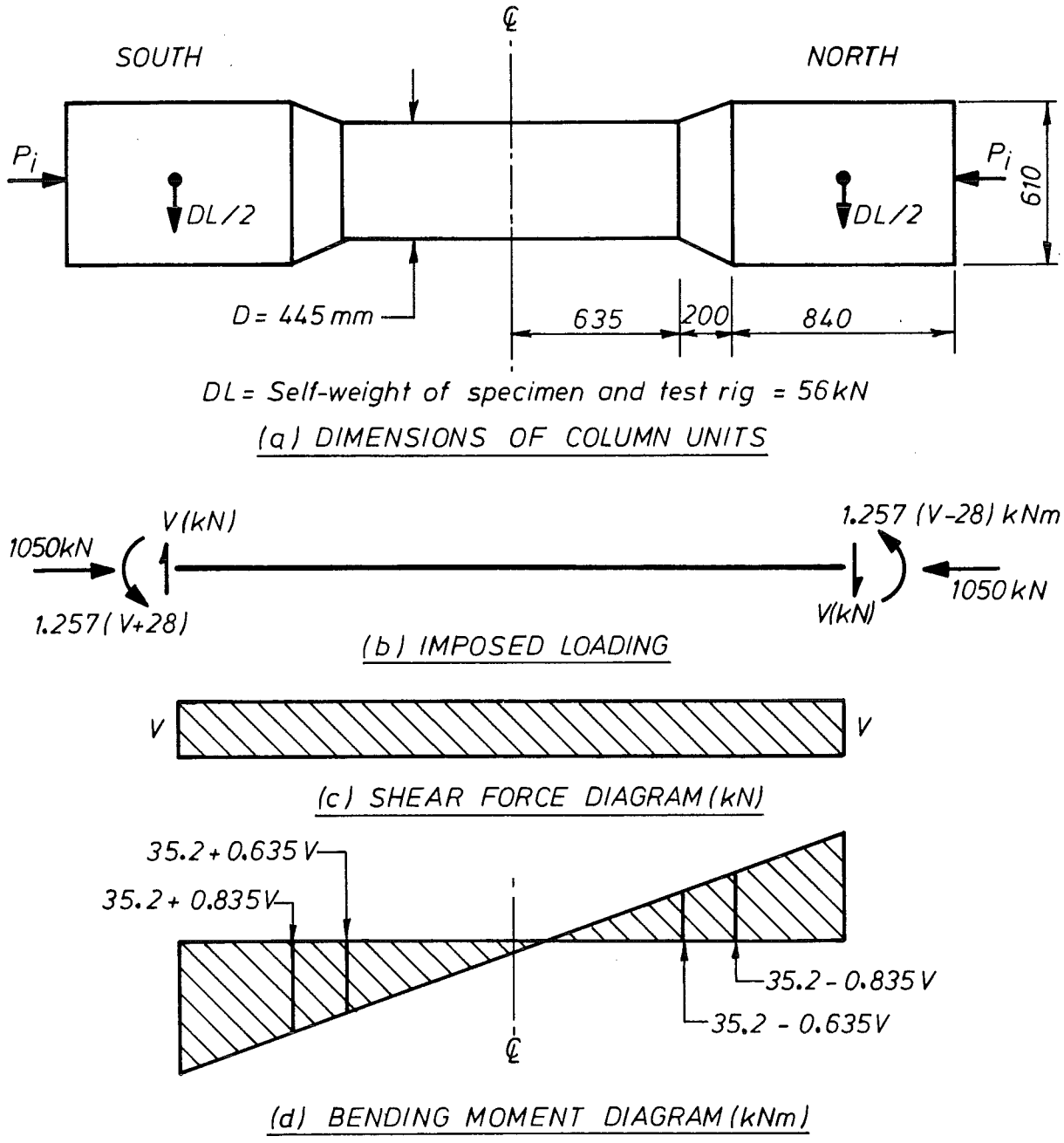

Fig. 5.9 : Loading details of circular column units tested at the University of Toronto[5.12]

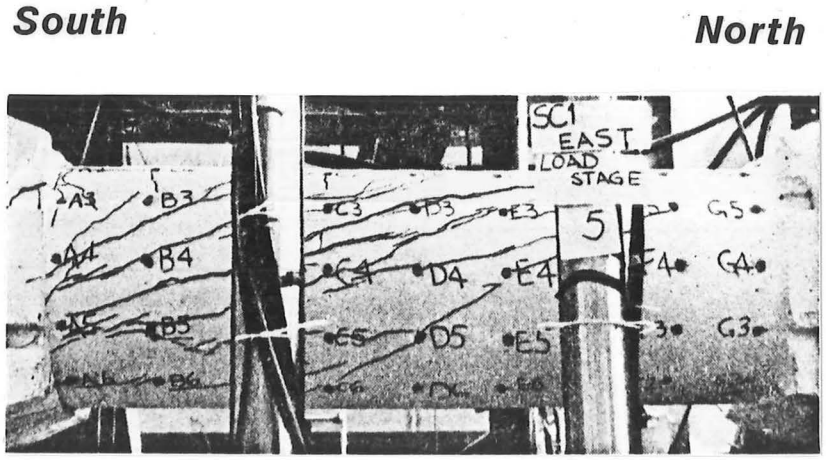

(a) Unit SC1

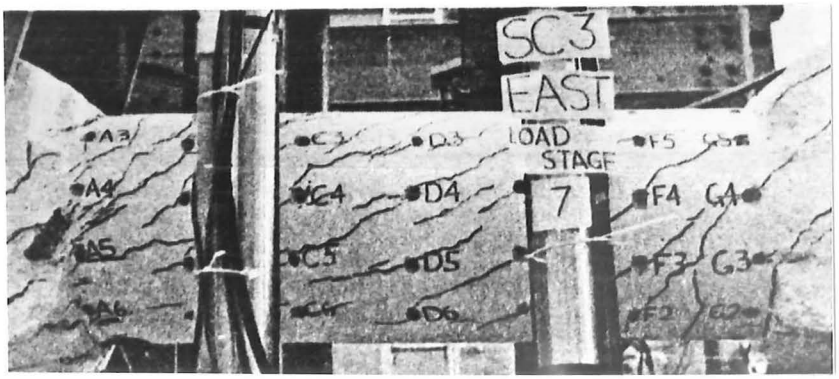

(b) Unit SC3

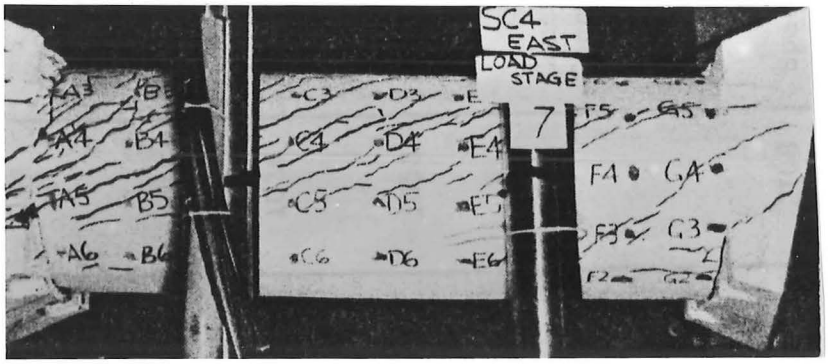

(c) Unit SC4

Fig. 5.10 : Final appearance of three circular column units tested at the University of Toronto[5.12]

Table 5.6 : Predicted Shear Strengths Of Column Units Tests At The University Of Toronto

UNIT	f'_c (MPa)	$\frac{P_i}{f'_c A_g}$	V_u (Expt.) (kN)	V_{si} (kN)	Case (a) V_{ci} (kN)	Case (a) V_i (kN)	$\frac{(4)}{(7)}$	Case (b) V_{ci} (kN)	Case (b) V_i (kN)	$\frac{(4)}{(10)}$
(1)	(2)	(3)	(4)	(5)	(6)	(7)	(8)	(9)	(10)	(11)
SC0	23.4	0.29	326	-	523	523	0.62	404	404	0.81
SC1	19.3	0.35	324	58	517	575	0.57	403	461	0.70
SC2	23.0	0.29	478	214	518	732	0.65	401	615	0.78
SC3	24.5	0.28	578	320	527	847	0.68	407	727	0.80
SC4	26.5	0.25	456	194	522	716	0.64	403	597	0.76
						Ave	0.63		Ave	0.77
						σ	0.04		σ	0.04

Referring to Fig. 5.9,

Case (a) : with effective fixity at the end of test region

Case (b) : with effective fixity at the end of transition

the circular section. The results are included in Table 5.6 as Case (b). The predicted shear strengths of the column units are reduced because an increase in $\frac{M}{VD}$ ratio means that the magnification factor α_1 ($= \frac{2.0}{\frac{M}{VD}}$) no longer applies. Although the accuracy of prediction is improved, the prediction still over-estimated the experimental shear strengths by a substantial margin. The average value of $\frac{V_u}{V_i}$ is 0.77 and the standard deviation is 0.04 . The discrepancy can be attributed to several differences between Khalifa's tests and the present series of tests.

First of all, it is doubtful whether the results from the present series of tests on cantilever column units are immediately applicable to Khalifa's tests which involved column units tested under double curvature bending. The difference in behaviour can be due to the manner in which the shear force is introduced. Fig. 5.11 illustrates the two different ways in which the shear force is introduced and shows the resulting steel force due to the diagonal compression. The shear force on the cantilever column shown in Fig. 5.11a, which is typical of that used in the present test series, is applied externally through some load application device. The possible path of the diagonal compression arising from the shear force is indicated by a dashed line in the figure. Similarly, Fig. 5.11c depicts a column under double curvature bending typical of that tested by Khalifa. The clear span of this column is taken to be twice the shear span of the cantilever column but the aspect ratio is the same. The shear force in this column at the point of contraflexure is introduced internally through some form of shear stress distribution. The introduction of shear force in this manner enables a smaller inclination, θ , of the diagonal compression to develop.

Assuming no axial load is present, the tension in the tensile reinforcement varies along the height of the cantilever column as shown in Fig. 5.11b. Effective but artificial anchorage for the tensile reinforcement was provided by welding them to a steel plate at the top of the column. The compression reinforcement at the critical section of this column still carries substantial compression. On the other hand, the variation of tensile force in the reinforcement in the column under double curvature bending is as shown in Fig. 5.11d. From the figure it can be seen that all the reinforcement is subjected to tension at the point of contraflexure, and since no axial load is assumed to be present, the tension in the reinforcement is balanced by the longitudinal component of diagonal compression acting at the centre. This axial tension and hence compression applied to the column at the point of zero moment is much larger than that in the case of the cantilever column.

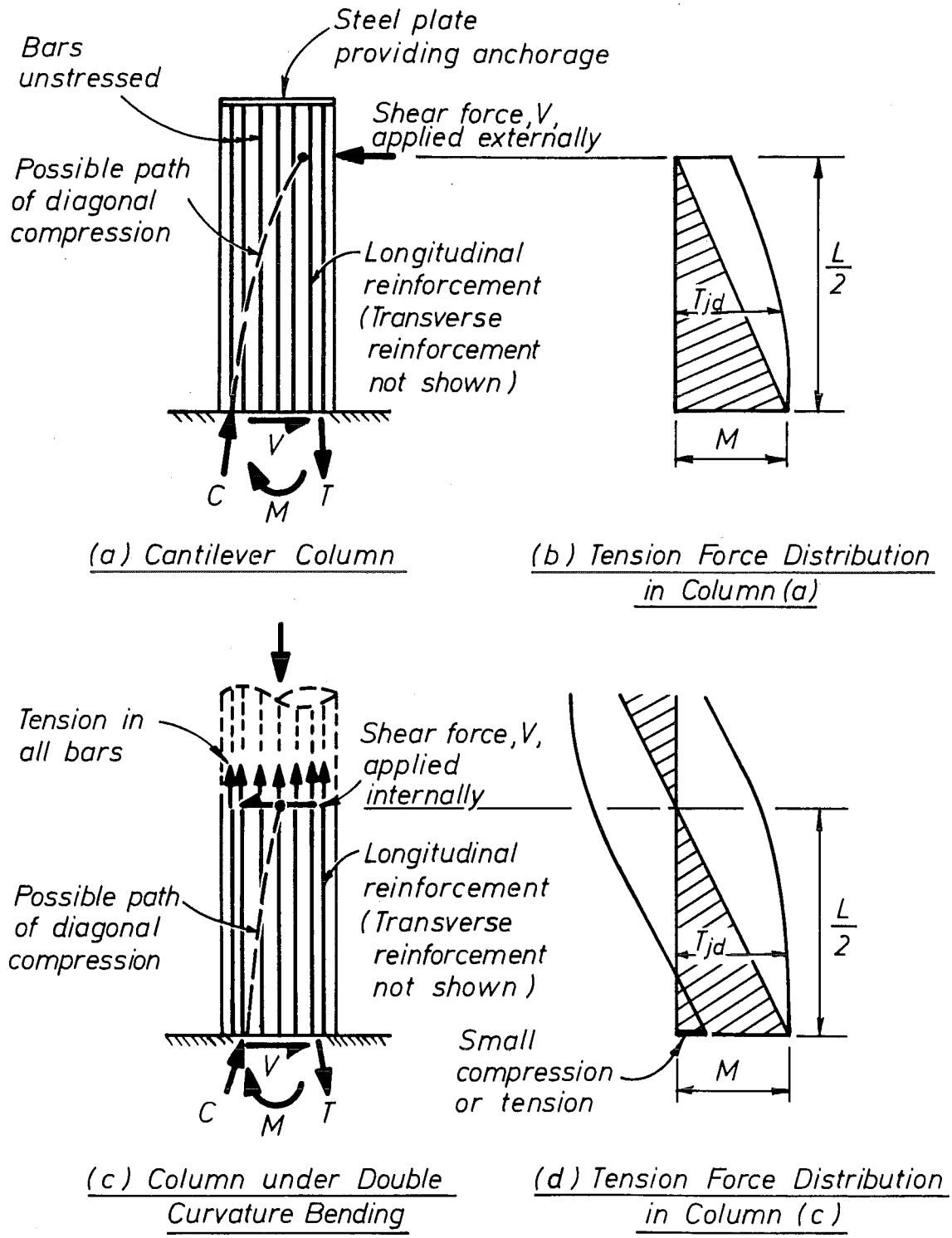

Fig. 5.11 : Different means of load application for cantilever column and column under double curvature bending

Furthermore, if the aspect ratio of the column is small the compression reinforcement at the critical section may be subjected to small axial tension as indicated in Fig. 5.11d. In such a situation the compression carried by concrete has to be increased and the lever arm is therefore reduced if the moments in the two columns are the same. All these differences may have a significant effect on the behaviour of Khalifa's columns.

Secondly, the difference in shear strengths may be due to the use of a different concrete mix. To facilitate vertical casting of his column units, Khalifa used a maximum aggregate size of 10 mm and a slump of 200 mm as compared to typical corresponding values of 20 mm and 75 mm used in the present project. The use of the non-standard mix might have affected the aggregate interlock performance in Khalifa's test units.

Finally, and most importantly, the base fixity of Khalifa's columns does not represent the actual situation in which the confinement effects at the base of columns by pile cap give rise to enhancement in concrete strength, The gradual transition of the test section into the end blocks of Khalifa's tests (Fig. 5.9) does not simulate the actual situation in the case of bridge piers. Moreover, the bending of longitudinal reinforcement at the beginning of the transition gives rise to detrimental effect due to the outward force $T \sin\alpha$ shown in Fig. 5.12 for the bottom bar in tension. This effect is more serious especially since no tie appears to have been provided at the bend of longitudinal reinforcement in Khalifa's column units. It is felt that both the lack of confinement from a strong end block and the radial tension due to the bend in the tensile reinforcement in Khalifa's tests are responsible for significant differences between the two series of tests.

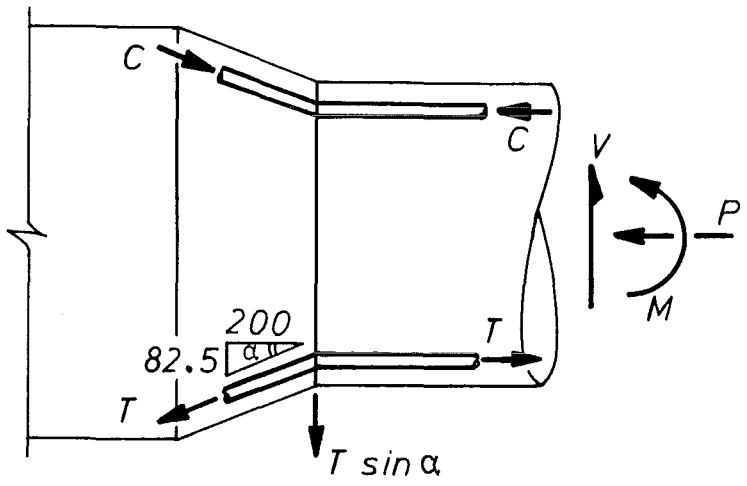

Fig. 5.12 : Outward force component in tensile reinforcement in Khalifa's columns[5.12]

5.4 COMPARISON BETWEEN NZS 3101 PROVISIONS AND THE PROPOSAL

The non-dimensional values of concrete shear stress ($\frac{v_c}{\sqrt{f'_c}}$) used by NZS 3101 and the proposal are plotted against axial load level in Fig. 5.13. The concrete shear stress, v_{ci}, used in Eq. 5.3b for the case where $\frac{M}{VD} \geq 2.0$ exceeds the non-seimsic provision of NZS 3101[5.13] by 85 percent.

It was found from tests (Chapter Four) that the NZS 3101 provision of no 'concrete contribution' at low axial level ($\frac{P_i}{f'_c A_g} \leq 0.1$) for ductile seismic response of circular piers is very conservative. On the other hand, the results indicated that it is non-conservative to assume that the concrete strength increases with axial load level (for $\frac{P_i}{f'_c A_g} > 0.1$) regardless of the amount of transverse reinforcement provided. It has also been noted by Priestley and Park[5.2] from a limited number of test results on squat octagonal columns that, with seismic load conditions, the value of v_c at high axial compression level may be substantially lower than the code specified value. Their results are as shown in Fig. 5.14.

For simplicity, the proposal assumes a constant v_{cf} value such that the prediction at low axial load levels is greater than the code specified value and vice versa. Unlike the NZS 3101 provisions, this value is further assumed to be proportional to the amount of spiral reinforcement provided, with an upper limit of $v_{cf} = 0.5\, v_b$ corresponding to a spiral reinforcement content of 1 percent or more.

Fig. 5.15 illustrates how the residual shear strength, V_f, is assumed to change, using the example of a typical column unit tested, The overall diameter, D, of the column used in the example is 400 mm with the typical 20-HD16 flexural reinforcement arrangement, giving a total longitudinal reinforcement content of 0.032. The yield strength of transverse steel is taken to be 325 MPa and the concrete strength is 30 MPa. The aspect ratio of the column is assumed such that it is governed by the limit $k = \cot 25^o$. Referring to Fig. 5.15, the shaded portion gives the available 'concrete contribution;, V_{cf}, according to Eq. 5.8. Added to this is the spiral contribution, V_{sf}, calculated using Eqs. 5.6a and 5.7c. The values of k are identified in the figure. At low spiral reinforcement content, the angle of diagonal strut inclination, θ, has to be lowered (i.e. larger k) but is limited by the lower limit of 25^o. The value of k, as given by Eq. 5.7c decreases as ρ_s is increased until the limit is $k = 1.0$ is reached. As the 45-deg truss is used to calculate V_{si}, the value of k is

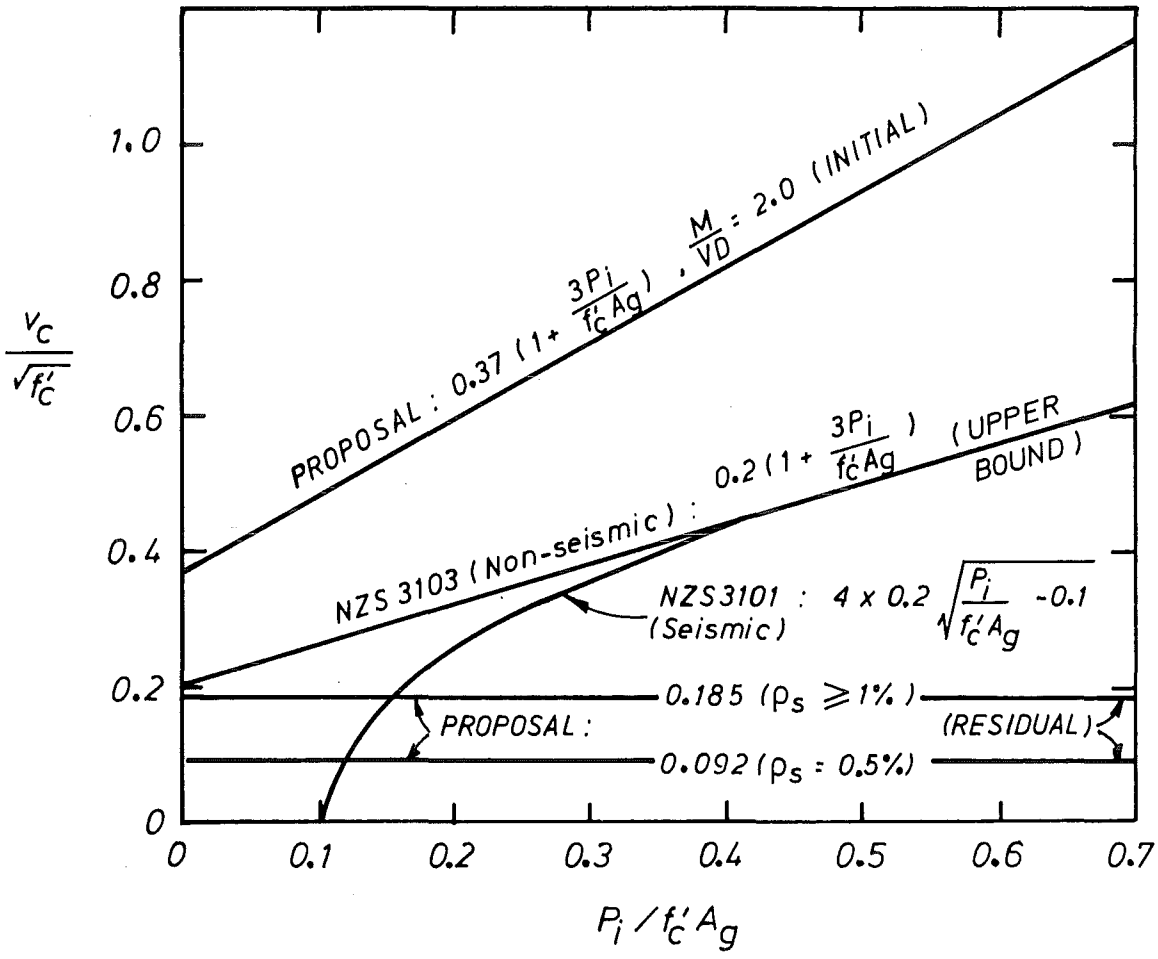

Fig. 5.13 : Comparison of concrete shear strength specified in NZS 3101[5.13] and in the design proposal for different axial load levels.

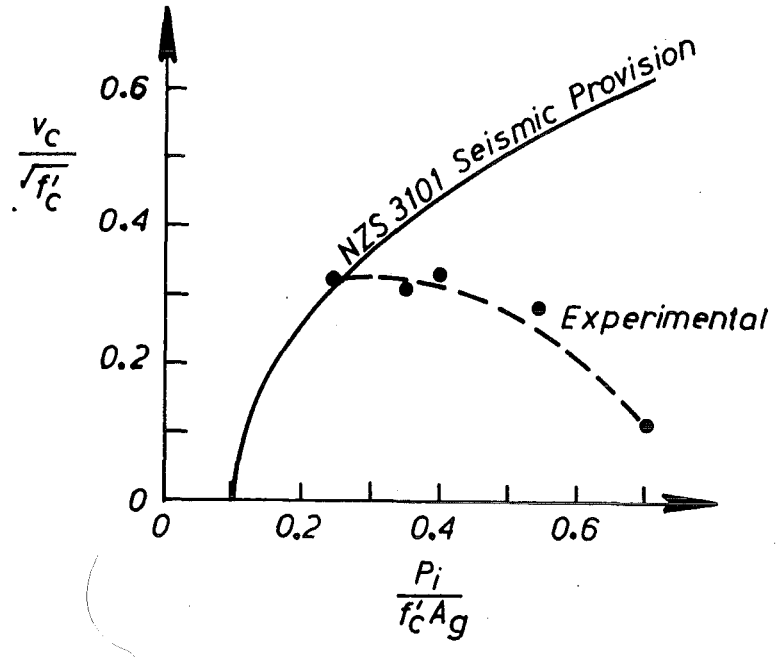

Fig. 5.14 : Shear carried by concrete at different axial load levels for squat octagonal columns at high displacement ductility level[5.2]

assumed to be no less than unity. In the absence of evidence, the higher upper bound on the ultimate shear stress of NZS 3101 is retained and is set at $0.9\sqrt{f'_c}$ as shown in the figure. Also shown in the figure is the seismic provision of NZS 3101 for different levels of axial compression. It can be seen that the seismic provision of NZS 3101 specifies lower shear strength than the proposal does at low axial load level when the 'concrete contribution' is ignored. On the other hand, the assumption that v_c increases with $\frac{P_i}{f'_c A_g}$ at higher axial load level results in greater code specified strength than that predicted by the proposal. It should be noted that the minimum level of v_s = 0.35 MPa is retained but the minimum transverse requirements of NZS 3101 for other purposes are not included in the comparison. It may well be that these other requirements are more critical at low shear stress levels.

5.5 AN INTEGRAL FLEXURE/SHEAR DUCTILE DESIGN APPROACH

Priestley and Park[5.2] have suggested a ductile design procedure for bridge columns based on the work carried out at the University of Canterbury. Their suggestion is further expanded in this section to include the proposal made in Section 5.2 and is illustrated by a flow

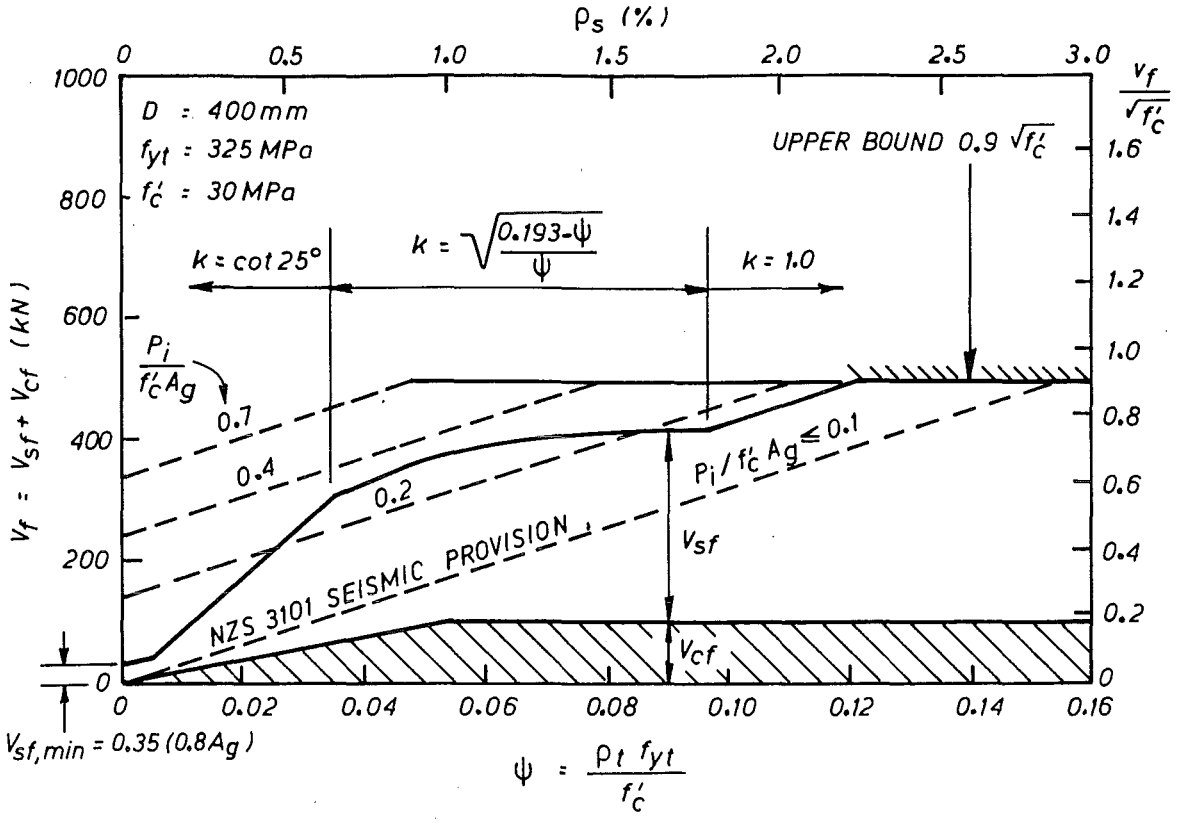

Fig. 5.15 : Comparison of residual shear strength in the design proposal with NZS 3101[5.13] shear provisions

chart shown in Fig. 5.16. Basically, Steps 1, 2 and 3 are as reported in Ref. 5.2 and Steps 4 and 5 are included based on the results of this project. The five steps are briefly summarized as follows:

Step 1: Determination of horizontal seismic design base shear force based on inelastic design spectra proposed by Berrill et al[5.14] such that

$$V_u = C_{H\mu} Z_H M g \tag{5.25}$$

where $C_{H\mu}$ is the basic horizontal force coefficient depending on the zone of earthquake activity, period of vibration and structural ductility, and is obtained from typical inelastic design spectra as shown in Fig. 5.17. The basic horizontal force coefficient is modified by a 'return period' coefficient, Z_H, which depends on the design life of the bridge and the acceptable probability of failure during the design life. The value of Z_H can be obtained from the design curve shown in Fig. 5.18.

Step 2: The dependable flexural strength, $M_{u,d}$ at critical plastic hinges is found by multiplying $M_{u,ACI}$ with a strength reduction factor, ϕ, and a strength enhancement factor, m, so that for a single stem cantilever pier of effective shear-span, L, subjected to a transverse earthquake attack,

$$M_u = V_u L$$
$$\leq M_{u,d}$$

where $M_{u,d} = \phi(m.M_{u,ACI})$ (5.26)

with $\phi = 0.9$

and m given by Eqs. 5.1a and b. The flexural strength $M_{u,ACI}$ is calculated using the ACI stress block for concrete in compression, nominal (specified) material strengths, and an ultimate concrete compression strain of 0.003. The flexural strength is calculated using the unspalled section dimensions.

Step 3: Design for confinement based on the required displacement ductility factor, μ, and the column aspect ratio. The value of μ is calculated from the actual structure ductility factor, μ_s, taking into account flexibility of foundation and bearing[5.2] given by Eq. 5.27

$$\mu_s = 1 + \frac{(\mu - 1)}{C} \tag{5.27}$$

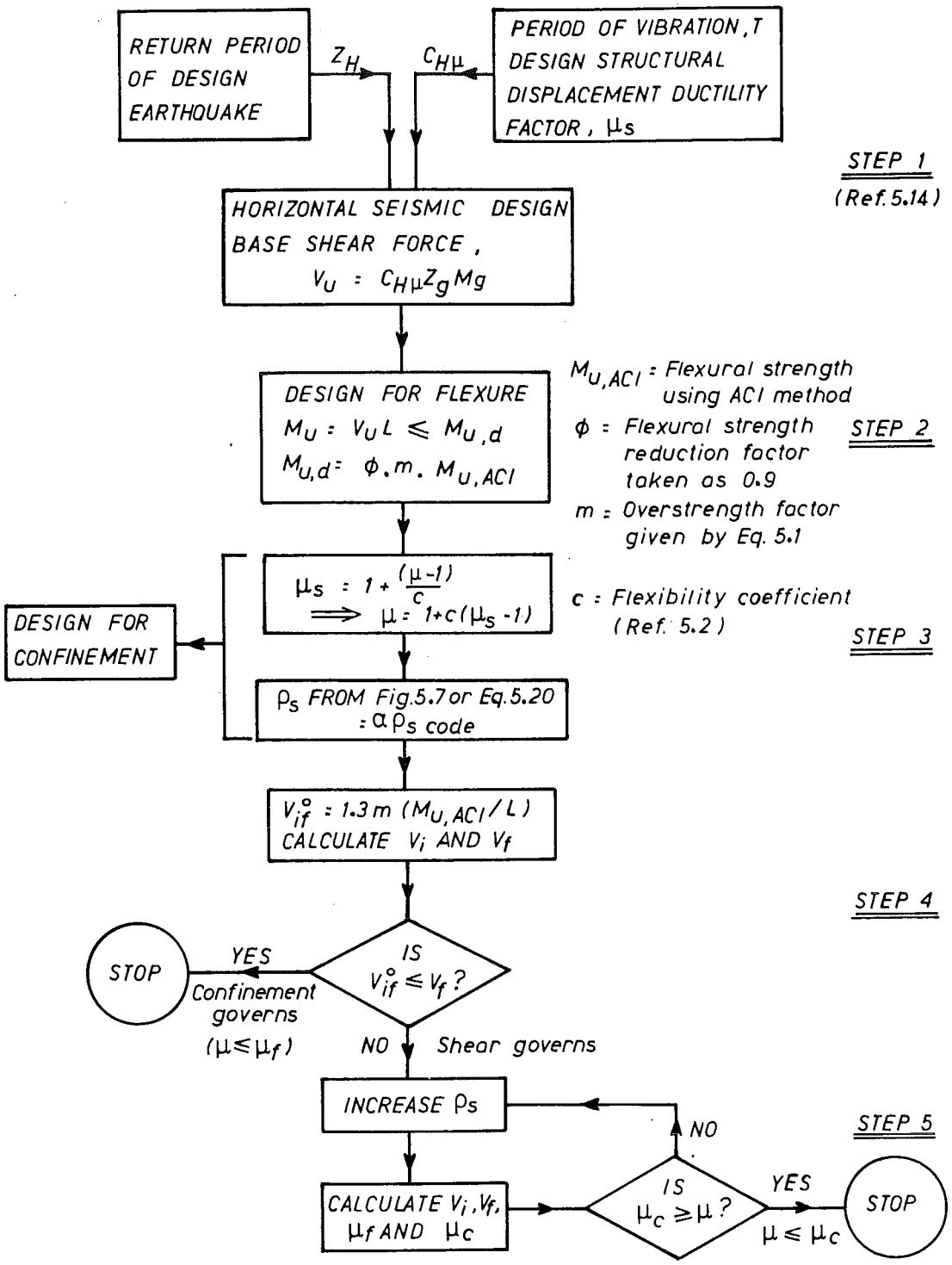

Fig. 5.16 : Flow chart showing the proposed design procedure

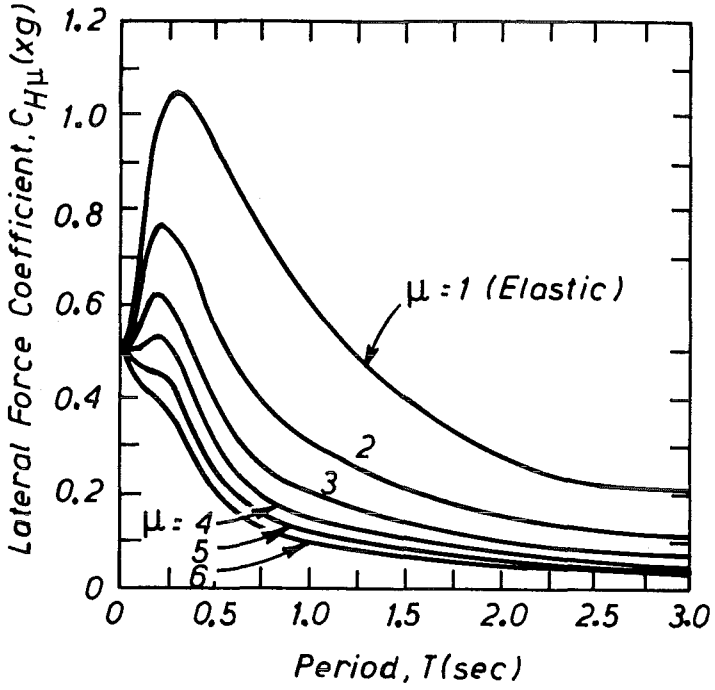

Fig. 5.17 : New Zealand Zone A inelastic design spectra[5.2]

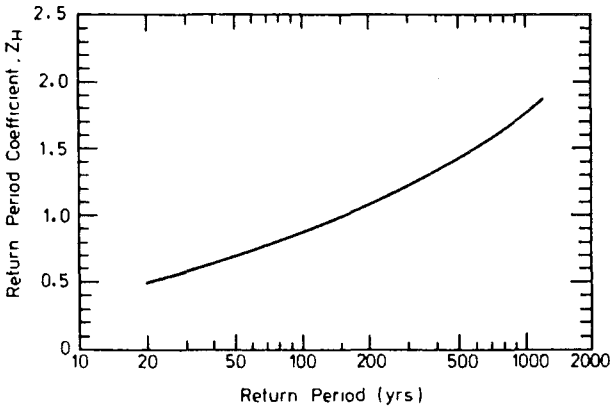

Fig. 5.18 : Relationship between Z_H and design return period[5.2]

where C (≥ 1.0) is a coefficient representing the increase in elastic flexibility of the system due to deformations of foundation and bearing. Hence,

$$\mu = 1 + C\,(\mu_s - 1) \tag{5.28}$$

The value of ρ_s is determined by multiplying the confinement reinforcement ratio $\rho_{s(code)}$ required by NZS 3101 with the factor α obtained from Fig. 5.7 or Eq. 5.22. According to NZS 3101, the value of $\rho_{s(code)}$ for circular sections is to be not less than

$$\rho_s = 0.45\left(\frac{A_g}{A_c} - 1\right)\frac{f'_c}{f_{yh}}\left(0.5 + 1.25\,\frac{P_e}{\phi f'_c A_g}\right) \tag{5.29a}$$

or

$$\rho_s = 0.12\,\frac{f'_c}{f_{yh}}\left(0.5 + 1.25\,\frac{P_e}{\phi f'_c A_g}\right) \tag{5.29b}$$

where A_g = gross area of column cross section,

A_c = concrete core area measured to the outside of spiral reinforcement,

P_e = column load in compression including earthquake effect, and

ϕ = strength reduction factor (= 0.9) for confined column.

Step 4: With the value of ρ_s decided, it is possible to calculate the initial shear strength, V_i, and the residual shear strength, V_f, using Eqs. 5.2 and 5.5 respectively. The value of spiral shear force, V_s, can be expressed in terms of ρ_s explicitly such that

$$V_s = \frac{\pi}{8}\left(\frac{4A_{sp}}{d_s\, s}\right) f_{yt}\, d_s^2$$

$$= \frac{\pi}{8}\, d_s^2\, \rho_s\, f_{yt} \tag{5.30}$$

If the value of V_f is greater than or equal to the shear force, V_{if}^o, at the development of flexural overstrength, the design is governed by confinement and, as shown in Fig. 5.1, the available ductility capacity will be no less than μ_f. Otherwise, the design is governed by shear requirements and Step 5 is followed. The shear force V_{if}^o is calculated using the overstrength factor given by Eqs. 5.1a and b but a factor

of 1.15 is introduced to safeguard against any underestimation by the best-fit equations. In addition, in order to allow for material strengths higher than the specified values, the recommended factor of 1.15 by NZS 3101 is used. Hence,

$$V_{if}^{o} = 1.15\ (1.15m\ \frac{M_{u,ACI}}{L}\ )$$

$$= 1.3m\ \frac{M_{u,ACI}}{L} \qquad (5.31)$$

with m_1 in Eqs. 5.1a and b equal to 1.13 when Grade 275 steel is used, and 1.22 if Grade 380 steel is used.

Step 5: If the design is governed by shear requirements, the value of ρ_s had to be increased. If one wishes one can go back to Step 1 to repeat the calculations using the increased value of μ_s due to the increase in ρ_s or else the calculations are repeated until the value of μ_c obtained using Eq. 5.23 is greater than or equal to the displacement ductility demand, μ .

5.6 CONCLUSIONS

A simple design proposal based on the results of static tests carried out in this project and other tests at the University of Canterbury gives good prediction of member strength and displacement ductility capacity. It allows an integral flexure/shear ductile design approach to be made. The proposal is of particular significance in the light of possible modification in the confinement requirements of NZS 3101 as an outcome of on-going research on ductility of bridge piers at the University of Canterbury, the results of which indicate that strength and ductility enhancement can be achieved through confinement. The benefit of such modification will be offset if the conservative shear provisions of NZS 3101 remain unchanged because as such, the possible relaxation in the provision for confinement reinforcement only means that the shear requirements will govern most of the time. The proposal therefore enables a more rational and more realistic assessment of shear strengths and ductility capacity of the member. However, it should be noted that the results were obtained from tests on circular columns and the application of the approach to other sectional shapes should therefore be verified with more research in this area. More research may also be needed to refine the approach to modify Eq. 5.4 to allow for the effect of ρ_w in calculating the basic shear stress, v_b , and also to include the effect of axial compression in the calculation of v_{cf} (i.e. Eq. 5.8). Finally, due to the

differences between cantilever columns and columns under double curvature bending highlighted in Section 5.3.3, investigation similar to that in the present project may have to be carried out on the latter, which is relevant for multi-column bridge piers, or longitudinal attack of piers with monolithic connection to the superstructure.

Chapter Six

THEORETICAL ANALYSES USING DIAGONAL COMPRESSION FIELD THEORY

6.1 INTRODUCTION

In this chapter the 'Diagonal Compression Field Theory' developed by Collins et al is extended to analyse the behaviour of column units of the static tests. The theory treats the concrete laminae, after discretization of the cross-section, as elements subjected to biaxial stresses (and strains) and therefore it requires a knowledge of biaxial stress-strain behaviour of concrete. Hence the chapter begins with discussions on the biaxial stress-strain relationship of concrete. In particular, the effect of tensile strain normal to the principal compressive stress (or strain) direction in reducing the concrete principal compressive strength is highlighted. A trial and error approach is used in the analytical process which involves several loops of iteration before a final solution satisfying the equilibrium and strain compatibility conditions can be obtained. The computational procedure is tedious and is elaborated in some detail in this chapter. The computer program with some brief notes and comments is given in Appendix II. The predicted performance of the column units is given mainly in the form of load-displacement response. The chapter, therefore, also involves discussions on components of displacement due to loading on the column units. Strictly, the theory is only applicable to monotonic loading. However, it is believed that the response predicted using such an approach provides an envelope to the response in repeated cyclic loading situations. As the analytical process will frequently refer to Mohr's circle of stresses and strains to obtain the various relationships between stress (or strain) parameters, the circles for a general case of biaxial loading are summarized in Fig. 6.1 for convenience of reference.

6.2 BIAXIAL STRESS-STRAIN RELATIONSHIP OF CRACKED CONCRETE

6.2.1 General

Similar to the theory commonly used in predicting flexural behaviour of reinforced concrete members, the 'Diagonal Compression Field Theory' developed by Collins et al, also adopts the plane section assumption in the process of analysis. Other than this assumption,

only the stress-strain behaviour of concrete and steel under a prescribed loading condition is required in both theories in order to make any prediction. The plane section assumption gives rise to linearly varying longitudinal strains across a section as shown in Fig. 6.8b. Usually, the concrete section is discretized into smaller elements (Fig. 6.8a) so that within each element the longitudinal strain can be taken as constant. The difference between the two theories lies in the way in which the stress (or strain) state of these elements are considered. In the flexural theory, the elements are considered to be in a state of uniaxial stress (or strain) and only the uniaxial stress-strain relationship, modified to allow for the confining effect of transverse reinforcement, is used in the prediction[6.1]. In the 'Diagonal Compression Field Theory', shear stress and transverse stress are considered together with the longitudinal stress as depicted in Fig. 6.2 for a typical element. These stresses acting simultaneously give rise to a state of biaxial stress and strain which can be represented by Mohr's circles of stress and strain respectively.

The uncoupling of overall stresses into steel and concrete stress components and the relations between them have been discussed in Chapter Two but it is emphasized again that the stress and strain considered are average values measured over a finite distance of the cracked concrete large enough to include several cracks. The principal compressive stress, f_{c2}, arising from the biaxial stress state may have to be transmitted across cracks previously formed at some other angle. The compressive strength of concrete is known to be weakened by the presence of principal tensile stress normal to the principal compressive stress[6.2]. More importantly, the ultimate strength of the member may be limited by the ability of the concrete to transmit stresses across the cracks and is therefore dependent on the crack width which, in turn, is related to the average principal tensile strain in the concrete[6.4]. Many research workers accounted for this effect by introducing an effectiveness factor, ν, in determining the concrete compressive strength. The factor was either a numerical constant less than unity or a function of f'_c. The reduced concrete compressive strength is obtained by multiplying f'_c with ν. Some typical examples[6.3] are

Thürlimann	:	$\nu = 0.6$ to 0.7
CEB-FIP Model Code	:	$\nu = 0.67$
Nielsen	:	$\nu = (0.8 - \frac{f'_c}{200})$
Ramirez	:	$\nu = \frac{2.5}{\sqrt{f'_c}}$

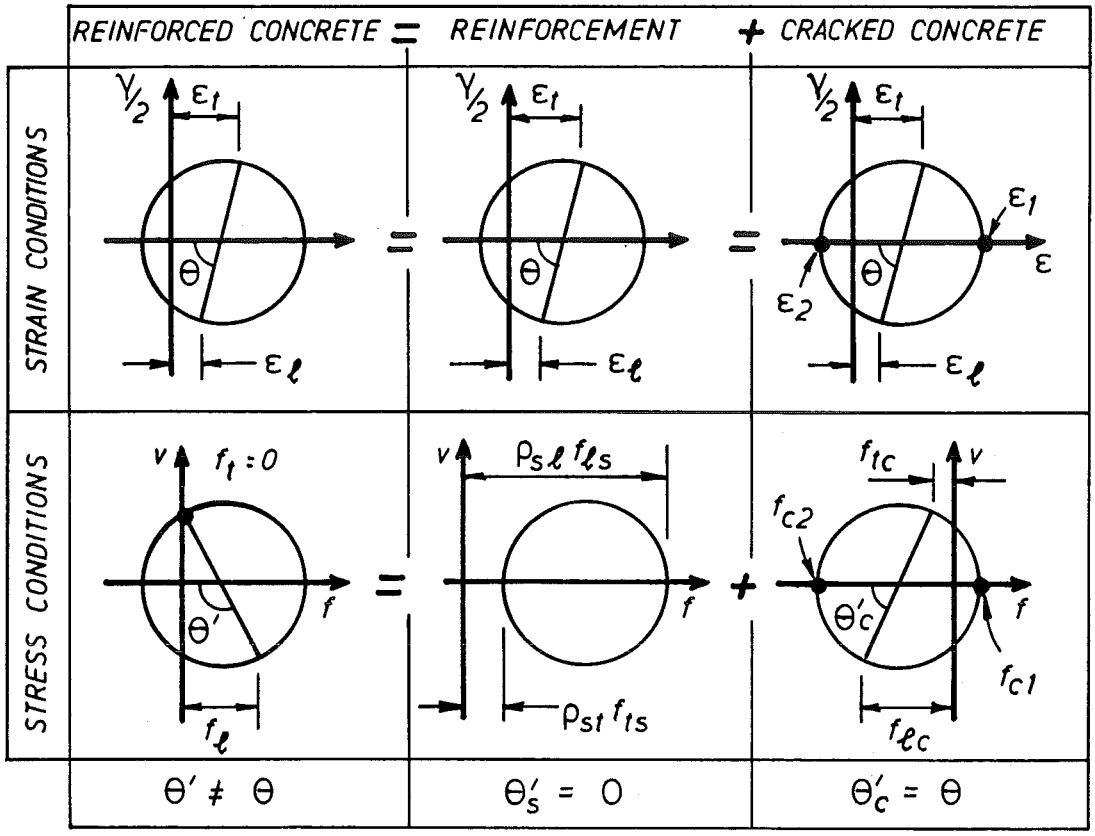

Fig. 6.1 : Mohr's circles of stress and strain for a general case of biaxial loading[6.9]

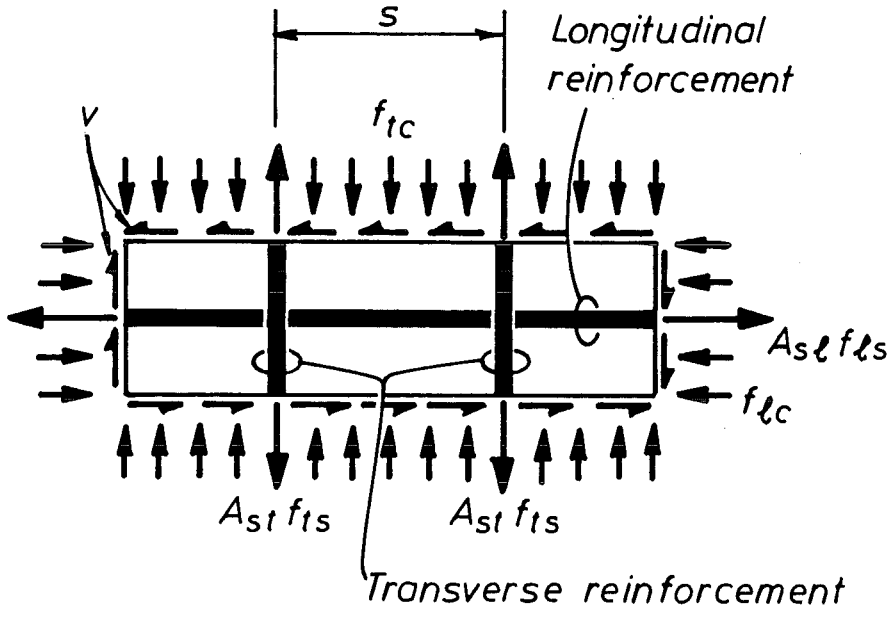

Fig. 6.2 : A typical biaxially stressed reinforced concrete element after discretization of cross-section

Rogowsky : $\nu = 0.85$

Braestrup : $\nu = 0.88$

6.2.2 Biaxial Compressive Stress-Strain Model Of Concrete Proposed By Collins et al

Experimental evidence from tests by Collins and his co-workers[6.5,6.9] revealed that the size of the stress circle is related to the size of the co-existing strain circle - i.e. for a given value of principal compressive strain, ε_2, in the concrete the resulting principal compressive stress f_{c2}, is not only a function of ε_2 but it also depends on the magnitude of the maximum co-existing shear strain, γ_m, which is the diameter of the Mohr's circle of strain. Over the years, the equation proposed by Collins[6.5] had been refined as a result of further research. Originally, the uniaxial stress-strain of concrete in compression was modified by multiplying with a factor, ν, to allow for the effect of straining in the direction normal to f_{c2}. The uniaxial stress-strain relationship of concrete in compression was assumed to be a parabola with a peak strength of f'_c at ε_o, i.e.

$$f_c = f'_c \left[2\left(\frac{\varepsilon_c}{\varepsilon_o}\right) - \left(\frac{\varepsilon_c}{\varepsilon_o}\right)^2 \right] \qquad (6.1)$$

The two earlier expressions proposed for ν were

$$\text{Refs. 6.4 :} \quad \nu = \frac{3.6}{1 - \frac{2\gamma_m}{\varepsilon_o}} \leq 1.0 \qquad (6.2a)$$

$$\text{Refs. 6.7 :} \quad \nu = \frac{5.5}{4 - \frac{\gamma_m}{\varepsilon_2}} \leq 1.0 \qquad (6.2b)$$

in which ε_o and ε_2 are negative for compressive strains.

A recent study by Vecchio[6.8,6.9] had produced more valuable information on biaxial stress-strain behaviour of reinforced concrete. He tested thirty 890 mm square by 70 mm thick reinforced concrete panels under pure shear and other loading combinations. The reinforcement was in the form of two layers of welded wire mesh with the wires parallel to the edges of the panel with cover of 6 mm. Unlike earlier work on plain concrete panels, Vecchio's test did not terminate at the onset of cracking and hence, information on post-cracking behaviour of biaxially stressed reinforced concrete could be gained. As a result of his work, the following expression was proposed[6.8],

$$f_{c2} = f'_c \left[2\left(\frac{\varepsilon_2}{\varepsilon_o}\right) - \nu_1 \left(\frac{\varepsilon_2}{\varepsilon_0}\right)^2 \right] \tag{6.3}$$

$$\text{where} \quad \nu_1 = \left(-\frac{\gamma_m}{\varepsilon_2} - 0.3 \right)^{0.5} \leq 1.0 \tag{6.4}$$

Eq. 6.3 is reduced to the usual parabolic equation, Eq. 6.1, for the uniaxially stressed concrete cylinder, the Mohr's circles of stress and strain of which are as shown in Fig. 6.3. The same equation gives a maximum concrete compressive strength, f'_p, at a compressive strain ε_p such that

$$f'_p = \frac{f'_c}{\nu_1} \tag{6.5a}$$

$$\text{and} \quad \varepsilon_p = \frac{\varepsilon_o}{\nu_1} \tag{6.5b}$$

In other words, the peak strengths lie on a straight line passing through the origin and the point (ε_o, f'_c). Eq. 6.4 was later modified to give the following expression[6.4],

$$\nu_1 = \frac{1}{0.58 - 0.27 \dfrac{\gamma_m}{\varepsilon_2}}$$

$$= \frac{1}{0.58 - 0.27 \dfrac{(\varepsilon_1 - \varepsilon_2)}{\varepsilon_2}}$$

$$= \frac{1}{0.85 - 0.27 \dfrac{\varepsilon_1}{\varepsilon_2}} \leq 1.0 \tag{6.6}$$

where ε_1 is the principal tensile strain.

The post-peak relationship was represented by another parabolic relationship between ε_p and $2\varepsilon_o$ and is given as follows:

$$f_{c2} = f'_p (1 - \eta^2) \tag{6.7}$$

$$\text{where} \quad \eta = \frac{(\varepsilon_2 - \varepsilon_p)}{(2\varepsilon_o - \varepsilon_p)} \tag{6.8}$$

The stress-strain relationship expressed by Eq. 6.3 and 6.7 is not convenient to use. It was further modified by Collins[6.10] as follows:

$$f_{c2} = \nu_1 f'_c \left[2\left(\frac{\varepsilon_2}{\varepsilon_o}\right) - \left(\frac{\varepsilon_2}{\varepsilon_o}\right)^2 \right] \tag{6.9}$$

$$\text{where } \nu_1 = \frac{1}{0.8 - 0.34 \frac{\varepsilon_1}{\varepsilon_o}} \leq 1.0 \qquad (6.10)$$

Fig. 6.4 compares the results of the last two proposed models for three ε_1 values. The values from the latest proposal are plotted as dots in the figure while the full lines are for Eqs. 6.3, 6.6, 6.7 and 6.8. It can be seen that the difference between them is small but the latest proposal has a computational advantage because ν_1, from Eq. 6.10, is only dependent on ε_1 and is uncoupled from the concrete stress-strain relationship. As noted by Vecchio[6.9], the parabolic expression of Eq. 6.1 has been adopted for the sake of simplicity and with this, a more accurate representation of the actual behaviour is possible. The form of Eq. 6.9 allows modification to the concrete stress-strain relationship to be made readily if necessary.

6.2.3 Concrete Confined By Spiral Reinforcement

It is unlikely that the arrangement of reinforcement in Vecchio's test panels would have given rise to effective confinement to the core concrete as in the case of reinforced concrete members confined with hoops or spirals. To use the parabolic stress-strain relationship to predict the behaviour of his panels was therefore justifiable. However, the enhancement in concrete strength and ductility due to confinement has been well established[6.1]. Hence, to extend the application of Eq. 6.9 to well confined reinforced concrete members, the stress-strain relationship may have to be modified to give a more realistic representation of the behaviour under effective but passive confinement. From both theoretical and experimental studies, Mander[6.1] proposed the following analytical model, for longitudinal compressive stress-strain behaviour of concrete, based on equation suggested by Popovics[6.11], viz.

$$f_c = \frac{f'_{cc} \times r}{r - 1 + x^r} \qquad (6.11)$$

$$\text{where } f'_{cc} = f'_{co} \left(2.254 \sqrt{1 + \frac{7.94\, f'_\ell}{f'_{co}}} - \frac{2 f'_\ell}{f'_{co}} - 1.254\right) \qquad (6.12)$$

is the peak longitudinal compressive strength of the confined concrete; f'_{co} is the peak strength of unconfined concrete and is taken to be the cylinder strength, f'_c, in the discussions that follow, and

$$f'_\ell = \frac{1}{2} k_e \rho_s f_{yt} \qquad (6.13)$$

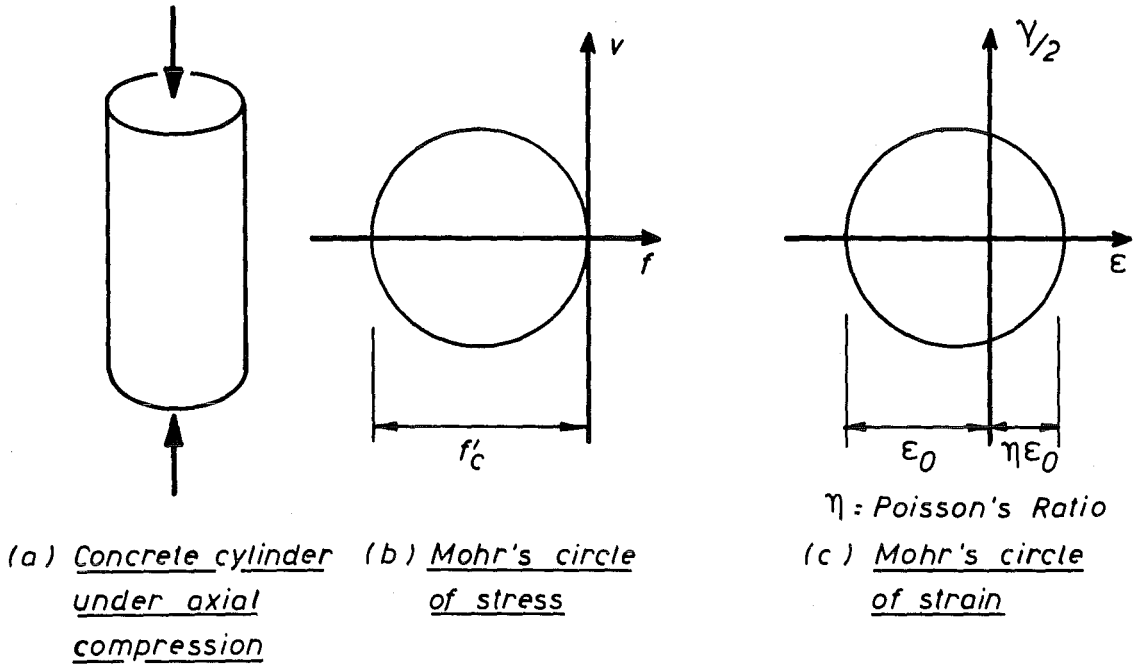

Fig. 6.3 : A uniaxially loaded concrete cylinder and the associated Mohr's circle of stress and strain

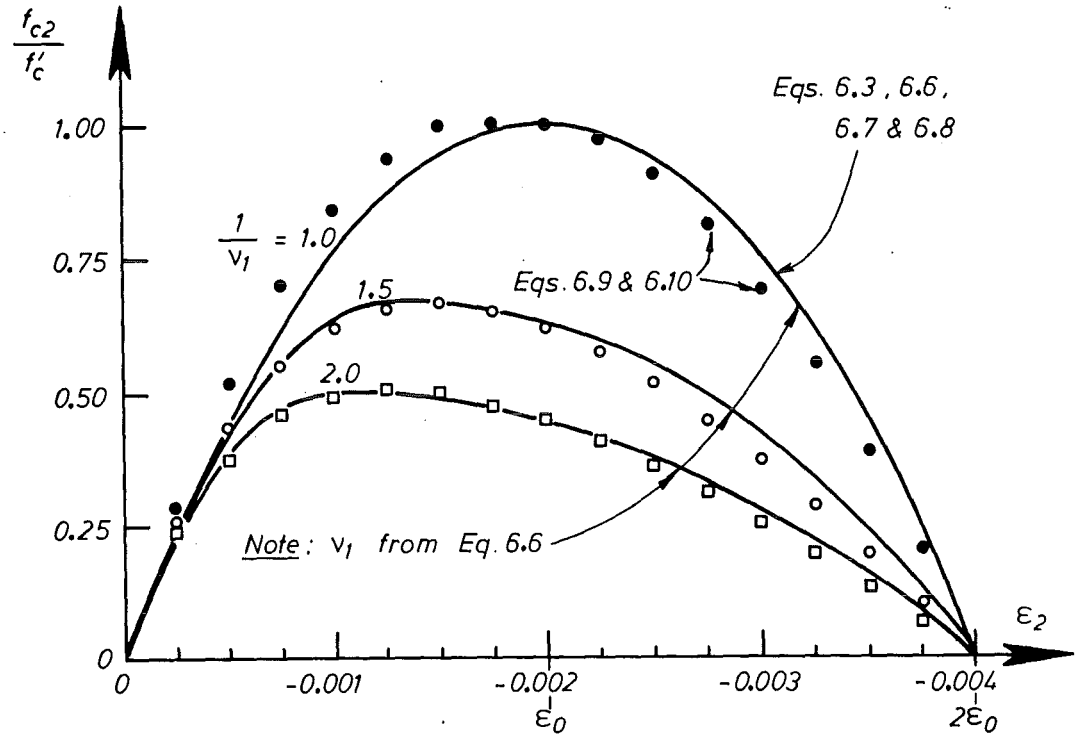

Fig. 6.4 : Comparison of two biaxial concrete compressive stress-strain relationships considering the effect of transverse tensile straining

is the effective lateral confining stress provided by transverse reinforcement at yield.

$$x = \frac{\varepsilon_c}{\varepsilon_{cc}} \tag{6.14}$$

is the ratio of concrete compressive strain to the strain at peak confined strength, f'_{cc}, with ε_{cc} given by Eq. 6.15 below.

$$\varepsilon_{cc} = \left[R \left(\frac{f'_{cc}}{f'_{co}} - 1 \right) + 1 \right] \varepsilon_{co} \tag{6.15}$$

in which R was found to have a value of 5 and ε_{co} is the compressive strain corresponding to f'_{co}. ε_{co} is assumed to be equal to ε_o in Eq. 6.1 and is taken to be -0.002 in the following discussions.

$$r = \frac{E_c}{E_c - E_{sec}} \tag{6.16}$$

where the initial tangent modulus of elasticity of concrete E_c, is given by

$$E_c = 5000 \sqrt{f'_c \ (\text{MPa})} \tag{6.17}$$

and the secant modulus of elasticity of concrete, E_{sec} is given by

$$E_{sec} = \frac{f'_{cc}}{\varepsilon_{cc}} \tag{6.18}$$

Eq. 6.13, giving the effective lateral confining stress depends on the confinement effectiveness coefficient, k_e, which relates the minimum fully confined core cross-sectional area to the full area Mander[6.1], showed that for sections confined by spirals

$$k_e = \frac{(1 - 0.5 \frac{s'}{d_s})}{1 - \rho_{cc}} \tag{6.19}$$

where ρ_{cc} is the ratio of volume of longitudinal steel to volume of concrete core, i.e.

$$\rho_{cc} = \rho_\ell \frac{A_g}{A_{cc}} \tag{6.20}$$

with A_{cc} equal to the core area; A_g = gross section area; s' is the clear spacing between the spirals and d_s is the effective core diameter measured to the bar centre of spirals.

The proposed equation (Eq. 6.11) substantially modifies the

commonly used compression stress-strain relationship for concrete, such as Eq. 6.1, to allow for the increase in strength and a flattening and elongation of the falling branch portion of th stress-strain curve as shown in Fig. 6.5. The form of Eq. 6.11 also has the advantage of obviating the need to establish separate rising and falling branch relations.

Previously, it has also been suggested[6.11], for concrete under biaxial compressive stress, that the increase in strength can be obtained from the following expression,

$$f'_{cc} = f'_{co} + k_1 f'_\ell \tag{6.21}$$

and, from Eqs. 6.15 and 6.21,

$$\varepsilon_{cc} = \left[R \left(\frac{f'_c}{f'_{co}} - 1 \right) + 1 \right] \varepsilon_{co}$$

$$= \left[R k_1 \frac{f'_\ell}{f'_{co}} + 1 \right] \varepsilon_{co} \tag{6.22}$$

Eqs. 6.22 and 6.21, after rearrangement and substituting f'_c for f'_{co}, are plotted in Fig. 6.6 with k_1 of Eq. 6.21 taken to be 5.5, as suggested by Mander[6.1]. It can be seen from the figure that the difference between the two expressions is not very great, and for simplicity, Eq. 6.21 is adopted in the present study, i.e.

$$f'_{cc} = f'_c + 5.5 f'_\ell \tag{6.23}$$

and, with $R = 5$ and $\varepsilon_o = - 0.002$,

$$\varepsilon_{cc} = (5 \times 5.5 \frac{f'_\ell}{f'_c} + 1) \varepsilon_o$$

$$= 0.002 \ (27.5 \frac{f'_\ell}{f'_c} + 1) \tag{6.24}$$

Hence, in the following discussions, extending the effects of the 'Diagonal Compression Field Theory' to confined concrete, the principal compressive stress is

$$f_{c2} = \nu_1 \left[\frac{f'_{cc} \ x \ r}{r - 1 + x^r} \right] \tag{6.25}$$

with all the terms as defined before and ν_1 is given by Eq. 6.10.

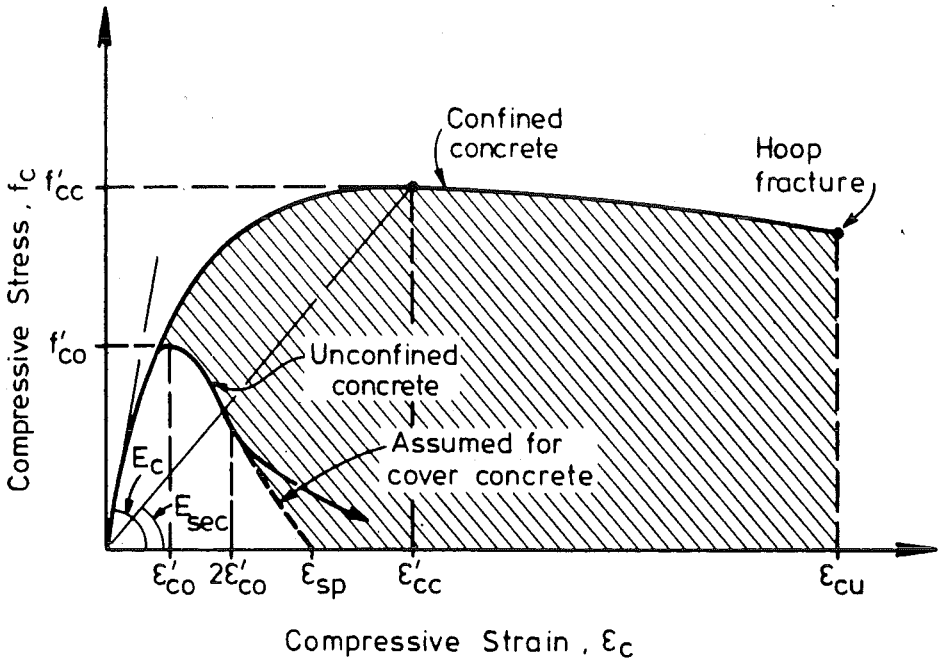

Fig. 6.5 : A concrete compressive stress-strain model proposed by Mander et al[6.1]

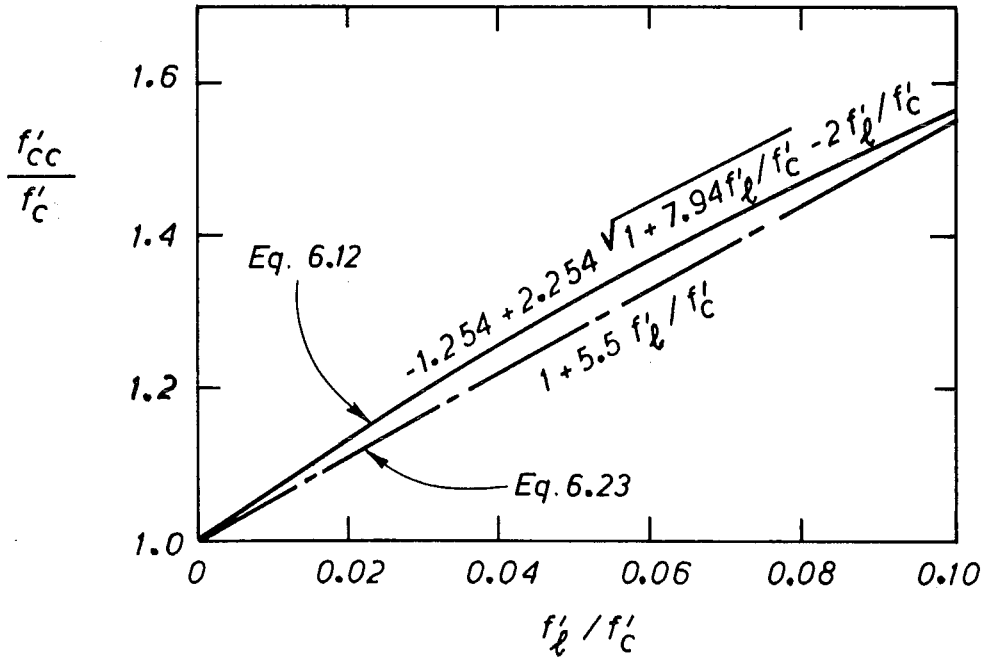

Fig. 6.6 : A linear approximation to Eq. 6.12 proposed by Mander et al[6.1]

For reinforced concrete members failing in shear the compressive strain in the concrete may not be very large, and therefore the beneficial effect due to confinement may not be fully utilized before the shear failure. This was found to be the case in a theoretical study (Section 6.4) to compare the predicted behaviour of a limited number of the static test columns using the unconfined (with $f'_\ell = 0$ in Eqs. 6.22 and 6.24) and the confined stress-strain relationship of concrete outlined earlier. At low strain level the difference between the two relationships is small and therefore the predicted behaviour did not differ significantly. Nevertheless, in order to unify the 'Diagonal Compression Field Theory' with flexural theory, the relationship given by Eq. 6.25 is adopted in the theoretical analysis reported herein.

6.2.4 Biaxial Tensile Stress-Strain Behaviour Of Concrete

In order to predict accurately the post-cracking behaviour of reinforced concrete elements, Vecchio[6.9] found that it was necessary to account for the average tensile stress which still exists in the concrete between cracks. To allow for this "tension stiffening" effect he specified a gradual unloading branch instead of an abrupt drop to zero stress level for the average tensile stress-strain relationship of concrete as shown in Fig. 6.7. The stress and strain at cracking are given by Eqs. 6.26 and 6.27 respectively.

$$f_{cr} = 0.33 \sqrt{f'_c} \ \text{(MPa)} \tag{6.26}$$

$$\varepsilon_{cr} = \frac{f_{cr}}{E_c} \tag{6.27}$$

Prior to cracking, a linear relationship was assumed such that

$$f_{cl} = E_c \, \varepsilon_1 \tag{6.28}$$

where f_{cl} is the average principal tensile stress. The falling branch after cracking is given by the following equation, viz.

$$f_{cl} = \frac{f_{cr}}{1 + \sqrt{\dfrac{\varepsilon_1}{0.005}}} \tag{6.29}$$

The results from which Vecchio derived the above relationships showed large scatter (see Fig. 6.7) but, since the tensile stresses are only a small part of the total stress circle, a large error in f_{cl}

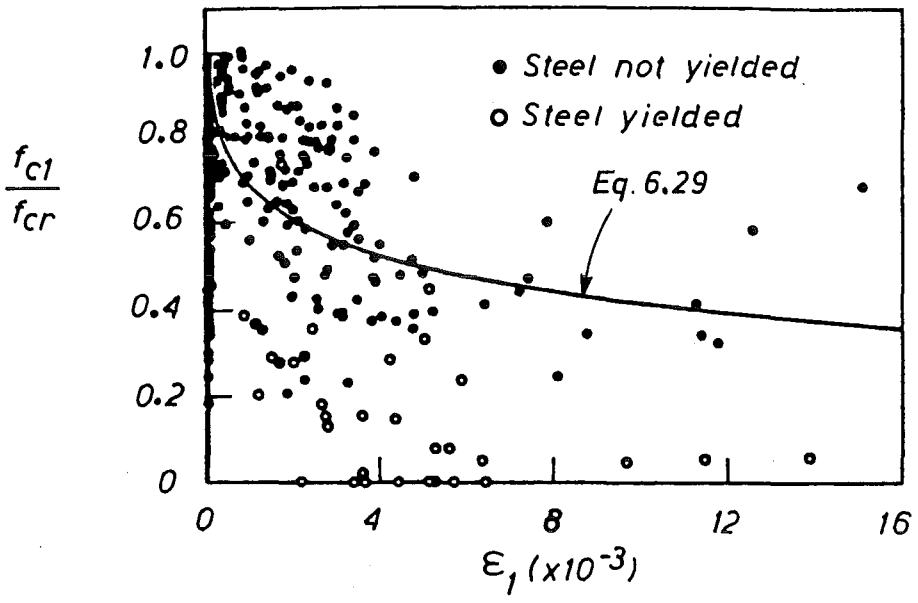

Fig. 6.7 : Principal tensile stress-strain relationship fitted to experimental data, after Vecchio[6.9]

does not necessarily result in a large error in the prediction. The equations were derived from monotonic test results and their application to cyclic loading situations is uncertain. Furthermore, it can be seen from Fig. 6.7 that the yielding of steel typically resulted in low values of f_{c1} which is relevant for inelastic cyclic loading situations where yielding of steel is to be expected.

The average stress-strain relationships for concrete and steel in the composite medium may differ from local stress-strain relationships as determined from standard material tests. In particular, the bond characteristic between the reinforcement and concrete influences the variation of local stress-strain values and therefore the average stress-strain relationships for the concrete and steel will not be completely independent of each other, as implied in the process of uncoupling. However, for the sake of simplicity, they are assumed to be independent of each other in the analysis.

6.3 COMPUTATION PROCEDURE TO ANALYSE REINFORCED CONCRETE SECTION SUBJECTED TO SHEAR, FLEXURE AND AXIAL LOAD

6.3.1 An Outline Of The Approach

The analytical process is similar to that of flexural theory. The composite reinforced concrete member is uncoupled into steel and concrete components. The concrete section is discretized into smaller elements over which the stresses and strains can be assumed to be uniform as shown in Fig. 6.8b. Unlike the flexural theory, the 'Diagonal Compression Field Theory' requires an assumption for the shear stress distribution over the section concerned (Fig. 6.8d). The two basic conditions to be satisfied are the strain compatibility requirement whereby the uncoupled concrete and steel elements are assumed to be subjected to equal strain if they are at the same level in the cross-section; and the equilibrium requirement whereby the sum of the element forces and moments must balance the applied force and moment at the section under consideration, i.e.

$$P = \sum^{all} f_{\ell c} \Delta A_c + \sum f_{\ell s} \Delta A_s \tag{6.30a}$$

$$M = \sum^{all} f_{\ell c} \Delta A_c \left(\frac{D}{2} - y_c\right) + \sum f_{\ell s} A_s \left(\frac{D}{2} - y_s\right) \tag{6.30b}$$

$$V = \sum^{all} v \Delta A_c \tag{6.30c}$$

where ΔA_c and ΔA_s are the area of concrete and steel elements respectively, and y_c and y_s are the corresponding distance of the centroid of the elements from the extreme compression fibre. A further equilibrium consideration required in the 'Diagonal Compression Field Theory' is that the sum of transverse forces must be zero (see Section 2.3.4) and this implies

$$f_{tc} + \rho_{st} f_{ts} = 0 \tag{6.30d}$$

From geometrical and material properties the right hand sides of Eqs. 6.30a and b can be determined. As was discussed in Chapter Two, a bi-linear relationship is assumed for the stress-strain property of the steel and the strain-hardening effect of steel is ignored. To analyse the concrete elements to obtain the longitudinal concrete stresses, $f_{\ell c}$, is a more complicated task. Out of a total of six variables required to define both the stress and strain circles (three for each), only the longitudinal strain, ε_ℓ, from the assumed longitudinal strain profile and the shear stress, v, from the assumed shear stress distribution are known. Therefore, the value of $f_{\ell c}$ has to be determined by a trial and error approach to satisfy the equilibrium and compatibility conditions outlined earlier and in Chapter Two. The

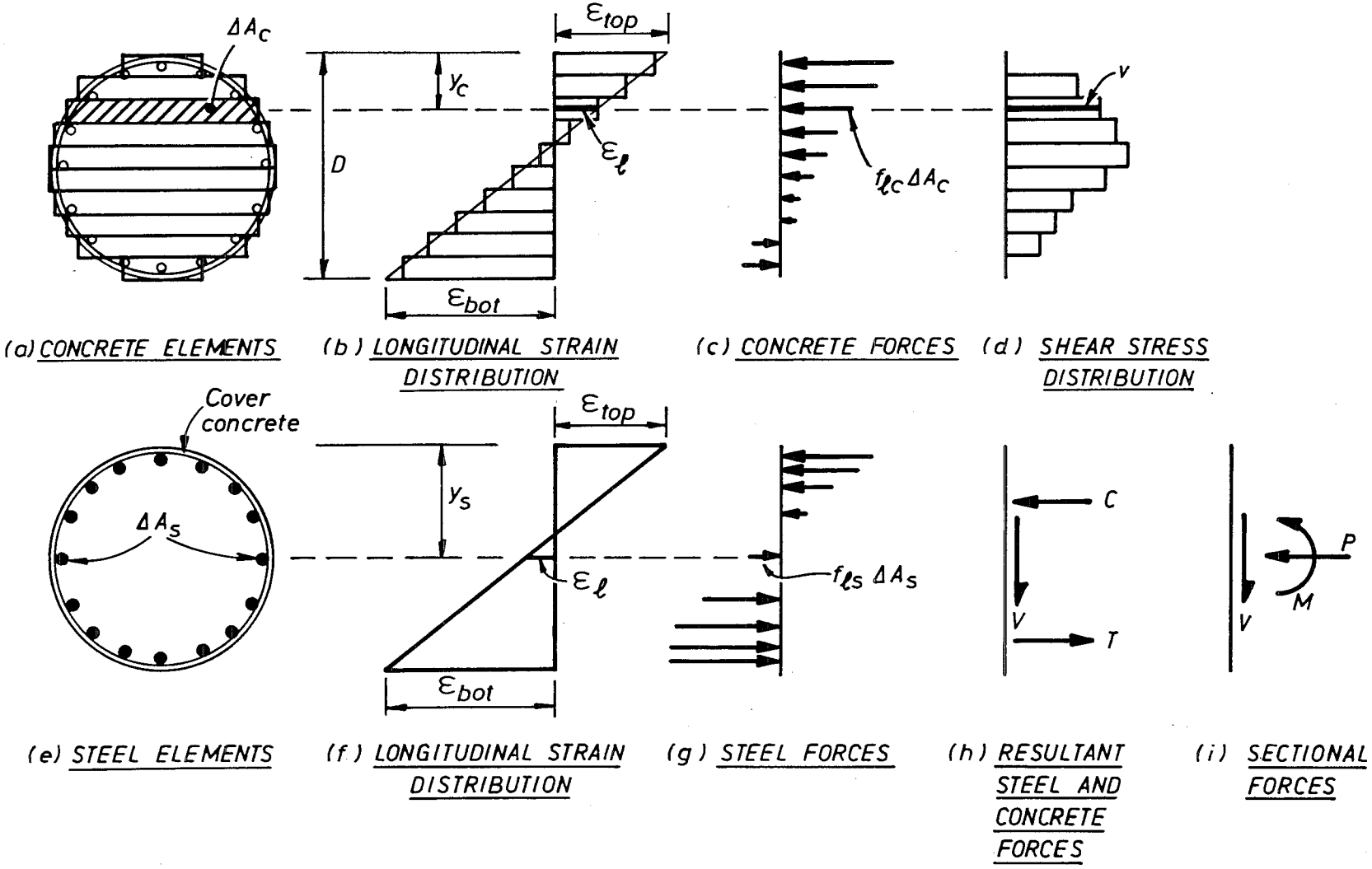

Fig. 6.8 : Concrete and steel element after discretization and the associated strain and stress conditions

procedure is discussed further in subsequent sub-sections.

The validity of the longitudinal strain distribution assumption can be checked using the equilibrium requirements of Eqs. 6.30a and b. The distribution is adjusted until these conditions are satisfied. However, this procedure is tedious because it involves two loops of iteration in order to reach convergence in both conditions. Hence, it was decided to carry out the analysis by fixing the top compressive strain, ε_{top}, while finding the bottom tensile strain, ε_{bot}, to achieve the requirement of Eq. 6.30a. Then the moment given by Eq. 5.30b was readily obtained. The procedure is then repeated with a new value of top strain to give another value of M and so on, as in the case of moment curvature analysis used in the flexural theory.

The assumed shear stress distribution is checked by considering another section a short distance away from the section concerned[6.6,6.9]. As shown in Fig. 6.9, the shear stress acting on the rth element can be calculated by considering the equilibrium of the element as a free body. From the figure, adding the algebraic sum of concrete and steel forces from the top layer to the (r-1)th layer gives

$$F_{r-1} = \sum_{i=1}^{r-1} (C_1 - C_2)_i + (T_1 - T_2)_i \qquad (6.31a)$$

where C_1 and C_2 are the products of concrete longitudinal stress, $f_{\ell c}$, and area of concrete element, ΔA_c, for sections 1 and 2 respectively, and similarly, T_1 and T_2 are the steel components. From equilibrium considerations of the free-body of rth element

$$F_r = F_{r-1} + (C_1 - C_2)_r + (T_1 - T_2)_r \qquad (6.31b)$$

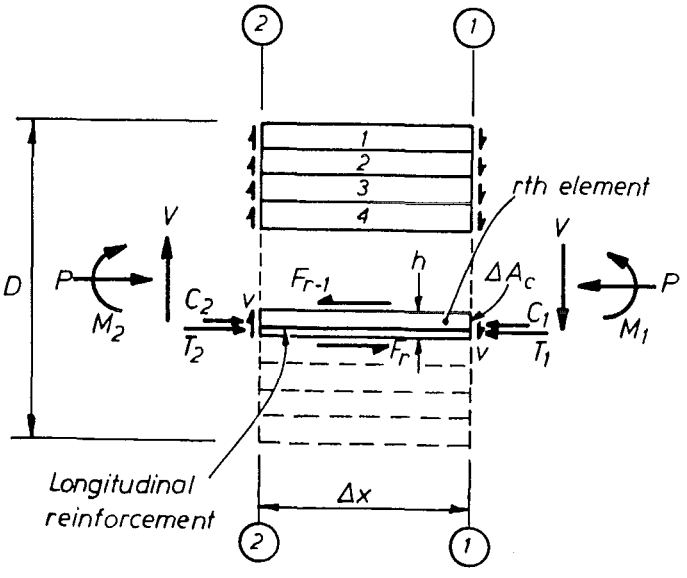

Fig. 6.9 : A free-body diagram of rth element used to compute the shear-stress acting on the element

The average shear stress acting on the element is therefore equal to

$$v_r = \frac{(F_r + F_{r-1})}{2 \Delta x \, b_r} \tag{6.32}$$

where b_r is the width of the element and Δx is the distance between the two sections given by the following expression:

$$\Delta x = \frac{|M_1 - M_2|}{V} \tag{6.33}$$

Each element is considered in turn to obtain the shear stress acting on the element using Eqs. 6.31 to 6.33. The resulting shear stress distribution is compared with the assumed distribution which is then adjusted accordingly and the analysis repeated until agreement is reached within acceptable limits.

The whole approach is summarized in the form of a flow chart shown in Fig. 6.10. As mentioned earlier, the overall procedure is similar to that of moment curvature analysis used in the flexural theory. However, in this case the moment-curvature curve obtained from the analyses is for a fixed value of shear force. Hence, as shown for a general case in Fig. 6.11, the maximum moment capacity for a fixed value of V, from the M-ϕ curve has to be greater than the moment encountered at the critical section, i.e. $M_{max} \leq Va$, where a is the shear span of the cantilever column. Failure would have taken place if the computed moment capacity is lower than Va. Otherwise the curvature of different sections along the column subjected to a particular shear force can be obtained as illustrated in Fig. 6.11.

The analytical procedure is carried out in a series of shear force increments until the above failure condition is reached, and the shear force at which this occurs is taken to be the theoretical ultimate strength of the member. The concrete elements are analysed using a subprogram. It is this subprogram which determines the efficiency of the computational process and whether convergence can be reached. The following sections discuss some important points about the main program and subprogram. Although the main program is essentially the same, the subprogram used in this project has been modified from the original one written by Vecchio[6.9].

6.3.2 Procedures Used to Analyse The Concrete Layers

As mentioned earlier, a trial and error iterative approach has to be used to obtain the longitudinal normal stress, $f_{\ell c}$, of the

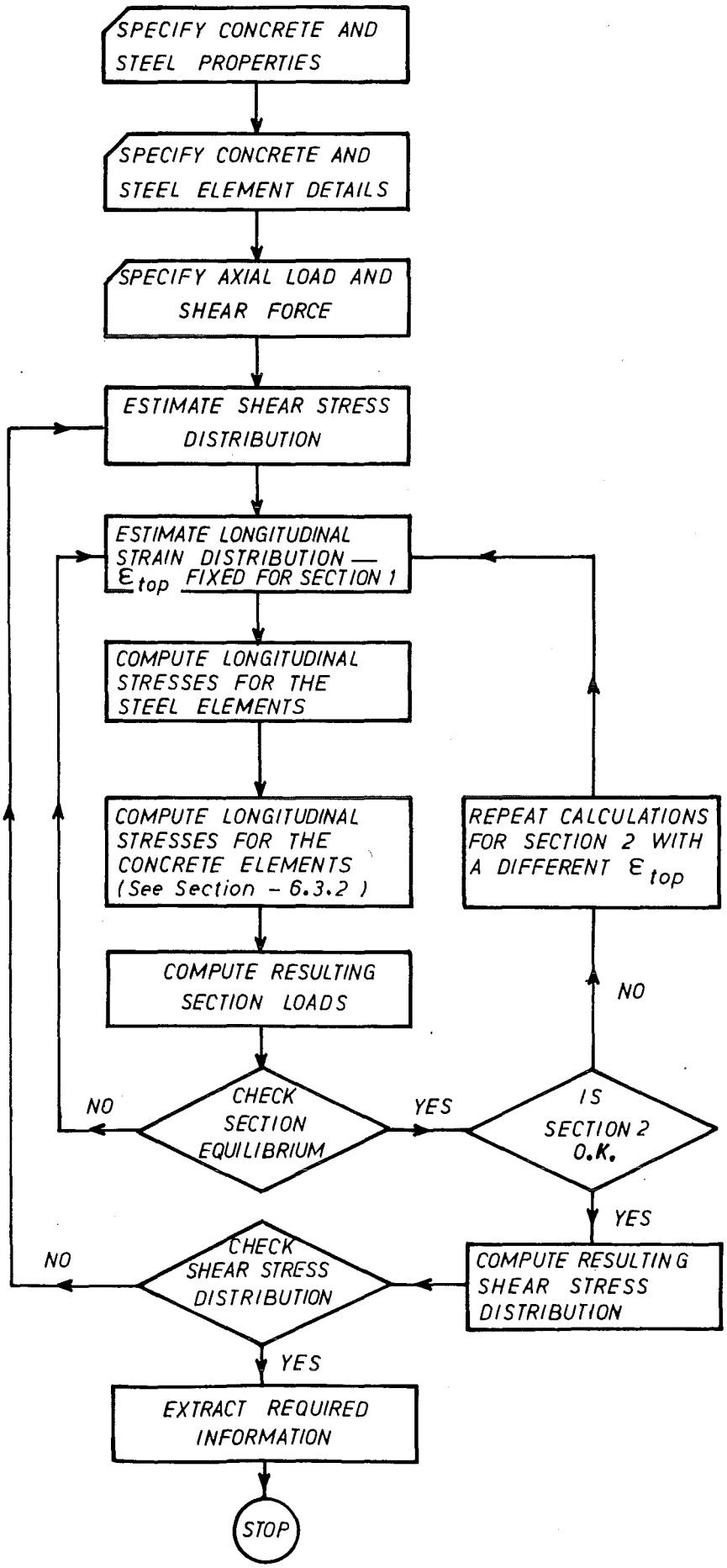

Fig. 6.10 : A flow-chart showing the overall computational procedure

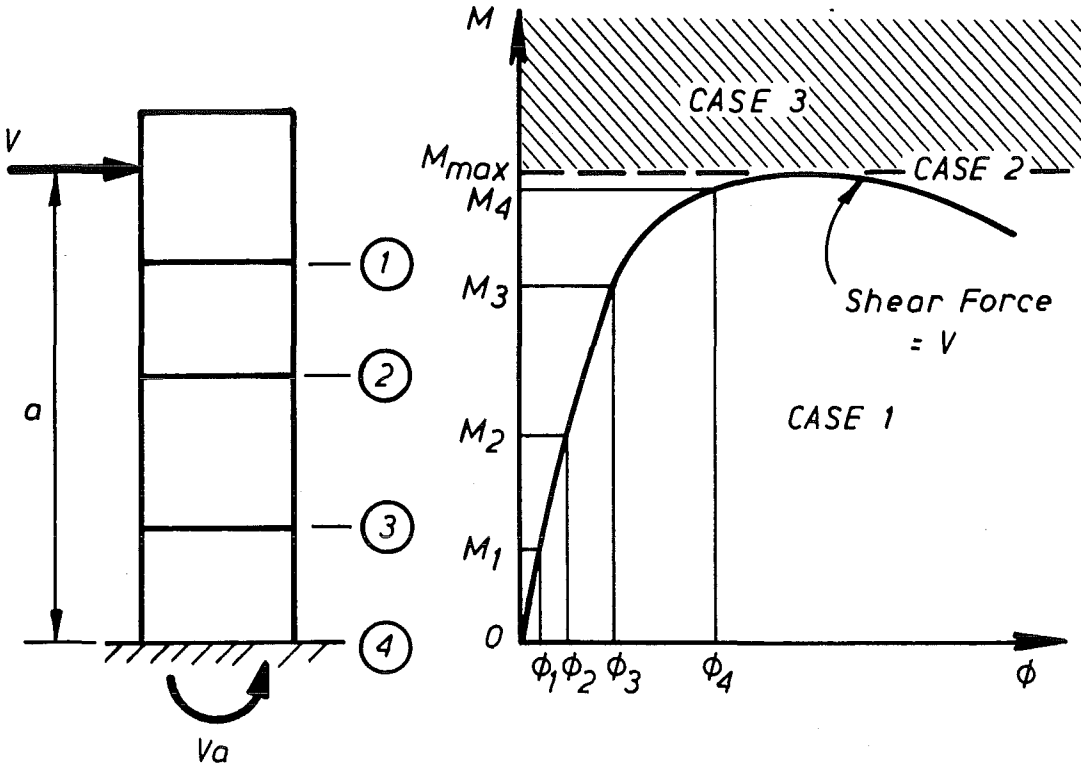

CASE 1 : $Va < M_{max}$ — Before Failure

CASE 2 : $Va = M_{max}$ — At Failure

CASE 3 : $Va > M_{max}$ — Failed

Fig. 6.11 : Moment-curvature diagram for a constant shear force and three different cases of consideration

concrete elements. Basically, two different computational procedures were adopted, depending on whether the assumed shear stress, v , on a concrete layer is more or less than the diagonal cracking shear stress, v_{cr} . Furthermore, there is also a possibility that the assumed shear stress on the concrete layer exceeds its capacity in shear. Hence there is a need to have an estimate of the maximum (or failure) shear stress, v_{max} , of the concrete layer (with a particular value of ε_ℓ) under consideration. The basic ideas of the approaches are derived and modified from those given in Ref. 6.10. The determination of v_{cr} is given in Section 6.3.2.1. The two computational procedures were incorporated in two separate subprograms and are discussed in the appropriate sections that follow. In the discussions, the sign convention for both stresses and strains is tension positive, compression negative.

6.3.2.1 The determination of the cracking shear stress, v_{cr}

The cracking shear stress, v_{cr} , is assumed to be the shear stress when the principal tensile strain, ε_1 , is equal to the cracking strain, ε_{cr} (Eq. 6.27). Hence, for a fixed value of ε_ℓ , a curve can be constructed for v_{cr} (normalized by dividing by f'_c) as a function of θ , where θ is the angle of inclination of principal compressive stress to the column axis. The curve is obtained using the following procedure.

Step 1 : From a fixed value of ε_ℓ , a chosen value of θ and with $\varepsilon_1 = \varepsilon_{cr}$, the value of principal compressive strain, ε_2 , can be obtained from strain circle, i.e.

$$\varepsilon_2 = \varepsilon_\ell - (\varepsilon_1 - \varepsilon_\ell) \tan^2\theta$$

Step 2 : From the calculated value of ε_2 , the principal compressive stress, f_{c2} , can be calculated using the stress-strain function of Eq. 6.25.

Step 3 : Knowing the values of f_{c2} , θ, $f_{c1} = f_{cr}$, the value of v_{cr} can be obtained from stress circle as follows:

$$v_{cr} = \frac{(f_{cr} - f_{c2})}{(\tan\theta + \cot\theta)}$$

Step 4 : Select a new value of θ and repeat Steps 1 to 3.

As an example, a series of such curves in solid lines for different values of ε_ℓ (≤ 0) were constructed and are shown in Fig. 6.12.

These curves do not give a unique value of v_{cr}, so a further condition has to be satisfied in order to obtain the unique solution. This condition involves the transverse stress and strain and requires equality between θ_1 and θ_2 determined from the following equations by considering the geometry of stress and strain circles,

$$\tan \theta_1 = \sqrt{\frac{f_{cr} - f_{tc}}{f_{tc} - f_{c2}}} = \frac{f_{cr} - f_{tc}}{v_{cr}} \tag{6.34a}$$

and

$$\tan \theta_2 = \sqrt{\frac{\varepsilon_{cr} - \varepsilon_t}{\varepsilon_t - \varepsilon_2}} = \sqrt{\frac{\varepsilon_{cr} - \varepsilon_t}{\varepsilon_{cr} - \varepsilon_\ell}} \tag{6.34b}$$

Assuming a value of ε_t, and hence f_{tc}, a value of v_{cr} may be obtained for a fixed value of ε_ℓ, if either of Eqs. 6.34a and b is considered separately. The results are plotted as two separate sets of curves for different values of ε_t in Fig. 6.12. The solutions can be obtained from the intersection points of these curves with the solid line. However, to obtain an exact unique solution the results should be the same regardless of which curve is considered. As can be seen from the figure, this agreement is only possible over a range of θ at $\varepsilon_t = 0$ and the results tend to vary in opposite directions as ε_t changes.

The solution becomes determinate if ε_t is assumed to be zero and v_{cr} can be found from the following equation,

$$v_{cr} = \sqrt{-f_{cr} f_{c2}} \tag{6.35}$$

But the divergence between θ_1 and θ_2 becomes greater as ε_ℓ becomes more negative and this phenomenon can be illustrated as shown in Fig. 6.13 in which the angle, θ_1, from consideration of the stress circle (Eq. 6.34a) is plotted against the angle, θ_2, from consideration of the strain circle (Eq. 6.34b). Also shown in the figure is a straight line indicating equality between θ_1 and θ_2. From the figure it can be seen that, for $\varepsilon_t = 0$, the difference between θ_1 and θ_2 increases as ε_ℓ decreases. In order to obtain a solution at high longitudinal compressive strain, ε_ℓ, the value of ε_t has to be slightly negative. This is evident from curves for two other values of ε_t in the figure. The solution is obtained from the intersection point of these curves with the straight line. Note that θ_1 remains relatively constant as the value of ε_t is lowered. The procedure to calculate v_{cr} is based on three observations and is given in the form of a flow chart in Fig. 6.14. In the subprogram, v_{cr} is given a very small value of 0.001 MPa

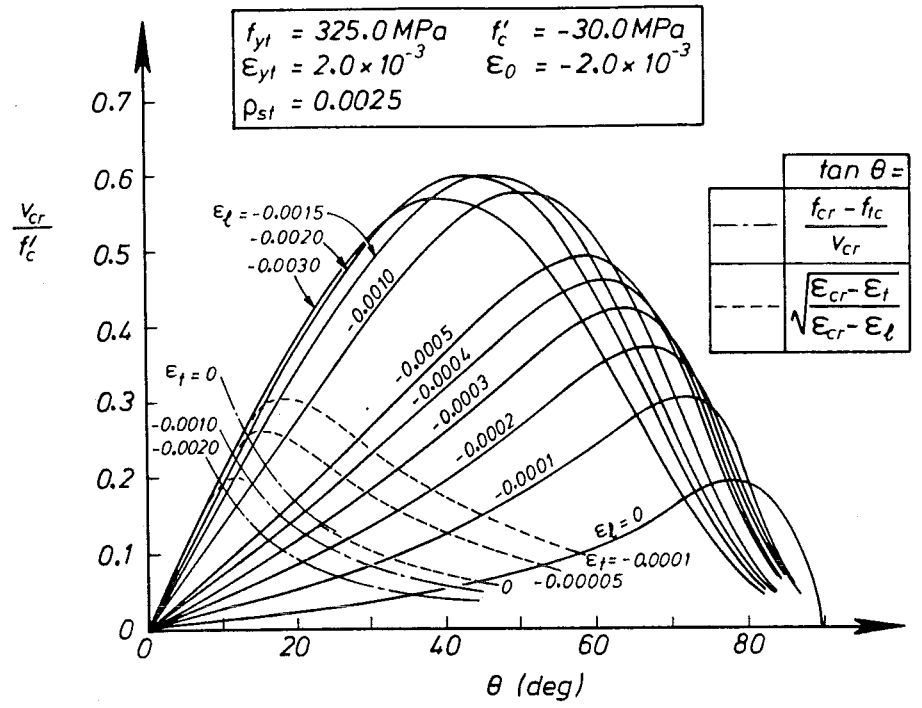

Fig. 6.12 : Determination of shear stress at diagonal cracking

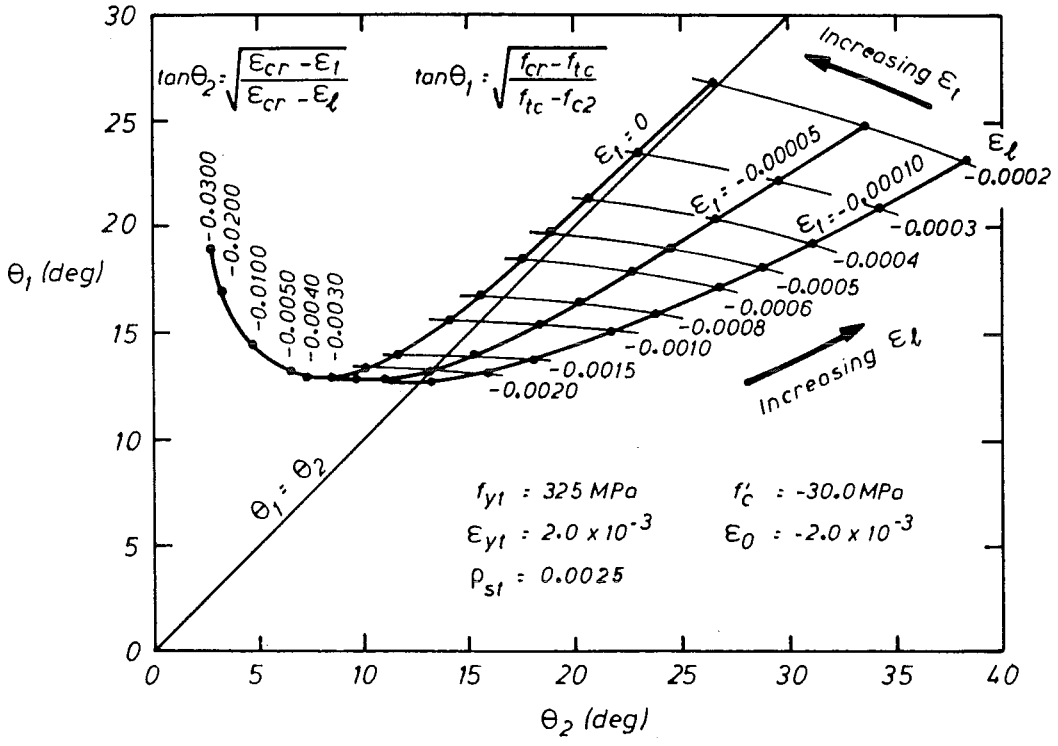

Fig. 6.13 : Difference between θ_1 and θ_2 obtained from stress and strain circles respectively at onset of diagonal cracking

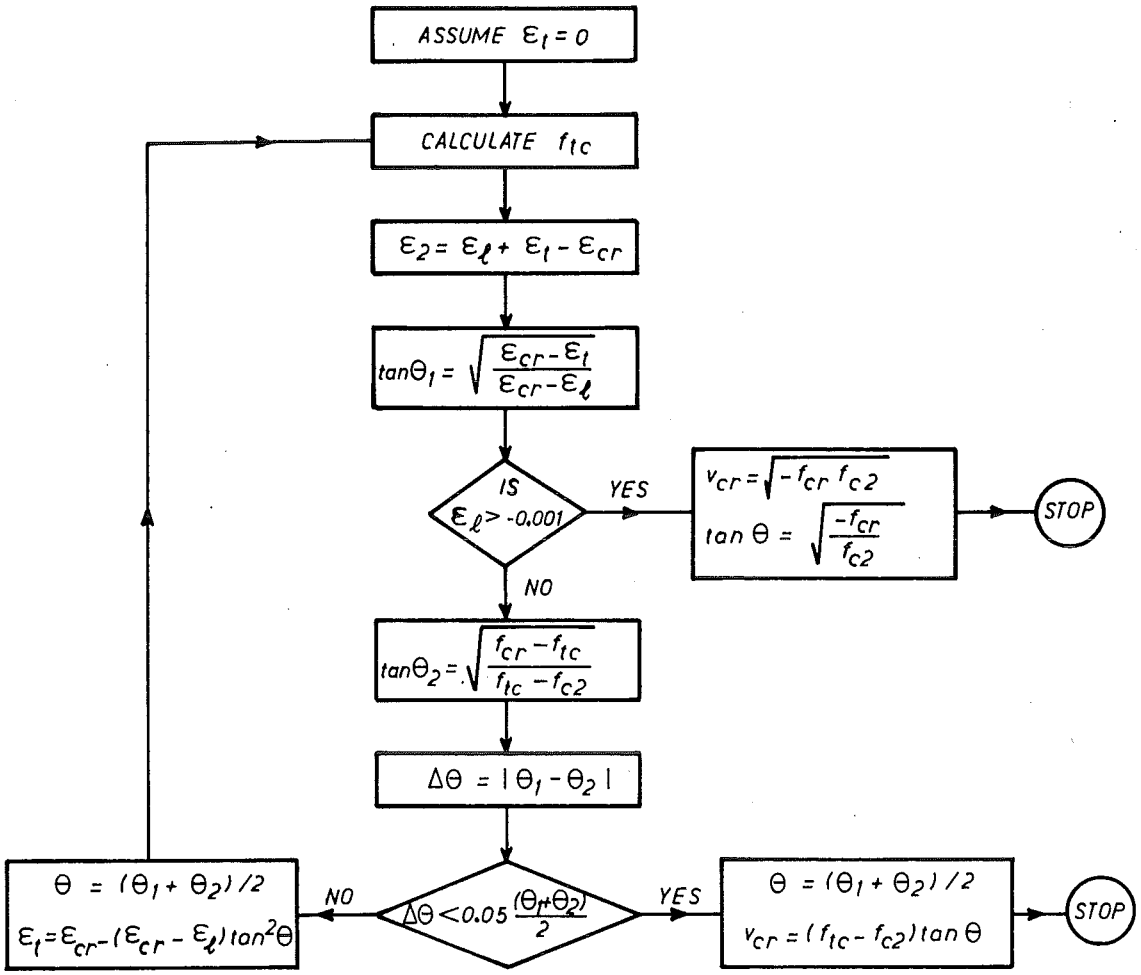

Fig. 6.14 : Flow chart showing the determination of diagonal cracking stress of a concrete element

for convenience of computation when $\varepsilon_\ell \geq \varepsilon_{cr}$ and the determination of v_{cr} is carried out only when $\varepsilon_\ell < \varepsilon_{cr}$.

6.3.2.2 To iterate when the shear stress, v , is less than the cracking shear stress, v_{cr}

As has been commonly noted before, that the transverse reinforcement is practically unstrained prior to diagonal cracking so the value of ε_t, and hence, f_{tc}, should remain close to zero if $v < v_{cr}$. If the shear stress acting on the concrete element is lower than the value of v_{cr} calculated in Section 6.3.2.1 and is non-zero, then the longitudinal normal stress, $f_{\ell c}$, of concrete is determined in the following manner:

Step 1 : Take $\varepsilon_t = 0$ as a first estimate

Step 2 : Use Eq. 6.25, with $\nu_1 = 1$ and $x = \dfrac{\varepsilon_\ell}{\varepsilon_{cc}}$, to obtain an initial estimate of $f_{\ell c}$

Step 3 : Calculate $f_{tc} = -\rho_{st} f_{ts}$ (from Eq. 6.30d) for transverse equilibrium, with f_{ts} determined from the stress-strain relationship of the transverse steel.

Step 4 : Calculate θ from the stress circle such that

$$\tan 2\theta = \frac{2v}{f_{tc} - f_{\ell c}}$$

Step 5 : With θ known, calculate ε_2 from the strain circle using the following equation

$$\varepsilon_2 = \frac{\varepsilon_\ell - \varepsilon_t \tan^2\theta}{1 - \tan^2\theta}$$

Step 6 : Calculate the principal compressive stress, f_{c2}, from the concrete stress-strain relationship given by Eq. 6.25 with ε_2 from Step 5.

Step 7 : Check the estimate of $f_{\ell c}$ from consideration of stress circle,

$$f^*_{\ell c} = f_{c2} + v \tan\theta$$

Step 8 : If the difference between $f_{\ell c}$ and $f^*_{\ell c}$ is not within acceptable limits, then return to Step 4 with a new estimate of $f_{\ell c}$.

Step 9 : If satisfied with the result from Step 7, calculate the principal tensile stress, f_{c1}, as follows,

$$f_{c1} = f_{\ell c} + f_{tc} - f_{c2}$$

Step 10 : Determine ε_1 from the concrete stress-strain relationship, and since ε_1 has to be lower than ε_{cr}, it can be obtained as follows:

$$\varepsilon_1 = \frac{f_{c1}}{E_c}$$

where E_c is given by Eq. 6.17.

Step 11 : Check estimate of ε_t from consideration of strain circle

$$\varepsilon_t^* = \varepsilon_1 + \varepsilon_2 - \varepsilon_\ell$$

Step 12 : If necessary, make a new estimate of ε_t and repeat the procedure from Step 3 until the agreement between the estimated and the computed values are within reasonable limits.

Step 13 : Extract the required information such as ε_t and $f_{\ell c}$.

Note that if no shear stress is acting on the concrete element, the procedure is straightforward and the value of $f_{\ell c}$ is determined using the uniaxial concrete stress-strain relationship (i.e. Eq. 6.25 with $\nu_1 = 1$) with $f_{\ell c} = 0$ for positive ε_ℓ values and the angle θ is equal to 0-deg or 90-deg depending on whether ε_ℓ is negative or positive. The stress and strain circles are therefore reduced to a point. Finally, if $\varepsilon_\ell = 0$ and $v < v_{cr}$, the angle θ is taken to be 45-deg and the stress circle is centred at the origin, with a radius equal to v.

6.3.2.3 To iterate when the shear stress, v , is greater than the cracking shear stress, v_{cr}

If the shear stress acting on the concrete element is greater than v_{cr}, the solution can be obtained by assuming two additional values on the strain (or stress) circle in order to define the circle, and from the stress-strain relationships of concrete and/or transverse steel, the co-existing stress (or strain) circle can be constructed. Then, the assumed values are adjusted until agreement between the values of angle θ obtained from the stress and strain circles is achieved. The

procedure is simpler with the assumption of ε_1 instead of the other two strain values (ε_t and ε_2) because of two computational conveniences. Firstly, it is because the principal tensile stress, f_{cl}, is independent of a second strain parameter as in the case of principal compressive stress, f_{c2}, and secondly, from the consideration of transverse equilibrium (Eq. 6.30d), the angle θ can be calculated without the need of an estimation. If $\rho_{st} > 0$ and the transverse steel is not yielding (i.e. $\varepsilon_t < \varepsilon_{yt}$), then

$$f_{tc} = - \rho_{st} E_{st} \varepsilon_t \tag{6.36}$$

and since $$\tan^2\theta = \frac{\varepsilon_1 - \varepsilon_t}{\varepsilon_1 - \varepsilon_\ell}$$

then $$\varepsilon_t = \varepsilon_1 (1 - \tan^2\theta) + \varepsilon_\ell \tan^2\theta \tag{6.37}$$

Substitute ε_t from Eq. 6.37 into Eq. 6.36 gives rise to a quadratic equation in terms of $\tan\theta$, i.e.

$$\rho_{st} E_{st} (\varepsilon_1 - \varepsilon_\ell)\tan^2\theta + v \tan\theta - (\rho_{st} E_{st}\varepsilon_1 + f_{cl}) = 0 \tag{6.38}$$

which can then be solved for θ. However, if the value of θ calculated is greater than that when the transverse reinforcement has yielded then the angle takes on a value such that

$$\tan\theta = \frac{f_{cl} + \rho_{st} f_{yt}}{v} \tag{6.39}$$

The computational procedure is summarized in nine steps as given below:

Step 1 : Take $\varepsilon_1 = 1.1\varepsilon_\ell + 0.00005 \geq 0.00005$ as a first estimate.

Step 2 : Calculate f_{cl} from concrete stress-strain relationship, i.e. Eq. 6.28 or 6.29.

Step 3 : Calculate θ, which is the smaller of the values given by Eqs. 6.38 and 6.39.

Step 4 : Calculate f_{c2} from the following equation from the consideration of stress circle.

$$f_{c2} = f_{cl} - v (\tan\theta + \cot\theta)$$

Step 5 : Check that the assumed value of ε_1 does not give rise to a magnitude of f_{c2} (from Step 3) that is greater than the

maximum possible value of $\nu_1 |f'_{cc}|$, i.e.

$$\frac{\nu_1 f'_{cc}}{f_{c2}} \geq 1$$

or

$$\frac{1}{\nu_1} \leq \frac{f'_{cc}}{f_{c2}}$$

$$(0.8 - 0.34 \frac{\varepsilon_1}{\varepsilon_o}) \leq \frac{f'_{cc}}{f_{c2}}$$

$$\varepsilon_1 \leq (0.8 - \frac{f'_{cc}}{f_{c2}}) \frac{\varepsilon_o}{0.34}$$

Otherwise return to Step 2 with a lower estimate of ε_1 . Combining Steps 4 and 5, the value of ε_1 for a typical example with f'_{cc} = - 34.4 MPa and f_{cr} = 1.81 MPa has to lie within the region shown in Fig. 6.15. The feasible range of ε_1 decreases as v increases. Note that from purely mathematical consideration the feasible value of ε_1 at low shear stress can be as high as 10 percent which is unlikely in real situations.

Step 6 : From the known values of f_{c2} and ε_1 the value of ε_2 can be obtained by solving Eq. 6.25 in a reversed manner. From Eq. 6.25,

$$f_{c2} = \nu_1 \frac{f'_{cc} \, x \, r}{(r-1) + x^r} \quad , \quad x = \frac{\varepsilon_2}{\varepsilon_{cc}}$$

Therefore, $$\frac{f_{c2}}{\nu_1 f'_{cc}} = \frac{xr}{(r-1) + x^r}$$

or $$\frac{f_{c2}}{\nu_1 f'_{cc}} \frac{x^r}{r} - x + \frac{f_{c2}}{\nu_1 f'_{cc}} \frac{(r-1)}{r} = 0$$

A solution of x , and hence ε_2 , can be found by solving the above polynomial equation using Newton-Raphson's method of iteration. The checking procedure in Step 5 is required to ensure that a solution of the above polynomial equation is possible. Fig. 6.16 illustrates graphically an example of how the determination of the solution is affected by the values of ε_1 , and hence ν_1 , in the polynomial equation.

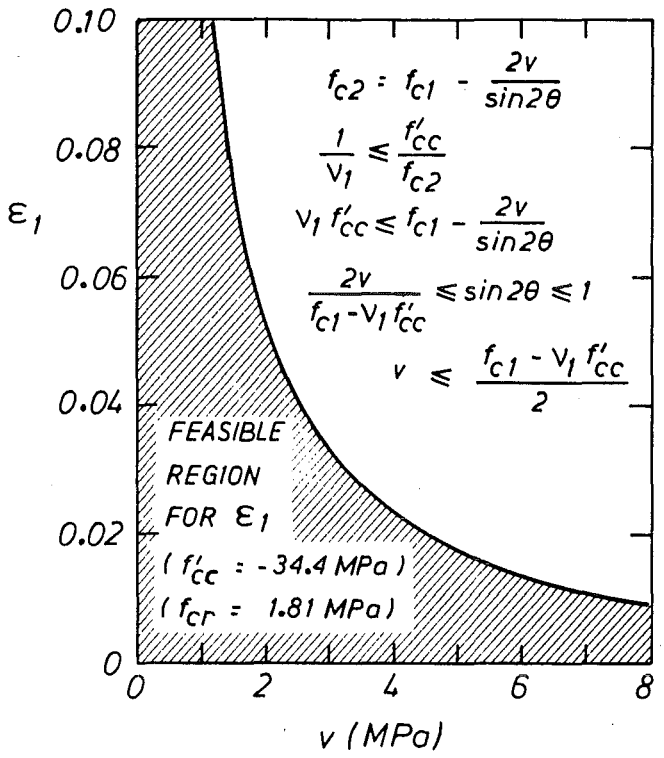

Fig. 6.15 : Feasible range of principal tensile strain, ε_1, for different levels of shear stress

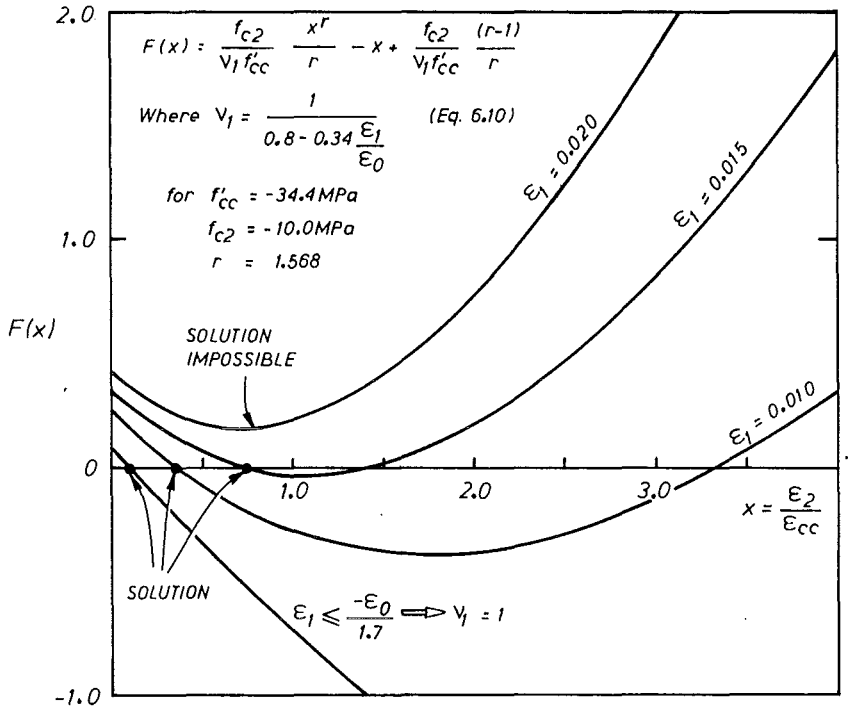

Fig. 6.16 : Graphical solution of polynomial equation, F(x), for different values of principal tensile strain

Step 7 : From the calculated value of ε_2, the assumed value of ε_1 can be checked using the following equation from consideration of strain circle.

$$\varepsilon_1^* = \frac{(\varepsilon_\ell - \varepsilon_2)}{\tan^2\theta} + \varepsilon_\ell$$

Step 8 : Repeat the procedure from Step 2 onwards if the agreement between ε_1 and ε_1^* is not satisfactory.

Step 9 : Extract the desired information from the stress and strain circles after convergence has been reached, e.g.

$$\varepsilon_t = \varepsilon_1 + \varepsilon_2 - \varepsilon_\ell$$

$$f_{\ell c} = f_{c1} - \frac{v}{\tan\theta}$$

Besides the condition discussed in Step 5, the value of ε_1 is also required to satisfy the condition that

$$\varepsilon_2 = \varepsilon_\ell - (\varepsilon_1 - \varepsilon_\ell)\tan^2\theta < 0$$

$$\Rightarrow \varepsilon_1 > \frac{\varepsilon_\ell}{\sin^2\theta} > 0 \qquad (6.40)$$

This condition provides a lower bound to the value of ε_1. On the other hand, the condition of Step 5 can be expressed in another form, i.e.

$$\frac{1}{\nu_1} \leq \frac{f'_{cc}}{f_{c2}}$$

$$\Rightarrow \sin 2\theta \geq \frac{2v}{f_{c1} - \nu_1 f'_{cc}} \qquad (6.41)$$

and it gives an upper bound to the volume of ε_1. These two conditions are illustrated in Fig. 6.17, using a typical example with $f'_{cc} = -34.4$ MPa and $f_{cr} = 1.81$ MPa. Two sets of curves for different values of v and ε_ℓ are shown. A solution may be possible only if the two curves intersect each other and the feasible region of ε_1 is shown shaded for the case when $v = 3$ MPa and $\varepsilon_\ell = 0.015$. Note that the size of this feasible region is reduced if v is increased for a fixed value of ε_ℓ, or if ε_ℓ is increased for a fixed value of v. Also shown in the figure is a curve showing the variation of ε_1 with θ when the transverse reinforcement has yielded, i.e. Eq. 6.39. In the example used, $\rho_{st} f_{yt}$ is taken to be 3 MPa and the feasible range of ε_1 is reduced to the solid line lying within the shaded region. Note that, since v

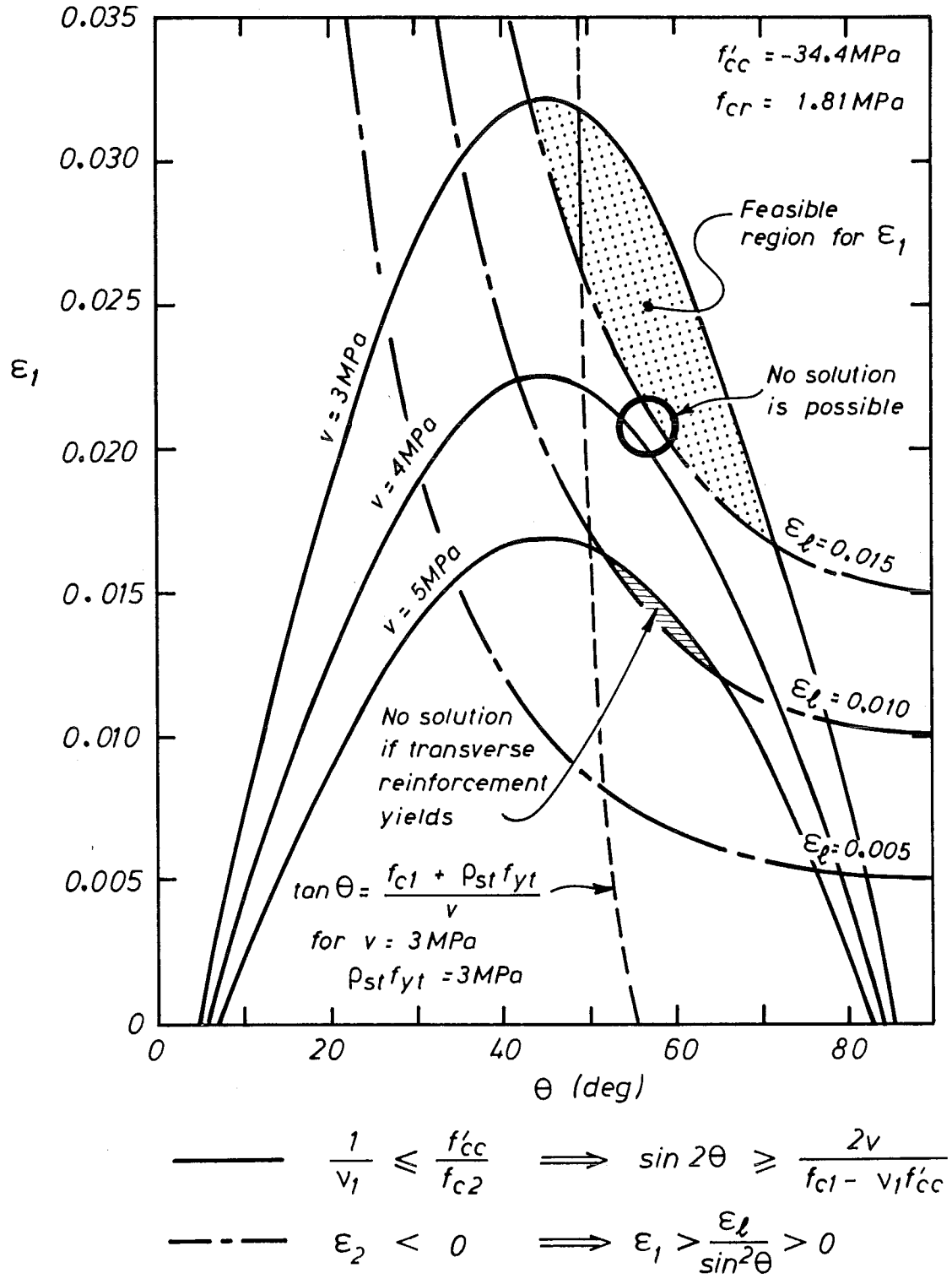

Fig. 6.17 : Upper and lower bounds of permissible ε_1 values

appears in the denominator in Eq. 6.39, the curve will move in the direction of decreasing θ if v increases. Hence, for the case of $v = 5$ MPa and $\varepsilon_\ell = 0.010$, no solution is possible if the transverse reinforcement has yielded. Nevertheless, the values of v and ε_ℓ cited for illustration are quite large, so in normal circumstances, it is usually the upper bound value of ν_1 that governs.

The algorithm outlined above is illustrated in graphical form in Fig. 6.18, in which the stresses are non-dimensionalised by dividing by f'_{cc}. The underlying idea of the approach can be thought of as finding a value of ε_1 that will result in an agreement between the f_{c2} values determined independently from the stress circle and the stress-strain behaviour of concrete, i.e.

$$f_{c2} = \frac{\nu_1 f'_{cc} \, xr}{(r-1+x^r)} = f_{c1} - v\,(\tan\theta + \cot\theta) \qquad (6.42)$$

In the figure it can be seen that the value of f_{c2} from consideration of the stress circle is rather insensitive to variation in ε_1 and ε_ℓ. On the other hand, the value obtained from the stress-strain relationship of concrete changes signigicantly as ε_1 and ε_ℓ are varied. The general shape of the curves is similar to that of the stress-strain relationship but there is a shift towards larger ε_1 values and a drop in the peak value of f_{c2} as ε_ℓ increases. A solution is possible only if the two curves intersect each other as for all the ε_ℓ values except $\varepsilon_\ell = 0.0025$ shown in the illustration. Note that the curves cross each other at two points but the one at higher ε_1 value corresponds to the situation when $f_{c2} = \nu_1 f'_{cc}$. In the case when no solution is possible, the determination of v_{max} (discussed in Section 6.3.2.4) is equivalent to lowering the shear stress in the concrete element so that the two curves touch each other at this higher value of ε_1. Also shown in Fig. 6.18 is the value of $f_{\ell c}$ obtained from the stress circle for different values of ε_1. As can be seen in the figure, $f_{\ell c}$ is also not very sensitive to ε_ℓ and ε_1 for a fixed value of v, unless the value of ε_1 is small.

If no solution can be found after going through the above procedure, the shear stress acting on the concrete element may be too large for that particular level of longitudinal strain, ε_ℓ, on the element with the transverse reinforcement content of ρ_{st}. Hence, the failure shear stress, v_{max}, of that element is calculated and the sub-program returns the appropriate information associated with $v_{max} (< v)$ to the main program. The determination of v_{max} is given in the next section.

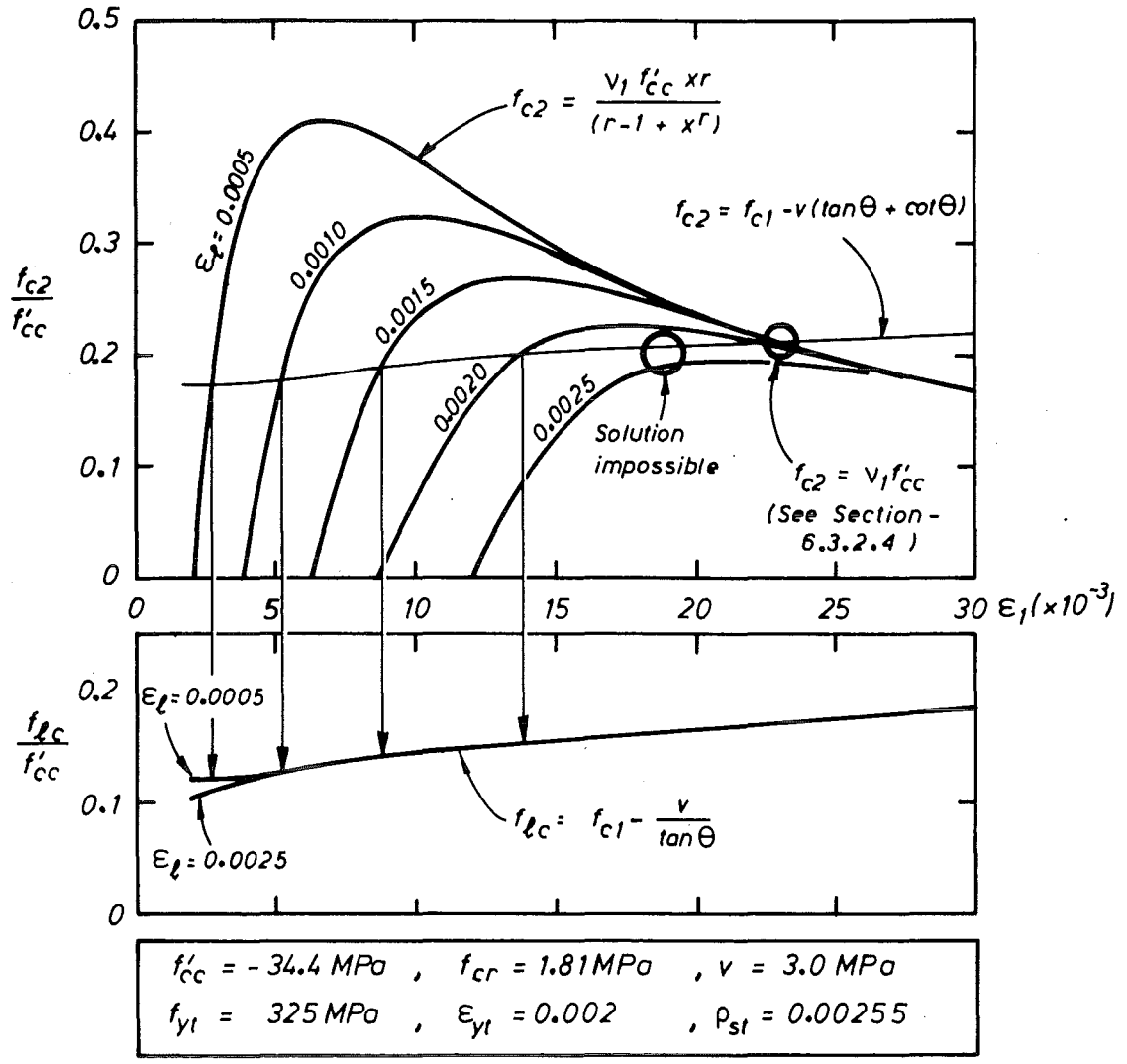

Fig. 6.18 : Determination of longitudinal concrete stress, $f_{\ell c}$, when the shear stress, v , is greater than the diagonal cracking stress, v_{cr}

6.3.2.4 The determination of failure stress, v_{max}

Two assumptions are involved in the determination of the maximum shear stress a concrete element is capable of resisting, with the given values of ε_ℓ, the reinforcing details and the material properties. These assumptions are:

(a) that the yielding of transverse reinforcement precedes the crushing of concrete under the principal compressive strain; and

(b) that the principal concrete compressive strain at failure reaches the value of ε_{cc}, and therefore $f_{c2} = \frac{f'_{cc}}{\nu_1}$

From the above assumptions, the value of the principal compressive stress can be determined independently in two different ways: from the consideration of the stress circle,

$$f_{c2} = f_{cl} - \frac{v}{\sin\theta \cos\theta} \tag{6.43a}$$

and, from the stress-strain relationship of concrete,

$$f_{c2} = \frac{f'_{cc}}{(0.8 - 0.34 \frac{\varepsilon_1}{\varepsilon_o})} \tag{6.43b}$$

By equating Eqs. 6.43a and b, the shear stress, v, can be found in terms of the other quantities, i.e.

$$f_{cl} - \frac{v}{\sin\theta \cos\theta} = \frac{f'_{cc}}{(0.8 - 9.34 \frac{\varepsilon_1}{\varepsilon_o})}$$

Therefore, $$v = \left[f_{cl} - \frac{f'_{cc}}{(0.8 - 0.34 \frac{\varepsilon_1}{\varepsilon_o})} \right] \sin\theta \cos\theta \tag{6.44}$$

But also from the stress circle,

$$v = \frac{f_{cl} - f_{tc}}{\tan\theta}$$

$$= \frac{f_{cl} + \rho_{st} f_{yt}}{\tan\theta} \tag{6.45}$$

Hence, equating Esq. 6.44 and 6.45,

$$\frac{f_{cl} + \rho_{st} f_{yt}}{\tan\theta} = \left[f_{cl} - \frac{f'_{cc}}{(0.8 - 0.34 \frac{\varepsilon_1}{\varepsilon_o})} \right] \sin\theta \cos\theta \tag{6.46}$$

Then, by rearranging Eq. 6.46

$$\frac{1}{\sin^2\theta} = \text{cosec}^2\theta = \frac{f_{cl} - \dfrac{f'_{cc}}{(0.8 - 0.34\,\frac{\varepsilon_1}{\varepsilon_o})}\,\frac{\varepsilon_1}{\varepsilon_o}}{f_{cl} + \rho_{st}\, f_{yt}} \qquad (6.47)$$

Since $\cot^2\theta = \text{cosec}^2\theta - 1$, therefore,

$$\cot^2\theta = \left[\frac{f_{cl} - \dfrac{f'_{cc}}{(0.8 - 0.34\,\frac{\varepsilon_1}{\varepsilon_o})}\,\frac{\varepsilon_1}{\varepsilon_o}}{f_{cl} + \rho_{st}\, f_{yt}} - 1\right]$$

$$= \left[\frac{-\dfrac{f'_{cc}}{(0.8 - 0.34\,\frac{\varepsilon_1}{\varepsilon_o})}\,\frac{\varepsilon_1}{\varepsilon_o} - \rho_{st}\, f_{yt}}{f_{cl} + \rho_{st}\, f_{yt}}\right] \qquad (6.48)$$

But, from the consideration of strain circle,

$$\cot^2\theta = \frac{\varepsilon_1 - \varepsilon_\ell}{\varepsilon_\ell - \varepsilon_{cc}}$$

Therefore

$$\frac{\varepsilon_1 - \varepsilon_\ell}{\varepsilon_\ell - \varepsilon_{cc}} = \left[\frac{-\dfrac{f'_{cc}}{(0.8 - 0.34\,\frac{\varepsilon_1}{\varepsilon_o})}\,\frac{\varepsilon_1}{\varepsilon_o} - \rho_{st}\, f_{yt}}{f_{cl} + \rho_{st}\, f_{yt}}\right] \qquad (6.49)$$

Eq. 6.49 after rearrangement gives rise to the following equation,

$$\left\{\frac{-0.35}{\varepsilon_o}[f_{cl} + \rho_{st}\, f_{yt}]\right\}\varepsilon_1^2 + \left\{0.8[f_{cl} + \rho_{st}\, f_{yt}] + \frac{0.34}{\varepsilon_o}[\varepsilon_\ell f_{cl} + \rho_{st}\, f_{yt}\, \varepsilon_{cc}]\right\}\varepsilon_1$$

$$- \{0.8[\varepsilon_\ell f_{cl} + \rho_{st}\, f_{yt}\, \varepsilon_{cc}] + [\varepsilon_{cc} - \varepsilon_\ell]\, f'_{cc}\} = 0 \qquad (6.50a)$$

Eq. 6.50a can be solved by an iterative approach to obtain the value of ε_1 . As a first approximation, f_{cl} can be taken to be zero, and Eq. 6.50a is reduced to a quadratic equation with ε_1 as the only unknown, viz.

$$-\frac{0.34}{\varepsilon_o}\varepsilon_1^2 + (0.8 + \frac{0.34}{\varepsilon_o}\varepsilon_{cc})\varepsilon_1 - \{0.8\varepsilon_{cc} + \frac{f'_{cc}(\varepsilon_{cc} - \varepsilon_\ell)}{\rho_{st}\, f_{yt}}\} = 0 \qquad (6.50b)$$

The value of f_{cl} can then be calculated using the value of ε_1 from the solution of Eq. 6.50b. This value is substituted into Eq. 6.50a

so that a quadratic equation, also in terms of ε_1, can be obtained and solved for a new value of ε_1. The procedure is repeated until convergence is achieved. Since the value of ε_1 at this stage is likely to be large, the value of f_{cl} is rather insensitive to the change of ε_1 during successive approximation. In fact, the value of ε_1 from the solution of Eq. 6.50b gives a good approximation of the final result using the more elaborate procedure. This value can be substituted into the appropriate equations to obtain the desired information such as

$$\varepsilon_t = \varepsilon_{cc} + \varepsilon_1 - \varepsilon_\ell$$

$$\tan\theta = \sqrt{\frac{\varepsilon_\ell - \varepsilon_{cc}}{\varepsilon_1 - \varepsilon_\ell}}$$

$$v_{max} = \frac{f_{cl} + \rho_{st} f_{yt}}{\tan\theta}$$

$$f_{\ell c} = f_{cl} - \frac{v_{max}}{\tan\theta}$$

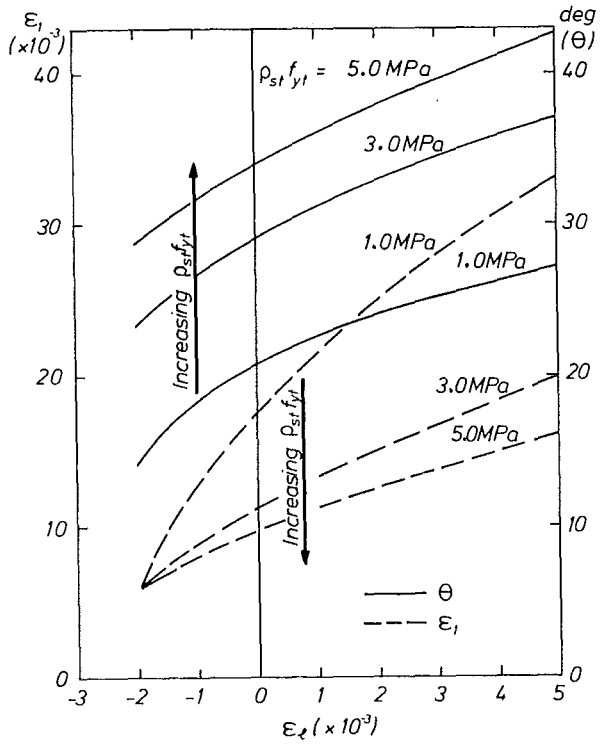

Fig. 6.19 : ε_1 and θ at failure shear stress, v_{max}, for different values of ε_ℓ (assuming $f_{cl} = 0$)

The results of ε_1 and θ calculated using Eq. 6.50b alone are plotted against ε_ℓ in Fig. 6.19 for three different values of $\rho_{st} f_{yt}$. Note that any variation in $\rho_s f_{yt}$ also results in a change in the values of ε_{cc} and f'_{cc} in Eq. 6.50b. The figure shows that θ increases and ε_1 decreases as the value of $\rho_{st} f_{yt}$ is increased if ε_ℓ remains constant. Also, for a fixed value of $\rho_{st} f_{yt}$, both θ and ε_1 decrease with decreasing value of ε_ℓ, which by virtues of the problem must not be lower than ε_{cc}. Hence in the subprogram, if $\varepsilon_\ell \leq \varepsilon_{cc}$ the maximum shear stress, v_{max}, is taken to be zero; the longitudinal normal stress, $f_{\ell c}$ is determined from uniaxial stress-strain relationship of concrete, and the angle θ is equal to 0-deg with respect to the column axis. In addition, if ε_ℓ is too small (i.e. more negative) there is a possibility that the value of ε_t computed is lower than the yield strain of the transverse steel and therefore the first assumption is violated. Hence, if this happens, the concrete element is treated as in the case when $\varepsilon_\ell \leq \varepsilon_{cc}$. On the other hand, if ε_1 is too large, there is a possibility that the transfer of shear stress across cracks is severed. So, the maximum shear stress, v_{max} is again taken to be zero but in this case, the angle θ is equal to 90-deg and the value of f_{cl} is zero.

6.3.2.5 The subprogram to analyse the concrete layers

The above procedures are combined into a subprogram to analyse the concrete layers. As it involves several loops of iterations, the maximum number of iterations in one loop is limited to 20. Usually, if a solution exists, only a few iterations are required to achieve convergence. If no solution is possible after going through 20 iterations, the next step in the subprogram is followed. Fig. 6.20 briefly summarizes the computational procedures involved in the form of flow chart.

The subprogram is entered with the necessary information from the main program and started with the determination of v_{cr}. If the longitudinal strain, ε_ℓ, is negative, or the shear stress is lower than v_{cr}, the procedure outlined in Section 6.3.2.2 is followed. Otherwise, or when no solution from this procedure is possible, the iteration procedure in Section 6.3.2.3 is used. As discussed earlier, the shear stress computed may be in excess of the failure shear stress, v_{max}, and in that situation, no solution is likely from these procedures. Hence, the failure stress is determined according to the procedure in Section 6.3.2.4 if no convergence is possible in the above procedures.

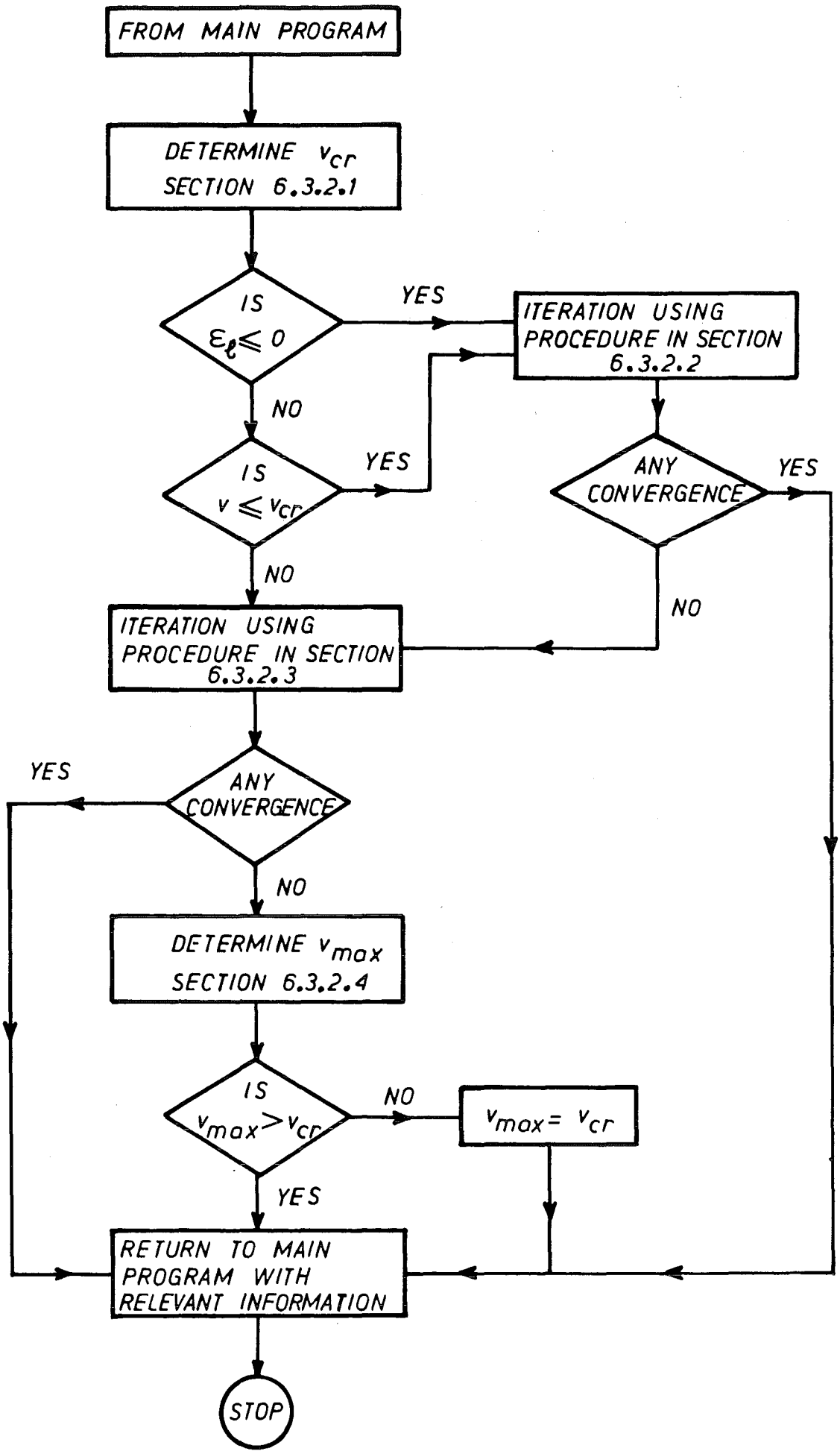

Fig. 6.20 : Flow chart showing how a biaxially stressed concrete element is analysed

However, if ε_ℓ has a large negative value, the value of v_{max} may be smaller than v_{cr}, so the failure stress is taken to be v_{cr}.

6.3.3 The Main Program

Two loops of iterations are required in the main program in order to arrive at compatible longitudinal and shear stress distributions, with the iteration on axial load carried out twice (once for each of the two sections concerned). Instead of describing the main program in detail, only some important features are discussed in this section.

(a) The program makes use of an interactive system so that the user has some control over the iteration procedure. Initially, the bottom strain, ε_{bot}, (see Fig. 6.8b) is input by the user and if no convergence is achieved after every five iterations, the user is asked to try a new value for ε_{bot} and the process is repeated. The user also has the freedom to vary the distance between the two sections (Fig. 6.9) by just changing the top strain, ε_{top}, of Section 2 allowed by the program through the interactive system.

(b) The section is discretized into no more than 20 layers of concrete laminae because of the time-consuming computational process involved. The first and last elements are taken to be the cover concrete measured to the centre-line of the transverse reinforcement and therefore, $\rho_{st} = 0$ and $v = 0$ in these elements. Consequently, only the uniaxial unconfined stress-strain behaviour is considered in the analysis of both these elements. As discussed in Section 2.4.4, the value of ρ_{st} in circular section with transverse spiral reinforcement is taken to be one-half the volumetric spiral reinforcement content, ρ_s.

(c) The spalling strain of the cover concrete is taken to be $2\varepsilon_o$, so if the longitudinal strain of the concrete element is such that $\varepsilon_\ell \leq 2\varepsilon_o$, the cover concrete is considered to have spalled and the area of the element is reduced by a factor $\frac{(D - 2 \times \text{cover})^2}{D^2}$ where D is the overall diameter of the column. In the case of the first concrete element at the top, the area is reduced to zero. All subsequent calculations are then based on the core area of the affected concrete elements.

(d) The program offers two options of a self generating initial parabolic shear stress distribution across the section and a user-specified initial shear stress distribution. A second section across the column is required in the analysis to check the validity

of the shear stress distribution as discussed in Section 6.3.1. This second section is chosen by specifying a different ε_{top} value, to give a different bending moment from that of Section 1. The same shear stress distribution is used in both sections. In the case of concrete element with large positive longitudinal strain, the yielding of longitudinal reinforcement may lead to a negative computed shear stress on that element. In such a situation the computed shear stress is taken to be zero. Sometimes, when the shear force acting is large and especially when the section is near the failure stage, the distance of the second section from section 1 may need to be as large as $\frac{D}{3}$ in order to ensure that a solution is possible. In other words, the top strain, ε_{top}, of section 2 specified may have to be substantially different from that of section 1.

(e) The relationship between the variables is usually unknown in most of the iterations in the main program and the subprograms. The iterations, therefore, have to be based on a modified form of Newton-Raphson's iteration procedure as illustrated in Fig. 6.21.

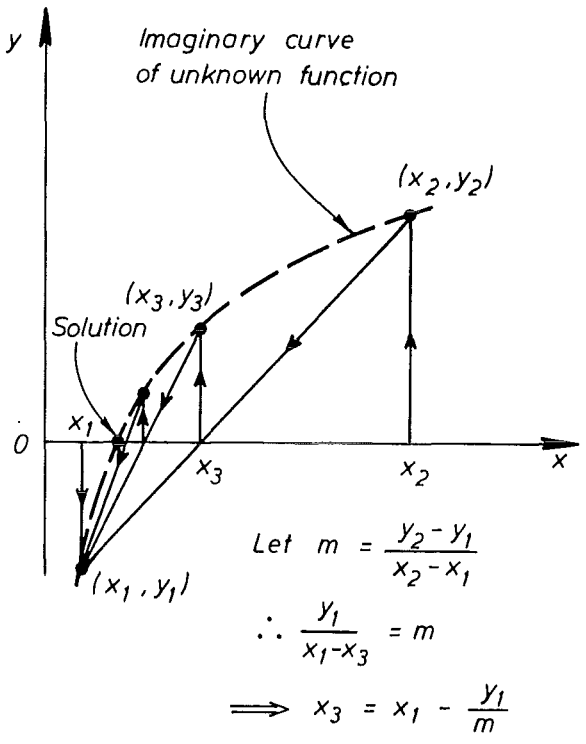

Fig. 6.21 : An iteration procedure using a modified Newton-Raphson's approach

The secant between two points on the unknown function instead of the tangent at a point of a known function is used in the iteration. Hence, as shown in Fig. 6.21, the iterations have to be started by choosing two initial values (x_1 and x_2) of x and calculating the corresponding values (y_1 and y_2) of y so that a straight line passing through both points can be fitted to obtain the next approximation. In the case of iteration on axial load in the main program, y corresponds to the difference between the computed and the specified axial load while x corresponds to bottom longitudinal strain. The user is therefore required to make a second estimate of ε_{bot} in order to start the iteration. No such provision is made in the subprogram for the other iterations because the program makes its own estimate for second approximation using the results from the initial calculation.

6.4 ANALYSIS OF THE STATIC TEST UNITS

The procedures outlined in the preceding section was used to analyse the behaviour of the static test units. The following subsections discuss the results obtained from the analyses.

6.4.1 Ultimate Shear Strength Of The Test Units

In the analyses, the shear force was increased in 50 kN increments until close to the ultimate stage. On approaching the ultimate stage the shear force increment was reduced to 5 kN, and the shear force above which convergence in the iterations could not be achieved was taken to be the ultimate shear strengths of the member. The analyses used shear force increments so that theoretical load-deflection curves (discussed in Section 6.4.2) could be constructed from the results. At each shear force level the top compressive strain, ε_{top}, was increased in 4-5 increments until the moment at the critical section, i.e. the column base, was reached or exceeded. Due to the restraining effect of the foundation beam, the condition of Eq. 6.30d requiring that $f_t = 0$ is no longer valid. Because of the confinement provided by the foundation beam, the critical section is shifted to a section some distance above the column base, and in the analyses it is assumed that this section is at a distance 0.25D (D = overall diameter of the column) away. This is based on a compression zone depth of approximately $\frac{D}{2}$, and a 45-deg core of influence from the base. A similar assumption was made by Priestley et al[6.13] in analysing results of squat bridge columns

under combined axial load and bending moment. It produced very close agreement with observed behaviour. Hence, if near the ultimate stage the moment at this 'relocated' critical section for a particular shear force cannot be reached then the number is considered to have failed earlier at smaller shear force, and the calculations are repeated with a smaller value of shear force. Due to time constraint for the project, a finer increment than 5 kN to get a more precise value of the ultimate shear strength was not used. A difference of 5 kN represents, in general, no more than 3 percent variation in the predicted value. The predicted ultimate strengths are compared with experimental values in Table 6.1. Also shown in the table are the ratios of the latter to the former. The average of the ratio is 1.08 with a standard deviation of 0.10. Compared with corresponding values of 1.00 and 0.06 (Table 5.3) predicted by the design proposal in Chapter Five, the agreement has been reasonable but the process involved is time consuming. The discrepancy tended to be greater in squatter columns in which failure along the corner-to-corner diagonal cracks was observed.

6.4.2 Load-Displacement Behaviour

6.4.2.1 The various displacement components

The lateral deflection of the cantilever column at the load application point was computed for each shear force increment to obtain

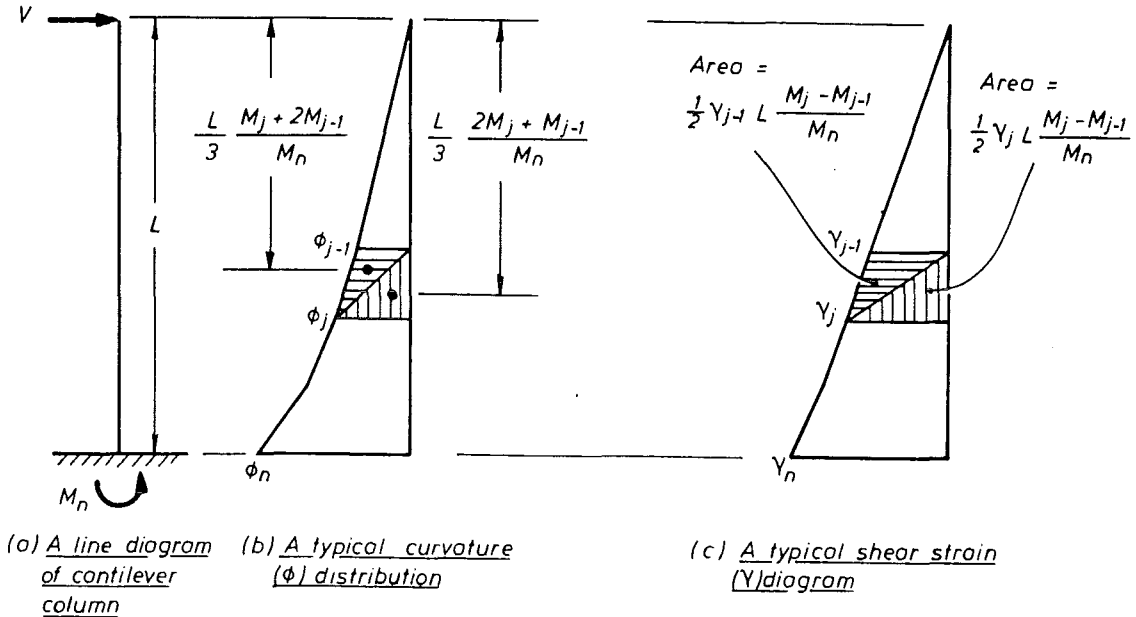

Fig. 6.22 : Typical curvature, ϕ , and shear strain, γ , distribution used in the determination of Δ_ϕ and Δ_γ

Table 6.1 : Comparison Of Predicted And Experimental Ultimate Strengths

Unit (1)	V_u (kN) (Expt) (2)	V_u (kN) (Theory) (3)	(2)/(3) (4)
1	320	300	1.067
2	228	240	0.950
3	298	270	1.104
4	295	300	0.983
5	340	320	1.063
6	390	360	1.083
7	280	295	0.949
8	475	405	1.173
9	385	335	1.149
10	450	420	1.071
11	404	380	1.063
12	527	450	1.171
13	443	400	1.108
14	311	300	1.037
15	230	220	1.045
16	379	350	1.083
17	329	300	1.097
18	507	400	1.267
19	436	365	1.195
20	487	365	1.334
21	258	290	0.890
22	280	285	0.982
23	339	320	1.059
24	338	325	1.040
25	233	-	-
		Ave	1.08
		σ	0.10

the load-displacement response of the column. The total deflection is the sum of component displacements due to curvature (Δ_ϕ) , shear strain (Δ_γ) , bending of foundation beam (Δ_B) and joint distortion (Δ_J) . The first two components were obtained from the computer analyses and the last two components had to be estimated with some assumptions.

(a) Displacement component due to curvature, Δ_ϕ

6.225

The displacement due to curvature can be computed by considering the curvature distribution along the column height, as shown for a typical example in Fig. 6.33b. The segment of the curvature diagram shown shaded can be approximated by two triangles. By summing the first moment of area of these triangles about the tip of the cantilever, its lateral deflection can be found. Hence, for the jth segment shown in the figure

$$\Delta_j = \frac{1}{2}\phi_j L \frac{(M_j - M_{j-1})}{M_n} \frac{L}{3} \frac{(2M_j + M_{j-1})}{M_n}$$

$$+ \frac{1}{2}\phi_{j-1} L \frac{(M_j - M_{j-1})}{M_n} \frac{L}{3} \frac{(M_j + 2M_{j-1})}{M_n} \qquad (6.51)$$

and by taking the summation, the total displacement due to curvature can be found from the following expression,

$$\Delta_\phi = \frac{1}{6}\left(\frac{L}{M_n}\right)^2 \sum_{j=1}^{n} (M_j - M_{j-1}) \left[\phi_j(2M_j + M_{j-1}) + \phi_{j-1}(M_j + 2M_{j-1})\right] \qquad (6.52)$$

where L is the distance from the load application point to the column base, and M_n and ϕ_n are the moment and curvature at the column base respectively. For each specified shear force level, variation in ε_{top} value gives rise to different values of moment and curvature and hence, the full curvature distribution along the column height can be obtained. As the critical section of the column, corresponding to the specified shear force level, was assumed to be at 0.25D (= 100 mm) above the column base, the curvature at the column base has to be obtained by extrapolation.

In addition, the effective fixity of the column was assumed to be at a distance equal to 0.25D ($\approx 6\, d_{b\ell}$, where $d_{b\ell}$ is the diameter of longitudinal bar diameter) into the foundation beam. The curvature within this region was assumed constant and equal to that at the column base obtained by extrapolation. The addition of this end region was to allow for the contribution to deflection due to possible yield

penetration and slippage of flexural rebars within the joint region, and is based on recommendations recently made by Priestley and Park[6.14].

(b) Displacement component due to shear strain, Δ_γ

The component displacement due to shear strain, Δ_γ, can be obtained in a similar manner as for the determination of Δ_ϕ. Because the shear stress and longitudinal strain vary across a particular section, the shear strain across the section is not a constant value. For the purpose of analysis, the maximum shear strain is used in the calculations. This shear strain value also varies along the column height. A shear strain diagram as shown in Fig. 6.22c can be obtained by analysing different sections of the column. From the shear strain diagram the displacement, Δ_γ, can be computed by finding the area of the diagram. Referring to Fig. 6.22c, the total area can be found by summing the area of the triangles shown, i.e.

$$\Delta_\gamma = \frac{1}{2}\left(\frac{R}{M_n}\right) \sum_{j=1}^{n} (M_j - M_{j-1})(\gamma_j + \gamma_{j-1}) \qquad (6.53)$$

Similar to the curvature distribution, the shear strain at the column base was obtained by extrapolation from the assumed critical section 100 mm away, and is assumed to vary linearly from the last section to the column base.

(c) Displacement component due to bending of foundation beam, Δ_B

The flexibility of the foundation beam, though small, also contributed to the deflection of the column. This component of displacement was estimated by considering the deflected shape of the structure, in line diagram, as shown in Fig. 6.23. The bending of the foundation beam resulted in additional displacement, Δ_B, which was obtained from the following consideration:

$$\theta = \frac{ML_B}{6E_B I_B}$$

Therefore $$\Delta_B = \theta(\ell + 225) = \frac{1}{6}\frac{ML_B}{E_B I_B}(\ell + 225)$$

$$= \frac{1}{6}\frac{VL_B}{E_B I_B}(\ell + 225)^2 \qquad (6.54)$$

where ℓ is the loading height from the column base, E_B, taken to be $5000\sqrt{f'_c}$, is the modulus of elasticity of the concrete in the foundation beam, and I_B is the moment of inertia of the cracked section assumed to be 60 percent of the gross moment of inertia of the beam section (i.e.

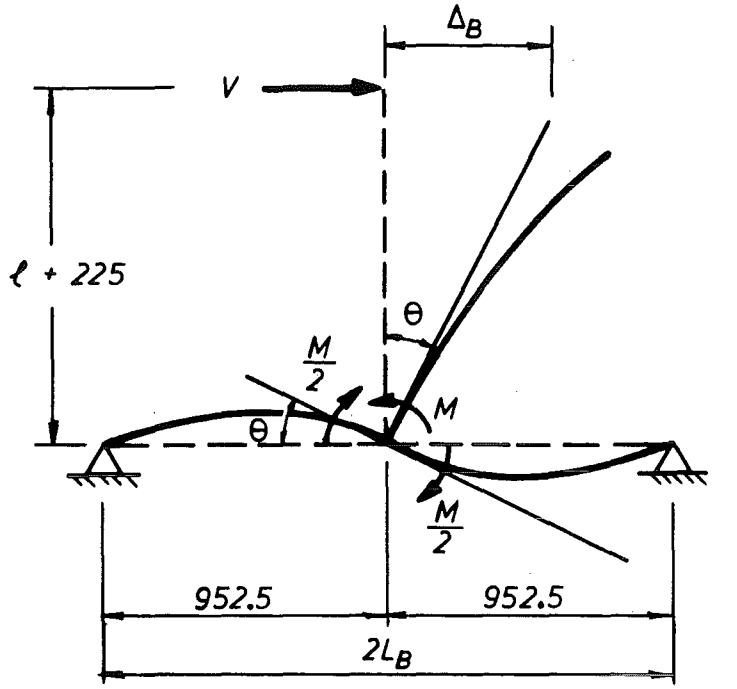

Fig. 6.23 : A line diagram of a deflected test structure

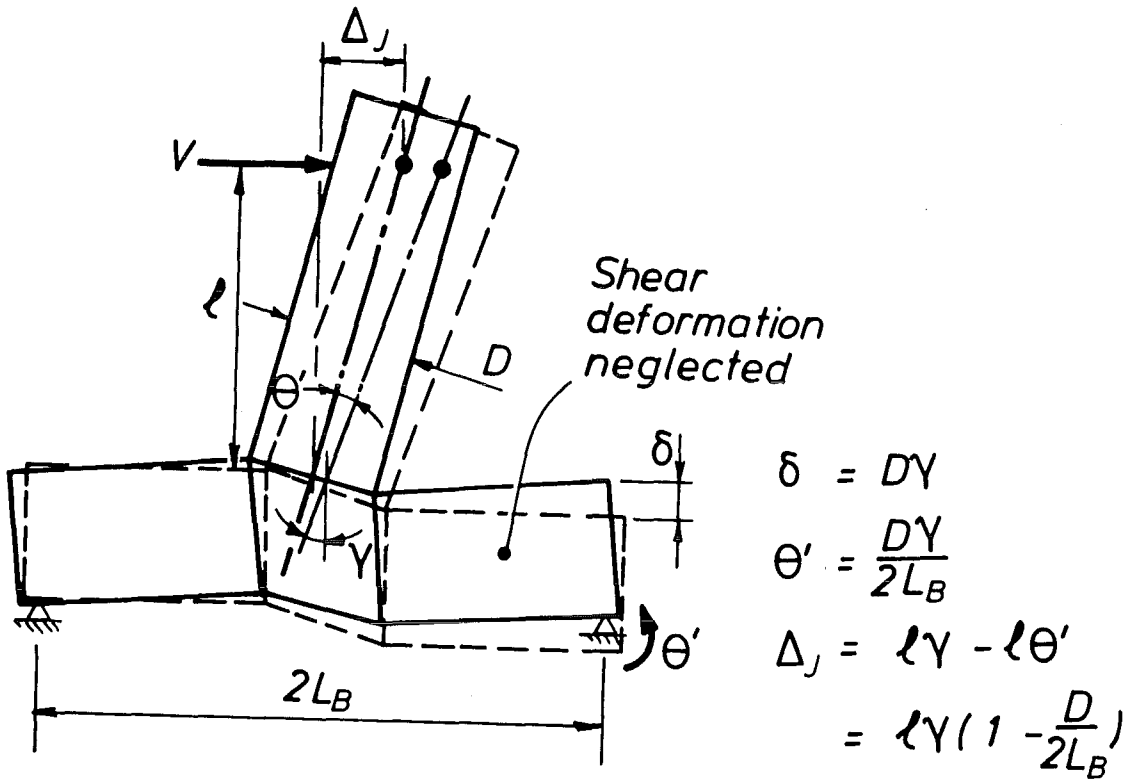

Fig. 6.24 : Deflection at load application point due to joint distortion

$0.6 \times \frac{550 \times 450^3}{12}$ mm^4) and L_B is the half span of the foundation beam.

(d) Displacement component due to joint distortion, Δ_J

The distortion of the beam column joint under the action of shear stress gives rise to another component of displacement. In order to estimate the magnitude of this distortion, the horizontal shear stress was assumed to act uniformly over an equivalent square joint of area 0.8D x 0.8D . The joint element was considered to be a panel subjected to pure shear and was analysed using the 'Diagonal Compression Field Theory'. From the resulting shear-stress-shear-strain response of the joint element, the value of Δ_J could be calculated as shown in Fig. 6.24, by substituting the appropriate value for D , ℓ and L_B . For simplicity, the presence of normal stress on the joint panel due to axial compression was ignored. The computation of this displacement component was subjected to greater uncertainty but since it is a relatively small contribution to the total column displacement, the error resulting from this computational uncertainty might not be very significant.

6.4.2.2 Load-displacement behaviour for loads less than the theoretical ultimate strength

(a) Comparison with experimental load-displacement response

The load-displacement response up to the development of the theoretical ultimate strength are compared with the experimental behaviour in Figs. 6.25a to j. In Fig. 6.25a the various displacement

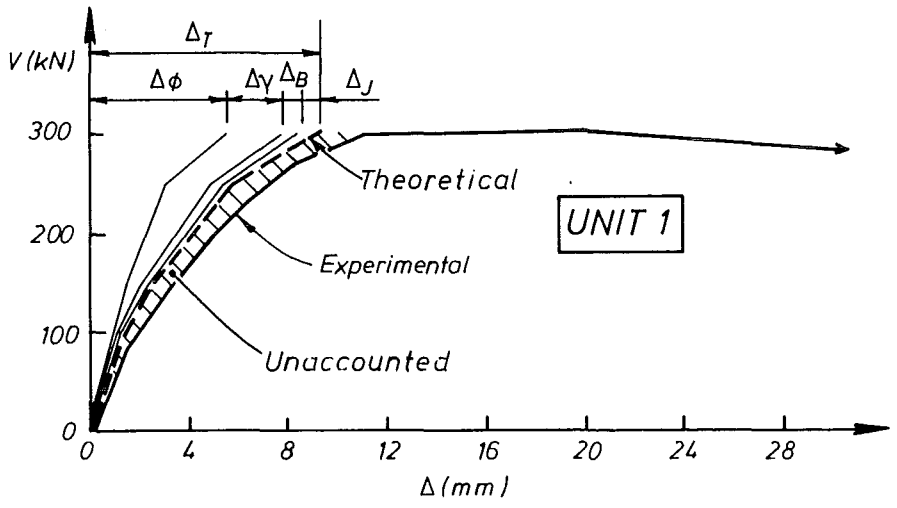

(a) Unit 1 ($\rho_s = 0.00509$, $\frac{M}{VD} = 2.0$, $\frac{P_i}{f'_c A_g} = 0$)

Fig. 6.25 : Comparison of predicted and experimental load-displacement response of static test columns

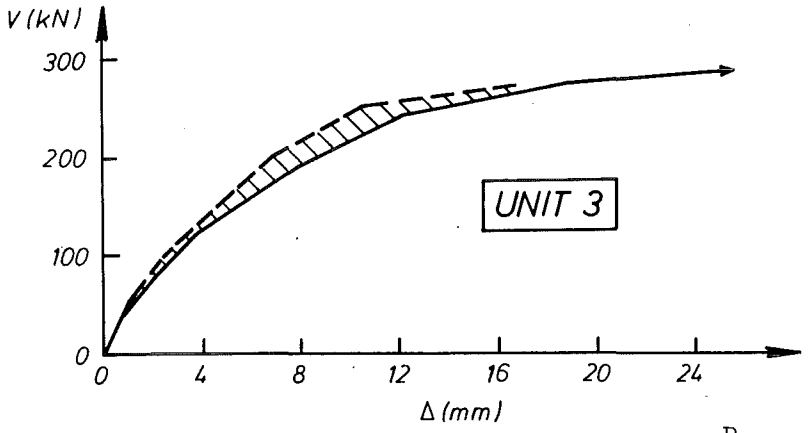

(b) Unit 3 ($\rho_s = 0.00509$, $\frac{M}{VD} = 2.5$, $\frac{P_i}{f'_c A_g} = 0$)

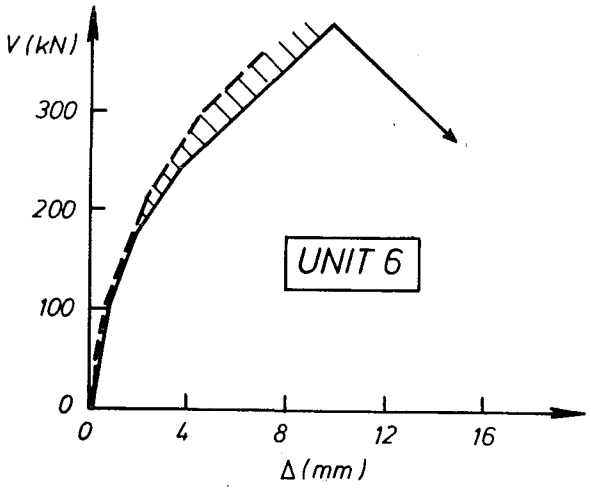

(c) Unit 6 ($\rho_s = 0.00509$, $\frac{M}{VD} = 1.5$, $\frac{P_i}{f'_c A_g} = 0$)

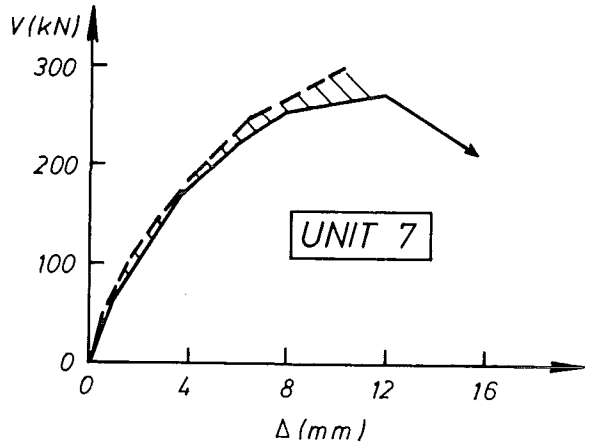

(d) Unit 7 ($\rho_s = 0.00382$, $\frac{M}{VD} = 2.0$, $\frac{P_i}{f'_c A_g} = 0$)

Fig. 6.25 (contd) : Comparison of predicted and experimental load-displacement response of static test columns.

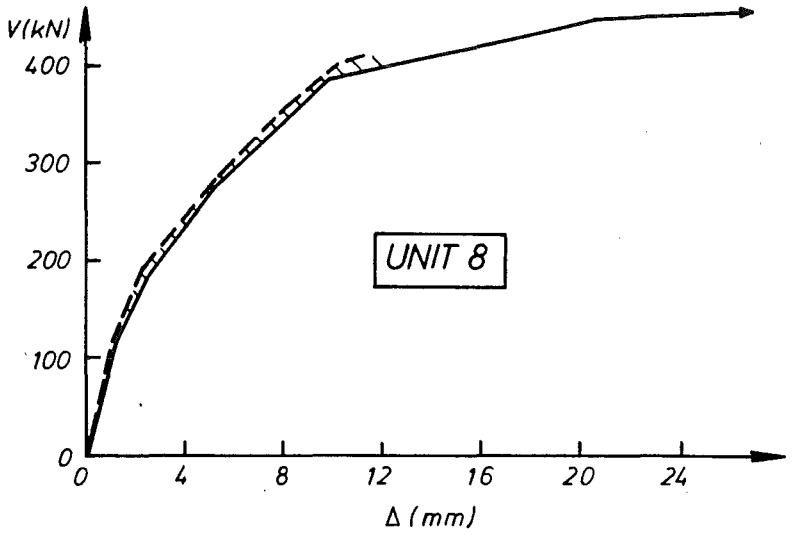

(e) Unit 8 ($\rho_s = 0.01019$, $\frac{M}{VD} = 2.0$, $\frac{P_i}{f'_c A_g} = 0.2$)

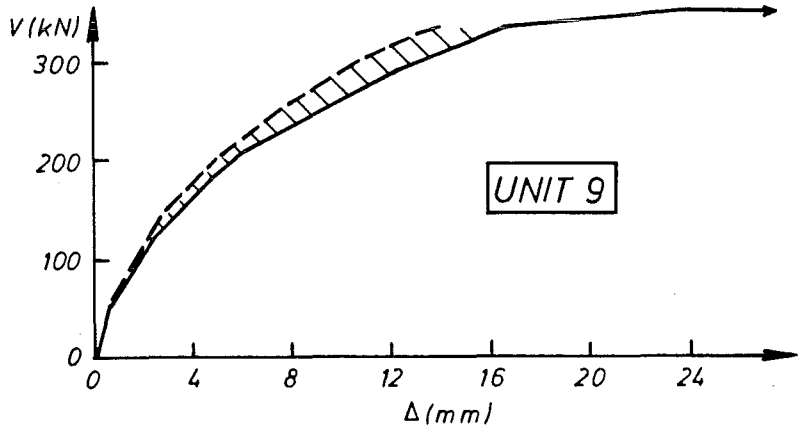

(f) Unit 9 ($\rho_s = 0.01019$, $\frac{M}{VD} = 2.5$, $\frac{P_i}{f'_c A_g} = 0.2$)

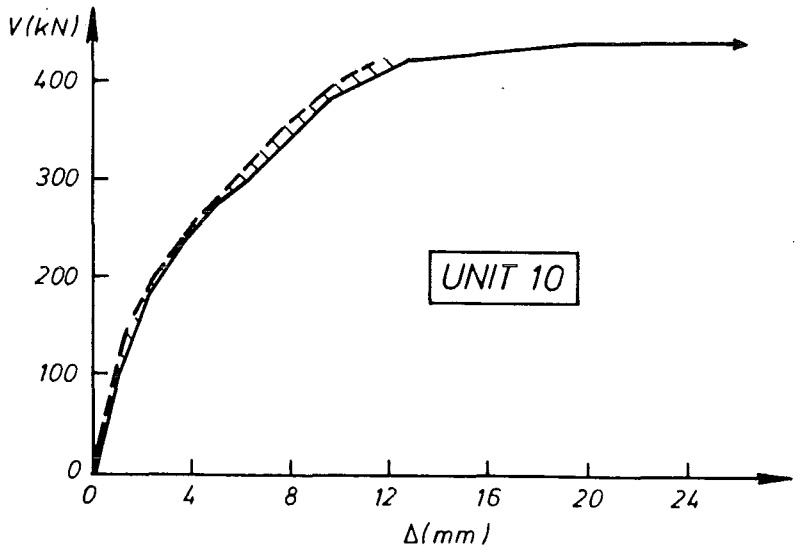

(g) Unit 10 ($\rho_s = 0.01019$, $\frac{M}{VD} = 2.0$, $\frac{P_i}{f'_c A_g} = 0.2$)

Fig. 6.25 (contd) : Comparison of predicted and experimental load-displacement response of static test columns.

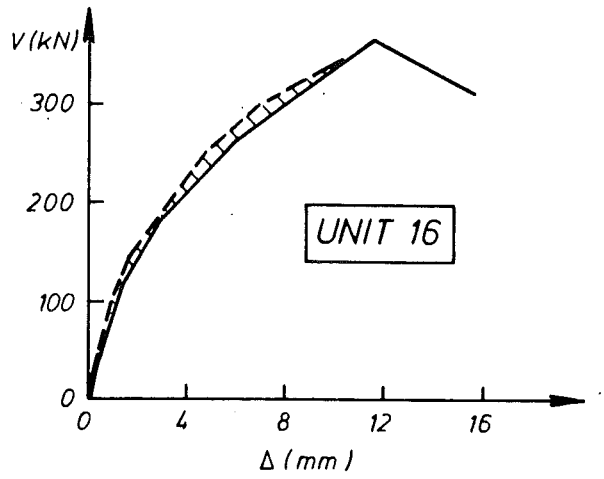

(h) Unit 16 (ρ_s = 0.00509 , $\frac{M}{VD}$ = 2.0 , $\frac{P_i}{f'_c A_g}$ = 0.1)

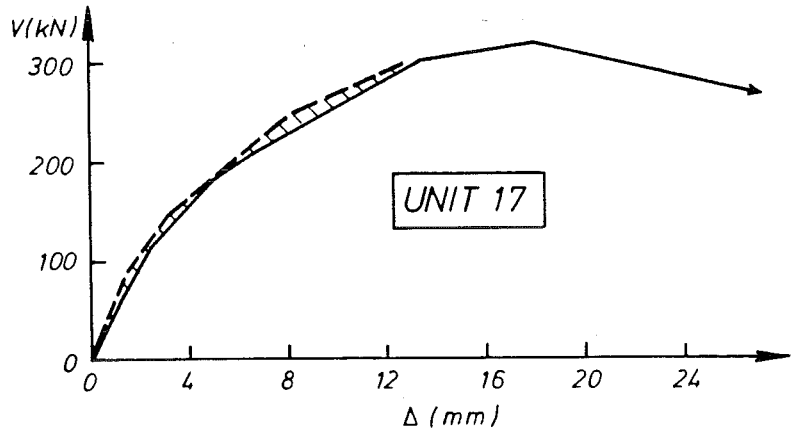

(i) Unit 17 (ρ_s = 0.00509 , $\frac{M}{VD}$ = 2.5 , $\frac{P_i}{f'_c A_g}$ = 0.1)

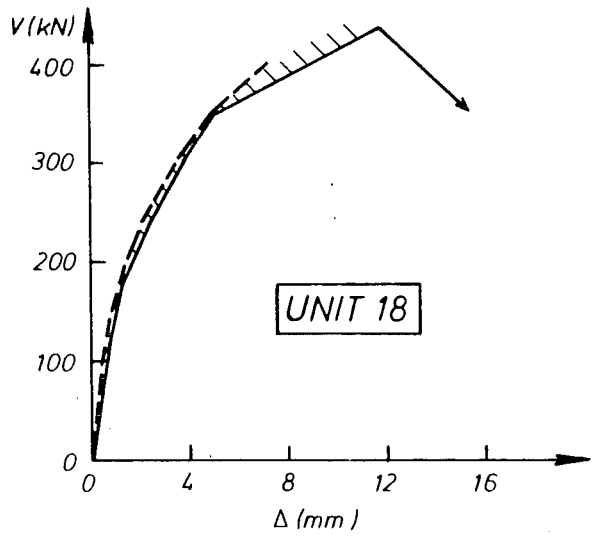

(j) Unit 18 (ρ_s = 0.00509 , $\frac{M}{VD}$ = 1.5 , $\frac{P_i}{f'_c A_g}$ = 0.1)

Fig. 6.25 (contd) : Comparison of predicted and experimental load-displacement response of static test columns.

components as discussed earlier, are shown to add up to the total theoretical tip displacement, Δ_T . In subsequent figures the shear force is plotted against the total displacement only. The experimental curves shown in the figures are obtained by joining the average of the first positive and negative peak values using straight lines. In general, though the agreement has been reasonable, the predicted displacements were smaller than the corresponding experimental values. The discrepancy is indicated by the shaded region in the figures. Besides the uncertainty in computation, the discrepancy between the experimental and the theoretical response might be due to the softening effect of the repeated load cycles and $P-\Delta$ effect when axial compression was acting. Because of computational difficulty the analysis had to be stopped short of the theoretical ultimate value and therefore the displacement at the achievement of ultimate strength cannot be duly compared.

(b) Comparison with displacement predicted by flexural theory

Parallel with the analyses using the 'Diagonal Compression Field Theory' the critical section was also analysed using conventional flexural theory. The latter analysis was carried out with the same steel and concrete stress-strain relationships, but the reduction in concrete compressive strength due to transverse tensile strain was not considered. Hence, the ν_1 factor in Eq. 6.25 was set to unity. As such the flexural theory considers only the uniaxial stress and strain of the concrete elements, and is therefore expected to provide an upper bound to the moment-curvature response of the critical section. Consequently, the load-deflection response from consideration of curvature distribution along the column is expected to indicate greater stiffness than the corresponding response using the 'Diagonal Compression Field Theory'. In Figs. 6.26 a to d for four selected column units, the two different analyses are compared in terms of $V-\Delta_\phi$, where Δ_ϕ is the deflection at the point of load application, resulting from flexural component only. The determination of Δ_ϕ is the same as that outlined in Section 6.4.2.1(a) for the two theories. As can be seen from the figures, the difference in the predicted displacements is negligible at low shear force levels. This is to be expected because the influence of shear force at that level could not have been significant. The deviation between the two predictions increases as the shear force is increased; the displacement predicted by the flexural theory is always smaller than that predicted by the 'Diagonal Compression Field Theory'. The difference is greater in column units which failed in shear with limited or no ductility, e.g. Units 1, 11 and 16, and is smaller in Unit 8 which failed in shear with

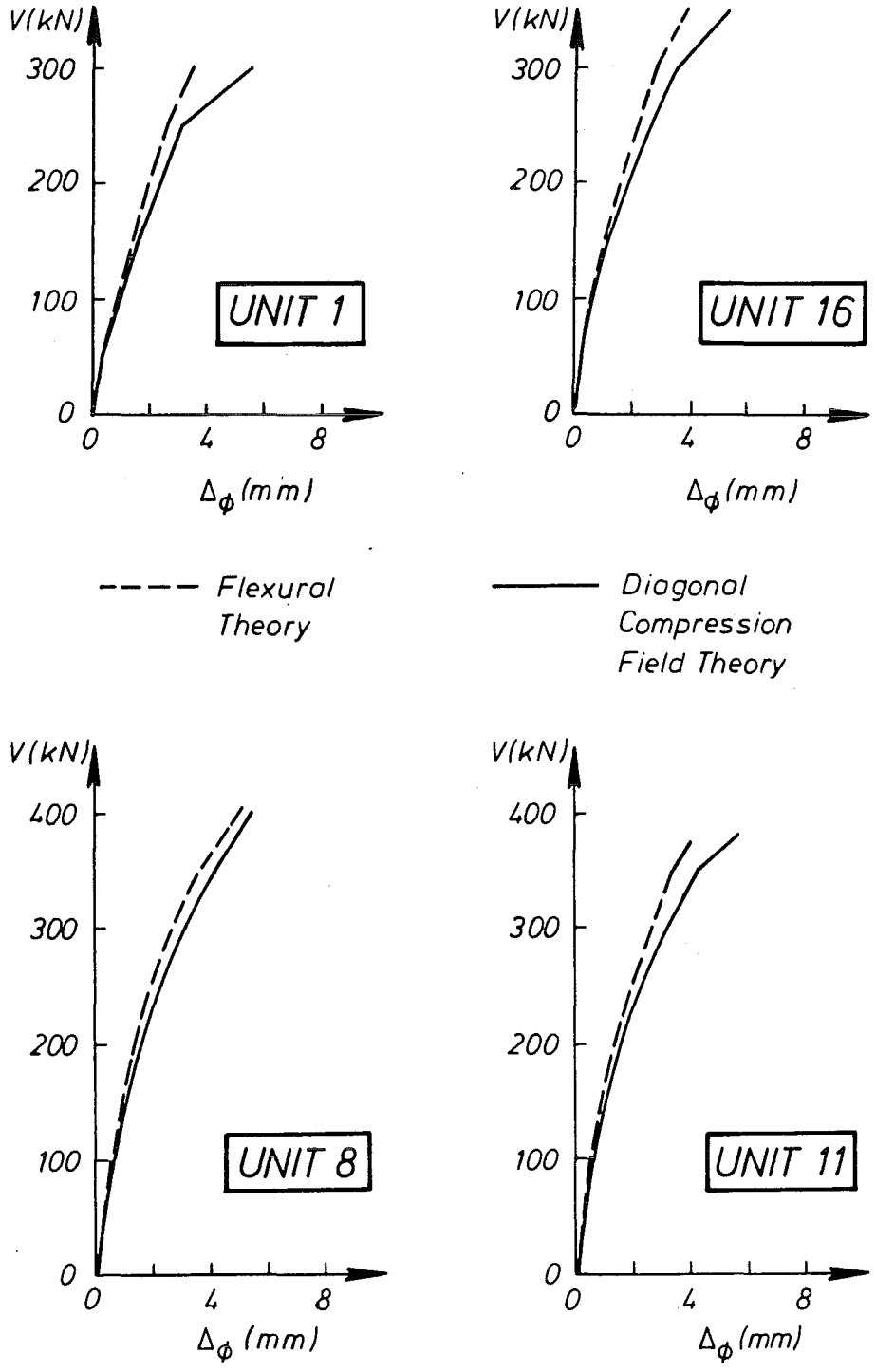

Fig. 6.26 : Comparison of displacement due to curvature distribution only from the 'Diagonal Compression Field Theory' and the flexural theory

moderate ductility, i.e. with more predominant flexural action. The ratios between the two predicted displacement values at the theoretical ultimate strength range from 0.66 (for Unit 1) to 0.82 (for Unit 8).

(c) Δ_ϕ and Δ_γ as proportions of the total predicted displacement, Δ_T

The two main displacement components (Δ_ϕ and Δ_γ) obtained from the computer analyses are expressed as fractions of the total predicted displacements and plotted against the shear force for a number of column units in Fig. 6.27 a to d. In general, the greater contribution towards the total predicted displacement comes from consideration of the curvature distribution, i.e. Δ_ϕ . The relative proportion of Δ_γ and Δ_ϕ in the total predicted displacement depends on how significant the influence of the shear force is. The contribution of Δ_γ tends to increase as the shear force is increased. Figs. 6.27a and b show the plots for two groups of column units which were observed to fail in shear with limited or no ductility during the static tests. As would be expected, the portion of Δ_T due to shear strain is greatest in these groups of column units in comparison with the other columns with different failure modes shown in Figs. 6.27c and d. On average, the contribution of Δ_γ was about 0.25 - 0.40 Δ_T for the first two groups of column units. The contribution of Δ_γ in the other cases shown in Fig. 6.27 c and d is relatively smaller and is about $0.20\Delta_T$ in the column units which failed either in shear with moderate ductility (e.g. Unit 10 of Fig. 6.27c) or in a ductile flexural manner (e.g. Unit 9 in Fig. 6.27d).

6.4.3 Shear Stress Distribution

As outlined in Section 6.3.1, the shear stresses obtained from the analyses actually represents averaged values of those acting above and below each concrete element as given by Eq. 6.32. Strictly, the shear stress does not remain constant within the concrete elements which contain longitudinal steel elements and there should be a local change in shear stress at that level of the concrete elements. Nevertheless, the averaged effect does give an idea how the shear stresses vary across the section. Typical examples of the shear stress distribution at different locations along the column obtained from the analysis are plotted in Figs. 6.28 a to c for three column units with different aspect ratios. Also shown in each case is the magnitude of the shear force under consideration. As can be seen from the figures, the shear stress distributions are more uniform near the load application point where the effect of flexure is minimal. As the bending moment increases towards the column base the effect of flexure becomes more significant. Near

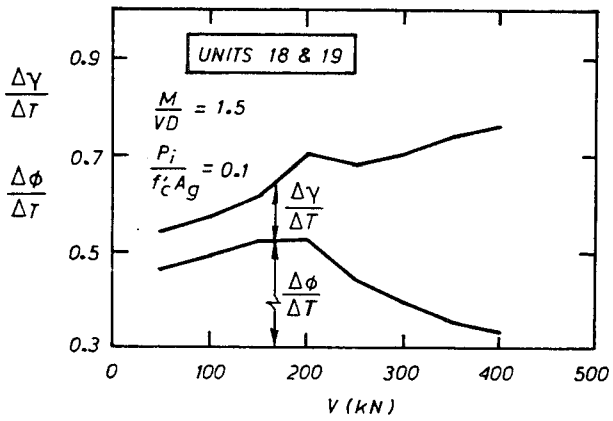

(a) Brittle shear failure

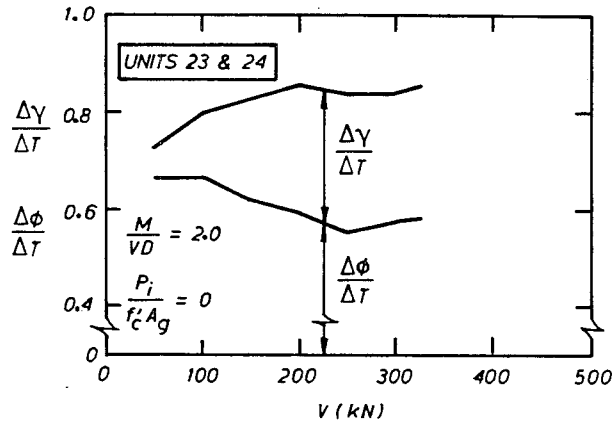

(b) Shear failure with limited ductility

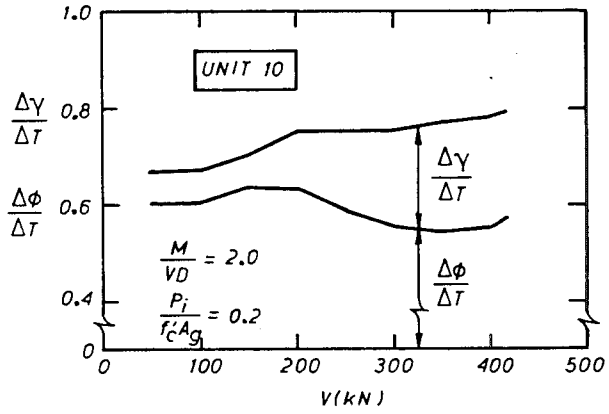

(c) Shear failure with moderate ductility

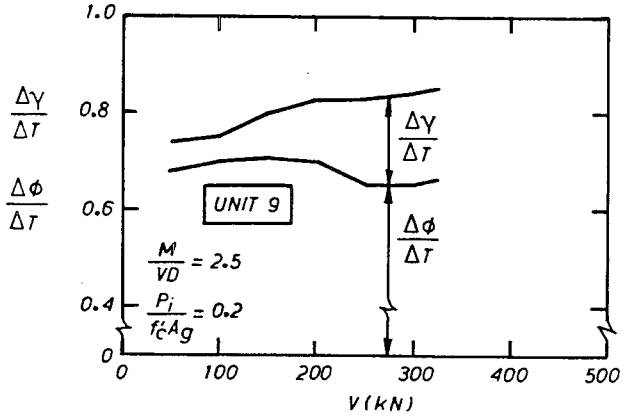

(d) Ductile flexure failure

Fig. 6.27 : Relative contribution of Δ_ϕ and Δ_γ towards total displacement of column units

the critical section the concrete in the flexure compression zone tends to have a greater share in carrying the shear force, especially if some of the longitudinal reinforcement has yielded in tension, e.g. Units 3 and 1 in Figs. 6.28 a and b respectively. The non-uniformity in shear stress distribution in the vicinity of the critical section is less pronounced in a squatter column (Fig. 6.28c) in which the yielding of tensile reinforcement occurs to a lesser extent according to the analysis. The re-distribution of shear stresses in this manner resulted in some concrete elements in the flexural compression zone carrying significantly higher shear stresses than the other elements, and eventually the maximum shear strength of these elements will be reached or exceeded on further load increments. Unless the other less heavily stressed concrete elements are capable of resisting additional shear stress shed from the 'failing' concrete elements, and the equilibrium conditions remain satisfied, the shear force has to be lowered when extensive yielding of longitudinal reinforcement has taken place in the tensile region, as is the case at high displacement ductility levels. This postulated behaviour appears to be a reasonable basis for the determination of shear strength versus displacement ductility capacity relationship during the post-ultimate stage. However, the inherent computational difficulty in achieving convergence in the iterations has to be overcome before further useful theoretical study can be carried out.

For the purpose of comparison plots for two columns (Units 11 and 16) are shown in Figs. 8.28 d and e . These units were similar to Unit 1 in every aspect except for the presence of axial compression. As is evident from Figs. 6.28 d and e, the presence of axial compression tends to maintain a more uniform shear stress distribution at the critical section if comparison is made with that of Unit 1 in Fig. 6.28b. The presence of axial compression implies a larger flexural compression zone and at the same time the yielding of tensile reinforcement is less extensive for the same shear force level. Hence, the distribution of shear stress is more uniform. This illustrates the beneficial effect of the axial compression in increasing the shear resistance of a reinforced concrete member.

From the analyses it is suggested that, in the case of distributed longitudinal reinforcement, such as used in the static test columns, a possibility to reduce the irregularity in shear stress distribution may be to distribute the longitudinal steel elements uniformly around the pitch circle diameter, as is commonly done in the flexural analysis, rather than treating as discrete elements. In this way, every concrete element, except the top and bottom concrete covers, contains longitudinal

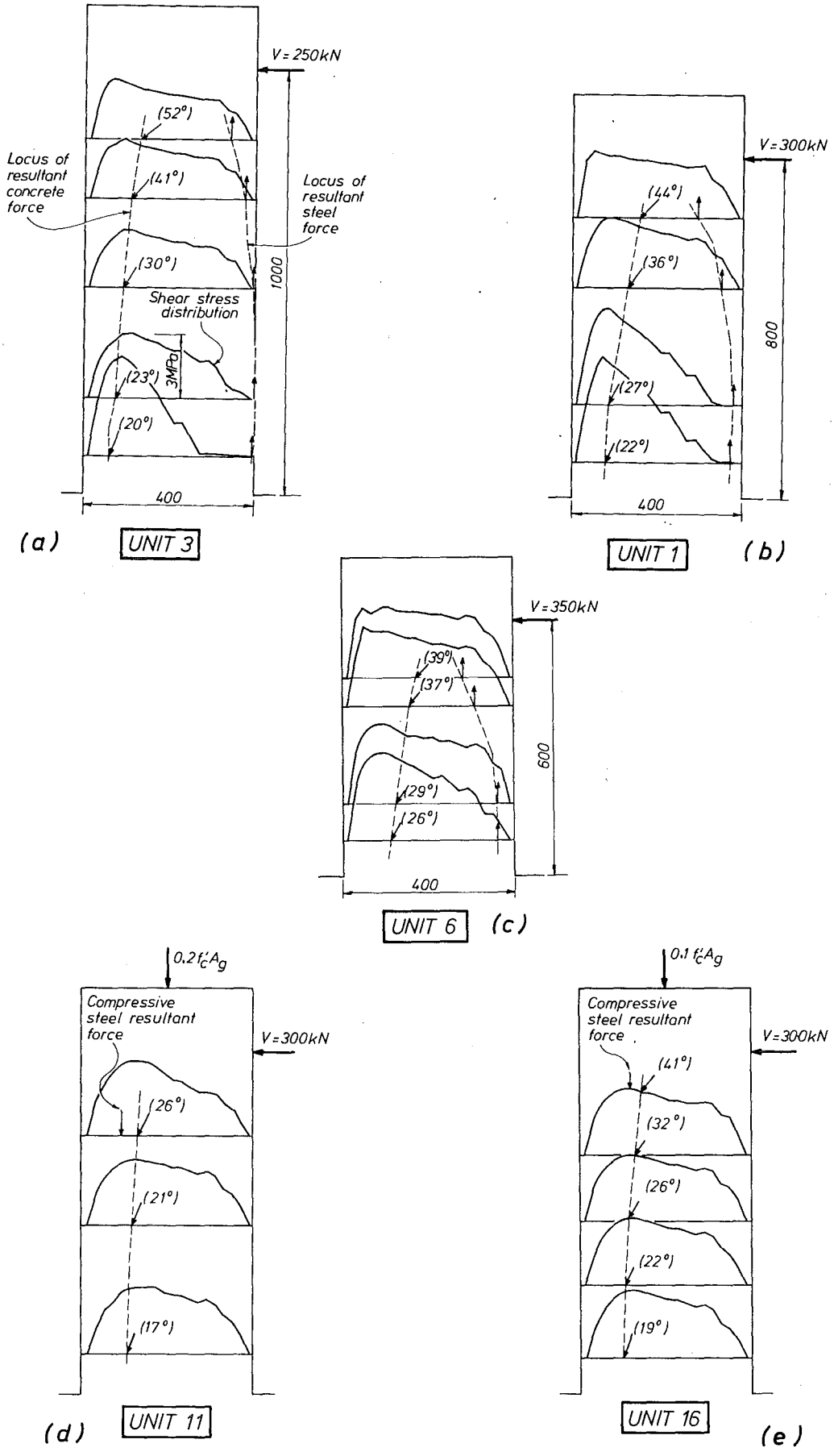

Fig. 6.28 : Theoretical shear stress distribution and resultant concrete and steel force trajectories

steel elements and hence the local variation in computed shear stresses due to steel forces is smeared over the entire section.

6.4.4 Resultant Force Trajectory

Also shown in Figs. 6.28 a to e are the trajectories of resultant concrete and steel forces obtained from the computer analyses. The points of action of the resultant concrete and steel forces were obtained from equilibrium analyses of relevant sections and were joined by straight lines to form the trajectories. Since the longitudinal reinforcement was assumed not to participate in shear resistance, all the resultant steel forces are therefore parallel to the column axis. On the other hand, the resultant concrete forces had to be inclined to the column axis so that the shear force is balanced by the transverse component of the compression forces. The angle of inclination of these forces are indicated in degrees within brackets. As can be seen in the figures, the line of concrete thrust tends to be closer to the column axes when the aspect ratio is smaller (Fig. 6.28c) or axial compression is present (Figs. 6.28 d and e). As expected, the angle of inclination of the resultant concrete forces decreases from the load application point towards the column base, and a smaller angle is obtained if the column is also subjected to axial compression.

6.4.5 Transverse Strain Distribution

The distribution of transverse strain across the section can also be obtained as an outcome of the computer analyses. Such distribution gives useful information with regard to how the transverse reinforcement at various locations is strained under the applied shear force. The pattern of transverse strain distribution at the assumed critical section is illustrated in Figs. 6.29 a to c for three column units similar in every aspect except the spiral pitch. Units 1, 5 and 7 contained R6 spirals at 60 mm, 40 mm and 80 mm respectively. Plotted in the figures are the transverse strain distributions across the section as the shear force is increased to the theoretical ultimate value. In general the magnitude of the transverse strain at low load level is negligible, and because of the assumption made in the analyses, the transverse strain in the first few concrete elements near the extreme compression fibre always remains at zero even at the ultimate stage. As can be seen from the figures the presence of a larger amount of transverse reinforcement due to smaller spiral pitch resulted in smaller transverse strain at the same shear force level, and delayed the onset of yielding of the trans-

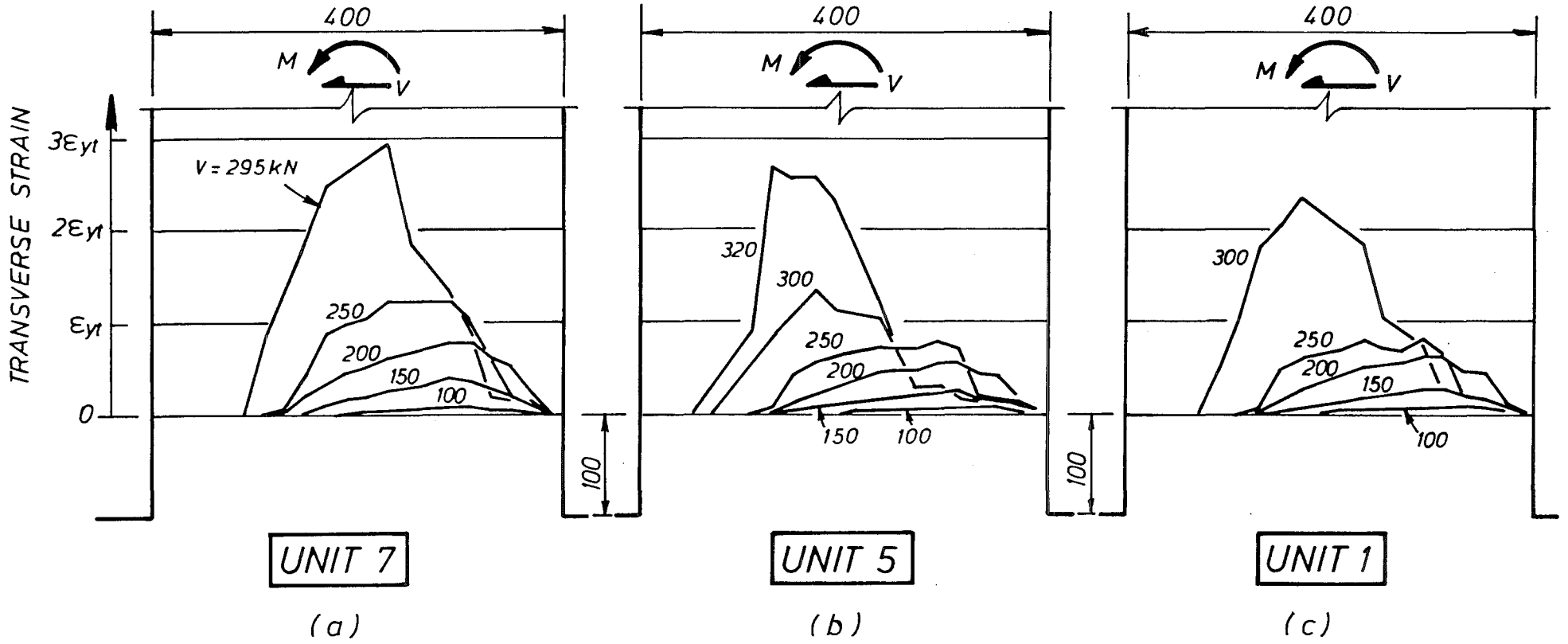

Fig. 6.29 : Theoretical transverse strain, ε_t , distribution at different load stages

verse reinforcement. It is interesting to see that the peak transverse strain moves from the tension zone to somewhere close to the centroidal axis as the ultimate stage is approached. The yielding of transverse reinforcement in the tension zone causes a drop in shear stresses carried by the concrete elements in this zone, and consequently, higher shear stress is imposed on concrete elements above this zone, resulting in higher transverse strain. The presence of high transverse strain associated with higher shear stress in the concrete element causes difficulty in iteration and no convergence can be achieved if the imposed shear stress is beyond the capacity of the concrete element concerned. This is particularly so if the maximum transverse stress is limited to that corresponding to yielding of the transverse reinforcement, i.e. disregarding the strain hardening effect of the transverse steel used.

6.5 LOCAL VARIATION OF STRESSES AT CRACKS

6.5.1 Aggregate Interlock

The results from the analysis using the 'Diagonal Compression Field Theory' are average values of stresses and strains. The theory assumes the element to contain several cracks, the influence of which is smeared over the entire element. The theory, therefore, does not provide any information concerning local variations at cracks. However, it is established that the steel stress at a crack is always higher than that between cracks, while concrete tensile stress between cracks is higher than at cracks. Hence, the ultimate capacity of the element can well be limited by its unability to transmit the high stresses of the reinforcement across the cracks.

To look at the local variation of stresses at a crack, the average stresses of the element are compared with the actual local values at a crack as shown in Fig. 6.30 a and b. The crack is assumed to occur parallel to the principal compressive stress direction. The element is reinforced with orthogonal reinforcement. The first set of stresses (Fig. 6.30a) represents stresses in the principal direction while the second set (Fig. 6.30b) represents those at a crack. Because of the shear stress, τ_g, arising from aggregate interlock and other actions these stresses are no longer the average principal stresses. Since both stress states represent the same system, Collins[6.10] obtained the following equations by comparing the two equivalent stresses in both directions.

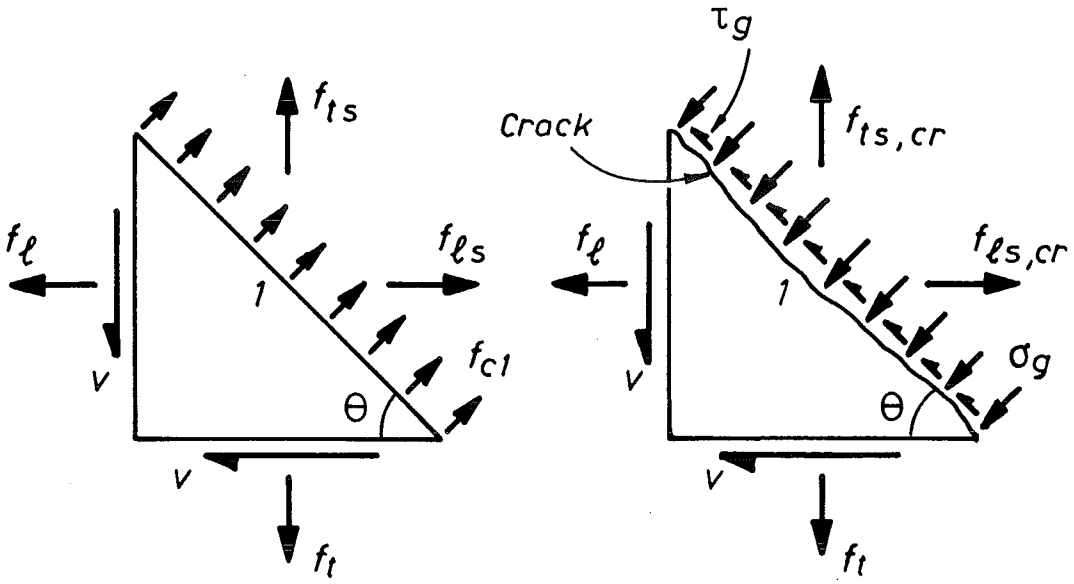

Fig. 6.30 : Equivalent average stresses and local stresses at a crack[6.10]

$$\rho_{s\ell} f_{\ell s} \sin\theta + f_{cl} \sin\theta = \rho_{s\ell} f_{\ell s,cr} \sin\theta - \sigma_g \sin\theta - \tau_g \cos\theta \qquad (6.55a)$$

$$\rho_{st} f_{ts} \cos\theta + f_{cl} \cos\theta = \rho_{st} f_{ts,cr} \cos\theta - \sigma_g \cos\theta + \tau_g \sin\theta \qquad (6.55b)$$

Rearranging the above equations gives

$$\rho_{s\ell} [f_{\ell s,cr} - f_{\ell s}] = f_{cl} + \sigma_g + \tau_g \cot\theta \qquad (6.56a)$$

$$\rho_{st} [f_{ts,cr} - f_{ts}] = f_{cl} + \sigma_g - \tau_g \tan\theta \qquad (6.56b)$$

Eqs. 6.56 a and b can be satisfied without mobilizing the interface shear transfer (i.e. with $\tau_g = 0$) if

$$\rho_{s\ell} [f_{\ell s,cr} - f_{\ell s}] = \rho_{st} [f_{ts,cr} - f_{ts}] = f_{cl} \qquad (6.57)$$

The condition given by Eq. 6.57 may not be able to be satisfied if the calculated average stresses in the reinforcement are large. In particular, yielding of reinforcement in either direction will immediately rule out the possibility of satisfying this condition because the steel stresses

at the crack cannot be increased further unless strain hardening is considered. Under this situation, stress redistribution has to take place so that the more lightly stressed elements will have to increase their share of shear carrying capacity while part of the shear stresses is relieved from the cracked zone. If this is not possible then failure is imminent.

Depending on which set of the reinforcement yields first, the values of τ_g and σ_g can be determined from either of Eqs. 6.56 a and b together with a consideration of the interface shear transfer behaviour. Many theoretical models have been proposed to relate τ_g and σ_g to the crack width and crack slip and it is not the intention of the author to discuss them here. Nevertheless, assuming there exists a solution from the above consideration, the value of τ_g and σ_g obtained when substituted into the remaining equation of Eqs. 6.56 a and b should satisfy the condition that the steel stress at the crack must not exceed the yield value. Thus, the main concern is whether the non-yielding set of reinforcement is able to adjust to the change in stress at the crack. Furthermore, if the section is subjected to bending moment in addition to shear and axial load, the change in bending moment resistance arises from change in concrete stresses at the crack must be able to be balanced by an equivalent but opposite change in moment due to a corresponding change in steel stresses[6.10].

If the above conditions cannot be satisfied or no solution is possible for the values of τ_g and σ_g, then equilibrium cannot be maintained and the cracks will open and slide. To avoid this, the value of f_{cl} in Eqs. 6.56 a and b has to be lowered. In other words, the effect of tension stiffening is reduced. However, if even the reduction in f_{cl} cannot solve the problem, the applied shear has to be lowered as a whole.

To incorporate the above checking process in the model requires a knowledge of crack width and shear slip along the crack as well as a valid aggregate interlock model. To obtain this information for cyclic loading situations is very difficult, if not impossible. The incorporation of such a checking process introduces another loop of iterations and thus complicates the already tedious computational procedure. Hence, the analyses reported in earlier sections were carried out without checking this local effect. Nevertheless, the results indicate that higher shear stress usually occurs near the neutral axis and in the flexural compression zone, and as such the increase in longitudinal

steel stress at the crack may not be a problem.

6.5.2 Dowel Action Of Longitudinal Bars

Dowel action is another means of interface shear transfer in addition to aggregate interlock. These two modes of interface shear transfer mechanism are interdependent. For the same slip, considerably larger aggregate interlock shear stress will be generated unless the crack width is large. Consequently, aggregate interlock action always predominates in the initial stage after diagonal cracking during which the crack opening and shear slip along the crack are still small. With further increase in load, the crack will inevitably widen and the shear slip will also increase. Until this shear displacement becomes substantial, no significant dowel action can probably be mobilized. In theory, the displacement across a potential diagonal crack relevant to dowel action can be very large and it is likely that, by the time the dowel action is mobilized, it may be too late to be of any use because the distortion may well exceed what is tolerable within the limits of structural usefulness.

Three possible modes of dowel action have been identified in Ref. 6.12 but these are not discussed here. Experimental observations during the static tests reported in Chapter Four indicate much mobility of the core concrete because of the lattice crack pattern, and to get good support for the dowels is difficult since the shape of the spirals does not furnish a tight corner bend for a firm support as in the case of rectangular hoops or stirrups. In addition to this, spalling of concrete cover and extensive yielding of flexural reinforcement imply that the dowels, instead of kinking at the potential inclined failure plane, may be displaced across several cracks so that a general bent shape over a longer length is imposed on them. This flexibility of the dowels suggests that at this stage of the response their contribution might be considerably less than conventional theory would indicate. Consequently, the contribution of dowel action was believed to be negligible within practical limits and was not considered in the analysis.

6.6 CONCLUSIONS

Theoretical study of the behaviour of the static test columns using the 'Diagonal Compression Field Theory' indicated that the correlation between the theoretical prediction and the experimental behaviour has been satisfactory. The behaviour in terms of load-displacement

response can be predicted within reasonable limits up to maximum load. The ultimate strength can be predicted within 10 percent accuracy with a standard deviation of less than 10 percent on average. If the same stress-strain relationship for confined concrete is used and the same critical section is considered, the prediction of ultimate strength by conventional flexural theory tends to be unconservative and the predicted load-deflection response, considering curvature alone, tends to exhibit greater stiffness. Other useful information can also be gained from the analyses. However, the process to arrive at a solution has been time consuming and effort to extend the theory to predict the inelastic behaviour after attaining maximum resistance has been unsuccessful due to inherent computation difficulty. Nevertheless, from the understanding of the theory it is believed that it can provide a sound basis to derive a relationship between degraded shear strength and displacement ductility level. Further modification to the computational algorithm may need to be done to include local variations at cracks and to strain hardening of steel during the post-ultimate inelastic stage.

Chapter Seven

— DYNAMIC TESTS OF CIRCULAR COLUMNS — DESIGN, CONSTRUCTION AND TESTING PROCESSES

7.1 INTRODUCTION

As a second stage of the test programme, a series of small circular column units were subjected to shake-table testing under sinusoidal or simulated earthquake ground motion. The purpose of the testing was to investigate the influence of dynamic loading on shear strength. In particular the effect of dynamic loading on the relationship between strength and ductility obtained from static test results would be examined under the more realistic dynamic situation. The intention of the tests was to eventually enforce a shear failure in the column units. Altogether eight single column units and two twin-column units were tested. The single column units allowed a direct evaluation of performance by comparing with static test results while the twin-column units gave a more realistic simulation of a typical situation in which axial load in the columns changed in magnitude during seismic response. This chapter discusses aspects of the design, construction and testing of the columns. Results are presented subsequently in Chapter Eight.

7.2 PROBLEMS RELATED TO DYNAMIC SIMULATION

D'Alembert's law of dynamic equilibrium implies a balance between the inertia and damping forces associated with the state of motion and the restoring forces representing the reaction to the movement. The restoring forces can be either gravitational or elastic in nature. It is these forces that play a basic role in the simulation problems.

Following Buckingham's π-theorem[7.1-7.2], the quantities involved in dyanmic simulation are defined by three fundamental units (i.e. mass, length and time) so only three physical quantities can be selected for independent scaling. However, in practice only two quanties can be chosen freely since the gravitational acceleration, g , will normally be the same for protoype and model. Consequently, the most restrictive requirement for perfect modelling comes from the similitude relation that

$$\lambda_L = \frac{\lambda_f}{\lambda_\rho} \tag{7.1}$$

where $\lambda_L = \frac{L_p}{L_m}$ is the geometrical scaling factor;

$\lambda_f = \frac{f_p}{f_m}$ is the stress scaling factor; and

$\lambda_\rho = \frac{\rho_p}{\rho_m}$ is the density scaling factor.

The subscripts p and m denote prototype and model quantities respectively. Since λ_L is greater than unity, Eq. 7.1 requires for perfect modelling that the model material must either have a much smaller stiffness (i.e. large λ_f) or much larger density (i.e. smaller λ_ρ) than that of the prototype material. In practice, unless full control over the scaling of gravitational acceleration can be achieved, the use of materials with similar strength and density rules out the use of exact models for dynamic studies. In fact, the practical difficulty in achieving the scaling conditions in the model leads to the consideration of two limiting cases of distorted modelling. For a distorted model, the effects of a possible alteration of a dimensionaless product (the π-factor) are offset by the alteration of another different dimensionless product so as to maintain the correspondence between the prediction equation of the prototype and that of the model.

Depending on the choice of restoring force, the two idealized extremes are as follows:

(a) In Cauchy's similitude, which neglects the gravitational forces, the similitude laws are derived from the relation

$$\left(\frac{\text{Inertia force}}{\text{Elastic force}}\right) = \left(\frac{\rho V^2}{E}\right)_m = \left(\frac{\rho V^2}{E}\right)_p \qquad (7.2a)$$

where ρ, V and E are density, velocity and modulus of elasticity respectively. Eq, 7.2a can be re-written by substituting $V = \frac{L}{T}$ so that

$$\left(\frac{\rho L^2}{ET^2}\right)_m = \left(\frac{\rho L^2}{ET^2}\right)_p \qquad (7.2b)$$

(b) In Froude's similitude, which ignores the elastic force, the similitude laws are derived from the relation

$$\left(\frac{\text{Inertia force}}{\text{gravity force}}\right) = \left(\frac{V^2}{Lg}\right)_m = \left(\frac{V^2}{Lg}\right)_p \qquad (7.3a)$$

Similarly, substitution of $V = \frac{L}{T}$ into Eq. 7.3a gives

$$\left(\frac{L}{T^2 g}\right)_m = \left(\frac{L}{T^2 g}\right)_p \qquad (7.3b)$$

Cauchy's similitude is more suitable in situations where the earthquake effects are very much greater than the gravitational effects. The advantage of adopting Cauchy's similitude lies in the freedom of choice of the density and stress scaling factors (i.e. λ_ρ and λ_E). If both factors are chosen to be unity, i.e. using the same material in the model as that in the prototype, Eq. 7.2b requires

$$\frac{L_p}{L_m} = \frac{T_p}{T_m}$$

$$\text{or} \quad \lambda_L = \lambda_T \tag{7.4}$$

In other words, the time scaling factor, λ_T, is equal to the geometrical scaling factor, λ_L. Hence, Cauchy's similitude requires a 'speeding up' of the earthquake for the model. From Eq. 7.4, the acceleration scaling factor, λ_a, can be derived as follows:

$$\lambda_a = \frac{a_p}{a_m} = \frac{\lambda_L}{\lambda_T^2} = \frac{1}{\lambda_L} \tag{7.5}$$

Hence,

$$a_m = a_p \lambda_L$$

$$= a_p \frac{L_p}{L_m} \tag{7.6}$$

i.e. the acceleration, a, used in model testing should be increased by a factor equal to $1/\lambda_L$.

The increase in time scale may lead to problems in measurement and in reproducing the dynamic excitation. It will also amplify strain rate effects on the material properties. Furthermore, the use of such a model is subjected to limitations in that it holds true only if the assumption that gravitational effects are negligible remains valid.

Although exact modelling was not necessary in this study, since specific prototype situations were not represented, the principles of Cauchy's similitude were essentially followed.

7.3 MODEL DESCRIPTION

7.3.1 Model Size

Even with distorted modelling outlined in the preceding section, simulation of other properties like bond and cracking can be rather difficult. Moreover, practical constraints do not guarantee that the scaling process can be strictly adhered to. In this project, the

physical constraints imposed by the shake-table were as follows:

maximum dynamic horizontal force capacity = 200 kN

maximum table acceleration (for model inertia mass of 5 tonnes) = 27 m/s^2 (2.76g)

maximum table velocity = 1 m/s

maximum table displacement (peak-peak) = 300 mm

The dynamic capacity of the table determined the magnitude of the maximum inertia load and hence, the size of column units for the twin-pier system. For simplicity, the size of single piers was chosen to be the same as that of the twin-piers. The final size of the models selected was such that they were effectively half scale models of the static test units, in terms of diameter, aspect ratio, concrete cover and reinforcement quantities. The column units all had an overall diameter of 200 mm and were founded on a 600 x 500 x 300 mm^3 footing. The general test set-up and overall column dimensions are shown in Fig. 7.1. Full details of column reinforcement are included in Table 7.1. Inertia loading was provided by pinning the units to a 5 tonne inertia mass as shown in Fig. 7.1. Details of the model design are described in the following sections.

7.3.2 The Paramaters Under Investigation

7.3.2.1 Aspect ratio ($\frac{M}{VD}$)

In this series of tests, aspect ratios of 1.5 and 2.0 were used. The difference in aspect ratio was achieved by keeping the diameter of the columns at 200 mm while the height to the pinned connection to the inertia mass (see Fig. 7.1) was changed. The resulting shear-span was 300 mm and 400 mm for $\frac{M}{VD}$ of 1.5 and 2.0 respectively. The largest aspect ratio of 2.5 used in static tests was not modelled.

7.3.2.2 Reinforcement quantities

All column units with the exception of Unit D3 had 10 gauge (3 mm diameter) wire as spiral reinforcement. Three different spacings, 30, 40 and 50 mm, were used to achieve variation in spiral reinforcement content, ρ_s, of 0.00509, 0.00382 and 0.00306 respectively. Reducing the spiral pitch below 30 mm would have caused difficulty in fabrication of reinforcement and placing of concrete. Hence Unit D3 with 6 gauge wire (5 mm diameter) at 40 mm (ρ_s = 0.01061) was included to give a higher spiral reinforcement content. Details of the reinforcement are listed in Table 7.1. The spiral reinforcement content was chosen based on the results

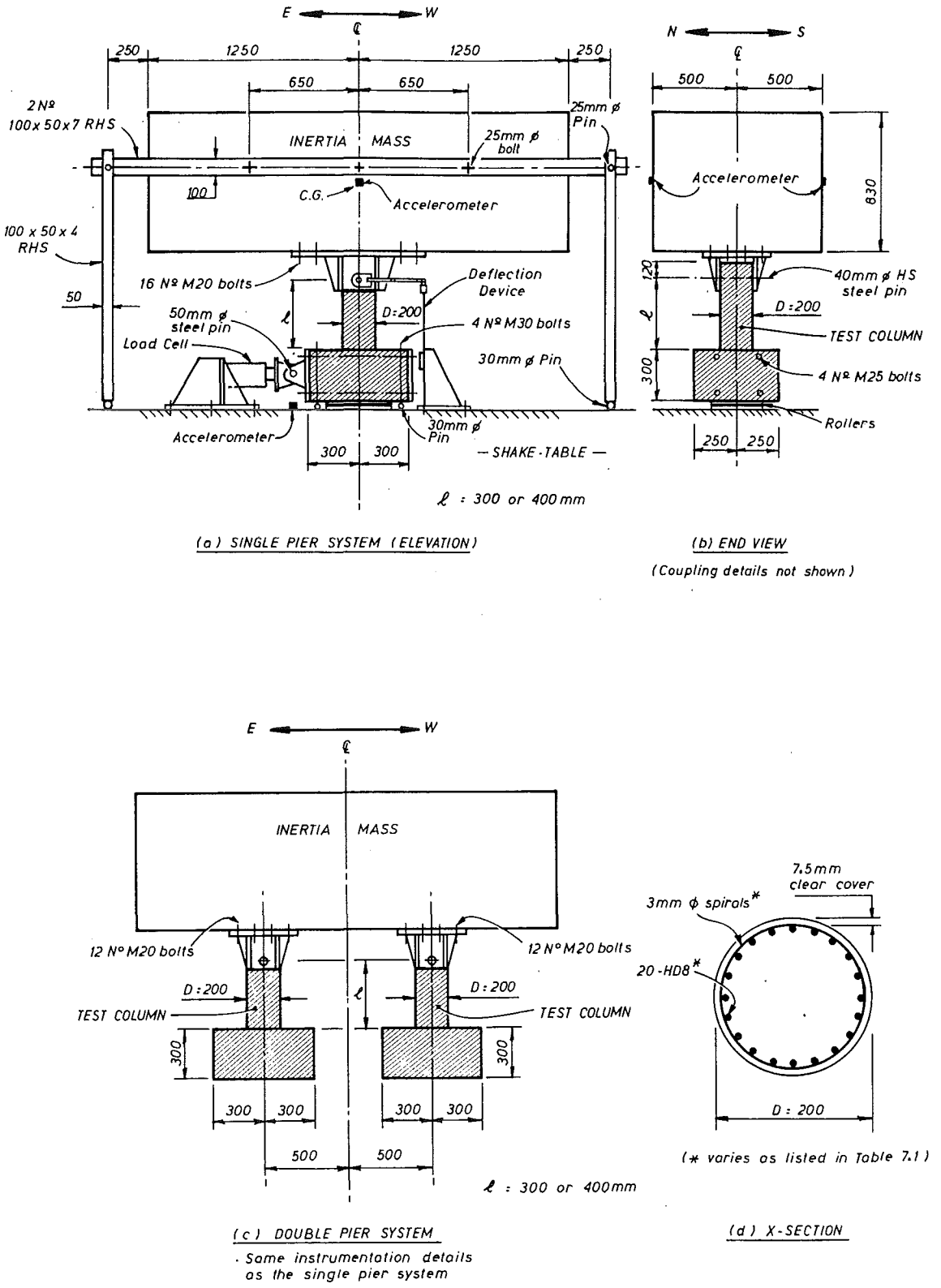

Fig. 7.1 : Test set-up and dimensions of column units

Table 7.1 : Details Of Column Units And Material Properties

UNIT	$\frac{M}{VD}$	$\frac{P_i}{f'_c A_g}$ (T)	$\frac{P_i}{f'_c A_g}$ (C)	Transverse Reinforcement: Quantity	Transverse Reinforcement: ρ_s ($\times 10^{-3}$)	Transverse Reinforcement: f_{yt} (MPa)*	Longitudinal Reinforcement: Quantity	Longitudinal Reinforcement: ρ_ℓ	Longitudinal Reinforcement: $f_{y\ell}$ (MPa)$^{\forall}$	f'_c (MPa)
DT1	1.5	0.13	0.20	10g @ 30	5.09	656	20-HD8	0.0320	436	20.9
DT2	2.0	0.09	0.16	10g @ 30	5.09	656	20-HD8	0.0320	436	21.1
D1	1.5	-	0.08	10g @ 30	5.09	656	20-HD8	0.0320	436	20.9
D2	1.5	-	0.08	10g @ 40	3.82	656	20-HD8	0.0320	436	20.2
D3	1.5	-	0.08	6g @ 40	10.61	380	20-HD8	0.0320	436	20.3
D4	1.5	-	0.08	10g @ 50	3.06	656	20-HD8	0.0320	436	20.8
D5	2.0	-	0.08	10g @ 30	5.09	656	20-HD8	0.0320	436	20.3
D6	2.0	-	0.08	10g @ 40	3.82	656	20-HD8	0.0320	436	19.6
D7	2.0	-	0.08	10g @ 50	3.06	656	20-HD8	0.0320	436	20.1
D8	2.0	-	0.08	10g @ 50	3.06	656	9-HD12	0.0324	450	19.4
									Ave	20.4
									σ	0.54

(T) : Tension (C) : Compression

10g = 10 gauge wire (3mm dia), 6g = 6 gauges wire (5mm dia)

* 0.2% proof stress (except D3)

$\forall$ 0.2% proof stress (except D8)

of the static tests to give a range of expected shear strengths and ductility capacities as listed in Table 7.2, using the analytical approach proposed in Chapter Five.

The longitudinal reinforcement used was typically half the size of HD 16 bars used in static tests. All the column units except Unit D8 had a typical arrangement of twenty HD8 bars as flexural reinforcement as shown in Fig. 7.1c. This arrangement resulted in a total longitudinal reinforcement content, ρ_ℓ , of 3.2 percent as in the case of the static tests. Unit D8 was provided with 9-HD12 instead of 20-HD8 bars as flexural reinforcement so as to investigate the influence of changing the number and size of bars while maintaining a fixed flexural reinforcement content of 0.032.

7.3.2.3 Axial load level $\left(\frac{P_i}{f'_c A_g}\right)$

The axial load on single piers was solely due to the dead weight of the inertia mass (see Section 7.5.1) and the resulting axial compression was $0.08 f'_c A_g$.

The level of axial load in the case of twin-piers was the algebraic sum of that due to the dead weight of the inertia mass and that due to the overturning effect. Fig. 7.2 shows a general case of twin-pier system with the piers at distance x apart. From the figure, the following expressions can be derived for axial loads, viz

$$P_1 = \frac{W}{2} - \frac{V(L-\ell)}{x} \qquad (7.7a)$$

and

$$P_2 = \frac{W}{2} + \frac{V(L-\ell)}{x} \qquad (7.7b)$$

for Pier 1 and Pier 2 respectively. In the expressions, W and V refer to the dead weight of inertia mass and the lateral inertia force respectively and the term $(L-\ell)$ is the distance from the pin to the centre of gravity of the inertia mass. In the tests, the value of $(L-\ell)$ was constant and equal to 590 mm and therefore the axial loads were independent of the loading height, ℓ .

Substituting $(L-\ell)$ = 590 mm and x = 1000 mm into Eqs. 7.7a and 7.7b gives

$$P_1 = 0.5W - 0.59\ (V_1 + V_2) \qquad (7.8a)$$

and

$$P_2 = 0.5W + 0.59\ (V_1 + V_2) \qquad (7.8b)$$

The resulting range of axial load levels at the development of ideal

flexural strength for Unit DT1, in terms of $f'_c A_g$, varied from 0.13 (tension) to 0.20 (compression) while the corresponding values were 0.09 (tension) and 0.16 (compression) for Unit DT2 which had a higher aspect ratio, and hence a lower value of V_{if}.

7.3.3 Construction Of Column Units

The design of piers and their footings followed the basic principles as outlined in Chapter Three. However, some variation did arise as a result of change in the loading system. Fig. 7.3 shows a drawing of typical column reinforcement. The use of an internal steel pin to connect the pier to the inertia mass required a steel tube to be placed at the desired height and welded to the locally displaced longitudinal reinforcement as shown in the figure. Extra reinforcement was also provided around the steel tube to prevent splitting failure at the pin.

The fabrication of the reinforcing cage followed the practice described in Chapter Three. However, unlike the previous series, the longitudinal reinforcement consisted of straight bars welded to steel plates at both ends (see Fig. 7.3) instead of the embedded 90-deg hooks used at the base in static tests (see Fig. 3.3). Because of this difference, the main reinforcement of the piers was welded to the bottom plate and held in position on top before the reinforcement for the footing was placed and tied together. Also, within the footing, four PVC tubes (as can be seen in Fig. 7.4b) were located along the loading direction. They were required to accommodate bolts for the load-cell coupling system (Section 7.6.3.3) used to monitor the lateral load input to the piers.

Spiral reinforcement was kept continuous over most of the column height. Because of their small size, the spirals were not welded together but were lapped for about half a turn with the free ends anchored into the concrete by a 90-deg bend with a minimum of 100 mm extension into the core. The spirals were lapped at no more than two locations along the entire height of the column.

The concrete block used for inertia mass simulation was cast first. The plywood mould was then modified for casting the twelve footings in a single operation. The plywood pieces were 20 mm thick and the bottom piece was grooved so that the vertical partition pieces could be set in place to divide the mould into twelve compartments of equal size as shown in Fig. 7.4a. For convenience the twelve piers were also cast together in one batch. The concrete was supplied by a commercial ready-mix contractor. Figs. 7.4a and b show the footings

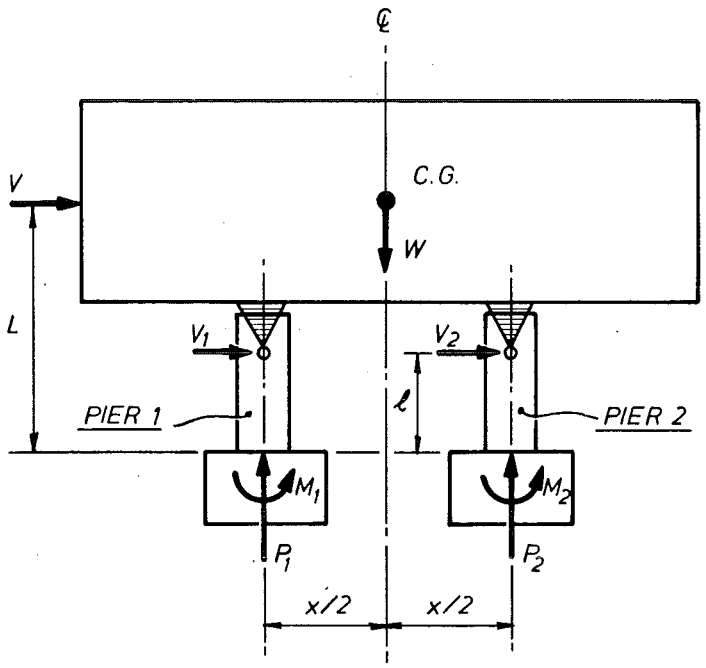

Fig. 7.2 : Loadings on twin-pier model

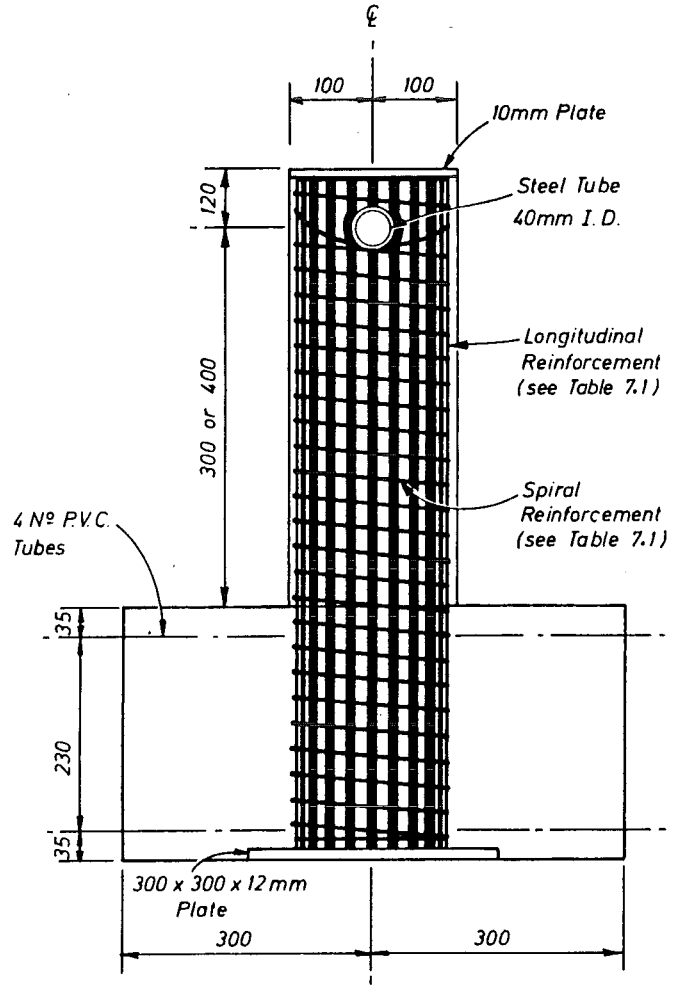

Fig. 7.3 : A typical column reinforcing cage

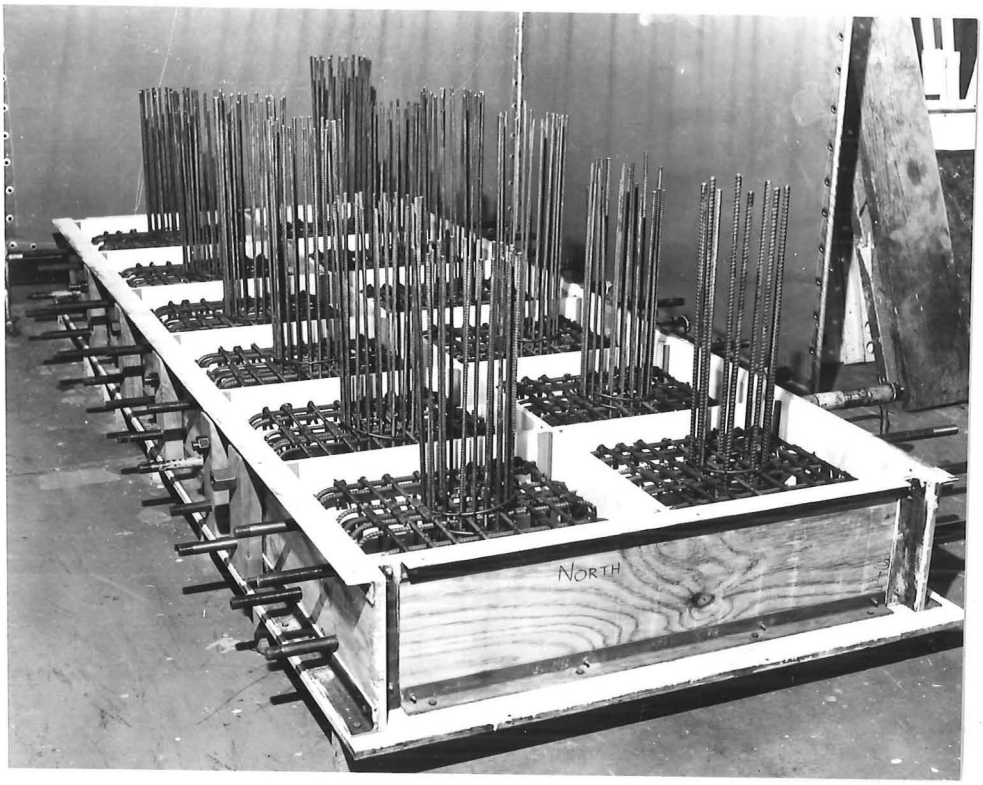

(a) Footings

(b) Columns

Fig. 7.4 : Footings and columns ready for casting

and the column units ready for casting.

7.4 MATERIAL PROPERTIES

7.4.1 Concrete

In order to reasonably scale concrete properties, maximum aggregate size was reduced to 10 mm (i.e. half of that for the static tests). Scaling of the complete aggregate grading curve was not practical and direct scaling of concrete mixes has some inherent difficulties as pointed out by Pehi and Priestley[7.3]. Moreover, according to Chana[7.4], even with correct similitude, a significant increase in shear strength due to the scale effect could still be observed in model testings. He found that the scale effect could not be wholly attributed to the lack of similitude of aggregate interlock action but rather the effect of increase in strain gradient due to the reduced size of the models. The increase in strain gradient had the effect of increasing the tensile strength of concrete. Hence the main concern was to make sure there was no excessive increase in the ratio of tensile to compressive strengths as a result of the scaling.

During casting of the inertia mass, footings and piers, three concrete prisms were taken together with the cylinders. These prisms were required for modulus of rupture tests to determine the tensile strength of concrete indirectly. The three concrete pours for the inertia mass, footings and the piers had different concrete cylinder strengths but the same maximum aggregate size of 10 mm. The results are plotted in Fig. 7.5; the points are well spread to give a good indication of the relationship between the tensile and compressive strengths. The results of 28 day strengths from Fig. 7.5 indicate that the tensile strength was about $0.77\sqrt{f'_c}$ MPa which is characteristic of concrete used in the prototype.

Concrete cylinder compressive strengths, f'_c, were also measured at the age of testing each pier and the results are included in Table 7.1. Due to an error by the ready-mix contractor, the concrete supplied was about 10 MPa weaker than the specified strength of 30 MPa.

7.4.2 Reinforcing Steel

For the model performance to be extrapolated to full size structure, the strength, the modulus of elasticity and the bond properties of the reinforcement need to be reproduced properly in the reinforcement for the model structure.

	①	②	③
f'_c	17.70	36.99	28.32
f'_t	3.04	4.80	4.25

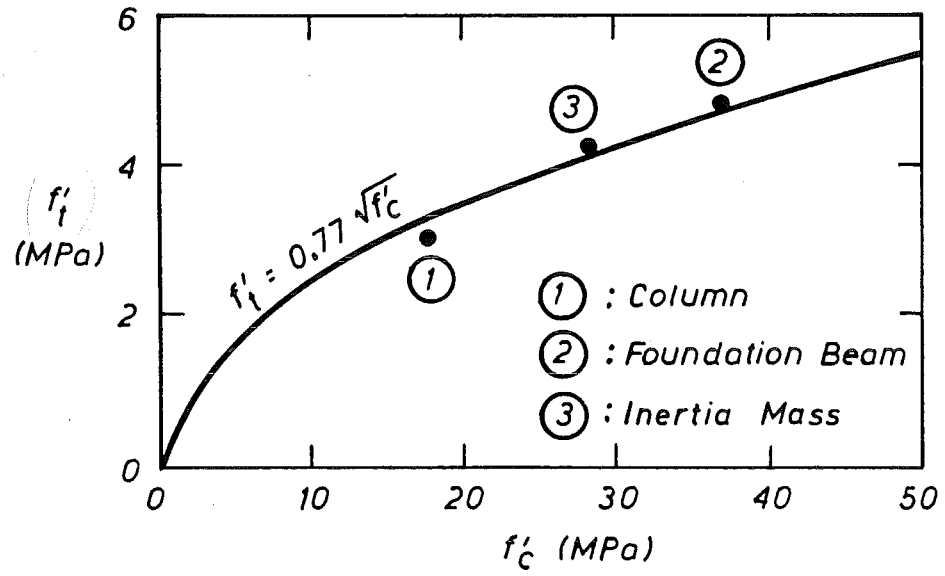

Fig. 7.5 : Tensile strength versus compressive strength of concrete used in the tests

The size of pier model chosen required a special run of HD8 deformed bars in order to have a one-half similitude of the HD16 reinforcement used in the static tests. Similarly, 10 gauge wire had to be used for spiral reinforcement so as to give a half scale similitude of R-6 reinforcement used typically in the static tests. All the steel was purchased from a commercial company. The stress-strain curves of the reinforcing steel are shown in Figs. 7.6a to d and tabulated in Table 7.1. The stress-strain curves for HD8 steel and 10 gauge wire did not show a distinct yield point so the 0.2 percent proof-stress was taken as the yield strengths in these cases and was used in the calculations of theoretical strengths of the test columns.

7.4.3 Change In Predicted Strength And Ductility Capacity Due To The Material Strengths Being Different From Specified Values

Table 7.2 summarizes the strengths and ductility capacities calculated using actual and specified material strengths. The designed values based on specified strengths (f'_c = 30 MPa and f_{yt} = 400 MPa) are

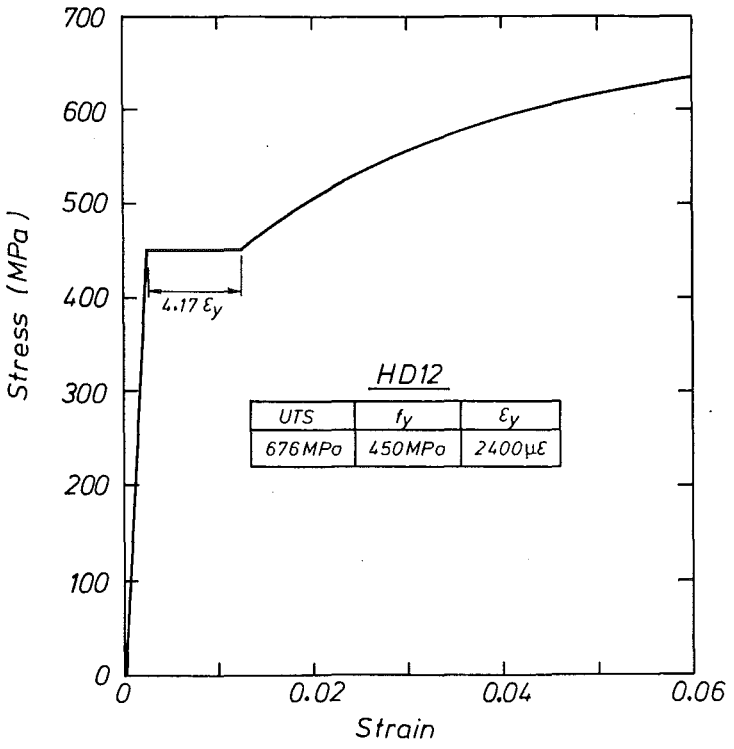

(a) Longitudinal reinforcement

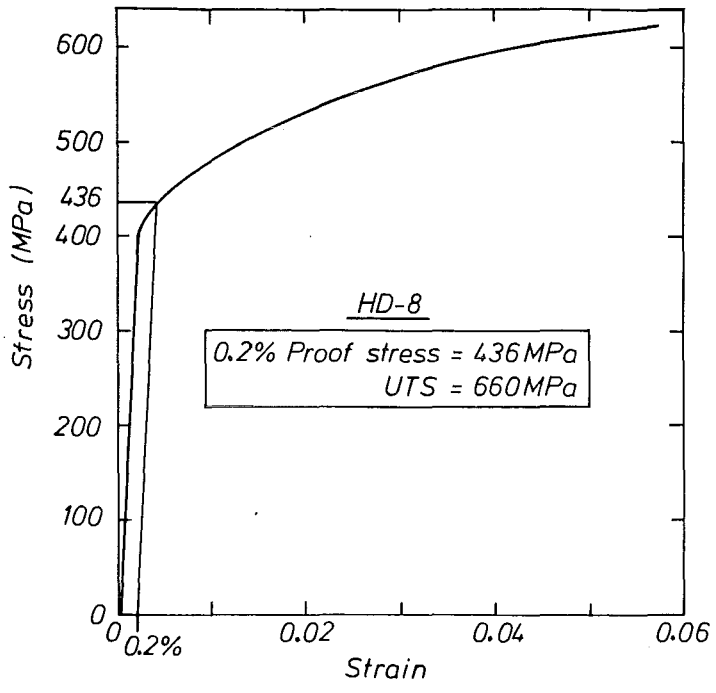

(b) Longitudinal reinforcement

Fig. 7.6 : Stress-strain curves for reinforcing steel

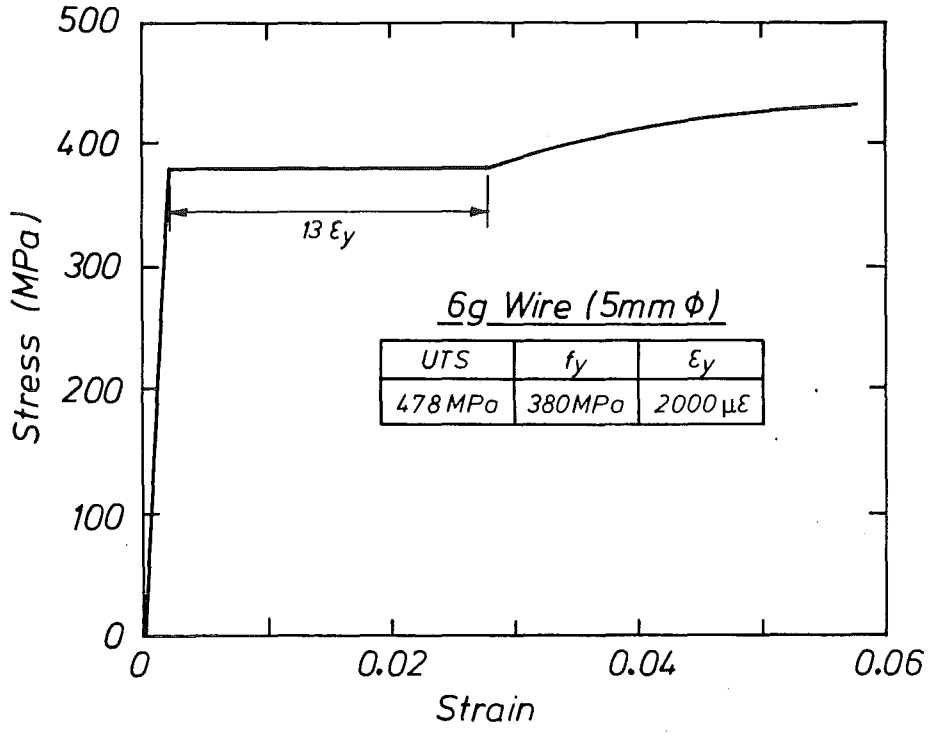

(c) Transverse reinforcement

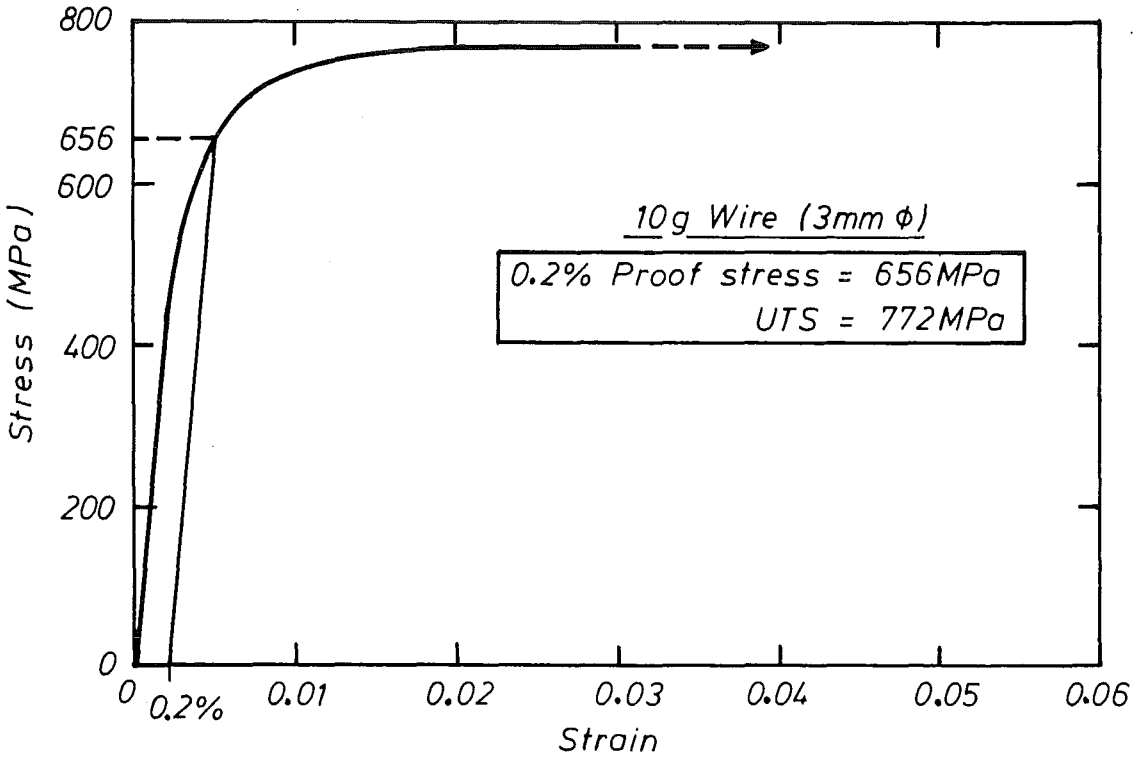

(d) Transverse reinforcement

Fig. 7.6 (contd.): Stress-strain curves for reinforcing steel

Table 7.2 : Theoretical Strength And Ductility Capacity Based On Actual and Specified Material Strengths

Unit	$\frac{M}{VD}$	$\frac{P_i}{f'_c A_g}$ (T)	$\frac{P_i}{f'_c A_g}$ (C)	Initial shear strength V_{si} (kN)	Initial shear strength V_{ci} (kN)	Initial shear strength V_i (kN)	Residual shear strength V_{sf}	Residual shear strength V_{cf}	Residual shear strength V_f	Flexural strength V_{if}	Flexural strength V_{if}^o	Displacement Ductility Capacity μ_c
DT1	1.5	0.13 (0.09)	0.20 (0.12)	49 (30)	91 (92)	140 (122)	58 (45)	11 (13)	69 (58)	107 (112)	133* (139)	-
DT2	2.0	0.09 (0.06)	0.16 (0.10)	49 (30)	63 (66)	112 (96)	59 (60)	11 (13)	70 (73)	80 (83)	98* (102)	-
D1	1.5	-	0.08 (0.05)	49 (30)	70 (78)	119* (108)	58 (45)	11 (13)	69 (58)	100 (103)	122 (126)	2.0 (2.0)
D2	1.5	-	0.08 (0.05)	37 (23)	69 (78)	106* (101)	54 (35)	8 (10)	62 (45)	100 (103)	122 (126)	2.0 (<1.0)
D3	1.5	-	0.08 (0.05)	53 (50)	69 (78)	122* (128)	53 (66)	21 (25)	74 (91)	100 (103)	122 (126)	2.0 (2.8)
D4	1.5	-	0.08 (0.05)	30 (18)	70 (78)	100* (96)	45 (27)	6 (8)	51 (35)	100 (103)	122 (126)	2.0 (<1.0)
D5	2.0	-	0.08 (0.05)	49 (30)	52 (59)	101 (89)	57 (60)	11 (13)	68 (73)	75 (77)	92* (94)	5.7 (2.0)
D6	2.0	-	0.08 (0.05)	37 (23)	51 (59)	88* (82)	53 (46)	8 (10)	61 (56)	75 (77)	92 (94)	2.0 (2.0)
D7	2.0	-	0.08 (0.05)	30 (18)	52 (59)	82* (77)	51 (36)	6 (8)	57 (44)	75 (77)	92 (94)	2.0 (2.0)
D8	2.0	-	0.08 (0.05)	30 (18)	51 (59)	81* (77)	50 (36)	6 (8)	56 (44)	75 (77)	92 (94)	2.0 (2.0)

T : Tension C : Compression * predicted ultimate strength value

NOTE: (1) The strength and ductility values are for columns with axial compression.

(2) The bracketed values are design values based on f'_c = 30 MPa and f_{yt} = 400 MPa, while the other values are calculated based on actual material strengths of $f'_c \approx$ 20 MPa and f_{yt} = 656 MPa (or 380 MPa in the case of Unit D3).

enclosed in brackets. The ideal flexural strengths for twin-pier models were determined such that the V_{if} values, when substituted into Eqs. 7.8a and b gave the levels of axial load that agreed with those used in calculating the V_{if} values. The change in flexural strengths due to difference in concrete strengths was not very significant while the greatest change in V_i and V_f was 17% (Unit DT2) and 46% (Unit D4) respectively. The predicted ductility capacity was rather insensitive to the change in material strengths except for Unit D5 in which the value based on actual material strengths gave a higher value (μ = 5.7) than that based on specified strength (μ = 2.0).

7.5 MODEL LOADING

7.5.1 Simulation Of Inertia Load

Previous dynamic testing of a bridge pier at the University of Canterbury[7.5] involved a column unit cast monolithically with a large mass of concrete representing the dead weight of superstructure at the top. This practice in the present series of tests would have resulted in unnecessary wastage of material and also, because of the monolithic casting, the rotational inertia of the concrete block would have affected the distribution of moments and shears up the pier height.

For the present series of tests, a reusable concrete block which could be coupled to the pier under test was designed. The inertia mass was designed to be large enough to avoid significant distortion of gravity load similitude. The target weight of the block was 50 kN, which was provided by a mass of concrete, the dimensions of which were 2500 x 1000 x 830 mm^3, as shown in Fig. 7.1. The weight of the block was chosen such that it was within the capacity of handling equipment in the laboratory and such that the inertia load due to maximum probable response was within the capacity of the table. The actual weight of the inertia mass was measured and found to be 49.26 kN (i.e. mass = 5.021 tonnes with $g = 9.81\ m/s^2$). Together with the mass of the coupling system and other steel fixings the total inertia mass was 5.2 tonnes.

As shown in Fig. 7.1, the column unit was connected to the concrete block via a 40 mm high strength steel pin. The connecting bracket was bolted to the concrete block through the anchorage provided beneath the block. In the case of single pier models, the inertia mass was supported by a special coupling system designed to maintain it in its horizontal position while the column was being tested. The coupling system shown in Figs. 7.1a and 7.7, consisted of two horizontal links

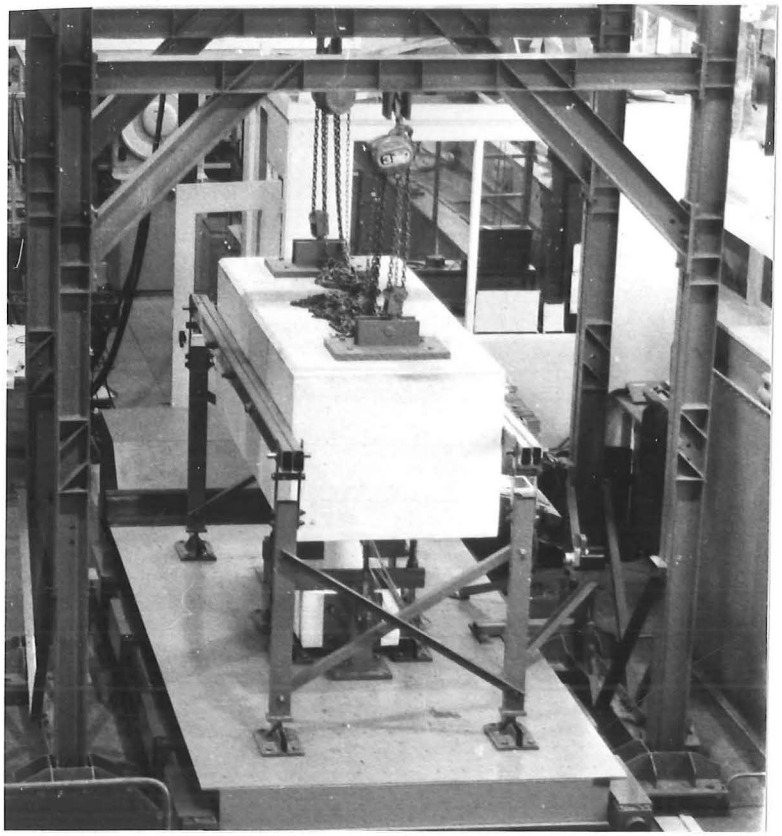

(a) End view

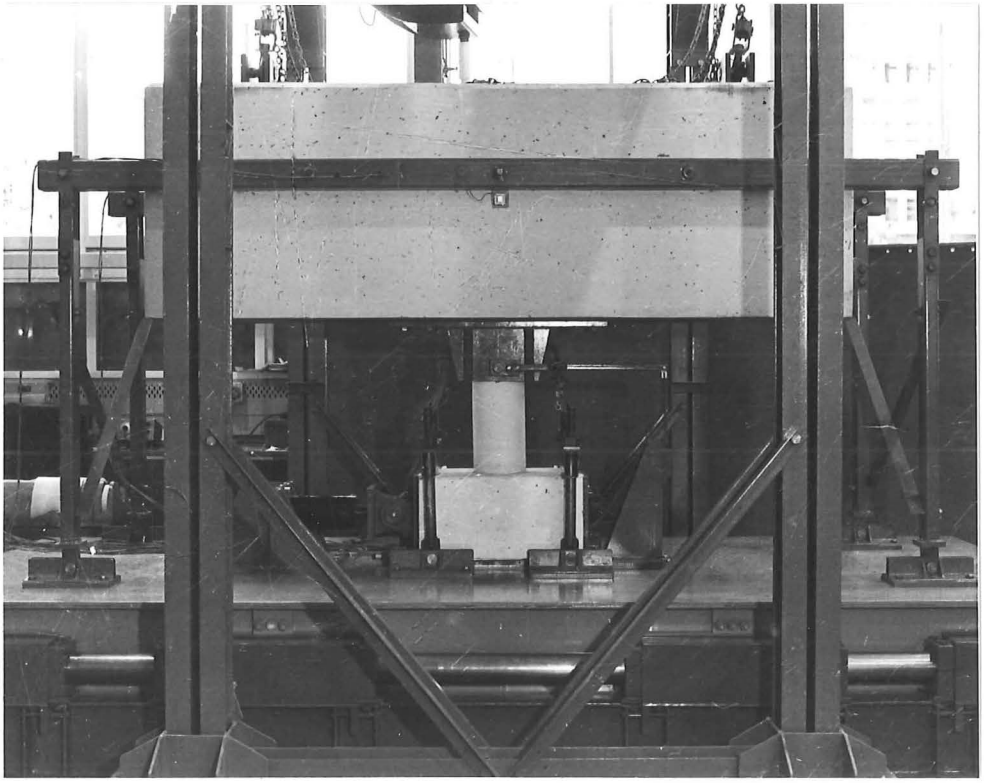

(b) Side view

Fig. 7.7 : Single pier test set-up

made up of two pairs of rectangular hollow steel sections and four vertical struts made up of similar sections. The vertical struts were pinned to the horizontal links at one end and hinged at the base to the shake-table. The mechanism was able to rotate in the planes parallel to the loading plane while keeping the block effectively horizontal. To prevent any movement in the transverse direction, angle sections were used to brace the pairs of struts at both ends of the block as shown in Fig. 7.7a. The horizontal links were bolted to the inertia mass through three PVC tubes provided at a short distance above the mid-depth of the block. They were designed such that they were flexible enough to transfer no more than 25 percent of the axial load to the four vertical struts as the column unit softened butwere strong enough to remain elastic when subjected to bending in the process of load transfer.

7.5.2 Testing Procedures

7.5.2.1 Single piers

Fig. 7.7 shows a typical single pier set-up ready for testing. The single piers were tested using five cycles of sinusoidal excitation of 5 Hz frequency. The tests were carried out in sequence of gradually increasing amplitude of table displacement of 2, 5, 7.5, 10, 15, 20 and 25 mm but earlier failure of some columns meant that the tests had to be terminated before the end of the above sequence in some cases. Sometimes, the same amplitude was repeated to check the behaviour of the column units if failure was felt to be imminent.

Five cycles of sinusoidal excitation were used in these tests so as to provide the best simulation of the static tests which were carried out with 5 cycles of loading to pre-determined displacement ductility levels. Although the static tests could have been better simulated by dynamic displacement to the top of the column units, the intention was to get as realistic a loading as possible, including the instability effect at failure which would not show up in displacement controlled testing.

The natural frequencies of the single piers based on the moment of inertia of cracked section, I_{cr} , (assumed to be 0.6 I_{gross}) and the modulus of elasticity of concrete, E_c (assumed to be $5000\sqrt{f'_c}$), were 24 Hz and 16 Hz for 300 mm and 400 mm tall columns respectively. Fig. 7.8 shows the variation of dynamic magnification factor, D, with the ratio of excitation to natural frequency, β , and the damping ratio, ξ . For a single degree of freedom response to harmonic loading, a forcing

frequency of 5 Hz, giving frequency ratios of $\frac{5}{24} = 0.21$ and $\frac{5}{16} = 0.31$ for two different heights of the column units, implied a dynamic magnification factor of a little over unity initially in the tests (see Fig. 7.8). However, as the stiffness degraded during the later stage of loading, the frequency ratio of the column units increased because of reductions in their natural frequency due to increasing flexibility. As such, the response of the columns became more intense because, as shown in Fig. 7.8, the dynamic magnification factor increases with β until resonance occurs at $\beta = 1$.

7.5.2.2 Twin piers

The presence of alternating axial tension and compression, discussed in Section 7.3.2.3, in the twin-piers made validity of a direct comparison of the dynamic test results with the static test results doubtful. Hence, it was decided to test the two twin-pier models with a more realistic simulation of seismic loading, using an actual earthquake record. For these tests, the May 1940 El Centro N-S earthquake acceleration record was numerically integrated twice to provide the ground motion in terms of displacement signals as shown in Fig. 7.9 with a time scaling factor of 7.5. Although the resulting acceleration trace obtained from table response may not exactly resemble that of the actual earthquake, it was believed to be reasonably representative of the selected excitation.

The tests were carried out with series of gradually increasing intensity. Actual duration of the earthquake excitation was about 9 seconds. The maximum measured table acceleration varied from about 0.5g to 5.0g corresponding to prototype values of 0.067g to 0.67g with the scaling factor of 7.5 used.

Fig. 7.10 shows the twin-pier test set-up ready for testing; in this case the coupling system outlined in the last section was not used, since the twin-pier set-up stabilized the inertia mass against uncontrolled rotation.

7.6 INSTRUMENTATION

7.6.1 Earthquake Simulating System

The basic components of the earthquake simulating system consisted of the shake-table, the Dartec testing facility and the external programming device to generate the command signals. The 2 m x 4 m shake-table was driven by a servohydraulic actuator and was designed as part of this

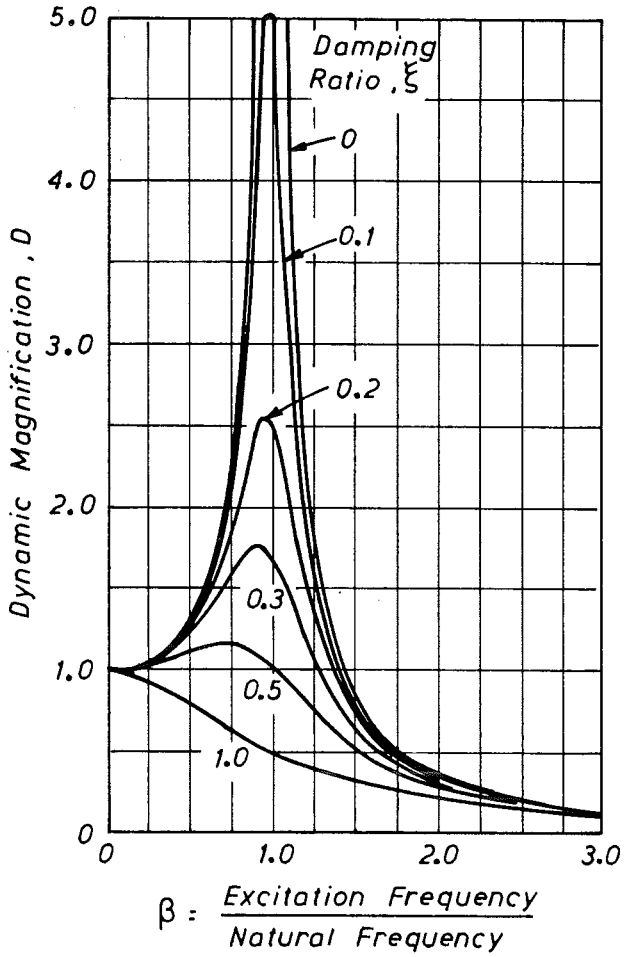

Fig. 7.8 : Variation of dynamic magnification factor with frequency ratio and damping ratio

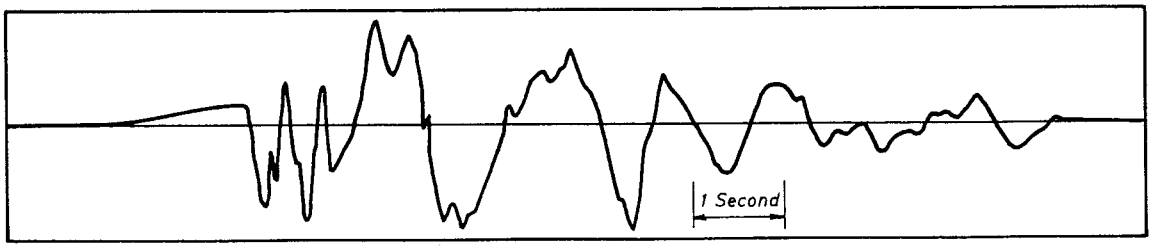

Fig. 7.9 : A typical trace of earthquake displacement record used in the testing of twin-pier models

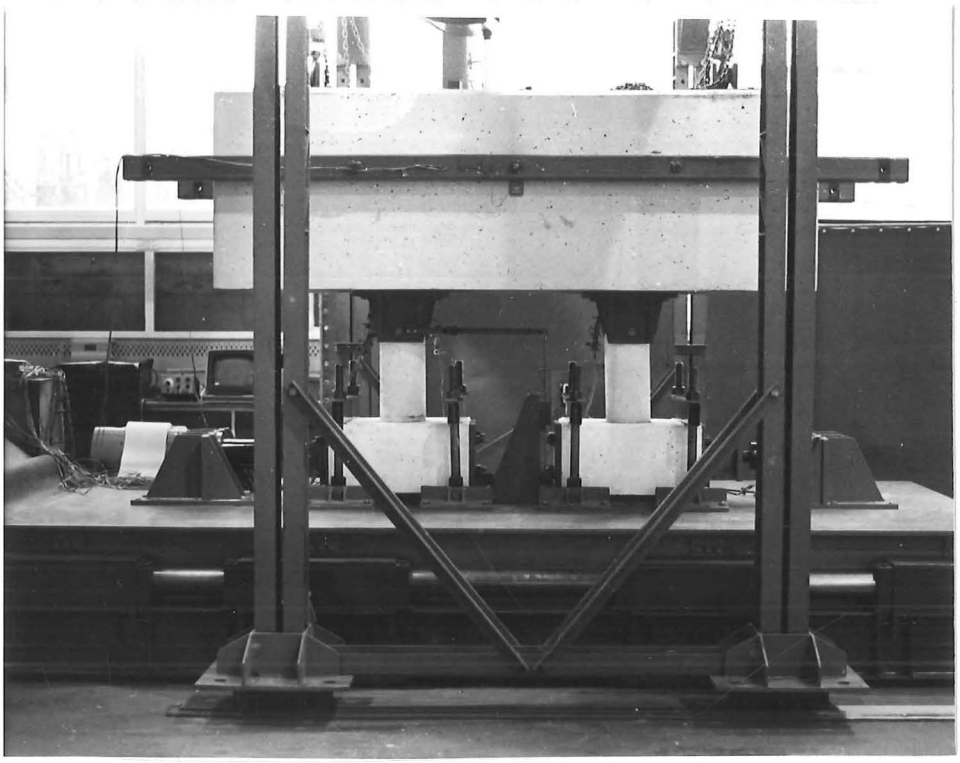

(a) Side view

(b) Oblique view

Fig. 7.10 : Twin-pier test set-up

project. Details of the design, and of mechanical and electronic components of the shake-table facility are described in Appendix III.

7.6.2 Data Acquisition System

As each test was completed in only a few seconds, the readings from various transducers had to be captured at high speed. Sufficient data points had to be acquired in order to allow response curves like load-deflection hysteresis loops to be constructed with reasonable accuracy. Data were recorded using the Civil Engineering Data Acquisition System (CEDACS) and a Bryans Southern Ultraviolet Oscillograph. The oscillograph provided an almost instantaneous display of time-history response of the column units being tested. No more than six channels of the oscillograph were selected in order to have reasonably clear traces of the time-history responses. Where necessary, the curves traced by the oscillograph were digitized for evaluation of results. Details of the CEDACS data logger are given in Appendix III.

7.6.3 Instruments To Monitor Column Performance

The performance of the column units was monitored continuously in terms of acceleration, displacement, base shear and spiral strain. The following sub-sections describe briefly the types of instruments used to measure these quantities.

7.6.3.1 Accelerometers

A Kistler 305A accelerometer was used to measure the table acceleration. It was located under the load cell close to the centre of the table as shown in Fig. 7.1a. The signal from this accelerometer was input to a channel of a Brush Mark 280 Recorder.

For single pier testings, two strain-gauged accelerometers (Showa BA-2L) were used to measure the concrete block acceleration. The accelerometers were placed at the level of centre of gravity of the block on both the north and south sides (Fig. 7.1a). A small piece of sheet metal glued to the block provided a smooth surface onto which the accelerometer could be stuck by means of double-sided tape. Both accelerometers had a maximum rating of 2g.

Higher response acceleration was anticipated in the case of twin-pier testings. Thus, the accelerometers used were replaced by a Showa BA-5L (5g) accelerometer on the north side and a Kyowa AS-10B (10g) accelerometer on the south.

In all the tests, one accelerometer was connected to the CEDACS data logger and the other to the oscillograph.

7.6.3.2 Displacement transducers

The internal LVDT in the Dartec actuator monitored the displacement response of the shake-table. The stroke readings were found to correspond very well with the displacement measured externally using a dial gauge during calibration run of the table. Hence, the stroke readings were used directly as an indication of the table movement and this was fed to the remaining channel of the Brush Mark 280 Recorder so that synchronised traces of table acceleration and displacement could be obtained.

To measure the displacement of the column units at the pin level, a deflection device was specially made. The device was designed as a simple vertical cantilever with strain gauges at the base to measure the bending strains. The relationship between strain and deflection was obtained by calibration. The cantilever was made from high strength spring steel of 3 mm thickness. Altogether two sets of strain gauges were used; one set was connected to the CEDACS data logger and the other to the oscillograph. The distance from the pin to the outermost set of strain gauges was 300 mm.

The base of the deflection device was clamped to a rigid bracket connected to the shake-table. The top of the device was connected by a pin-ended strut to the pin joining the column to the inertia mass as shown in Fig. 7.11, where the deflected device at the end of the test can be seen. Several such devices were made and calibrated in anticipation of damage due to excessive bending during failure of column units. The sensitivity of the device was typically 34 mm/V , enabling a resolution of 0.034 mm.

7.6.3.3 Load cells

Load cells were used to measure the base shear input to the piers. The readings taken served as a check on the acceleration results and in the case of twin-piers, they give an indication of the proportion of lateral force input into each pier. They were designed to have a capacity of 200 kN and were rear-mounted on a rigid bracket bolted to the shake-table. The load cell was connected to the footing of the test column via a 50 mm steel pin as shown in Fig. 7.12. The load cells were strain gauged with two sets of strain-gauges, one of which was connected to the CEDACS data logger and the other to the oscillograph.

The footing of each pier was separated from the shake-table by a bed of rollers so as to reduce the frictional force, and ensure maximum shear transfer through the load cell. As shown in Fig. 7.13, the rollers were placed between a pair of machined stainless steel plates. The four holding-down bolts for each pier were also pinned at their base to allow some freedom in rotation to accommodate any movement that might arise. The details of the base connection of these bolts can also be seen in Fig. 7.13.

The frictional force of the roller system was measured using two load cells and a hydraulic jack pushing from one end of the footing while the column was in position. The two load cells, one at each end of the footing, measured the load before and after frictional loss and hence the difference between the two readings give an indication of the magnitude of the frictional force in the roller system. In this way, the frictional force was found to be about 13 kN, but it depended on the level of clamping force provided by the holding-down bolts.

7.6.3.4 Strain gauges

The strain gauges and the self-adhesive terminal strips were the same as those used in the static tests. They were mounted on the spirals following the pattern described in Section 3.4.2.

7.6.4 Filming And Photographing Facilities

A video camera and a Super 8 movie camera were used to film the column behaviour during testing. The movie camera was mounted on a rigid supporting frame bolted to the shake-table and thus recorded the behaviour relative to the table. Besides the video and the movie cameras, still photographs were also taken to record the damage at any point of interest. Cracks were marked in-between tests before taking any photograph.

Fig. 7.11 : A deflected displacement transducer at the end of a test.

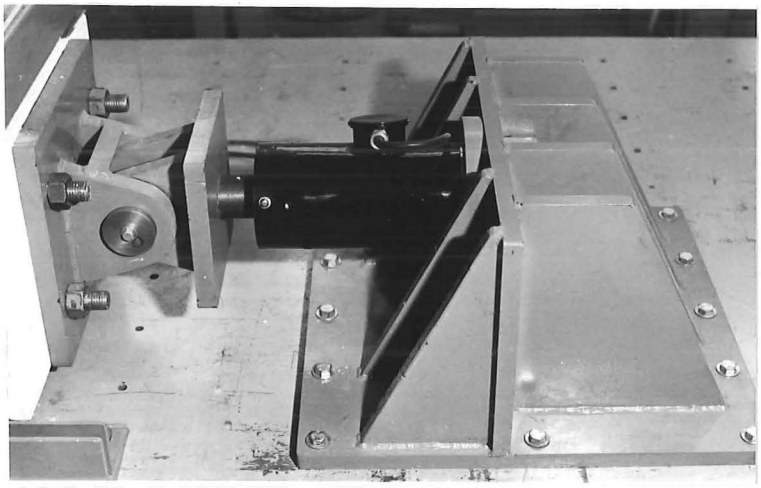

Fig. 7.12 : Load cell and the coupling system

Fig. 7.13 : Rollers and base details of holding down bolts

Chapter Eight

— DYNAMIC TESTS OF CIRCULAR COLUMNS — RESULTS AND OBSERVATIONS

8.1 INTRODUCTION

The results obtained from the dynamic tests described in Chapter Seven are presented in this chapter. General observations of behaviour of the column units are briefly described first. The rapid nature of the tests did not allow a close observation of the behaviour during tests but video-tapes and films provided a good record of the sequence of events leading to failure of the column units. As in the case of the earlier static tests, the performance was mainly gauged in terms of strength and displacement ductility. Data recorded in digital or analogue form were used to plot the shear force-deflection hysteresis response of the column units. As is pointed out later, the actual shear force acting on the column units was better represented by the response acceleration results (i.e. inertia load) rather than the base-reactions measured by load cell, so the strength of the column units were discussed in terms of the former. The rather irregular nature of the hysteresis loops made assessment of relative energy dissipated in a cycle (relative to perfectly plastic elasto-plastic response) of doubtful validity. Hence, the energy dissipation property of the column units are not discussed. Also, since no attempt was made to measure column curvatures, the concrete strains at crushing and spalling can not be presented. However, from measured spiral strains and estimated crack inclinations, shear force resisted by the spiral reinforcement and hence the 'concrete contribution' could be calculated. Comparison with static test results was made wherever possible.

8.2 GENERAL OBSERVATIONS

The single pier units were subjected to a sequence of tests with sinusoidal excitation of 5 Hz and with increasing amplitude levels between tests. Five cycle of such excitation at table displacement amplitudes of 2, 5, 7.5, 10, 15, 20 and 25 mm were used. The corresponding maximum theoretical table accelerations (i.e. $(2\pi f)^2$ x amplitude) are listed in Table 8.1. Fig. 8.1 shows typical traces of input displacement and acceleration records. The high frequency components in the table acceleration record were due to the natural frequency of the

Table 8.1 : Maximum Theoretical Table Accelerations
(Single Pier Units)

TEST	Table Displacement Δ_{table} (mm)	Table Acceleration * (m/s^2)	(xg)
1	2	1.97	0.2
2	5	4.93	0.5
3	7.5	7.40	0.75
4	10	9.87	1.0
5	15	14.80	1.5
6	20	19.74	2.0
7	25	24.67	2.5

* $(2\pi f)^2 \Delta_{table}$

f : excitation frequency

g : gravitational acceleration

Table 8.2 : Maximum Measured Table Acceleration
(Twin-Pier Units)

TEST	Table Acceleration (xg)	
	DT1	DT2
1	0.6	0.5
2	1.1	1.0
3	1.5	1.7
4	1.9	1.9
5	2.6	2.4
6	3.5	3.5
7	4.7	3.9

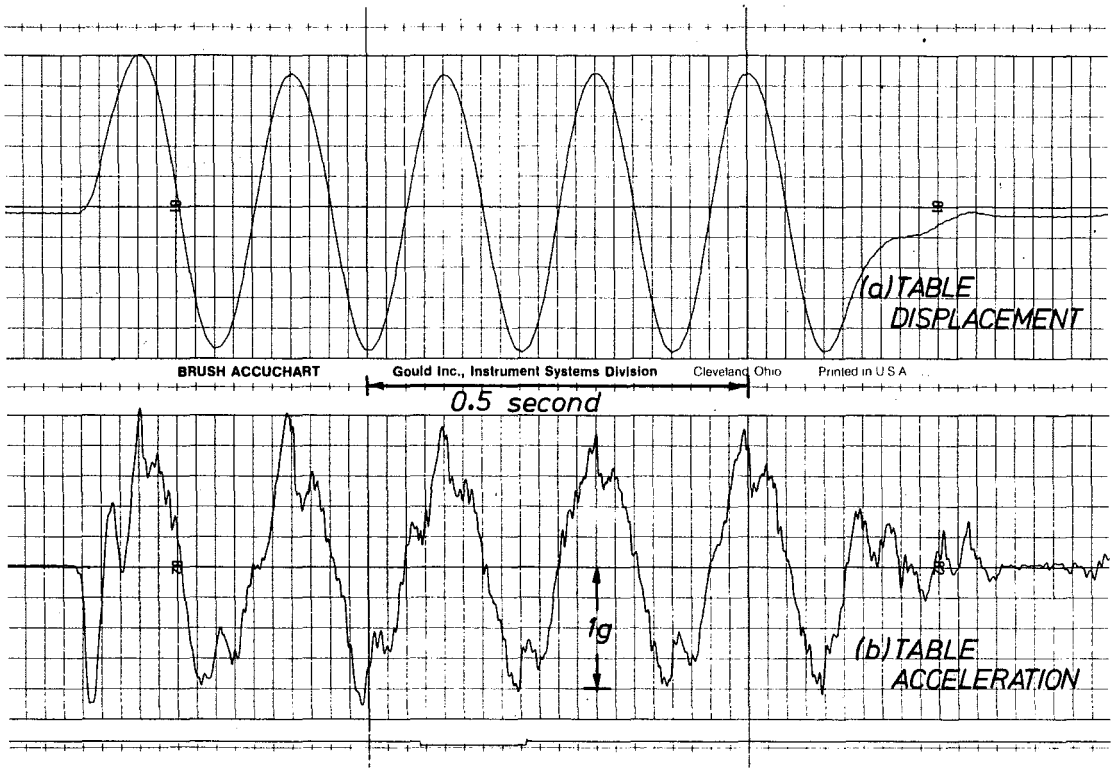

Fig. 8.1 : Typical displacement and acceleration traces of sinusoidal excitation (5Hz at 7.5 mm)

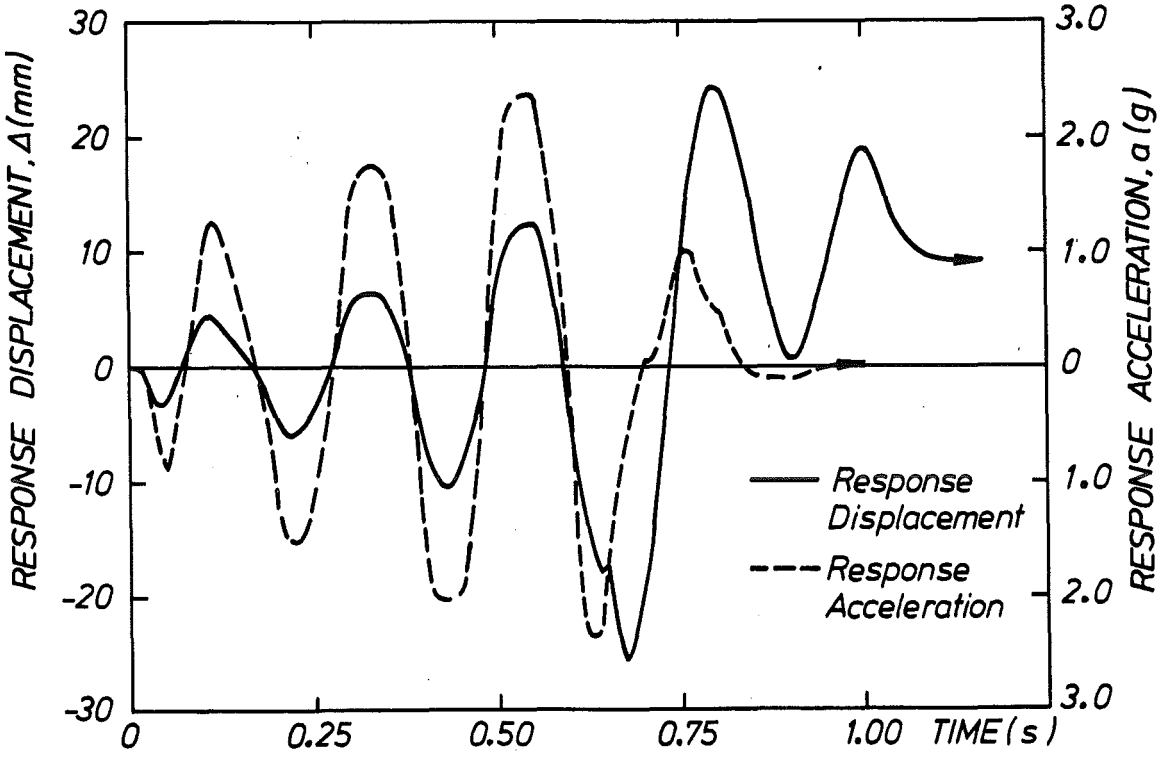

Fig. 8.2 : Time-history of response acceleration and displacement of a typical single column unit to sinusoidal excitation of 5 Hz frequency at 7.5 mm amplitude.

table mass on the hydraulic system, and the servovalve response frequency, but were considered unlikely to have significantly influenced column unit response. This was confirmed by response acceleration records, as shown typically in Fig. 8.2, which indicated column response was dictated by the fundamental excitation frequency of 5 Hz.

The two twin-piers were tested using earthquake ground motion obtained by numerically integrating the N-S component of the acceleration record of May, 1940 El Centro Earthquake twice to get a displacement record (see Fig. 7.9). A time scaling factor of 7.5 was used and the units were also subjected to a series of tests with increasing amplitudes. The maximum table acceleration measured for a given test varied from 0.5g to 4.7g and typical traces of table displacement and acceleration records are shown in Fig. 8.3. The peak table accelerations during the testing of the two twin-piers were scaled from such acceleration traces and are summarized in Table 8.2. Note that the high frequency component on both displacement and acceleration traces in Fig. 8.3 is due to 50 Hz interference on the recorder, and were not present in the table.

8.2.1 Single Pier Units D1 To D4 ($\frac{M}{VD} = 1.5$)

Based on the design proposal of Chapter Five, Units D1 to D4 were expected to fail in shear with limited or no ductility. In fact all of them failed during Test 3 when the amplitude of excitation was 7.5 mm, with low response ductility level. No obvious damage was detected in any of them during Test 1. Diagonal cracking was initiated during Test 2, but the column units still responded in their elastic range. Due to stress concentration, some minor cracks appeared around the pin connecting the pier to the inertia mass. These cracks did not propogate further nor affected behaviour in subsequent tests. Failure was generally sudden and explosive, with a diagonal failure plane forming and leading to immediate physical disintegration.

Units D1 to D4 differed only in the quantity of transverse reinforcement provided, which varied between $\rho_s = 0.00306$ and $\rho_s = 0.01061$. Unit D1 ($\rho_s = 0.00509$) failed in shear during the first half of Cycle 4 of Test 3. The failure was explosive and several spirals were broken. The final appearance of this column unit is as shown in Fig. 8.4. The failure planes are apparent in the figure and the angle of inclination was found to be about 45-deg.

Shear failure in Unit D2 ($\rho_s = 0.00382$) was initiated during the

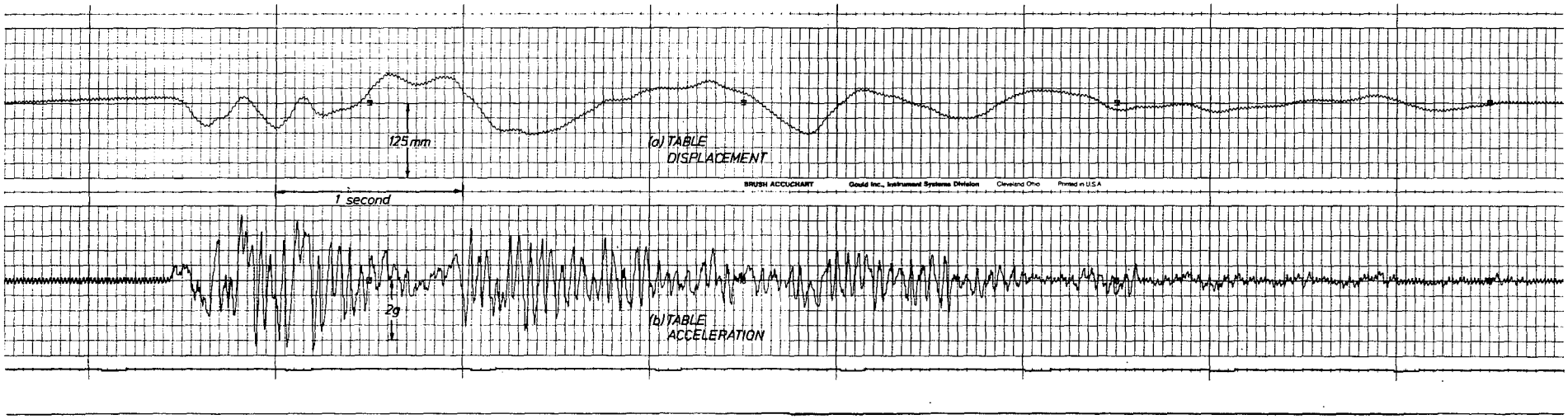

Fig. 8.3 : Typical displacement and acceleration traces of earthquake excitation

second half of Cyle 4 of Test 3. The unit failed predominantly along a main diagonal crack which followed an approximately 40-deg failure plane. Extensive spalling along the main crack can be seen in Fig. 8.5. Fracture of a number of spirals also took place.

6 gauge wire (5 mm diameter) was used in Unit 3 (ρ_s = 0.01061) instead of the 10 gauge wire (3 mm diameter) used in all the other column units. This wire had a more ductile behaviour and a higher ultimate strain. Consequently, there was no fracture of spiral reinforcement during the tests. This column unit failed in Test 3 after extensive spalling of concrete cover and collapse of core concrete had taken place. More tests with larger amplitudes were conducted subsequent to Test 3 and this led to complete disintegration of concrete, the extent of which can be seen in Fig. 8.6.

Figs. 8.7 a and b are photographs taken during testing of Unit D4 (ρ_s = 0.00306). The initial explosive nature of the formation of the failure plane is apparent in Fig. 8.7a. Failure in this column unit took place during the second half of Cycle 3 of Test 3. The damage concentrated mainly in the main inclined failure plane that formed first (see Fig. 8.7a). The angle of inclination of this failure plane was estimated to be about 45-deg. Fracture of spirals, extensive spalling and collapse of the concrete core took place as the column unit failed in shear. A close-up view of the failed region is shown in Fig. 8.7c.

8.2.2 Single Pier Units D5 To D8 ($\frac{M}{VD}$ = 2.0)

The main variable in these column units was again the spiral reinforcement content which varied between ρ_s = 0.00306 and ρ_s = 0.00509. Besides this variation a reduced number of bars of larger diameter (12 mm diameter) were used for flexural reinforcement in Unit D8 instead of the HD-8 bars in all the other columns. Based on the design proposal of Chapter Five, all these column units except D5 were expected to fail in shear with limited or no ductility. Unit D5 was expected to fail in shear with a displacement ductility capacity of 5.7.

Five cycles with amplitude of 2 mm in Test 1 did not cause any damage to any of the column units. Diagonal cracking took place in Units D7 and D8 during Test 2 (5 Hz at 5 mm) but no damage could be detected in Units D5 and D6. Units D7 and D8 possessed smaller spiral reinforcement content (ρ_s = 0.00306) than Units D5 (ρ_s = 0.00509) and D6 (ρ_s = 0.00382) and as a consequence, failed earlier than Units D5 and D6, when subjected to Test 3. Unit D6 failed during Test 6 when the amplitude of excitation was 20 mm but Unit D5 survived in Test 6 and

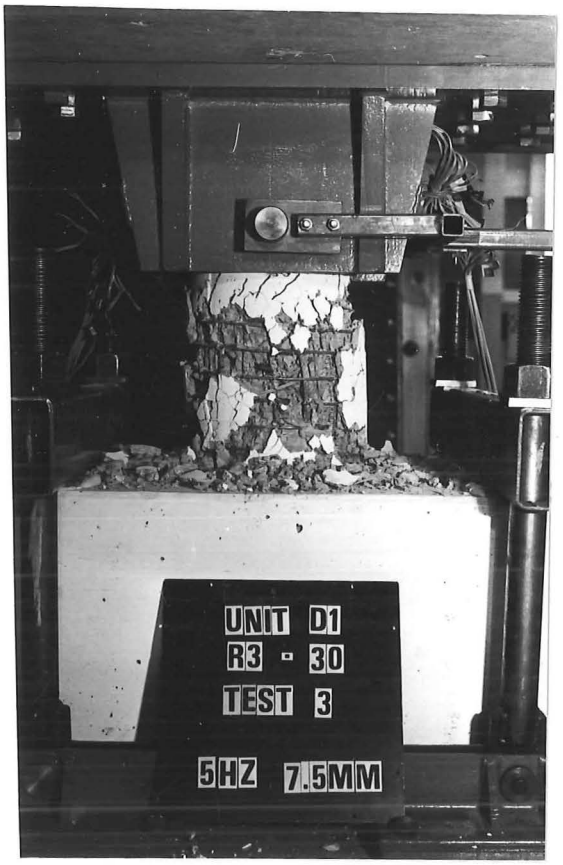

Fig. 8.4 : Final appearance of Unit Dl

Fig. 8.5 : Final appearance of Unit D2

Fig. 8.6 : Final appearance of Unit D3

failed in Test 7 under a table displacement amplitude of 25 mm.

On the basis of the proposal outlined in Chapter Five, Unit D5 (ρ_s = 0.00509) was expected to fail at μ = 5.7 . It indeed failed at a displacement ductility of about μ = 5 with distinct plastic hinging. However, unlike comparable column units tested statically, flexural cracks appeared only after diagonal cracking had already occurred. This phenomenon was also observed in the other column units within this group. The diagonal cracking load for this unit was estimated to be about 38 kN (see Table 8.6) and if based on a concrete tensile strength of $0.77\sqrt{f'_c}$ obtained from indirect modulus of rupture test on concrete prisms given in Chapter Seven, flexural cracks are expected to appear at a load of about 13 kN. Hence, unless flexural cracks occurred but were not detected during earlier tests of lower response level, these values represent at least a three-fold increase in the flexural tensile strength in the column unit under the dynamic loading situation, and are typical of this group of column units. Shear failure with fracture of spirals took place in Unit D5 during the second half of Cycle 1 of Test 7. Fig. 8.8 shows Unit D5 after failure. The more dramatic collapse of this unit was due to lack of support of the concrete block by means other than the column after failure. Unit D5 was the second unit, after Unit D6, tested in this series. During the testing of both of these units, a more flexible coupling system to overcome the rotational inertia of the concrete block (see Section 7.5.1) was used and this flexible system had poor control on the movement of the block as the test unit failed. Subsequent to the testing of Units D5 and D6 the coupling system was stiffened substantially and the inertia block was supported loosely by a chain which took the weight after column failure, enabling a better examination of the failure to be made.

Unit D6 (ρ_s = 0.00382) failed during the second half of Cycle 1 of Test 6. Several spirals were broken along the failure plane which was inclined at about 50-deg to the column axis. The appearance of the unit after failure is shown in Fig. 8.9.

The appearance of Unit D7 (ρ_s = 0.00306) at the end of the tests is shown in Fig. 8.10. The failure plane was estimated to be 35-deg with respect to the column axis. This column unit failed during the second half of Cycle 2 of Test 3 and it failed predominantly in one direction. Though the failure of this column unit occurred earlier, the damage was not as extensive as in Units D5 and D6 shown in Figs. 8.8 and 8.9 because of the reasons given earlier. Fracture of spirals and extensive spalling of concrete occurred.

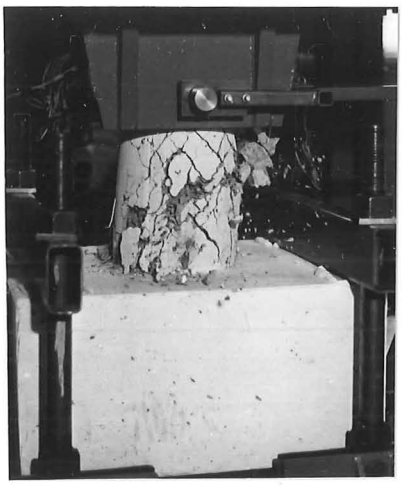

(a) Formation of failure plane

(b) After failure

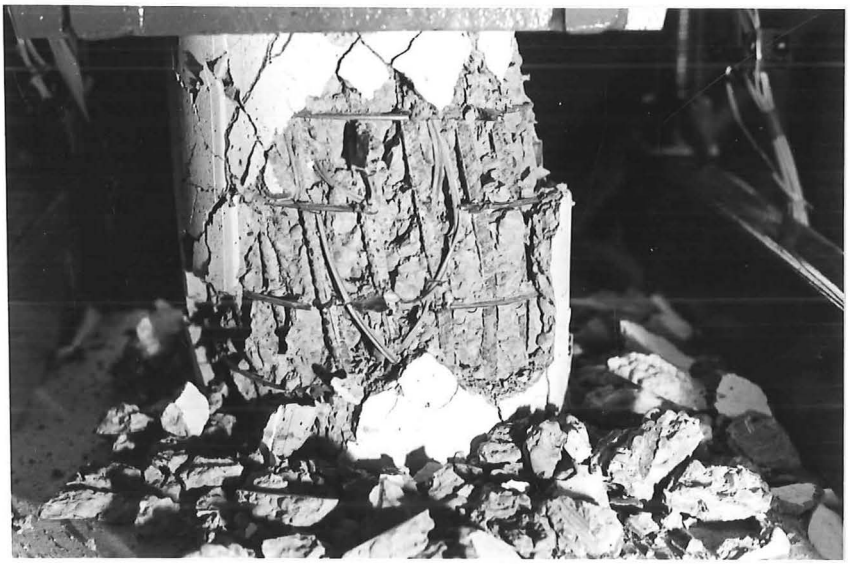

(c) A close up view after failure

Fig. 8.7 : Damage in Unit D4

Fig. 8.8 : Final appearance of Unit D5

A reduced number of bars of larger diameter (12 mm) were used for flexural reinforcement in Unit D8 (ρ_s = 0.00306) to give the same total longitudinal reinforcement content of 0.00320. The stress-strain curve of the flexural steel showed a distinct yield plateau but the strength ($f_{y\ell}$ = 450 MPa) was of the same magnitude as that of HD-8 bars (0.2% proof stress = 436 MPa) used in all the other column units. This column unit failed along an inclined plane, at about 40-deg to the column axis, as shown in Fig. 8.11. The bond between the flexural bars and the concrete was lost and a number of spirals fractured.

8.2.3 Twin-Pier Units DT1 And DT2

Unit DT1 consisted of two columns with aspect ratio of 1.5 and spiral reinforcement content of 0.00509. No obvious damage or cracking could be detected after the first two tests, with maximum table excitation of about 1.1g. Diagonal cracking initiated during Test 3 while the columns were still responding in their elastic range. As shown in Fig. 8.12a, the inclination of the diagonal cracks in the columns indicated that the cracks were initiated while the columns were in tension. At this stage, diagonal cracking did not occur while the columns were subjected to maximum compression. The cracks were at about 45-deg to the column axis. Diagonal cracking in the other direction, and flexural cracking, were first noted in Test 5 (2.6g table excitation). Incipient spalling at the column base was detected after the completion of Test 5. Fig. 8.12b shows the appearance of the column after Test 5. Spalling of concrete became more extensive in Test 6 (3.5g table excitation) and ductile flexure plastic hinging was apparent. Failure took place along an inclined plane in both columns but the one at the west (DT1-W) failed marginally earlier, while subjected to axial tension. The sudden reduction in shear carrying capacity in Column DT1-W forced additional load onto the compression column, DT1-E, which failed subsequently. Fig. 8.11c shows the final appearance of Unit DT1 after the tests were completed.

Columns of Unit DT2 had an aspect ratio of 2.0. The spiral reinforcement content used was 0.00509. Since the higher aspect ratio implied a lower shear at the development of flexural strength, a more ductile response was therefore expected compared with Unit DT1. The first two tests did not induce visible cracking in the columns. Diagonal cracking was initiated during Test 3 only in the east column, DT2-E. Diagonal cracks at about 40-deg to the column axis appeared in both columns during Test 4 and flexural cracks appeared during Test 5

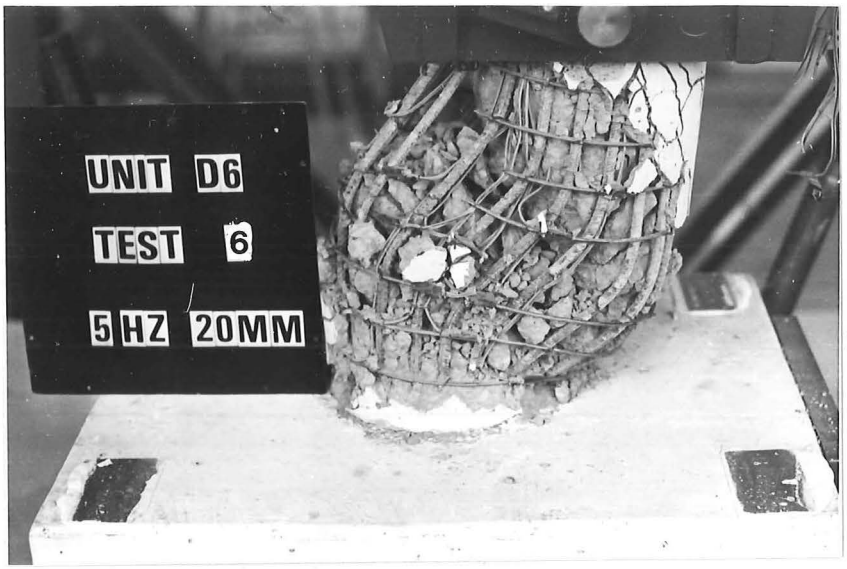

Fig. 8.9 : Final appearance of Unit D6

Fig. 8.10 : Final appearance of Unit D7

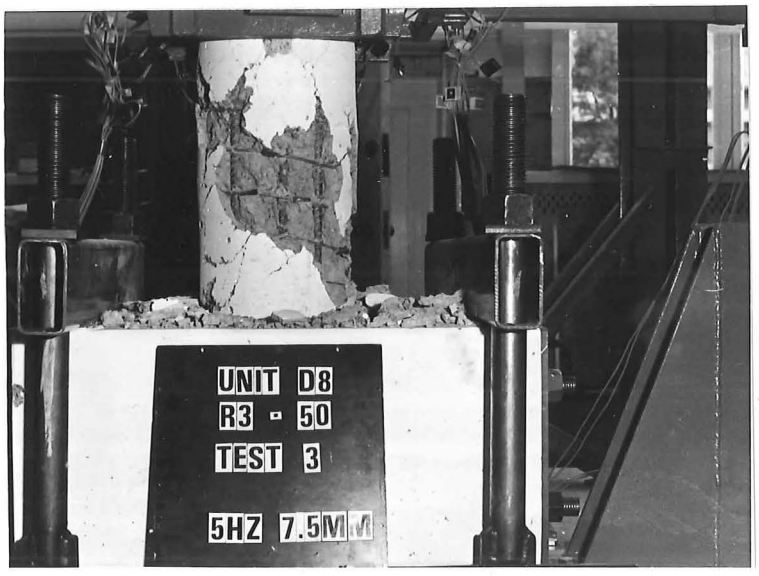

Fig. 8.11 : Final appearance of Unit D8

East West

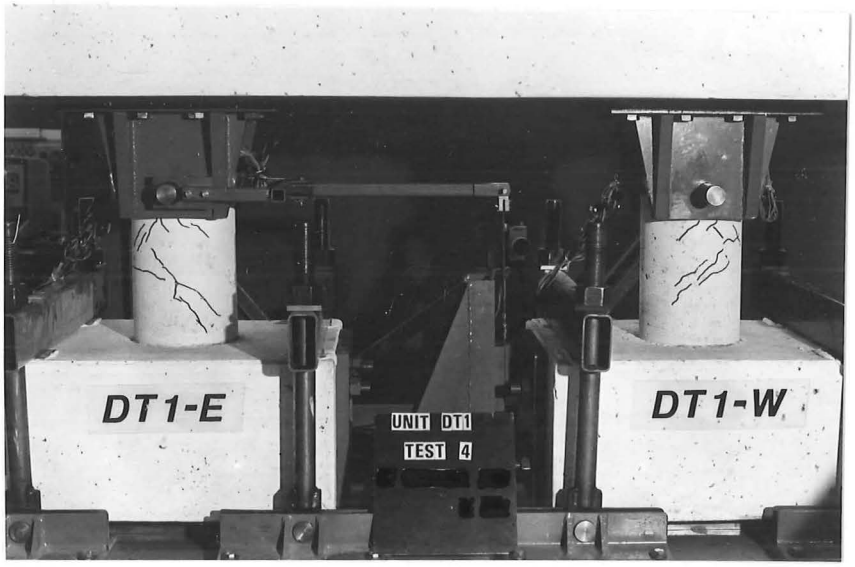

(a) After Test 4 (max. table accel. ≈ 1.9g)

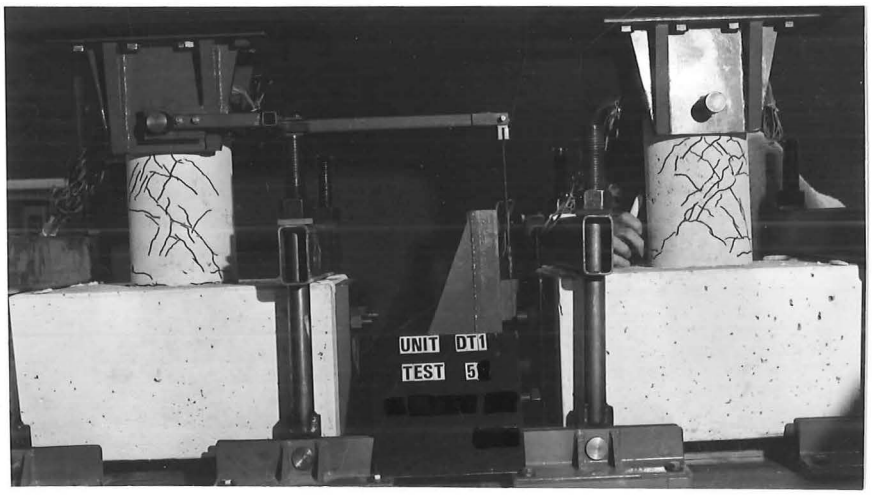

(b) After Test 5 (max. table accel. ≈ 2.6g)

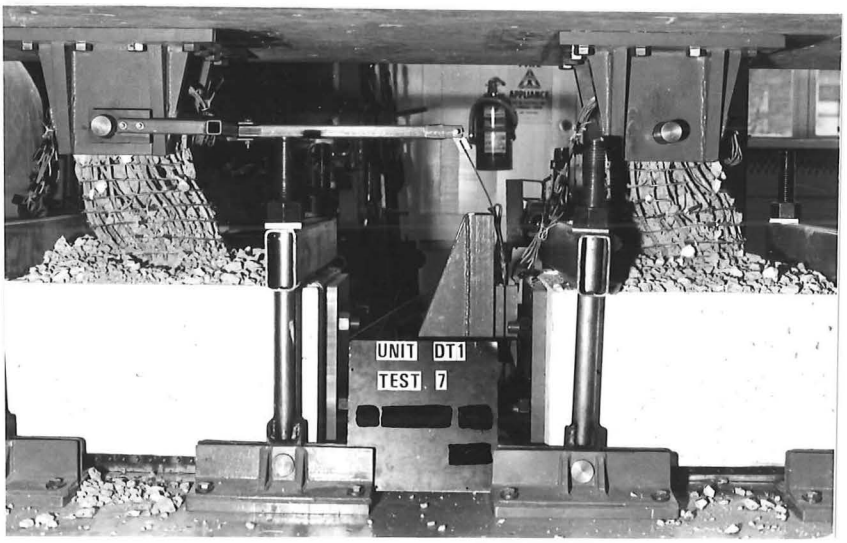

(c) After Test 7 (max. table accel. ≈ 4.7g)

Fig. 8.12 : Damage in Unit DT1 at different stages of the tests

(2.4g table excitation). Spalling of concrete at the column base was also detected after Test 5 (see Fig. 8.13a). Diagonal cracking and spalling of concrete became extensive during Test 6 (see Fig. 8.13b) and the columns eventually failed in Test 7. The columns failed along an inclined plane and the east column (DT2-E) was the first to fail. The west column (DT-W) failed about 0.8 seconds later. Figs. 8.14 a to f record the failure of the columns. Note that in this case the first column to fail was in compression. From the figures, the inclination of the failure planes was found to be approximately 40-deg with respect to the column axis. The final appearance of the columns is shown in two close-up views in Figs. 8.13c and d.

8.3 LOAD-DEFLECTION HYSTERESIS RESPONSE

8.3.1 Column Shear Force

The horizontal base reaction was measured directly by load cell connected to the base of the column units (Section 7.6.3.3). The maximum readings from the load cell as recorded by the CEDACS data logger and oscillograph are listed in Table 8.3 for single piers. Also listed in the table are the corresponding values as computed from inertia mass response acceleration recorded by the same two instruments, i.e. $9.81\ Ma$, where M $(5.2 \times 10^3 kg)$ is the total inertia mass and a is the response acceleration as a proportion of g, the acceleration due to gravity. Comparison between the two differently obtained shear forces at ultimate indicates that the load cell readings are, on average, about 10 percent higher than the results calculated from the response accelerations. This discrepancy is apparent in the results recorded by both the CEDACS data logger and the oscillograph. The discrepancy can be explained with reference to Fig. 8.15. As the load-cell is pinned to the column unit at the mid-depth of its footing, there is a tendency for the column to rotate as a rigid body about this pivoted position as the shake-table is moved. Consequently, the frictional force on the base rollers acted in the same direction as that of the inertia force (i.e. $9.81\ Ma$) which acted through the pin at the top of the column unit. The horizontal base reaction measured by the load cell was the sum of these two forces. It was therefore larger than the inertia force and did not represent the actual shear force acting on the column unit. Hence, the shear forces acting on the columns were more truly represented by the results calculated from response acceleration readings. The difference between the two results was of about the same magnitude as the measured frictional force of the roller system (Section 7.6.3.3).

(a) After Test 5 (maximum table acceleration ≈ 2.4g)

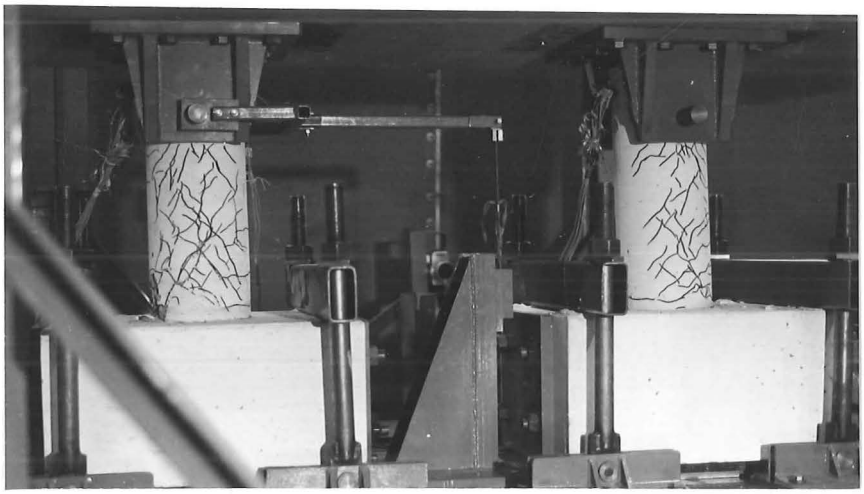

(b) After Test 6 (maximum table acceleration ≈ 3.5g)

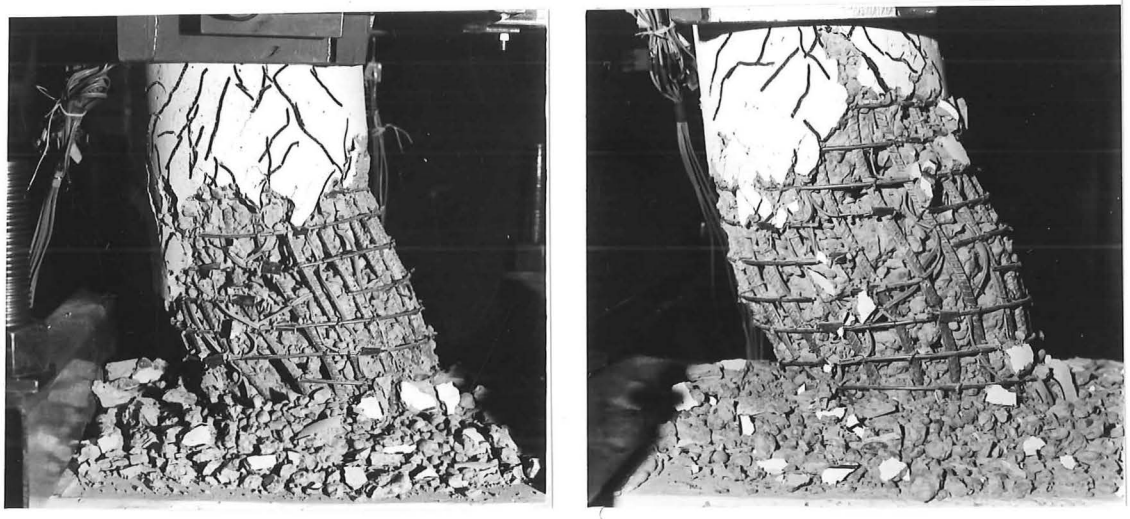

(c) DT2-E after Test 7 (d) DT2-W after Test 7

(maximum table acceleration ≈ 3.9g)

Fig. 8.13 : Damage in Unit DT2 at different stages of the tests

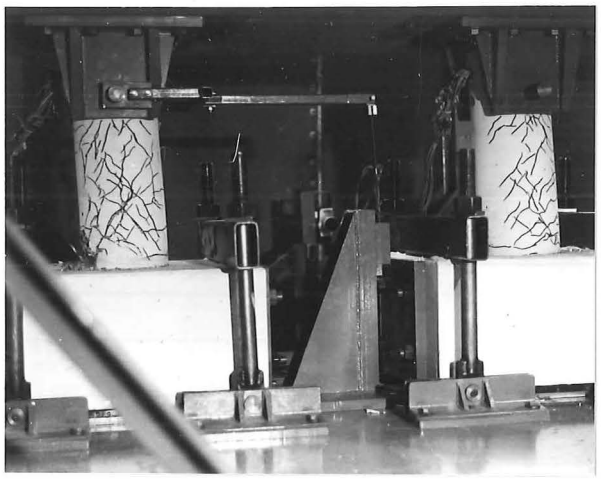

(a)

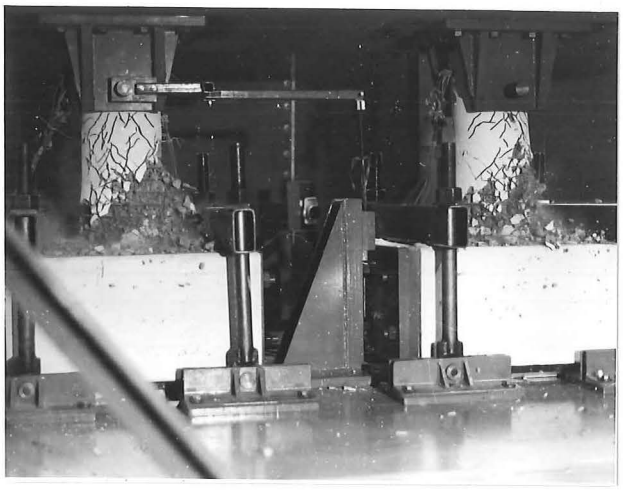

(d)

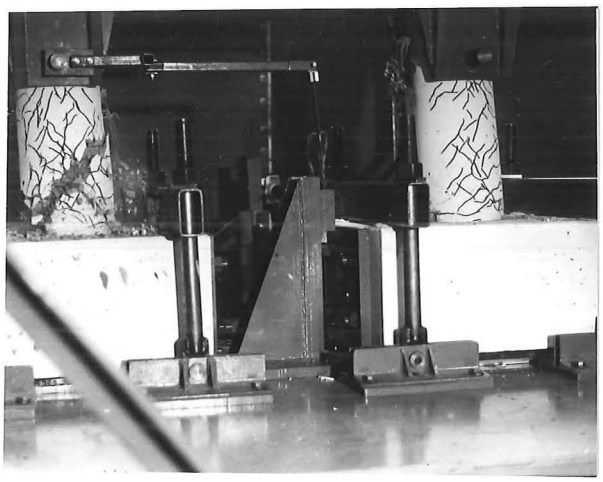

(b)

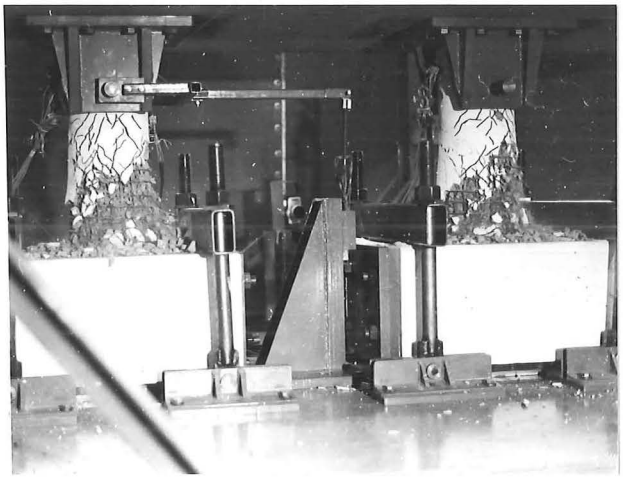

(e)

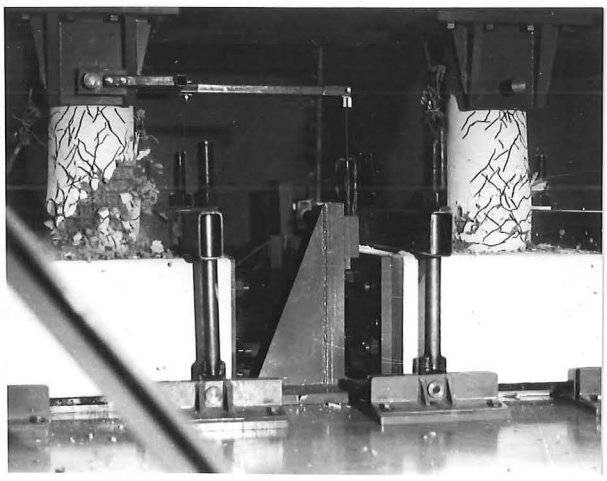

(c)

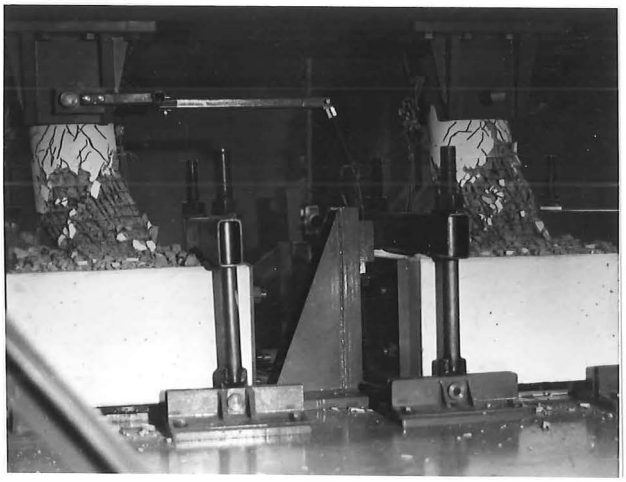

(f)

Fig. 8.14 : Photosequence of failure of Unit DT2 (time lapse between frames $\approx$ 0.33s)

Table 8.3 : Comparison Between Maximum Horizontal Base Reaction and Inertia Load (Single Pier Units)

UNIT	CEDACS V_{Base} (kN)	CEDACS V_{Accel} (kN)	$\frac{(2)}{(3)}$	BSO V_{Base} (kN)	BSO V_{Accel} (kN)	$\frac{(5)}{(6)}$	$V_u = \frac{(3)+(6)}{2}$ (kN)
(1)	(2)	(3)	(4)	(5)	(6)	(7)	(8)
D1	133	121	1.10	118	122	0.97	122
D2	127	118	1.08	129	117	1.10	118
D3	139	123	1.13	141	125	1.13	124
D4	113	108	1.05	116	105	1.10	107
D5	-	-	-	108	97	1.11	97
D6	102	96	1.06	107	97	1.10	97
D7	91	79	1.15	95	80	1.19	80
D8	83	77	1.08	86	-	-	77
			Ave 1.09			Ave 1.10	

CEDACS = High speed data logger (digital)

BSO = Bryan Southern Oscillograph (analogue)

V_{Base} = Base horizontal reaction measured by load cell

V_{Accel} = Inertia load calculated from response acceleration

= Mga (with M = 5200 kg and g = 9.81 m^2/s)

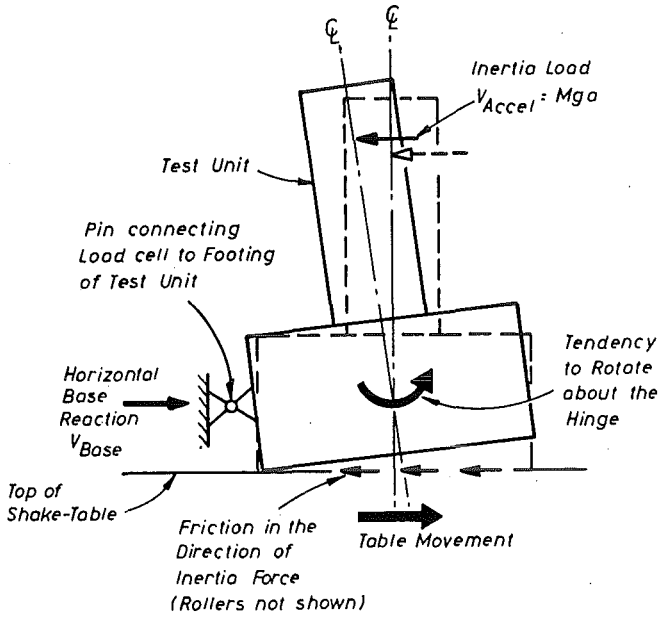

Fig. 8.15 : Rigid body rotation of test unit during testing

In the case of twin-pier models, the sum of the two load-cell readings also exceeded the inertia force calculated from the response accelerations. Figs. 8.16 a and b show two plots of the inertia force versus the sum of horizontal base reactions for Units DT1 and DT2 respectively. Only the envelope curve for each test is shown in the figures. Also included in the plots is a straight line indicating equality between the inertia force and the sum of horizontal base reactions. In general, especially when the magnitude of the load was large, the envelope curves tend to fall in-between this straight line and the horizontal axis, indicating that the sum of horizontal base reactions is greater than the inertia force most of the time. The results at maximum response acceleration are listed in Table 8.4. The frictional force in the roller system was dependent on the clamping force of the four holding-down bolts in each pier and was also dependent on the dead weight and the vertical reaction due to the overturning moment. Consequently, the magnitude of the frictional force in the piers would not necessarily be the same. However, for simplicity, the shear force acting on each leg of the twin-pier is obtained by proportion, i.e.

$$V_E = \frac{V_{east}}{(V_{east} + V_{west})} \cdot Mga \qquad (8.1a)$$

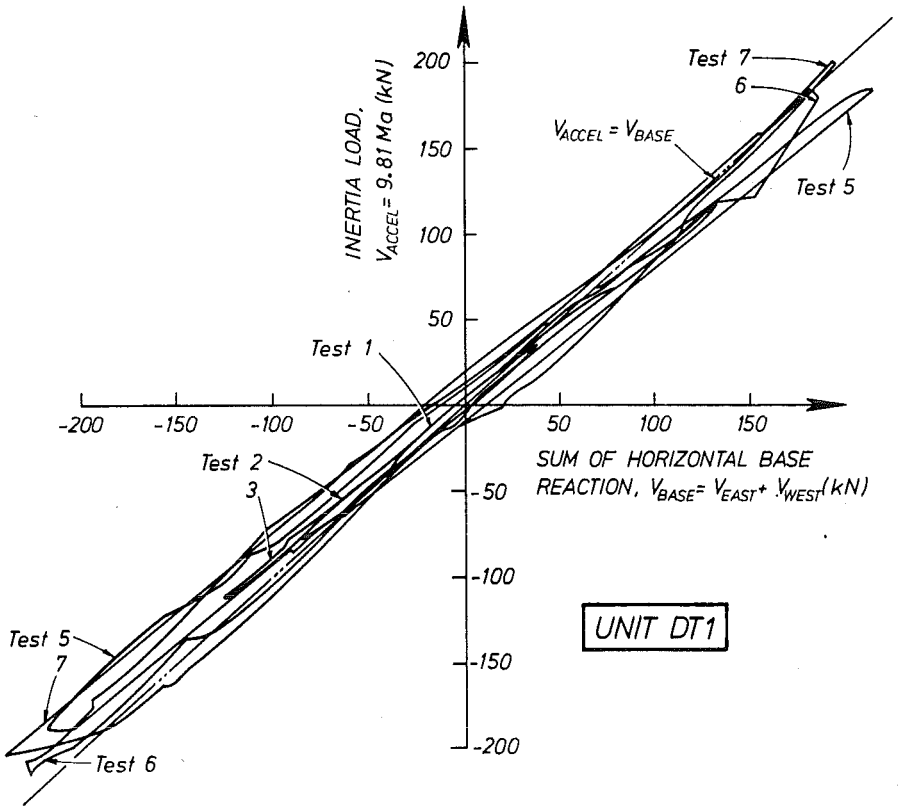

(a) Unit DT1

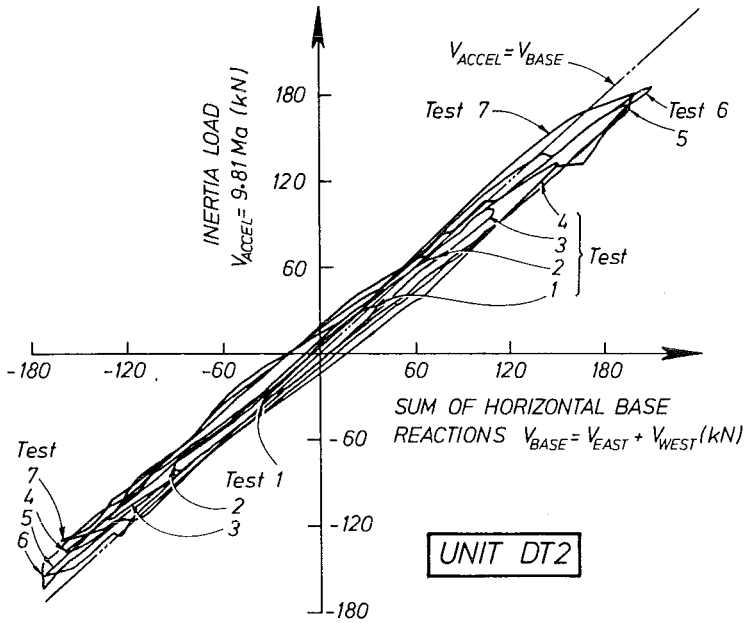

(b) Unit DT2

Fig. 8.16 : Calculated inertia load versus measured sum of horizontal base shear of twin-pier units

$$V_W = \frac{V_{west}}{(V_{east} + V_{west})} \cdot Mga \qquad (8.1b)$$

where V_E and V_W are the corrected shear force of the east and the west columns respectively. V_{east} and V_{west} are the corresponding horizontal base reactions measured by the load cells.

8.3.2 Construction Of Load-Deflection Hysteresis Curves

The inertia mass response acceleration, the horizontal base reaction and the column lateral displacement readings recorded by the CEDACS data logger were reduced with the aid of a data reduction program. Subsequently the column shear versus displacement hysteresis curves were plotted. Since the shear force acting on the column units were better represented by the response acceleration results, only the hysteresis curves obtained from the response acceleration results are referred to in the discussion that follows. However, the overall shape of the hysteresis loops of the column units resulting from the horizontal base reaction or the response acceleration were quite similar, as is illustrated for two typical examples in Figs. 8.17 and 8.18. The hysteresis curves of the column units began in the negative direction first. Comparison between the two plots is provided by the ratio $\frac{V}{V_{if}}$, where V is the column shear obtained from the response acceleration or the horizontal base reaction, and V_{if} is the ideal flexural strength computed using measured material strengths and the column design charts[8.1] with strength reduction factor set to unity. The theoretical ultimate load taken to be V_{if} is shown as a dashed line in the plots and this dashed line dips with higher displacements because of the P-Δ effect. From the figures, it can be seen that the hysteresis loops from the horizontal base reaction are broader, as would be expected from the consideration of frictional reversal as the direction of table movement was reversed.

Also shown in the plots of hysteresis loops is the displacement ductility factor, μ, defined as the ratio of the displacement in the inelastic range to the yield displacement Δ_y. The yield displacement was obtained by linearly scaling the maximum displacement obtained during initial elastic response of no more than $0.75V_{if}$, by the ratio of $\frac{V_{if}}{V_e}$, where V_e was the actual shear corresponding to the maximum elastic displacement. The average of the values obtained in the two directions of response was taken to be Δ_y and used to estimate the displacement ductility factor. The values of Δ_y obtained in this

Table 8.4 : Comparison Between The Sum Of Horizontal Base Reactions And Inertia Load At Maximum Response Acceleration (Twin-Pier Units)

UNIT	CEDACS V_{Base} (kN)	CEDACS V_{Accel}* (kN)	Ratio	BSO V_{Base} (kN)	BSO V_{Accel}* (kN)	Ratio
(1)	(2)	(3)	(4)	(5)	(6)	(7)
DT1-E	184	203	$\frac{(184+115)}{203}$ = 1.47	179	191	$\frac{(179+110)}{191}$ = 1.51
DT1-W	115			110		
DT2-E	111	184	$\frac{(111+98)}{184}$ = 1.14	117	178	$\frac{(117+101)}{178}$ = 1.22
DT2-W	98			101		

* at maximum acceleration

CEDACS = High speed data logger (digital)

BSO = Bryan Southern Oscillograph (analogue)

V_{Base} = Base horizontal reaction measured by load cell

V_{Accel} = Inertia load calculated from response acceleration

= Mga (with M = 5200 kg and g = 9.81 m^2/s)

Table 8.5 : Yield Displacement (Δ_y) Of Comparable Column Units From Dynamic And Static Tests (Single Pier Units)

$\frac{M}{VD} = 1.5, \frac{P_i}{f'_c A_g} \approx 0.1$		$\frac{M}{VD} = 2.0, \frac{P_i}{f'_c A_g} \approx 0.1$	
Unit	Δ_y (mm)	Unit	Δ_y (mm)
D1	6.7	D5	7.1
D2	5.9	D6	6.7
D3	6.0	D7	5.4
D4	5.8	D8	7.1
12	4.6	16	7.8
18	6.7		
19	6.4		

manner are listed together with those obtained from comparable units of the static tests in Table 8.5. The results show that the Δ_y values from this test series are of the same magnitude as those from the static tests whereas scaling laws would require the displacement to be half the static displacements because of a model scale of 0.5 between the dynamic and the static columns. The discrepancy can be explained by two factors:

(a) A reduced modulus of elasticity of the concrete in the column units of the dynamic test series;

(b) the way the yield displacement was determined. — Elastic cycles of response prior to the cycle which was used to determine the yield displacement could have 'softened' the column units somewhat as compared to the first cycle to $0.75V_{if}$ in the static tests in which there was no 'damage' due to prior loading.

8.3.3 Single Pier Units D1 To D4 ($\frac{M}{VD} = 1.5$)

In general, these column units responded elastically during the first two tests (i.e. Tests 1 and 2 with 5 Hz at 2 and 5 mm respectively). Their hysteresis loops remained narrow and the peak loads were below the theoretical ultimate strength represented by the dashed line in the figures. However, there was an increase in peak response acceleration and displacement with the number of cycles before failure in Test 3. This behaviour is illustrated for a typical response in Fig. 8.2, which shows a time-history response of Unit D1 during Test 3. Damage during Tests 1 and 3 and the initial cycles of Test 3 must have softened the column unit and hence, its natural frequency was decreased. With the forcing frequency of 5 Hz remaining unchanged, the frequency ratio was therefore increased and so there was an increase in response from the initially stiff column until it eventually failed.

The ideal flexural strength of Unit D1 was exceeded during Cycle 3 of Test 3 in both directions. A maximum load of $1.22V_{if}$ was achieved in the first half (i.e. the negative direction) of Cycle 4 at $\mu = 2.4$ but failure followed soon at about $\mu = 2.7$. As can be seen in Fig. 8.17a, there was a sudden drop in load carrying capacity which was caused by fracture of the spirals. On load reversals, the strength and stiffness remained low but the displacement continued to increase. The loss in strength and stiffness after this cycle is evident in the hysteresis curves shown in Fig. 8.17a.

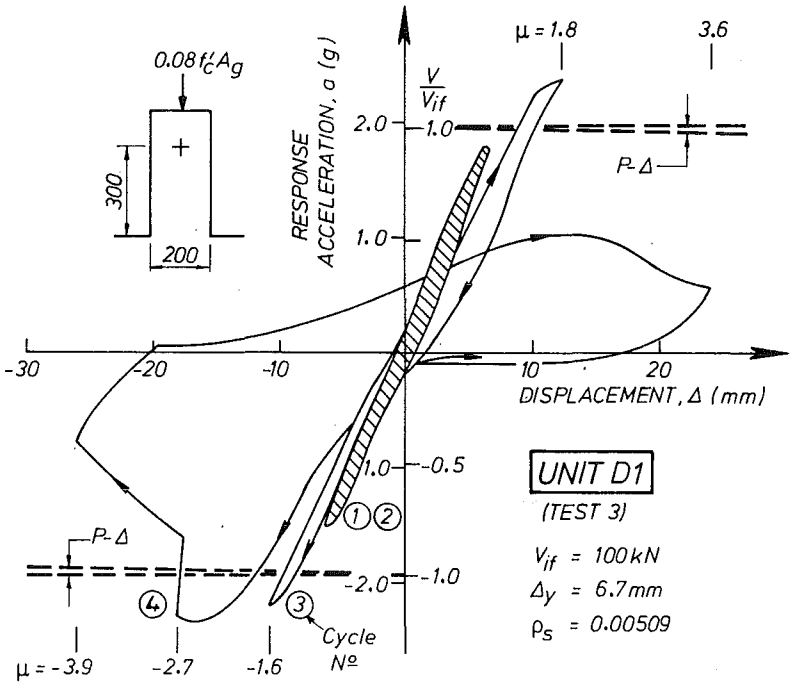

(a) Response acceleration versus lateral displacement

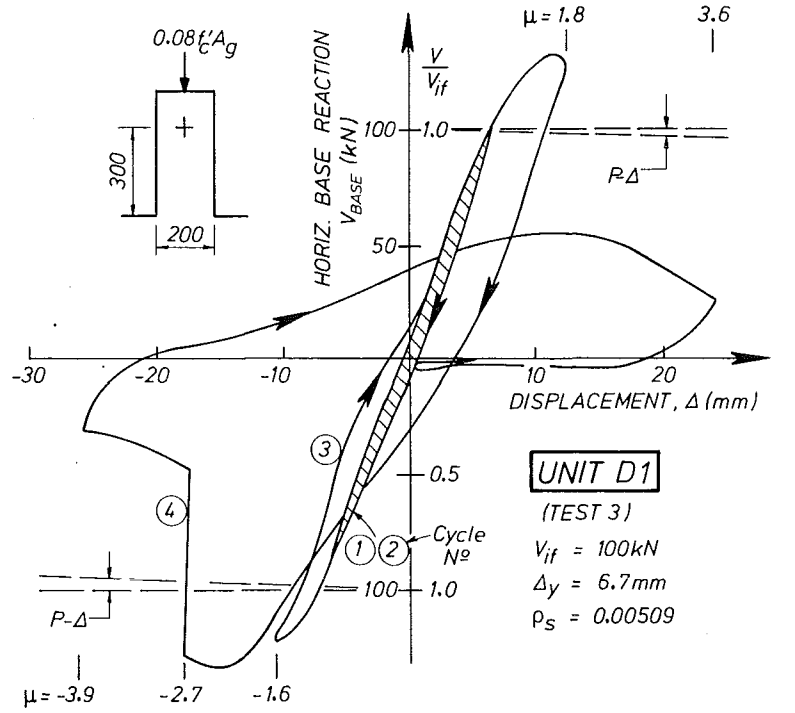

(b) Horizontal base reaction versus lateral displacement

Fig. 8.17 : Hysteresis curves of Unit D1 during Test 3

As shown in Fig. 8.18a, the ideal flexural strength of Unit D2 was exceeded during Cycle 3 of Test 3 in both positive and negative directions. The peak load in the first half (i.e. the negative direction) of the following cycle reached a maximum value of $1.18V_{if}$ at $\mu = 2.6$. On subsequent load reversal the peak load in the opposite direction could not attain the previous peak value in that direction but it still exceeded the ideal flexural strength by about 4 percent. The column unit failed at approximately $\mu = 3$ in this direction. The load carrying capacity degraded rapidly and the strength and stiffness of the column were almost completely lost, as can be seen in Fig. 8.17a in the response following the failure.

Unit D3 possessed the largest amount of spiral reinforcement (ρ_s = 0.01061). It was therefore expected to perform better than the other three within this group of column units. The peak load of this column unit in Cycle 3 of Test 3 exceeded the V_{if} value and a maximum of $1.24\,V_{if}$ was achieved in the positive half at $\mu = 2.4$ of the same cycle. The hysteresis loops for Test 3 shown in Fig. 8.19 were broader than the corresponding plots of Units D1, D2 and D4 shown in Figs. 8.17, 8.18 and 8.20, respectively, indicating that more energy was dissipated. The good performance could not be maintained in Cycle 5 of the same test. The peak load in both positive and negative directions of Cycle 5 did not reach the value of V_{if}, though the displacement ductility at this stage reached about 2.5 and 3.7 in positive and negative directions respectively. Three more tests with larger excitation amplitude equal to 10, 15 and 20 mm were conducted but the hysteresis loops for these tests are not shown. In general, the peak loads of these three tests were lower than $0.8\,V_{if}$; a maximum displacement ductility of about $\mu = 6$ (in positive direction) with a peak load of $0.6\,V_{if}$ was achieved during the last test. However, the stiffness and therefore the energy dissipation capacity were greatly reduced. The ductility capacity of this column unit is taken to be 3.7 which occurred in the negative half of Cycle 4 of Test 3 before failure in the following cycle commenced (see Fig. 8.19).

The behaviour of Unit D4 was similar to that of Units D1 and D2 during Test 3. The hysteresis curves of this column unit are shown in Fig. 8.20. The peak load and displacement increased with the number of cycles during the first three cycles. A maximum load of $1.07\,V_{if}$ was achieved in the first (negative) half of Cycle 3 and $\mu = 2.1$. The peak load in the opposite direction also reached the value of V_{if} but was immediately followed by failure at about $\mu = 2.5$. Significant degradation in strength and stiffness took place and the column possessed

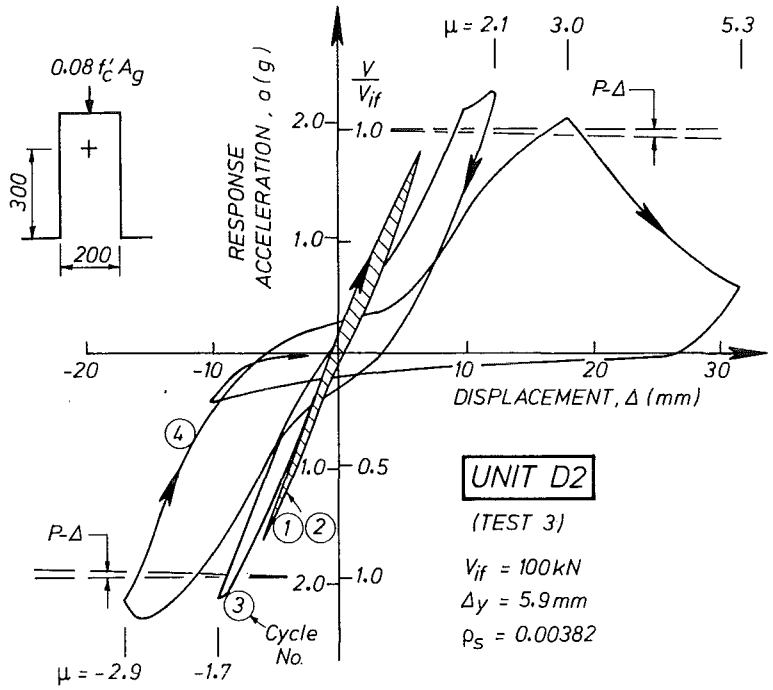

(a) Response acceleration versus lateral displacement

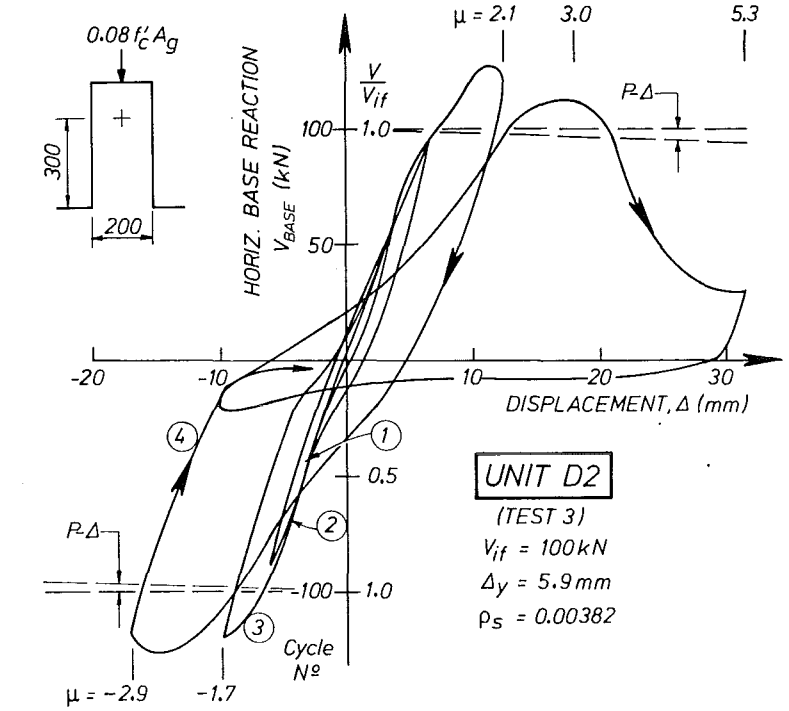

(b) Horizontal base reaction versus lateral displacement

Fig. 8.18 : Hystersis curves of Unit D2 during Test 3

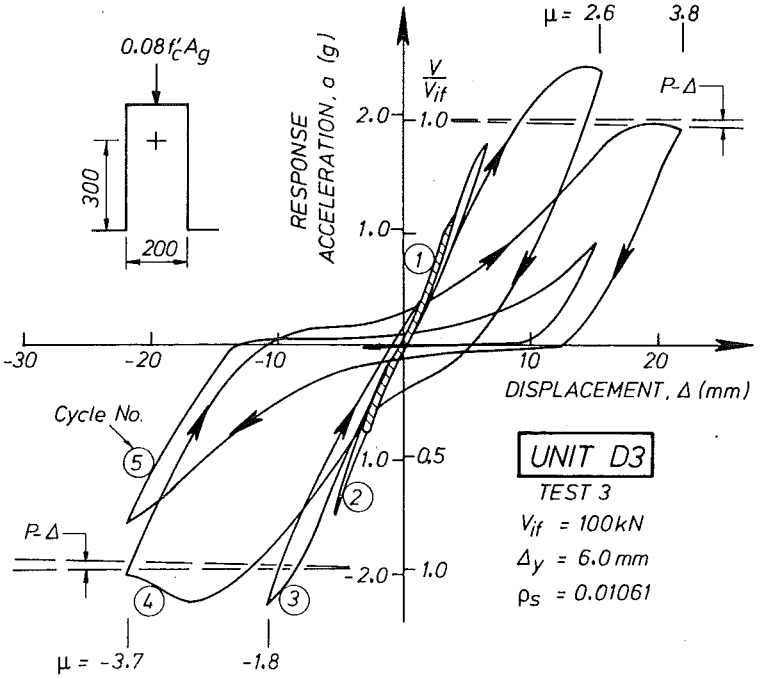

Fig. 8.19 : Hystersis curves of Unit D3 during Test 3

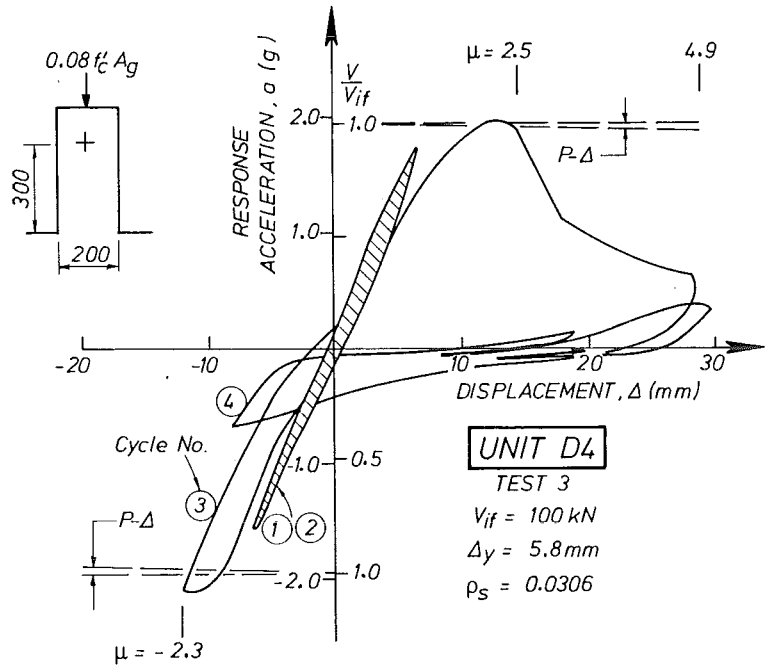

Fig. 8.20 : Hysteresis curves of Unit D4 during Test 3

negligible strength and stiffness at the conclusion of the test.

8.3.4 Single Pier Units D5 To D8 ($\frac{M}{VD} = 2.0$)

In the absence of readings from CEDACS data logger due to a breakdown of the instrument, the digitised results of time-history plots from the oscillograph were used to plot the hysteresis curves for Units D5 and D6. The resulting plots of these two columns (Figs. 8.21 and 8.22) indicate that they responded elastically during the first three tests. However, in the case of Units D7 and D8 (Figs. 8.23 and 8.24), the response remained elastic only during Test 1. This apparent difference in behaviour between the two pairs of column units might be due to the use of a more flexible coupling system as explained in Section 8.2.2. The flexible coupling system resulted in significant rotation of the inertia mass and part of the effect of the inertia load might have been offset by the rotational effect of the concrete block. Subsequent to the testing of Units D5 and D6 the coupling system was stiffened substantially and the rotation of the inertia mass was greatly reduced during the testing of all the other columns.

As can be seen in Fig. 8.21a, the ideal flexural strength of Unit D5 was exceeded in the first negative half cycle of Test 5 (5 Hz ar 15 mm) at about $\mu = 1.7$. The response of this column unit subsequent to Test 5 was greater in the negative direction during Test 6 (5 Hz at 20 mm). During this cycle, obvious plastic hinging was first noted. A maximum load of $1.3\,V_{if}$ was achieved in the first negative half cyle of Test 6 at $\mu = 3.5$. However, the peak load in the other direction was only $1.07\,V_{if}$ and was achieved at a lower displacement ductility of about 1.5. Subsequent response, shown shaded in Fig. 8.21a, during the same test was smaller than the first cycle response. The increase in flexibility due to damage in the first cycle and earlier tests must have caused a reduction in the response from the critical domain as a result of a reduction in frequency ratio. Failure of the column took place during Test 7 (5 Hz at 25 mm) after the first negative peak load of about $1.2\,V_{if}$ was achieved at $\mu \approx 4.9$ and a continuous decrease in load carrying capacity followed as shown in Fig. 8.21b.

Unit D6 was not tested with excitation amplitude of 7.5 mm but was instead tested twice with excitation amplitude of 10 mm. As Fig. 8.22a shows, the ideal flexural strength of this column was reached during the first negative cycle of Test 4. As with Unit D5, the subsequent response also tended to be greater in the negative direction, though in this case the difference was not as great (Fig. 8.22a). A

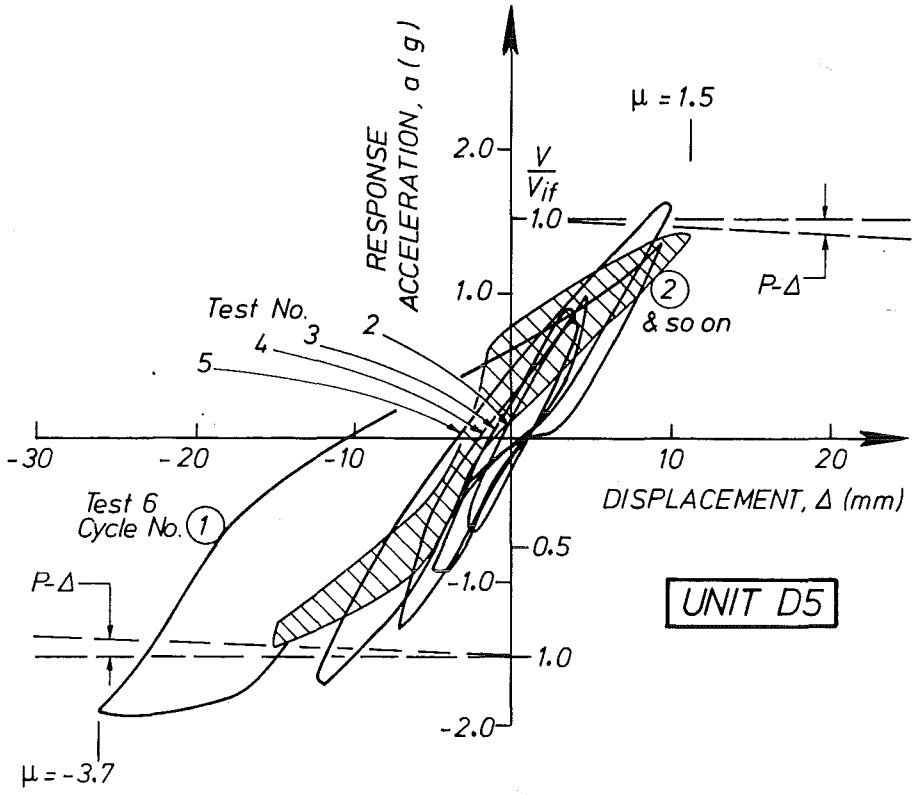

(a) Tests 2 to 6

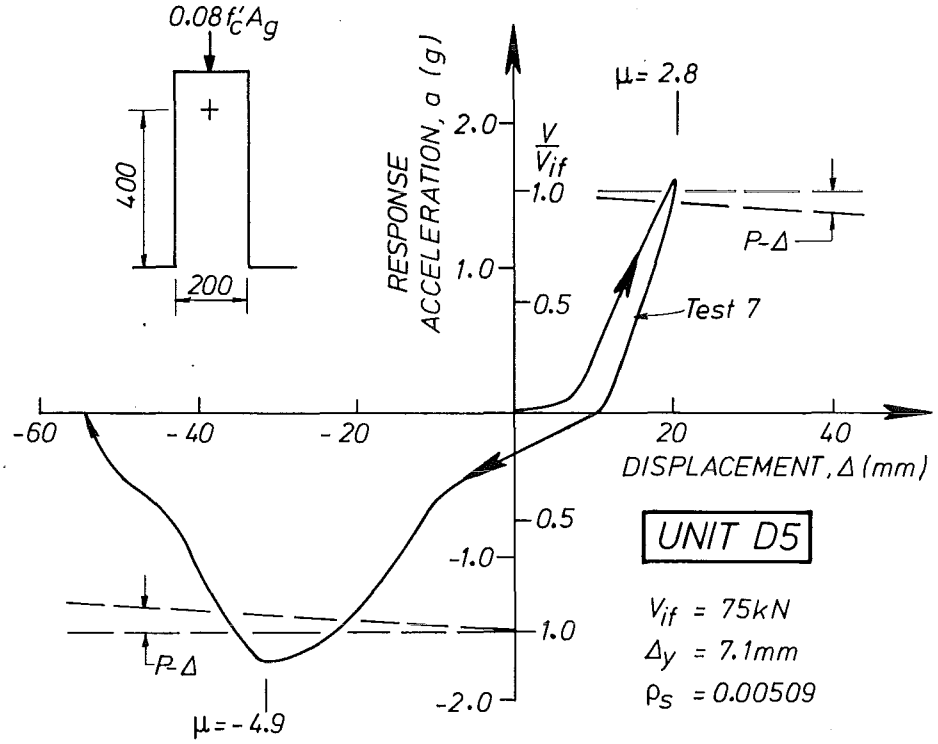

(b) Test 7

Fig. 8.21 : Hysteresis curves of Unit D5

maximum load of about $1.3\,V_{if}$ was achieved at approximately $\mu = 2.9$ in the negative direction during Cycle 2 of Test 5 (5 Hz at 15 mm). During the same test, the peak load in the other direction was just equal to $1.0\,V_{if}$ and was reached during the third cycle at $\mu = 1.3$. For similar reasons given in the last paragraph, the response during subsequent cycles in this test was much reduced, and the curves, shown shaded, is an envelope curve to the responses. The column failed during Cycle 1 of Test 6 (5 Hz at 20 mm) and the load carrying capacity prior to failure did not reach the ideal flexural strength. A large increase in displacement followed the failure as shown in Fig. 8.22b.

The peak load and displacement of Unit D7, as seen in Fig. 8.23, increased with the number of cycles during the first five cycles of Test 2 and exceeded the ideal flexural strength during Cycles 4 and 5. The peak load at Cycle 5 ($\mu = 2.0$) was the maximum achieved for this column unit and was equal to $1.07\,V_{if}$. The loop for Test 2 shown shaded in Fig. 8.23 is an envelope curve enclosing the peak loads and displacements of this test. The column failed after two cycles in Test 3. The failure took place during the positive half cycle at a displacement ductility of about $\mu = 2.8$. The load carrying capacity in the next half cycle was approximately $0.35\,V_{if}$ and the stiffness remained low. A maximum displacement ductility of about 4.0 was achieved in this direction. As can be seen in Fig. 8.23, the strength and stiffness of the column subsequent to this peak degraded to a very low level.

The behaviour of Unit D8 was similar to that of Unit D7. Fig. 8.24 shows that the peak load and displacement also increased with the number of cycles during Test 2 until a maximum load of $1.03\,V_{if}$ was reached at about $\mu = 1.5$ during the positive half of Cycle 4. The envelope curve for Test 2, shown shaded in Fig. 8.24, again represents the range of peak loads and displacements of the test. The failure of this column occurred at $\mu = 2.5$ (in the negative direction) during Cycle 3 of Test 3. The peak loads in this test did not reach the value of V_{if}.

8.3.5 Twin-Pier Units DT1 And DT2

The lateral force input into either of the columns of the twin-pier system was calculated from the response acceleration results using Eqs. 8.1a and b. The results are plotted in Figs. 8.25 to 8.28 against column lateral displacements to obtain the hysteresis curves for individual columns. The axial load acting on the columns varied with the magnitude of the lateral inertia. It also changed its direction as the

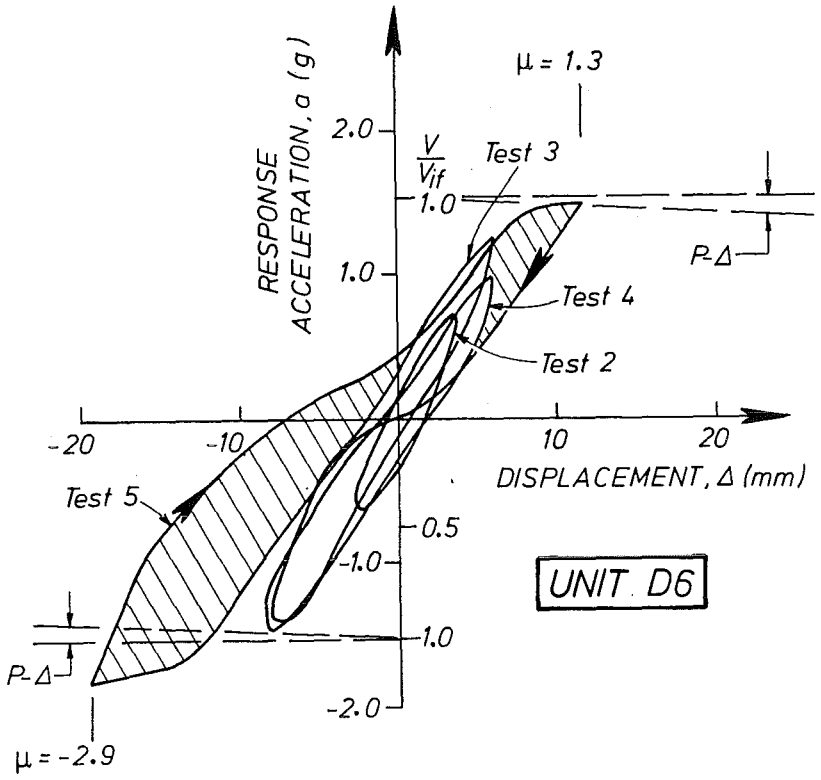

(a) Tests 2 to 5

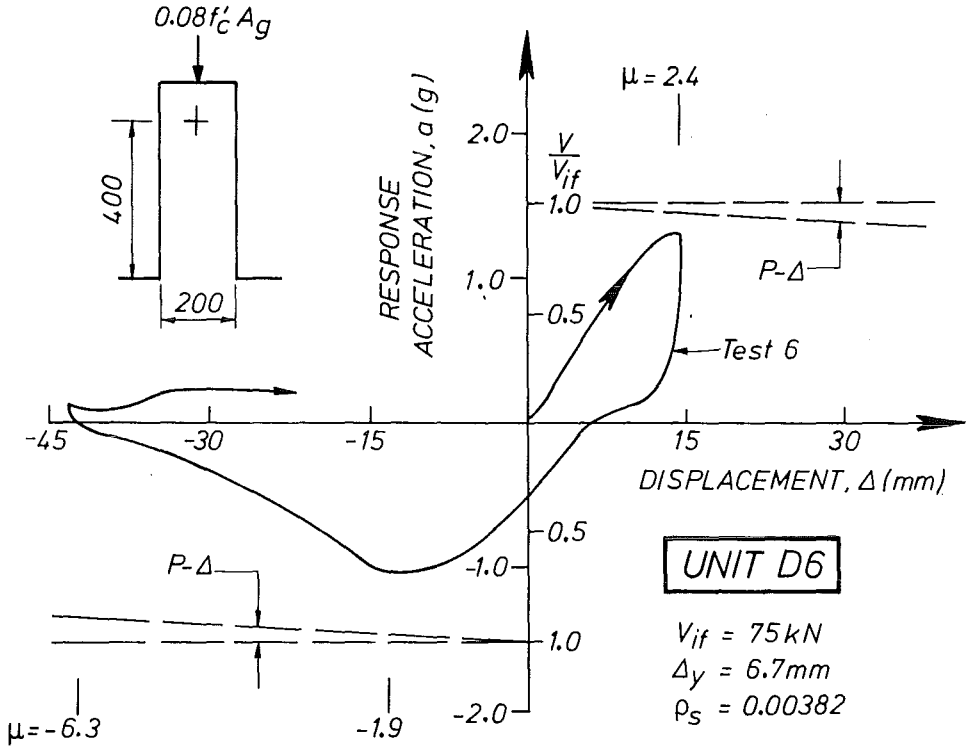

(b) Test 6

Fig. 8.22 : Hysteresis curves of Unit D6

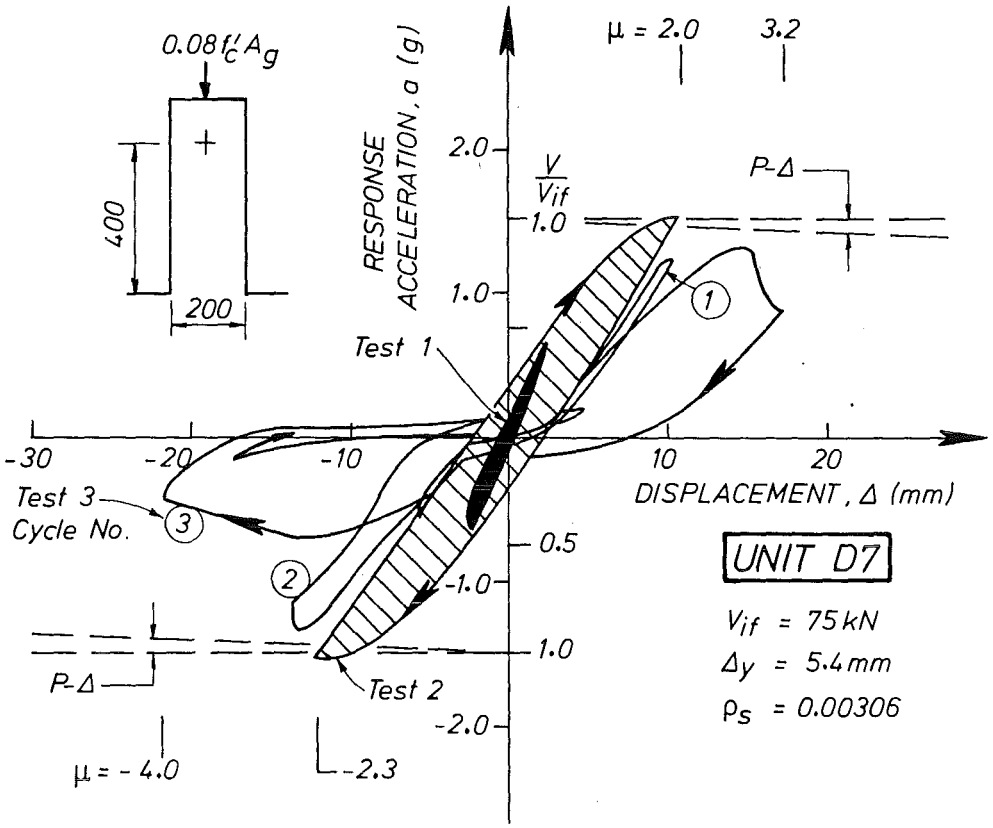

Fig. 8.23 : Hysteresis curves of Unit D7 (Tests 1 to 3)

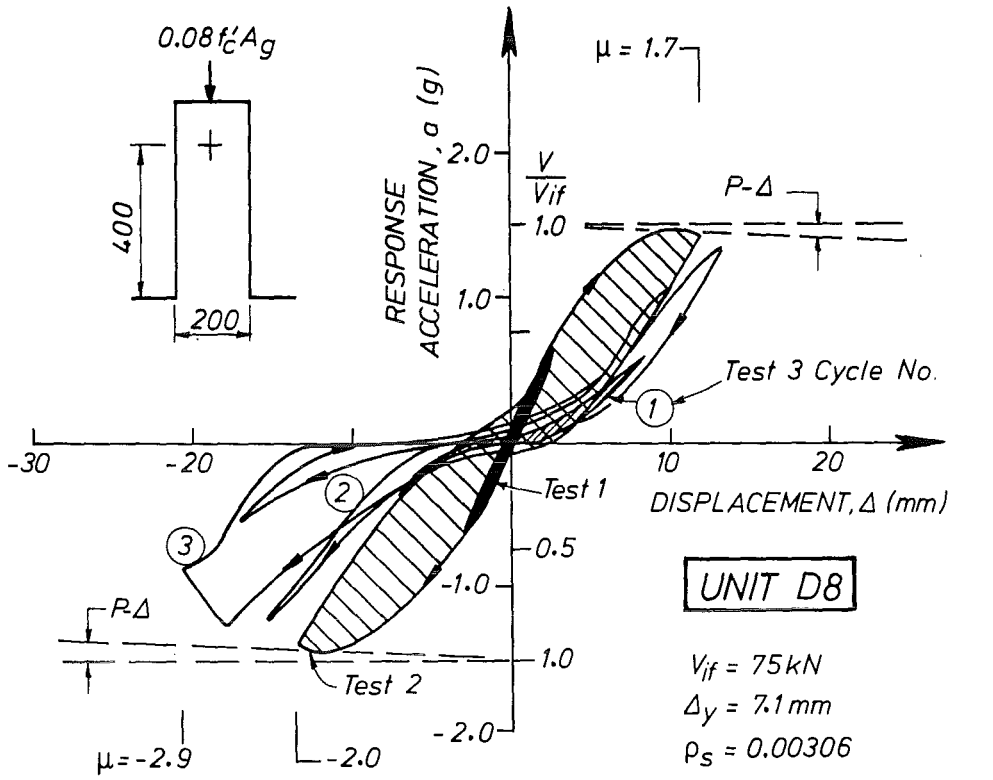

Fig. 8.24 : Hysteresis curves of Unit D8 (Tests 1 to 3)

direction of the lateral inertia force changed. For simplicity, the axial loads shown in the figures are the ones corresponding to those at the development of ideal flexural strengths shown with the dashed lines in the figures. The curves are plotted such that the negative load cycles correspond to the case when axial tension was acting on the column concerned. Note that there was a negative P-Δ effect in the case when axial tension was acting. Therefore the dashed line representing the theoretical ultimate strength in Figs. 8.25 to 8.28 inclines in a direction opposite to that when axial compression was acting. From the hysteresis curves shown in Figs. 8.25 and 8.27, it can be seen that both the twin-piers responded elastically during the first three tests when the maximum measured table acceleration was about 1.5-1.7g.

Due to the two levels of axial load, there were two different values of ideal flexural strengths. These are identified as $V_{if}(C)$ when the column was in compression and $V_{if}(T)$ when it was in tension. The values of $V_{if}(C)$ and $V_{if}(T)$ for Unit DT1 are 107 kN and 77 kN respectively while those of Unit DT2 are 80 kN and 60 kN respectively.

As shown in Figs. 8.25a and b, the ideal flexural strengths of the east (DT1-E) and the west (DT1-W) columns of Unit DT1 were exceeded during Test 5. The ideal flexural strength, $V_{if}(T)$, of Column DT1-W was first exceeded (by about 8 percent) at $\mu = 1.5$ (Fig. 8.25b). In the case of Column DT1-E, the ideal flexural strength in tension, $V_{if}(T)$, was exceeded (by about 2 percent) during the following cycle of the same test (Fig. 8.25a). The response in subsequent tests tended to be greater in one direction than the other. As can be seen in Figs. 8.25a and b, the response of Column DT1-W was greater while it was in tension whereas that of Column DT1-E was greater while it was in compression, indicating that the stronger response occurred when the inertia force was acting in the eastward direction. The peak load of Column DT1-W in Test 6 exceeded $V_{if}(T)$ by about 26 percent (see Fig. 8.25b). The displacement ductility at this peak was about 2.1. However, there was a slight drop in load carrying capacity from this peak to a lower value of about $1.09\,V_{if}(T)$ with an increase in displacement ductility to about $\mu = 2.5$. The peak load of Column DT1-E during the same cycle while it was in compression was $1.23\,V_{if}(C)$ and it occurred at $\mu = 2.1$. This was the maximum load (in compression) achieved for this column. A drop in load carrying capacity also took place and the peak load decreased to about $1.05\,V_{if}(C)$ while the displacement ductility increased to $\mu = 2.3$. A maximum load of $1.14\,V_{if}(T)$ was also achieved for the same column in tension later during Test 6 at $\mu = 1.3$. The maximum load of Column DT1-W in compression ($= 1.06\,V_{if}(C)$) was

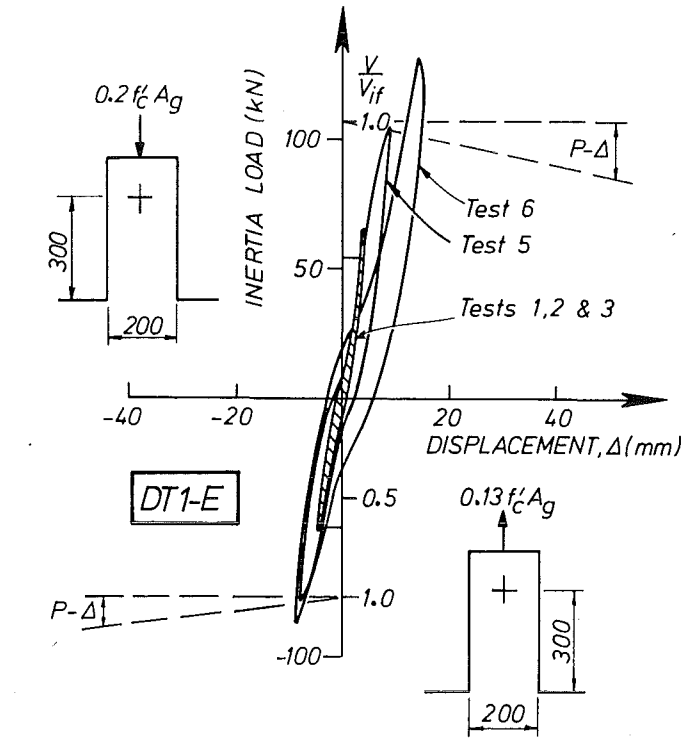

(a) DT1-E

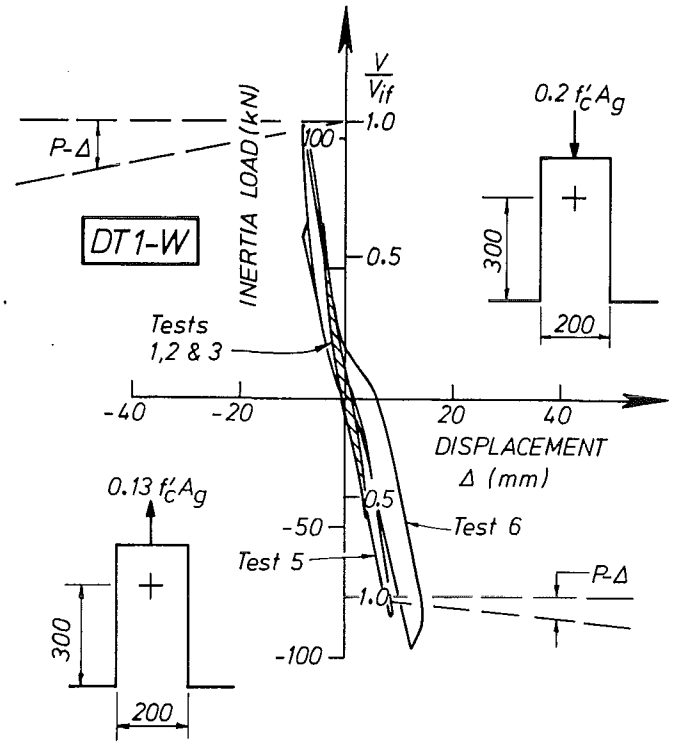

(b) DT1-W

Fig. 8.25 : Hysteresis curves of Unit DT1 (Tests 1 to 6)

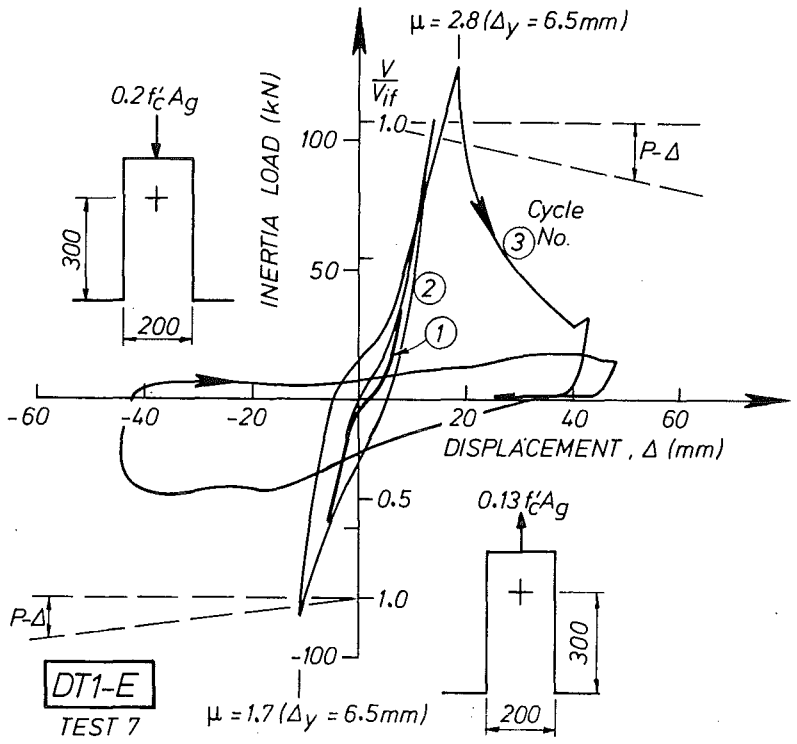

(a) DT1-E

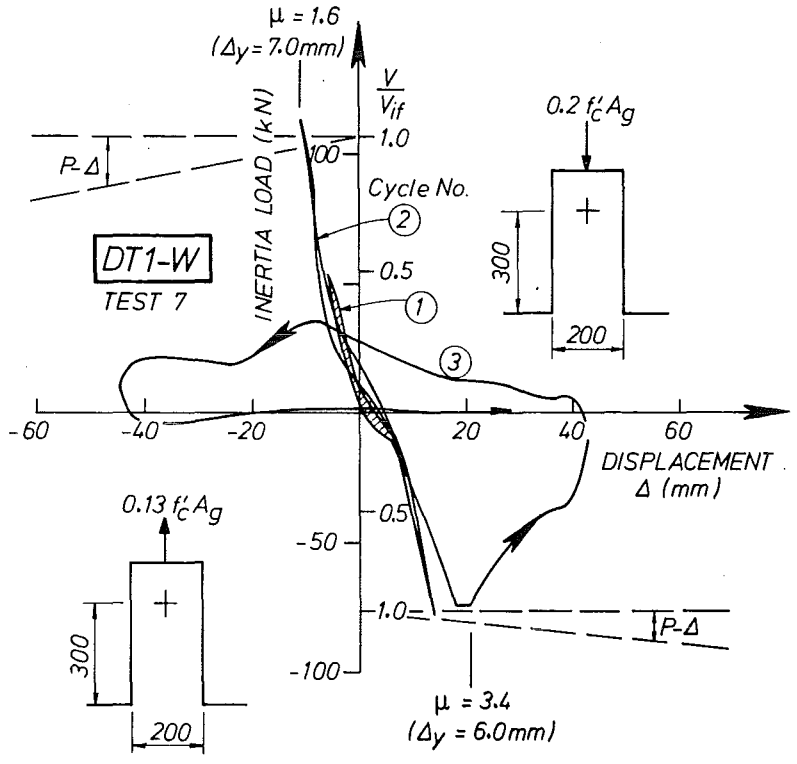

(b) DT1-W

Fig. 8.26 : Hysteresis curves of Unit DT1 (Test 7)

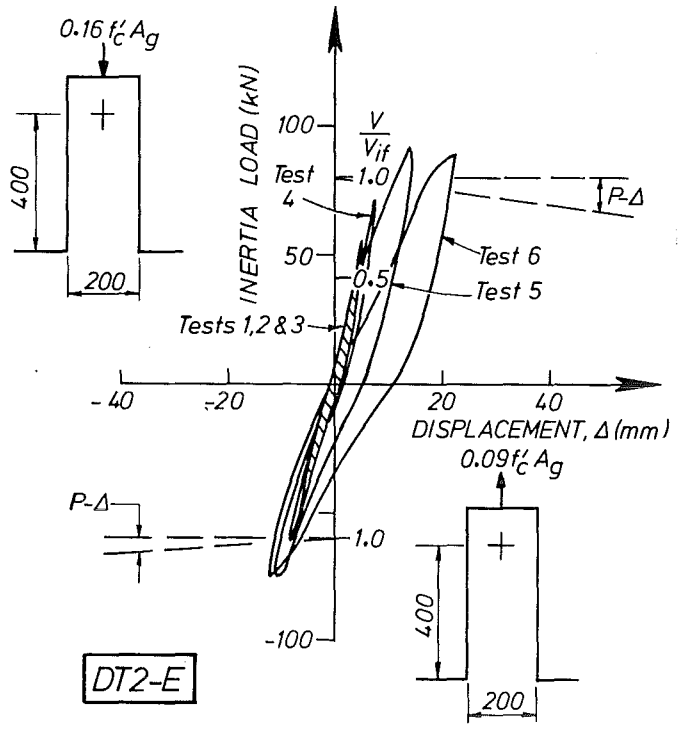

(a) DT2-E

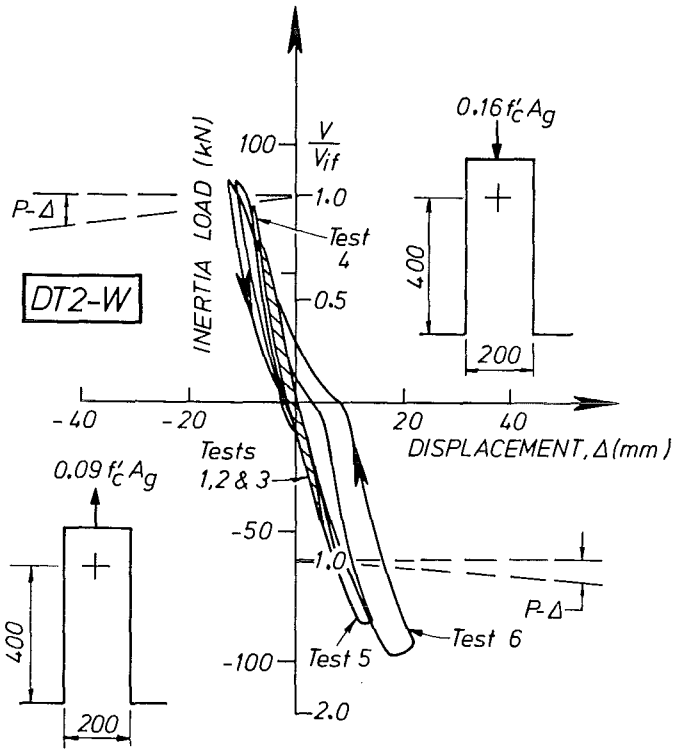

(b) DT2-W

Fig. 8.27 : Hysteresis curves of Unit DT2 (Tests 1 to 6)

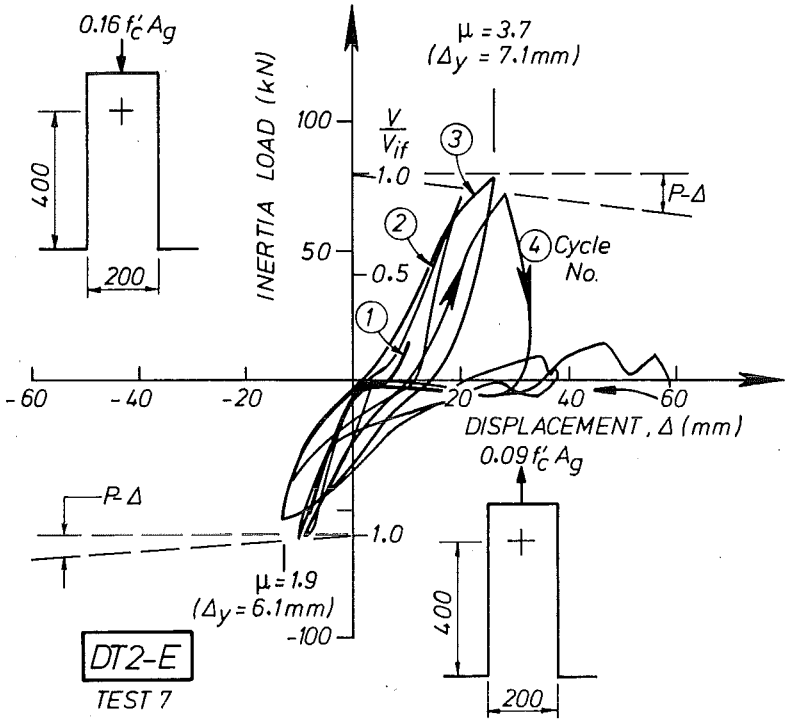

(a) DT2-E

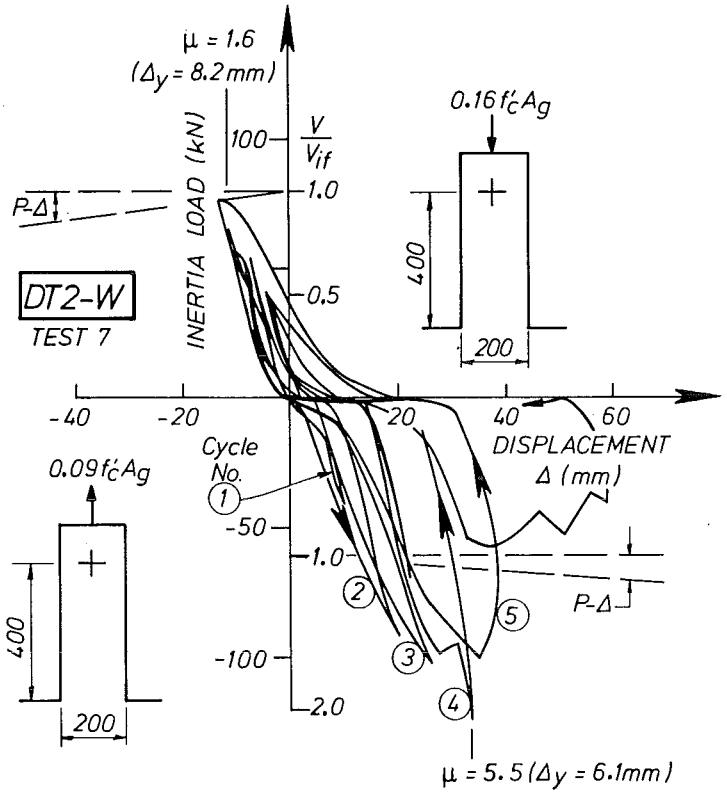

(b) DT2-W

Fig. 8.28 : Hysteresis curves for Unit DT2 (Test 7)

reached in Test 7 (Fig. 8.26b) at a displacement ductility of about 1.6. Failure took place in the cycle that followed when the west column (DT1-W) was in tension. There was a sudden drop in load carrying capacity and the strengths and stiffnesses of both columns remained low on load reversal, as can be seen in Figs. 8.26a and b.

The hysteresis curves for Columns DT2-W and DT2-E of Unit DT2 are shown in Figs. 8.27 and 8.28. The ideal flexural strength in tension, $V_{if}(T)$, was reached in both columns during different load cycles of Test 4 at about $\mu = 2$. The ideal flexural strength in compression, $V_{if}(C)$, was exceeded in both Columns DT2-E and DT2-W in Test 5. This took place at about $\mu = 1.9$ and $\mu = 1.3$ for Columns DT2-E and DT2-W respectively. The peak loads were $1.14\,V_{if}(C)$ for Column DT2-E and $1.08\,V_{if}(C)$ for Column DT2-W. This peak load is the maxumum load (in compression) achieved in the case of Column DT2-E. During the same test, the peak load of Column DT2-W in tension increased and reached a value of $1.37\,V_{if}(T)$ at $\mu = 2.3$. Similar to the behaviour of Unit DT1, the response of Unit DT2 in subsequent tests appears to be greater in one direction than in the other, with the response being greater while Column DT2-W and Column DT2-E were in tension and compression respectively. The maximum load on Column DT2-W while in compression ($= 1.09\,V_{if}(C)$) was achieved in Test 6 at $\mu = 1.6$. The peak load of the same column while in tension continued to increase and reached a value of $1.61\,V_{if}(T)$ at $\mu = 2.8$. Column DT2-E responded more strongly while it was in compression. However, the peak load decreased slightly from the maximum value of $1.14\,V_{if}(C)$ to about $1.12\,V_{if}(C)$ at $\mu = 3.0$. As seen in Fig. 8.28 failure of this column occurred while it was in compression. This caused a sudden increase in lateral load to be carried by Column DT2-W while in tension. The load on this latter column reached a value of $2.08\,V_{if}(T)$, but due to the instantaneous nature of the load increase resulting from failure of the other column, it is believed not to represent a true enhanced strength value. The strengths and stiffness of both columns degraded significantly after Cycle 5 as shown in Figs. 8.28a and b.

8.4 SHEAR STRENGTH AND DISPLACEMENT DUCTILITY CAPACITY

As was discussed earlier, the shear force acting on the column units was taken to be the inertia force calculated from response acceleration of the inertia mass. The average of the results from the CEDACS data logger and the oscillograph was used. The experimental and predicted shear strengths at onset of diagonal cracking and at ultimate, and the displacement ductility are presented in the following sections. Since

the alternating tension and compression in the twin-pier models would have a different effect on the shear strengths and ductility capacity on the columns making up the twin-pier, the results of these column units are discussed in a separate section.

8.4.1 Shear Strength At Onset Of Diagonal Cracking

As discussed in Chapter Four, the spiral reinforcement remained effectively unstrained until onset of diagonal cracking. The diagonal cracking load can, therefore, be taken as the load from which the spiral reinforcement began to be significantly strained. The diagonal cracking loads obtained in this manner for the eight single pier models are listed in Table 8.6. The shear stresses, assumed acting over an effective area of $0.8A_g$, at onset of diagonal cracking, given in Table 8.6, are normalised by dividing by $\sqrt{f'_c}$ in MPa. The non-dimensional shear stress, $\frac{v_{cr}}{\sqrt{f'_c}}$, remained relatively constant within each of the two groups of column units with aspect ratios of 1.5 and 2.0. The values tended to be greater in the shorter than in the taller columns. The average value for the former is 0.417 while that for the latter is 0.346.

Also included in the table are the corresponding values determined from the equation derived from static test results, viz

$$\frac{v_{cr}}{\sqrt{f'_c}} = 0.28 \left(1 + 3.1 \frac{P_i}{f'_c A_g}\right) \alpha_1 \qquad (8.2)$$

where $\alpha_1 = \frac{2.0}{\frac{M}{VD}} \geq 1.0$

From the table, it appears that the dynamic test results, on average, are about 6 percent lower than the predicted results with a standard deviation of 0.06. The discrepancy between the experimental and predicted results for shorter column units ($\frac{M}{VD} = 1.5$) tended to be greater. This could be due to the different ways the shear force was applied to the column units. The introduction of shear force through an internal pin in the dynamic test columns, instead of the loading collar (by bearing stresses) used in the static tests (see Fig. 3.5), might have reduced the influence of the term α_1 used in Eq. 8.2. Also the lower concrete strength used in the models might have increased the significance of the ratio $\frac{P_i}{f'_c A_g}$ in Eq. 8.2. Nevertheless the accuracy of the prediction indicates that the static and dynamic test results are comparable.

Table 8.6 : Shear Stress At Onset Of Diagonal Cracking (Single Pier Units)

UNIT	$\frac{M}{VD}$	$\frac{P_i}{f'_c A_g}$	V_{cr} (kN)	$\frac{v_{cr}}{\sqrt{f'_c}}$ Expt.	$\frac{v_{cr}}{\sqrt{f'_c}}$ Predicted (Eq. 8.2)	$\frac{(5)}{(6)}$
(1)	(2)	(3)	(4)	(5)	(6)	(7)
D1	1.5	0.08	47	0.409	0.466	0.88
D2	1.5	0.08	49	0.434	0.466	0.93
D3	1.5	0.08	46	0.406	0.466	0.87
D4	1.5	0.08	48	0.419	0.466	0.90
D5	2.0	0.08	38	0.336	0.349	0.96
D6	2.0	0.08	36	0.324	0.349	0.93
D7	2.0	0.08	40	0.355	0.349	1.02
D8	2.0	0.08	41	0.370	0.349	1.06
					Ave	0.94
					σ	0.06

Table 8.7 : Shear Strength And Concrete Shear Stress At Ultimate (Single Pier Units)

UNIT	$\frac{M}{VD}$	ρ_s ($\times 10^{-3}$)	V_u (kN)	$\frac{v_u}{\sqrt{f'_c}}$	V_s (45-deg truss) (kN)	$\frac{v_c}{\sqrt{f'_c}}$ Expt.	$\frac{v_c}{\sqrt{f'_c}}$ Predicted (Eq. 8.4)	$\frac{(7)}{(8)}$
(1)	(2)	(3)	(4)	(5)	(6)	(7)	(8)	(9)
D1	1.5	5.09	122	1.062	49	0.635	0.612	1.04
D2	1.5	3.82	118	1.045	37	0.717	0.612	1.17
D3	1.5	10.61	124	1.095	53	0.616	0.612	1.01
D4	1.5	3.06	107	0.933	30	0.672	0.612	1.10
D5	2.0	5.09	97	0.857	49	-	-	-
D6	2.0	3.82	97	0.872	37	0.486	0.459	1.06
D7	2.0	3.06	80	0.710	30	0.450	0.459	0.98
D8	2.0	3.06	77	0.696	30	0.486	0.459	1.06
							Ave	1.06
							σ	0.06

8.4.2 Shear Strength at Ultimate

The ultimate shear strength of the column units was taken to be the maximum value achieved during the tests. The values in terms of shear force, V_u (in kN) and non-dimensional shear stress, $\frac{v_u}{\sqrt{f'_c}}$ (with $v_u = \frac{V_u}{0.8A_g}$), are listed in Table 8.7.

In order to have a valid comparison of results between the dynamic and the static test columns with singificantly different material properties, the results are plotted in Fig. 8.29 where influences due to differences in steel and concrete strengths are taken into account by the parameter $\frac{\rho_s f_{yt}}{\sqrt{f'_c}}$. Three groups of column units classified according to aspect ratio and axial load level are considered in Fig. 8.29 and the results are also listed in Table 8.8. Note that the third group consists solely of column units from the static tests. In general, the results show that there is a strong linear relation between $\frac{v_u}{\sqrt{f'_c}}$ and $\frac{\rho_s f_{yt}}{\sqrt{f'_c}}$, even when the dynamic and static test results are considered together. The average gradient of the best-fit straight lines to the results of first and third groups of column units is 0.512. Since the second group consists of only four column units, the above average gradient was used to fit a straight line to the results, and as can be seen from the figure, only Unit D6 with exceptionally high $\frac{v_u}{\sqrt{f'_c}}$ is poorly represented by the straight line. Note the value of 0.512 for the average gradient of the straight lines is in agreement with that from theoretical consideration using a 45-deg truss, as follows:

$$V_u = V_s + V_c$$

$$\text{or} \quad \frac{v_u}{\sqrt{f'_c}} = \frac{V_u}{0.8A_g\sqrt{f'_c}} = \frac{\frac{\pi}{2} A_{sp} f_{yt} \frac{d_s}{s}}{0.8A_g\sqrt{f'_c}} + \frac{v_c}{\sqrt{f'_c}}$$

$$= \frac{\frac{\pi}{8} d_s^2}{0.8 A_g} \left(\frac{\rho_s f_{yt}}{\sqrt{f'_c}} \right) + \frac{v_c}{\sqrt{f'_c}}$$

$$= \frac{(\frac{d_s}{D})^2}{1.6} \left(\frac{\rho_s f_{yt}}{\sqrt{f'_c}} \right) + \frac{v_c}{\sqrt{f'_c}}$$

$$= 0.518 \left(\frac{\rho_s f_{yt}}{\sqrt{f'_c}} \right) + \frac{v_c}{\sqrt{f'_c}} \quad , \qquad (8.3)$$

since $\frac{d_s}{D} = 0.91$ in both the static and dynamic test units. A comparison of the vertical intercepts of the straight lines, i.e. the value of $\frac{v_u}{\sqrt{f'_c}}$

when $\rho_s = 0$, in Fig. 8.29 with that of Eq. 8.3 shows that the value of 'concrete contribution', v_c , increases with decreasing aspect ratio and increasing axial load level. As a whole the results show that the ultimate shear strength of dynamic test columns is comparable with that of the static test columns if material and geometrical properties and axial load level are similar.

Table 8.8 : Non-Dimensional Shear Stress At Ultimate Versus $\frac{\rho_t f_{yt}}{\sqrt{f'_c}}$

$\frac{M}{VD} = 1.5$, $\frac{P_i}{f'_c A_g} \approx 0.1$			$\frac{M}{VD} = 2.0$, $\frac{P_i}{f'_c A_g} \approx 0.1$			$\frac{M}{VD} = 2.0$, $\frac{P_i}{f'_c A_g} = 0$		
Unit	$\frac{v_u}{\sqrt{f'_c}}$	$\frac{\rho_s f_{yt}}{\sqrt{f'_c}}$	Unit	$\frac{v_u}{\sqrt{f'_c}}$	$\frac{\rho_s f_{yt}}{\sqrt{f'_c}}$	Unit	$\frac{v_u}{\sqrt{f'_c}}$	$\frac{\rho_s f_{yt}}{\sqrt{f'_c}}$
D1	1.062	0.730	D6	0.872	0.566	1	0.520	0.276
D2	1.045	0.558	D7	0.710	0.447	4	0.530	0.295
D3	1.095	0.895	D8	0.696	0.456	5	0.606	0.451
D4	0.933	0.440	16	0.652	0.286	7	0.513	0.262
12	0.980	0.629				14	0.533	0.285
18	0.852	0.279				21	0.445	0.217
19	0.739	0.213				22	0.501	0.214
						23	0.593	0.419
						24	0.584	0.418

To examine further the magnitude of the 'concrete contribution' at ultimate, the spiral shear force, V_s , assuming a 45-deg truss, and using measured steel stresses was subtracted from the measured maximum shear stress, v_u , and this was non-dimensionalized by dividing by $\sqrt{f'_c}$. The results are included in Table 8.7 and compared with predicted results using the following equation derived from the static test results in Chapter Four, i.e.

$$\frac{v_c}{\sqrt{f'_c}} = 0.37\ \alpha_1\ (1 + 3.0\ \frac{P_i}{f'_c A_g}) \qquad (8.4)$$

where $$\alpha_1 = \frac{2.0}{\frac{M}{VD}} \geq 1.0$$

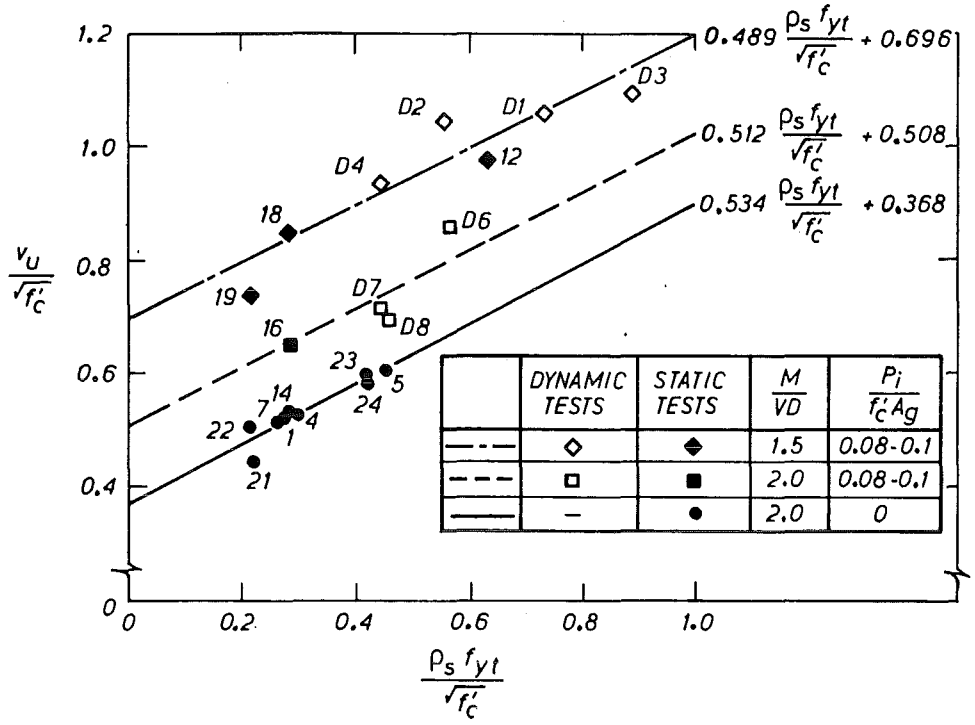

Fig. 8.29 : Non-dimensional shear stress at ultimate versus $\frac{\rho_s f_{yt}}{\sqrt{f'_c}}$

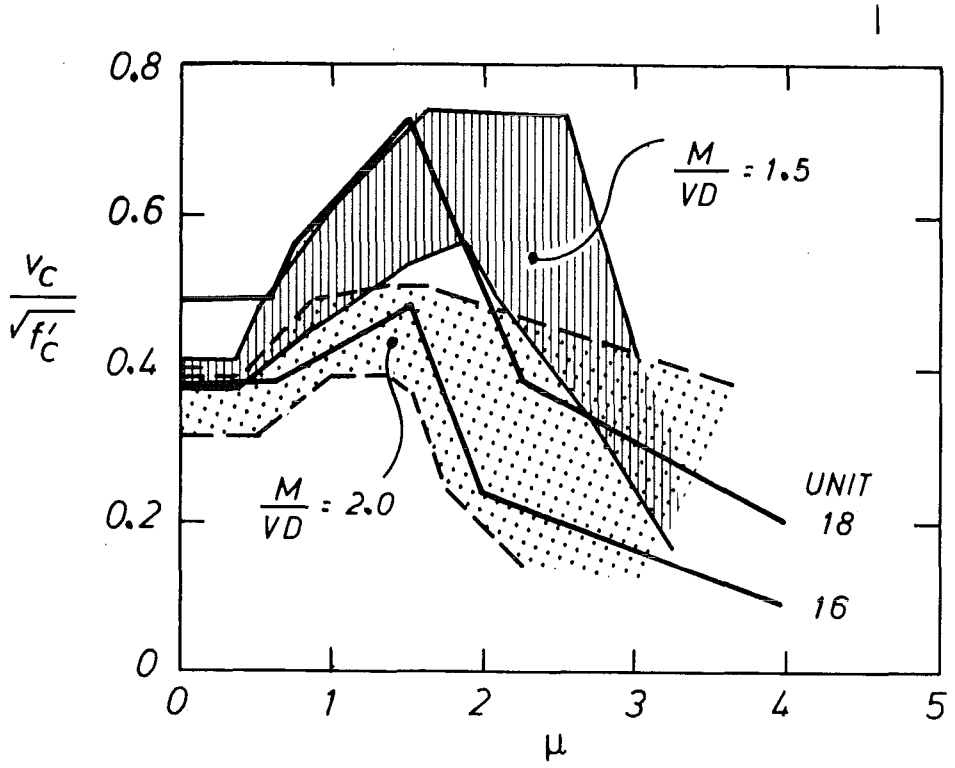

Fig. 8.30 : Non-dimensional shear stress carried by concrete at different displacement ductility levels

The data from Table 8.7 indicate that, on average the dynamic test results are about 6 percent higher than those predicted by Eq. 8.4 and the standard deviation of the ratios of the former to the latter is 0.06. This good agreement shows that the 'concrete contribution' of the static test results at ultimate is attainable in the dynamic loading situation and that it has a similar relationship with the aspect ratio and axial load level in both cases.

The variation of shear stress carried by concrete with displacement ductility for the single pier units is shown in Fig. 8.30. The figure only shows the upper and lower envelopes of the two different groups of single pier models with $\frac{M}{VD} = 1.5$ and 2.0 . The curves suggest increasing v_c with ductility after diagonal cracking until the ultimate stage and a drop in v_c thereafter. In general, the v_c values for shorter columns tended to be higher than those with larger aspect ratios. Also included in the figure are two similar curves, one for Unit 16 and one for Unit 18. These are from the static tests with aspect ratio of 2.0 and 1.5 respectively. These columns were reinforced transversely with R6 spirals at 60 mm pitch ($\rho_s = 0.00509$) and were subjected to an axial compression of $0.1f'_c A_g$ in addition to the lateral load. From the comparison, it appears that the results of the static and dynamic tests are compatible except that the results from the static tests tended to be closer to the lower envelopes after the maximum shear strength had been achieved. This might be expected since these column units from the static tests were subjected to more severe loading of five cycles each at a fixed displacement ductility level, even after maximum load had been attained. In the case of the dynamic tests, because of the uncontrollable instability effect associated with failure, the displacement tended to increase with the number of cycles and consequently the response was seldom repeated at the same displacement ductility level.

8.4.3 Shear Force At The Development Of Flexural Overstrength

In the design proposal discussed in Chapter Five, the strength enhancement factor, m_1 , was calculated from the following equation:

$$\frac{M_u}{M_i} = m = 2.35 \left(\frac{P_i}{f'_c A_g} - 0.1 \right)^2 + m_1 \quad \text{for} \quad \frac{P_i}{f'_c A_g} > 0.1 \qquad (8.5a)$$

$$= m_1 \quad \text{for} \quad \frac{P_i}{f'_c A_g} \leq 0.1 \qquad (8.5b)$$

Therefore,

$$m_1 = \frac{M_u}{M_i} - 2.35 \left(\frac{P_i}{f'_c A_g} - 0.1 \right)^2 \quad \text{for} \quad \frac{P_i}{f'_c A_g} > 0.1 \qquad (8.6a)$$

$$= \frac{M_u}{M_i} \quad \text{for} \quad \frac{P_i}{f'_c A_g} \leq 0.1 \qquad (8.6b)$$

where $\frac{M_u}{M_i}$ ($= \frac{V_u}{V_{if}}$) is the ratio of experimental ultimate strength to theoretical ultimate strength. The latter is taken as the ideal flexural strength. In the dynamic tests, only Unit D5 can be considered to be sufficiently ductile ($\mu_v \approx 5$) to have developed the full flexural overstrength and its $\frac{u}{V_{if}}$ value is compared with that of five comparable column units from the static tests. The values of $\frac{V_u}{V_{if}}$ and m_1 calculated using Eqs. 8.6a and b are listed in Table 8.9. The average value of m_1 for these six column units with high strength steel are flexural reinforcement is 1.25 with a standard deviation of 0.07. From the above consideration, it appears that the value of 1.22 suggested for m_1 in Section 5.2.2 for members with grade 380 steel may be non-conservative and a more suitable value for m_1 would be 1.25.

Table 8.9 : Flexural Strength Enhancement Factor, m_1

Unit	$\frac{P_i}{f'_c A_g}$	V_u (kN)	V_{if} (kN)	$\frac{V_u}{V_{if}}$	m_1
D5	0.08	97	75	1.293	1.293
8	0.2	475	356	1.334	1.311
9	0.2	385	281	1.370	1.347
10	0.2	450	360	1.250	1.227
13	0.1	443	363	1.220	1.220
15	0	230	204	1.127	1.127
				Ave	1.25
				σ	0.07

8.4.4 Comparison With the Design Proposal Of Chapter Five

On the basis of the design proposal made in Chapter Five, the initial shear strength, V_i , the residual shear strength, V_f , and the flexural overstrength, V_{if}^o , for the single pier units were calculated, and are listed in Table 8.10. Actual material strengths from Chapter Seven were used in the calculations and the value of m_1 was taken to be 1.22 instead of the newly suggested value of 1.25. The results show that only Unit D5 possessed a theoretical initial shear

Table 8.10 : Comparison Of Experimental Ultimate Strengths With The Values Predicted By The proposal From Chapter Five

(Single Pier Units)

UNIT	V_{si} (kN)	V_{ci} (kN)	V_i (kN)	V_{sf} (kN)	V_{cf} (kN)	V_f (kN)	Ideal Flexural Strength V_{if} (kN)	Enhanced Flexural Strength V_{if}^o (kN)	V_u (kN) Expt.	V_u (kN) Predicted	(10)/(11)
(1)	(2)	(3)	(4)	(5)	(6)	(7)	(8)	(9)	(10)	(11)	(12)
D1	49	70	(119)*	58	11	69	100	122	122	119	1.03
D2	37	69	(106)	54	8	62	100	122	118	106	1.11
D3	53	69	(122)	53	21	74	100	122	124	122	1.02
D4	30	70	(100)	45	6	51	100	122	107	100	1.07
D5	49	52	101	57	11	68	75	(92)	97	92	1.05
D6	37	51	(88)	53	8	61	75	92	97	88	1.10
D7	30	52	(82)	51	6	57	75	92	80	82	0.98
D8	30	51	(81)	50	6	56	75	92	77	81	0.95
										Ave	1.04
										σ	0.05

* Value within brackets give the predicted ultimate strength

strength in excess of the flexural overstrength (by approximately 10 percent) and all the other column units did not have adequate theoretical initial shear strength to match the anticipated flexural overstrength. According to the proposal, the predicted ultimate strength is taken to be the smaller of V_i and V_{if}^o. The ratios of the experimental to the predicted ultimate shear strength are listed in the last column of Table 8.10. This ratio was found to average 1.04 with standard deviation of 0.05.

8.4.5 Displacement Ductility Capacity

Besides the prediction of shear and flexural strengths, the design proposal presented in Chapter Five also allows the displacement ductility capacity of the column units to be assessed. Based on the procedure outlined in Chapter Five, all the single pier units, except Unit D5, were expected to fail in shear with limited ductility while Unit D5 was predicted to exhibit a moderate ductility of 5.7 before failure. The predicted results are listed together with the experimental values of Table 8.11. In general, the prediction tends to be conservative for column units failing in shear with limited ductility. From an assessment of the dynamic test results in Table 8.11 and the static test results in Table 5.3, it appears that a more realistic value of 2.5 instead of 2.0 can be used for the displacement ductility corresponding to the beginning of the transition between V_i and V_f, i.e. point B of line BC shown in Fig. 5.1, for the design proposal.

The experimental displacement ductility capacity of Unit D5 was calculated based on the displacement result obtained from the record of the oscillograph, and because the displacement trace went out of the range of the instrument, the maximum displacement result can only be estimated and thus it may be subject to error as a result of extrapolation.

On the whole, it can be said that the results of the two series of tests are compatible not only in terms of shear strengths but also displacement ductility capacity. However, it is recommended that more dynamic tests should be carried out on column units which fail in shear with moderate ductility, or exhibit fully ductile behaviour, in order to check the validity of the procedure used to calculate the displacement ductility capacity in the design proposal.

8.4.6 Shear Strength And Ductility Capacity Of Twin-Pier Units

8.4.6.1 Shear strength at onset of diagonal cracking

Table 8.11 : Experimental And Predicted Displacement Ductility Capacity

(Single Pier Units)

Unit	V_i (kN)	V_f (kN)	V_{if}^o (kN)	μ_f (Eq.5.22)	Ductility Capacity		Predicted Failure Mode*
					Expt	Predicted	
D1	119	69	122	17.5	2.7	2.0	LD-S
D2	106	62	122	14.1	3.0	2.0	LD-S
D3	122	74	122	21.1	3.7	2.0	LD-S
D4	100	51	122	11.4	2.5	2.0	LD-S
D5	101	68	92	15.4	4.9†	5.7	MD-S
D6	88	61	92	12.4	2.9	2.0	LD-S
D7	82	57	92	10.2	3.0	2.0	LD-S
D8	81	56	92	12.9	2.5	2.0	LD-S

* MD-S : Shear failure with moderate ductility ($4 \leq \mu < 6$)

LD-S : Shear failure with limited ductility ($2 \leq \mu < 4$)

† Conservative estimate - displacement off-scale of oscillograph

The shear force and non-dimensional shear stress at the onset of diagonal cracking for twin-pier models were calculated as for the single pier models (Section 8.4.1). These are tabulated in Table 8.12. Also included in the table is the axial load level associated with the diagonal cracking load. In the case of twin pier units, due to the presence of alternating tension and compression, the diagonal cracks tended to be initiated when the column unit was in tension, as is evident in three of the columns listed in Table 8.12. The results of Column DT2-W indicate that the diagonal cracking occurred while it was in axial compression but this was found to be at a lower load level ($\frac{v_{cr}}{\sqrt{f'_c}} = 0.28$) than that predicted by Eq. 8.2 ($\frac{v_{cr}}{\sqrt{f'_c}} = 0.37$). Eq. 8.2 was also used to predict the diagonal cracking load of the other three columns, with the term $\frac{P_i}{f'_c A_g}$ taken as negative for axial tension. It can be seen from the results in Table 8.12 that the agreement, though reasonable, is not as good as in the case of single pier models (see Table 8.6).

8.4.6.2 Shear strength at ultimate

The corrected ultimate strengths of twin-pier units based on Eqs. 8.1a and b are listed in Table 8.13 together with the associated axial load level for both the tension and compression cases. With the exception of Column DT2-W, the strength of the columns in compression is greater in tension, as would be expected. It should be noted that Column DT2-W sustained an exceptionally high ultimate strength in tension equal to 2.08 $V_{if}(T)$, but because of the instantaneous nature of the loading, it is doubtful that it represents the true value of enhanced strength.

Also included in Table 8.13 is the ultimate shear stress normalized with respect to $\sqrt{f'_c}$. The results show that the shear stress level was high even while axial tension was acting. Comparison with the results in Table 8.7 indicates that, while the value of $\frac{v_u}{\sqrt{f'_c}}$ are compatible in shorter columns of both single and twin-pier models (i.e. D1, DT1-W and DT1-E) in compression, the results of taller columns of the twin-pier model (Unit DT2) is lower than that of the companion single pier model (Unit D5).

Comparison of theoretical initial shear strength, V_i , with the predicted enhanced flexural strength, V_{if}^o , in Table 8.14 indicates that the ultimate strength for all the columns in compression was expected to be limited by the V_{if}^o value. The ratios of the experimental to the predicted ultimate strengths of columns in compression had an average value of 0.91. This indicates that the columns in compression were 'weaker' than expected, probably due to the effect of

Table 8.12 : Shear Stress At Onset Of Diagonal Cracking (Twin-Pier Units)

Unit	$\frac{M}{VD}$	$\frac{P_i}{f'_c A_g}$	V_{cr} (kN)	$\frac{v_{cr}}{\sqrt{f'_c}}$ Expt.	$\frac{v_{cr}}{\sqrt{f'_c}}$ Predicted (Eq.8.2)	$\frac{(15)}{(16)}$
(1)	(2)	(3)	(4)	(5)	(6)	(7)
DT1-W	1.5	-0.03	34.4	0.30	0.34	0.88
DT1-E	1.5	-0.02	30.3	0.26	0.35	0.74
DT2-W	2.0	0.10	32.7	0.28	0.37	0.76
DT2-E	2.0	-0.02	33.1	0.29	0.26	1.12
					Ave	0.88
					σ	0.15

* Negative sign denotes axial tension

Table 8.13 : Shear Strength At Ultimate (Twin-Pier Units)

Unit	$\frac{M}{VD}$	Axial Compression			Axial Tension		
		$\frac{P_i}{f'_c A_g}$	V_u (kN)	$\frac{v_u}{\sqrt{f'_c}}$	$\frac{P_i}{f'_c A_g}$ *	V_u (kN)	$\frac{v_u}{\sqrt{f'_c}}$
DT1-W	1.5	0.22	113	0.983	-0.15	97	0.844
DT1-E	1.5	0.22	132	1.149	-0.13	87	0.757
DT2-W	2.0	0.18	87	0.754	-0.07	125	1.082
DT2-E	2.0	0.19	92	0.797	-0.11	75	0.650

* Negative sign denotes axial tension

Table 8.14 : Comparison of Experimental Ultimate Strengths With The Values Predicted By The Proposal From Chapter Five

(Twin-Pier Units)

UNIT	$\frac{P_i}{f'_c A_g}$	Initial Shear Strength			Residual Shear Strength			Ideal Flexural Strength V_{if} (kN)	Enhanced Flexural Strength V_{if}^o (kN)	V_u (kN)		$\frac{(10)}{(11)}$
		V_{si} (kN)	V_{ci} (kN)	V_i (kN)	V_{sf} (kN)	V_{cf} (kN)	V_f (kN)			Expt.	Predicted	
		(2)	(3)	(4)	(5)	(6)	(7)	(8)	(9)	(10)	(11)	
DT1-W(C)	0.22	49	94	143	58	11	69	107	(134)*	113	134	0.84
(T)	-0.15		31	(80)				77	94	97	80	1.21
DT1-E(C)	0.22	49	94	143	58	11	69	107	(134)	132	134	0.99
(T)	-0.13		34	(83)				77	94	87	83	1.05
DT2-W(C)	0.18	49	66	115	59	11	70	80	(99)	87	99	0.88
(T)	-0.07		33	82				60	(73)	125	73	1.71
DT2-E(C)	0.19	49	67	116	59	11	70	80	(99)	92	99	0.93
(T)	-0.11		29	78				60	(73)	75	73	1.02

(T) : Tension (C) : Compression

Ave (C) 0.91

(T) 1.10

* Value within brackets gives the predicted ultimate strength

alternating tension and compression. The theoretical initial shear strength of columns in tension was calculated with $\frac{P_i}{f'_c A_g}$ taken as negative, and the enhanced flexural strength was calculated as for the case of $\frac{P_i}{f'_c A_g} < 0.1$ in compression (i.e. m = 1.22 from Section 5.2.2). The ultimate strengths of shorter columns (DT1-W and DT1-E) in tension were expected to be limited by the value of V_i while those of the taller columns (DT2-W and DT2-E) by the value of V_{if}^o. Excluding the exceptional case of DT2-W, the ratios of the experimental to the predicted ultimate strength of columns in tension (see Table 8.14) had an average value of 1.10.

Table 8.15 : Enhancement In Flexural Strength (Twin-Pier Units)

Unit	Axial Compression			Axial Tension			Overall System		
	V_u (kN)	V_{if} (kN)	$\frac{V_u}{V_{if}}$	V_u (kN)	V_{if} (kN)	$\frac{V_u}{V_{if}}$	V_u (kN)	V_{if} (kN)	$\frac{V_u}{V_{if}}$
DT1-W	113	107	1.06	97	77	1.26	212	184	1.15
DT1-E	132	107	1.23	87	77	1.13			
DT2-W	87	80	1.09	125	60	2.08	184	140	1.31
DT2-E	92	80	1.15	75	60	1.25			

Assuming that flexural overstrength is the limiting factor and to assess the extent of this enhancement, the values of $\frac{V_u}{V_{if}}$ are listed in Table 8.15 for both cases of axial compression and tension as well as the overall system considering the twin pier model as a whole unit. The results show that an average value of $\frac{V_u}{V_{if}}$ for columns in compression is 1.13 with a standard deviation of 0.06 as compared with 1.29 for Unit D5 and the average value of 1.25 for all the units listed in Table 8.9. For the case of column units with axial tension, as noted earlier, Column DT2-W gave an exceptionally high value of $\frac{V_u}{V_{if}}$, and if this value is disregarded, the average value of $\frac{V_u}{V_{if}}$ is 1.21 with a standard deviation of 0.06. Because of the absence of a yield plateau in the stress-strain curve of the flexural steel (Chapter Seven), strength enhancement due to strain hardening effect is more pronounced and begins earlier in the case when the column units were subjected to axial tension as is reflected in the larger average value of the ratio

of $\frac{V_u}{V_{if}}$. Finally, if the maximum horizontal inertia force calculated from the maximum response acceleration is divided by the sum of the ideal flexural strengths of the component columns, with one in tension and the other in compression, the strength enhancement ratio for the overall system was found to be 1.15 and 1.31 for Units DT1 and DT2 respectively.

8.4.6.3 Displacement ductility capacity

The experimental displacement ductility capacity for the twin-pier models is compared with the predicted value in Table 8.16. The failure mode predicted based on the design proposal given in Chapter Five are also included. The value listed are for columns in compression only because the confinement ratio, α ($\frac{\rho_{s(provided)}}{\rho_{s(code)}}$) used to calculate the value of μ_f (see Section 5.2.5) was not defined for columns in tension. The predicted ductility capacities are larger than the experimental values particularly in the case of the taller columns (DT2-W and DT2-E). The poor agreement indicates that the method of displacement ductility prediction which was based on the results of single stem cantilever columns may not be suitable for the case of twin-pier systems. The effect of alternating axial tension and compression might have some influence on the ductility capacity of individual columns.

Table 8.16 : Experimental And Predicted Displacement Ductility Capacity
(Twin-Pier Units - Columns in Axial Compression)

Unit	V_i (kN)	V_f (kN)	V_{if}^o (kN)	μ_f (Eq. 5.22)	Ductility Capacity		Predicted Failure Mode *
					Expt.	Predicted	
DT1-W	143	69	134	14.0	1.6	3.5	LD-S
DT1-E	143	69	134	14.0	2.8	3.5	LD-S
DT2-W	115	70	99	12.7	1.6	5.8	MD-S
DT2-E	116	70	99	12.7	3.9	6.0	MD-S

* MD-S : Shear failure with moderate ductility ($4 \leq \mu < 6$)

LD-S : Shear failure with limited ductility ($2 \leq \mu < 4$)

8.5 CONCLUSIONS

From the analyses of results of dynamic tests the following conclusions can be drawn:

(a) The behaviour of single pier units under dynamic loading was generally well predicted by equations based on the results of static testing. In particular for observed shear forces it was found that the:

(i) average shear stress at diagonal cracking ≈ 94% of predicted value,

(ii) ultimate shear stress carried by concrete ≈ 106% of predicted value,

and (iii) ultimate shear strength ≈ 104% of predicted value.

(b) Flexural cracking was apparently delayed during dynamic testing but the delay did not influence the ultimate strength and the displacement ductility capacity.

(c) Dynamic strength enhancement was much less than values recorded for previous axial tests of concrete and steel with dynamic loading, despite the very high loading rate[8.2]. It is felt that this may be due to the cyclic nature of testing as compared to the monotonic loading used for the determination of material strengths.

(d) The behaviour of dynamically tested twin-pier models was less predictable than the single pier models. Strengths of columns with axial compression were rather lower than predicted, while columns with axial tension had higher ultimate strengths. Ductility capacity was less than that predicted using the design method of Chapter Five. More testing is therefore required to have a better understanding of the twin-pier behaviour.

Chapter Nine

CONCLUSIONS AND RECOMMENDATIONS

9.1 CONCLUSIONS

Research into shear behaviour of circular reinforced concrete columns under cyclic loading was found to be lacking from a review of relevant literature. The project was therefore carried out with the specific aim of improving knowledge in this area. Extensive static and dynamic tests were carried out on bridge pier models to provide an experimental data base. As an outcome of the experimental work, a proposal regarding the design of circular reinforced concrete members for shear strength and ductility capacity was put forward. The 'variable-angle truss' model was found to provide a rational approach to the problem, and therefore, the 'Diagonal Compression Field Theory' was adapted in a limited theoretical investigation of shear behaviour. The following points are brief summaries of conclusions drawn on various aspects of the project.

(a) Twenty-five column units were subjected to incremental reversed cyclic loadings in the static tests. The main variables were the aspect ratio, the axial load level and the spiral reinforcement content. Four failure modes were identified according to the displacement ductility achieved before degradation of strength occurred. The results suggested that the strength of concrete shear resisting mechanisms was dependent on the displacement ductility level, and was increased by decreasing aspect ratio and increasing axial compression level. However, increasing the axial compression enhanced the rate of strength decay after maximum load was reached. An increase in spiral reinforcement content enhanced the shear strength and ductility performance as well as energy dissipation capacity.

(b) The current New Zealand concrete design code provisions for shear, when applied to circular sections with uniformly distributed flexural reinforcement, were found to be very conservative even when the non-seismic provisions were used. On average, observed strengths were about 56 percent higher than the shear strength specified by the non-seismic provisions of the code. However, it should be noted that current code equations are based on results of rectangular sections with flexural reinforcement

concentrated in opposite faces. Similar conservatism was also noted in other code provisions; the ratios of observed to specified strengths ranging between 1.27 and 1.76. The 'variable-angle truss' model was found to be conservative because of the limitation on the angle of inclination controlled by the geometry of the column units. The shear strength of the column units, therefore, could not be predicted by reducing the diagonal strut inclination and considering solely the spiral contribution.

(c) A proposal for the design for shear strength of circular reinforced concrete members was put forward, based on the experimental results of the static tests. The proposed approach required checking the flexural overstrength against two levels of shear strength, namely the initial shear strength applicable at low ductility levels, and the residual shear strength applicable at high ductility levels when degradation has taken place. The initial shear strength is calculated using the 45-deg truss. The equation for concrete contribution to shear strength was derived from the static test results. The residual shear strength was calculated with reduced concrete contribution and increased spiral contribution through a smaller diagonal strut inclination. The design approach not only allows the shear strength but also the displacement ductility capacity to be assessed. Good agreement with experimental values was achieved using this simple design approach. The proposal has also been incorporated into an integral flexure/shear design methodology that also considers ductility. In this the transverse reinforcement is required for confinement as well as shear resistance for a particular displacement ductility demand.

(d) As a second stage of the experimental work, half scale models of the static test units were subjected to more realistic dynamic tests on a shake-table. Eight single pier models and two twin-pier models were tested. The single piers were subjected to a sequence of sinusoidal excitation of 5 Hz frequency, with increasing amplitude between tests. The twin-pier models were tested using excitation obtained from an actual earthquake accelerogram. On the whole the behaviour of single pier units was comparable to those of the static tests. The design proposal gave reasonable prediction of the model behaviour. The behaviour of dynamically tested twin-pier models was less predictable; strengths of columns with axial compression was rather lower than predicted while

columns with axial tension had higher observed ultimate strengths. The enhancement in material strength due to the rate of loading, which has been observed in material testing, was not reflected in enhancement of section strength in the dynamic tests.

(e) The 'Diagonal Compression Field Theory' was adapted in the analyses with the use of concrete stress-strain relationship developed for confined concrete. The ultimate strength and the load-displacement response up to the theoretical ultimate load predicted by the theory agreed reasonably well with experimental observations. The computational process was time consuming and the analytical formulation was unsuitable for predicting the falling branch portion of the load-displacement response. However, from the analytical work, it appears that the theory could be extended to form a basis for obtaining the relationship between degraded strength and displacement ductility capacity.

9.2 RECOMMENDATIONS FOR FUTURE RESEARCH

Due to time-constraint the study undertaken in this project could not be extended to cover a wider range of topics. Other related areas of interest and concern were revealed in the process of investigation. The following recommendations refer to areas considered to be important. Such further investigations would enhance the knowledge of shear behaviour of reinforced concrete columns under seismic attack and would complement the present project.

(a) The behaviour of twin-pier models under dynamic testing indicated significant differences from static testing of single column piers. Hence, further investigation is recommended to study systems where the axial load varies in magnitude. Some preliminary static tests could be conducted on such twin-pier systems, or on single pier units with varying axial load acting in conjunction with the lateral shear force.

(b) Bridge piers under double curvature bending can behave rather differently from cantilever piers because of the way the shear force is introduced. Bridge piers may be subjected to double curvature bending under longitudinal seismic attack, or in multiple pier systems under a transverse earthquake attack. Hence, it is essential to obtain information, through more experimental work in this area.

(c) As the dynamic testing was limited to columns failing mainly in shear with limited ductility, more dynamic tests are recommended so that other categories of failure mode can be investigated. In particular, more dynamic tests on column units designed according to the design proposal and expected to fail in shear with moderate ductility, or exhibiting a ductile flexural failure mode should be carried out to check the validity of the proposal, especially the availability of displacement ductility capacity.

(d) In order to improve the design proposal more experimental work is needed to investigate the influence of other parameters such as the flexural reinforcement content and the presence of axial tension. Columns of other cross-sectional shape should be studied if the design proposal is to be generally applicable.

(e) The 'Diagonal Compression Field Theory' can be a useful analytical tool to carry out parametric studies to investigate moment-shear interaction. Some important parameters to be studied are, the compressive strength, tensile reinforcement content and distribution of tensile reinforcement within a section. In particular, the relationship between degraded shear strength and displacement ductility capacity should be further investigated using the theory, with emphasis placed on overcoming the inherent computational difficulty in the approach.

Appendix I

REFERENCES

CHAPTER ONE

1.1 CHAPMAN, H.E., 'An Overview of the State of Practice in Earthquake Resistant Design of Bridges in New Zealand', Proceedings of a Workshop on Earthquake Resistance of Highway Bridges, Applied Technology Council, Jan. 29-31, 1979, pp. 67-97.

1.2 20 AUTHORS, 'Papers Resulting from the Deliberation of the Society's Discussion Groups on the Seismic Design of Bridges', Bulletin of the N.Z. National Society for Earthquake Engineering, Vol.13, No.3, Sept. 1980, pp. 226-309.

1.3 SUZUKI, Z. (Chief Editor), 'General Report on the Tokachi-Oki Earthquake of 1968', Tokyo, 1971, 754 pp.

1.4 SOZEN, M.A. et al, 'Engineering Report on the Caracas Earthquake of 29th July 1967', National Research Council, National Academy of Engineering, Washington, D.C. 1968, 84 pp.

1.5 JENNINGS, P.C. (Editor), 'Engineering Features of the San Fernando Earthquake', California Institute of Technology, Pasadena, California, 1971, 512 pp.

1.6 BLAKELEY, R.W.G., 'Analysis and Design of Bridges Incorporating Mechanical Energy Dissipating Devices for Earthquake Resistance', Proceedings of a Workshop on Earthquake Resistance of Highway Bridges, Applied Technology Council, Jan. 29-31, 1979, pp. 313-342.

1.7 BLAKELEY, R.W.G., 'Design of Bridges Incorporating Mechanical Energy Dissipating Devices', Part 2, Seismic Design of Bridges, RRU Bulletin 43, National Roads Board, Wellington, New Zealand, 1979, pp. 71-145.

1.8 NZS 3101, 'New Zealand Code of Practice for the Design of Concrete Structures', Standards Association of New Zealand, Wellington, 1982.

1.9 PRIESTLEY, M.J.N., and PARK, R., 'Strength and Ductility of Bridge Substructures', RRU Bulletin 71, National Roads Board, Wellington, New Zealand, 1984, 120 pp.

CHAPTER TWO

2.1 HOGNESTED, E., 'What Do We Know About Diagonal Tension and Web Reinforcement in Concrete? A Historical Study', University of Illinois Engineering Experiment Station, Circular Series No. 64, March 1952, 47 pp.

2.2 ACI-ASCE COMMITTEE 326, 'Shear and Diagonal Tension', ACI Journal, Vol. 59, Jan, Feb, March 1962, pp. 1-30, 277-334, 352-396.

2.3 JOINT ACI-ASCE TASK COMMITTEE 426, 'The Shear Strength of Reinforced Concrete Members', Journal of the Structural Division, ASCE, Vol. 99, No.ST6, June 1973, pp. 1091-1187.

2.4 ACI BIBLIOGRAPHY No. 4, 'Shear, Diagonal Tension and Torsion in Structural Concrete', ACI Publication, 1962, 121 pp.

2.5 JIRSA, J.O., 'Applicability to Bridges of Experimental Seismic Test Results Performed on Subassemblages of Buildings', Proceedings of a Workshop on Earthquake Resistance of Highway Bridges, Applied Technology Council, Jan. 29-31, 1979, pp.547-565.

2.6 JIRSA, J.O., MARUYAMA, K. and RAMIREZ, R., 'Development of Loading System and Initial Tests - Short Columns Under Bidirectional Loading', CESRL Report No. 78-2, Department of Civil Engineering, University of Texas, Austin, Sept. 1978, 70 pp.

2.7 MARUYAMA, K. and JIRSA, J.O., 'Shear Behaviour of Reinforced Concrete Members Under Bidirectional Reversed Lateral Loading', CESRL Report No. 79-1, Department of Civil Engineering, University of Texas, Austin, Aug. 1979, 161 pp.

2.8 RAMIREZ, H. and JIRSA, J.O., 'Effects of Axial Load on Shear Behaviour of Short Reinforced Concrete Columns Under Cyclic Lateral Deformations', PMFSEL Report No. 80-1, Department of Civil Engineering, University of Texas, Austin, June 1980, 162 pp.

2.9 WOODWARD, K.A. and JIRSA, J.O., 'Behaviour Classification of Short Reinforced Concrete Columns Subjected to Cyclic Deformations', PMFSEL Report No. 80-2, Department of Civil Engineering, University of Texas, Austin, July 1980, 339 pp.

2.10 JIRSA, J.D., MARUYAMA, K., and RAMIREZ, H., 'The Influence of Load History on the Shear Behaviour of Short Reinforced Concrete Columns', Proceedings of the Seventh World Conference on Earthquake Engineering, Vol. 6., Istanbul, Turkey, 1980, pp. 339-346.

2.11 WOODWARD, K.A., 'Behaviour of Short Reinforced Concrete Columns Subjected to Cyclic Bilateral Deformations', Proceedings of the Seventh World Conference on Earthquake Engineering, Vol. 6, Istanbul, Turkey, 1980, pp. 347-354.

2.12 MARUYAMA, K., RAMIREZ, H. and JIRSA, J.O., 'Behaviour of Reinforced Concrete Columns Under Biaxial Lateral Loading', Sixth European Conference on Earthquake Engineering, Dubronik, Yugoslavia, Sept. 18-22, 1978, pp. 135-141.

2.13 RAMIREZ, H. and JIRSA, J.O., 'The Influence of Axial Load on the Response of Columns Under Bidirectional Loadings', Bulletin D'Information No. 132, Comite Euro-International Du Beton, pp. 133-140.

2.14 WOODWARD, K.A. and JIRSA, J.O., 'Influence of Reinforcement on Reinforced Concrete Short Column Lateral Resistance', Journal of the Structural Division, ASCE, Vol.110, No. ST1, Jan. 1984, pp. 90-104.

2.15 MARUYAMA, K., RAMIREZ, H. and JIRSA, J.O., 'Short Reinforced Concrete Columns Under Bilateral Load Histories', Journal of the Structural Division, ASCE, Vol. 110, No. ST1, Jan. 1984, pp. 120-137.

2.16 UMEHARA, H. and JIRSA, J.O., 'Short Rectangular Reinforced Concrete Columns Under Bidirectional Loadings', Journal of the Structural Division, ASCE, Vol. 110, No. ST3, March 1984, pp. 605-618.

2.17 PARK, R., 'Ductile Design of Bridge Piers', Part 1, Seismic Design of Bridges, RRU Bulletin 43, National Roads Board, Wellington, New Zealand , 1979, pp. 1-70.

2.18 PRIESTLEY, M.J.N., and PARK, R., 'Seismic Resistance of Reinforced Concrete Bridge Columns', Proceedings of a Workshop on Earthquake Resistance of Highway Bridges, Applied Technology Council, Jan. 29-31, 1979, pp. 253-283.

2.19 PARK, R., 'Ductility Investigation of Piers and Columns', Comparison of United States and New Zealand Seismic Design Practices for Highway Bridges, Applied Technology Council, Aug. 1982, pp. 61-68.

2.20 PRIESTLEY, M.J.N. and PARK, R., 'Strength and Ductility of Bridge Substructures', RRU Bulletin 71, National Roads Board, Wellington, New Zealand, 1984, 120 pp.

2.21 PRIESTLEY, M.J.N., PARK, R., and POTANGAROA, R.T., 'Ductility of Spirally Confined Concrete Columns', Journal of the Structural Division, ASCE, Vol. 107, No. ST1, Jan. 1981, pp. 181-202.

2.22 KUBOTA, T. and SOZEN, M.A., 'A Study of Methods Used in Japan and the U.S.A. for Design of Web Reinforcement in Reinforced Concrete', Civil Engineering Studies, Structural Research Series No. 452, University of Illinois, Urbana, Aug. 1978, 141 pp.

2.23 HIROSAWA, M., OZAKI, M. and WAKABAYASHI, 'Experimental Study on Large Models of Reinforced Concrete Columns', Vol. 1, Fifth World Conference on Earthquake Engineering, Rome, Italy, 1974, pp.815-824.

2.24 BROWN, R.H. and JIRSA, J.O., 'Reinforced Concrete Beams Under Load Reversals', ACI Journal, Vol. 68, May 1071, pp. 380-390.

2.25 GOSAIN, N.K., BROWN, R.H. and JIRSA, J.O., 'Shear Requirements for Load Reversals on Reinforced Concrete Members', Journal of the Structural Division, ASCE, Vol. 103, No. ST7, July 1977, pp.1461-1476.

2.26 WIGHT, J.K., 'Shear Strength Decay in Reinforced Concrete Columns Subjected to Large Deflection Reversals', Ph.D. Thesis, Department of Civil Engineering, University of Illinois, Urbana, 1973, 291 pp.

2.27 WIGHT, J.K. and SOZEN, M.A., 'Strength Decay of Reinforced Concrete Columns Under Shear Reversals', Journal of the Structural Division, ASCE, Vol. 101, No. ST5, May 1975, pp. 1053-1065.

2.28 WIGHT, J.K. and KANOH, Y., 'Shear Failure of Reinforced Concrete Columns Subjected to Cyclic Loading', Proceedings of the Fifth World Conference on Earthquake Engineering, Vol. I, Rome, Italy, 1974, pp. 807-810.

2.29 SCRIBNER, C.F., and WIGHT, J.K., 'Strength Decay in Reinforced Concrete Beams Under Load Reversals', Journal of the Structural Division, ASCE, Vol. 106, No. ST4, April 1980, pp. 861-876.

2.30 SCRIBNER, C.F. and WIGHT, J.K., 'Delaying Shear Strength Decay in Reinforced Concrete Flexural Members Under Large Load Reversals', Proceedings of the Seventh World Conference on Earthquake Engineering, Vol. 7, Istanbul, Turkey, 1980, pp. 31-38.

2.31 BERTERO, V.V., 'Seismic Behaviour of Linear Element (Beams and Columns)', State-of-the-Art in Earthquake Engineering, Istanbul, Turkey, 1981, pp. 323-364.

2.32 BERTERO, V.V., BRESLER, B. and LIAO, H., 'Stiffness Degradation of Reinforced Concrete Members Subjected to Cyclic Flexural Moments', Report No. EERC 69-12, University of California, Berkeley, Dec. 1969, 111 pp.

2.33 POPOV, E.P., BERTERO, V.V. and KRAWINKLER, H., 'Cyclic Behaviour of Three Reinforced Concrete Flexural Members with High Shear', Report No. EERC 72-5, University of California, Berkeley, Oct. 1972, 78 pp.

2.34 CELEBI, M. and PENZION, J., 'Experimental Investigation into the Seismic Behavior of Critical Regions of Reinforced Concrete Components as Influenced by Moments and Shears', Report No. EERC 73-4, University of California, Berkeley, Jan. 1973, 103 pp.

2.35 BERTERO, V.V., POPOV, E.P. and WANG, T.Y., 'Hysteretic Behavior of Reinforced Concrete Flexural Members with Special Web Reinforcement', Report No. EERC 74-9, University of California, Berkeley, Aug. 1974, 126 pp.

2.36 BERTERO, V.V. and POPOV, E.P., 'Hysteretic Behavior of Ductile Moment-Resisting Reinforced Concrete Components' Report No. EERC 75-16, University of California, Berkeley, April 1975, 126 pp.

2.37 ATALAY, M.B. and PENZIEN, J., 'The Seismic Behavior of Critical Regions of Reinforced Concrete Components as Influenced by Moment, Shear and Axial Force', Report No. EERC 75-19, University of California, Berkeley, Dec. 1975, 226 pp.

2.38 MA, S.M., BERTERO, V.V., and POPOV, E.P., 'Experimental and Analytical Studies on the Hysteretic Behavior of Reinforced Concrete Rectangular and T-Beams', Report No. EERC 76-2, University of California, Berkeley, May 1976, 241 pp.

2.39 ZAGAJESKI, S.W., BERTERO, V.V., and BONWKAMP, J.G., 'Hysteretic Behavior of Reinforced Concrete Columns Subjected to High Axial and Cyclic Shear Forces', Report No. EERC 78-5, University of California, Berkeley, April 1978, 208 pp.

2.40 CELEBI, M. and PENZIEN, J., 'Behavior of Reinforced Concrete Beams Under Combined Moment and Shear Reversal', Preliminary Report, International Association for Bridge and Structural Engineering, Lisbon, 1973, pp. 193-198.

2.41 BERTERO, V.V. and POPOV, E.P., 'Seismic Behavior of Ductile Moment Resisting Reinforced Concrete Frames', Reinforced Concrete Structures in Seismic Zones, San Francisco, 1974, Special Publication SP-53, ACI, pp. 247-291.

2.42 ZAGAJESKI, S.W. and BERTERO, V.V., 'Hysteretic Behavior of Reinforced Concrete Columns Subjected to High Axial Forces and Cyclic Shear Forces', Sixth European Conference on Earthquake Engineering, Vol. 3, Sept. 18-22, Dubrovnik, Yugoslavia, pp. 159-166.

2.43 BERTERO, V.V. and BRESLER, B., 'Seismic Behavior of Reinforced Concrete Framed Structures', Proceedings of the Fourth World Conference on Earthquake Engineering, Vol. I, Santiago, Chile, 1969, pp. 109-124.

2.44 FENWICK, R.C. and FONG, A., 'The Behaviour of Reinforced Concrete Beams Under Cyclic Loadings', Report No. 176, Department of Civil Engineering, University of Auckland, Auckland, Dec. 1979, 46 pp.

2.45 FENWICK, R.C. and THOM, C.W., 'Shear Deformation in Reinforced Concrete Beams Subjected to Inelastic Cyclic Loading', Report No. 279, Department of Civil Engineering, University of Auckland, Auckland, June 1982, 50 pp.

2.46 FENWICK, R.C., 'Strength Degradation of Reinforced Concrete Beams Under Cyclic Loading', Report No. 304, Department of Civil Engineering, Universiry of Auckland, Auckland, April 1983, 42 pp.

2.47 THOM, C.W., 'The Effects of Inelastic Shear on the Seismic Response of Structures', Ph.D. Thesis, Department of Civil Engineering, University of Auckland, Auckland, New Zealand, 1983.

2.48 FENWICK, R.C., and FONG, A., 'The Behaviour of Reinforced Concrete Beams Under Cyclic Loading', Proceedings of the Second South Pacific Regional Conference on Earthquake Engineering, Wellington, New Zealand, May 1979, pp. 533-552.

2.49 FENWICK, R.C., 'Strength Degradation of Concrete Beams Under Cyclic Loading', Proceedings of the Third South Pacific Regional Conference on Earthquake Engineering, Wellington, New Zealand, May 1983, pp. 137-155.

2.50 FENWICK, R.C., 'Shear Deformation in Seismic Frame Structures', Journal of the Structural Division, ASCE, Vol. 109, No. ST4, April 1982, pp. 965-976.

2.51 FENWICK, R.C., and FONG, A., 'The Behaviour of Reinforced Concrete Beams Under Cyclic Loading', Bulletin of the New Zealand National Society for Earthquake Engineering, Vol. 12, No.2, June 1979, pp. 158-167.

2.52 KARLSSON, B.I., AOYAMA, H., and SOZEN, M.A., 'Spirally Reinforced Concrete Columns Subjected to Loading Reversals Simulating Earthquake Effects', Proceedings of the Fifth World Conference on Earthquake Engineering, Vol. I, Rome, Italy, 1973, pp. 803-806.

2.53 PARK, R., and PAULAY, T., 'Reinforced Concrete Structures', John Wiley and Sons, New York, 1975, 769 pp.

2.54 LEONHARDT, F. and WALTHER, R., 'The Stuttgart Shear Tests, 1961', Cement and Concrete Association Library, Translation No. 111, London, England, 1964, 134 pp.

2.55 LEONHARDT, F., 'On the Reduction of Shear Reinforcement as Derived from the Stuttgart Shear Tests 1961-1963', Final Report, Seventh Congress, International Association for Bridge and Structural Engineering, Rio de Janeiro, 1964, pp. 323-345.

2.56 LEONHARDT, F., 'Reducing the Shear Reinforcement in Reinforced Concrete Beams and Slabs', Magazine of Concrete Research, Vol. 17, No. 53, Dec. 1965, pp. 187-198.

2.57 LEONHARDT, F., 'Shear in Concrete Structures', Bulletin D'Information No. 126, Comite Euro-International Du Beton, June 1978, pp. 66-124.

2.58 BRESLER, B. and SCORDELIS, A.C., 'Shear Strength of Reinforced Concrete Beams', ACI Journal, Vol. 60, No.1, Jan. 1963, pp.51-72.

2.59 ATTIOGBE, E.K., PALASKAS, M.N. and DARWIN, D., 'Shear Cracking and Stirrup Effectiveness of Lightly Reinforced Concrete Beams', SM Report No. 1, Structural Engineering and Engineering Materials, University of Kansas Center for Research, Inc., July 1980, 138 pp.

2.60 HADDADIN, M.J., HONG, S.T., and MATTOCK, A.H., 'Stirrup Effectiveness in Reinforced Concrete Beams with Axial Forces', Journal of the Structural Division, ASCE, Vol. 97, No. ST9, Sept. 1971, pp. 2277-2298.

2.61 GROB, J., and THÜRLIMANN, B., 'Ultimate Strength and Design of Reinforced Concrete Beams Under Bending and Shear'. IABSE Publication, Vol. 3-II, Zurich, 1976, pp. 105-120.

2.62 THÜRLIMANN, B., 'Shear Strength of Reinforced and Prestressed Concrete Beams - CEB Approach', Proceedings of the Symposium on Concrete Design: U.S. and European Practices, Detroit, 1979, Special Publication, SP-59, ACI, pp. 93-115.

2.63 THÜRLIMANN, B., 'Plastic Analysis of Reinforced Concrete Beams, IABSE Colloquium, Kopenhagen, 1979, pp. 71-90.

2.64 BRAESTRUP, M.W., 'Plastic Analysis of Shear in Reinforced Concrete', Magazine of Concrete Research, Vol. 26, No. 89, Dec. 1974, pp. 221-228.

2.65 NIELSEN, M.P. et al, 'Concrete Plasticity - Shear in Beams', Bulletin D'Information No. 126, Comite Euro-International Du Beton, June 1978, pp. 285-357.

2.66 NIELSEN, N.P., BRAESTRUP, M.W. and BACH, F., 'Rational Analysis of Shear in Reinforced Concrete Beams', IABSE Proceedings, P-15/78, pp. 1-16.

2.67 NIELSEN, M.P., 'Some Examples of Lower-Bound Design of Reinforcement in Plane Stress Problems', IABSE Colloquium, Copenhagen, 1979, pp. 317-324.

2.68 BRAESTRUP, M.W., 'Structural Concrete as a Plastic Material, IABSE Colloquium, Delft, 1981, pp. 3-16.

2.69 CHEN, W.F., 'Plasticity in Reinforced Concrete', McGraw-Hill Book Company, New York, 1982, 474 pp.

2.70 RABBAT, B.G., and COLLINS, M.P., 'A Variable Angle Space Truss Model for Structural Concrete Members Subjected to Complex Loading', Douglas McHenry International Symposium on Concrete and Concrete Structures, Mexico City, 1976, Special Publication, SP-55, ACI, pp. 547-588.

2.71 COLLINS, M.P., 'Towards a Rational Theory for Reinforced Concrete Members in Shear', Journal of the Structural Division, ASCE, Vol. 104, No. ST4, April 1978, pp. 649-665.

2.72 COLLINS, M.P., 'Investigating the Stress-Strain Characteristics of Diagonally Cracked Concrete', IABSE Colloquium, Copenhagen, 1979, pp. 27-34.

2.73 COLLINS, M.P., 'Reinforced Concrete Members in Torsion and Shear', IABSE Colloquium, Copenhagen, 1979, pp. 119-130.

2.74 COLLINS, M.P. and MITCHELL, D., 'Shear and Torsion Design of Prestressed and Non-prestressed Concrete Beams' PCI Journal, Vol. 25, No.5, Sept-Oct. 1980, pp. 32-100.

2.75 VECCHIO, F. and COLLINS, M.P., 'Stress-Strain Characteristics of Reinforced Concrete in Pure Shear', IABSE Colloquium, Delft, 1981, pp. 211-225.

2.76 VECCHIO, F., 'The Response of Reinforced Concrete to In-Plane Shear and Normal Stresses', Ph.D. Thesis, Department of Civil Engineering, University of Toronto, Toronto, 1981, 332 pp.

2.77 KHALIFA, J.U. and COLLINS, M.P., 'Circular Reinforced Concrete Members Subjected to Shear', Publication No. 81-08, Department of Civil Engineering, University or Toronto, Toronto, Dec. 181, 103 pp.

2.78 COLLINS, M.P., 'Prestressed Concrete Structures', Lecture Notes for a Postgraduate Course at the University of Canterbury, May-Aug. 1983.

2.79 ACI COMMITTEE 318, 'Building Code Requirements for Reinforced Concrete' American Concrete Institute, Detroit, Michigan, 1969, 1971, 1977 and 1983.

2.80 NZS 3101, 'New Zealand Code of Practice for the Design of Concrete Structures', Standards Association of New Zealand, Wellington, 1982.

2.81 'CEB-FIP Model Code for Concrete Structures' (English Translation). Third Edition, April 1978.

2.82 CSA COMMITTEE A23.3-M84, 'Design of Concrete Structures for Buildings, CAN-A23.3-M84', National Standard of Canada, Canadian Standards Association, Rexdale, 1984.

2.83 OHNO, K., SHIBATA, T. and HATTORI, T., 'Strength and Lateral Deformability of Columns of Reinforced Concrete at Shear Failure', Preliminary Report, International Association for Bridge and Structural Engineering, Lisbon, 1973, pp. 213-218.

2.84 ARAKAWA, T., ARAI, Y. and FUJITA, Y., 'Effectiveness of Shear Reinforcement on the Deformation Behaviour of Reinforced Concrete Columns Under Cyclic Loadings', Transactions of the Japan Concrete Institute, Vol. 2, 1980, pp. 439-446.

2.85 'Application of New Zealand Standard Code of Practice for the Design of Concrete Structures NZS 3101:1982', Seminar Notes, New Zealand Concrete Society, Aug. 1983.

2.86 MacGREGOR, J.G. and GERGELY, P., 'Suggested Revisions to ACI Building Code Clauses Dealing with Shear in Beams', ACI Jourhal, Vol. 74, No.10, Oct. 1977, pp. 493-500.

2,87 MAQUOI, R. and RONDAL, R., 'Optimal Shear Design of Beams in CEB-FIP Model Code' IABSE Colloquium, Copenhagen 1979, pp. 333-340.

2.88 RAJAGOPALAN, K.S. and FERGUSON, P.M., 'Explatory Shear Tests Emphasising Percentage of Longitudinal Steel, ACI Journal, Vol. 65, No. 8, Aug. 1968, pp. 634-638.

2.89 'Colloquium on Shear Analysis of Reinforced Concrete Structures', Introductory Report, Proceedings of Japanese Concrete Institute, Tokyo, Japan, June 1982.

CHAPTER THREE

3.1 NZS 3101, 'New Zealand Code of Practice for the Design of Concrete Structures', Standards Association of New Zealand, Wellington, 1982.

3.2 'New Zealand Reinforced Concrete Design Handbook', Wellington, New Zealand.

CHAPTER FOUR

4.1 'New Zealand Reinforced Concrete Design Handbook', Wellington, New Zealand.

4.2 NZS 3101, 'New Zealand Code of Practice for the Design of Concrete Structures', Standards Association of New Zealand, Wellington, 1982.

4.3 CSA COMMITTEE A23.3-M84, 'Design of Concrete Structures for Buildings, CAN-A23.3-M84', National Standard of Canada, Canadian Standards Association, Rexdale, 1984.

4.4 ACI COMMITTEE 318, 'Building Code Requirements for Reinforced Concrete', American Concrete Institute, Detroit, Michigan, 1983.

4.5 'CEB-FIP Model Code for Concrete Structures' (English Translation), Third Edition, April, 1978.

4.6 Architectural Institute of Japan, AIJ Standard for Structural Calculation of Reinforced Concrete Structures, 1971 (in Japanese).

4.7 GOSAIN, N.K., BROWN, R.H., and JIRSA, J.O., 'Shear Requirements for Load Reversals on Reinforced Concrete Members', Journal of the Structural Division, ASCE, Vol. 103, No. ST7, July 1977, pp. 1461-1476.

CHAPTER FIVE

5.1 ATC-6-2, 'Seismic Retrofitting Guidelines for Highway Bridges', Applied Technology Council, Palo Alto, California, Aug. 1983.

5.2 PRIESTLEY, M.J.N. and PARK, R., 'Strength and Ductility of Bridge Substructures', RRU Bulletin 71, National Roads Board, Wellington, New Zealand, 1984, 120 pp.

5.3 DAVEY, B.E., 'Reinforced Concrete Bridge Piers Under Seismic Loading', M.E. Report, Department of Civil Engineering, University of Canterbury, Christchurch, Feb. 1975, 100 pp.

5.4 MUNRO, I.R.M., 'Seismic Behaviour of Reinforced Concrete Bridge Piers', M.E. Report, Department of Civil Engineering, University of Canterbury, Christchurch, Feb. 1975, 106 pp.

5.5 NG, K.H., 'Seismic Behaviour of Circular Reinforced Concrete Bridge Piers', M.E. Report, Department of Civil Engineering, University of Canterbury, Christchurch, Feb. 1978, 129 pp.

5.6 POTANGAROA, R.T., 'Ductility of Spirally Reinforced Concrete Columns Under Sesismic Loading', M.E. Report, Department of Civil Engineering. University of Canterbury, Christchurch, Feb. 1979, 116 pp.

5.7 GILL, W.D., 'Ductility of Rectangular Reinforced Concrete Columns with Axial Load', M.E. Report, Department of Civil Engineering, University of Canterbury, Christchurch, Feb. 1979, 136 pp.

5.8 ANG, B.G., 'Ductility of Reinforced Concrete Bridge Piers Under Seismic Loading', M.E. Report, Department of Civil Engineering, University of Canterbury, Christchurch, Feb. 1981, 109 pp.

5.9 ZAHN, F.A., PARK, R. and PRIESTLEY, M.J.N., 'Strength and Ductility of Reinforced Concrete Piers - A Summary Report', Report 83-7, Department of Civil Engineering, University of Canterbury, Christchurch, Dec. 1983, 43 pp.

5.10 MANDER, J.B., PRIESTLEY, M.J.N, and PARK, R., 'Seismic Design of Bridge Piers', Report No. 84-2, Department of Civil Engineering, University of Canterbury, Christchurch, Feb. 1984, 483 pp.

5.11 THÜRLIMANN, B. 'Shear Strength of Reinforced and Prestressed Concrete Beams - CEB Approach', Proceedings of the Sympoisum on Concrete Design: U.S. and European Practices, Detroit, 1979, Special Publication, SP-59, ACI, pp. 93-115.

5.12 KHALIFA, J.U. and COLLINS, M.P., 'Circular Reinforced Concrete Members Subjected to Shear', Publication No. 81-08, Department of Civil Engineering, University of Toronto, Toronto, Dec. 1981, 103 pp.

5.13 NZS 3101, 'New Zealand Code of Practice for the Design of Concrete Structures', Standards Association of New Zealand, Wellington, 1982.

5.14 BERRILL, J.B., PRIESTLEY, M.J.N. and PEEK, R., 'Further Comments on Seismic Design Loads for Bridges', Bulletin of the New Zealand National Society for Earthquake Engineering, Vol.14, No.1, March 1981, pp. 3-11.

CHAPTER SIX

6.1 MANDER, J.B., PRIESTLEY, M.J.N., and PARK, R., 'Seismic Design of Bridge Piers', Report No. 84-2, Department of Civil Engineering, University of Canterbury, Christchurch, Feb. 1984, 483 pp.

6.2 KUPFER, H.B., HILSDORF, H.K., and RÜSCH, H., 'Behavior of Concrete Under Biaxial Stress' ACI Journal, Vol. 66, No. 8, Aug. 1969, pp. 656-666.

6.3 MacGREGOR, J.G., 'Design of Deep Beams', Background Notes for a Series of Seminars given in Australia and New Zealand, May-June 1984.

6.4 COLLINS, M.P., 'Towards a Rational Theory for Reinforced Concrete Members in Shear', Journal of the Structural Division, ASCE, Vol. 104, No. ST4, April 1978, pp. 649-665.

6.5 COLLINS, M.P., 'Investigating the Stress-Strain Characteristics of Diagonally Cracked Concrete', IABSE Colloquium, Copenhagen, 1979, pp. 27-34.

6.6 COLLINS, M.P., 'Reinforced Concrete Members in Torsion and Shear', IABSE Colloquium, Copenhagen, 1979, pp. 119-130.

6.7 COLLINS, M.P. and MITCHELL, D., 'Shear and Torsion Design of Prestressed and Non-Prestressed Concrete Beams', PCI Journal, Vol. 25, No. 5, Sept.-Oct. 1980, pp. 32-100.

6.8 VECCHIO, F. and COLLINS, M.P., 'Stress-Strain Characteristics of Reinforced Concrete in Pure Shear', IABSE Colloquium, Delft, 1981, pp. 211-225.

6.9 VECCHIO, F., 'The Response of Reinforced Concrete to In-Plane Shear and Normal Stresses', Ph.D. Thesis, Department of Civil Engineering, University of Toronto, Toronto, 1981, 332 pp.

6.10 COLLINS, M.P., 'Prestressed Concrete Structures', Lecture Notes for a Postgraduate Course at the University of Canterbury, May-Aug. 1983.

6.11 POPOVICS, S., 'A Numerical Approach to the Complete Stress-Strain Curves of Concrete', Cement and Concrete Research, Vol. 3, No. 5, Sept. 1973, pp. 583-599.

6.12 PARK, R. and PAULAY, T., 'Reinforced Concrete Structures', John Wiley and Sons, New York, 1975, 769 pp.

6.13 PRIESTLEY, M.J.N., PARK, R. and POTANGAROA, R.T., 'Ductility of Spirally Confined Concrete Columns', Journal of the Structural Division, ASCE, Vol. 107, No. ST1, Jan. 1981, pp. 181-202.

6.14 PRIESTLEY, M.J.N. and PARK, R., 'Strength and Ductility of Bridge Substructures', RRU Bulletin 71, National Roads Board, Wellington, New Zealand, 1984, 120 pp.

CHAPTER SEVEN

7.1 KRAWINKLER, H. and MONCARZ, P.D., 'Similitude Requirements for Dynamic Models', Dynamic Modelling of Concrete Structures, Special Publication SP-73, ACI, 1982, pp. 1-22.

7.2 ZIA, P., WHITE, R.N., and VAN HORN, D.A., 'Principles of Model Analysis', Models for Concrete Structures, Special Publication SP-24, ACI, 1970, pp. 19-40.

7.3 PEHI, W.B. and PRIESTLEY, M.J.N., 'Mangare Motorway Bridge Microconcrete Model of Pier 6', Report No. 495, Ministry of Works and Development, Lower Hutt, New Zealand, Feb. 1974, 109 pp.

7.4 CHANA, P.S., 'Some Aspects of Modelling the Behaviour of Reinforced Concrete Under Shear Loading', Technical Report 543, Cement and Concrete Association, July 1981, 22 pp.

7.5 MUNRO, I.R.M., 'Seismic Behaviour of Reinforced Concrete Bridge Piers', M.E. Report, Department of Civil Engineering, University of Canterbury, Christchurch, Feb. 1975, 106 pp.

CHAPTER EIGHT

8.1 'New Zealand Reinforced Concrete Design Handbook', Wellington, New Zealand.

8.2 PRIESTLEY, M.J.N. and PARK, R. 'Strength and Ductility of Bridge Structures', RRU Bulletin 71, National Roads Board, Wellington, New Zealand, 1984, 120 pp.

Appendix II

COMPUTER PROGRAM — MODIFIED "SMAL"

(1) Introduction

The solution procedures discussed in Chapter Six are coded in a computer program called 'SMAL'. The program solves for stress and strain conditions in a reinforced concrete member subjected to a given set of section loads. It is coded in Fortran and requires the use of an interactive system. It is suitable for computers with Fortran IV compiler.

(2) Sign Convention

Positive for tensile stresses and strains and negative for compressive values.

(3) Units

Linear dimension	:	mm
Area	:	mm^2
Force	:	kN
Stress	:	MPa
Moment	:	kNm
Modulus of Elasticity	:	GPa
Strain	:	dimensionless but has been multiplied by 10^3
Curvature	:	rad/m

(4) Input and Output File

The program reads the data cards defining the properties of concrete and element properties from a data file and writes the results into a separate output file. Unless the user directs the computer to do otherwise, these section details will be printed preceding the analytical results. The data deck is headed by a title card which is treated as a comment card, and except for this card, the only valid input characters for the data cards are the digits '0 1 2 3 4 5 6 7 8 9' together with the necessary plus (+) or minus (-) sign and/or the decimal point. The section details are defined by the following sequence of data cards.

(a) Title card

Field	Parameter	Description	Format
1	TITLE	Description of job using any of the normal alphanumeric key-punch characters.	80A1

(b) Concrete properties

Field	Parameter	Description	Format
1	FCP	Concrete compressive strength, f'_c (MPa)	F10.5
2	ENOT	Concrete strain, ε_o, at f'_c	F10.5
3	FLP	Passive lateral confining pressure, f'_ℓ (MPa)	F10.5

(Note: all are negative values)

(c) Steel properties

Field	Parameter	Description	Format
1	FYL	Yield stress of longitudinal reinforcement, $f_{y\ell}$ (MPa)	F10.5
2	EYL	Yield strain for longitudinal reinforcement, $\varepsilon_{y\ell}$	F10.5
3	FYT	Yield stress of transverse reinforcement, f_{yt} (MPa)	F10.5
4	EYT	Yield strain of transverse reinforcement, ε_{yt}	F10.5
5	RHOS	Spiral reinforcement content, ρ_s or twice transverse reinforcement content ($2\rho_t$)	F10.5

(Note: all are positive values)

(d) Cross-section dimensions

Field	Parameter	Description	Format
1	D	Overall depth or diameter of cross-section (mm)	F10.5
2	COVER	Concrete cover thickness to the centreline of transverse reinforcement (mm)	F10.5

(e) Discretization details

Field	Parameter	Description	Format
1	NS	Number of steel elements	I5
2	NC	Number of concrete elements	I5

(Note: $1 \leq NS \leq 20$, $1 \leq NC \leq 20$)

(f) Details of concrete elements

Field	Parameter	Description	Format
1	AC	Area of concrete layer (mm^2)	F10.5
2	DH	Thickness of concrete layer (mm)	F10.5

(Note: one card per element)

(g) Details of steel elements

Field	Parameter	Description	Format
1	AS	Area of steel element (mm^2)	F10.5
2	YS	Centroidal depth of steel element from the extreme compression fibre (mm)	F10.5

(Note: one card per element)

(5) Operating Instructions and Comments

The program makes use of an interactive system so that the user has some control over the iteration procedure. The user has to decide when to stop the iteration on axial load and shear-stress distribution, depending on the chosen criteria for convergence. The user can only answer Yes (Y) or No (N) to any question asked by the computer. After logging in to the system, the computer will display the following questions and comments on the user's VDU terminal in the order listed. Only the characters in block capital letters are displayed by the computer and the comments in *italics* are just some explanatory notes.

DO YOU WANT TO PRINT SECTION DETAILS? (Yes or No)

INPUT AXIAL LOAD: (Input value in F-format)

INPUT SHEAR FORCE: (Input value in F-format)

THIS IS SECTION: 1

INPUT TOP STRAIN: (Input value in F-format)

Comment: The top part is assumed to be under compressive strain and must have the appropriate negative sign.

INITIAL GUESS OF BOTTOM STRAIN: (Input value in F-format)

INPUT SHEAR STRESS DISTRIBUTION? (Yes or No)

Comment: If the answer to the above question is 'yes' then type in the shear stresses in F-format, one per line for every concrete element.

Comment: During the computational process, the computer displays the conditions of each concrete layer and the current subprogram involved in the calculations.

LAYER: 1 EL: _ _ . _ _ _ V: _ _ . _ _ _

- - SUBROUTINE CLAYER - -

- - SUBROUTINE FV1 - -

LAYER: 2 EL: _ _ . _ _ _ V: _ _ . _ _ _

- - SUBROUTINE CLAYER - -

- - SUBROUTINE FV1 - -

- - SUBROUTINE FV2 - -

LAYER: 3 EL: _ _ . _ _ _ V: _ _ . _ _ _

.
.
.
.

THIS IS ITERATION 1

(NP-N) : _ _ _ _ . _ _ _ _ _

EBOT : _ _ _ _ . _ _ _ _ _

Comment: (NP-N) is the difference between the computed and the applied axial load and EBOT is the value of bottom strain.

ARE YOU SATISFIED WITH THESE VALUES? (Yes or No)

SECOND GUESS OF BOTTOM STRAIN: (Input value in F-format)

Comment: The user is asked to try a second guess of EBOT if the answer to the above question is 'No' and this is done only after every fifth iteration.

THIS IS SECTION: 2

INPUT TOP STRAIN: (Input value in F-format)

Comment: Input a slightly less negative strain from that of Section 1 and the process is repeated.

.
.
.
.

ARE YOU SATISFIED WITH THESE VALUES? (Yes or No)

S/D : _ _ _ _ . _ _ _ _ _

Comment: The computer displays the distance, S , bwteeen the two sections as a fraction of the overall depth, D .

ARE YOU SATISFIED WITH THIS VALUE? (Yes or No)

TRY ANOTHER ETOP2: (Input value in F-format)

Comment: The user is asked to try another value of top strain for the second section if the distance

between the two sections in previous calculations is not satisfactory and the process is repeated.

.
.
.
.

MAXIMUM DIFFERENCE IN VC(I): _ _ _ _ . _ _ _ _

Comment: *The computer displays the maximum difference between the computed and assumed shear stresses.*

ARE YOU SATISFIED WITH THIS VALUE? (Yes or No)

Comment: *If the answer is 'No' the shear-stress distribution is adjusted and the whole process is repeated. If the answer is 'Yes' the following question is asked.*

DO YOU WANT TO CONTINUE? (Yes or No)

Comment: *If the answer is 'Yes' the user is asked to input the new axial load and shear force and the process is repeated. If the answer is 'No' the files are closed and the computation is stopped.*

General Comment: *The user may choose to iterate for the axial load in a less precise manner and adjust the shear-stress distribution first before iterating the axial load to the desired accuracy, by giving the appropriate answer to the questions asked.*

(6) Source Listing and Program Output

A program source listing and an illustrative program output are given as follows. The notations used in the program output are:

AC : Area of a concrete element (mm^2)

AS : Area of a steel element (mm^2)

B : Width of a concrete element (mm)

C : Longitudinal compressive force in a concrete element (kN)

DH : Thickness of a concrete element (mm)

EBOT : Strain at the extreme bottom fibre, ε_{bot} ($\times 10^{-3}$)

EC : Modulus of elasticity of concrete, E_c (GPa)

ECC : Strain, ε_{cc}, at maximum concrete stress f'_{cc} ($\times 10^{-3}$)

ECR : Strain, ε_{cr}, at diagonal cracking ($\times 10^{-3}$)

EL : Longitudinal strain, ε_{ℓ} ($\times 10^{-3}$)

ENOT : Strain, ε_o, at concrete stress f'_c (= - 2.0 $\times 10^{-3}$)

ESL : Young's Modulus of longitudinal steel (GPa)

EST : Young's Modulus of transverse steel (GPa)

ET : Transverse strain, ε_t ($\times 10^{-3}$)

ETOP : Strain (negative) at the extreme top fibre, ε_{top} ($\times 10^{-3}$)

EYL : Yield strain of longitudinal steel ($\times 10^{-3}$)

EYT : Yield strain of transverse steel ($\times 10^{-3}$)

E2 : Principal compressive strain in concrete ($\times 10^{-3}$)

FCL : Longitudinal stress in a concrete element, $f_{\ell c}$ (MPa)

FCP : Concrete compressive cylinder strength, f'_c (MPa)

FCR : Concrete stress at diagonal cracking, f_{cr} (MPa)

FCT : Transverse stress in a concrete element, f_{tc} (MPa)

FCCP : Maximum strength of confined concrete, f'_{cc} (MPa)

FSL : Stress in a longitudinal steel element, $f_{\ell s}$ (MPa)

FYL : Yield stress of longitudinal steel, $f_{y\ell}$ (MPa)

FYT : Yield stress of transverse steel, f_{yt} (MPa)

FC2 : Principal compressive stress in concrete, f_{c2} (MPa)

GLT : Shear strain in a concrete element, $\gamma_{\ell t}$ ($\times 10^{-3}$)

MP : Moment resistance of a section (kNm)

N : Axial load acting on a section (kN)

NP : Resulting axial load from internal forces (kN)

RHOT : Transverse reinforcement ratio, ρ_{st}

STAGE : An indicator of the stage of a concrete element

- 0.0 - no shear stress acting
- 1.0 - before diagonal cracking
- 2.0 - after diagonal cracking
- 3.0 - shear stress exceeded the capacity of concrete element
- 4.0 - shear stress exceeded the capacity of concrete element and $v_{max} < v_{cr}$

T : Tensile force in longitudinal steel element (kN)

THETA : Angle of inclination of principal compressive stress (or strain with longitudinal axis (deg)

V : Shear force acting on a section (kN) or shear stress acting in a concrete element (MPa)

VB : Shear stress at the bottom face of a concrete element (MPa)

VP : Permissible shear force of a section (kN) or permissible shear stress of a concrete element (MPa)

VQ : Computed shear stress of a concrete element (MPa)

YC : Centroid of concrete element from extreme compression fibre (mm)

YS : Centroid of steel element from extreme compression fibre (mm)

```
C
C     ===============================================
C     THIS IS A MODIFIED VERSION OF 'SMAL' PROGRAM
C     BY : ANG BENG GHEE
C     ===============================================
C
      INTEGER FLG,FLG1,FLG2
      REAL MP,MCC,MST,N,NP,MAC
C
      DIMENSION TITLE(80)
      DIMENSION CS(20,2),FS(20,2)
      DIMENSION X(20),Y(10),LF(20)
      DIMENSION AS(20),YS(20),RHOT(20)
      DIMENSION VC(20),VQ(20),VMAX(20),VBOT(20),VB(20)
      DIMENSION AC(20),ACC(20),B(20),DH(20),XC(20),YC(20)
C
    1 CONTINUE
      OPEN(UNIT=1,NAME='DATA.DAT',TYPE='OLD',READONLY,ERR=2)
      OPEN(UNIT=2,NAME='RESU.DAT',TYPE='NEW')
      GO TO 5
    2 STOP 'WRONG DATA FILE NAME'
C
C     READ SPECIMEN PARAMETERS
C
    5 CONTINUE
      READ(1,720) (TITLE(I),I=1,80)
      READ(1,730) FCP,ENOT,FLP
      READ(1,730) FYL,EYL,FYT,EYT,RHOS
      READ(1,730) D,COVER
      READ(1,700) NS,NC
C
      ESL=FYL/EYL
      EST=FYT/EYT
      FCR=0.33*SQRT(-FCP)
      EC=5.0*SQRT(-FCP)
      ECR=FCR/EC
      FCCP=FCP+5.5*FLP
      ECC=ENOT*(1.0+5.0*5.5*FLP/FCP)
C
      TYPE 6
    6 FORMAT(/' DO YOU WANT TO PRINT SECTION DETAILS ? '$)
      ACCEPT 720, ANS
      IF(ANS.EQ.'N') GO TO 7
      WRITE(2,800) (TITLE(I),I=1,80)
      WRITE(2,810) FCP,ENOT,FCR,ECR,FCCP,ECC,EC
      WRITE(2,815) FYL,EYL,ESL,FYT,EYT,EST
      WRITE(2,820) NC,NS,D
      WRITE(2,830)
C
C     READ CONCRETE STRIP PROPERTIES
C
    7 CONTINUE
      MAC=0.0
      DO 10 I=1,NC
      READ(1,730) AC(I),DH(I)
      RHOT(I)=RHOS/2.0
      IF(I.EQ.1) RHOT(I)=0.0
      IF(I.EQ.NC) RHOT(I)=0.0
      YC(I)=(I-0.5)*DH(I)
      B(I)=AC(I)/DH(I)
      MAC=MAC+YC(I)*AC(I)
      IF(ANS.EQ.'Y') WRITE(2,840)I,DH(I),B(I),AC(I),YC(I),RHOT(I)
   10 CONTINUE
      ACG=3.14159*D**2.0/4.0
      CGC=MAC/ACG
      IF(ANS.EQ.'Y') WRITE(2,850)CGC
C
C     READ STEEL ELEMENT PROPERTIES
C
      AST=0.0
      DO 20 I=1,NS
      READ(1,730) AS(I),YS(I)
      AST=AST+AS(I)
      IF(ANS.EQ.'Y') WRITE(2,860)I,AS(I),YS(I)
   20 CONTINUE
      RHOL=AST/ACG
      IF(ANS.EQ.'Y') WRITE(2,865)RHOL
C
C     ACCEPT SECTION LOADS AND STRAINS
C
      J=1
      LN=1
      TYPE 30
   30 FORMAT(/' INPUT AXIAL LOAD : '$)
      ACCEPT 730, N
      TYPE 31
   31 FORMAT(/' INPUT SHEAR FORCE : '$)
      ACCEPT 730, TV
C
   40 CONTINUE
      TYPE 41, J
   41 FORMAT(/' THIS IS SECTION ',I2)
      TYPE 42
   42 FORMAT(/' INPUT TOP STRAIN : '$)
      ACCEPT 730, ETOP
      IF(J.EQ.2) GO TO 200
      TYPE 43
   43 FORMAT(/' INITIAL GUESS OF BOTTOM STRAIN : '$)
      ACCEPT 730, EBOT
```

```
C
C     DETERMINE INITIAL SHEAR STRESS DISTRIBUTION
C
      TQ=0.0
      TC=0.0
      TYPE 100
  100 FORMAT(/' INPUT SHEAR STRESS DISTRIBUTION ? '$)
      ACCEPT 720, ANS
      IF(ANS.EQ.'Y') GO TO 115
      D1=D/2.0
      DO 110 I=1,NC
      XC(I)=1.0-((D1-YC(I))/(D1-YC(1)))**2.0
      TC=TC+XC(I)*AC(I)
  110 CONTINUE
      VM=TV/TC*1000.0
  115 CONTINUE
      DO 120 I=1,NC
      IF(ANS.EQ.'N') VC(I)=XC(I)*VM
      IF(ANS.EQ.'Y') ACCEPT 730, VC(I)
      TQ=TQ+VC(I)*AC(I)*0.001
  120 CONTINUE
      DO 160 I=1,NC
      VC(I)=VC(I)*TV/TQ
  160 CONTINUE
C
C     ITERATION ON AXIAL LOAD STARTS HERE
C
      FLG=0
      FLG2=0
  200 CONTINUE
      NCALC=1
      FLG1=0
      NF=0.0
      IF(LN.GT.1.AND.FLG.NE.1) TYPE 210, J
  210 FORMAT(/' THIS IS SECTION ',I2)
  220 CONTINUE
      IF(NCALC.GT.5) NCALC=1
      PHI=(EBOT-ETOP)/D
      D1=ETOP/(ETOP-EBOT)*D
      IF(FLG.EQ.1) WRITE(2,870)J
      IF(FLG.EQ.1) WRITE(2,900)ETOP,EBOT,D1,PHI
C
C     COMPUTE STEEL STRAINS AND FORCES
C
      T=0.0
      MST=0.0
      DO 230 I=1,NS
      EL=ETOP-YS(I)/D*(ETOP-EBOT)
      FSL=FNS(EL,FYL,EYL,ESL)
      FS(I,J)=FSL*AS(I)*0.001
      T=T+FS(I,J)
      MST=MST+FS(I,J)*(YS(I)-CGC)*0.001
      IF(FLG.EQ.1) WRITE(2,910)I,EL,FSL,AS(I),FS(I,J)
  230 CONTINUE
      IF(FLG.EQ.1) WRITE(2,920)T,MST
C
C     COMPUTE CONCRETE STRAINS AND FORCES
C
      C=0.0
      MCC=0.0
      TVP=0.0
      TGLT=0.0
      CGLT=0.0
      IF(FLG.EQ.1) WRITE(2,930)
C
      DO 250 I=1,NC
      EL=ETOP-YC(I)/D*(ETOP-EBOT)
      ACC(I)=AC(I)
      SPAL=((D-2.0*COVER)/D)**2.0
      IF(I.EQ.1.AND.EL.LE.(2.0*ENOT)) ACC(I)=0.0
      IF(I.NE.1.AND.EL.LE.(2.0*ENOT)) ACC(I)=AC(I)*SPAL
      IF(ACC(I).NE.0.0) V=VC(I)*AC(I)/ACC(I)
      IF(ACC(I).EQ.0.0) V=0.0
      IF(FLG.NE.1) TYPE 235, I,EL,V
  235 FORMAT(/' LAYER:',I3,2X,' EL:',F6.3,2X,' V:',F6.3)
      IF(J.EQ.1) LF(I)=0
C
      X(1)=EL
      X(2)=ENOT
      X(3)=FCR
      X(4)=ECR
      X(5)=FCCP
      X(6)=ECC
      X(7)=EC
      X(8)=RHOT(I)
      X(9)=FYT
      X(10)=EYT
      X(11)=EST
      X(12)=V
      IF(I.EQ.1) X(5)=FCP
      IF(I.EQ.1) X(6)=ENOT
C
      CALL CLAYER(X,Y,FLG)
      ET=Y(1)
      E1=Y(2)
      E2=Y(3)
      FCL=Y(4)
      FC1=Y(5)
      FC2=Y(6)
      THETA=Y(7)
      VP=Y(8)
      STAGE=Y(9)
C
      IF(J.EQ.1) VMAX(I)=VP
      IF(J.EQ.1.AND.V.GT.VP) LF(I)=1
      FCT=-RHOT(I)*FNS(ET,FYT,EYT,EST)
      TT=THETA*3.14159/180.0
      TANG=SIN(TT)/COS(TT)
      GLT=0.0
```

```
      IF(THETA.LT.90.0.AND.THETA.GT.0.0) GLT=(EL-E2)/TANG*2.0
      TGLT=TGLT+GLT
      CGLT=CGLT+1.0
      IF(GLT.EQ.0.0) CGLT=CGLT-1.0
      CS(I,J)=FCL*ACC(I)*0.001
      C=C+CS(I,J)
      MCC=MCC+CS(I,J)*(YC(I)-CGC)*0.001
      TVP=TVP+VP*ACC(I)*0.001
      IF(FLG.EQ.1) WRITE(2,940)I,CS(I,J),EL,ET,E2,GLT,
     1FCL,FCT,FC2,THETA,V,VMAX(I),VB(I),VQ(I),STAGE
  250 CONTINUE
      IF(CGLT.NE.0.0) AGLT=TGLT/CGLT
      IF(CGLT.EQ.0.0) AGLT=0.0
      IF(FLG.EQ.1) WRITE(2,950)C,MCC,AGLT
C
C     CHECK AXIAL LOAD
C
      NP=T+C
      MP=MCC+MST
      IF(FLG.EQ.1) WRITE(2,960)MP,NP,N,TVP,TV
      IF(J.EQ.1.AND.FLG.EQ.1) GO TO 411
      IF(J.EQ.2.AND.FLG.EQ.1) GO TO 600
      TYPE 316, NCALC
  316 FORMAT(/' THIS IS ITERATION ',I2)
      TYPE 317, (NP-N)
  317 FORMAT(/' (NP-N): ',F10.5)
      TYPE 318, EBOT
  318 FORMAT(/' EBOT  : ',F10.5)
      TYPE 319
  319 FORMAT(/' ARE YOU SATISFIED WITH THESE VALUES ? '$)
      ACCEPT 720, ANS
      IF(ANS.EQ.'Y') GO TO 400
      IF(NCALC.GT.1) GO TO 328
      X1=EBOT
      Y1=NP-N
      TYPE 320
  320 FORMAT(/' SECOND GUESS OF BOTTOM STRAIN : '$)
      ACCEPT 730, EBOT
      NCALC=NCALC+1
      GO TO 220
  328 X2=EBOT
      Y2=NP-N
      EBOT=FIN(X1,Y1,X2,Y2)
      AD1=ABS(EBOT-X1)
      AD2=ABS(EBOT-X2)
      IF(AD1.GT.AD2) X1=X2
      IF(AD1.GT.AD2) Y1=Y2
      NCALC=NCALC+1
      GO TO 220
C
  400 CONTINUE
      IF(J.EQ.2) FLG1=1
      IF(J.EQ.1) BM1=MP
      IF(J.EQ.2) BM2=MP
      IF(J.EQ.1) GO TO 410
      S=ABS(BM1-BM2)/TV*1000.0
      TYPE 401, S/D
  401 FORMAT(/' S/D:',F10.5)
      TYPE 402
  402 FORMAT(/' ARE YOU SATISFIED WITH THIS VALUE ? '$)
      ACCEPT 720, ANS
      ETOP2=ETOP
      EBOT2=EBOT
      IF(ANS.EQ.'Y') GO TO 500
      TYPE 404
  404 FORMAT(/' TRY ANOTHER ETOP2 : '$)
      ACCEPT 730, ETOP
      GO TO 200
  410 IF(J.EQ.1) ETOP1=ETOP
      IF(J.EQ.1) EBOT1=EBOT
  411 J=2
      IF(LN.EQ.1) GO TO 40
      ETOP=ETOP2
      EBOT=EBOT2
      GO TO 200
C
C     COMPUTE SHEAR STRESS DISTRIBUTION
C
  500 CONTINUE
      TQ=0.0
      V1=0.0
      SGNN=0.0
      SGNP=0.0
      DO 520 I=1,NC
      V1=V1+CS(I,2)-CS(I,1)
      V2=0.0
      DO 510 K=1,NS
      IF(YS(K).GT.(YC(I)+0.5*DH(I))) GO TO 510
      V2=V2+FS(K,2)-FS(K,1)
  510 CONTINUE
      VBOT(I)=(V1+V2)/(S*B(I))*1000.0
      IF(VBOT(I).LE.0.0) SGNN=-1.0
      IF(VBOT(I).GT.0.0) SGNP=1.0
      IF(I.EQ.1.AND.SGNN.EQ.-1.0) SGNN=0.0
      SIGN=SGNN+SGNP
      VB(I)=VBOT(I)
      VBOT(I)=VBOT(I)*SIGN
      IF(I.EQ.1) VQ(I)=VBOT(I)/2.0
      IF(I.GT.1) VQ(I)=(VBOT(I)+VBOT(I-1))/2.0
      IF(ACC(I).NE.0.0) VQ(I)=VQ(I)*AC(I)/ACC(I)
      IF(I.EQ.1.OR.I.EQ.NC) VQ(I)=0.0
      TQ=TQ+VQ(I)*ACC(I)*0.001
  520 CONTINUE
      DO 530 I=1,NC
      VQ(I)=VQ(I)*TV/TQ
  530 CONTINUE
```

```
C
C     CHECK ESTIMATE OF SHEAR STRESSES
C
      FLG2=1
      DQP=0.0
      DO 540 I=1,NC
      DQ=ABS(VC(I)-VQ(I))
      IF(DQP.LT.DQ) DQP=DQ
  540 CONTINUE
      TYPE 541, DQP
  541 FORMAT(/' MAXIMUM DIFFERENCE IN VC(I) : ',F10.5)
      TYPE 542
  542 FORMAT(/' ARE YOU SATISFIED WITH THIS VALUE ? '$)
      ACCEPT 720, ANS
      IF(ANS.EQ.'N') FLG2=0
      IF(FLG2.EQ.1) GO TO 565
C
C     OBTAIN NEW SHEAR STRESS DISTRIBUTION
C
      TQ1=0.0
      TQ2=0.0
      DO 550 I=1,NC
      VC(I)=0.25*VC(I)+0.75*VQ(I)
      IF(LF(I).EQ.1.AND.VC(I).GT.VMAX(I)) VC(I)=VMAX(I)
      IF(I.EQ.1.OR.I.EQ.NC) VC(I)=0.0
      IF(LF(I).EQ.0) TQ1=TQ1+VC(I)*ACC(I)*0.001
      IF(LF(I).EQ.1) TQ2=TQ2+VC(I)*ACC(I)*0.001
  550 CONTINUE
      IF(TQ1.NE.0.0) FAC=(TV-TQ2)/TQ1
      IF(TQ1.EQ.0.0) FAC=1.0
      IF(TQ1.EQ.0.0) FLG2=1
      DO 560 I=1,NC
      IF(LF(I).EQ.0) VC(I)=VC(I)*FAC
      IF(LF(I).EQ.1) VC(I)=VC(I)*1.0
      IF(VC(I).LT.0.0) VC(I)=0.0
  560 CONTINUE
C
  565 CONTINUE
      FLG=FLG1*FLG2
      J=1
      ETOP=ETOP1
      EBOT=EBOT1
      LN=LN+1
      GO TO 200
C
  600 CONTINUE
      TYPE 610
  610 FORMAT(/' DO YOU WANT TO CONTINUE ? '$)
      ACCEPT 720, ANS
      IF(ANS.EQ.'N') STOP ' -- GOOD LUCK --'
      CLOSE(UNIT=1,DISPOSE='SAVE')
      CLOSE(UNIT=2,DISPOSE='SAVE')
      GO TO 1
```

```
C
C     READ FORMAT
C
  700 FORMAT(10I5)
  720 FORMAT(80A1)
  730 FORMAT(8F10.5)
C
C     WRITE FORMAT
C
  800 FORMAT('1',/'0',10X,80A1,/' ',10X,80('='))
  810 FORMAT('0',10X,'SPECIMEN PARAMETERS:',/
     1' ',20X,'FCP =',2X,F7.2,'  MPA',5X,'ENOT=',2X,F7.3,'  E-3',/
     2' ',20X,'FCR =',2X,F7.2,'  MPA',5X,'ECR =',2X,F7.3,'  E-3',/
     3' ',20X,'FCCP=',2X,F7.2,'  MPA',5X,'ECC =',2X,F7.3,'  E-3',
     45X,'EC  =',F9.2,'  GPA')
  815 FORMAT(' ',20X,'FYL =',2X,F7.2,'  MPA',5X,'EYL =',2X,F7.3,
     1'  E-3',5X,'ESL =',F9.2,'  GPA',/
     2' ',20X,'FYT =',2X,F7.2,'  MPA',5X,'EYT =',2X,F7.3,'  E-3',
     35X,'EST =',F9.2,'  GPA')
  820 FORMAT('0',10X,'NO. OF CONCRETE STRIPS   =',2X,I3,/
     1' ',10X,'NO. OF STEEL ELEMENTS    =',2X,I3,/
     2' ',10X,'DIAMETER OF COLUMNS      =',2X,F6.2,'  MM')
  830 FORMAT('0',10X,'CONCRETE STRIP DATA:',/' ',22X,'STRIP',7X,
     1'DH',10X,'B',10X,'AC',10X,'YC',8X,'RHOT')
  840 FORMAT(' ',20X,I5,4(2X,F10.1),3X,F8.5)
  850 FORMAT('0',10X,'DEPTH OF CENTROIDAL AXIS=',F7.2,'  MM',
     1/'0',10X,'STEEL ELEMENT DATA:',/' ',23X,'NO.'8X,'AS',
     210X,'YS')
  860 FORMAT(' '20X,I5,2F12.1)
  865 FORMAT('0',10X,'TOTAL LONGITUDINAL STEEL CONTENT=',F8.5)
  870 FORMAT('1',11X,'SECTION',I2,/' ',10X,9('-'))
  900 FORMAT('0',15X,'ETOP=',2X,F8.3,'  E-3',/
     1' ',15X,'EBOT=',2X,F8.3,'  E-3',/
     2' ',10X,'N-A DEPTH=',2X,F8.3,'  MM',/
     3' ',10X,'CURVATURE=',2X,F8.5,'  RAD PER M',/
     4'0',1X,'STEEL ELEMENT CONDITIONS:',/
     5' ',10X,'NO.',8X,'EL',9X,'FSL',10X,'AS',10X,'T')
  910 FORMAT(' ',7X,I5,F12.3,2F12.1,F12.2)
  920 FORMAT('0',10X,'TOTAL STEEL FORCE =',F10.2,'  KN',/
     1' ',10X,'TOTAL STEEL MOMENT=',F10.2,'  KN-M')
  930 FORMAT('0',1X,'CONCRETE STRIP CONDITIONS:',/
     1' ',8X,'STRIP',4X,'C',6X,'EL',5X,'ET',5X,'E2',4X,'GLT',5X,'FCL',
     24X,'FCT',5X,'FC2',3X,'THETA',4X,'V',5X,'VP',5X,'VB',5X,'VQ',
     34X,'STAGE')
  940 FORMAT(' ',10X,I2,F8.2,4F7.3,F8.3,F7.3,F8.3,F7.2,4F7.3,F6.1)
  950 FORMAT('0',10X,'TOTAL CONCRETE FORCE =',F10.2,'  KN',/
     1' ',10X,'TOTAL CONCRETE MOMENT=',F10.2,'  KN-M',/
     2' ',10X,'AVERAGE SHEAR STRAIN =',F10.5,'  E-3')
  960 FORMAT('0',1X,'RESULTING FORCE AND MOMENT:',/
     1' ',10X,'MP=',F8.2,2X,'KN-M',/
     2' ',10X,'NP=',F8.2,2X,'KN',5X,'N=',F8.2,2X,'KN',/
     3' ',10X,'VP=',F8.2,2X,'KN',5X,'V=',F8.2,2X,'KN')
C
C
      RETURN
      END
```

```
C
C     ====================================
C     SUBPROGRAM TO ANALYSE CONCRETE LAYERS
C     ====================================
C
      SUBROUTINE CLAYER(X,Y,IFLG)
      DIMENSION X(20),Y(10)
      EL=X(1)
      ENOT=X(2)
      FCR=X(3)
      ECR=X(4)
      FCCP=X(5)
      ECC=X(6)
      EC=X(7)
      RHOT=X(8)
      FYT=X(9)
      EYT=X(10)
      EST=X(11)
      V=X(12)
C
      IF(IFLG.NE.1) TYPE 1000
 1000 FORMAT(/' -- SUBROUTINE CLAYER --')
      IF(EL.GE.ECR) VCR=0.001
      IF(EL.GE.ECR) GO TO 1030
      ET=0.0
 1020 FCT=-RHOT*FNS(ET,FYT,EYT,EST)
      E2=EL+ET-ECR
      T1=ATAN(SQRT((ECR-ET)/(ECR-EL)))
      FC2=FNC(E2,FCCP,ECC,FCR,ECR,EC)
      IF(EL.GT.-1.0) VCR=SQRT(-FC2*FCR)
      IF(EL.GT.-1.0) TANG=SQRT(-FCR/FC2)
      IF(EL.GT.-1.0) GO TO 1030
      T2=ATAN(SQRT((FCR-FCT)/(FCT-FC2)))
      CON=ABS(T1-T2)
      T12=(T1+T2)/2.0
      TANG=SIN(T12)/COS(T12)
      IF(CON.LT.0.05*T12) GO TO 1021
      ET=ECR-(ECR-EL)*TANG**2.0
      GO TO 1020
 1021 VCR=(FCT-FC2)*TANG
C
 1030 CONTINUE
      IF(EL.LE.0.0.OR.V.LT.VCR) CALL FV1(X,Y,IFLG)
      IF(Y(9).EQ.2.0.OR.V.GE.VCR) CALL FV2(X,Y,IFLG)
      IF(Y(9).NE.3.0) GO TO 1085
      IF(Y(8).GE.VCR) GO TO 1085
      Y(1)=ET
      Y(2)=ECR
      Y(3)=E2
      Y(4)=FC2+FC1-FCT
      Y(5)=FCR
      Y(6)=FC2
      Y(7)=ATAN(TANG)*180.0/3.14159
      Y(8)=VCR
      Y(9)=4.0
C
 1085 CONTINUE
      RETURN
      END
C
C     ========================
C     BEFORE DIAGONAL CRACKING
C     ========================
C
      SUBROUTINE FV1(X,Y,IFLG)
      DIMENSION X(20),Y(10)
      EL=X(1)
      ENOT=X(2)
      FCR=X(3)
      ECR=X(4)
      FCCP=X(5)
      ECC=X(6)
      EC=X(7)
      RHOT=X(8)
      FYT=X(9)
      EYT=X(10)
      EST=X(11)
      V=X(12)
C
      IF(IFLG.NE.1) TYPE 1200
 1200 FORMAT(/' -- SUBROUTINE FV1 --')
      ET=0.0
      FCT=0.0
      STAGE=1.0
      IF(V.LT.0.001) STAGE=0.0
      IF(V.GE.0.001) GO TO 1241
      IF(EL.GE.0.0) GO TO 1240
C
C     COMPRESSIVE STRAIN WITHOUT SHEAR STRESS
C
      FCL=FNC(EL,FCCP,ECC,FCR,ECR,EC)
      FC2=FCL
      FC1=0.0
      E2=EL
      E1=0.0
      THETA=0.0
      VP=V
      GO TO 1285
C
C     TENSILE STRAIN WITHOUT SHEAR STRESS
C
 1240 FCL=0.0
      FC2=0.0
      FC1=FCL
      E2=0.0
      E1=EL
      THETA=90.0
      VP=V
      GO TO 1285
```

```
C
C     AT NEUTRAL AXIS
C
 1241 IF(EL.NE.0.0) GO TO 1242
      FCL=0.0
      FC1=V
      FC2=-V
      ET=0.0
      E1=FC1/EC
      E2=-E1
      THETA=45.0
      VP=V
      GO TO 1285
C
C     NOT AT NEUTRAL AXIS
C
 1242 ICALC=1
      JCALC=1
      FCL=FNC(EL,FCCP,ECC,FCR,ECR,EC)
 1243 IF(FCL.EQ.FCT) FCT=0.99*FCL
      IF(FCL.EQ.FCT) E2=-E1
      T=0.5*ATAN(2.0*V/(FCT-FCL))
      IF(T.LT.0.0) T=3.14159/2.0+T
      TANG=SIN(T)/COS(T)
      IF(FCL.EQ.FCT) TANG=1.0
      IF(TANG.EQ.1.0) TANG=0.99
      E2=(EL-ET*TANG**2.0)/(1.0-TANG**2.0)
      G=0.8-0.34*E1/ENOT
      IF(G.LT.1.0) G=1.0
      FC2=FNC(E2,FCCP,ECC,FCR,ECR,EC)
      FCLP=FC2+V*TANG
      CON=ABS(FCLP-FCL)
      IF(FCL.NE.0.0) CON=CON/ABS(FCL)
      IF(FCL.EQ.0.0.AND.CON.LT.0.005) GO TO 1245
      IF(FCL.NE.0.0.AND.CON.LT.0.05) GO TO 1245
      IF(ICALC.GE.20) STAGE=2.0
      IF(ICALC.GE.20) GO TO 1285
      IF(ICALC.GT.1) GO TO 1244
      X1=FCL
      Y1=(FCLP-FCL)
      FCL=FCL
      ICALC=ICALC+1
      GO TO 1243
 1244 X2=FCL
      Y2=(FCLP-FCL)
      FCL=FIN(X1,Y1,X2,Y2)
      AD1=ABS(FCL-X1)
      AD2=ABS(FCL-X2)
      ICALC=ICALC+1
      GO TO 1243
 1245 FCL=(FCLP+FCL)/2.0
      FC1=FCL+V/TANG
      IF(FC1.GT.FCR) FC1=FCR
      IF(FC1.LT.0.0) FC1=0.0
      E1=FC1/EC
      ETP=E1+E2-EL
      CON=ABS(ETP-ET)
      IF(CON.LT.0.005) GO TO 1260
      ET=(ETP+ET)/2.0
      FCT=-RHOT*FNS(ET,FYT,EYT,EST)
      IF(JCALC.GE.20) STAGE=2.0
      IF(JCALC.GE.20) GO TO 1285
      JCALC=JCALC+1
      ICALC=1
      GO TO 1243
 1260 THETA=ATAN(TANG)*180.0/3.14159
      VP=V
C
 1285 CONTINUE
      Y(1)=ET
      Y(2)=E1
      Y(3)=E2
      Y(4)=FCL
      Y(5)=FC1
      Y(6)=FC2
      Y(7)=THETA
      Y(8)=VP
      Y(9)=STAGE
      RETURN
      END
C
C     ======================
C     AFTER DIAGONAL CRACKING
C     ======================
C
      SUBROUTINE FV2(X,Y,IFLG)
      DIMENSION X(20),Y(10),Z(10)
      EL=X(1)
      ENOT=X(2)
      FCR=X(3)
      ECR=X(4)
      FCCP=X(5)
      ECC=X(6)
      EC=X(7)
      RHOT=X(8)
      FYT=X(9)
      EYT=X(10)
      EST=X(11)
      V=X(12)
C
      IF(IFLG.NE.1) TYPE 1300
 1300 FORMAT(/' -- SUBROUTINE FV2 --')
      STAGE=2.0
      ICALC=1
      E1=1.1*EL+0.05
      IF(E1.LE.0.0) E1=0.05
```

```
1330 FC1=FNC(E1,FCCP,ECC,FCR,ECR,EC)
     A=RHOT*EST*(E1-EL)
     B=V
     C=-RHOT*EST*E1-FC1
     TANG=(-B+SQRT(B*B-4.0*A*C))/(2.0*A)
     TANP=(FC1+RHOT*FYT)/V
     IF(TANG.GT.TANP) TANG=TANP
     FC2=FC1-V*(TANG+1.0/TANG)
     IF(FC2.GT.0.0) FC2=-V*(TANG+1.0/TANG)
     E1P=ENOT*(0.8-FCCP/FC2)/0.34
     IF(E1P.GE.E1) GO TO 1331
     IF(E1P.LE.EL) GO TO 1360
     E1=ABS(E1P)
     GO TO 1330
1331 G=0.8-0.34*E1/ENOT
     IF(G.LT.1.0) G=1.0
     IF(ICALC.EQ.1.OR.E2.GT.0.0) E2=0.5*ECC
     E2=FIT(G,FC2,E2,FCCP,ECC,EC)
     E1P=(EL-E2)/TANG**2.0+EL
     CON=ABS(E1P-E1)
     IF(E1.NE.0.0) CON=CON/ABS(E1)
     IF(E1.EQ.0.0.AND.CON.LT.0.005) GO TO 1350
     IF(E1.NE.0.0.AND.CON.LT.0.05) GO TO 1350
     IF(ICALC.GE.20) GO TO 1360
     IF(ICALC.GT.1) GO TO 1340
     X1=E1
     Y1=(E1P-E1)
     E1=ABS(E1P)
     ICALC=ICALC+1
     GO TO 1330
1340 X2=E1
     Y2=(E1P-E1)
     E1=FIN(X1,Y1,X2,Y2)
     IF(E1.LE.EL) E1=ABS(E1P)
     AD1=ABS(E1-X1)
     AD2=ABS(E1-X2)
     IF(AD1.GT.AD2) X1=X2
     IF(AD1.GT.AD2) Y1=Y2
     ICALC=ICALC+1
     GO TO 1330
C
1350 CONTINUE
     E1=(E1+E1P)/2.0
     G=0.8-0.34*E1/ENOT
     IF(G.LT.1.0) G=1.0
     ET=E1+E2-EL
     FC2=FNC(E2,FCCP,ECC,FCR,ECR,EC)/G
     FCL=FC1-V/TANG
     THETA=ATAN(TANG)*180.0/3.14159
     VP=V
     GO TO 1385
C
1360 STAGE=3.0
     IF(EL.LE.ECC) GO TO 1370
     JCALC=1
     FC1=0.0
     FCT=-RHOT*FYT
1361 A=-0.34*(FC1-FCT)/ENOT
     B=0.8*(FC1-FCT)+0.34*(EL*FC1-ECC*FCT)/ENOT
     C=-0.8*(EL*FC1-ECC*FCT)-(ECC-EL)*FCCP
     E1P=(-B+SQRT(B*B-4.0*A*C))/(2.0*A)
     FC1=FNC(E1P,FCCP,ECC,FCR,ECR,EC)
     IF(JCALC.EQ.1) GO TO 1362
     CON=ABS(E1P-E1)/E1
     IF(CON.LT.0.01) GO TO 1363
1362 E1=E1P
     JCALC=JCALC+1
     GO TO 1361
1363 G=0.8-0.34*E1/ENOT
     IF(G.GT.10.0) GO TO 1380
     E2=ECC
     ET=E1+E2-EL
     IF(ET.LT.EYT) GO TO 1370
     FC2=FCCP/G
     TANG=SQRT((EL-ECC)/(E1-EL))
     THETA=ATAN(TANG)*180.0/3.14159
     VP=(FC1-FCT)/TANG
     FCL=FC1-VP/TANG
     GO TO 1385
1370 E1=0.0
     E2=EL
     ET=0.0
     FC1=0.0
     FC2=FNC(E2,FCCP,ECC,FCR,ECR,EC)
     FCL=FC2
     THETA=0.0
     VP=0.0
     GO TO 1385
1380 E1=EL
     E2=0.0
     ET=0.0
     FC1=0.0
     FC2=0.0
     FCL=FC1
     THETA=90.0
     VP=0.0
C
1385 CONTINUE
     Y(1)=ET
     Y(2)=E1
     Y(3)=E2
     Y(4)=FCL
     Y(5)=FC1
     Y(6)=FC2
     Y(7)=THETA
     Y(8)=VP
     Y(9)=STAGE
     RETURN
     END
```

```
C
C     ==================
C     ITERATION FUNCTION
C     ==================
C
      FUNCTION FIT(G,FC2,E2,FCCP,ECC,EC)
      ITER=1
      ESEC=FCCP/ECC
      R=EC/(EC-ESEC)
      A=G*FC2/(R*FCCP)
      X1=E2/ECC
 1510 F=A*X1**R-X1+A*(R-1.0)
      FP=A*R*X1**(R-1.0)-1.0
      X2=X1-F/FP
      CON=ABS(X2-X1)
      IF(CON.LT.0.001) GO TO 1520
      IF(ITER.GE.20) GO TO 1520
      IF(X2.LE.0.0) X2=0.5*X1
      X1=X2
      ITER=ITER+1
      GO TO 1510
 1520 FIT=(X1+X2)/2.0*ECC
      RETURN
      END
C
C     ======================
C     INTERPOLATION FUNCTION
C     ======================
C
      FUNCTION FIN(X1,Y1,X2,Y2)
      IF(X2.EQ.X1) X2=0.99*X1
      IF(X2.EQ.X1.AND.X1.EQ.0.0) X2=0.001
      GRAD=(Y1-Y2)/(X1-X2)
      IF(GRAD.EQ.0.0) GRAD=0.001
      FIN=X1-Y1/GRAD
      RETURN
      END
C
C     ================================
C     STRESS-STRAIN FUNCTION OF CONCRETE
C     ================================
C
      FUNCTION FNC(E,FCCP,ECC,FCR,ECR,EC)
      ESEC=FCCP/ECC
      R=EC/(EC-ESEC)
      X=E/ECC
      IF(E.GE.0.0) FNC=E*EC
      IF(E.GT.ECR) FNC=FCR/(1.0+SQRT(0.2*E))
      IF(E.LT.0.0) FNC=FCCP*R*X/(R-1.0+X**R)
      RETURN
      END
C
C     ==============================
C     STRESS-STRAIN FUNCTION OF STEEL
C     ==============================
C
      FUNCTION FNS(E,FY,EY,ES)
      FNS=ES*E
      IF(E.GE.EY) FNS=FY
      IF(E.LE.-EY) FNS=-FY
      RETURN
      END
```

UNITS 16,17 AND 18 --- R6 AT 60 MM

SPECIMEN PARAMETERS:

FCP =	-34.80	MPA	ENOT=	-2.000	E-3			
FCR =	1.95	MPA	ECR =	0.066	E-3			
FCCP=	-39.20	MPA	ECC =	-3.264	E-3	EC =	29.50	GPA
FYL =	436.00	MPA	EYL =	2.000	E-3	ESL =	218.00	GPA
FYT =	326.00	MPA	EYT =	2.000	E-3	EST =	163.00	GPA

NO. OF CONCRETE STRIPS = 20
NO. OF STEEL ELEMENTS = 11
DIAMETER OF COLUMNS = 400.00 MM

CONCRETE STRIP DATA:

STRIP	DH	B	AC	YC	RHOT
1	20.0	117.4	2349.0	10.0	0.00000
2	20.0	209.6	4191.0	30.0	0.00255
3	20.0	264.0	5280.0	50.0	0.00255
4	20.0	303.6	6071.8	70.0	0.00255
5	20.0	333.8	6675.6	90.0	0.00255
6	20.0	357.0	7139.6	110.0	0.00255
7	20.0	374.5	7490.0	130.0	0.00255
8	20.0	387.1	7742.2	150.0	0.00255
9	20.0	395.3	7906.0	170.0	0.00255
10	20.0	399.3	7986.6	190.0	0.00255
11	20.0	399.3	7986.6	210.0	0.00255
12	20.0	395.3	7906.0	230.0	0.00255
13	20.0	387.1	7742.2	250.0	0.00255
14	20.0	374.5	7490.0	270.0	0.00255
15	20.0	357.0	7139.6	290.0	0.00255
16	20.0	333.8	6675.6	310.0	0.00255
17	20.0	303.6	6071.8	330.0	0.00255
18	20.0	264.0	5280.0	350.0	0.00255
19	20.0	209.6	4191.0	370.0	0.00255
20	20.0	117.4	2349.0	390.0	0.00000

DEPTH OF CENTROIDAL AXIS= 200.00 MM

STEEL ELEMENT DATA:

NO.	AS	YS
1	201.0	29.0
2	402.0	37.4
3	402.0	61.7
4	402.0	99.5
5	402.0	147.2
6	402.0	200.0
7	402.0	252.8
8	402.0	300.5
9	402.0	338.3
10	402.0	362.6
11	201.0	371.0

TOTAL LONGITUDINAL STEEL CONTENT= 0.03199

SECTION 1

ETOP= -1.200 E-3
EBOT= 1.743 E-3
N-A DEPTH= 163.125 MM
CURVATURE= 0.00736 RAD PER M

STEEL ELEMENT CONDITIONS:

NO.	EL	FSL	AS	T
1	-0.987	-215.1	201.0	-43.23
2	-0.925	-201.6	402.0	-81.05
3	-0.746	-162.7	402.0	-65.39
4	-0.468	-102.0	402.0	-41.02
5	-0.117	-25.5	402.0	-10.27
6	0.271	59.1	402.0	23.77
7	0.660	143.8	402.0	57.81
8	1.011	220.3	402.0	88.56
9	1.289	280.9	402.0	112.93
10	1.467	319.9	402.0	128.60
11	1.529	333.4	201.0	67.01

TOTAL STEEL FORCE = 237.73 KN
TOTAL STEEL MOMENT= 94.22 KN-M

CONCRETE STRIP CONDITIONS:

STRIP	C	EL	ET	E2	GLT	FCL	FCT	FC2	THETA	V	VP	VB	VQ	STAGE
1	-66.62	-1.126	0.000	-1.126	0.000	-28.363	0.000	-28.363	0.00	0.000	0.000	0.485	0.000	0.0
2	-101.61	-0.979	0.000	-0.981	0.079	-24.245	0.000	-24.279	2.30	0.974	0.974	1.385	0.928	1.0
3	-113.11	-0.832	0.000	-0.836	0.116	-21.422	0.000	-21.514	3.96	1.490	1.490	1.491	1.428	1.0
4	-110.99	-0.685	0.000	-0.691	0.130	-18.280	0.000	-18.429	5.36	1.730	1.730	1.863	1.665	1.0
5	-98.93	-0.538	0.000	-0.548	0.145	-14.820	0.000	-15.069	7.54	1.998	1.998	2.062	1.949	1.0
6	-79.00	-0.391	0.000	-0.404	0.147	-11.064	0.000	-11.432	10.33	2.088	2.088	2.094	2.064	1.0
7	-52.80	-0.244	0.000	-0.263	0.143	-7.049	0.000	-7.604	15.23	2.075	2.075	2.057	2.061	1.0
8	-21.93	-0.097	0.000	-0.131	0.135	-2.832	0.000	-3.843	27.18	1.979	1.979	1.917	1.973	1.0
9	-4.64	0.051	0.092	-0.075	0.290	-0.587	-0.038	-2.205	40.90	1.904	1.904	1.901	1.896	2.0
10	-5.20	0.198	0.291	-0.075	0.632	-0.651	-0.121	-2.219	40.86	1.824	1.824	1.762	1.819	2.0
11	-4.70	0.345	0.454	-0.073	0.936	-0.588	-0.188	-2.140	41.74	1.750	1.750	1.772	1.755	2.0
12	-5.41	0.492	0.645	-0.077	1.279	-0.684	-0.268	-2.240	41.64	1.767	1.767	1.796	1.772	2.0
13	-3.78	0.639	0.727	-0.072	1.505	-0.488	-0.302	-2.031	43.38	1.659	1.659	1.580	1.677	2.0
14	-2.51	0.786	0.794	-0.069	1.713	-0.335	-0.330	-1.871	44.94	1.567	1.567	1.639	1.599	2.0
15	-3.48	0.933	0.989	-0.080	2.076	-0.488	-0.411	-2.056	44.31	1.639	1.639	1.723	1.670	2.0
16	-1.79	1.080	0.987	-0.072	2.202	-0.268	-0.410	-1.817	46.31	1.512	1.512	1.417	1.560	2.0
17	1.96	1.228	0.709	-0.044	1.948	0.323	-0.294	-1.132	52.54	1.136	1.136	0.982	1.192	2.0
18	2.58	1.375	0.649	-0.037	1.960	0.488	-0.269	-0.954	55.24	1.004	1.004	1.138	1.053	2.0
19	4.24	1.522	0.205	-0.014	1.206	1.011	-0.085	-0.385	68.57	0.548	0.548	-0.002	0.565	2.0
20	0.00	1.669	0.000	0.000	0.000	0.000	0.000	0.000	90.00	0.000	0.000	-0.003	0.000	0.0

TOTAL CONCRETE FORCE = -667.71 KN
TOTAL CONCRETE MOMENT= 84.58 KN-M
AVERAGE SHEAR STRAIN = 0.92448 E-3

RESULTING FORCE AND MOMENT:
MP= 178.80 KN-M
NP= -429.99 KN N= -430.00 KN
VP= 200.00 KN V= 200.00 KN

SECTION 2

ETOP= -1.000 E-3
EBOT= 1.373 E-3
N-A DEPTH= 168.566 MM
CURVATURE= 0.00593 RAD PER M

STEEL ELEMENT CONDITIONS:

NO.	EL	FSL	AS	T
1	-0.828	-180.5	201.0	-36.28
2	-0.778	-169.6	402.0	-68.19
3	-0.634	-138.2	402.0	-55.56
4	-0.410	-89.3	402.0	-35.91
5	-0.127	-27.6	402.0	-11.11
6	0.186	40.7	402.0	16.34
7	0.500	108.9	402.0	43.79
8	0.783	170.6	402.0	68.59
9	1.007	219.5	402.0	88.24
10	1.151	250.9	402.0	100.88
11	1.201	261.8	201.0	52.62

TOTAL STEEL FORCE = 163.42 KN
TOTAL STEEL MOMENT= 75.98 KN-M

CONCRETE STRIP CONDITIONS:

STRIP	C	EL	ET	E2	GLT	FCL	FCT	FC2	THETA	V	VP	VB	VQ	STAGE
1	-58.69	-0.941	0.000	-0.941	0.000	-24.986	0.000	-24.986	0.00	0.000	0.000	0.485	0.000	0.0
2	-88.94	-0.822	0.000	-0.824	0.075	-21.222	0.000	-21.262	2.62	0.974	0.974	1.385	0.928	1.0
3	-98.69	-0.703	0.000	-0.708	0.112	-18.692	0.000	-18.800	4.53	1.490	1.490	1.491	1.428	1.0
4	-96.89	-0.585	0.000	-0.592	0.127	-15.957	0.000	-16.130	6.11	1.730	1.730	1.863	1.665	1.0
5	-86.93	-0.466	0.000	-0.477	0.143	-13.022	0.000	-13.308	8.52	1.998	1.998	2.062	1.949	1.0
6	-70.72	-0.347	0.000	-0.362	0.146	-9.906	0.000	-10.315	11.42	2.088	2.088	2.094	2.064	1.0
7	-49.66	-0.229	0.000	-0.249	0.143	-6.630	0.000	-7.216	16.01	2.075	2.075	2.057	2.061	1.0
8	-24.99	-0.110	0.000	-0.142	0.135	-3.228	0.000	-4.161	25.38	1.979	1.979	1.917	1.973	1.0
9	-3.34	0.009	0.028	-0.072	0.179	-0.423	-0.011	-2.114	41.92	1.904	1.904	1.901	1.896	2.0
10	-4.44	0.127	0.188	-0.073	0.456	-0.556	-0.078	-2.148	41.26	1.824	1.824	1.762	1.819	2.0
11	-4.15	0.246	0.325	-0.071	0.706	-0.520	-0.135	-2.079	41.86	1.750	1.750	1.772	1.755	2.0
12	-5.05	0.364	0.489	-0.075	0.993	-0.638	-0.203	-2.192	41.49	1.767	1.767	1.796	1.772	2.0
13	-3.46	0.483	0.561	-0.068	1.175	-0.447	-0.233	-1.993	43.15	1.659	1.659	1.580	1.677	2.0
14	-2.21	0.602	0.621	-0.063	1.346	-0.295	-0.258	-1.821	44.65	1.567	1.567	1.639	1.599	2.0
15	-3.31	0.720	0.793	-0.073	1.654	-0.464	-0.329	-2.010	43.81	1.639	1.639	1.723	1.670	2.0
16	-1.59	0.839	0.792	-0.065	1.757	-0.239	-0.329	-1.768	45.83	1.512	1.512	1.417	1.560	2.0
17	2.28	0.958	0.554	-0.039	1.533	0.376	-0.230	-1.081	52.43	1.136	1.136	0.982	1.192	2.0
18	2.88	1.076	0.504	-0.033	1.539	0.545	-0.209	-0.898	55.24	1.004	1.004	1.138	1.053	2.0
19	4.45	1.195	0.167	-0.012	0.951	1.063	-0.069	-0.329	68.50	0.548	0.548	-0.002	0.565	2.0
20	0.00	1.314	0.000	0.000	0.000	0.000	0.000	0.000	90.00	0.000	0.000	-0.003	0.000	0.0

TOTAL CONCRETE FORCE = -593.46 KN
TOTAL CONCRETE MOMENT= 74.96 KN-M
AVERAGE SHEAR STRAIN = 0.73173 E-3

RESULTING FORCE AND MOMENT:
MP= 150.94 KN-M
NP= -430.04 KN N= -430.00 KN
VP= 200.00 KN V= 200.00 KN

Appendix III

DYNAMIC TESTING FACILITIES

(A) THE SHAKING TABLE

As part of this project, a new shaking table was designed to enable the dynamic testing reported in Chapters Seven and Eight to be carried out. Fig. A1 shows typical applications and the maximum design loadings for which the table was designed. Both approximate hand calculation and computer analysis were made to check the stresses and deformation of the table under the prescribed loading conditions. The maximum values of these quantities under the prescribed loading conditions are listed together with other details of the shaking table in Table A1.

Fig. A2 shows a schematic diagram of the earthquake simulating system. It consists of

(i) the shake table : see descriptions in following paragraphs.

(ii) the actuator (Dartec M1000/A) : The actuator is a single channel closed loop electro-hydraulic system and is double acting with a total (peak-peak) stroke of 300 mm. It has a static capacity of 250 kN and a nominal dynamic capacity of 200 kN. Details of the actuator are given in Table A2 and the theoretical performance curves of the actuator, incorporating limits imposed by servo-valves and hydraulic power units, are as shown in Fig. A3 in terms of amplitude frequency response.

(iii) the control system (Dartec M1000-D1) : The control system has the function of providing the excitation and amplification of feedback signals, selecting the control feedback and providing the command signals. The output waveform generated by a function generator (M1000-P2) can be sinusoidal, square or triangular but the system also allows the use of external command signals, such as earthquake ground motion.

(iv) the servo-valves : The two servo-valves regulating the flow of oil have a rating of 230 ℓ/m each.

(v) the hydraulic power unit : The unit consists of three separate motor pumps, each draining oil from a common

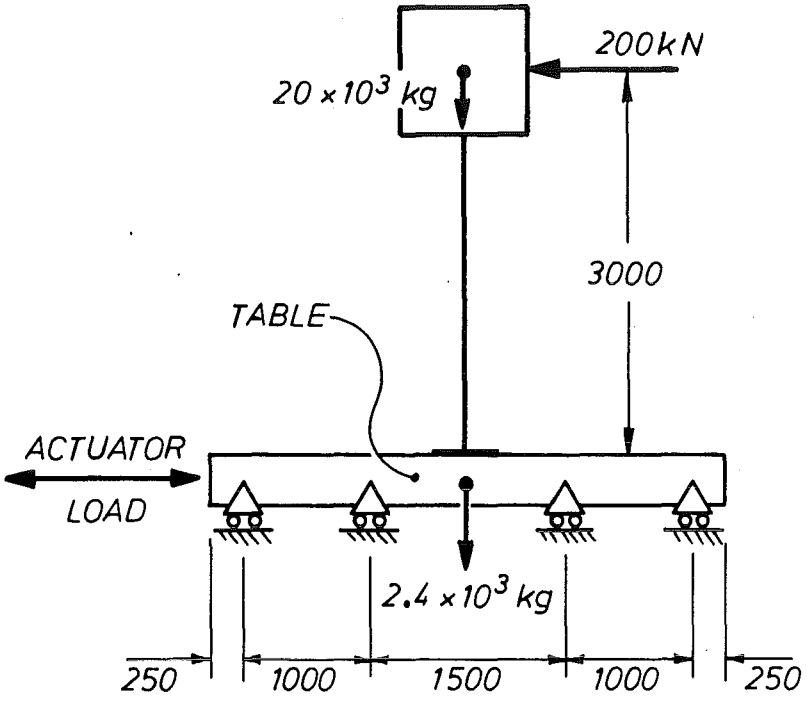

(a) Single column unit

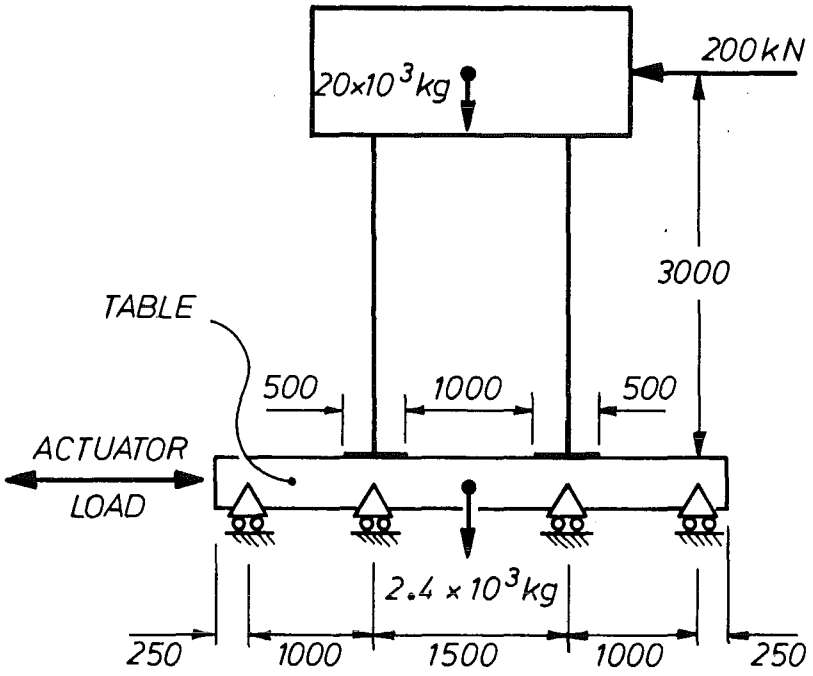

(b) Twin column unit

Fig. A1 : Design loadings for shaking table

Table A1 : A Summary of Table Details

Plan area	2 m by 4 m
Height above ground	700 mm
Material	Steel
Weight	2.4×10^3 kg
Maximum travel	300 mm
Natural frequency (unloaded)	≈ 20 Hz
Maximum out of plane deflection under design loadings	0.44 mm
Maximum stress under design loadings	28 MPa (+) 45 MPa (-)
Support details	4 Glacier DU Bearings on stationary shaft (100 mm dia) along either side of the table
Table top	12 mm steel plate
Longitudinal stiffeners	4 - 410 UB54
Transverse stiffeners	12 mm full depth steel plate at 500 mm intervals
Hole pattern	drilled and tapped for M12 bolts at 250 mm lengthwise and 125 mm transversely

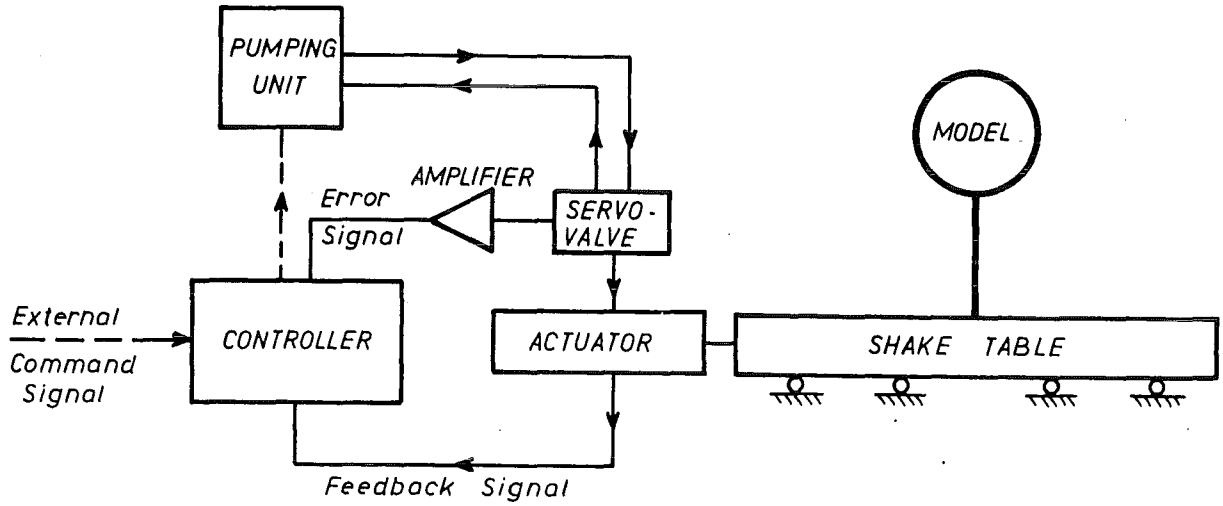

Fig. A2 : Schematic diagram of earthquake simulating system

Table A2 : A summary of actuator details

Static capacity	±250 kN
Dynamic capacity (nominal)	±200 kN
Total stroke	300 mm
Effective piston area	9677 mm^2
Servovalve rating	2 x 230 ℓ/m
Maximum velocity attainable	1 m/s
Supply pressure	300 bar

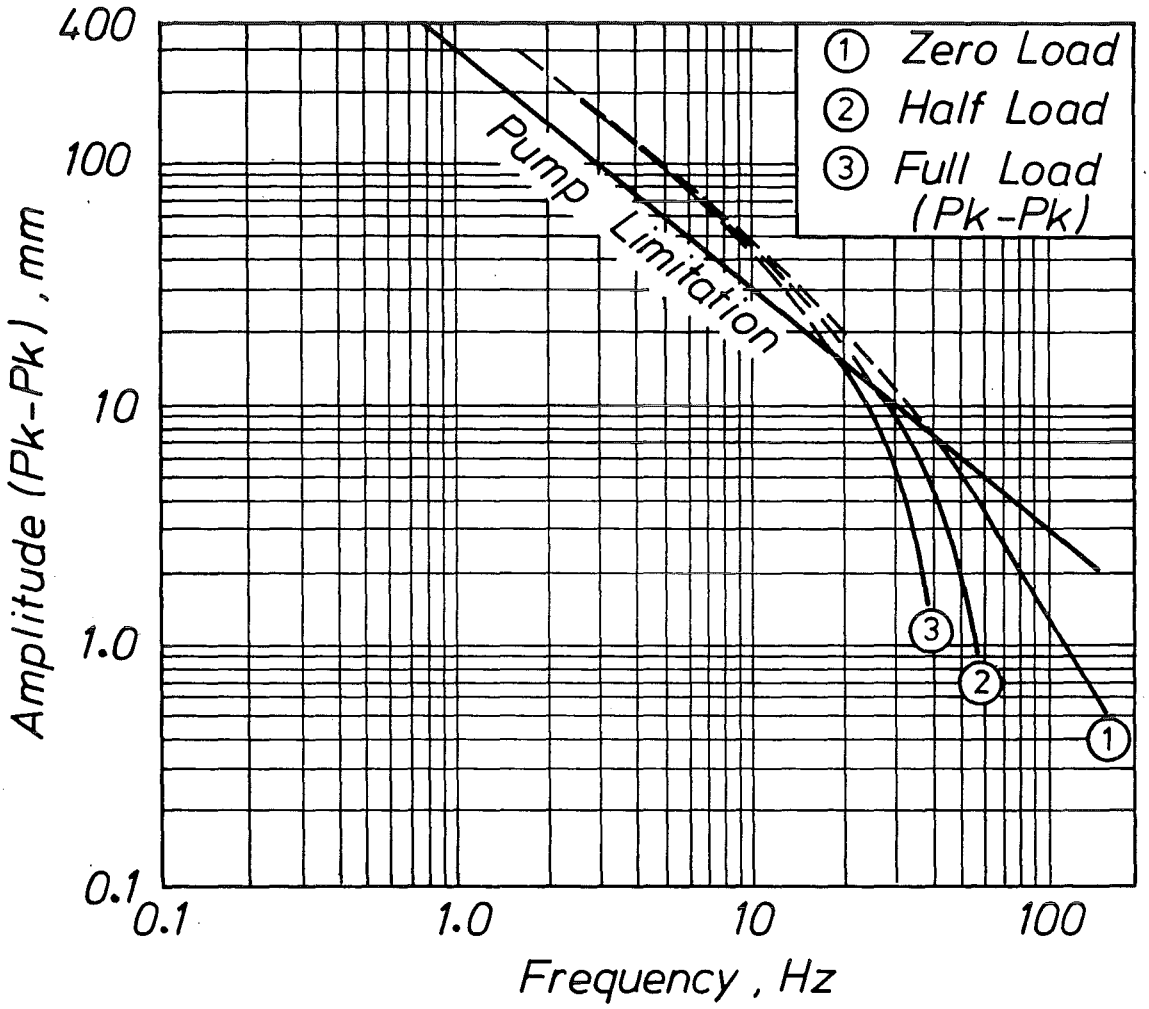

Fig. A3 : Theoretical performance curve for Dartec actuator

reservoir and delivers to a common supply line. The delivery rate is 115 ℓ/m each at a pressure of 300 bar (4350 psi).

(vi) the external programming device: The external common signal is fed through the system with the aid of an APPLE IIE computer. The original acceleration records were integrated twice numerically to provide ground displacement, and are stored in the APPLE IIE computer. The stored earthquake data in terms of displacements can be fed to the Dartec system in the form of voltage analog signals. Several earthquake options are available and the program allows a range of 1 to 50 to be selected for the scaling factor. A scale factor of 1 output the data at their natural frequencies of 50 pps while a scale factor of n(> 1) gave an output value of 50 n pps.

Fig. A4 shows detail drawings of the table. The total weight of the table was approximately 2.4 tonnes and the table surface was about 700 mm above the structures laboratory strong floor.

The table was supported on either side by four Glacie DU bushes (MB110115 DU) which ran on 100 mm diameter bright steel shafts as shown in Fig. A5. The bushes were made up of steel backing strips with a porous bronze matrix impregnated and overlaid with the PTFE (polytetrafluoroethylene)/lead material. The bushes operated along only a short length of about 315 mm along the shafts which were held stationary by means of steel chucks at the extreme end of the travel (see Fig. A5(b)). The shafts were aligned very carefully until they were effectively parallel and horizontal. Detail drawings of the bearings and support system are as shown in Fig. A6. The table was mounted on a supporting frame made from two universal beams (250 UB 37) as shown in Fig. A7.

The actuator was connected to the table via a lock-nut and a 50 mm thick steel matching plate. The matching plate was screwed onto the free threaded end of the piston and secured onto the table by 16 high strength bolts. The round nut which was part of the actuator was then locked against the matching plate. Detail drawings of the jack to table connection can be found in Fig. A8. Successful performance of the table depended on the precision in the alignment of the actuator and the shafts. The design of the above and connecting systems allowed ample adjustment to achieve this.

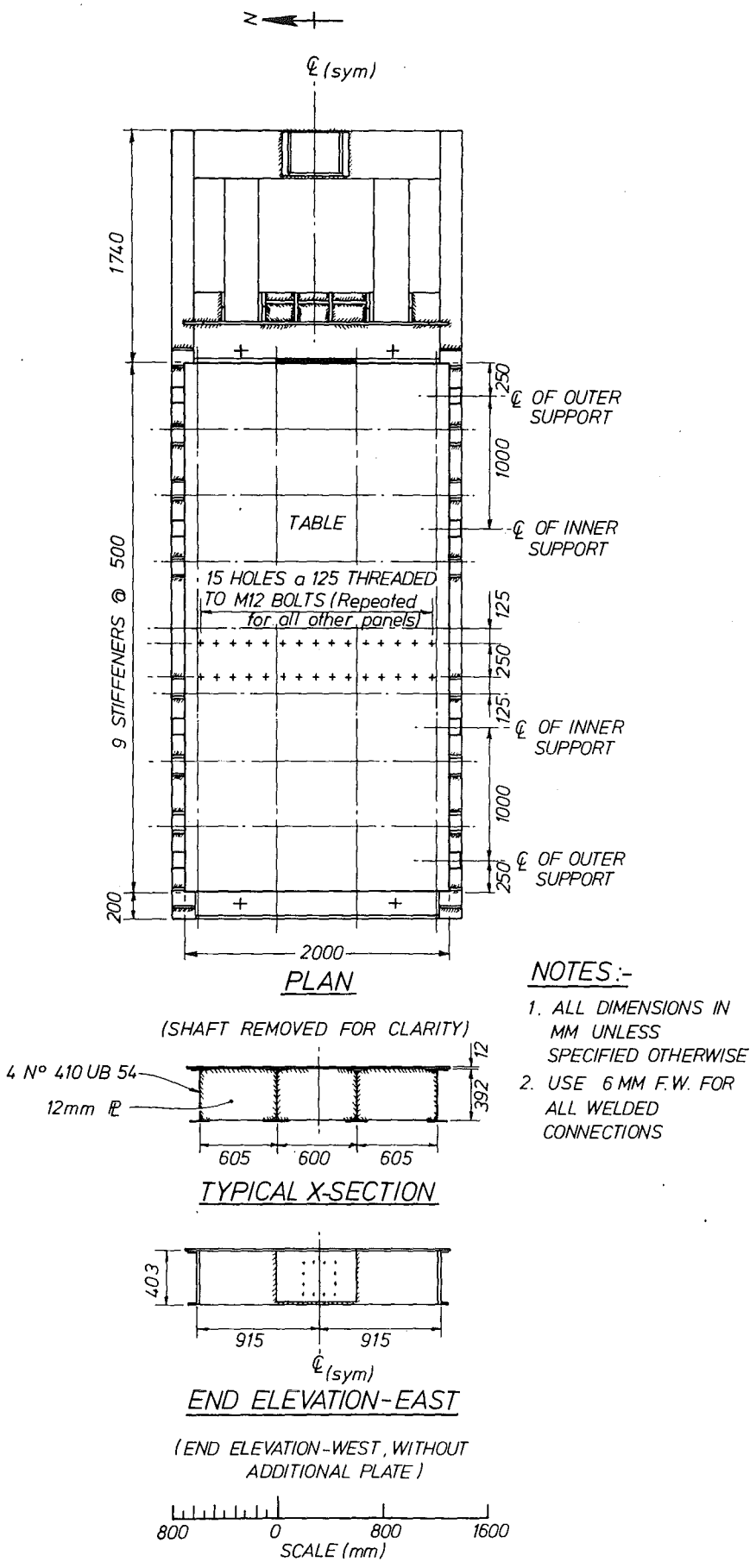

Fig. A4 : Dimensions of shaking table

(a) general view

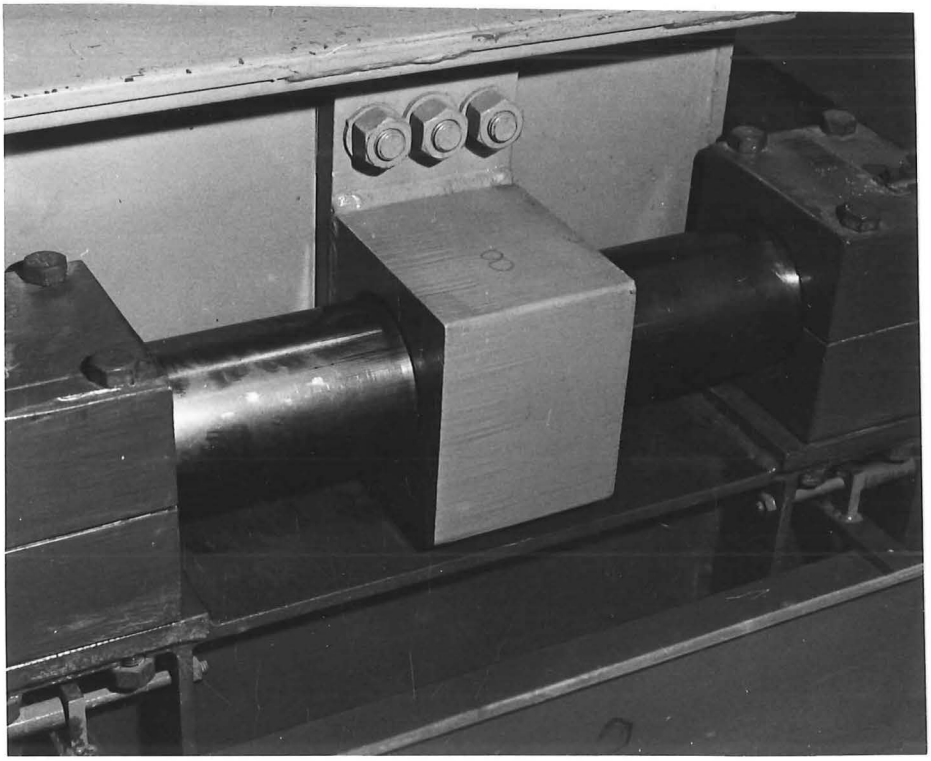

(b) close-up view

Fig. A5 : Table support details

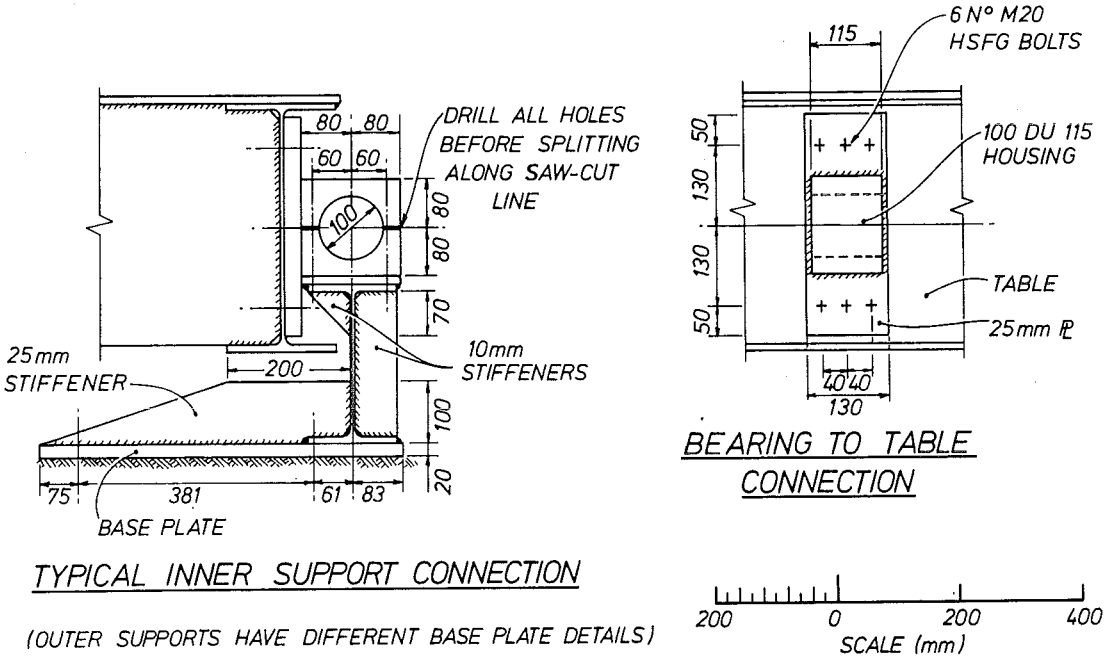

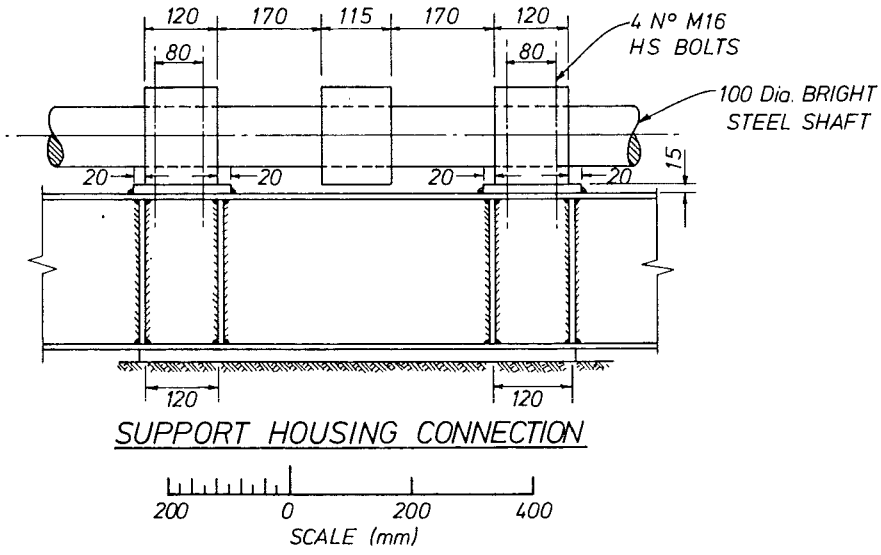

Fig. A6 : Details of bearing and support system of the shaking table

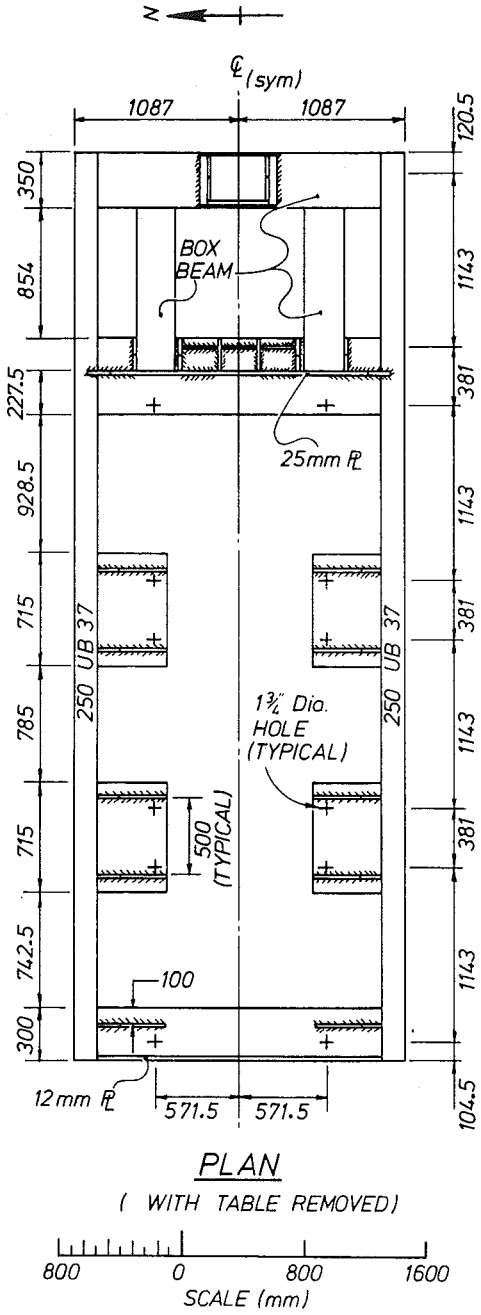

Fig. A7 : Details of supporting frame for shaking table

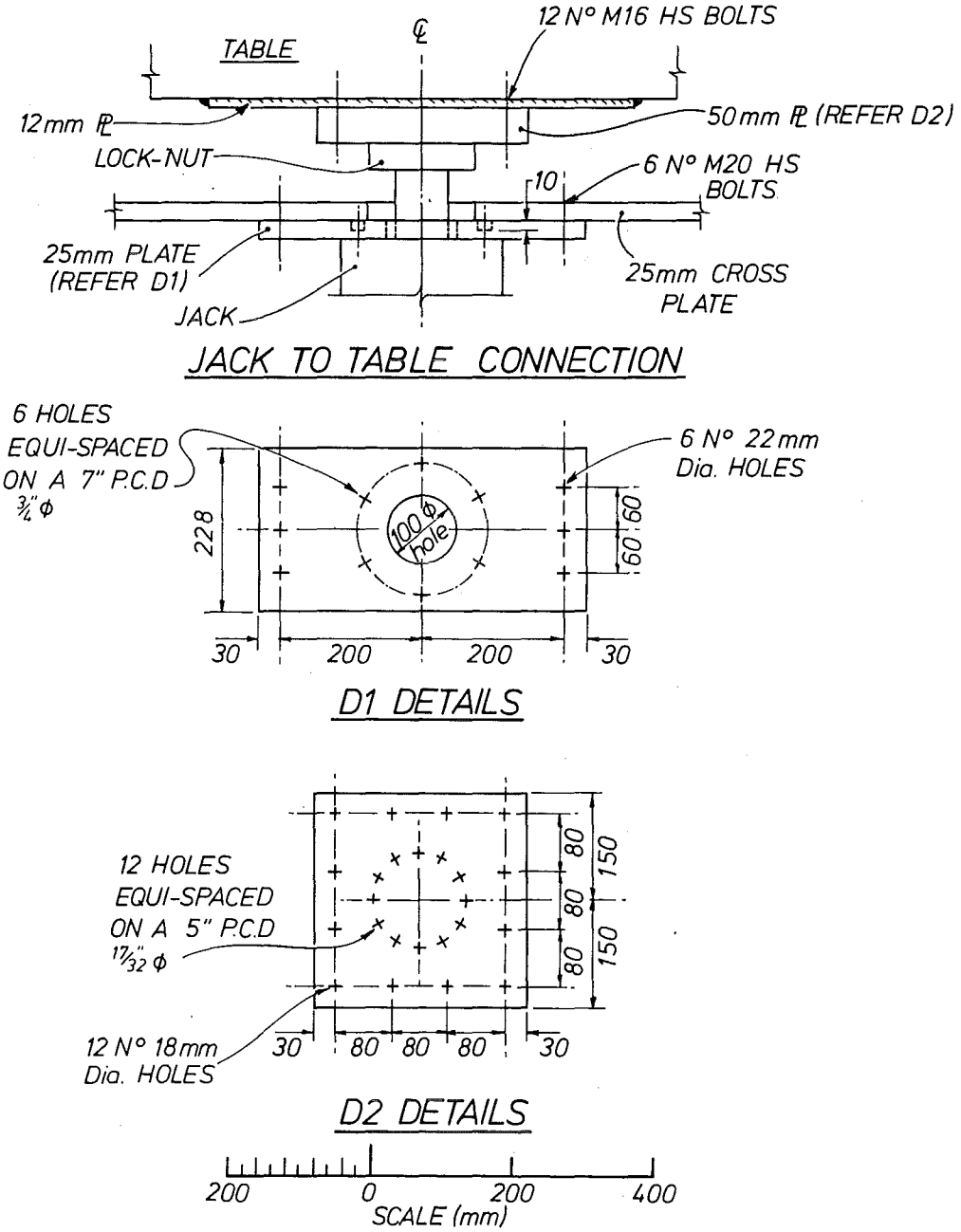

Fig. A8 : Details of actuator to table connection

(B) DYNAMIC DATA ACQUISITION SYSTEM

The system utilized a PDP 11/10 computer to control the channel selection and scan rate and a PDP 11/34 computer to store the readings obtained. Two analog to digital converters (A-D converters) on the PDP 11/10 read the electrical output of the transducers connected to them and converted the analog signals present at their input to digital number. One of the A-D converters had 16 channels (the A-channels), 0-5 volt range and a 10 bit resolution. The readings obtained were in the range of 0-1023 (i.e. $2^{10}-1$). The other A-D converter had 256 channels (the B- channels), a basic range of -2.5 to +2.5 volts and a 12 bit resolution. Similarly, the readings obtained were in the range of 0-4095 (i.e. $2^{12}-1$). Any number of channels could be selected from A- and/or B- channels but the maximum of the total number allowed was 255. Only the range of B- channels could be altered by changing the gains. A range of down to -1.25 to +1.25 mV was possible.

Table A3 lists the gains together with the range, the readability, the precision attainable and the delay time for an accuracy of 0.01 percent based on a full bridge excited at 5 volt dc. The delay time was needed to allow the analog signal to settle before conversion took place. This settling time was especially important for accuracy when higher gains (> 100) were used. During the tests, all transducers except for strain gauges were excited with a 4 volt dc. The strain gauges were excited at 1 volt dc so as to get a wider range of readings without changing the gain setting.

During the tests the scan rate was fixed at 80 scans per second and the scan duration was 3 seconds for single pier testings and 11 seconds for twin-pier testings. The longer time span for the latter was required to cover the duration of earthquake excitation used. Only the B- channels were used in the tests and because of the high scan rate only a maximum of 15-16 channels could be selected for the smooth running of the system. In the case of twin piers, the conversion time (about 24 microseconds originally) had to be lowered so that the same number of channels could be selected.

As part of the system, a data reduction program and a plotting program were written to convert the raw data into useful information and to plot the results if the user so wishes. The plotting program had four options for plotting time-history, strain-history, load-deformation hysteresis and monotonic load-deformation response.

Table A3 : Performance details of B- channels of CEDACS at different gain settings

Gain	Range		Readability	Precision *	Delay time † for 0.01% accuracy (microsecond)
	Volts	με	(με/unit)	(LSB)	
1	-2.5 to 2.5	-1×10^{6} to 1×10^{6}	488	1	< 300
100	-0.025 to 0.025	-10×10^{3} to 10×10^{3}	4.88	1	500
500	-0.005 to 0.005	-2×10^{3} to 2×10^{3}	0.977	1	800
1000	-2.5×10^{-3} to 2.5×10^{-3}	-1×10^{3} to 1×10^{3}	0.488	2	1000
2000	-1.25×10^{-3} to 1.25×10^{-3}	-0.5×10^{3} to 0.5×10^{3}	0.244	4	2000

* The precision can be no better than 1 LSB (least significant bit)

1 LSB = 1 unit; 2 LSB = 3 units and 4 LSB = 15 units

† Delay time is necessary to allow the analogue signals to settle before actual conversion takes place. It may be shorter if lesser accuracy is acceptable.